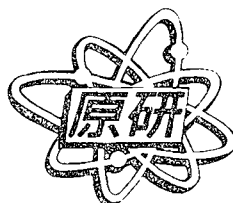


JAERI-Conf  
2003-006



JP0350310



PROCEEDINGS OF THE 2002 SYMPOSIUM  
ON NUCLEAR DATA  
NOVEMBER 21-22, 2002, JAERI, TOKAI, JAPAN

June 2003

(Eds.) Takaaki OHSAWA\* and Tokio FUKAHORI

日本原子力研究所  
Japan Atomic Energy Research Institute

本レポートは、日本原子力研究所が不定期に公刊している研究報告書です。

入手の問合わせは、日本原子力研究所研究情報部研究情報課（〒319-1195 茨城県那珂郡東海村）あて、お申し越してください。なお、このほかに財団法人原子力弘済会資料センター（〒319-1195 茨城県那珂郡東海村日本原子力研究所内）で複写による実費頒布をおこなっております。

This report is issued irregularly.

Inquiries about availability of the reports should be addressed to Research Information Division, Department of Intellectual Resources, Japan Atomic Energy Research Institute, Tokai-mura, Naka-gun, Ibaraki-ken, 319-1195, Japan.

© Japan Atomic Energy Research Institute, 2003

編集兼発行 日本原子力研究所

Proceedings of the 2002 Symposium on Nuclear Data  
November 21-22, 2002, JAERI, Tokai, Japan

(Eds.) Takaaki OHSAWA\* and Tokio FUKAHORI

Japanese Nuclear Data Committee  
Tokai Research Establishment  
Japan Atomic Energy Research Institute  
Tokai-mura, Naka-gun, Ibaraki-ken

(Received February 20, 2003)

The 2002 Symposium on Nuclear Data was held at Tokai Research Establishment, Japan Atomic Energy Research Institute (JAERI), on 21st and 22nd of November 2002. Japanese Nuclear Data Committee and Nuclear Data Center, JAERI organized this symposium. In the oral sessions, presented were 18 papers on topics of release of JENDL-3.3, requests from users, status of FP nuclear data, international activities and other subjects. In the poster session, presented were 33 papers concerning experiments, evaluations, benchmark tests and on-line database on nuclear data. Those presented papers are compiled in the proceedings.

Keywords: Nuclear Data, Symposium, Proceedings, Nuclear Reaction, JENDL,  
Experiment, Evaluation, Benchmark Test, Cross Section.

---

\*Kinki University

2002 年核データ研究会報文集  
2002 年 11 月 21 日～22 日，東海研究所，東海村

日本原子力研究所東海研究所

シグマ研究委員会

(編) 大澤 孝明\*・深堀 智生

(2003 年 2 月 20 日受理)

2002 年核データ研究会が、2002 年 11 月 21 日と 22 日の両日、日本原子力研究所東海研究所において開催された。この研究会は、日本原子力研究所のシグマ研究委員会と核データセンターが主催して開いたものである。口頭発表では、JENDL-3.3 の完成、産業界からの要望、FP 核データの現状、国際セッション、その他のトピックスについての 18 件の報告があった。ポスター発表では、33 件の発表があり、それらは、核データの測定、評価や評価済核データのベンチマークテスト、オンラインデータベース等に関するものであった。本報文集は、それらの論文をまとめたものである。

---

東海研究所：〒319-1195 茨城県那珂郡東海村白方白根 2-4

\* 近畿大学



**Program Committee**

Takaaki OHSAWA(Chairman)	Kinki University
Satoshi CHIBA	Japan Atomic Energy Research Institute
Tokio FUKAHORI	Japan Atomic Energy Research Institute
Tetsuo IGUCHI	Nagoya University
Makoto ISHIKAWA	Japan Nuclear Cycle Development Institute
Osamu IWAMOTO	Japan Atomic Energy Research Institute
Tomohiko IWASAKI	Tohoku University
Shigeaki OKAJIMA	Japan Atomic Energy Research Institute
Yoshihisa TAHARA	Mitsubishi Heavy Industries, Ltd.

**プログラム委員会**

大澤	孝明 (委員長)	近畿大学
千葉	敏	日本原子力研究所
深堀	智生	日本原子力研究所
井口	哲夫	名古屋大学
石川	眞	核燃料サイクル開発機構
岩本	修	日本原子力研究所
岩崎	智彦	東北大学
岡嶋	成晃	日本原子力研究所
田原	義壽	三菱重工業 (株)

This is a blank page.

## Contents

1. Introduction .....	1
2. Papers Presented at Oral Sessions .....	7
2.1 Outline of Evaluations for JENDL-3.3 .....	9
K. Shibata	
2.2 Integral Test of JENDL-3.3 for Thermal Reactors .....	15
K. Okumura, T. Mori	
2.3 Integral Test of JENDL-3.3 for Fast Reactors .....	22
G. Chiba	
2.4 Integral Test of JENDL-3.3 with Shielding Benchmarks .....	28
N. Yamano	
2.5 Nuclear Mass Formulas and its Application for Astrophysics .....	34
H. Koura	
2.6 Fragment Mass Distribution of the $^{239}\text{Pu}(\text{d,pf})$ Reaction at the Super-deformed $\beta$ -vibrational Resonance .....	40
K. Nishio, H. Ikezoe, Y. Nagame, S. Mitsuoka, I. Nishinaka, L. Duan, K. Satou, M. Asai, H. Haba, K. Tsukada, N. Shinohara, S. Ichikawa, T. Ohsawa	
2.7 Requests on Domestic Nuclear Data Library from BWR Design .....	46
H. Maruyama	
2.8 Proposals for Nuclear Data Activities from PWR Core Design .....	51
Y. Tahara	
2.9 Requests on Nuclear Data in the Backend Field through PIE Analysis .....	54
Y. Ando, Y. Ohkawachi	
2.10 Analysis of MISTRAL Experiments with JENDL-3.2 .....	61
T. Umamo, T. Yamamoto, R. Kanda, M. Sasagawa, T. Kan, K. Ishii, Y. Ando, M. Tatsumi	
2.11 Request from Radiation Damage Evaluation in Materials .....	66
K. Fukuya, I. Kimura	
2.12 Calculation of $\text{n}+^{232}\text{Th}$ Reaction Cross Sections in the $E_n \leq 20$ MeV Energy Range .....	72
Y. Han	
2.13 Progress in the KAERI High Energy Nuclear Data Library: Proton-induced Neutron Emission Spectra .....	86
Y.-O. Lee, J. Chang	
2.14 Benchmark Tests of JENDL-3.3 and ENDF/B-VI Data Files using Monte	

Carlo Simulation of the 3MW TRIGA MARK II Research Reactor .....	92
M.Q. Huda, T.K. Chakroborty, M.J.H. Khan, M.M. Sarker	
2.15 History of FP Nuclear Data Evaluation .....	100
M. Kawai	
2.16 Recent Experimental Data .....	113
M. Igashira, K. Ohgama	
2.17 Present Status and Plans of JENDL FP Data Evaluation Project .....	119
T. Kawano, FP Nuclear Data Evaluation Working Group	
3. Papers Presented at Poster Sessions .....	125
3.1 Neutron Capture Cross Section Measurement of Pr in the Energy Region from 0.003 eV to 140 keV by Linac Time-of-flight Method .....	127
Samyol Lee, S. Yamamoto, K. Kobayashi, Jungran Yoon, Taeik Ro	
3.2 Measurement of Cross Sections of the $^{210}\text{Po}$ Production Reaction by keV-neutron Capture of $^{209}\text{Bi}$ .....	133
K. Saito, M. Igashira, T. Ohsaki, T. Obara, H. Sekimoto	
3.3 Measurements of Activation Cross Sections Producing Short-lived Nuclei in the Energy Range of 2-3 MeV with Pulsed Neutron Beam .....	138
T. Shimizu, H. Yamamoto, M. Kasaishi, I. Miyazaki, M. Shibata, K. Kawade, J. Hori, T. Nishitani	
3.4 Measurement of (n,2n) Reaction Cross Section Using a 14MeV Pencil Beam Source .....	144
M. Mitsuda, R. Tanaka, Y. Yamamoto, N. Mori, I. Murata, A. Takahashi, K. Ochiai, T. Nishitani	
3.5 Neutron Production by 0.8 and 1.5 GeV Protons on Fe and Pb Targets at the Most-forward Region .....	150
D. Satoh, N. Shigyo, K. Ishibashi, Y. Takayama, S. Ishimoto, Y. Iwamoto, H. Tenzou, T. Nakamoto, M. Numajiri, S. Meigo	
3.6 The Measurement of Energy Spectra for $^9\text{Be}(p,p'\alpha)$ Reaction at 392 MeV .....	156
T. Kin, F. Saiho, S. Hohara, K. Ikeda, F. Kondo, I. Fukuchi, K. Ichikawa, G. Wakabayashi, Y. Uozumi, N. Ikeda, M. Matoba, N. Koori	
3.7 Measurements of Differential Thick Target Yield for C, Al, Ta, W, $\text{Pb}(p,xn)$ Reactions at 50 and 70 MeV .....	160
N. Kawata, M. Baba, T. Aoki, M. Hagiwara, T. Itoga, N. Hirabayashi, S. Yonai, T. Nakamura	
3.8 Measurements of Neutron Emission Spectra and $^7\text{Be}$ Production in $\text{Li}(d,n)$ and $\text{Be}(d,n)$ Reactions for 25 and 40 MeV Deuterons .....	166

	M. Hagiwara, M. Baba, T. Aoki, N. Kawata, N. Hirabayashi, T. Itoga	
3.9	Method of Measurement of Cross Sections of Heavy Nuclei Fission Induced by Intermediate Energy Protons .....	172
	A. Kotov, A. Chtchetkovski, O. Fedorov, T. Fukahori, Y. Gavrikov, Y. Chestnov, V. Poliakov, L. Vaishnene, V. Vovchenko	
3.10	$^{100}\text{Mo}(p,d)^{99}\text{Mo}$ Reaction at 50 MeV and Direct Reaction Analysis .....	178
	F. Aramaki, Syafarudin, G. Wakabayashi, Y. Uozumi, N. Ikeda, M. Matoba, T. Sakae, N. Koori	
3.11	Evaluation of Cross Sections for Nucleons up to 3 GeV on $^{12}\text{C}$ .....	183
	Y. Watanabe, O. Iwamoto, T. Fukahori, S. Chiba, E.Sh. Sukhovitskiĭ	
3.12	Brief Note on the Statistical Calculation of Final Continuum Reaction Cross Sections of Light Nuclides .....	189
	T. Murata	
3.13	Evaluation of Cross Sections of $^{63}\text{Cu}$ and $^{65}\text{Cu}$ for JENDL High Energy File... ..	195
	N. Yamano, T. Fukahori, S. Chiba	
3.14	Nuclear Data Evaluations of Neutron and Proton Incidence on Zr, Nb, and W for Energy up to 200 MeV .....	201
	S. Kunieda, N. Shigyo, K. Ishibashi	
3.15	Thick Target Benchmark Test for the Code Used in the Design of High Intensity Proton Accelerator Project .....	207
	S. Meigo, M. Harada	
3.16	Comment to VITAMIN-B6 .....	213
	C. Konno, H. Nakashima, R.A. Lillie	
3.17	NMLIB .....	219
	C. Konno, Y. Ikeda, K. Niita	
3.18	Neutron Optical Potentials in Unstable Nuclei and the Equation of State of Asymmetric Nuclear Matter .....	225
	K. Oyamatsu, K. Iida	
3.19	Light Output Response of GSO(Ce) Scintillator to Deuterons .....	232
	F. Saiho, T. Kin, S. Hohara, K. Ikeda, F. Kondo, K. Ichikawa, I. Fukuchi, Y. Uozumi, N. Ikeda, G. Wakabayashi, M. Matoba	
3.20	The Development of Melamine-D for the Precise Measurement of Detection Efficiencies of High Energy $\gamma$ -rays .....	237
	S. Nakamura, H. Harada, H. Takayama, K. Kawade	
3.21	Measurement of the Westcott Conventionality Thermal Neutron Flux and Suchlike at Irradiation Facilities of the KUR .....	241
	H. Chatani	

3.22	Effects of Nucleon Correlations in $(p,d)$ , $(e,e'p)$ and $(\gamma,p)$ Reactions .....	247
	M.K. Gaidarov, K.A. Pavlova, A.N. Antonov, M.V. Stoitsov, S.S. Dimitrova, M.V. Ivanov, C. Giusti, S.E. Massen, Ch.C. Moustakidis	
3.23	Energy Dependence of Microscopic Corrections for Nuclear Droplet Model ...	253
	H. Nakamura	
3.24	Recurrence of the Excited States of Nuclei and Time Coherency of the de Broglie Wave in $^{16}\text{O}+n$ Resonances .....	259
	M. Ohkubo	
3.25	Analysis of Cosmic Ray Neutron-induced Single-event Phenomena .....	265
	Y. Tsukamoto, Y. Watanabe, H. Nakashima	
3.26	Soft Errors of Semiconductors Caused by Secondary Cosmic-ray Neutrons .....	271
	H. Sawamura, T. Iguchi, T. Handa	
3.27	PRA (Probabilistic Risk Assessment) for Spent Fuel Decommissioning of the Fugen Nuclear Power Station .....	277
	D.T. Sony Tjahyani, Y. Iguchi, S. Kiyota	
3.28	Radiation Damage Calculation by NPRIM Computer Code with JENDL3.3 ....	283
	S. Shimakawa, N. Sekimura, N. Nojiri	
3.29	MCNP and MATXS Cross Section Libraries Based on JENDL-3.3 .....	289
	K. Kosako, C. Konno, T. Fukahori, K. Shibata	
3.30	JOYO MK-II Core Characteristics Database - Upgrade to JENDL-3.2 - .....	294
	Y. Ohkawachi, S. Maeda, T. Sekine	
3.31	Measurement of Total Cross-sections of Natural Dy, In and Cu at the Pohang Neutron Facility .....	300
	G. Kim, R. Machrafi, H. Ahmed, D. Son, Vadim Skoy, Y.S. Lee, H. Kang, M.-H. Cho, I.S. Ko, N. Won	
3.32	Proposal of Experimental Facilities for Studies of Nuclear Data and Radiation Engineering in the Intense Proton Accelerator Project .....	310
	M. Baba, M. Igashira, Y. Nagai, K. Ishibashi	
Appendix: Participant List .....		317

## 目 次

1. はじめに .....	1
2. 口頭発表論文 .....	7
2.1 JENDL-3.3評価の概要 .....	9
柴田 恵一	
2.2 熱中性子炉に対するJENDL-3.3の積分テスト .....	15
奥村 啓介、森 貴正	
2.3 JENDL-3.3の高速炉での積分テスト .....	22
千葉 豪	
2.4 遮蔽に対するJENDL-3.3の積分テスト .....	28
山野 直樹	
2.5 原子核質量公式とその周辺（天体物理への応用） .....	34
小浦 寛之	
2.6 超変形 $\beta$ 振動共鳴における $^{239}\text{Pu}(\text{d},\text{pf})$ 反応からの核分裂片質量数分布 .....	40
西尾 勝久、池添 博、永目 諭一郎、光岡 真一、西中 一郎、 L. Duan、佐藤 健一郎、浅井 雅人、羽場 宏光、塚田 和明、 篠原 伸夫、市川 進一、大澤 孝明	
2.7 BWR設計からの国産核データライブラリーに対する要望 .....	46
丸山 博見	
2.8 PWR炉心設計からの核データ整備に対する提案 .....	51
田原 義壽	
2.9 照射後解析から見たバックエンドからの核データに対する要望 .....	54
安藤 良平、大川内 靖	
2.10 JENDL-3.2を用いたMISTRAL実験解析 .....	61
馬野 琢也、山本 徹、神田 僚司、笹川 勝、菅 太郎、 石井 一弥、安藤 良平、巽 雅洋	
2.11 材料損傷評価の観点からの要望 .....	66
福谷 耕司、木村 逸郎	
2.12 20MeV以下における $\text{n}+^{232}\text{Th}$ 反応断面積の計算 .....	72
Y. Han	
2.13 KAERI 高エネルギー核データライブラリーの進展 一陽子入射による放出中性子スペクトルー .....	86
Y.-O. Lee、J. Chang	
2.14 3MW TRIGA MARK II研究炉のモンテカルロシミュレーションを 用いたJENDL -3.3及びENDF/B-VIのベンチマークテスト .....	92

M.Q. Huda, T.K. Chakrobortty, M.J.H. Khan, M.M. Sarker	
2.15	FP核データ評価の歴史 ..... 100 川合 將義
2.16	最近の実験データ ..... 113 井頭 政之、大釜 和也
2.17	JENDL FP核データ評価計画の現状と予定 ..... 119 河野 俊彦、FP核データ評価WG
3.	ポスター発表論文 ..... 125
3.1	飛行時間分析法を用いた 0.003eV~140keV 領域における Pr の中性 子捕獲断面積の測定 ..... 127 李三烈、山本 修二、小林 捷平、Jungran Yoon、Taeik Ro
3.2	$^{209}\text{Bi}$ のkeV中性子捕獲反応による $^{210}\text{Po}$ 生成断面積の測定 ..... 133 齋藤 浩介、井頭 政之、大崎 敏郎、小原 徹、関本 博
3.3	パルス中性子ビームを用いた2~3MeV領域における短寿命核種生 成断面積の測定 ..... 138 清水 俊明、山本 弘法、笠石 昌史、宮崎 格、柴田 理尋、 河出 清、堀 順一、西谷 健夫
3.4	ビーム状14 MeV中性子を用いた(n,2n)反応断面積の測定 ..... 144 満田 幹之、田中 良平、山本 康史、森 匡教、村田 勲、 高橋 亮人、落合 謙太郎、西谷 健夫
3.5	0.8GeVと1.5GeV陽子入射反応によるFeとPbからの最前方への中性 子生成 ..... 150 佐藤 大樹、執行 信寛、石橋 健二、高山 尉志、石本 俊輔、 岩元 洋介、天造 秀樹、中本 達志、沼尻 正晴、明午 伸一郎
3.6	392MeVにおける $^9\text{Be}(\text{p},\text{p}'\text{x})$ 反応のエネルギースペクトルの測定 ..... 156 金 政浩、才保 文伸、芳原 新也、池田 克彦、近藤 史哲、 福地 郁生、市川 聖久、若林 源一郎、魚住 裕介、池田 伸夫、 的場 優、桑折 範彦
3.7	厚いターゲットを用いた50及び70MeVにおけるC, Al, Ta, W, Pbの (p,xn)反応による生成中性子の測定 ..... 160 川田 直輝、馬場 護、青木 伯夫、萩原 雅之、糸賀 俊朗、 平林 直哉、米内 俊祐、中村 尚司
3.8	25MeVと40MeV重陽子を用いたLi(d,n)及びBe(d,n)反応による中性 子スペクトルと $^7\text{Be}$ 生成量の測定 ..... 166 萩原 雅之、馬場 護、青木 伯夫、川田 直輝、平林 直哉、 糸賀 俊朗



3.9	重核の中高エネルギー陽子入射核分裂断面積測定法 .....	172
	A. Kotov, A. Chtchetkovski, O. Fedorov, 深堀 智生, Y. Gavrikov, Y. Chestnov, V. Poliakov, L. Vaishnene, V. Vovchenko	
3.10	50MeVにおける $^{100}\text{Mo}(\text{p},\text{d})^{99}\text{Mo}$ 反応と直接反応モデルによる解析 .....	178
	荒巻 富士夫, Syafarudin, 若林 源一郎, 魚住 裕介, 池田 伸夫, 的場 優, 榮 武二, 桑折 範彦	
3.11	3GeVまでの核子に対する $^{12}\text{C}$ の核データ評価 .....	183
	渡辺 幸信, 岩本 修, 深堀 智生, 千葉 敏, E.Sh. Sukhovitskii	
3.12	軽核の連続領域への核反応断面積の統計モデル計算に関する考察 .....	189
	村田 徹	
3.13	JENDL高エネルギーファイルのためのCu-63,65の評価 .....	195
	山野 直樹, 深堀 智生, 千葉 敏	
3.14	200 MeVまでのZr, Nb, Wに対する中性子及び陽子入射の核データ 評価 .....	201
	国枝 賢, 執行 信寛, 石橋 健二	
3.15	大強度陽子加速器計画の設計に用いられるコードに対する厚いタ ーゲットのベンチマークテスト .....	207
	明午 伸一郎, 原田 正英	
3.16	VITAMIN-B6に対するコメント .....	213
	今野 力, 中島 宏, R.A. Lillie	
3.17	NMLIB .....	219
	今野 力, 池田 裕二郎, 仁井田 浩二	
3.18	不安定核の中性子光学ポテンシャルと非対称核物質の状態方程式 .....	225
	親松 和浩, 飯田 圭	
3.19	重陽子に対するGSO(Ce)シンチレータの発光応答 .....	232
	才保 文伸, 金 政浩, 芳原 新也, 池田 克彦, 近藤 史哲, 市川 聖久, 福地 郁生, 魚住 裕介, 池田 伸夫, 若林 源一郎, 的場 優	
3.20	高エネルギーガンマ線検出効率の高精度測定のための重水素置換 メラミン開発 .....	237
	中村 詔司, 原田 秀郎, 高山 寛和, 河出 清	
3.21	KUR照射設備におけるWestcott流熱中性子束などの測定 .....	241
	茶谷 浩	
3.22	(p,d), (e,e'p)及び( $\gamma$ ,p)反応における核子相関の影響 .....	247
	M.K. Gaidarov, K.A. Pavlova, A.N. Antonov, M.V. Stoitsov, S.S. Dimitrova, M.V. Ivanov, C. Giusti, S.E. Massen, Ch.C. Moustakidis	
3.23	原子核液滴模型における微視的補正項のエネルギー依存性 .....	253

中村 久	
3.24 核励起状態の回帰と $^{16}\text{O}+n$ 共鳴に於けるドブロイ波との時間コヒーレンス .....	259
大久保 牧夫	
3.25 宇宙線中性子誘起シングルイベント現象の解析 .....	265
塚本 泰幸、渡辺 幸信、中島 秀紀	
3.26 2次宇宙線中性子による半導体のソフトエラー .....	271
澤村 英範、井口 哲夫、半田 隆信	
3.27 ふげん原子力発電所の使用済み燃料解体に対する確率論的リスク評価 ..	277
D.T. Sony Tjahyani、井口 幸弘、清田 史功	
3.28 NPRIMコードによるJENDL3.3を用いた照射損傷計算.....	283
島川 聡司、関村 直人、野尻 直喜	
3.29 JENDL-3.3に基づくMCNPとMATXS断面積ライブラリー .....	289
小迫 和明、今野 力、深堀 智生、柴田 恵一	
3.30 「常陽」MK-II炉心特性データベース –JENDL-3.2への改訂– .....	294
大川内 靖、前田 茂貴、関根 隆	
3.31 Pohang Neutron FacilityにおけるDy, In, Cuの全断面積の測定 .....	300
G. Kim、R. Machrafi、H. Ahmed、D. Son、Vadim Skoy、Y.S. Lee、 H. Kang、M.-H. Cho、I.S. Ko、N. Won	
3.32 大強度陽子加速器プロジェクトにおける核データと放射線工学研究のための実験設備に関する提案 .....	310
馬場 護、井頭 政之、永井 泰樹、石橋 健二	
付録： 参加者リスト .....	317

# 1. Introduction

The 2002 symposium on nuclear data was held at Tokai Research Establishment, Japan Atomic Energy Research Institute (JAERI), on 21st and 22nd of November 2002, with about 150 participants. Japanese Nuclear Data Committee and Nuclear Data Center, JAERI organized the symposium.

The program of the symposium is listed below. In the oral sessions, presented were 18 papers on topics of release of JENDL-3.3, requests from users, status of FP nuclear data, international activities and other subjects. In the poster session, presented were 33 papers concerning experiments, evaluations, benchmark tests and on-line database on nuclear data. Those presented papers are compiled in the proceedings.

## Program of 2002 Symposium on Nuclear Data

**Nov. 21 (Thu.)**

10:00-10:05

1. Opening Address

H. Nakajima (JAERI)

10:10-11:50

2. Release of JENDL-3.3

Chairman: T. Yoshida (Musashi Tech.)

2.1 Outline of Evaluations for JENDL-3.3 [25+5]

K. Shibata (JAERI)

2.2 Integral Test of JENDL-3.3 in Thermal Reactors [30+10]

K. Okumura (JAERI)

2.3 Integral Test of JENDL-3.3 for Fast Reactors [30+10]

G. Chiba (JNC)

12:00-12:10    Taking Photo

12:10-13:00    Lunch

13:00-13:45

2. Release of JENDL-3.3

Chairman: T. Yoshida (Musashi Tech.)

2.4 Integral Test of JENDL-3.3 with Shielding Benchmarks [30+10]

N. Yamano (SAE)

13:45-16:00

3. Poster Presentation (Odd Numbers)

16:00-17:55

4. Topics Chairman: K. Oyamatsu (Aichi Shukutoku U.)
- 4.1 New Development of Neutrino Physics [40+10] K. Niwa (NagoyaU.)
- 4.2 Nuclear Mass Formula and its Application for Astrophysics [30+10]  
H. Koura (RIKEN)
- 4.3 Fragment Mass Distribution of  $^{239}\text{Pu}(\text{d},\text{pf})$  Reaction at the Super-deformed  
 $\beta$ -vibrational Resonance [20+5] K. Nishio (JAERI)

18:20-20:00 Reception (Akogi-ga-ura Club)

Nov. 22 (Fri.)

9:30-12:00

5. Request about Domestic Nuclear Data Library from the Industrial Circles  
Chairman: T. Matsumura (CRIEPI)
- 5.1 Requests on Domestic Nuclear Data Library from BWR Design [15+10]  
H. Maruyama (GNF-J)
- 5.2 Proposals for Nuclear Data Activities from PWR Core Design [15+10]  
Y. Tahara (MHI)
- 5.3 Requests on Nuclear Data in the Backend Field through PIE Analysis [15+10]  
Y. Ando (Toshiba)
- 5.4 Analysis of MISTRAL Experiments with JENDL-3.2 [15+10] T. Umamo (NUPEC)
- 5.5 Request from Radiation Damage Evaluation in Materials [15+10]  
K. Fukuya (INSS)

12:00-13:00 Lunch

13:00-14:00

6. Poster Presentation (Even Numbers)

14:00-15:00

7. International Session Chairman: T. Fukahori (JAERI)
- 7.1 Calculation and Analysis of  $n+^{232}\text{Th}$  Reaction Cross Sections [15+5]  
Y. Han (CIAE)
- 7.2 Progress in the KAERI High Energy Nuclear Data Library -  
Proton-induced Neutron Emission Spectra [15+5] Y.-O. Lee (KAERI)
- 7.3 Benchmark Tests of JENDL-3.3 and ENDF/B-VI Data Files using Monte Carlo

Simulation of the 3MW TRIGA MARK II Research Reactor [15+5]

M.Q. Huda (INST)

15:00-15:15 Coffee Break

15:15-16:25

8. Present Status and Future of Evaluation of JENDL FP Nuclear Data

Chairman: K. Kobayashi (KUR)

8.1 History of FP Nuclear Data Evaluation [15+5]

M. Kawai (KEK)

8.2 Recent Experimental Data [20+5]

M. Igashira (TIT)

8.3 Present Status and Plans of JENDL FP Data Evaluation Project [20+5]

T. Kawano (Kyushu U.)

16:25-16:30

9. Poster Award and Closing Address

T. Ohsawa (Kinki U.)

**Poster Presentations**

Nov. 21 (Thu.) 13:45-16:00 (Odd Numbers)

Nov. 21 (Fri.) 13:00-14:00 (Even Numbers)

P.1 Neutron Capture Cross Section Measurement of Pr in the Energy Region  
from 0.003 eV to 140 keV by Linac Time-of-Flight Method

K. Kobayashi (KUR)

P.2 Measurement of Cross Sections of the  $^{210}\text{Po}$  Production Reaction by  
keV-Neutron Capture of  $^{209}\text{Bi}$

K. Saito (TIT)

P.3 Measurement of Activation Cross Sections Producing Short-lived Nuclei  
in the Energy Range of 2-3 MeV with Pulsed Neutron Beam

T. Shimizu (Nagoya U.)

P.4 Measurement of (n,2n) Reaction Cross Section Using a 14MeV Pencil Beam Source

M. Mitsuda (Osaka U.)

P.5 Neutron Production by 0.8 and 1.5 GeV Protons on Fe and Pb Targets at  
the Most-Forward Region

N. Shigyo (Kyushu U.)

P.6 The Measurement of Energy Spectra for  $^9\text{Be}(p,p'x)$  Reaction

T. Kin (Kyushu U.)

P.7 Measurements of Differential Thick Target Yield for C, Al, Ta, W,  
Pb(p,n) Reactions at 50 and 70 MeV

N. Kawata (Tohoku U.)

- P.8 Measurements of Neutron Emission Spectra and  $^7\text{Be}$  Production in  $\text{Li(d,n)}$  and  $\text{Be(d,n)}$  Reactions for 25 and 40 MeV Deuterons M. Hagiwara (Tohoku U.)
- P.9 Measurements of Proton Induced Fission Cross Sections for  $^{\text{nat}}\text{Pb}$ ,  $^{209}\text{Bi}$ ,  $^{235}\text{U}$  and  $^{238}\text{U}$  in the Incident Energy Range 200-1000 MeV T. Fukahori (JAERI)
- P.10  $^{100}\text{Mo(p,d)}^{99}\text{Mo}$  Reaction at 50MeV and Direct Reaction Analysis F. Aramaki (KIIS)
- P.11 Evaluation of Cross Sections for Nucleons up to 3 GeV on  $^{12}\text{C}$  Y. Watanabe (Kyushu U.)
- P.12 Brief Note on the Statistical Calculation of Final Continuum Reaction Cross Sections of Light Nuclides T. Murata (Aitel)
- P.13 Evaluation of Cross Sections of  $^{63}\text{Cu}$  and  $^{65}\text{Cu}$  for JENDL High Energy File N.Yamano (SAE)
- P.14 Nuclear Data Evaluations of Neutron and Proton Incidence on Zr, Nb, and W for Energy up to 200 MeV N. Shigyo (Kyushu U.)
- P.15 Thick Target Benchmark Test for the Code Used in the Design of High Intensity Proton Accelerator Project S. Meigo (JAERI)
- P.16 Comment to VITAMIN-B6 C. Konno (JAERI)
- P.17 NMLIB C. Konno (JAERI)
- P.18 Neutron Optical Potentials in Unstable Nuclei and the Equation of State of Asymmetric Nuclear Matter K. Oyamatsu (Aichi Shukutoku U.)
- P.20 Light Output Response of GSO(Ce) Scintillator to Deuterons F. Saiho (Kyushu U.)
- P.21 The Development of Melamine-D for the Precise Measurement of Detection Efficiencies of High Energy  $\gamma$ -rays S. Nakamura (JNC)
- P.22 Measurement of the Westcott Conventionality Thermal Neutron Flux and Suchlike at Some Irradiation Facilities of the KUR H.Chatani (KUR)
- P.23 Effects of Nucleon Correlations in  $(p,d)$ ,  $(e,e'p)$  and  $(\gamma,p)$  Reactions M.K. Gaidarov (Kyushu U.)
- P.24 Energy Dependence of Microscopic Corrections for Nuclear Droplet Model H. Nakamura (--)
- P.25 Recurrence of the Excited States of Nuclei and Time Coherence of the de Broglie wave in O-16 Resonances M. Ohkubo (--)
- P.26 Web-based Editor for Nuclear Reaction Data N. Otuka (Hokkaido U.)
- P.27 Analysis of Cosmic Ray Neutron-induced Single-event Phenomena Y. Tsukamoto (Kyushu U.)
- P.28 Soft Errors of Semiconductors Caused by Secondary Cosmic-ray Neutrons H. Sawamura (Nagoya U.)

- P.29 PRA (Probabilistic Risk Assessment) for Spent Fuel Pool During  
Decommissioning of the Fugen Nuclear Power Station D.T.S. Tjahyani (BATAN)
- P.30 Radiation Damage Calculation by NPRIM Computer Code with JENDL3.3  
S. Shimakawa (JAERI)
- P.31 MCNP and MATXS Cross Section Libraries Based on JENDL-3.3  
K. Kosako (SAE)
- P.32 JOYO MK-II Core Characteristics Database - Update to JENDL-3.2 -  
Y. Ohkawachi (JNC)
- P.33 Measurement of Total Cross Sections of Natural Dy, In and Cu  
at Pohang Neutron Facility G.N. Kim (Kyungpook National U.)
- P.34 Proposal of Experimental Facilities for Studies of Nuclear Data and Radiation  
Engineering in the Intense Proton Accelerator Project M. Baba (Tohoku U.)

This is a blank page.



## **2. Papers Presented at Oral Sessions**

This is a blank page.



## 2.1 Outline of Evaluations for JENDL-3.3

Keiichi SHIBATA

Nuclear Data Center, Japan Atomic Energy Research Institute

Tokai-mura, Naka-gun, Ibaraki-ken 319-1195

e-mail: shibata@ndc.tokai.jaeri.go.jp

Evaluation for JENDL-3.3 was performed by considering the accumulated feedback information and various benchmark tests of the previous library JENDL-3.2. The major problems of JENDL-3.2 were solved with the new library. This paper describes what was done for JENDL-3.3.

### 1. Introduction

The JENDL-3.2 data [1] have been used in various application fields since the library was released in 1994. However, some drawbacks of the library were pointed out by comparing with differential and integral measurements. The evaluation work for JENDL-3.3 started in 1997 in order to remove the drawbacks. The compilation of the new library was finished in March 2002, and then it was officially released in May 2002 as JENDL-3.3, which provides the neutron-induced reaction data for 337 nuclides in the incident energy region from  $10^{-5}$  eV to 20 MeV.

This paper briefly describes the data for light & medium-heavy nuclides, heavy nuclides, and minor actinides, together with covariances.

### 2. Summary of the Problems in JENDL-3.2

The major problems of JENDL-3.2 are summarized as follows:

- (1) There exists a large difference in the criticalities of light water reactors between the JENDL-3.1 [2] and -3.2 calculations. The JENDL-3.2 values are by 0.3-1.1% larger than those of JENDL-3.1 for thermal reactors.
- (2) It was found that the JENDL-3.2 calculations yield by 0.7-1.3% larger criticalities for fast cores which contain  $^{233}\text{U}$ .
- (3) Energy distributions of secondary neutrons were found to be incorrect for several heavy nuclei.
- (4) There is inconsistency between elemental and isotopic data for medium-heavy nuclides.
- (5) In the MeV region, capture cross sections of many nuclei decrease rapidly with incident

energy, which is not likely to occur.

- (6) Covariances are needed for several important nuclei.

### 3. Evaluation

#### 3.1 Light and Medium-heavy Nuclide Data

##### (1) Resolved Resonance Parameters

Resolved resonance parameters were revised for V,  $^{46,48,49,50}\text{Ti}$ ,  $^{50,52,53,54}\text{Cr}$ ,  $^{54,56}\text{Fe}$ ,  $^{58}\text{Ni}$ ,  $^{59}\text{Co}$ ,  $^{99}\text{Ru}$ , and  $^{186}\text{W}$  by examining experimental data. The resolved resonance parameters of  $^{56}\text{Fe}$  were taken from JEF-2.2 [3] with the Reich-Moore formalism. As for  $^{186}\text{W}$ , it was pointed out that the capture resonance integral of JENDL-3.2 (347.0 b) is too small as compared with the value of  $485.0 \pm 15.0$  b recommended by Mughabghab [4]. In the JENDL-3.3 evaluation, the parameters at the 18.8-eV resonance were modified and a negative resonance was deleted. As a result, the resonance integral led to a larger value of 528 b, being consistent with a value of  $510.7 \pm 24.3$  b measured by Kobayashi *et al.* [5]

##### (2) Total Cross Sections

Elemental data files were not produced in order to avoid the inconsistency between the elemental and isotopic data seen in JENDL-3.2. However, there are a lot of measured total cross-section data on natural elements in the MeV region. These measurements were taken into account in the present evaluation. In principle, a weighted sum of the evaluated cross section of an isotope should reflect the measured total cross section of the element. For instance, in the MeV region, the total cross sections of  $^{57,58}\text{Fe}$  were obtained from the optical model calculations, while that of  $^{54}\text{Fe}$  was derived from the measurements [6,7]. The total cross section of elemental iron was evaluated on the basis of the experimental data [8-10] in the energy region from 700 keV to 20 MeV. Then, the total cross section of  $^{56}\text{Fe}$  was obtained by subtracting the contributions of  $^{54,57,58}\text{Fe}$  from the cross section of elemental iron.

##### (3) Reaction Cross Sections

The cross sections of  $^{162,164,166,167,168,170}\text{Er}$  were evaluated mainly by nuclear model calculations. The optical model parameters were obtained so as to reproduce the measured total cross sections of elemental erbium. The capture cross sections of  $^{166,167,168,170}\text{Er}$  measured by the Tokyo Institute of Technology group [11-13] were taken into account in the present evaluation.

##### (4) Gamma-ray Production and Double-differential Neutron Emission Cross Sections

In JENDL-3.2, gamma-ray production data were included for 66 nuclides. However, no isotopic data were available for 9 elements: Mg, S, K, Ti, Cr, Mo, Cd, Eu, and W. The gamma-ray production cross sections and emitted gamma-ray spectra for the isotopes of these elements were calculated by using the SINCROS code system [14] for JENDL-3.3.

Double-differential neutron emission cross sections, *i.e.*, angle-dependent neutron

emission spectra, were not contained in JENDL-3.2. In the present work, the double differential cross sections were included for 60 nuclides; most of them were taken from JENDL/F-99 [15].

#### (5) Cross Sections of Light Nuclei

Minor modification was made for the cross sections of  $^{11}\text{B}$ ,  $\text{C}$ ,  $^{14,15}\text{N}$ , and  $^{16}\text{O}$ . According to the preliminary benchmark analyses of the thermal critical assemblies (STACY and TRACY) with uranyl nitrate solution, the  $(n,p)$  cross section of  $^{14}\text{N}$  was found to be too small at the thermal energy. The JENDL-3.3 evaluation adopted Mughabghab's recommendation [16], which led to an improvement of criticality values for the STACY and TRACY cores. As for the  $^{15}\text{N}(n,\gamma)$  reaction that is important for  $s$ -process nucleosynthesis, the  $p$ -wave capture contributes to cross sections predominantly above 10 eV, although the JENDL-3.2 cross sections exhibit an inverse of velocity behavior up to 10 keV. We adopted the cross-section formula obtained by Meissner *et al.* [17] for JENDL-3.3.

### 3.2 Heavy Nuclide Data

#### (1) Resonance Parameters and Prompt Fission Neutron Spectra for $^{235}\text{U}$

The overestimation of  $k_{\text{eff}}$  is the biggest problem concerning JENDL-3.2 when the library is applied to thermal fission reactors. In order to solve this problem, we re-evaluated the resonance parameters of  $^{235}\text{U}$  and the prompt fission neutron spectra from  $^{235}\text{U}$ . The resonance parameters were replaced with those obtained by Leal *et al.* [18]. The fission neutron spectra were re-evaluated by Ohsawa [19] with a multi-modal fission analysis.

#### (2) Simultaneous Evaluation of Fission Cross Sections

Fission cross sections above the resonance region are also important for reactor calculations. We adopted a simultaneous evaluation [20] to obtain the fission cross sections of major actinides above 30 keV. The experimental data on  $^{233}\text{U}$  were included in the present evaluation, while the  $^{233}\text{U}$  data were evaluated separately from the simultaneous evaluation for JENDL-3.2. The fission cross sections of  $^{233}\text{U}$  obtained for JENDL-3.3 are lower than those for JENDL-3.2 in the energy range above several hundred keV.

#### (3) Secondary Neutron Spectra

Secondary neutron spectra for the  $(n,n')$ ,  $(n,2n)$ , and  $(n,3n)$  reactions compiled in JENDL-3.2 have been criticized for a long time. We performed spectrum calculation with the GNASH code [21] and the results were processed with GAMFIL code [22]. With this procedure, the crucial problems concerning the energy distributions of secondary neutrons were obviously solved.

#### (4) Direct/Semi-direct Capture

In the JENDL-3.2 evaluation, the capture cross sections at higher energies were often ignored, because these cross sections became extremely small when the Hauser-Feshbach statistical model was used to calculate them. It is known that the direct/semi-direct (DSD)

capture model should be applied to calculate capture cross sections in this energy region. In the present work, we took account of the DSD contributions.

#### (5) Delayed Neutrons

The number of delayed neutrons per fission for  $^{235}\text{U}$  and  $^{238}\text{U}$  were re-evaluated on the basis of available experimental data.. It was found that the re-evaluated results are consistent with the values obtained by Sakurai and Okajima [23] considering the integral measurements at FCA, TCA, and MASURCA. The delayed neutron spectra were taken from the summation calculation results obtained by Brady and England [24] for six temporal groups.

### 3.3 Minor Actinide Data

#### (1) $^{237}\text{Np}$

The resonance parameters were revised on the basis of the new experimental data obtained at CEA Saclay [25]. As a result, the upper boundary of the resolved resonance region was extended from 130 eV to 500 eV. In the energy range above the resonance region, the total, inelastic scattering, capture and (n,3n) reaction cross sections were replaced with the new evaluation by Ignatyuk *et al.* [26]. The fission cross section was obtained by least-squares fitting to experimental data. The (n,2n) reaction cross section is the same as that given in JENDL-3.2.

#### (2) $^{241}\text{Am}$

The resonance parameters of Maslov *et al.* [27] were modified so as to reproduce slightly larger thermal cross sections. The present evaluation gives a capture cross section of 639.47 b at 0.0253 eV which is 6.6% larger than JENDL-3.2. The fission cross section above 100 keV was obtained by fitting to experimental data. The evaluation of Maslov *et al.* was adopted for the capture, (n,2n), (n,3n) and inelastic scattering cross sections. For the capture cross section, the isomeric ratio was evaluated from experimental data and the GNASH calculations, as seen in Fig. 1.

### 3.4 Covariance Data

The previous library JENDL-3.2 contains covariance data only for  $^{55}\text{Mn}$ , although we were requested to prepare covariances for the nuclides which were required to evaluate the characteristics of fast reactors. In order to meet the needs, covariance data were evaluated for selected nuclides in JENDL-3.2, and they were made available as the JENDL-3.2 Covariance File [28]. These covariance data were obtained from measurements or nuclear model calculations which the evaluated mean data were based on. Most of the covariance data were also adopted in JENDL-3.3 with a slight modification.

The simultaneous evaluation yielded the covariance matrices for the fission cross sections of  $^{233,235,238}\text{U}$  and  $^{239,240,241}\text{Pu}$  in the energy region above several tens of keV. The matrices represent not only the correlation of individual fission cross sections between

different incident energies but also that of a fission cross section with another fission cross section.

In JENDL-3.3, covariances are included for 20 nuclides. The covariances for  $^{48}\text{Ti}$ , V, and  $^{59}\text{Co}$  were newly evaluated for JENDL-3.3.

#### 4. Conclusions

Evaluation and compilation were performed for JENDL-3.3. Only the significant changes from JENDL-3.2 were described in this report, although data for more than a hundred nuclides were revised. The major problems of JENDL-3.2 were solved with the present library.

#### Acknowledgments

This work was performed in cooperation with the Japanese Nuclear Data Committee (JNDC). The author would like to thank all the members of JNDC for the cooperation.

#### References

- [1] T. Nakagawa, *et al.*: J. Nucl. Sci. Technol., **32**, 1259 (1995).
- [2] K. Shibata, *et al.*: JAERI 1319 (1990).
- [3] C. Nordborg, M. Salvatores: Proc. Int. Conf. on Nuclear Data for Science and Technology, Gatlinburg 1994, Vol. 2, p.680 (1994).
- [4] S.F. Mughabghab: "Neutron Cross Sections," Vol. 1, Part B, Academic Press (1984).
- [5] K. Kobayashi, *et al.*: Proc. Conf. Neutron Physics, Kiev 1987, Vol. 4, p. 238 (1988).
- [6] E.M. Cornelis, *et al.*: Proc. Int. Conf. Nuclear Data for Science and Technology, Antwerp 1982, p.135 (1983).
- [7] R.F. Carlton, *et al.*: Bull. Am. Phys. Soc., **30**, 1252 (1985).
- [8] K. Berthold, *et al.*: Proc. Int. Conf. Nuclear Data for Science and Technology, Gatlinburg 1994, Vol. 1, p.218 (1994).
- [9] A.D. Carlson, R.J. Cerbone: Nucl. Sci. Eng., **42**, 28 (1970).
- [10] F.G. Perey, *et al.*: ORNL-4823 (1972).
- [11] A.K.M. Harun-ar-Rashid: Ph.D. Thesis, Tokyo Institute of Technology (2000).
- [12] A.K.M. Harun-ar-Rashid, *et al.*: J. Nucl. Sci. Technol., **37**, 421 (2000).
- [13] M. Igashira: Private communication (2002).
- [14] N. Yamamuro: JAERI-M 90-006 (1990).
- [15] S. Chiba, *et al.*: J. Nucl. Sci. Technol., **39**, 187 (2002).
- [16] S.F. Mughabghab, *et al.*: "Neutron Cross Sections," Vol. 1, Part A, Academic Press (1981).
- [17] J. Meissner, *et al.*: Phys. Rev., **C53**, 977 (1996).

- [18] L.C. Leal, *et al.*: Nucl. Sci. Eng., **131**, 230 (1999).  
 [19] T. Ohsawa: JAERI-Conf 2001-006, p.157 (2001).  
 [20] T. Kawano, *et al.*: J. Nucl. Sci. Technol., **37**, 327 (2000).  
 [21] P.G. Young, E.D. Arthur: LA-6947 (1977).  
 [22] K. Hida: JAERI-M 86-150 (1986) [in Japanese].  
 [23] T. Sakurai, S. Okajima: J. Nucl. Sci. Technol., **39**, 19 (2002).  
 [24] M.C. Brady, T.R. England: Nucl. Sci. Eng., **103**, 129 (1989).  
 [25] V. Gressier, *et al.*: Annals Nucl. Energy, **27**, 1115 (2000).  
 [26] A.V. Ignatyuk, *et al.*: ISTC-304-95 (1997), and private communication (1999).  
 [27] V.M. Maslov, *et al.*: INDC(BLR)-005 (1996).  
 [28] K. Shibata, *et al.*: J. Nucl. Sci. Technol., **Suppl. 2**, 40 (2002).

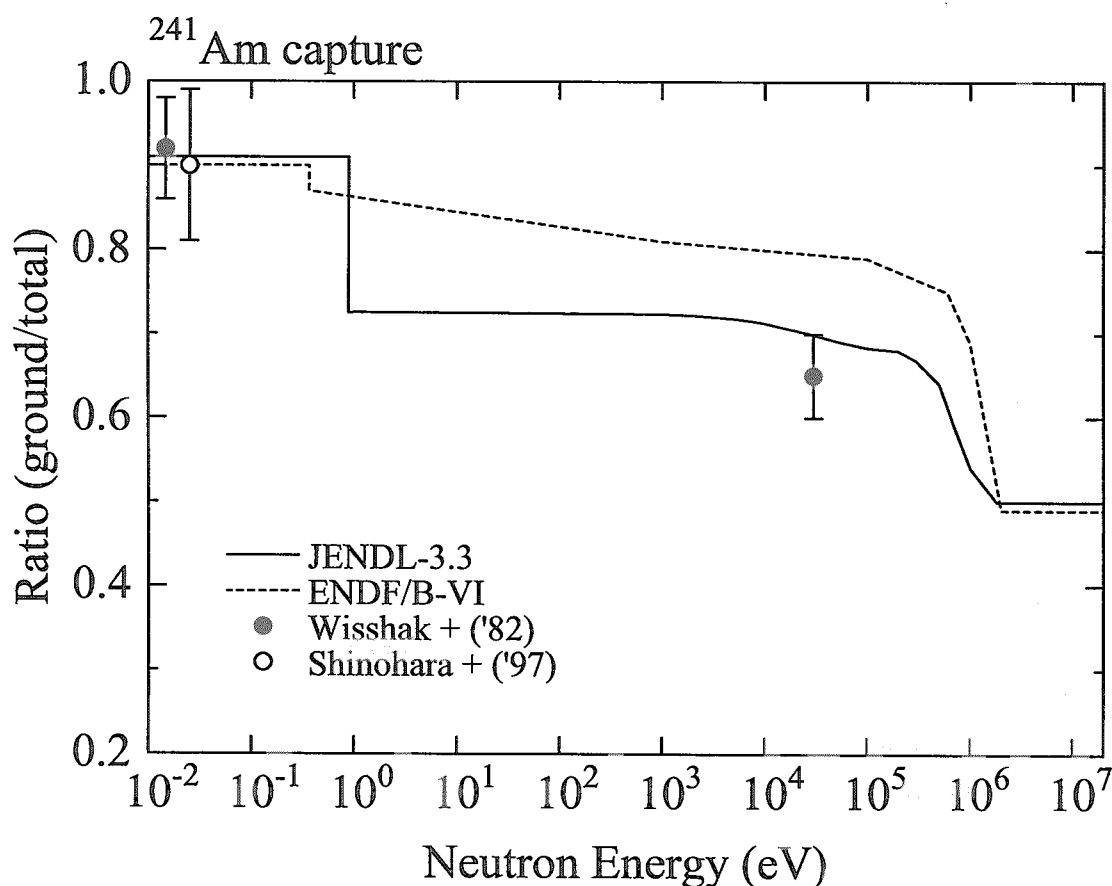


Fig. 1 Ratio of Ground-state Transitions to Total Capture Cross Section of  $^{241}\text{Am}$





## 2.2 Integral Test of JENDL-3.3 for Thermal Reactors

Keisuke OKUMURA and Takamasa MORI

Japan Atomic Energy Research Institute

Tokai-mura, Naka-gun, Ibaraki-ken 319-1195

e-mail: okumura@mike.tokai.jaeri.go.jp, mori@mike.tokai.jaeri.go.jp

Criticality benchmark testing was carried out for 59 experiments in various thermal reactors using a continuous-energy Monte Carlo code MVP and its different libraries generated from JENDL-3.2, JENDL-3.3, JEF-2.2 and ENDF/B-VI (R8). From the benchmark results, we can say JENDL-3.3 generally gives better  $k_{eff}$  values compared with other nuclear data libraries. However, further modification of JENDL-3.3 is expected to solve the following problems: 1) systematic underestimation of  $k_{eff}$  depending on  $^{235}\text{U}$  enrichment for the cores with low (less than 3wt.%) enriched uranium fueled cores, 2) dependence of C/E value of  $k_{eff}$  on neutron spectrum and plutonium composition for MOX fueled cores. These are common problems for all of the nuclear data libraries used in this study.

### 1. INTRODUCTION

The latest version of Japanese Evaluated Nuclear Data Library (JENDL-3.3) [1] was released in May, 2002. When it was completed, a criticality benchmark testing [1] of JENDL-3.3 had been carried out for various types of fast and thermal reactors by Reactor Integral Test Working Group in JNDC. As far as thermal reactors, however, further test is necessary, because the previous benchmark calculation was made only for 13 experiments carried out in JAERI facilities TCA, STACY, TRACY and JRR4. Especially for  $\text{UO}_2$  or MOX fueled thermal-neutron cores, the test was done only for TCA experiments. Although the lattice pitches and loading patterns can be varied in TCA, fuels are limited to 2.6wt.% enriched  $\text{UO}_2$  and 3.0wt.% MOX. Thus integral test covering more cores with different fuel specifications are required. In the present study, results of the extended integral test of JENDL-3.3 by using a continuous-energy Monte Carlo code are shown for totally 59 experiments in various thermal reactors including the previous benchmark cores. Results with JENDL-3.2[2], JEF-2.2 [3], and ENDF/B-VI (R8) [4] are also shown for comparison.

### 2. BENCHMARK CORES

Table 1 shows the benchmark cores selected in this study. Most of them are light water moderated  $\text{UO}_2$  or MOX fueled uniform lattices at room temperature. Exceptions are as follows:

- Fuel material of TRX is metal uranium (Al clad cylindrical rod),
- Temperature of KRITZ-2 in hot condition is about 245°C,

- Fuels of STACY and TRACY are homogeneous uranyl nitrate solutions,
- JRR4 is a light water moderated research reactor which uses MTR type fuel elements. In 1998, the fuel material of JRR4 was changed from 93% enriched U-Al alloy to 20% enriched  $U_3Si_3$ -Al dispersed alloy. Two minimum critical cores (JRR4-U93 and JRR4-U20) at room temperature with the above different fuels are selected in this study,

Except for JRR4, TRACY and MISTRAL, the benchmark problems are taken from public international benchmark literatures, in which details of experimental procedures, material compositions, calculation modeling and evaluated benchmark uncertainties are described. See the literatures given in Table 1 for details.

Table 1 Benchmark cores

Lattice names	H/HM	Fuel (Enrichment)	Remarks	Ref.
TRX-1	3.3	Metal-U (1.3 % $^{235}U$ ), Al cladding	Triangular pitch=1.806cm, 764 rods	[5]
TRX-2	5.6		Triangular pitch=2.174cm, 578 rods	
KRITZ2:1 Cold	3.4	$UO_2$ (1.86% $^{235}U$ ) Zry-2 cladding	Pitch=1.485cm, 44x44 rods, Temp.=19.7°C, Boron: 218ppm, Hc=65.28cm	[6] [7]
KRITZ2:1 Hot	2.8		Pitch=1.485cm, 44x44 rods, Temp.=248.5°C, Boron: 26ppm, Hc=105.5cm	
KRITZ2:13 Cold	5.0		Pitch=1.635cm, 40x40 rods, 22.1°C, Boron: 452ppm, Hc=96.17cm	
KRITZ2:13 Hot	4.1		Pitch=1.635cm, 40x40 rods, 243.0°C, Boron: 280ppm, Hc=110.9cm	
B&W-Core XI	5.4	$UO_2$ (2.5% $^{235}U$ ) Al cladding	LEU-COMP-THERM-008-001* 4961 rods, Boron: 1511ppm	[8]
TCA-1.50U (3 cases)	4.3	$UO_2$ (2.6% $^{235}U$ ) Al cladding	LEU-COMP-THERM-006-001 ~ 003* Pitch=1.849cm, 19x19,20x20,21x21 rods	[8]
TCA-1.83U (5 cases)	5.3		LEU-COMP-THERM-006-004 ~ 008* Pitch=1.956cm, 17x17,18x18,19x19,20x20,21x21	
TCA-2.48U (5 cases)	7.2		LEU-COMP-THERM-006-009 ~ 013* Pitch=2.150cm, 16x16,17x17,18x18,19x19,20x20	
TCA-3.00U (5 cases)	8.6		LEU-COMP-THERM-006-014 ~ 018* Pitch=2.293cm, 15x15,16x16,17x17,18x18,19x19	
DIMPLE3	3.0	$UO_2$ (3.0% $^{235}U$ )	LEU-COMP-THERM-048-001*	[8]
MISTRAL Core 1	5.1	$UO_2$ (3.7% $^{235}U$ )	Boron: 300ppm	[9] [10]
DIMPLE7	8.4	$UO_2$ (7.0% $^{235}U$ )	LEU-COMP-THERM-018* Pitch=1.32cm, 376 rods, Hc=53.9cm	[8]
STACY (7 cases)	from 73 to 103	uranyl nitrate solution (10% $^{235}U$ )	LEU-SOL-THERM-005-001 ~ 007* 7 cases of solution fueled cores with different uranium concentrations from 225 to 310 gU/liter in a water reflected 60cm $\phi$ cylindrical tank	[8]
TRACY	52	uranyl nitrate solution (10% $^{235}U$ )	Solution fuele in a 50cm $\phi$ cylindrical tank with a channel for a transient rod (out of core) Run-64, Temp.=27.8C, 430gU/l, Hc=45.3cm	[11]
JRR4-U20	-	$U_3Si_3$ -Al dispersed alloy (20% $^{235}U$ )	Minimum critical core with 12 MTR type fuel elements	[12]
JRR4-U93	-	U-Al alloy (93% $^{235}U$ )	Minimum critical core with 12 MTR type fuel elements	
KRITZ2:19 Cold	10.4	MOX (1.5% Pu-t) $^{239}Pu/Pu=0.914$	Pitch=1.80cm, 25x24 rods, Temp.=21.1°C, Boron: 4.8ppm, Hc=66.56cm	[6]
KRITZ2:19 Hot	8.5		Pitch=1.80cm, 25x24 rods, Temp.=235.9°C, Boron: 5.2ppm, Hc=104.2cm	[7]

TCA-2.42PU (3 cases)	12.0	MOX (3.0% Pu-t) Pu-fiss./Pu~0.75	MIX-COMP-THERM-004-001~003* Pitch=1.825cm, 23x23 rods, Date:1972-1974	[8]
TCA-2.98PU (3 cases)	14.8		MIX-COMP-THERM-004-004~006* Pitch=1.956cm, 21x21 rods, Date:1972-1975	
TCA-4.28PU (3 cases)	21.1		MIX-COMP-THERM-004-007~009* Pitch=2.225cm, 20x20 rods, Date:1972-1974	
TCA-5.50PU (2 cases)	27.6		MIX-COMP-THERM-004-010~011* Pitch=2.474cm, 21x21 rods, Date:1972-1973	
CRX-Case 1	4.9	MOX (6.6% Pu-t) <sup>239</sup> Pu/Pu=0.906	MIX-COMP-THERM-003-001* Pitch=1.3208cm, 23x22 rods, Hc=82.90cm	[8]
CRX-Case 2	6.4		MIX-COMP-THERM-003-002* Pitch=1.4224cm, 19x19 rods, Hc=81.295cm	
CRX-Case 3	6.4		MIX-COMP-THERM-003-003* (Boron:337ppm) Pitch=1.4224cm, 21x21 rods, Hc=88.06cm	
CRX-Case 4	13.8		MIX-COMP-THERM-003-004* Pitch=1.8679cm, 13x13 rods, Hc=68.41cm	
CRX-Case 5	16.7		MIX-COMP-THERM-003-005* Pitch=2.01158cm, 12x12 rods, Hc=76.76cm	
CRX-Case 6	31.6		MIX-COMP-THERM-003-006* Pitch=2.6416cm, 11x11 rods, Hc=79.50cm	
MISTRAL Core 2	5.1	MOX (7.0% Pu-t)	Pitch=1.32cm, Boron: 0ppm	[9]
MISTRAL Core 3	6.0		Pitch=1.39cm, Boron: 230ppm	[10]

\* Benchmark identification numbers in the "Handbook of International Criticality Safety Benchmark Evaluation Project (ICSBEP)" [8],

H/HM: ratio of atomic number densities of hydrogen and all heavy metal nuclides in fuel, Pitch: rectangular lattice pitch, NxN: loading pattern of fuel rods in rectangular lattice, Hc: critical water height, Date: measurement date in Pu core, Temp: system temperature, Boron: boron concentration in water moderator if any

### 3. MVP CALCULATION

A series of benchmark calculations was performed by using a continuous-energy Monte Carlo code MVP [13, 14] and its four different nuclear data libraries generated from JENDL-3.2, JENDL-3.3, JEF-2.2 and ENDF/B-VI(R8). The library generation was performed with the LICEM code system [15, 16]. The thermal scattering law data  $S(\alpha, \beta)$  for the JENDL-3.3 and ENDF/B-VI(R8) libraries were taken from ENDF/B-VI, while the data for the other libraries were taken from ENDF/B-III. The resonance shielding effects in unresolved resonance region was treated by the probability table.

In each of the MVP calculations, the first 30 cycles were skipped, followed by 1,000 active cycles, each with 10,000 particles per cycle. Statistical errors ( $1\sigma$ ) of  $k_{eff}$  values are within the range from 0.00015 to 0.00025.

As far as the MISTRAL cores are concerned, MVP results are referred from the literatures [9, 10] published by NUPEC members, because detailed information to construct 3D modeling of the MISTRAL cores are not opened. The JENDL-3.3 result for the MISTRAL cores has not been reported yet.

### 4. RESULTS AND DISCUSSIONS

#### (1) Uranium fueled cores

Figure 1 shows the C/E values of  $k_{eff}$  for the uranium fueled benchmark cores. In this figure, the values for the TCA cores (TCA1.50U, TCA-1.83U, TCA-2.48U and TCA3.00U) are the averages for the three or five experiments in which fuel loading patterns (See in Table 1) are different but the lattice pitches are the

same. The averaging was done because meaningful differences or systematic tendency were not observed for the C/E values among the experiments. The value for the STACY core is also averaged one for the seven experiments in which uranium concentration are different in the range specified in Table 1. In Fig.1, benchmark cores are lined up in the order of  $^{235}\text{U}$  enrichment and in the order of H/HM values for the cores with the same enrichment.

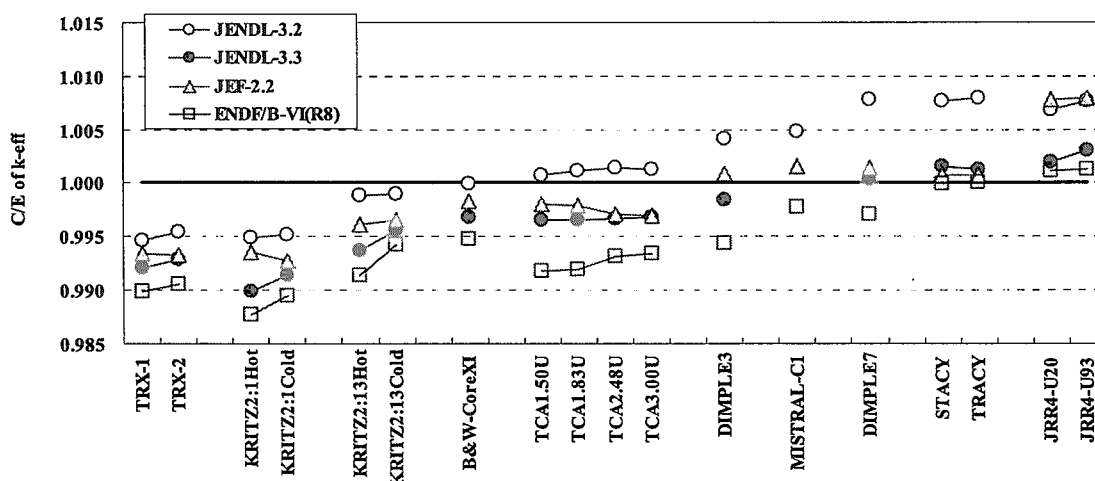


Fig.1 C/E values of  $k_{eff}$  for uranium fueled benchmark cores

From Fig.1, the followings are observed:

- The calculated  $k_{eff}$  values are larger in the order of the JENDL-3.2, JEF-2.2, JENDL-3.3 and ENDF/B-VI (R8) results.
- JENDL-3.2 overestimates criticality by about 0.5% $\Delta k$  or more for the core in which  $^{235}\text{U}$  enrichment is higher than 3.0wt.% (e.g. MISTRAL-C1, DIMPLE-3/-7, STACY, TRACY, JRR4), whereas it underestimates criticality of the core in which the enrichment is lower than 2.0 wt.% (e.g. TRX-1/-2, KRITZ2:1, KRITZ2:13).
- In the JENDL-3.3 results, the overestimations observed in the JENDL-3.2 results are improved. This is mainly due to the modification [1] of thermal cross section data of  $^{235}\text{U}$ . For the STACY and TRACY results, modification of thermal cross section of  $^{14}\text{N}(n,p)$  is also contributing to the improvement by about 0.2% $\Delta k$ . [17]
- For the cores with relatively lower  $^{235}\text{U}$  enriched fuels, all nuclear data libraries give underestimated results. It is significant especially for ENDF/B-VI (R8) which gives lower  $k_{eff}$ , compared with other libraries. The underestimation depends on  $^{235}\text{U}$  enrichment systematically.
- The KRITZ2 benchmark gives information on the prediction accuracy for total temperature coefficient. From the difference of the C/E values among hot and cold conditions in KRITZ2:1 and KRITZ2:13, JENDL-3.2 gives the most accuracy result.

## (2) MOX fueled cores

Table 2 shows the plutonium compositions of the MOX fueled benchmark cores. For the MISTRAL cores, it is reported that the plutonium fuel has regular plutonium composition. The KRITZ2:19 and CRX benchmarks are useful to test cross section data of  $^{239}\text{Pu}$ , because  $^{239}\text{Pu}$  contents in these cores are more than 90wt.% and the reactivity contribution of higher-order plutonium isotopes and  $^{241}\text{Am}$  is small. In addition, the two experiments in KRITZ2:19 and six experiments in CRX were performed within four and three months, respectively. Therefore, plutonium aging effects, which is reactivity loss due to decay from  $^{241}\text{Pu}$  to  $^{241}\text{Am}$  with half-life of 14.4 years, can be neglected in these benchmarks. On the other hand, the TCA-MOX and MISTRAL benchmarks are important because their fuel compositions are similar to those of MOX fueled LWRs. In these cores, plutonium aging effects should be taken into account.

Table 2 Composition of Pu composition (wt.% including Am241)

Lattice name	Pu238	Pu239	Pu240	Pu241	Pu242	Am241
KRITZ2:19	-	91.4	7.9	0.4	0.03	0.3
CRX	-	90.5	8.6	0.8	0.04	0.1
TCA-4.24PU*	0.5	68.1	22.0	7.1	2.0	0.3
TCA-2.98PU**	0.5	68.1	22.0	6.1	2.0	1.3

\*oldest (13, Apr., 1972) and \*\* latest (21, May, 1975) experiments in the TCA-MOX benchmark

At first, time dependence of the C/E values was investigated for eleven experiments in the TCA-MOX benchmark. The MVP results with JENDL-3.2 and JENDL-3.3 are shown in Fig. 2. In the JENDL-3.2 results, the C/E values have a tendency to increase slightly as time passes. It was improved in the JENDL-3.3 results due to the modification [1] of  $^{241}\text{Am}$  capture cross section in JENDL-3.3.

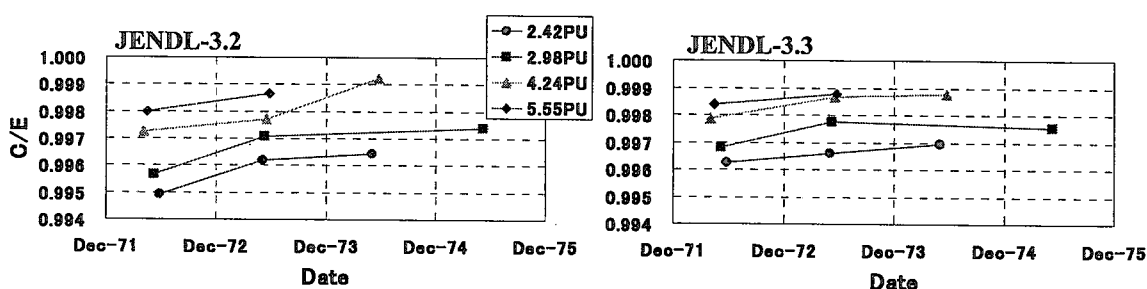


Fig.2 Time dependence of C/E values ( $k_{eff}$ ) for MOX fueled TCA cores

Figure 3 shows the C/E values of  $k_{eff}$  for all of the MOX fueled benchmark cores. In this figure, the values for the TCA cores (2.42PU, 2.98PU, 4.28PU, 5.50PU) are not averaged ones but values for the 4 experiments measured within 24 days. This is for excluding the plutonium aging effect. From Fig.3, the followings are observed:

- Remarkable differences are not observed between the  $k_{eff}$  values of JENDL-3.2 and JENDL-3.3 results. The  $k_{eff}$  values obtained with JEF-2.2 and ENDF/B-VI(rev.8) are smaller than those with JENDL-3.2 and JENDL-3.3.

- From the results for the TCA and CRX cores, where H/HM values varied from about 5.0 to 30.0, it is said that the C/E values depend on neutron spectra in MOX fueled cores. The dependency seems to be attributed to  $^{239}\text{Pu}$  cross section data, because the dependency is observed in CRX, where contributions of higher-order plutonium isotopes and  $^{241}\text{Am}$  are small in CRX.
- From the comparison between the KRITZ2:19 and CRX results, significant dependency of the C/E values on plutonium enrichment is not observed in the MOX cores with high  $^{239}\text{Pu}$  content. On the other hand, the C/E values are quite different between the results for TCA and MISTRAL, in which MOX fuels have more contents of higher-order plutonium and  $^{241}\text{Am}$ , compared with KRITZ2 and CRX cores.
- In the KRITZ2 results, difference of the C/E values between hot and cold conditions is almost equivalent to those in the  $\text{UO}_2$  fueled KRITZ2 cores. The differences are almost same among the results with the different nuclear data libraries.

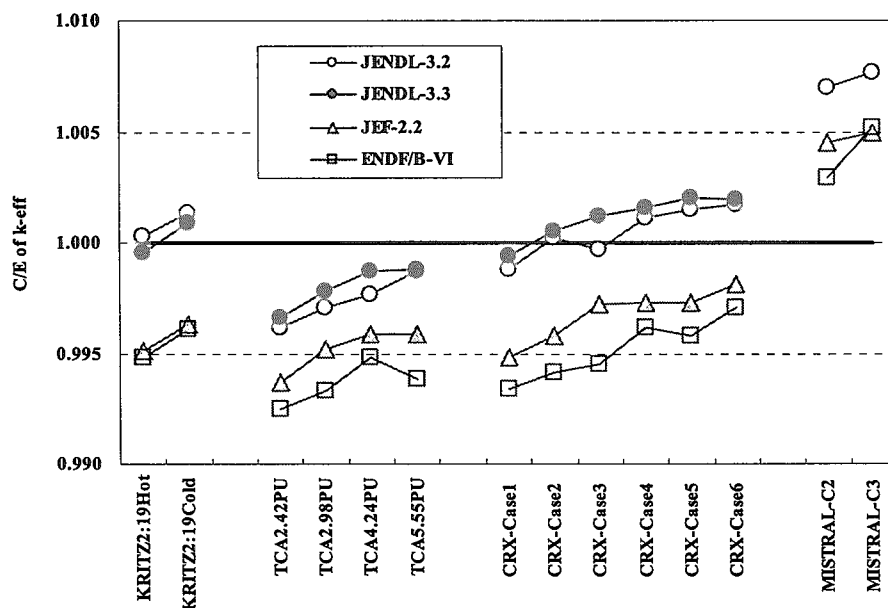


Fig.3 C/E values of  $k_{eff}$  for MOX fueled benchmark cores

## 5. CONCLUSIONS

Criticality benchmark testing of JENDL-3.3 was performed for 59 experiments in various thermal reactors. From the benchmark results, we can say JENDL-3.3 generally gives better  $k_{eff}$  values, compared with JENDL-3.2, JEF-2.2 and ENDF/B-VI (R8). However, further modification of JENDL-3.3 is expected to solve the following problems: 1) systematic underestimation of  $k_{eff}$  depending on  $^{235}\text{U}$  enrichment for the cores with low (less than 3wt.%) enriched uranium fueled cores, 2) dependence of C/E value for  $k_{eff}$  on neutron spectrum and plutonium composition for MOX fueled cores. These are common problems for all of the nuclear data libraries used in this study.

## REFERENCES

- [1] K. Shibata, *et al.*: "Japanese Evaluated Nuclear Data Library Version 3 Revision-3: JENDL-3.3," J. Nucl. Sci. Technol. **39**, 1125, (2002).
- [2] T. Nakagawa, K. Shibata and S. Chiba: "Japanese Evaluated Nuclear Data Library version 3 revision-2: JENDL-3.2," J. Nucl. Sci. Technol. **32**, 1259, (1995).
- [3] C. Nordborg and M. Salvatore: "Status of the JEF evaluated data library," Proc. Int. Conf. on Nuclear Data for Science and Technology, Gatlinburg 1994, Vol.2, p.680 (1994).
- [4] Cross Section Evaluation Working Group: "ENDF/B-VI Summary Documentation," BNL-NCS-17541 (ENDF-201) (1991).
- [5] J. Hardy: "A Study of Physics Parameters in Several Water Moderated Lattices of Slightly Enriched and Natural Uranium," WAPD-TM-931 (1970).
- [6] E. Johansson: "Data and Results from KRITZ Experiments on Regular H<sub>2</sub>O / Fuel Pin Lattices at Temperatures up to 245 °C," STUDSVIK/NS-90/133, Studsvik AB, Sweden, (1990).
- [7] I. Remec, *et al.*: "OECD/NEA KRITZ-2 UO<sub>2</sub> and MOX Benchmark," Proc. of Int. Conf. PHYSOR2002, 11B-03, Seoul, Korea, 7-10 October, (2002).
- [8] NEA Nuclear Science Committee: "International Handbook of Evaluated Criticality Safety Benchmark Experiments," NEA/NSC/DOC(95)03, September 2002 Edition. (ICSBEP Handbook)
- [9] K. Hibi, *et al.*: "Analysis of MISTRAL and EPICURE Experiments with SRAC and MVP Code Systems," Proc. of Int. Conf. PHYSOR2000.
- [10] T. Yamamoto *et al.*: "Core Physics Experiment of 100% MOX Core: MISTRAL," Proc. of Int. Conf. Global'97, Vol.1, 395 (1997).
- [11] K. Nakajima, *et al.*: "Experimental Study on Criticality Accidents Using the TRACY," Proc. of Int. Conf. PHYSOR96, Vol.4, L-83, Mito, Japan, 16-20 September (1996).
- [12] Y. Nakano: "Neutronic Analysis of JRR-4 with Low Enriched Uranium Silicon Dispersion Type Fuel of 3.8g/cm<sup>3</sup> Uranium Density," JAERI-Tech 95-002 (1995), and Private communication, (2002).
- [13] T. Mori, M. Nakagawa, "MVP/GMVP: General Purpose Monte Carlo Codes for Neutron and Photon Transport Calculations based on Continuous Energy and Multigroup Methods," JAERI-Data/Code 96-018, (1996) (in Japanese).
- [14] T. Mori, K. Okumura and Y. Nagaya: "Status of JAERI's Monte Carlo Code MVP for Neutron and Photon Transport Problems," Proc. of Int. Conf. MC2000, p.625, Lisbon, 23-26, October, (2000).
- [15] T. Mori, M. Nakagawa and K. Kaneko: "Neutron Cross Section Library Production Code System for Continuous Energy Monte Carlo Code MVP: LICEM," JAERI-Data/Code 96-018, (1996) (in Japanese).
- [16] T. Mori, K. Okumura, Y. Nagaya and M. Nakagawa: "Application of Continuous Energy Monte Carlo Code MVP to Burn-up and Whole Core Calculations Using Cross Sections at Arbitrary Temperatures," Proc. of Int. Conf. M&C'99, Vol.2, p.987, Madrid, (1999).
- [17] K. Okumura and K. Shibata: "Re-evaluation of (n,p) Cross Section of <sup>14</sup>N for JENDL-3.3 and Its Effects to Critical Benchmark Test of STACY Experiments Using 10wt.% Enriched Uranyl Nitrate Solution," p.26 JAERI-Review 2002-005 (2002).



## 2.3 Integral test of JENDL-3.3 for fast reactors

Gou Chiba

Japan Nuclear Cycle Development institute

Oarai-machi, Ibaraki-ken 311-1311

e-mail:go\_chiba@oec.jnc.go.jp

An integral test of JENDL-3.3 was performed for fast reactors. Various types of fast reactors were analyzed. Calculation values of the nuclear characteristics were greatly especially affected by the revisions of the cross sections of U-235 capture and elastic scattering reactions. The C/E values were improved for ZPPR cores where plutonium is mainly fueled, but not for BFS cores where uranium is mainly fueled.

### 1. Introduction

The updated version of JENDL-3 nuclear data library, JENDL-3.3, was released. It is important to validate an application of JENDL-3.3 to the fast reactor analysis because a revision of nuclear data library affects accuracy of calculation values greatly.

This integral test was performed in several fast cores. These are ZPPR, FCA, JOYO, MOZART and BFS. Features of these cores are different to each other.

Analyzed nuclear characteristics are effective multiplication factor( $k_{\text{eff}}$ ), reaction rate distribution, reactivity of sodium void, Doppler and control rod insertion, and so on. The calculations were performed both with JENDL-3.3 and JENDL-3.2 and effects of the revision were evaluated.

### 2. Tested cores and its characteristics

Features of tested cores are summarized in Table 1. ZPPR cores are categorized into four "JUPITER" experiments. Many types of cores were used in this test. Small or large cores, uranium or plutonium fueled cores are there.

### 3. Calculation method

JUPITER standard calculation scheme[1] was adopted. The scheme has been used in many analyses of fast reactors. Figure 1 shows an outline of the scheme.

JFS-3-J3.3 was used as an application library to fast reactor analysis. JFS-3-J3.3 is the Bondarenko type library with 70-group structure. Effective cell-averaged cross sections are calculated by the cell calculation and condensed to smaller (18 or 7) energy groups. The condensed cross sections are used in the core calculation based on the diffusion or transport theory. After that, the value of the nuclear characteristics can be obtained.

In addition to the standard calculation scheme, the new group constant system was used. The system has been developed to improve an insufficient treatment of resonance self shielding effects[2]. Correction factors for the improvement were evaluated based on JENDL-3.2 and applied to some nuclear characteristics.



Table 1 Features of tested cores

	Core size	Feature	Fuel	Outer region*
JUPITER-I JUPITER-II JUPITER-III JUPITER-1o	Large, Medium	Homogeneous Radial heterogeneous Axial heterogeneous Homogeneous	Pu Pu Pu Pu,U	Blanket
BFS-62-1 BFS-62-2 BFS-62-3A BFS-62-4	Medium	Homogeneous	U U U,Pu U,Pu	Blanket Reflector, Blanket Reflector, Blanket Blanket
JOYO MK-I JOYO MK-II	Small	Homogeneous	U,Pu	Blanket Reflector
FCA X-1 FCA XVII-1	Small	Homogeneous	U,Pu	Blanket
MOZART MZA MOZART MZB(1)	Medium	Homogeneous	Pu	Blanket

\*"Outer region" means the region adjacent to the fuel region.

#### 4. Results

Figure 2 shows results of  $k_{\text{eff}}$  in ZPPR cores.  $k_{\text{eff}}$  increases about 0.2%dk/k by the revision and underestimations were slightly improved except for ZPPR-18, -19 cores, in which uranium is fueled partly. C/E values become similar to each other. Figure 3 shows results of sensitivity analyses. The revision of U-235 capture cross section causes the difference of

the  $k_{\text{eff}}$  change. The revision of Fe capture cross section mainly contributes to the improvement of the underestimations.

Figure 4 shows results in other cores. It can be seen that C/E values become worse in BFS cores while MOZART cores have better results. The changes of  $k_{\text{eff}}$  in BFS cores were caused by the revision of U-235 capture cross section. Improvements in MOZART cores were mainly contributed by the revision of Fe capture and elastic scattering cross sections.

It can be said in general, improvements were observed in  $k_{\text{eff}}$  of most of the tested cores when JENDL-3.3 was used. However,  $k_{\text{eff}}$  of all cores were still underestimated.

Control rod worth was affected by the revision only in uranium fueled cores. Figure 5 shows results of ZPPR-18, -19 cores. Decreases were observed in control rod worth for uranium fueled regions. As the result, discrepancy of C/E values becomes smaller. This is due

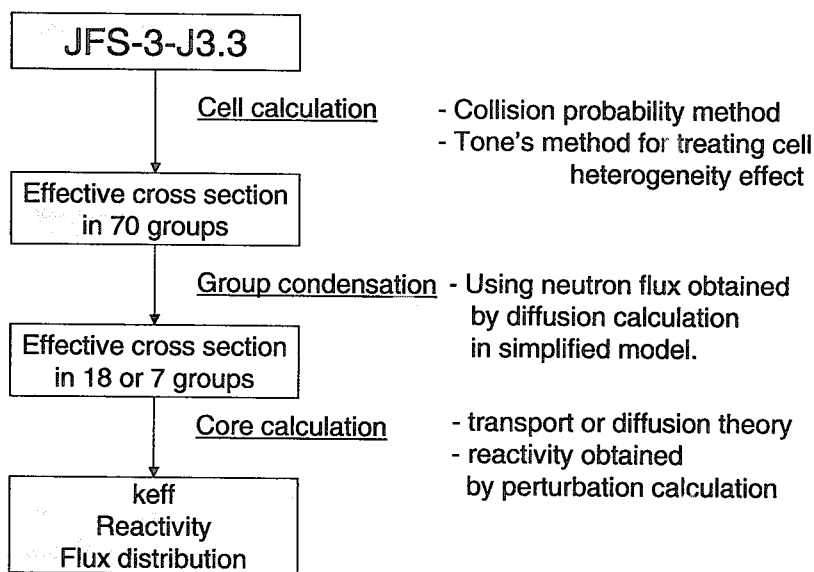


Fig. 1 Outline of the JUPITER standard calculation scheme

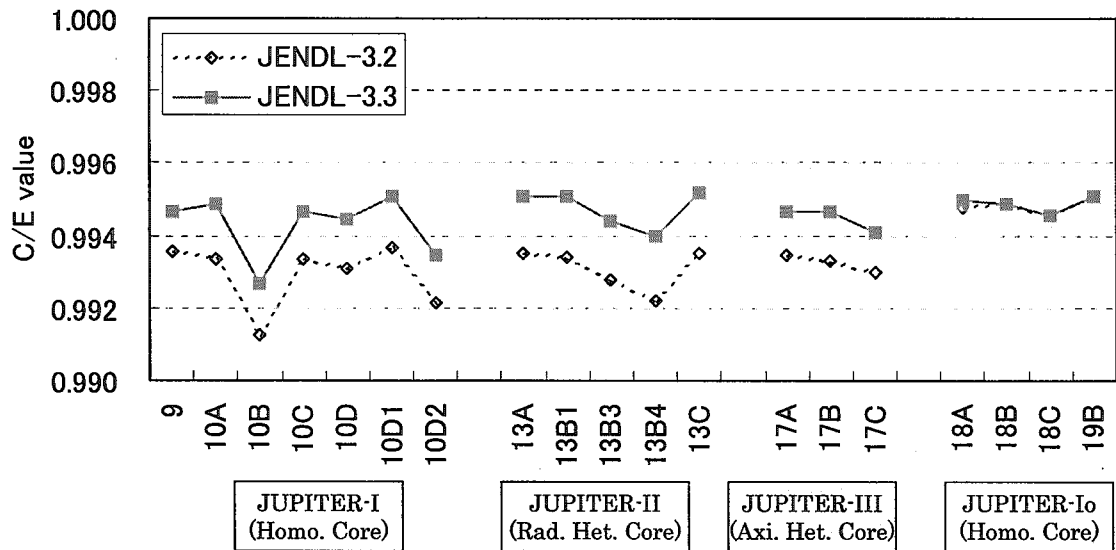


Fig.2 Results of k-eff in ZPPR cores

to the revision of U-235 capture cross section. However, in BFS cores, C/E values are not improved by the revision. The results are shown in Fig. 6.

Small sample worth analysis was also performed in ZPPR-9 cores. A significant effect was observed when sample is a stainless steel. The result is shown in Fig. 7. The average of C/E values changed from 1.095 to 1.046. Overestimations were improved about 5% by using JENDL-3.3. It is due to the revision of Fe capture cross section.

Figure 8 shows results of high Pu-240 zone substitution reactivity analysis in

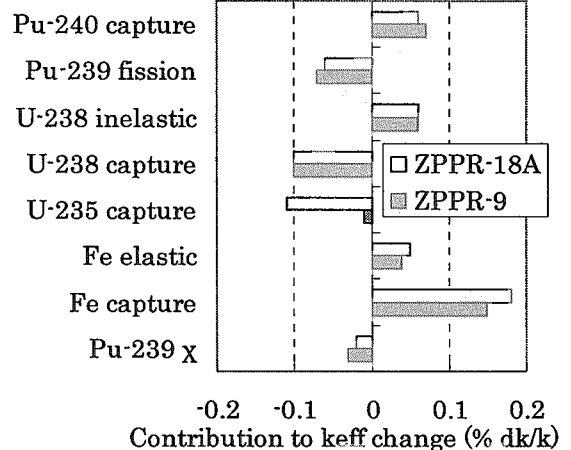


Fig.3 Results of sensitivity analyses of k-eff in ZPPR cores

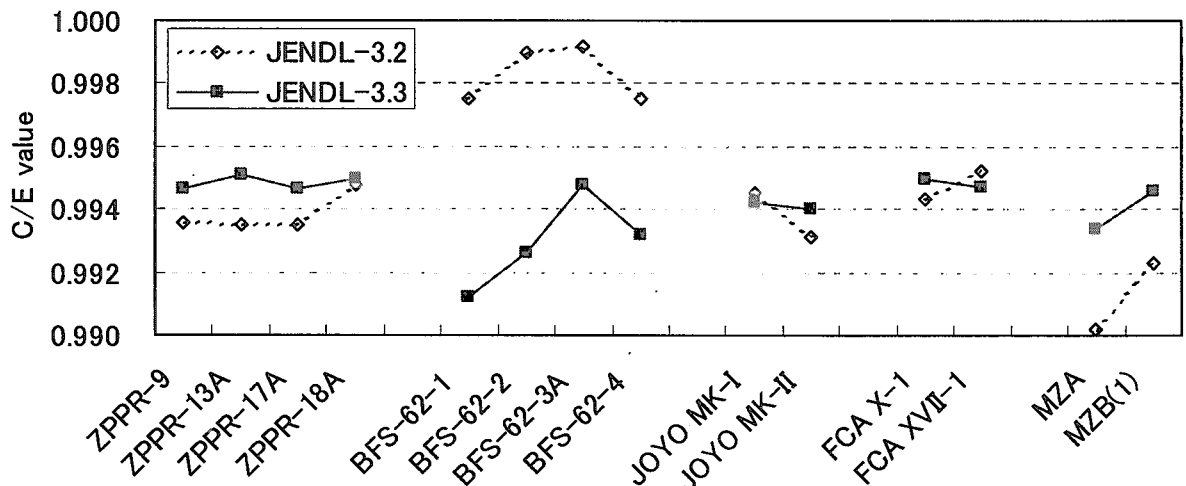


Fig.4 Results of k-eff in other cores

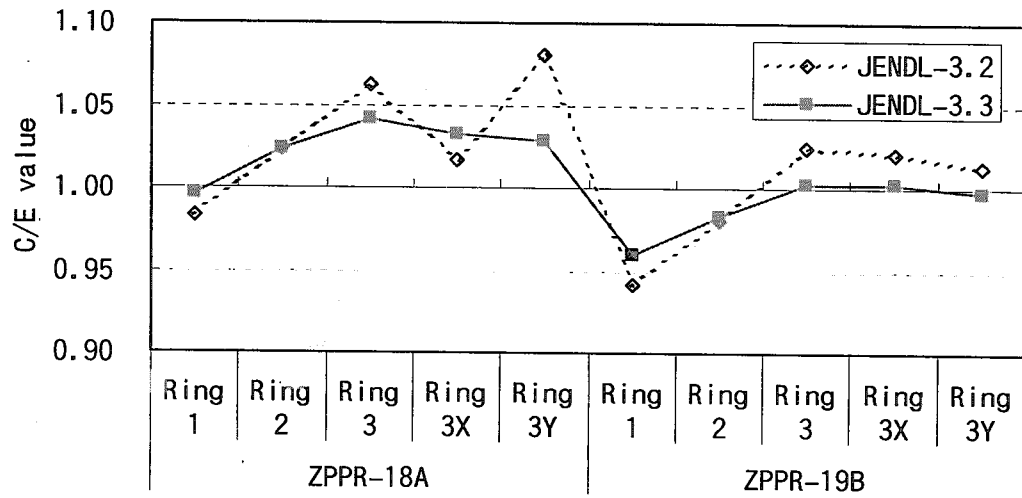


Fig.5 Results of control rod worth in ZPPR cores

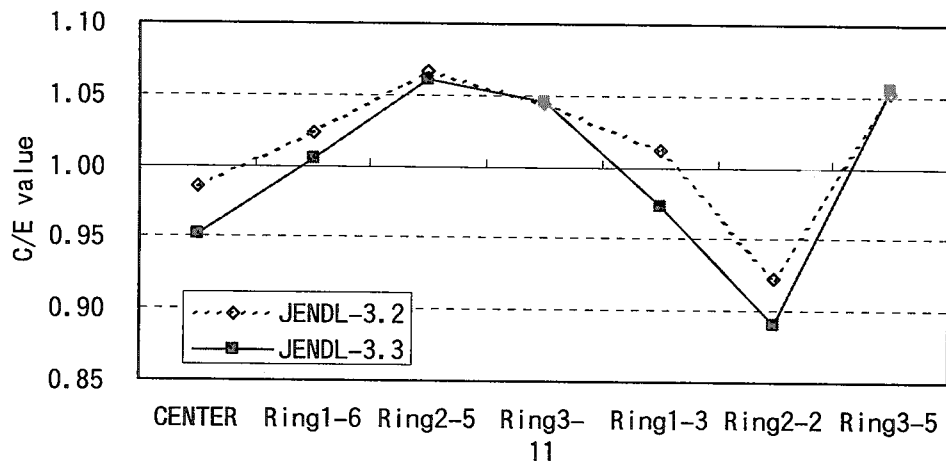


Fig.6 Results of control rod worth in BFS cores

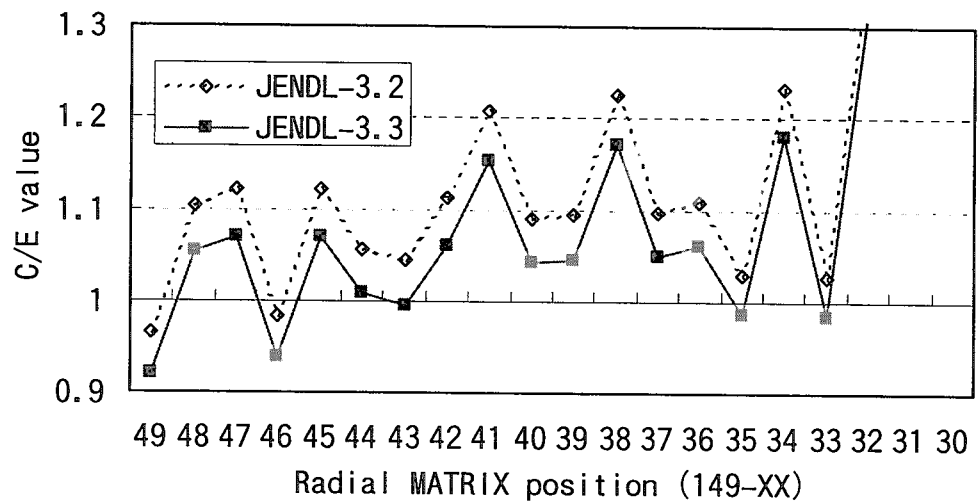


Fig.7 Results of small sample reactivity (ZPPR-9)

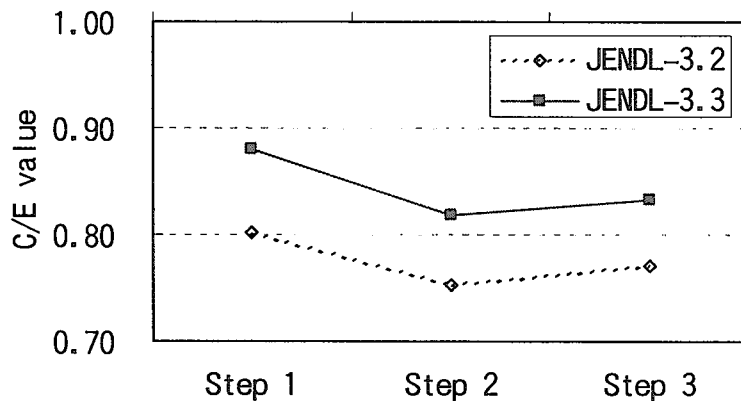


Fig.8 Results of high Pu-240 substitution reactivity

ZPPR-13C. In this experiment, the ordinary fuel (Pu-240 enrichment is 12%) was substituted to high Pu-240 fuel (enrichment is 26%) and the reactivity was measured. Underestimation was improved by the revision of Pu-240 capture cross section.

Figure 9 shows results of sodium void reactivity analysis in ZPPR cores. C/E values decrease and were not improved by the revision. Figure 10 shows

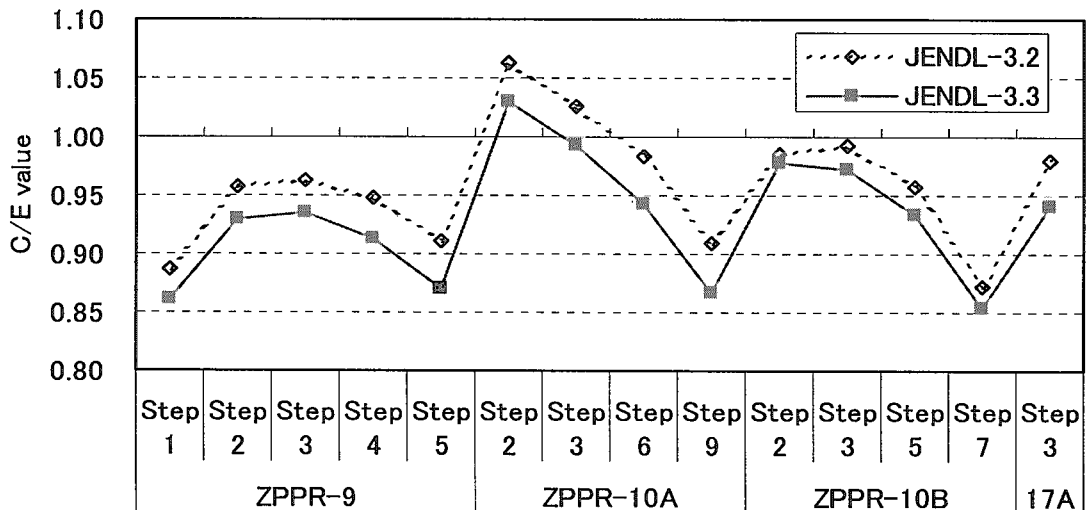


Fig.9 Results of sodium void reactivity in ZPPR cores

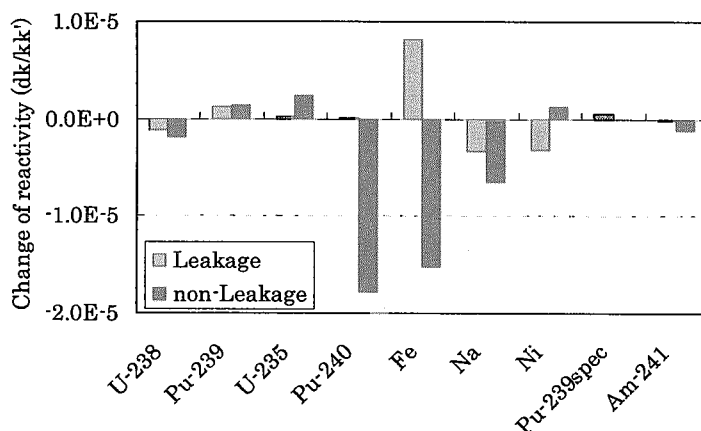


Fig.10 Result of sensitivity analysis of sodium void reactivity (ZPPR-9 void step 5)

results of sensitivity analysis. The revision of Pu-240 and sodium cross section made the C/E values smaller. The revision of Fe affects a little because a cancel of effects was occurred between the leakage term and the non-leakage term. Figure 11 shows C/E values in BFS cores. The revision of U-235 capture cross section mainly contributed to the changes of C/E values, which did not lead to an improvement.

Overestimation was observed in Pu-239 fission reaction rate distribution on the reflector region in

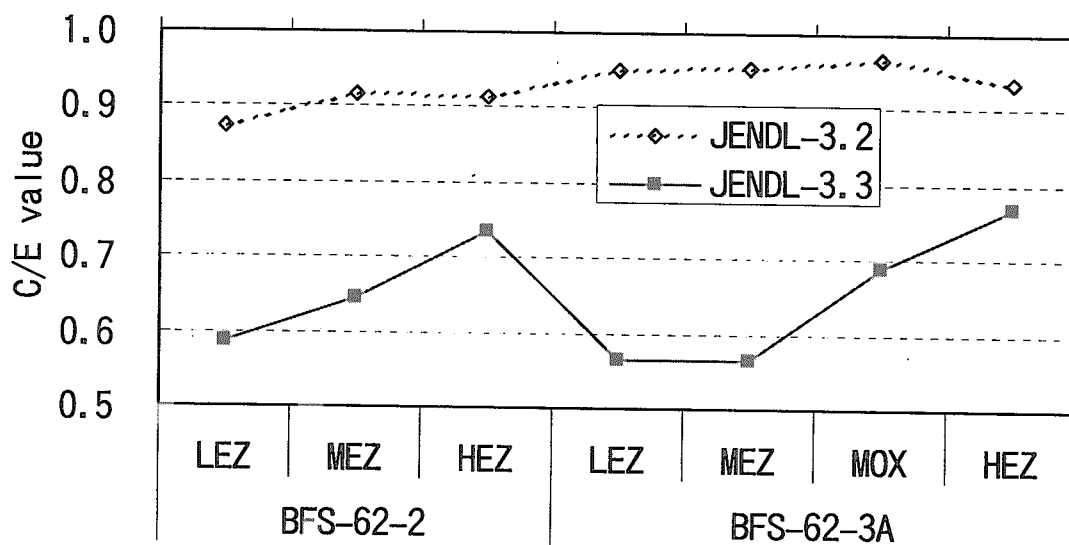


Fig.11 Results of sodium void reactivity in BFS cores

BFS cores when JENDL-3.2 was used. It have been pointed out by many researchers that the overestimation was originated from an error of the nuclear data because Monte Carlo methods can not improve the problem. Figure 12 shows results obtained by using JENDL-3.3. There is no improvement.

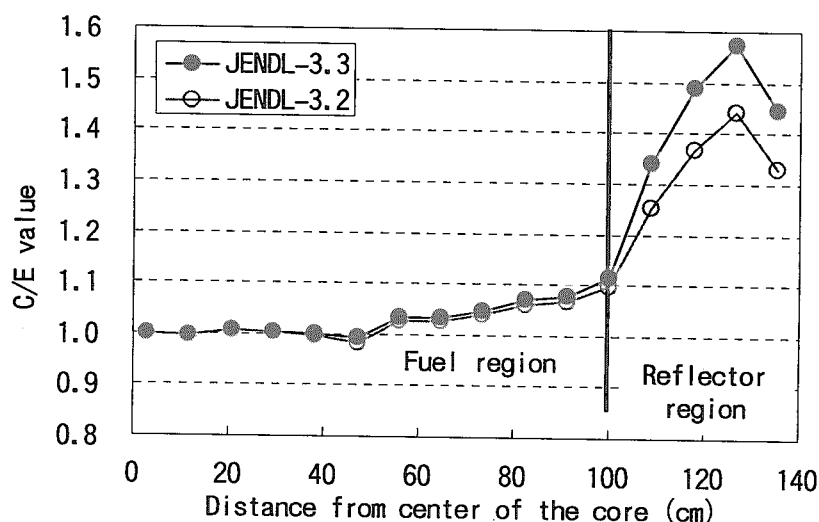


Fig.12 Results of Pu-239 fission reaction rate distribution(BFS-62-2)

## 5. Conclusion

An integral test of JENDL-3.3 was performed for fast reactors. The nuclear characteristics were mainly affected by the revision of U-235 capture cross section, Fe capture cross section, Fe elastic scattering cross section and Pu-240 capture cross section. In ZPPR cores, C/E values of many characteristics were improved by using JENDL-3.3. However, C/E values deteriorate in BFS cores which have strong sensitivity to U-235 cross section.

## References

- [1] Ishikawa, M. : "Consistency Evaluation of JUPITER Experiment and Analysis for Large FBR Cores," *Proc. of Int. Conf. on the Physics of Reactors(PHYSOR96)*, Mito, Japan, Vol.2, p.E-36 (1996).
- [2] Sugino, K. : "JUPITER Experiment Analyses Using a New Constant Set Based on JENDL-3.2," *J. of Nucl. Technol. Supp.* 2 p.1002 (2002).



## 2.4 Integral Test of JENDL-3.3 with Shielding Benchmarks

Naoki YAMANO<sup>\*†</sup>

<sup>\*</sup>Shielding Integral Test Working Group, Japanese Nuclear Data Committee

<sup>†</sup>Department of Nuclear Design, Sumitomo Atomic Energy Industries, Ltd.,

2-10-14 Ryogoku, Sumida-ku, Tokyo 130-0026, Japan

e-mail: yamano@sae.co.jp

Integral tests of neutron and gamma-ray production data for cross-section libraries based on the Japanese Evaluated Nuclear Data Library, Version 3.3 (JENDL-3.3) have been performed by using shielding benchmarks. An evaluation scheme for shielding benchmark analysis established in Japanese Nuclear Data Committee (JNDC) was applied to the integral test for medium-heavy nuclei such as Oxygen, Sodium, Aluminum, Silicon, Titanium, Vanadium, Chromium, Iron, Cobalt, Nickel, Copper, Zirconium, Niobium, Molybdenum, Tungsten and Mercury. Calculations were made based on a continuous-energy Monte Carlo code MCNP4C and multi-group discrete ordinates codes ANISN, DORT and TORT. Calculations with JENDL-3.2, ENDF/B-VI, EFF-2, FENDL-1 and FENDL-2 were also made for comparison. The results of JENDL-3.3 were generally satisfactory and the cross-section libraries generated with JENDL-3.3 were verified to shielding applications for fission and fusion reactors.

### 1. Introduction

The latest Japanese Evaluated Nuclear Data Library, Version 3.3 (JENDL-3.3) was released on May 2002. The Shielding Integral Test Working Group in the Japanese Nuclear Data Committee (JNDC) has been in charge of verification work for JENDL-3.3 through shielding benchmark tests. Recently, a point-wise cross-section library, FSXLIB-J33, and a multi-group library, MATXS-J33 were produced by Japan Atomic Energy Research Institute (JAERI) and Sumitomo Atomic Energy (SAE).<sup>1)</sup> In order to verify the cross-section libraries based on JENDL-3.3, integral tests with shielding benchmarks have been performed for medium-heavy nuclei such as Oxygen, Sodium, Aluminum, Silicon, Titanium, Vanadium, Chromium, Iron, Cobalt, Nickel, Copper, Zirconium, Niobium, Molybdenum, Tungsten and Mercury. An evaluation scheme<sup>2)</sup> established in JNDC was adopted in the present study.

### 2. Evaluation Scheme

For the integral test of cross sections by using shielding benchmarks, we should select appropriate integral measurements of different types. In the present study, we selected a number of spectrum measurements listed in Table 1 that were characterized as having high sensitivity to the nuclear data of interest. For calculation, we used a continuous-energy Monte Carlo code MCNP4C<sup>3)</sup> and multi-group discrete ordinates codes ANISN<sup>4)</sup>, DORT<sup>5)</sup> and TORT<sup>6)</sup>. A systematic analysis procedure was introduced to specify the accuracy and definite problems for typical reactions of nuclear data when discrepancy was found between calculation result and measurement. Calculations with JENDL-3.2<sup>7)</sup>, ENDF/B-VI<sup>8)</sup>, EFF-2<sup>9)</sup>, FENDL-1<sup>10)</sup> and FENDL-2<sup>11)</sup> were also made for comparison.

### 3. Results and Discussions

#### 1. Oxygen

A JAERI-FNS benchmark result for liquid oxygen measured at 0 degree from 20 cm penetration is shown in Fig. 1. The neutron spectrum calculated with JENDL-3.3 shows a good agreement with experiment, and it is improved compared with JENDL-3.2. Gamma-ray spectrum measurement at FNS for LiAlO<sub>2</sub> is shown in Fig. 2. The gamma-ray peaks from discrete inelastic reactions are well reproduced with JENDL-3.3, while a peak around at 6 MeV is missing in JENDL-3.2.

<sup>\*</sup> C. Ichihara (KURRI), K. Ueki (NMRI), Y. Matsumoto (MES), F. Maekawa (JAERI), C. Konno (JAERI), Y. Hoshiai (CRC), K. Sasaki (ARTECH), M. Takemura (KHI), T. Nishitani (JAERI), O. Sato (JAERI), S. Maeda (JNC), M. Kawai (KEK), A. Hasegawa (JAERI)

## 2. Sodium

For thick neutron penetration problems, JASPER IVFS-IC/Pb.9 and IHX-IB/Pb benchmarks are shown in Figs. 3 and 4, respectively. The results with JENDL-3.3 indicate a good agreement with both measurements, while results with ENDF/B-VI show overestimation compared with experiments in the energy range below 1.5 MeV. The difference is attributed to inelastic reactions based on the sensitivity analysis.

## 3. Iron

For relatively thin neutron transmission benchmarks, we selected KfK and NIST experiments from iron spheres with a  $^{252}\text{Cf}$  source in the center. The result is shown in Fig. 5 for the KfK iron sphere of 40 cm in diameter. Neutron spectrum calculated with MCNP4C shows good agreement except for resonance minima below 400 keV, but a good agreement is generally obtained between calculation and measurement. Figure 6 shows the result of the NIST iron sphere of 50.7 cm in diameter. The result with JENDL-3.3 is similar to that with JENDL-3.2, however JENDL-3.3 indicates slightly larger than that of ENDF/B-VI in the energy range between 1.6 and 2 MeV. This tendency also appears in the KfK benchmark.

For relatively thick neutron penetration benchmarks, we adopted ASPIS and FNS experiments. Figure 7 shows comparison between calculated results and the ASPIS measurement at 113.98-cm depth of iron slabs. Figure 8 indicates comparisons between calculated results with MCNP4C/DORT and the FNS measurement at 81-cm depth of large iron cylinder. In these benchmarks, neutron fluxes calculated with JENDL-3.3 in the energy range between 0.7 and 1 MeV are slightly underestimated compared with experiments. On the contrary, results with ENDF/B-VI are much better in this energy region. Two calculation results with DORT and MCNP4C show the same flux profile, so that we recommend improvement should be made in the energy range. For lower energy region below the 24 keV s-wave resonance, JENDL-3.3 slightly indicates overestimation compared with measurement as shown in Fig. 8. The calculation to experimental (C/E) ratio integrated over between 1 and 1000 eV is relatively large for JENDL-3.3, whereas the C/E deviations with JENDL-3.3 at each measured position are relatively smaller than those with another libraries.

For gamma-ray production benchmarks, we employed KfK and FNS measurements. The results with JENDL-3.3 indicate good agreement with measurements as shown in Figs. 9 and 10, and the results are better than those with JENDL-3.2.

## 3. Vanadium

Figures 11 and 12 show neutron and gamma ray benchmarks performed by FNS, respectively. Neutron flux calculated with JENDL-3.3 shows underestimation below 1 keV, while it makes better compared with JENDL-3.2 as shown in Fig. 11. In the energy region above 20 keV, a good agreement is generally obtained except between 0.1 and 1 MeV. For gamma-ray production data, JENDL-3.3 is improved from JENDL-3.2 as shown in Fig. 12.

## 4. Tungsten

Neutron flux measurements of FNS and OKTAVIAN are shown in Figs. 13 and 14, respectively. Neutron spectrum above 150 keV is slightly underestimated compared with the FNS experiment. For leakage gamma-ray measurements of FNS and OKTAVIAN, the profile of photon flux is generally acceptable compared with JENDL-3.2 as shown in Figs. 15 and 16.

## 5. Mercury

Neutron flux measurement of FNS is shown in Fig. 17. Neutron spectra at thickness of 7 and 14 cm are generally acceptable while the calculated values slightly show underestimation. Gamma-ray heating rate measurement of FNS indicates underestimation as shown in Fig. 18.

## 6. Titanium and Niobium

Neutron flux measurements of OKATVIAN for Titanium and Niobium are shown in Figs. 19 and 20, respectively. Neutron spectra show overestimation below 1 MeV. Gamma-ray spectra for Titanium and Niobium are generally acceptable as shown in Figs. 21 and 22, respectively.

## 7. Aluminum, Silicon, Chromium, Cobalt, Nickel, Copper, Zirconium and Molybdenum

Figures 23 and 24 show the comparisons between calculation and measurement for FNS and OKTAVIAN Copper experiments, respectively. The results of JENDL-3.3 are in good agreement with experiments except below 1 keV for the FNS benchmark. Comparisons of neutron fluxes between calculations and measurements for Aluminum, Silicon, Chromium, Cobalt, Nickel, Zirconium and Molybdenum are similar results to those of JENDL-3.2.

## 4. Conclusion

Integral tests with the FSXLIB-J33 and the MATXS-J33 libraries based on JENDL-3.3 have been performed for Oxygen, Sodium, Aluminum, Silicon, Titanium, Vanadium, Chromium, Iron, Cobalt, Nickel, Copper,

Zirconium, Niobium, Molybdenum, Tungsten and Mercury for various shielding benchmarks. The results were generally satisfactory and the new libraries would be acceptable for shielding applications for fission and fusion reactors. However, some problems in JENDL-3.3 remained, and the improvement should be made in the next release of JENDL.

### Acknowledgments

Authors are indebted to M. Wada of Startcom Co. Ltd. for his calculations of the FNS benchmarks. The work was performed as an activity of the Shielding Integral Test Working Group of JNDC.

### References

- 1) K. Kosako, C. Konno, T. Fukahori, K. Shibata, "MCNP and MATXS Cross Section Libraries Based on JENDL-3.3," to be presented in this Symposium (2002).
- 2) N. Yamano, "On the Integral Test Method for Neutron Nuclear Data Evaluation," *Ann. Nucl. Energy*, **24**, 1085 (1997).
- 3) J.F. Briesmeister, (Ed.), "MCNP-A General Monte Carlo N-Particle Transport Code, Version 4C," LA-13709-M (2000).
- 4) W.W. Engle Jr., "A USER'S MANUAL FOR ANISN: A One Dimensional Discrete Ordinates Transport Code with Anisotropic Scattering," K-1693 (1967).
- 5) W.A. Rhodes, R.L. Childs, "The DORT Two-Dimensional Discrete Ordinates Transport Code," *Nucl. Sci. Eng.*, **99**, 88 (1988).
- 6) W.A. Rhoades, D.B. Simpson, "The TORT Three-Dimensional Discrete Ordinates Neutron/Photon Transport Code (TORT Version 3)," ORNL/TM-13221 (1998).
- 7) T. Nakagawa, K. Shibata, S. Chiba, et al., "Japanese evaluated nuclear data library version 3 revision-2: JENDL-3.2," *J. Nucl. Sci. Technol.*, **32**, 1259 (1995).
- 8) P.F. Rose, (Ed.), "ENDF-201 ENDF/B-VI Summary Documentation," BNL-NCS-17541 (1991).
- 9) H.D. Lemmel, et al., IAEA-NDS-170 (1995).
- 10) S. Ganesan, P.K. McLaughlin, "FENDL/E Evaluated Nuclear Data Library of Neutron Nuclear Interaction Cross-Sections and Photon Production Cross-Sections and Photon-Atom Interaction Cross Sections for Fusion Applications Version 1.0 of May 1994," IAEA-NDS-128 (1995).
- 11) A.B. Pashchenko, et al., "FENDL-2: An Improved Nuclear Data Library for Fusion Applications," *Proc. Int. Conf. on Nuclear Data for Science and Technology*, Trieste, Italy, 19-24 May 1997, Vol. 59, Part II, p.1150 (1997).
- 12) N. Yamano, et al., *J. Nucl. Sci. Technol., Supplement 2*, pp. 841-846 (2002).

**Table 1** Shielding Benchmark Experiments for Integral Test of JENDL-3.3\*

Nuclide	Benchmark Experiments
Oxygen	FNS
Sodium	SDT4, SDT12, JASPER (IVFS-IC/Pb.9, IHX-IB/Pb)
Aluminum	OKTAVIAN, IPPE
Silicon	OKTAVIAN
Titanium	OKTAVIAN
Vanadium	FNS
Chromium	OKTAVIAN
Iron	SDT1, SDT11, FNS, ASPIS, KfK, NIST
Cobalt-59	OKTAVIAN
Nickel (include SS)	IPPE, ORNL, FNS
Copper	OKTAVIAN, FNS
Zirconium	OKTAVIAN
Niobium	OKTAVIAN
Molybdenum	OTRAVIAN
Tungsten	OKTAVIAN, FNS
Mercury	FNS

\* Benchmarks adopted in this study are referred in elsewhere.<sup>12)</sup>



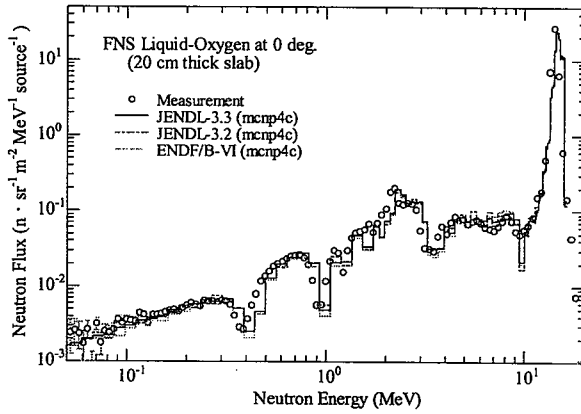


Fig. 1 Results of FNS Oxygen benchmark.

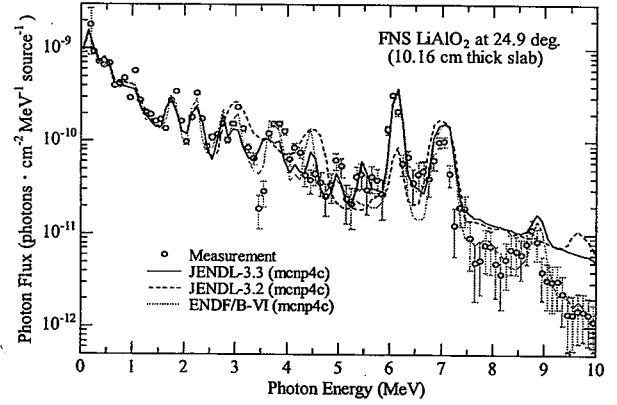
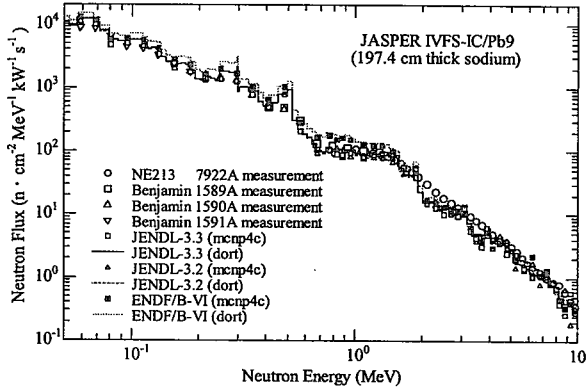

Fig. 2 Results of FNS LiAlO<sub>2</sub> benchmark.


Fig. 3 Results of JASPER IVFS-IC/Pb benchmark.

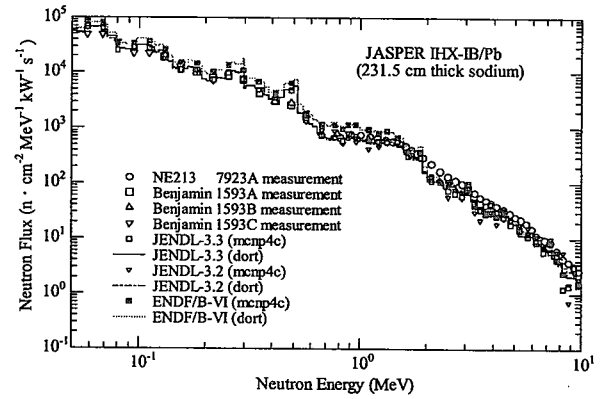


Fig. 4 Results of JASPER IHX-IB/Pb benchmark.

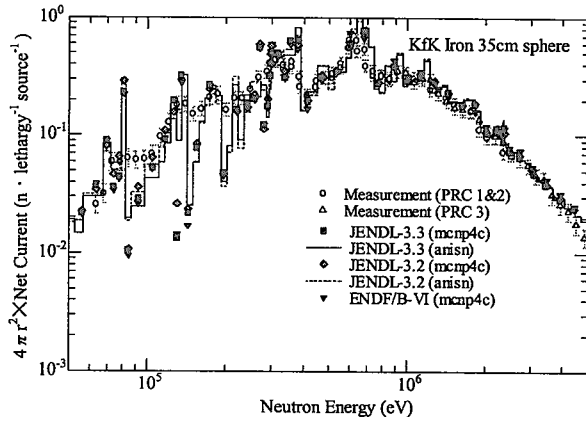


Fig. 5 Results of KfK Iron benchmark.

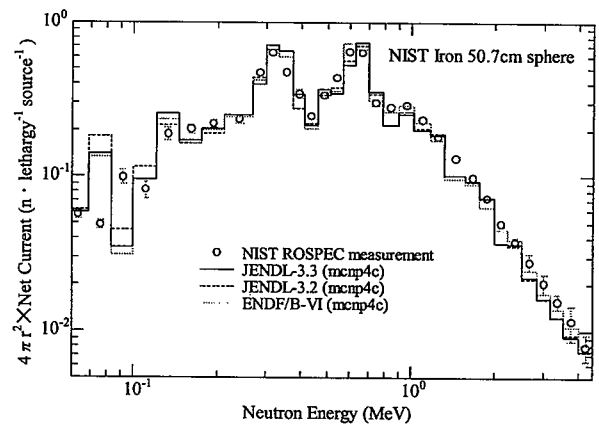


Fig. 6 Results of NIST Iron benchmark.

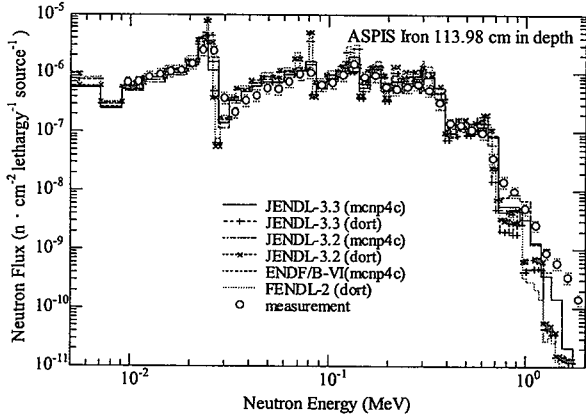


Fig. 7 Results of ASPIS Iron benchmark.

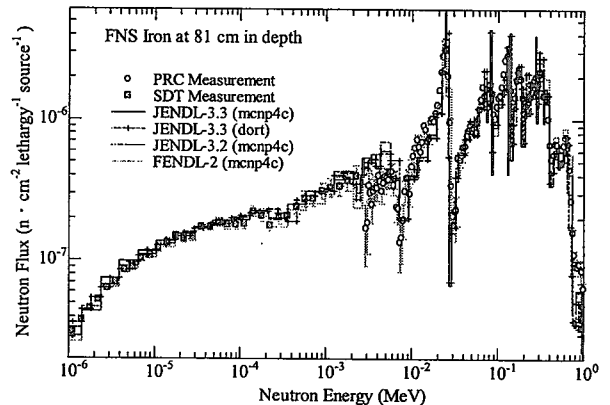


Fig. 8 Results of FNS Iron benchmark.

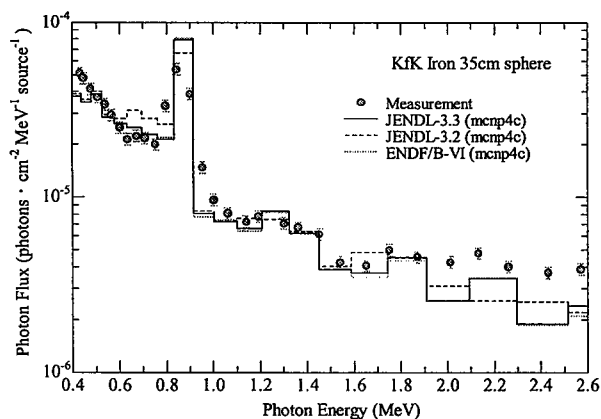


Fig. 9 Results of KfK Iron benchmark.

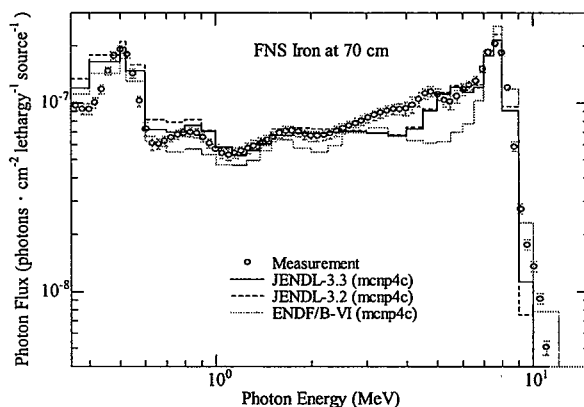


Fig. 10 Results of FNS Iron benchmark.

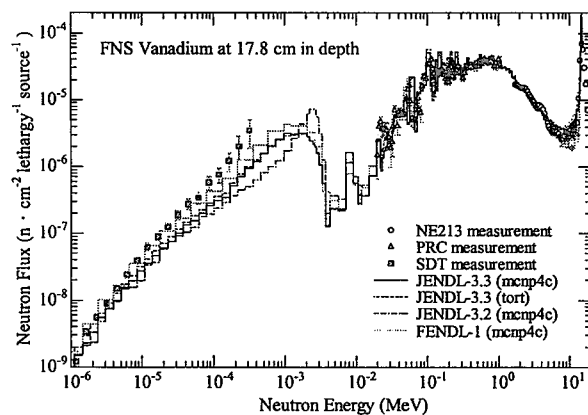


Fig. 11 Results of FNS Vanadium benchmark.

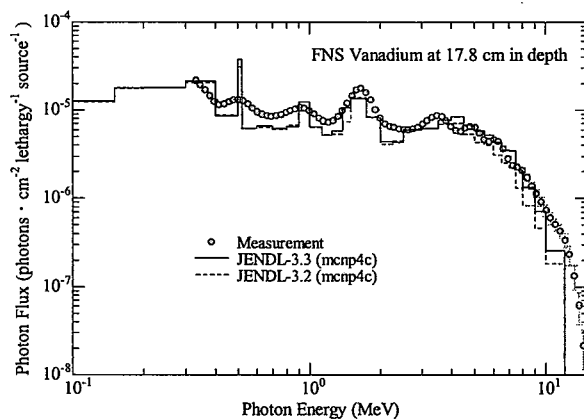


Fig. 12 Results of FNS Vanadium benchmark.

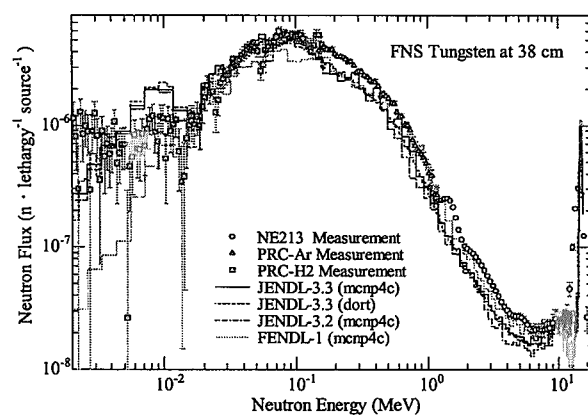


Fig. 13 Results of FNS Tungsten benchmark.

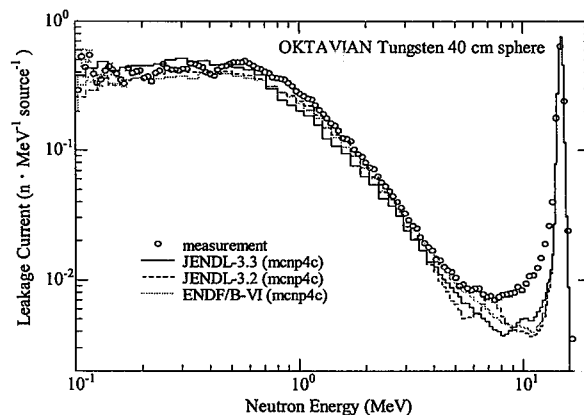


Fig. 14 Results of OKTAVIAN Tungsten benchmark.

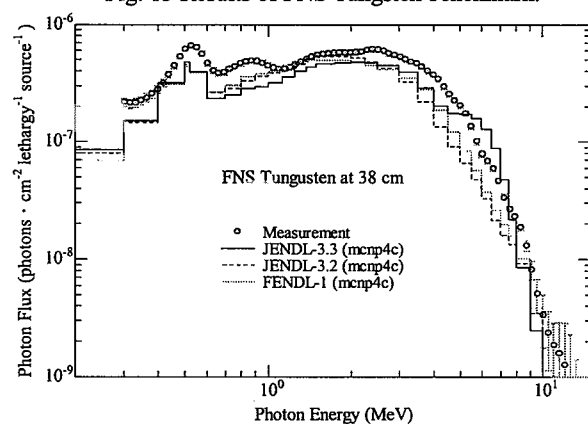


Fig. 15 Results of FNS Tungsten benchmark.

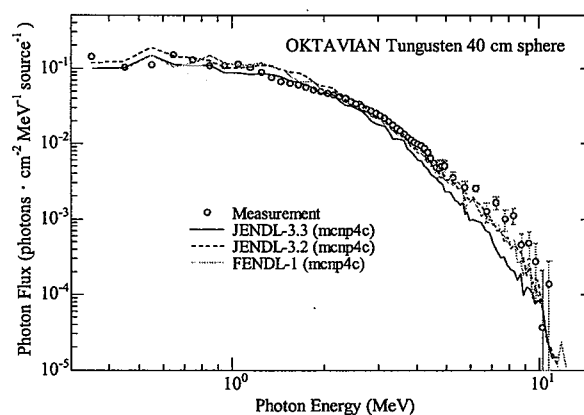


Fig. 16 Results of OKTAVIAN Tungsten benchmark.

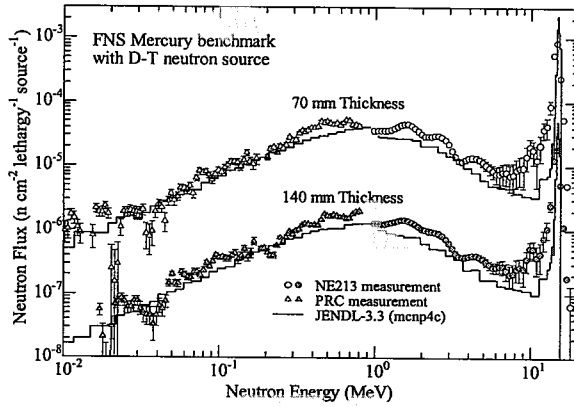


Fig. 17 Results of FNS Mercury benchmark.

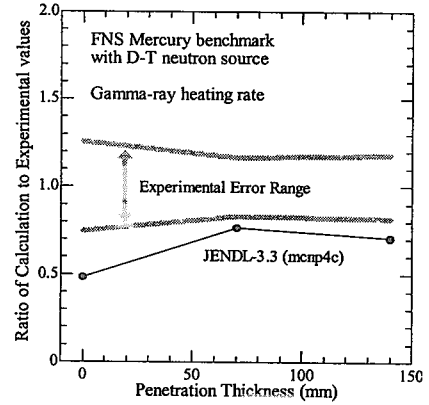


Fig. 18 Results of FNS Mercury benchmark.

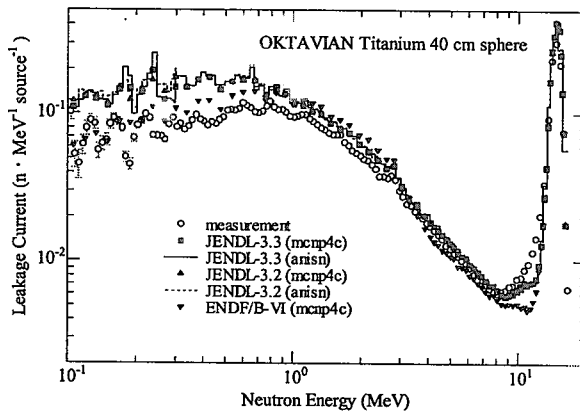


Fig. 19 Results of OKTAVIAN Titanium benchmark.

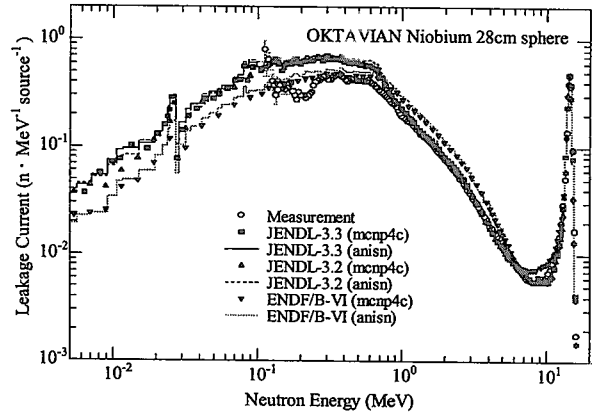


Fig. 20 Results of OKTAVIAN Niobium benchmark.

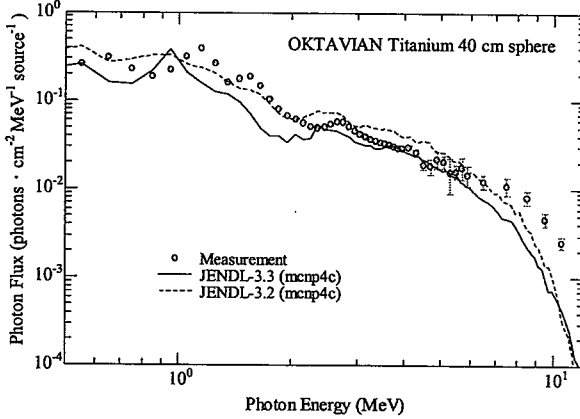


Fig. 21 Results of OKTAVIAN Titanium benchmark.

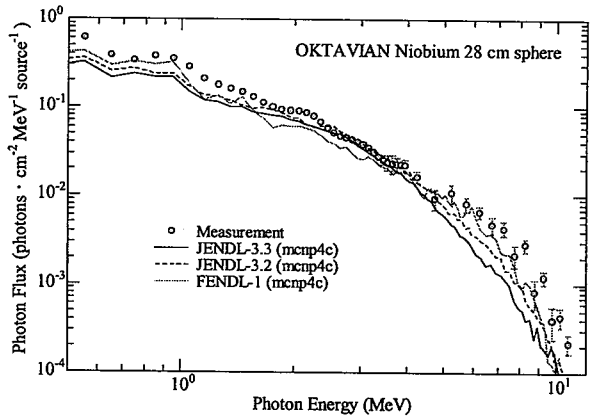


Fig. 22 Results of OKTAVIAN Niobium benchmark.

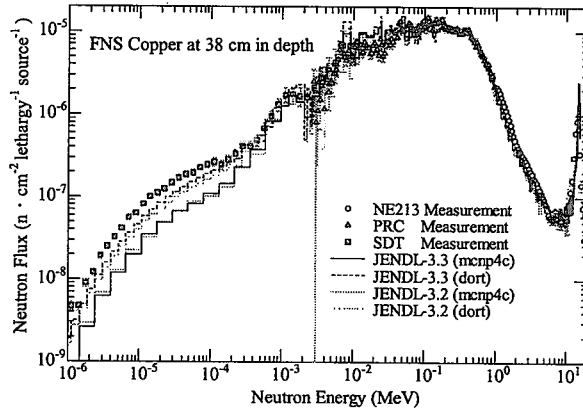


Fig. 23 Results of FNS Copper benchmark.

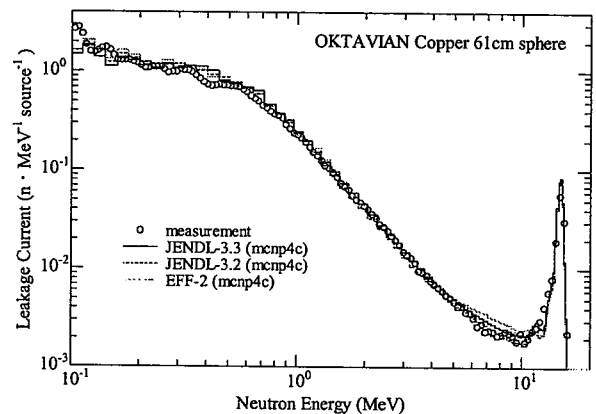


Fig. 24 Results of OKTAVIAN Copper benchmark.



## 2.5 Nuclear Mass Formulas and its application for Astrophysics

Hiroyuki Koura

*The Institute of Physical and Chemical Research (RIKEN),*

*Hirosawa 2-1, Wako, Saitama 1351-0198, JAPAN*

*Advanced Research Institute for Science and Engineering, Waseda University,*

*Okubo 3-4-1, Shinjuku-ku, Tokyo 169-8555, JAPAN*

koura@postman.riken.go.jp

koura@aoni.waseda.jp

Some nuclear mass formulas are reviewed and applied for the calculation of the rapid neutron-capture-process (r-process) nucleosynthesis. A new mass formula composed of the gross term, the even-odd term, and the shell term is also presented. The new mass formula is a revised version of the spherical basis mass formula published in 2000, that is, the even-odd term is treated more carefully, and a considerable improvement is brought about. The root-mean-square deviation of the new formula from experimental masses is 641 keV for  $Z \geq 8$  and  $N \geq 8$ . Properties on systematic of the neutron-separation energy is compared with some mass formulas. The calculated abundances of the r-process from different mass formulas are compared with use of a simple reaction model, and the relation between the calculated abundances and the corresponding masses are discussed. Furthermore, fission barriers for the superheavy and neutron-rich nuclei are also applied for the endpoint of the r-process.

### 1 Introduction

Nuclear masses are important quantities to determine the ground-state properties and reactions. Since the Weizsäcker-Bethe nuclear mass formula [1, 2], many mass predictions were presented. At the present time, the main purpose of the study on mass formulas is not only to give more precise mass values of known nuclides but also to predict reliable masses of unknown nuclides, especially the superheavy nuclides and neutron-rich nuclides. As related to the latter, the mass predictions are required in the study of the abundance of the rapid-neutron-capture-process (r-process) nucleosynthesis because there are few experimental masses of neutron-rich nuclei related to the r-process.

In this report, we briefly review some mass formulas and outline our mass formula. The calculated r-process abundances with a simple reaction model from different mass formulas are compared. In our method of obtaining shell energies, fission barriers for the heavy and superheavy nuclei can be estimated. The application of these fission barriers for the r-process is also discussed.

### 2 Mass formula

One of the way to reproduce the known nuclear mass values is to use the mass systematics. For examples, the mass formulas by Comay et al. and Jänecke et al. [4] are based on the Garvey-Kelson-like systematics [3], and the root-mean-square (RMS) deviations from then current experimental masses are 350-450 keV. There is also the mass formula by Tachibana et al. [5] (TUYU formula) composed of a gross term with the Coulomb energy treated elaborately, an even-odd term, and an empirical shell term. The RMS deviation of it is about 550 keV. These phenomenological mass formulas are usable to reproduce known masses and unknown ones in the vicinity of known nuclei, however, these cannot be extrapolated to the region of superheavy nuclei where no empirical data are available: the above-mentioned mass formulas can be applied only for  $N \leq 157$ -160. These formulas may also be difficult to predict the possibility of increasing or decreasing the strength of magicity far from the  $\beta$ -stability line. Moreover, no predictions of the nuclear shapes are available.

On the other hand, some approaches considering the nuclear force and the nuclear deformation have been done based on the models, or kinds of assumptions. The mass formula by Myers et al. [6] is the

early study of the liquid-drop model, which is composed of the macroscopic liquid-drop part and the microscopic shell part. (This early version were still in the similar problem to the above-mentioned systematics without the nuclear shapes). As examples of assumptions, we mention only two methods: the Skyrme-Hartree-Fock calculation and the relativistic mean-field calculation.

In the last decade, some mass predictions designed for the wide nuclidic regions were presented. We mention three mass predictions. One is the Finite-range droplet model (FRDM, 1995) formula, which is composed of the macroscopic droplet term and microscopic shell term [7]. The shell term is calculated from the folded-Yukawa single-particle potential. Other is the Hartree-Fock plus the BCS-type pairing method with the MSk7 Skyrme force (HFBCS-1, 2001) [8]. The last one is the mass formula by our groups published in 2000 [9], namely KUTY00. This formula is composed of the gross term, the even-odd term, and the shell term, and the first two terms are almost the same as those of TUYU formula. The method of obtaining the shell term is based on the spherical basis, and we solve some problems on the TUYU formula. These three methods can predict the nuclear shapes. The RMS deviations of these three predicted masses are about 600-800 keV in a current status. The differences of properties of these formulas will be discussed in the next section.

We now construct a new mass formula as a revised version of the KUTY00, that is, the even-odd term is treated more carefully, and a considerable improvement is brought about [11]. In the following, we give a brief explanation of the method of obtaining the shell energy and of the improved even-odd term.

## Spherical basis mass formula with an improved even-odd term

### Shell energy on a spherical basis

We first calculate shell energies for neutron groups and for proton groups in spherical nuclei using a spherical single-particle potential [10]. The potential parameters are assumed to be smooth functions of  $Z$  and  $N$  with the consideration of the charge symmetry, and this potential reproduces fairly well the single-particle levels of double-magic or magic-submagic nuclei in a wide nuclidic region. With this spherical potential, spherical shell energies can be obtained. For a spherical nucleus the nuclear shell energy is simply the sum of the refined spherical neutron and proton shell energies. The shell energy of a deformed nucleus is expressed as the sum of the intrinsic shell energy and the average deformation energy. The key point of the method to obtain the intrinsic shell energy is to treat the deformed nucleus as a particular superposition of spherical nuclei [9].

### Improved even-odd term

The even-odd term of the new and the previous ones is expressed as

$$M_{eo}(Z, N) = M_{oddN}(Z, N)\delta_{oddN} + M_{oddZ}(Z, N)\delta_{oddZ} - M_{oo}(Z, N)\delta_{oddN}\delta_{oddZ} \quad (1)$$

with

$$\delta_{oddi} = \begin{cases} 0 & \text{for even-}i \\ 1 & \text{for odd-}i, i=N \text{ and } Z. \end{cases} \quad (2)$$

In the previous mass formula [5, 9], the construction of the even-odd term was insufficient mainly in two points. One is the functional form of  $M_{oddZ}(Z, N)$  and  $M_{oddN}(Z, N)$ . Considering the charge symmetry of the nuclear force, we also take the functional form of the charge symmetry for odd- $N$  and odd- $Z$  terms as treated generally. The charge symmetry requires that the magnitudes of  $M_{oddZ}(Z, N)$  and  $M_{oddN}(Z, N)$  between mirror nuclei are equal to each other. When we have compared the "experimental"  $M_{oddZ}^{\text{exp}}(Z, N)$  and  $M_{oddN}^{\text{exp}}(Z, N)$  between mirror nuclei, however, the result is different. There are 45 pairs of mirror nuclei in the experimental data and almost all of  $M_{oddN}^{\text{exp}}(a, b) - M_{oddZ}^{\text{exp}}(b, a)$  ( $a$ : even,  $b$ : odd) is positive, and the average is about 100 keV. This means that the even-odd term for a proton is somewhat smaller than that for a neutron. Undoubtedly, the main reason for this is the Coulomb repulsive force between protons. (More precise discussion, see Ref. [11]). Considering the above features of "experimental" even-odd term, we make the functional form of the even-odd term. The other point is the odd-odd term  $M_{oo}(Z, N)$ . In the previous formula,  $M_{oo}(Z, N)$  is a function independent on

$M_{\text{odd}Z}(Z, N)$  and  $M_{\text{odd}N}(Z, N)$ .  $M_{\text{oo}}(Z, N)$  is caused by the interaction between the last odd-neutron and the last odd-proton. This interaction seems to be weaker than the pairing interaction, and  $M_{\text{oo}}(Z, N)$  should be smaller than either of  $M_{\text{odd}Z}(Z, N)$  and  $M_{\text{odd}N}(Z, N)$ . In the new formula, we impose this constraint on the form of  $M_{\text{oo}}(Z, N)$ .

### 3 Properties of recent mass formulas

The root-mean-square (RMS) deviation is given in Table 1. The RMS deviation of our present formula, we refer to as KTUY02, is 657.7 keV for 1835 experimental masses [12], which is smaller than that of the KUYT00 mass formula [9], 680.2 keV. In Table 1, we also list the RMS deviations of two other recent mass formulas, FRDM [7] and HFBCS-1 [8]. Among them, our mass formula has the smallest RMS deviation. Although there is not much difference in the RMS deviations among these three mass formulas, there still remain fairly large differences of the estimated masses for some individual nuclides. The RMS deviation of the separation energies of KTUY02 mass formula is listed in Table 2 together with those of the two others. Our RMS deviation is significantly smaller than those of the others.

Figure 1 shows the two-neutron separation energies  $S_{2n}$  for even- $N$ , the experimental data in (a), our results in (b), ones of FRDM in (c), and HFBCS in (d). We connect the nuclei with the same  $N$  by solid lines. In such a figure, magicities are seen as large gaps between two lines. In the panel (a), we see large gaps between  $N=8$  and 10 (abbreviated as “at  $N=8$ ”), and at  $N=20, 28, 50, 82, 126$  except for the region with very small values of  $S_{2n}$ . Similar gaps are seen in the other panels without ones at  $N=8$  and  $N=20$ . On the very neutron-rich region, which corresponds to the region near the  $S_{2n}=0$  line, the large gaps of  $S_{2n}$  for (b) at  $N=20, 28, 50$  decrease, and the gaps at  $N=16, 32$  (or 34), 58 become larger compared with the neighboring ones. On the other hand, in the panel (c) the decreasing the magic gaps are not so clear, and unreasonable crossing of the solid lines are shown in the region of the very neutron-rich nuclei. In the panel (d), the similar tendencies on increasing the gaps seem to be seen at  $N=16$  and 34, but the gap at  $N=20$  and 28 is not so clear compared with those of experimental data and ours, and some unreasonable zigzag lines are seen in the region of heavy and neutron-rich nuclei.

### 4 Application for astrophysics

#### 4.1 R-process abundances

It is considered that about half of the stable nuclides heavier than iron observed in nature are synthesized by the rapid neutron-capture process (r-process). We estimate the nuclidic abundances produced in the r-process nucleosynthesis in the canonical model with the waiting point approximation [13]. For each  $N$ , the most abundant isotope has an even neutron number  $N$ , and its two-neutron separation energies  $S_{2n}(Z, N)$  satisfies the constraints [14]

$$S_{2n}(Z, N+2)/2 \leq S_a^0 \equiv (34.075 - \log N_n + 1.5 \log T_9) \times T_9/5.04 \leq S_{2n}(Z, N)/2, \quad (3)$$

where  $N_n$  is the neutron number density in  $\text{cm}^{-3}$  and  $T_9$  is the temperature in  $10^9$  K. The r-process path in the  $N$ - $Z$  plane is defined as the ensemble of the nuclides satisfying the above equation. The equation of the time evolution is written as

$$\frac{dY_Z(t)}{dt} = -\lambda_Z Y_Z(t) + \lambda_{Z-1} Y_{Z-1}(t), \quad (4)$$

where  $Y_Z$  is the sum of abundance  $Y(Z, N)$  and  $\lambda_Z$  is the sum of the decay constant  $\lambda$  with the same  $Z$ .

We take the  $S_{2n}$  from some mass formulas, and the values of  $\lambda$  are estimated from theoretical  $\beta$ -decay half-lives [16] with  $Q_\beta$  of mass formulas, and  $N_n, T_9, \tau$  are chosen so as to reproduce the abundance peak at  $A=130$ . Figure 2 shows the r-process abundances for three mass formulas. Focused on the abundance around  $A=130$ , the lack of the abundances is seen at  $A \approx 110$  for those of KUTY, and the deeper dips are seen for those of FRDM. These results could be explained with the tendencies of the neutron-separation energies. Figure 3 shows two-neutron separation energies  $S_{2n}$  connected with isotopes. In the panels of TUYU and KUTY, the isotope lines of  $S_{2n}$  go regularly. In the right panel of FRDM, however, the lines of  $Z=36-40$  and some neighboring ones have the dips around  $N=40-44$  and  $N=70-80$ . Because experimental

$S_{2n}$  of the nuclei around  $Z=38$  and  $N=40$  exist and no corresponding dips are seen, the dips of FRDM around  $N=40-44$  seem to be incorrect. On the other hand, there are no experimental data corresponding nuclei with the dips of FRDM around  $N=70-80$ , but the both TUYU and KUTY formulas have no corresponding dips. The dips around  $N=70-80$  correspond to  $A \approx 110$  on the r-process abundances. If the isotope lines have the dips and these values satisfy the condition of Eq. (3), the calculated abundances diffuse into the nuclei with the different  $N$ , and consequently there are fewer abundances compared with the neighboring ones. The dips around  $N=70-80$  of FRDM also cause the lack of the abundances at  $A \approx 110$ . It is noted that the predicted nuclear shapes by FRDM change from the prolate shapes to the oblate ones in the two regions. As for the lack of abundances around  $A \approx 110$  of KUTY, the isotope lines with  $Z=36-40$  of KUTY have gentler slopes in the corresponding region compared with those of TUYU. The difference of steepness causes less abundances of KUTY than those of TUYU, although more than those of FRDM. Figure 2 also shows the decreasing of the abundances in the region of  $A > 150$  for KUTY and FRDM. These differences are caused by the different mass surfaces. These results are not so critical, at present, because we take a simple reaction model in which such a bulk feature cannot be considered. If we take more realistic reaction model, the situation seems to change, but the problem related to the dips on the above-mentioned  $S_{2n}$  systematics is still remaining.

#### 4.2 Fission-barrier height relevant to r-process

After the end of the rapid neutron capture, the synthesized nuclei go to the beta-stable region by the beta-decay. However, if the fission barrier  $B_{\text{fiss}}$  of a daughter nucleus is lower than the beta-decay  $Q$ -value  $Q_\beta$  of a parent nucleus, such a nucleus is not expected to reach the beta-stable nuclei because of the fission. Now, we estimate the beta-decay  $Q$ -values from the present mass formula, KTUY02, and the fission-barrier heights with use of the method of obtaining the spherical basis shell term [15]. Figure 4 shows the region with  $Q_\beta - B_{\text{fiss}} > 0$ . The r-process paths obtained the previous subsection are also seen. This figure shows the existence of the nuclei with  $Q_\beta - B_{\text{fiss}} > 0$  in the region with nuclei around  $Z \approx 106$  and  $N \approx 192$ . These nuclei are located between the r-process path and the  $\beta$ -stability line. This indicates that superheavy nucleus  $^{298}[114]_{184}$  is not expected to be synthesized from the r-process.

#### Acknowledgement

The author thanks Dr. Tachibana for helpful discussions. The numerical calculations were mainly made with the computer VPP700 at Computer and Information Division, RIKEN.

#### References

- [1] C.F. von Weizsäcker, Z. Phys. **96** (1935) 431.
- [2] H.A. Bethe and R.F. Bacher, Rev. Mod. Phys. **8** (1936) 829.
- [3] G.T. Garvey, *et al.*, Rev. Mod. Phys. **41**, (1969) S1.
- [4] P.E. Haustein, Special Editor: "1988-89 Atomic Mass Predictions", ATOMIC DATA AND NUCLEAR DATA TABLES **39** (1988) 185.
- [5] T. Tachibana, M. Uno, M. Yamada, S. Yamada, ATOMIC DATA AND NUCLEAR DATA TABLES **39** (1988) 251.
- [6] W.D. Myers, W.J. Swiatecki, Nucl. Phys. **81** (1966) 1.
- [7] P. Möller, J.R. Nix, W.D. Myers, J. Swiatecki, ATOMIC DATA AND NUCLEAR DATA TABLES **59**, (1995) 185.
- [8] S. Goriely, F. Tondeur, J.M. Pearson, ATOMIC DATA AND NUCLEAR DATA TABLES **77** (2001) 311.
- [9] H. Koura, M. Uno, T. Tachibana, M. Yamada, Nucl. Phys. **A674** (2000) 47; H. Koura, M. Uno, T. Tachibana, M. Yamada, RIKEN-AF-NP-394, RIKEN (2001).
- [10] H. Koura and M. Yamada, Nucl. Phys. **A 671** (2000) 96.
- [11] H. Koura, T. Tachibana, M. Uno, M. Yamada, in preparation.
- [12] G. Audi and A.H. Wapstra, Nucl. Phys. **A 595** (1995) 409.
- [13] T. Kodama, K. Takahashi, Nucl. Phys. **A239** (1975) 489.
- [14] T. Tachibana, M. Arnould, Nucl. Phys. **A588** (1995) 333c.
- [15] H. Koura, J. Nucl. Radiochem. Sci. **3** (2002) 201.
- [16] T. Tachibana, M. Yamada, T. Yoshida, Prog. Theor. Phys. **84** (1990) 641.

Table 1: RMS deviations of mass formulas from experimental data in keV. The values in the parentheses are the numbers of nuclei.

Mass formula	nuclidic region	
	$Z, N \geq 2$ (1835)	$Z, N \geq 8$ (1768)
KTUY02 (this work)	657.7	640.8
KUTY00	680.2	656.1
FRDM	-	678.3
HFBCS-1	-	718.0

Table 2: RMS deviations of separation energies from experimental data for their mass formulas in keV. The values in the parentheses are the numbers of nuclei.

Mass formula	neutron		proton	
	$S_n$	$S_{2n}$	$S_p$	$S_{2p}$
$Z, N \geq 2$	(1648)	(1572)	(1592)	(1483)
KTUY02	361.7	466.0	403.1	542.0
$Z, N \geq 8$	(1585)	(1515)	(1527)	(1424)
KTUY02	319.1	391.9	344.4	465.8
FRDM	416.7	551.6	409.0	514.2
HFBCS-1	464.6	506.1	483.3	529.0

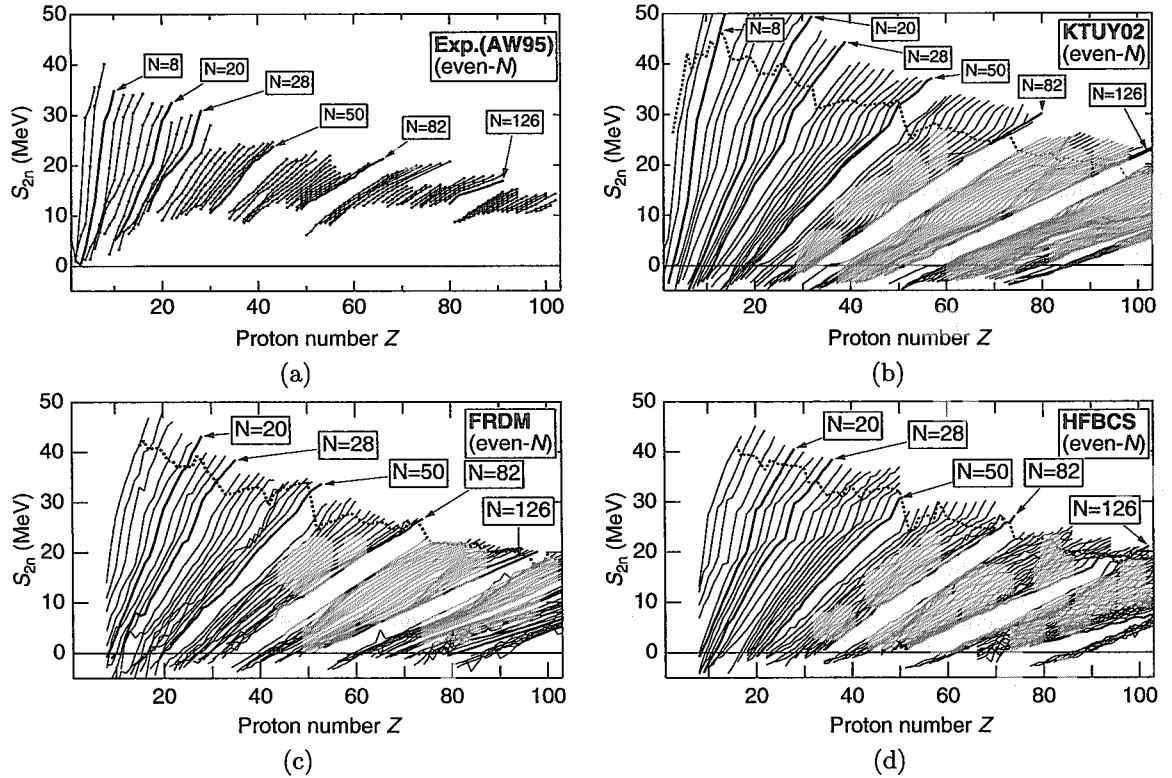


Figure 1: Two-neutron separation energies  $S_{2n}$  for even- $N$ . The solid lines connect the nuclei with the same  $N$ , and dashed line comments the proton-drip nuclei for fixed  $N$ 's. (a): experimental data, (b): KTUY02 (present formula), (c): FRDM, (d): HFBCS.



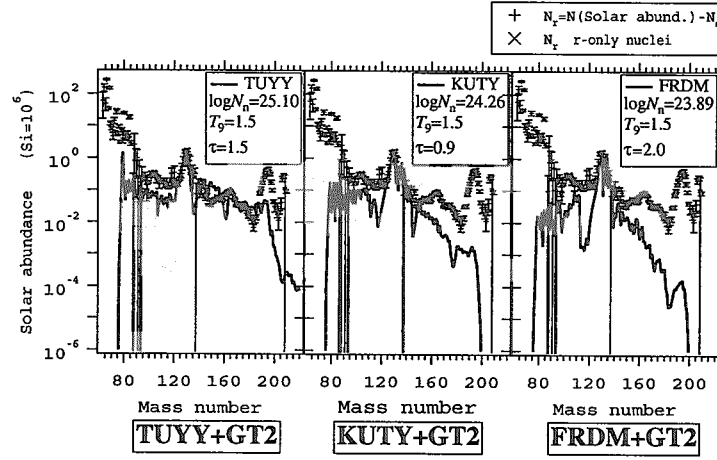


Figure 2: Relative r-process abundances estimated by using the canonical model. The crosses represent the solar system r-process abundances. Observed and calculated abundances are normalized to  $^{130}\text{Te}$ .

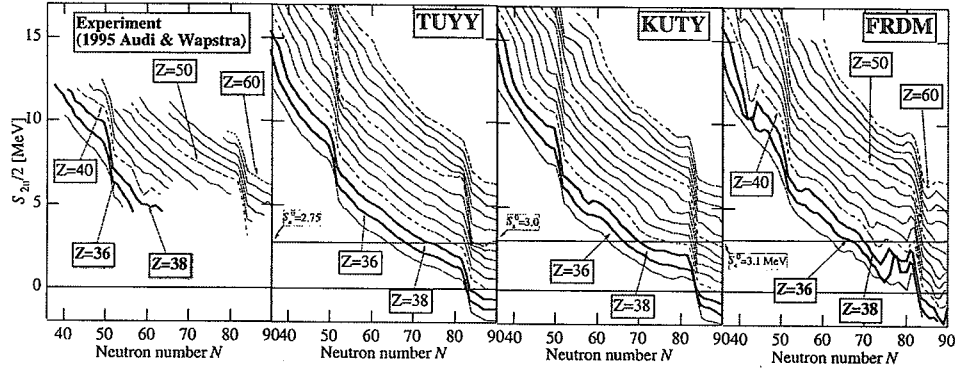


Figure 3: Two-neutron separation energies  $S_{2n}$  for even- $Z$ . The solid lines connect the nuclei with the same  $Z$ . The  $S_a^0$  line defined in Eq. (3) for each mass formula is also shown.

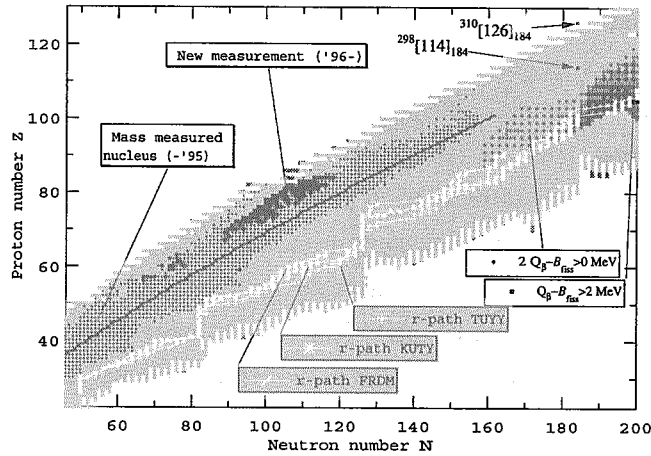


Figure 4: The r-process paths for each mass formula and the nuclei with  $Q_{\beta} - B_{\text{fiss}} > 0$  estimated from the KUTY mass formula.



## 2.6 Fragment Mass Distribution of the $^{239}\text{Pu}(\text{d}, \text{pf})$ Reaction at the Super-deformed $\beta$ -vibrational Resonance

K. Nishio<sup>1</sup>, H. Ikezoe<sup>1</sup>, Y. Nagame<sup>1</sup>, S. Mitsuoka<sup>1</sup>, I. Nishinaka<sup>1</sup>, L. Duan<sup>2</sup>, K. Satou<sup>1</sup>, M. Asai<sup>1</sup>, H. Haba<sup>1</sup>, K. Tsukada<sup>1</sup>, N. Shinohara<sup>1</sup>, S. Ichikawa<sup>1</sup>, T. Ohsawa<sup>3</sup>

1. *Advanced Science Research Center, Japan Atomic Energy Research Institute, Tokai-mura, Ibaraki 319-1195, Japan*

2. *Institute of Modern Physics, Chinese Academy of Sciences, 730000 Lanzhou, China*

3. *Department of Electrical & Electronic Engineering, School of Science & Engineering, Kinki University, Osaka 577-8502, Japan*

We measured, for the first time, the mass distribution of  $^{240}\text{Pu}$  fission fragments following the  $\beta$ -vibrational resonance, whose level is formed on the second minimum of the double-humped fission barrier. The distribution shows an asymmetric mass distribution similar to the one observed for thermal neutron-induced fission of  $^{239}\text{Pu}$  and isomeric fission of  $^{240}\text{Pu}$ . This indicates that the  $^{240}\text{Pu}$  system following the  $\beta$ -vibrational resonance descends into a fission valley which is identical to the fission valley of the  $^{240}\text{Pu}$ -isomer and  $^{239}\text{Pu}(\text{n}_{\text{th}}, \text{f})$ .

### 1. Introduction

For neutron-induced fission of  $^{239}\text{Pu}$ , there is an old investigation on the mass division following the neutron capture resonance [1,2]. The results [2] show, in the abundance of  $^{99}\text{Mo}$  and  $^{115}\text{Cd}$ , that fission through the  $J^\pi = 1^+$  state enhances the relative abundance of mass-asymmetric fission products ( $^{99}\text{Mo}$ ) compared to fission through the  $J^\pi = 0^+$  state. This was interpreted in [3] as an effect of the collective motion at the saddle point that the octupole vibration of  $K^\pi = 1^+$  with mirror asymmetry results in the enhanced mass asymmetry compared to the ground state of  $K^\pi = 0^+$ , namely the vibrational motion at the saddle point drives the system to the asymmetric fission mode (path). Supporting this interpretation, it would be natural to presume that when the  $\beta$ -vibration with  $K^\pi = 0^+$  is populated at the middle stage of the fission process the resulting fission may have a symmetric fission component larger than the thermal neutron-induced fission due to vibrational motion with mirror symmetry. We can find the  $\beta$ -vibrational state on the second minimum of the double-humped fission barrier (super-deformed minimum : SD). This state is observed below the threshold energy in the form of an enhanced fission cross section due to resonance tunneling induced when the excitation energy ( $E_{\text{ex}}$ ) of the compound nucleus matches the level [4,5,6,7].

We are interested in resonance fission through the  $\beta$ -vibrational state of  $K^\pi = 0^+$  built on the SD which has a mass symmetric shape [8]. We expect for this specific case that near-symmetric fission would be enhanced. In this paper we measured the mass distribution of fission fragments by gating on the  $\beta$ -vibrational resonance. Our choice for this study was  $^{240}\text{Pu}$  populated by  $^{239}\text{Pu}(\text{d}, \text{p})$

reaction. Plutonium-240 is one of the nuclei for which the properties of the  $\beta$ -vibrational state were extensively investigated. We have determined the excitation energy of  $^{240}\text{Pu}$  by measuring protons using silicon detectors as in [4].

## 2. Experimental Methods

The experimental setup is shown schematically in Fig. 1. The reaction  $^{239}\text{Pu}(d,pf)$  was used to study resonance fission of  $^{240}\text{Pu}$ . The 13.5 MeV deuteron beam was supplied by the JAERI-tandem accelerator, and the typical beam current was 5 nA. The  $^{239}\text{Pu}$  target was made by electrodeposition of  $^{239}\text{PuO}_2(\text{NO}_3)_2$  on a  $90 \mu\text{g}/\text{cm}^2$  thick nickel foil, and the target thickness was  $35 \mu\text{g}/\text{cm}^2$ .

The outgoing protons resulting from the (d,p) reaction were detected by a  $\Delta E$ -E telescope which consisted of  $300 \mu\text{m}$  ( $\Delta E$ ) and  $1500 \mu\text{m}$  (E) thick silicon detectors. The telescope was set at  $135^\circ$  relative to the beam direction with a solid angle of 45 msr. The protons were easily distinguished from deuterons and tritons on the  $\Delta$ -E map, allowing the selection of neutron transfer events.

Two fission fragments were coincidentally detected by two silicon PIN diodes, which were equipped on both sides of the target with a similar aperture. The center of the PIN diodes were set at  $90^\circ$  to the beam direction. The diodes which have an active area of  $1000 \text{ mm}^2$ , each, were masked by plates having a circular hole of 31.9 mm diameter, and each diode was viewed by the target at a solid angle of 1.25 sr.

## 3. Data Analysis

The energy resolution  $\Delta E$ -E telescope, namely the energy resolution for protons, was 55 keV(FWHM), which was determined by the elastic peak of the deuteron. The resolution includes the energy spread of about 30 keV arising from the kinetic effect. The proton energy was transformed to the excitation energy of  $^{240}\text{Pu}$  using the mass table of Ref. [9] (The  $Q$ -value for the ground state nuclear transfer in  $^{239}\text{Pu}(d,p)^{240}\text{Pu}$  is 4.31 MeV).

The calibration of the fission detectors is made by using the Schmidt formula [10] as follows. First, we constructed a pulse height spectrum,  $S(X)$ , by selecting the events in  $6.0 < E_{\text{ex}} < 7.0 \text{ MeV}$  as in Fig.2. This spectrum is close to that for the thermal neutron-induced fission of  $^{239}\text{Pu}$ , whose compound nucleus  $^{240}\text{Pu}$  has an excitation energy of 6.53 MeV. The solid curve in Fig.2 is the result of decomposing the experimental data to two Gaussian distributions having the same area. The centroid of two Gaussian components,  $P_L$  and  $P_H$ , obtained in the fitting process were used to determine the calibration constants in the Schmidt formula,

$$E(X, m) = (a + a' m) X + b + b' m, \quad (1)$$

$$a = c_1 / (P_L - P_H), \quad (2)$$

$$a' = c_2 / (P_L - P_H), \quad (3)$$

$$b = d_1 - a P_L, \quad (4)$$

$$b' = d_2 - a' P_H. \quad (5)$$

where  $E$  and  $m$  are the fragment kinetic energy and mass. We used the parameters  $(c_1, c_2, d_1, d_2) = (27.6654, 0.04106, 89.0064, 0.1362)$  for the  $^{239}\text{Pu}(n_{\text{th}}, f)$  given by Neiler *et al.* [11].

Fission fragment masses,  $m_1$  and  $m_2$ , were determined from the pulse height of both fragments,  $X_1$  and  $X_2$ , by following the mass and momentum conservation law. An iteration procedure was used to numerically determine the mass number of the fission fragment. In this analysis, we determined the primary fragment mass, i.e. mass before neutron evaporation. This needs a number of neutron emission as a function of fragment mass,  $\nu(m)$ , for which data of Tsuchiya *et al.* [12] were used.

#### 4. Experimental Results and Discussions

Figure 3 shows the proton-fission coincidence events plotted as a function of excitation energy of  $^{240}\text{Pu}$ . The energy bin is set at 50 keV corresponding to the present resolution. The resonance peak is observed at 5.05 MeV. For excitation energies below the neutron binding energy (6.53 MeV), where neutron emission is energetically hindered and the  $\gamma$ -ray emission is the only decay mode competing with fission in the decay channel, the spectrum in Fig.3 is related to the 'fission probability' multiplied by the 'population probability' of the compound nucleus in the transfer reaction  $^{239}\text{Pu}(d, p)^{240}\text{Pu}$ . The resonance energy of 5.05 MeV obtained in this work is close to that measured by Glassel *et al.* [6] and Hunyadi *et al.* [7].

By measuring the  $^{239}\text{Pu}(d, pf)$  reaction, fission events resulting from excitation energies near the first fission barrier height ( $E_A=5.80$  MeV [4]) could be obtained. We show firstly in Fig.4(A) the mass yield curve following the excited compound nucleus of  $6.0 > E_{\text{ex}} > 5.3$  MeV. The yield is normalized such that the sum of the yields becomes 200 %. The mass bin is set at 2.0 amu to gain statistics. This spectrum agrees with that for thermal neutron-induced fission of  $^{239}\text{Pu}$  by Wagemans *et al.* ( $E_{\text{ex}} = 6.53$  MeV) [13] shown by the solid curve. The data of [13] were obtained by measuring the kinetic energies of both fragments (2E method) by using silicon detectors similar to our experimental method.

Fission events through the vibrational resonance being characterized by their excitation energy between  $4.78 < E_{\text{ex}} < 5.30$  MeV (see Fig.3) result in the mass yield in Fig.4 (B). We set the mass bin as 5 amu. Although the mass yield curve constructed by using only about 80 events has a large uncertainty, the asymmetric fission character is evident, and the yield agrees with that for  $^{239}\text{Pu}(n_{\text{th}}, f)$  as well as the gross trend that the sharp rise in the near symmetric region when going from the heavy fragment mass  $m_H = 125$  amu to 135 amu and the gradual decrease in the far asymmetric region from  $m_H = 140$  amu to 160 amu. The yield reaches the maximum at around  $m_H = 135$  amu for all spectra shown in Fig.4. We have determined the average value of the heavy fragment mass as  $\langle m_H \rangle = 140.2 \pm 2.8$  amu, where the error comes from the binning and the uncertainty arising from the energy calibration process. This agrees with the value  $139.8 \pm 1.1$  amu obtained from the spectra in Fig.4(A) within the error and with the value 139.7 amu for  $^{239}\text{Pu}(n_{\text{th}}, f)$  [13]. The present data then lead to the conclusion that fission through the  $\beta$ -vibrational resonance does not show any significant

enhancement in the symmetric mass division within the error.

We want to show in Fig.4(C) the mass yield for the fission of shape isomer in  $^{240}\text{Pu}$  [14] (half-life is 3.8 ns [15]). This is localized in the SD of the double-humped fission barrier (2.25 MeV above the ground state) [7], and has the  $(J^\pi, K)$  value of  $(0^+, 0)$ . Isomeric fission forms a good reference in the sense that the nuclear shape is the same as that experienced by the  $\beta$ -vibrational fission. Isomeric fission forms a mass distribution similar to that for  $^{239}\text{Pu}(n_{\text{th}}, f)$  and hence to the  $\beta$ -vibrational fission in Fig.4(B).

## 5. Conclusions

Motivated by the speculation that the  $\beta$ -vibration on the SD of the double-humped fission barrier would result in an enhancement of the symmetric mass components, the mass distribution of  $^{240}\text{Pu}$  following the resonance tunneling originating from this level was measured for the first time. The obtained distribution shows an asymmetric mass division similar to the one for the thermal neutron-induced fission of  $^{239}\text{Pu}$  and the isomeric fission of  $^{240}\text{Pu}$ . This indicates that the system through  $\beta$ -vibrational resonance comes out in the asymmetric fission valley that the  $^{240}\text{Pu}$ -isomer and  $^{239}\text{Pu}(n_{\text{th}}, f)$  descend.

## Acknowledgments

The authors thank the crew of the JAERI-tandem facility for the beam operation. Special thanks are due to Dr. T. Nakagawa of Nuclear Data Center in JAERI for the calculation of thermal neutron-induced fission cross section from the  $J^\pi=0^+$  and  $1^+$  states. The present study is supported by the REIMEI Research Resources of Japan Atomic Energy Research Institute.

## References

- [1] R.B. Regier, W.H. Burgus, R.L. Tromp, and B.H. Sorensen, *Phys. Rev.* **119** (1960) 2017.
- [2] G.A. Cowan, B.P. Bayhurst, R.J. Prestwood, J.S. Gilmore, and G.W. Knobeloch, *Phys. Rev.* **144**, 979 (1966).
- [3] A. Michaudon, *Advances in Nuclear Physics*, Presum Press (1973), Vol.6, p.1.
- [4] B.B. Back, J.P. Bondorf, G.A. Otroschenko, J. Pedersen, B. Rasmussen, in *Proceedings of the IAEA Symposium in Physics and Chemistry of Fission*, Vienna, IAEA, p.351 (1969). B.B. Back, J. Bondorf, G. Otroschenko, J. Pederson and B. Rasmussen, *Nucl. Phys. A* **165**, 449 (1971). B.B. Back, O. Hansen, H.C. Britt, J.D. Garrett, *Phys. Rev. C* **9**, 1924 (1974).
- [5] H.J. Specht, J.S. Fraser, J.C.D. Milton, W.G. Davies, in *Proceedings of the IAEA Symposium in Physics and Chemistry of Fission*, Vienna, IAEA, p.363 (1969)
- [6] P. Glassel, H. Rosler and H.J. Specht, *Nucl. Phys. A* **256**, 220 (1976).
- [7] M. Hunyadi, D. Gassmann, A. Krasznahorkay, D. Habs, P.G. Thirolf, M. Csatos, Y. Eisermann, T. Faestermann, G. Graw, J. Gulyas, R. Hertenberger, H.J. Maier, Z. Mate, A. Metz, M.J. Chromik, *Phys. Lett. B* **505**, 27 (2001).

- [8] Mass symmetry at the second minimum (SD) is predicted in the calculation of the potential energy surface as seen in P.A. Butler, W. Nazarewicz, Rev. Mod. Phys. **68**, 349 (1996).
- [9] G. Audi, and A.H. Wapstra, Nucl. Phys. **A595**, 409 (1995).
- [10] H.W. Schmitt, W.M. Gibson, J.H. Neiler, F.J. Walter and T.D. Thomas, in Proceedings of the Symposium on Physics and Chemistry of Fission, Vol.1, IAEA (1965) p.531.
- [11] J.N. Neiler, F.J. Walter and H.W.Schmitt, Phys. Rev. **149**, 894 (1966).
- [12] C. Tsuchiya, Y. Nakagome, H. Yamana, H. Moriyama, K. Nishio, I. Kanno, K. Shin and I. Kimura, J. Nucl. Sci. Technol. **37**, 941 (2000).
- [13] C. Wagemans, E. Allaert, A. Deruytter, R. Barthelémy, and P. Schillebeeckx, Phys. Rev. C **30**, 218 (1984).
- [14] J. Weber, H.J. Specht, E. Konecny, and D. Heunemann, Nucl. Phys. **A221**, 414 (1974).
- [15] H.C. Britt, B.H. Erkkila and B.B. Back, Phys. Rev. C **6**, 1090 (1972).

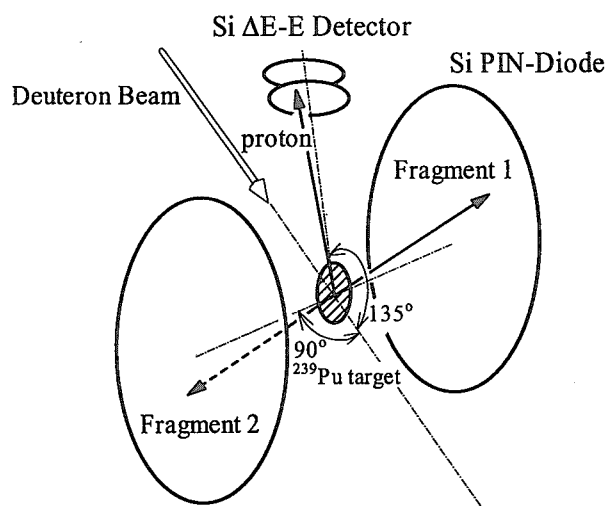


Fig. 1 Experimental setup for the fission fragment mass distribution in the  $^{239}\text{Pu}(\text{d,pf})$  reaction.

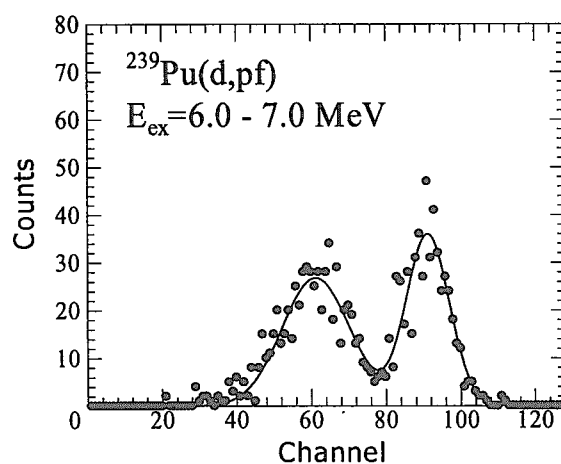


Fig. 2 Pulse height spectrum  $S(X)$  of fission fragment obtained in the silicon PIN diode. Curve is the result of the fitting of the spectrum to two Gaussian distributions with equal areas.

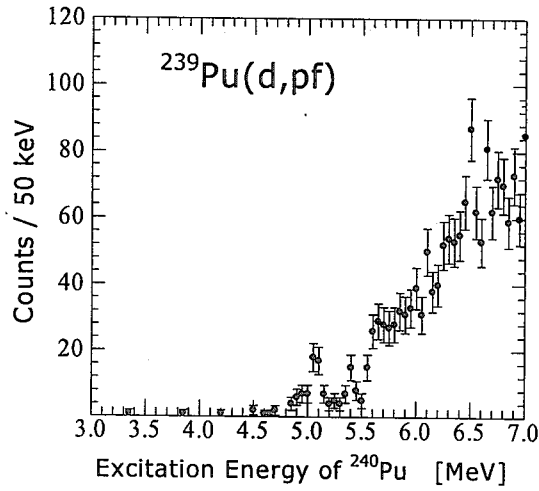


Fig. 3 Number of coincidence events between fission fragments and proton plotted as a function of excitation energy of  $^{240}\text{Pu}$ .

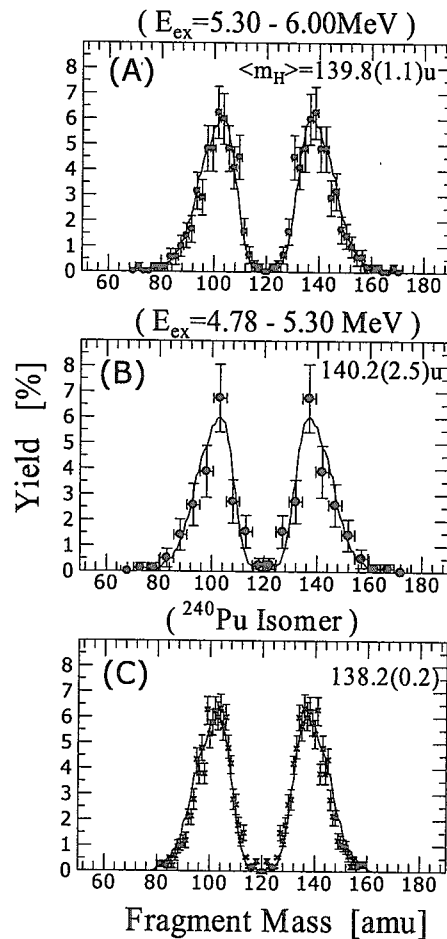


Fig. 4 Mass yield curves obtained for the  $^{239}\text{Pu}(d, pf)$  reaction ( (A) and (B) ). These spectra are made by setting the excitation energy range as (A)  $6.0 > E_{\text{ex}} > 5.3$  MeV and (B)  $5.30 > E_{\text{ex}} > 4.78$  MeV. The average value for the heavy fragment mass  $\langle m_H \rangle$  is shown in each section of the figure. The error shown in (A) and (B) comes from the binning and the uncertainty arising from the energy calibration process. Mass yield curve for the isomer fission [14] is shown in (C). Solid curve appearing in the every section is the data for  $^{239}\text{Pu}(n_{\text{th}}, f)$  [13].



## 2.7 Requests on Domestic Nuclear Data Library from BWR Design

Hiromi MARUYAMA

Global Nuclear Fuel - Japan Co., Ltd.

3-1, Uchikawa 2-Chome, Yokosuka-Shi, Kanagawa-Ken 239-0836

E-mail: Hiromi.Maruyama@gnf.com

Requests on the domestic nuclear data library JENDL and activities of the Nuclear Data Center have been presented from the perspective of BWR design and design code development. The requests include a standard multi-group cross section library, technical supports, and clarification of advantage of JENDL as well as requests from physical aspects.

### 1 Introduction

The domestic nuclear data library JENDL3.3 [1] was released in May 2002. In order that the efforts made for the domestic nuclear data library development may not end up being a waste, it is important to prepare a way for use of the domestic nuclear data library in design works. User's opinions will be informative for this purpose. This paper summarizes requests on the domestic nuclear data library and activities of the Nuclear Data Center from various viewpoints of BWR design; requests from the viewpoint of physical aspects in BWR fuel/core designs are described in Chapter 2, those from the standpoint of design code development in Chapter 3, and those from the angle of the domestic nuclear data library utilization in Chapter 4.

### 2 Physical Aspects in BWR Fuel and Core Design

#### 2.1 Improvement of Current BWR

Recent BWR core designs are characterized with

- high burn-up,
- plutonium utilization in thermal reactors,
- long-cycle operation, and
- up-rate of reactor power

in the extension of a current BWR design.

High burn-up design is effective for reducing the amount of spent fuel disposal and fuel cycle cost. High burn-up BWR fuel designs [2] are proceeding step by step; a target discharge exposure of conventional 8x8 fuel was 28GWd/t, and those of high burn-up fuels Step-I, Step-II, Step-III were 33GWd/t, 39.5GWd/t, and 45GWd/t, respectively, as shown in Fig.1. From Step-I to Step-III fuel, various items such as reliability and thermal margin were



improved so as to keep fuel integrity. The fuel cycle cost of Step-III was reduced by 30% compared with conventional 8x8 fuel.

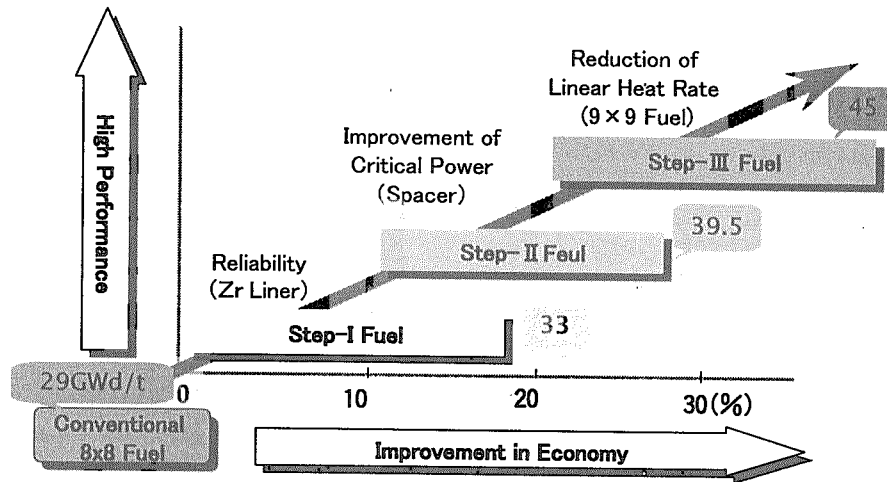


Fig. 1 High Burn-Up Fuels Used in BWR

Figure 2 shows the FP contribution to total absorption rate in a fuel rod as a function of discharge exposure. The FP absorption contribution increases with exposure; for example, the FP contribution increases by 50% when discharge exposure increases from 30 GWd/t to 60 GWd/t. Therefore, accurate evaluation of the FP absorption contribution is important for the high burn-up designs.

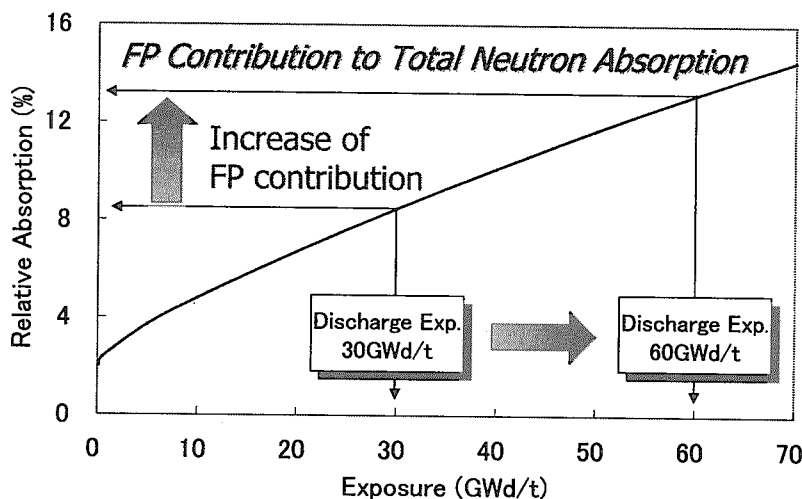


Fig. 2 FP Contribution to Total Neutron Absorption in UO<sub>2</sub> Fuel

In the plutonium utilization in thermal reactors (Pu thermal utilization), the higher actinide contribution to the total absorption rate increases as shown in Fig. 3. This figure shows that this contribution is more significant in MOX fuel than in UO<sub>2</sub> fuel. Hence, more attention should be paid to the accuracy of higher actinide cross sections in MOX fuel design.

than in UO<sub>2</sub> fuel design.

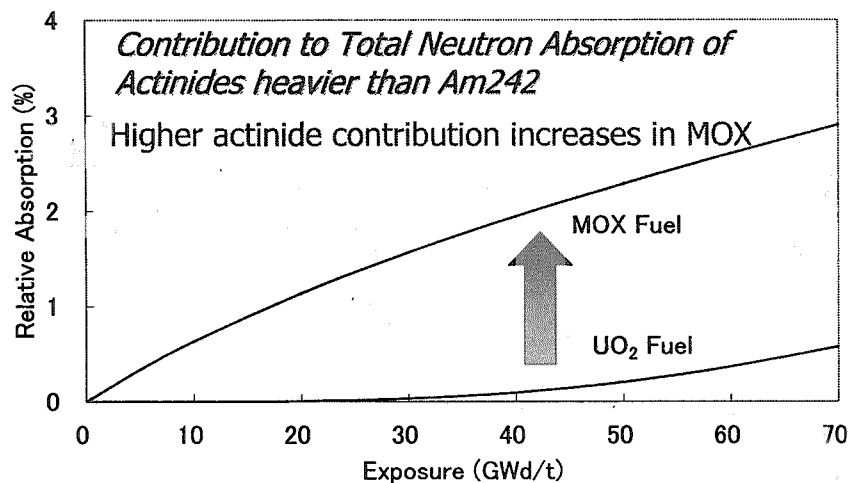


Fig. 3 Higher Actinide Contribution to Total Neutron Absorption

Long-cycle operation improves the plant utilization factor. In this operation, a control of excess reactivity is a key technique, and new kinds of burnable absorber might be adopted in place of gadolinia. Therefore, the cross section of various absorber materials must be prepared for the long-cycle operation design. Accurate thermal margin evaluation is important for up-rate of reactor power. For this purpose, every type of cross sections must be prepared with sufficient accuracy as basic data of the design works.

## 2.2 Next Generation BWR

New core concepts for next generation BWR [3] are investigated these days in order to maintain stable energy supply in the future. Some of these designs improve a conversion ratio up to 1.0 or more, using tight-pitch lattices with low H/HM ratios. Others [4] aim at an effective use of Pu for saving uranium resources, in which design high moderation MOX core is used. Further refinement in resonance treatment is required for evaluations of core performances such as conversion (or breeding) ratio in the former design. In the latter design, higher actinide and FP contributions are important as in Pu thermal utilization. These new designs also require various cross-sections and chain data for a sufficient number of nuclides.

## 3 Design Code Development

We are concerned about the decreasing number of nuclear data specialists in the BWR fuel/plant makers. The fact that very few nuclear data specialists are in the analysis method development staff makes it difficult to get various kinds of information on nuclear data and to investigate group constants processing methods. The design codes use the processed group constants, instead of nuclear data themselves given in the nuclear data library such as

JENDL. Therefore, even if the nuclear data were accurate and elaborate, the group constants processed incorrectly from the nuclear data library would result in poor design codes. Accuracy of nuclear data library strongly links with group constant processing methods in design use.

We request that the nuclear data center should provide the following technical supports in this field:

- To provide nuclear data information,
- To provide a standard multi-group cross-section library, and
- To provide handling techniques for effective cross-sections and kinetic parameters.

It is desirable that the standard multi-group cross-section library with 200 or more energy groups is commonly used for fast and thermal reactors. Standardization of the cross-section library and its handling technique makes open environments and make it easy to accumulate experience of nuclear data library usage, leading to a highly accurate nuclear data library.

#### 4 Domestic Nuclear Data Library Utilization

A merit of maintaining the domestic nuclear data library is that it can reflect our design activities such as critical experiments and reactor operation tracking. A good example is Am241 absorption cross section reflected in JENDL3.3, which was thought to be a primary cause of a critical eigenvalue overprediction in the MISTRAL full MOX critical experiments conducted by NUPEC. In the future, when Japan must select its original reactor such as the next generation BWR described above in its particular resource situation, the domestic nuclear data library will play a more important role than now.

However, the fact is that very few design codes adopt JENDL in the official design procedures even in Japan. Why?

Japanese design codes have something to do with foreign companies as their developers or users. Moreover, chances to collaborate in design work or method development with foreign companies are increasing recently. In these collaborations, common nuclear data such as cross-sections, nuclide chain data and kinetic data are required, because differences in such fundamental data make essential discussion difficult. However, the choice of nuclear data library is not so easy because the accuracy of the nuclear data library is not clear. As a result, we are apt to select a well-known nuclear data library such as ENDF.

The request on the use of the domestic nuclear data library is that the advantage of JENDL should be clarified compared with other libraries such as ENDF and JEF through international benchmark analysis, including operating reactor cases, for nuclear data library comparison. It is more preferable that the domestic nuclear data library provides cross-sections, nuclide chain data, and kinetic parameters consistent with those of other libraries.

## 5 Conclusion

The requests on the domestic nuclear data library from the standpoint of BWR design and design method development are summarized as follows:

- (1) To provide the neutron and photon cross-sections for a sufficient number of higher actinides, FP nuclides and burnable absorbers with sufficient accuracy,
- (2) To provide technical support related to nuclear data use, such as standard multi-group cross-section libraries and their handling methods, and
- (3) To clarify the advantage of JENDL nuclear data compared with other nuclear data files such as ENDF and JEF, or to provide cross-sections, kinetic-related data and nuclide chain data consistent with those files.

## Reference

- [1] Shibata K. et al.: J. Nucl. Sci. Technol., 39[11], p.1125 (2002)
- [2] Tanabe A. et al.: "Advances in Nuclear Fuel Technology- (2) Advances in Nuclear Fuel Technology for LWRs" (in Japanese), Journal of Atomic Energy Society of Japan, 44[7], p.536 (2002)
- [3] Okubo T. et al.: "Present Status of Study on Reduced-Moderation Water Reactors", JAERI-CONF-2001-013, p4, 117(2001)
- [4] Hamamoto K. et al.: "High Moderation MOX Cores for Effective Use of Plutonium in LWRs" (in Japanese), Journal of Atomic Energy Society of Japan, 43[5], p.503 (2001)



## 2.8 Proposals for Nuclear Data Activities from PWR Core Design

Yoshihisa Tahara

Reactor Core Engineering Department Mitsubishi Heavy Industries, Ltd.

3-1, Minatomirai 3-chome, Nishi-ku Yokohama, 220-8401 Japan

e-mail: tahara@atom.hq.mhi.co.jp

A direction of nuclear data activities and requirements are discussed in this paper. The discussions suggest actual guides to promote utilization of nuclear data.

### 1. Introduction and discussions

A nuclear data file of JENDL-3.3 was opened this year[1]. This is good news to those relating to atomic energy in Japan. But, I remember that Dr. Kimura pointed out that the Japanese evaluated nuclear data are seldom adopted in safety design and safety evaluation of light water reactors and hardly found in related safety regulatory guidelines and standards except the decay heat [2].

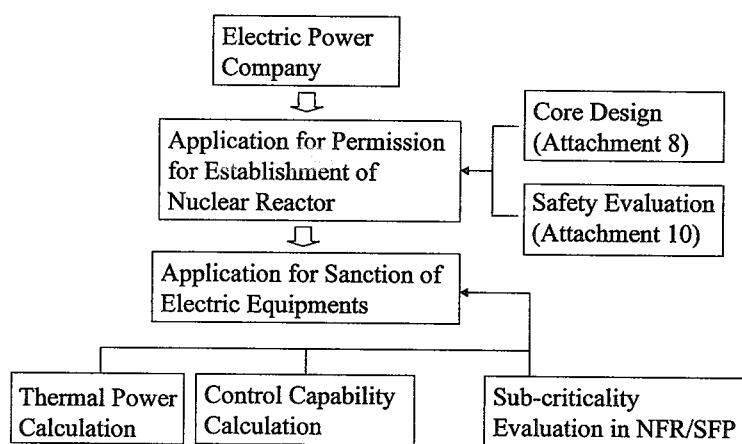


Fig. 1 Plant licensing application flow in Japan

Originally, nuclear data libraries were imported from U.S. with core design codes. However, Japan has already its own evaluated nuclear data. Although even the important nuclear data such as  $^{235}\text{U}$  and  $^{238}\text{U}$  are still being reevaluated and may be revised in future, now is the best time to begin using Japanese nuclear data. Plant licensing application flow is shown in Fig.1. Nuclear data are used in Core Design (Attachment 8), Control Capability Calculation and Sub-criticality Evaluation in New Fuel Rack (NFR)/ Spent Fuel Pit (SFP). Decay heat is used in Safety Evaluation (Attachment 10). It takes long time to validate nuclear data in core design and nuclear data can hardly changed from viewpoint of licensing. However, once Japanese nuclear data are used, the utilization will be accelerated and they will be widely used in reactor core design calculations and safety analyses. Therefore, Japanese nuclear data must be used first in plant licensing application to promote its use. To achieve this, I think the followings are needed: (a)

Establish a user support system; (b) Clarify the core parameter prediction uncertainty due to nuclear data uncertainties; (c) Assure activity of nuclear data evaluation and user support.

## 2. Proposals

I propose the following practical guides to reflect the above discussions.

### (1) Nuclear data should be opened with its processing code

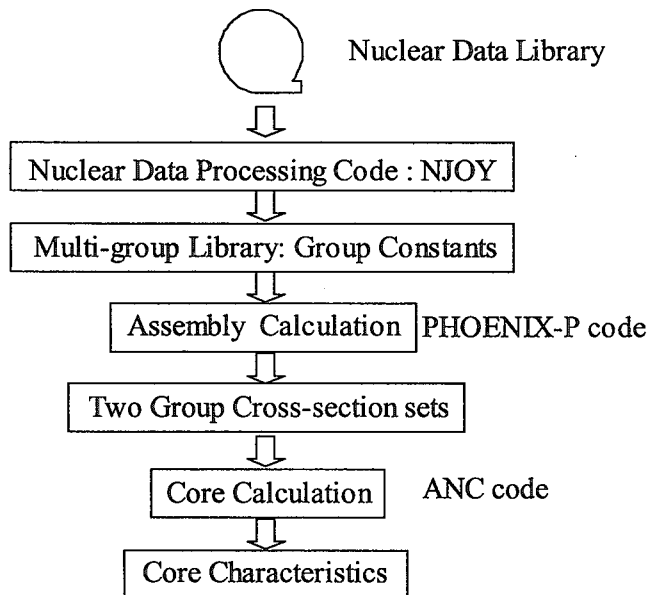


Fig. 2 Flow of Neutronics Calculation

The flow of neutronics calculation is shown in Fig.2. Multigroup library for assembly transport calculation code is generated using NJOY code. However, a lot of troubles have occurred in processing JENDL-3.3 nuclear data with the NJOY code. So, nuclear data processing code should be opened and maintained with nuclear data.

### (2) Benchmark problems with detailed specifications and information should be opened

To verify the adequacy of nuclear data, Benchmark calculations were performed using TCA, TRX critical experiments. However, recalculation and

confirmation of adequacy of nuclear data were never done and reported by any plant makers or software companies because the details of the benchmark calculations were not opened. To promote use of Japanese nuclear data, confirmation is needed and benchmark problems and reference solutions should be opened with detailed input lists for the codes used in the reference calculations.

Moreover, the benchmark calculations were done at cold conditions (20°C), but commercial reactor cores are operating at higher temperatures, therefore, benchmark analyses should be done using high temperature experiments for instance KRITZ performed at 20°C to 245°C.

Such analyses are beneficial to evaluation of Doppler effect from cold to hot conditions. In addition to critical experiments, PIE analyses and Core analyses should be performed to verify nuclear data of higher actinides and fission products during fuel depletion. These tasks should be shared in nuclear data committee and done by working groups. The results should be integrated and opened as an evaluation result of nuclear data.

### (3) Establish a user support system

To avoid the difficulties as described above (1), users are hoping that a user support sys-

tem will be established in Nuclear Data Center. They will feel rather strongly that the nuclear data is reliable and that they are supported if the benchmark problems described above (2) are discussed and communication with the support center is maintained.

(4) Uncertainty should be evaluated using benchmark problems

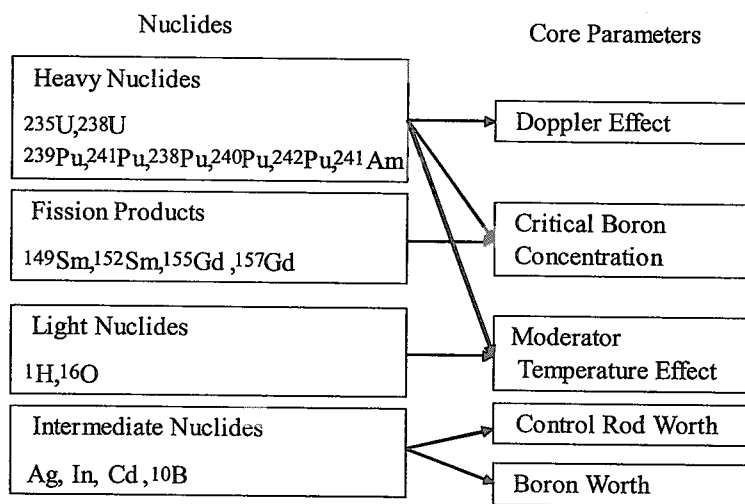


Fig. 3 Nuclides affecting core parameters

The relation of core parameters and nuclides that affect them are shown in Fig.3. In actual core design, critical boron concentration is one of the most important parameters from safety and economical efficiency viewpoint. That is, the core reactivity with fuel depletion must be predicted accurately. Therefore, uncertainty of  $k_{\text{eff}}$  due to nuclear data uncertainty should be evaluated and opened with nuclear data.

For this purpose, benchmark problems should be established first. Nuclear

parameters to be evaluated ( $k_{\text{eff}}$ , Doppler effect etc.) should be also determined. These benchmark problems may be critical experiments, unit pin cell calculation, unit assembly calculation or core calculation.

(5) Standard nuclear data libraries should be prepared for common use

When developing or comparing calculation methods, and clarify the calculation accuracy, standard or common libraries will play a very important role and produce useful and beneficial results. Multigroup libraries and continuous energy libraries should be prepared based on the same nuclear data. For multigroup libraries, energy shielding methods of F-table method (SRAC type library) and resonance integral table method (WIMS type library) should be prepared for extended use of the libraries. ORIGEN is widely used for simple and extensive study. So, ORIGEN libraries should be also prepared.

(6) Assure activity of nuclear data evaluation and user support

Nuclear data are basis of neutronics calculations and used in plant licensing applications. Therefore they must be reliable and valid and maintained for some period. In order to continue to improve nuclear data quality and keep user support, activity of nuclear data must be assured to Nuclear Data Center.

## References

- [1] JENDL HP: [http://www.ndc.tokai.jaeri.go.jp/jendl/jendl\\_J.html](http://www.ndc.tokai.jaeri.go.jp/jendl/jendl_J.html)
- [2] Kimura I.: JAERI-Conf 2000-005 p.9 (2000).



## 2.9 Requests on Nuclear Data in the Backend Field through PIE Analysis

Yoshihira Ando<sup>1)</sup>, Yasushi Ohkawachi<sup>2)</sup>

1) TOSHIBA Corporation  
Power System & Services Company  
Power & Industrial Systems Research & Development Center  
4-1 Ukishima-cho, Kawasaki-ku, Kawasaki 210-0862, Japan  
E-mail:yoshihira.ando@toshiba.co.jp

2) Experimental Reactor Division, Irradiation Center, O-arai Engineering Center  
Japan Nuclear Cycle Development Institute  
4002 Narita, O-arai, Ibaraki 311-1393 JAPAN  
E-mail:okawachi@oec.jnc.go.jp

### 1. Introduction

The working group on evaluation of nuclide generation and depletion is active in response to requests from the industry group in the backend field.

Accurate evaluations of fuel composition, neutron/gamma production, radioactivity and decay heat for spent fuel are requested in the backend field. The ORIGEN2 code is widely used to evaluate these quantities in the industry. This WG, therefore, prepares ORIGEN2 libraries for LWR and FBR based on JENDL-3.2 reflecting user requests[1]. Fuel compositions for spent fuels are basic quantities to be used in the criticality safety analysis and radiation shielding. So, the accuracy of fuel compositions for LWR and FBR spent fuels have been investigated through PIE analysis using recent nuclear data such as JENDL-3.2.

Hereafter, the present status of fuel composition analysis for LWR and FBR (fast reactor spent fuel) and the requests for nuclear data are described. After that, the reason of discrepancies between measured and calculated values will be studied by the sensitivity analysis.

### 2. Present status of fuel composition analysis for LWR and fast reactor spent fuels

#### 2.1 Fuel composition analysis for LWR spent fuels

In JAERI, spent fuel composition irradiated in commercial PWR and BWR have been measured and analyzed by burn-up code[2].

Irradiation data on measured fuels are shown in Table 1 and measured nuclides are shown in Table 2.

Results of fuel composition analyses by burn-up code SWAT (SRAC-ORIGEN2) are shown in Fig. 1, in which nuclear data are JENDL-3.2+JNDC-V2 and unit-cell models mock-up the sample rods considering actual irradiation histories are used.

Accuracy of analyses for U and Pu isotopes are quite good ( $|C/E-1| < 5\%$ ). But, errors for Am-241 are  $+10 \sim 20\%$  and those for major neutron production nuclide (Cm-242 and Cm-244) are large ( $-15 \sim 50\%$  for Cm-242,  $-23 \sim 26\%$  for Cm-244).

On the other hand, accuracy of analyses for fission products are good ( $|C/E-1| < 10\%$ ) except Sm-152.

From the above results, we have the following remarks..

- It is possible to reduce large margin assumed in the present criticality analysis for spent fuels based on the burnup code considering actual irradiation histories
- It is desired that the insufficient accuracy for Cm242 and Cm244 will be improved

#### 2.2 Fuel composition analysis for fast reactor spent fuel

Post irradiation examination (PIE) analysis of for the fast reactor JOYO mixed oxide spent fuel has been carried out. The outline of the measured spent fuel is shown in Table 3. It has been originally irradiated at the 2<sup>nd</sup> row and it was later moved to the



4<sup>th</sup> row and irradiation has been continued until the fuel burn-up reached approximately 58.2GWd/Mt. The irradiation position of the measured spent fuel and PIE positions are shown in Fig. 2. The PIE has been carried out for three fuel pins (No.7, 76, C1). Axial positions examined are the core center height, as well as the upper and lower ends of the fuel region.

Burn-up composition is calculated using ORIGEN2 code. One-group cross-section was collapsed from the 73 group constant set based on JENDL-3.2, using the neutron spectrum of each PIE position, which was calculated using CITATION. The neutron flux used as an input to the ORIGEN2 was calculated by the JOYO core management code system.

The comparison between the calculated and measured burn-up composition is shown in Fig. 3. Calculated results of U, Pu and <sup>148</sup>Nd agree well with measured values. Am isotopes, <sup>242</sup>Cm and <sup>244</sup>Cm are overestimated, and <sup>237</sup>Np and <sup>243</sup>Cm are underestimated. The reason for the disagreement is understood to be that the capture cross-section of Am isotopes are underestimated, and that of <sup>237</sup>Np and <sup>243</sup>Cm are overestimated.

### 3. Studied on capture cross sections for TRUs

Large errors for TRUs capture cross section on JEF2.2 were indicated from the CEA experiment mock-up thermal and epi-thermal reactor[3]

Discrepancies for capture cross sections of heavy nuclides between APOLLO-1 calculations using JEF-2.2 and experiments are shown in Table 4.

The comparison for capture cross section of TRUs between JENDL-3.2 and JEF-2.2 is shown in Table 5.

Errors for capture cross sections of TRUs in JENDL-3.2 assumed from the combination of Table 4 and 5 are shown in Table 6.

We study through PIE analysis with cross section considering assumed error for Am-241 capture cross section shown in Table 5. The analysis by burn-up code MCNP-ORIGEN2[4] has been performed for the one of BWR sample rods shown in Table 1, in which JENDL-3.2+JNDC-V2 is used and analytical model is BWR assembly model with reflective boundary condition shown in Fig.4.

To investigate the effect of error on Am-241 capture cross section, we perform the calculation with +25% correction for Am-241 capture cross section at all burnup steps in addition to the no correction calculation.

The results of comparison for actinide compositions between two calculations are shown in Fig.5 for U-isotopes, Fig. 6 for Np and Pu-isotopes and Fig.7 for Am and Cm-isotopes.

The effect to actinide compositions caused by the correction of Am-241 capture cross section are

- U-234~238: very small (<0.3%)
- Np-237: small (~3%)
- Pu- 238~242 : small (<1%)
- Am-241: large (-15%)
- Am-242,242m: large (+7%)
- Cm-242: large (+9%)
- Cm-244: small (+0.1%)

Accuracy of TRUs compositions in the analysis for LWR spent fuels considering the above effects are summarized as follows.

The overestimation of Am-241(10~20%) is well solved, but the underestimations of Cm-242 (-15~50%) and Cm244 (-23~26%) are solved partly in the analysis using the +25% correction for Am241 capture cross section in JENDL-3.2.

We, therefore, wish that the improvement of cross sections for actinides beyond Pu are very important to improve the accuracy of PIE analysis.

#### 4. Conclusion

From studies on nuclear data related to the backend field based on activities of our WG, we have the following remarks..

- The burnup codes used in our WG such as SRAC, SWAT and ORIGEN with cross sections considering actual neutron spectrum has been verified through PIE analysis based on JENDL-3.2
- It is possible to reduce large margin assumed in the present criticality analysis for spent fuels using the verified burnup codes
- It is desired that the nuclear data files for Cm-242 and Cm-244 will be revised to improve the accuracy of PIE analysis

Our wishes is to use improved nuclear data to be solved the problems in our studies.

#### Acknowledgment

This report is supported by the activity of the working group on evaluation of nuclide generation and depletion The authors would like to express thanks to members of the working group.

#### References

- [1] K.Suyama, J.Katakura, Y.Ohkawauchi, M.Ishikawa "Libraries based on JENDL-3.2 for ORIGEN2 code : ORLIBJ32", *JAERI-Data/Code* 99-003, (1999)
- [2] Y.Nakahara, K.Suyama, T.Suzaki eds "Technical Development on Burn-up Credit for Spent LWR Fuel", *JAERI-Data/Tech* 2000-071, (2000)
- [3] S. Cathalau and A.Benslimane, "Qualification of JEF-2.2 Capture Cross-Sections for Heavy Nuclides and Fission Products" Proc. of Global'95 pp1537-1544 (1995)
- [4] Y.Ando, K.Yoshioka, I.Mitsubishi and K.Sakurada, "Development and Verification of Monte Carlo Burnup Calculation System" to be published in ICNC-2003 (2003)

Table.1 Irradiation Data on Measured LWR Fuels

Reactor Type	BWR	PWR
Irradiation Plant	Fukushima-2	Takahama-3
Burnup (GWd/Mt)	4~44	8~48
Void History (%)	0~73	—
No. of Data	17	16

Table.2 Measured Nuclides for LWR Fuels

Actinide (18 Nuclides)		Fission Product (17 Nuclides)	
Element	Nuclides	Element	Nuclides
U	U 234, U 235, U 236, U 238	Cs	Cs134, Cs137
Np	Np237	Ce	Ce144
Pu	Pu238, Pu239, Pu240, Pu241, Pu242	Nd	Nd143, Nd144, Nd145, Nd146, Nd148, Nd150
Am	Am241, Am242m, Am243	Eu	Eu154
Cm	Cm242, Cm243, Cm244, Cm245, Cm246	Sm	Sm147, Sm148, Sm149, Sm150, Sm151, Sm152, Sm154

Table 3 Outline of the Measured Spent Fuel

MOX Fuel Content	U-235 Enrichment : 18.6wt%	
	Pu Content : 28.5wt%	
Irradiation Condition	Core Resident Period : Dec. 14, 1990~Sep. 24, 1997	
	Address : 2 <sup>nd</sup> Row(2B1)	Address: 4 <sup>th</sup> Row(4D1)
	Irradiation Days:171	Irradiation Days:285
	$\Phi_{\text{total}} : 3.3 \times 10^{15} \text{n/cm}^2 \text{s}$ (Subassembly Averaged)	$\Phi_{\text{total}} : 2.1 \times 10^{15} \text{n/cm}^2 \text{s}$ (Subassembly Averaged)
$\Phi_{\text{total}}$ (Subassembly) Averaged	$9.9 \times 10^{22} \text{n/cm}^2$	
Burn-up (Subassembly Averaged)	58.2GWd/Mt	

Table 4 %-(C/E-1) for capture cross sections of heavy nuclides between APOLLO-1 calculations using JEF-2.2 and experiments

Nuclide	SHERWOOD	ICARE/S
U238	$+1.1 \pm 1.8$	$+5.3 \pm 2.5$
Pu238	—	$+16.0 \pm 12.0$
Pu239	$+2.6 \pm 1.6$	$+1.0 \pm 8.0$
Pu240	$+1.9 \pm 1.6$	$+0.1 \pm 3.2$
Pu241	$+5.6 \pm 10.0$	$-4.7 \pm 6.1$
Pu242	$-0.3 \pm 3.2$	$-12.3 \pm 6.4$
Am241	$-20.0 \pm 15.0$	$-20.0 \pm 11.0$
Am243	$-22.4 \pm 5.0$	—
Cm244	$+7.9 \pm 12.3$	—

Value :  $(C/E-1) \pm 2\sigma$  in %

SHERWOOD : Square lattice experiment mock-up thermal reactor

ICARE/S : Tight lattice experiment mock-up epi-thermal reactor

Table 5 Comparison for TRUs capture cross section between JENDL-3.2 and JEF2.2

Nuclide	Thermal (2200m/sec)			Resonance Integral		
	JENDL-3.2	JEF-2.2	JENDL/JEF	JENDL-3.2	JEF-2.2	JENDL/JEF
Am241	600.4	616	0.97	1305	1450	0.90
Am243	78.50	75.94	1.03	1823	1810	1.01
Cm244	15.10	14.41	1.05	660	634	1.04

Where, cross sections are in barns

Table 6 %-errors for capture cross sections of TRUs in JENDL-3.2  
assumed from the combination of Table 3 and 4

Nuclide	Thermal	Epi-thermal
Am241	$-23.0 \pm 15.0$	$-30.0 \pm 11.0$
Am243	$-21.7 \pm 5.0$	—
Cm244	$+8.3 \pm 12.3$	—

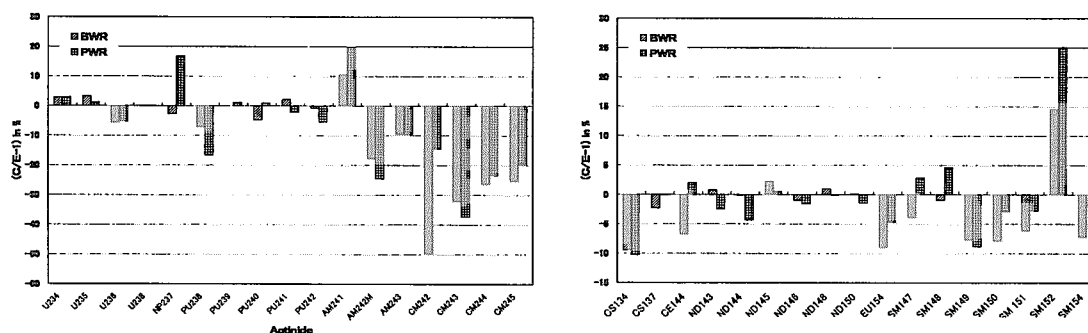


Fig.1 Results of SWAT Analyses for LWR Spent Fuels based on JENDL-3.2

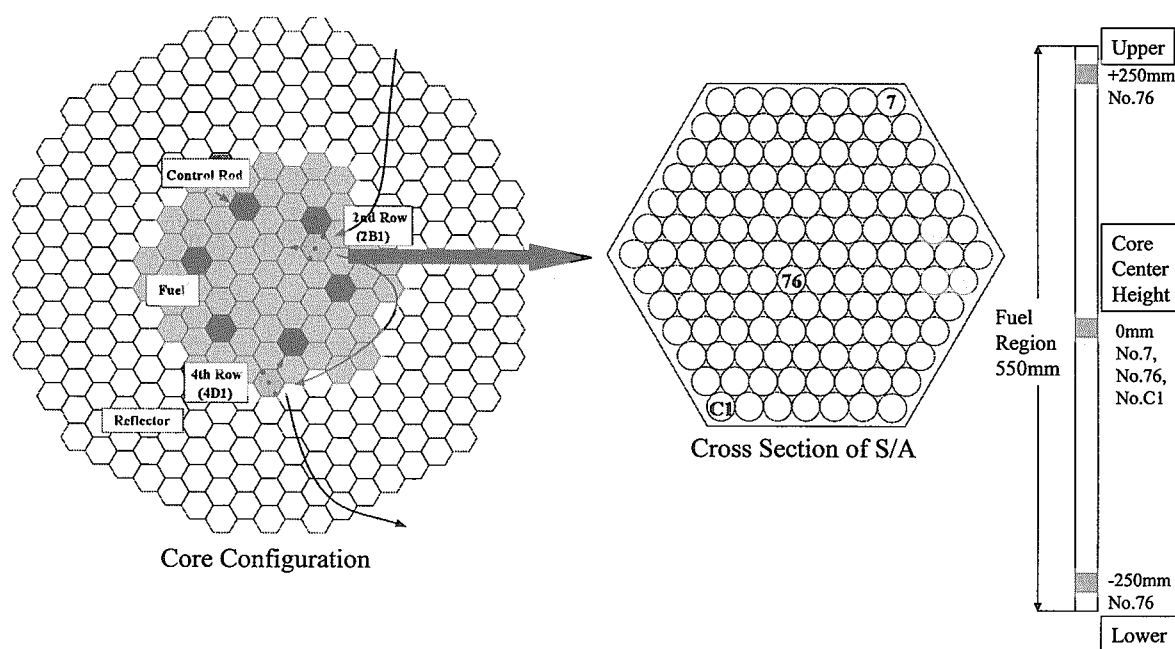


Fig.2 Irradiation Position and PIE Position of JOYO MK-II Measured Fuel

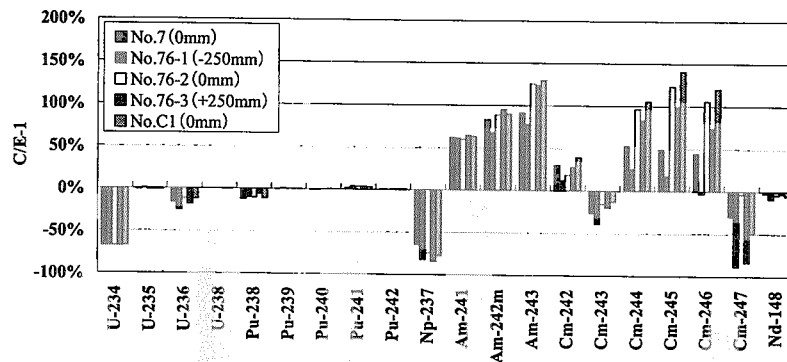


Fig.3 Comparison of Calculated and PIE Results of JOYO MK-II Spent Fuel

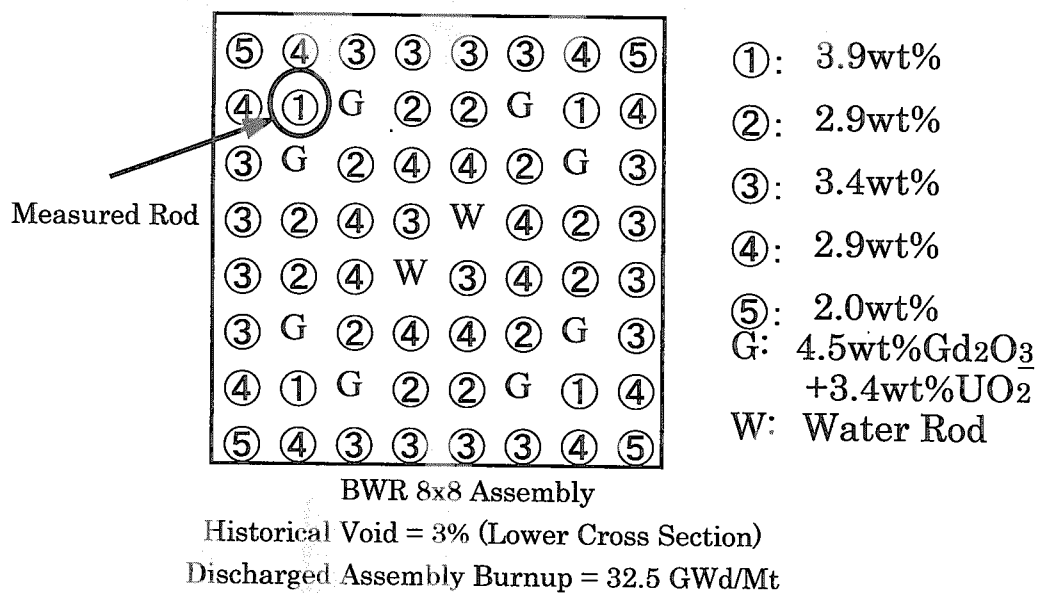


Fig.4 Analytical Model in MCNP-ORIGEN Burnup Calculation for BWR sample rod

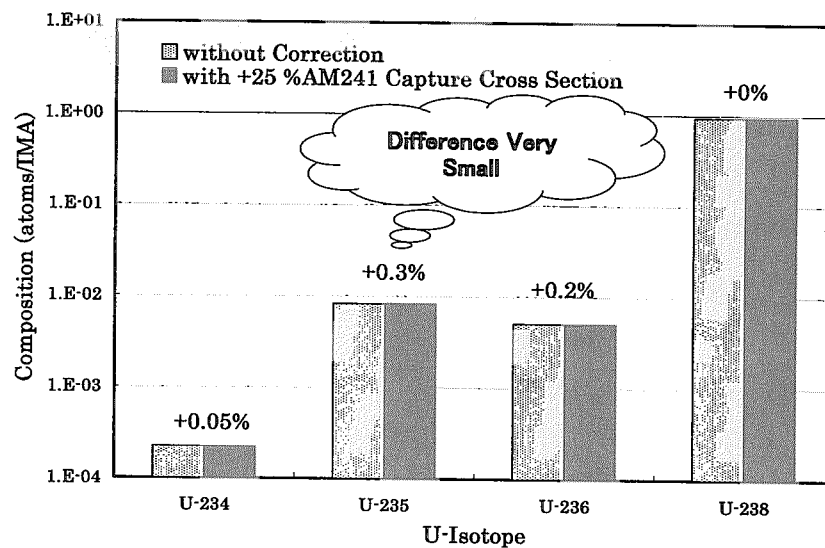


Fig.5 The comparison of vo,positions for U-isotopes between two calculations

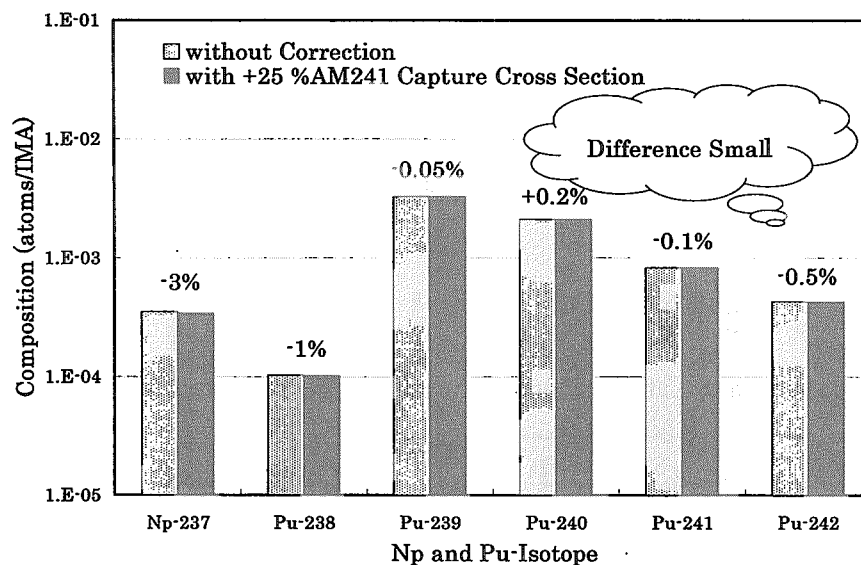


Fig.6 The comparison of compositions for Np&amp;Pu-isotopes between two calculations

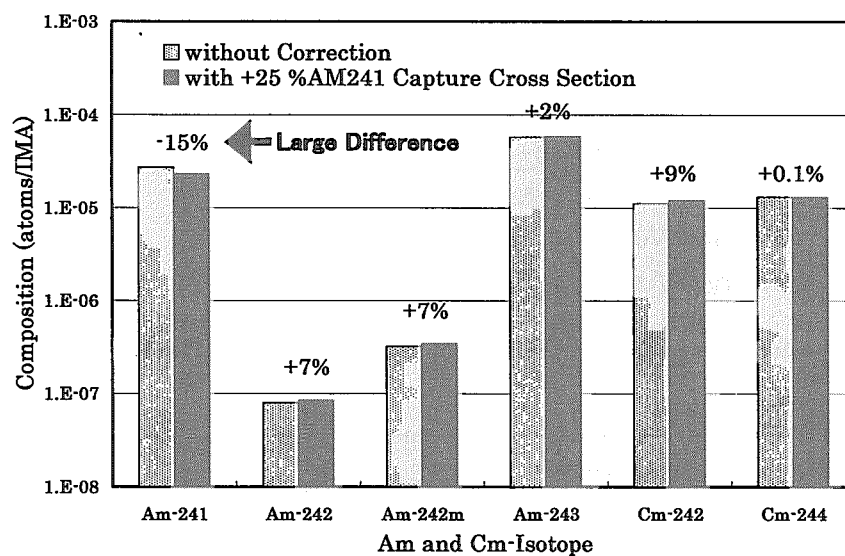


Fig.7 The comparison of compositions for Am&amp;Cm-isotopes between two calculations



## 2.10 Analysis of MISTRAL Experiments with JENDL-3.2

Takuya UMANO

Nuclear Power Engineering Corporation (NUPEC)

FUJITA KANKO TORANOMON BLDG., 5F 17-1, 3-CHOME TORANOMON,  
MINATO-KU, TOKYO 105-0001 Japan

E-mail: umano@nupec.or.jp

Toru YAMAMOTO, Ryoji KANDA, Masaru SASAGAWA (NUPEC)

Taro KAN (MHI), Kazuya ISHII (Hitachi), Yoshihira ANDO (Toshiba),  
Masahiro TATSUMI (NFI)

NUPEC and CEA have launched an extensive experimental program called MISTRAL to study highly moderated MOX cores for the advanced LWRs. The analyses using the SRAC system and the MVP code with the JENDL-3.2 library are in progress on the experiments of the MISTRAL program and also the EPICURE program that was carried out by CEA before the MISTRAL program. Various comparisons have been made between the calculation results and the measurement values.

### 1. Introduction

Nuclear Power Engineering Corporation (NUPEC), French Atomic Commission (CEA) and CEA's industrial partners have launched an extensive experimental program called MISTRAL (MOX: Investigation of Systems Technically Relevant of Advanced Light water reactors) [1,2,3,4,5] in order to obtain the basic core physical parameters of the highly moderated MOX cores that will be used to validate and improve core analysis methods. This experimental program was conducted in the EOLE facility at the Cadarache center and successfully completed in July 2000. As a part of the MISTRAL program, NUPEC also obtained some of the experimental data of the EPICURE program that CEA had conducted for 30% MOX loading in PWRs.

### 2. EOLE critical facility

The experiments have been performed in the EOLE facility that is a tank type critical facility. A cylindrical Aluminum vessel (diameter = 2.3 m, height = 3m) is installed with a cylindrical core tank (diameter = 1.0 m, height = 1.0 m) and stainless steel over structures. Fuel pins used in the facility are a standard PWR type and the active length of the pins is about 80 cm. Four types of enrichment are prepared for MOX pins and one type for UO<sub>2</sub> pins. The reactivity of the core is mainly controlled with the boron (boric acid) concentration in water and the core size. Core excess reactivity is determined through the in-hour equation with measuring the doubling time after the withdrawal of the pilot rod.

### 3. Core configurations and measurements in the MISTRAL program

The core configuration of MISTRAL-1 is shown in Figure 1. It consisted of about 750 regular enriched UO<sub>2</sub> (3.7% in <sup>235</sup>U) fuel pins in a lattice pitch of 1.32 cm and was designed as a reference for the highly moderated MOX cores. The core configuration of MISTRAL-2 is shown in Figure 2. This is a highly moderated full-MOX core consisting of about 1600 MOX (7% enrichment) fuel pins with the same lattice pitch of MISTRAL-1. Figure 3 shows the core configuration of MISTRAL-4 which is a PWR mock-up configuration. The UO<sub>2</sub>-Reference configuration in MISTRAL-4 is shown in Figure 4. In this configuration the 17×17 type of UO<sub>2</sub> zone was installed at the center

of the core, and on account of the large reactivity of  $\text{UO}_2$  pins, the core size was smaller than that of the full-MOX cores. Measurement items were carefully selected from the followings :

- (1) Critical mass and boron concentration                      (2) Boron worth
- (3) Buckling measurement using reaction rate distribution measurements
- (4) Spectrum indices      (5) Modified conversion factor :  $^{238}\text{U}$  capture/total fission
- (6) Isothermal temperature coefficients
- (7) Reactivity worth and associated reaction rate distribution of a single absorber  
(Natural  $\text{B}_4\text{C}$ , enriched  $\text{B}_4\text{C}$ , Ag-In-Cd alloy, and  $\text{UO}_2\text{-Gd}_2\text{O}_3$ ) at the center of the core )
- (8) Reactivity worth and associated reaction rate distribution of a cluster absorber
- (9) Reactivity worth and associated reaction rate distribution of the substitution of 9 central fuel pins by water holes / Void coefficient
- (10)  $\beta_{\text{eff}}$

#### 4. Experimental methods

The number of fuel pins, the core temperature, the boron concentration and the doubling time were measured to determine the core critical mass. The neutron source multiplication method (the sub-critical method) was utilized for the reactivity measurement. The integral gamma scanning method was applied to determine the fission distributions of the fuel pins. The miniature fission chambers of several kinds of isotopes were adopted for the determination of energy dependent neutron flux and also for the spectrum index measurements. The effective delayed neutron fraction of the core ( $\beta_{\text{eff}}$ ) was measured using of the core noise method which had been utilized in the international benchmark of  $\beta_{\text{eff}}$ 's at the MASURCA and the FCA facilities.

#### 5. Calculation methods

The analysis has been performed using the SRAC system and the MVP code that have been developed at Japan Atomic Energy Research Institute (JAERI) with the JENDL-3.2 library. The SRAC system consists of deterministic codes. A processed nuclear data library with 107-energy group structure is prepared for it. MVP is a continuous energy Monte Carlo code that is utilized to obtain reference calculation results for the SRAC system such as core eigen-values. In the SRAC system, the collision probability method is applied for generating the 16-group collapsed and homogenized unit cell cross sections. The neutron energy spectrum affected by the neutron leakage is calculated with the B1 approximation taking into account the measured geometrical buckling. The resonance absorption of Pu isotopes should be precisely evaluated in epi-thermal and thermal ranges for MOX fuels. Thereby an ultra fine group resonance reaction calculation module, PEACO, is utilized throughout for the effective cross section calculation. The thermal cut-off energy was carefully chosen and determined to be 1.855eV through a sensitivity study. After generating 16-group cell cross sections (fast range - 8 groups and thermal range - 8 groups) , core calculations in 1/4 symmetry configuration were performed using the CITATION and/or TWOTRAN modules of the SRAC system. In two-dimensional calculation model, axial leakage is implicitly taken into account using the measured axial buckling.

#### 6. Calculation results and discussion

Varieties of comparisons between the calculations and the measurements have been carried out for MH1.2 (which is devoted to study on basic characteristics of a 30% MOX core in the EPICURE program), MISTRAL-1, -2 -3 and -4. The critical  $k_{\text{eff}}$  for 4 core reference configurations is shown in Table 1. The calculation results of MVP with



JENDL-3.2 overestimated all the critical keff both for the UO<sub>2</sub> core and the MOX cores. For MISTRAL-1, the overestimation is about 0.5%. On the other hand, the calculation results of SRAC for MISTRAL-1 underestimated the critical keff because of the calculation errors for such a very small core. Among the MOX cores, a small trend of increasing of the critical keff with the experiment date is observed. This increase is considered to be related with the change of the atomic number densities of the materials in MOX pins (the Pu aging effect). After the additional study, the underestimation of the neutron capture cross section of <sup>241</sup>Am of JENDL-3.2 would be a main reason. Among the 7 core configurations of MISTRAL-4 experiments, the partial UO<sub>2</sub> configurations are of much interest because they provide the UO<sub>2</sub> and MOX combined critical mass and complicated radial power distributions. The critical keff for the 7 configurations of MISTRAL-4 is shown in Table 2. For the full-MOX core configuration, the calculation results of MVP agree very well each other and the overestimation of the critical keff is always about 0.9%. Compared with this, the calculation result for the UO<sub>2</sub>-Reference configuration is smaller. Because the UO<sub>2</sub>-zone is installed at the center of the core hence the overestimation was little reduced by the features of the UO<sub>2</sub> core with JENDL-3.2. In the UO<sub>2</sub>-B<sub>4</sub>C configuration, the ratio of the outer MOX-zone was increased and the character of a UO<sub>2</sub> core was diminished. Thereby it showed almost the same critical keff of MOX cores in MISTRAL-4. The root-mean-square (R.M.S) differences of the radial power distribution is shown in Table 3. The differences are as much as the uncertainty of measurement. Further studies both for the critical keff and the power distribution are required and still ongoing.

#### Acknowledgment

This study is supported by the Japanese Ministry of Economy, Trade and Industry (METI). The authors thank Dr. K. Kanda, Director of Japan Energy Policy Institute and other members of the implementation committee of "Study of Advanced LWR Cores for Effective Use of Plutonium," in NUPEC for their technical advices and suggestions.

#### References

- [1] S. Cathalau and J.C. Cabrilhat et al: "MISTRAL: an experimental program in the EOLE facility devoted to 100% MOX core physics", International Conference on Physics of Reactors: PHYSOR 96, Vol. 3 (H- 84-92) September 16-20,1996 Mito. Japan.
- [2] Yamamoto T. et al: "CORE PHYSICS EXPERIMENT OF 100% MOX CORE: MISTRAL" Proc. of Int. Conf. on Future Nuclear Systems, Global '97, Vol.1, pp395 1997.
- [3] Kanda K. and Yamamoto T. et al: "MOX fuel core physics experiments and analysis - aiming for Plutonium effective use ", (in Japanese) Journal of the Atomic Energy Society of Japan, No.11, Vol. 40. 1998.
- [4] Hibi K. et al: "ANALYSIS OF MISTRAL AND EPICURE EXPERIMENTS WITH SRAC AND MVP CODE SYSTEMS", Proc. of Int. Conf. Physics of Reactor Operation, Design and Computation, PHYSOR 2000.
- [5] S. Cathalau and P. Fougeras et al: "Full MOX recycling in ALWR: Lessons Drawn through the MISTRAL Program", International Conference on Physics of Reactors: PHYSOR 2002, Seoul, South Korea.

Table.1 Critical keff for 4 Core Reference Configurations

PROGRAM	EPIURE	MISTRAL			
CORE NAME	MH 1.2	CORE 1	CORE 2	CORE 3	CORE 4 (MOX-Ref)
FEATURE	Partial MOX	Uranium CORE	Full MOX	Full MOX	PWR Mock-up
FUEL PIN	3.7%UO <sub>2</sub> + 7% MOX	3.7% UO <sub>2</sub>	7% MOX (Mainly)	7% MOX	7% MOX
LATTICE PITCH	1.26 cm	1.32 cm	1.32 cm	1.39 cm	1.32 cm
H/HM	3.7	5.1	5.1	6.2	5.8
CORE DIAMETER	69 cm	41 cm	60 cm	59 cm	62 cm
EXPERIMENT DATE	June 1996	—	April 1997	August 1998	August 1999
MVP	1.0027 $\pm 0.02 \% (1\sigma)$	1.0048 $\pm 0.03 \% (1\sigma)$	1.0070 $\pm 0.02 \% (1\sigma)$	1.0077 $\pm 0.02 \% (1\sigma)$	1.0093 $\pm 0.02 \% (1\sigma)$
SRAC (Pij + TWOTRAN )	1.0013	0.9981	1.0041	1.0042	1.0074

Table. 2 Critical keff of 7 Core Configurations in MISTRAL-4

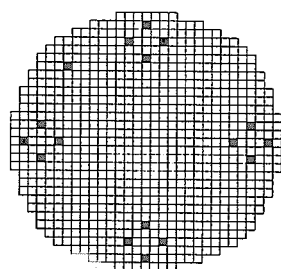
Core Configuration		Calculation Method		
		SRAC (Pij + CITATION )	SRAC (Pij + TWOTRAN )	MVP
Full-MOX	MOX - Reference	1.0074	1.0074	1.0093 $\pm 0.02 \% (1\sigma)$
	MOX - SUS	1.0074	1.0072	1.0093 $\pm 0.02 \% (1\sigma)$
	MOX - Hf *	1.0054	1.0072	1.0091 $\pm 0.02 \% (1\sigma)$
	MOX-AIC *	1.0054	1.0073	1.0094 $\pm 0.02 \% (1\sigma)$
	MOX -B <sub>4</sub> C *	1.0049	1.0092	1.0098 $\pm 0.02 \% (1\sigma)$
Partial UO <sub>2</sub> ( UO <sub>2</sub> + MOX )	UO <sub>2</sub> - Reference	0.9990	1.0024	1.0060 $\pm 0.02 \% (1\sigma)$
	UO <sub>2</sub> - B <sub>4</sub> C	1.0017	1.0071	1.0089 $\pm 0.02 \% (1\sigma)$

\* UO<sub>2</sub> pins were put in the outer part of the core

Table. 3 R.M.S Differences of Radial Power Distribution between  
Calculation and Measurement for each Experimental Core

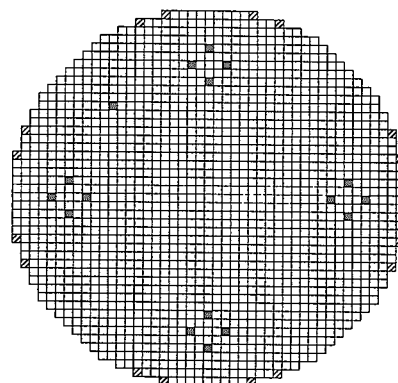
PROGRAM	EPIURE	MISTRAL			
CORE NAME	MH 1.2	CORE 1	CORE 2	CORE 3	CORE 4
FEATURE	Partial MOX	Uranium CORE	Full MOX	Full MOX	PWR Mock-up
MVP	1.2 %	1.7 %	1.7 %	1.4 %	1.3 %
SRAC (Pij + CITATION )	0.9 %	2.0 %	1.1 %	1.3 %	1.0 %

Measurement uncertainty UO<sub>2</sub> rod  $\sim 1.0 \%$  : MOX rod  $\sim 1.5 \% (1\sigma)$



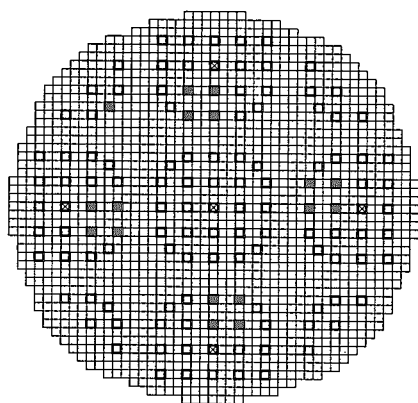
- MOX(7.0%) fuel rod
- Guide tube for safty and control rod

Fig.1 Core Configuration of MISTRAL-1



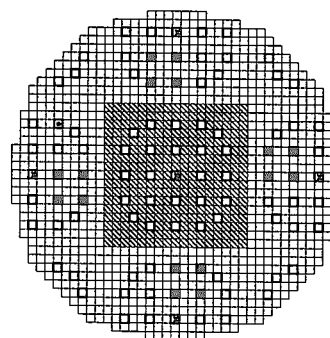
- MOX(7.0%) fuel rod
- ▨ MOX(8.7%) fuel rod
- Guide tube for safty and control rod

Fig.2 Core Configuration of MISTRAL-2



- MOX(7.0%) fuel rod
- Mock-up thimble tube
- ⊗ Instrumentation tube
- Guide tube for safty and control rod

Fig.3 Core Configuration of MISTRAL-4  
MOX-Reference configuration



- MOX(7.0%) fuel rod
- ▨ UO<sub>2</sub>(3.7%) fuel rod
- ⊗ Instrumentation tube
- Guide tube for safety and control rod

Fig.4 Core Configuration of MISTRAL-4  
UO<sub>2</sub>-Reference configuration



## 2.11 Request from Radiation Damage Evaluation in Materials

Koji FUKUYA and Itsuro KIMURA

*Institute of Nuclear Safety System*

*64 Sata, Mihama-cho, Mikata-gun, Fukui 919-0125, Japan*

*e-mail: fukuya@inss.co.jp, kimura@inss.co.jp*

Radiation transport calculations in a PWR using cross-section data sets based on JENDL3.2 showed that the calculated neutron fluence agreed well with the dosimeter measurements and that the fast neutron flux and dpa rate differed within 10% from those calculated using ENDF/B-IV and ENDF/B-VI based data sets. Calculations of helium generation in structural materials in the PWR using ENDF/B-VI showed that the dominant source of helium is the  $(n, \alpha)$  reaction of  $^{59}\text{Ni}$  and that the calculated helium content agreed with the measurements. For accurate estimation of radiation field from a material viewpoint, it is desirable to construct proper cross-section libraries, which have a proper energy group structure and contain sufficient elements including  $^{59}\text{Ni}$  as an indispensable element.

### 1. Introduction

Accurate characterization of radiation field is essential for precise life prediction of structural materials and understanding of material degradation mechanisms in nuclear reactors. Nuclear cross-section data (nuclear data) are used for evaluating fluxes and spectra of neutron and gamma ray in near-core components such as reactor vessels, for measuring radiation fields using dosimeters and for modeling microstructural evolution based on radiation damage parameters such as cascade formation and gas generation.

Material property changes under radiation field are determined by parameters such as radiation fluence, flux, temperature, stress and material composition. Fast neutron fluence with the energy higher than 1MeV or 0.1MeV is widely used as a traditional exposure for prediction of material properties in various reactors. Displacement per atom (dpa) is also used as an exposure parameter. Procedures of dpa calculation and dpa cross-section of iron under neutron irradiation have been standardized in ASTM E693. This standard has been derived from ENDF/B and widely used in nuclear industry. The dpa induced by gamma rays is evaluated for structural materials in which the gamma ray flux is expected much higher than neutron flux.<sup>1)</sup> Nuclear transmutation reactions cause a gradual change in material composition. Although the change in material composition is negligible for major metallic elements in structural materials, the production of helium and hydrogen through  $(n, \alpha)$  and  $(n, p)$  reactions is known to have a strong effect on material property change such as swelling and creep. Recently it has been demonstrated that the helium generation has a detrimental influence on weldability of irradiated materials.<sup>2)</sup> The weldability of irradiated stainless steels is degraded by the existence of 0.1 - 1 appm helium. The accurate estimation of helium generation is important to assess applicability of welding to irradiated structural materials. Recent experiments showed that swelling initiation is sensitive to material temperature during irradiation and that an increase of 10 °C resulted in a larger swelling.<sup>3)</sup> The temperature of structural materials during reactor operation is estimated using heat transfer calculations considering gamma heating and coolant flow distribution. The accuracy of gamma heating is a key factor for the accuracy of temperature estimation.

As mentioned above, the accuracy of parameters that determined material behaviors under reactor radiation environment depends on accuracy of nuclear data and calculation modeling. In this paper, results of radiation transport calculations and dpa calculations inside the reactor vessel of a two-loop pressurized water reactor (PWR) using JNEDL data are presented and compared with those using ENDF/B data. Estimation of helium generation in core materials of the PWR is also presented. Finally requests for domestic nuclear data are summarized from the viewpoint of material evaluation under radiation field.

## 2. Neutron flux and dpa calculated using JENDL3.2

The transport calculations in a two-loop PWR (1456MWth) were carried out using DORT code with three cross-section libraries (JSSTD<sup>4</sup>), BUGLE-96<sup>5</sup>) and JSD-100<sup>6</sup>), TORT code with BUGLE-96 and MCNP with JENDL3.2. The JSSTD library is generated from JENDL3.2 and has a 100-neutron and 40-gamma group structure. The JSD-100 data set was generated from the JSD-100 library (100-neutron and 40-gamma group, based on ENDF/B-IV) and has a 21-neutron and 13-gamma group structure collapsed using the spectrum calculated with the one-dimensional ANISN code for the PWR. This data set has been used for fluence evaluation in PWRs in Japan for almost two decades. In this paper it is simply designated as JSD-100. The BUGLE-96 is generated from ENDF/B-VI and has a 47-neutron and 20-gamma group structure. The one-eighth horizontal geometry model is shown in Fig.1. The detailed calculation procedure was described elsewhere.<sup>7</sup>) Figure 2 shows the spectra of neutrons and gamma rays at the inner surface of the reactor vessel. The spectra calculated with various code and libraries are well coincident with each other. Table 1 shows the C/M ratios for the surveillance dosimeters (Fe, Ni, Cu,  $^{238}\text{U}$  and  $^{239}\text{Np}$ ) installed at the outer surface of the thermal shield. The three libraries used in the calculation gave almost the same average C/M ratio (0.98 – 1.05) for the surveillance dosimeters, indicating that these libraries gave sufficiently precise estimation of neutron flux at almost the same level. The fast neutron fluxes at the surveillance position and the reactor vessel calculated with JSSTD agreed within 10% with those calculated with BUGLE-96 and JSD-100.

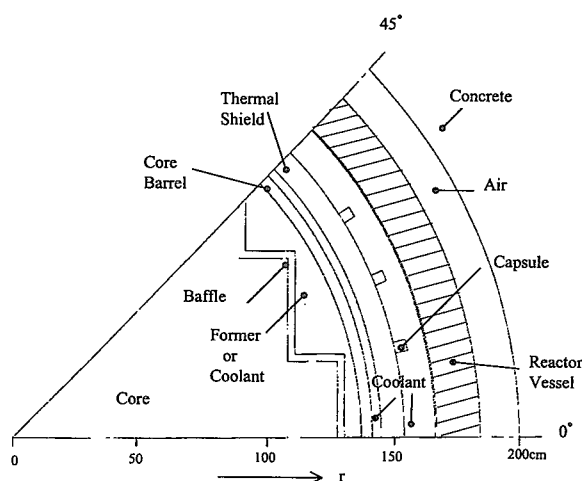


Fig.1 One-eighth horizontal geometry of a two-loop PWR

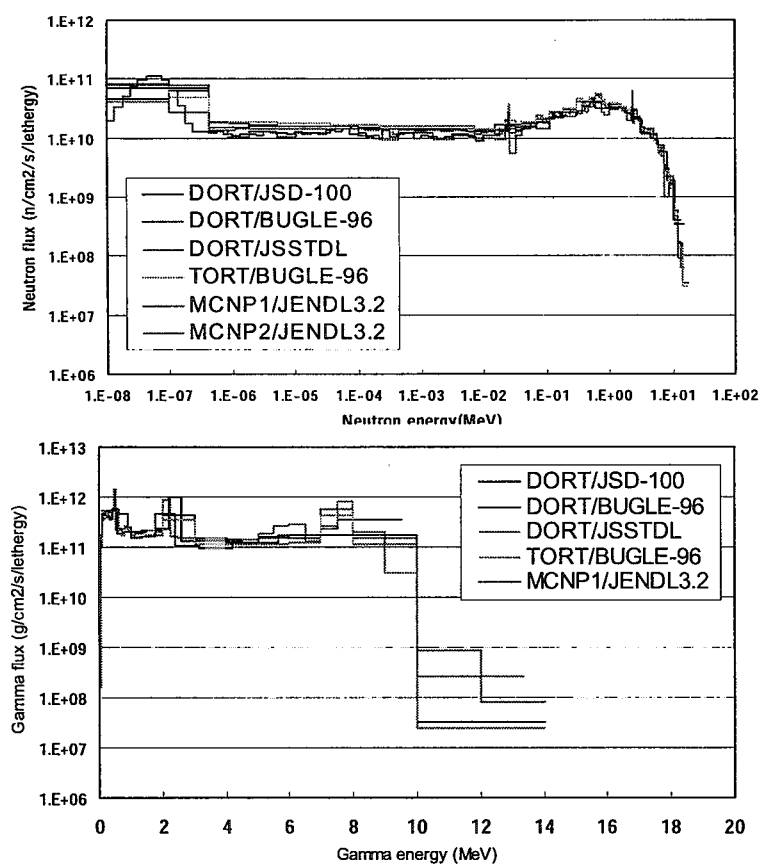


Fig.2 Spectra of neutrons (upper) and gamma rays (lower) at the inner surface of reactor vessel calculated using various codes and libraries.

Table 1 C/M ratios for surveillance dosimetry

Code and data set		$^{54}\text{Fe}$ ( $n, p$ ) $^{54}\text{Mn}$	$^{58}\text{Ni}$ ( $n, p$ ) $^{58}\text{Co}$	$^{63}\text{Cu}$ ( $n, \alpha$ ) $^{60}\text{Co}$	$^{238}\text{U}$ ( $n, f$ ) $^{137}\text{Cs}$	$^{237}\text{Np}$ ( $n, f$ ) $^{137}\text{Cs}$	Average (Standard Deviation)
TORT	BUGLE-96	0.94	1.12	0.91	0.96	1.12	1.01 (0.10)
DORT	JSD-100	0.90	1.04	1.19	0.92	1.19	1.05 (0.14)
	BUGLE-96	0.94	1.13	0.95	0.96	1.14	1.03 (0.10)
	JSSTD	0.91	1.09	0.96	0.92	1.04	0.98 (0.08)
MCNP1	JENDL3.2	0.90	1.05	0.96	0.76	0.80	0.89 (0.12)
MCNP2	JENDL3.2	0.88	1.04	0.96	0.79	0.83	0.90 (0.10)

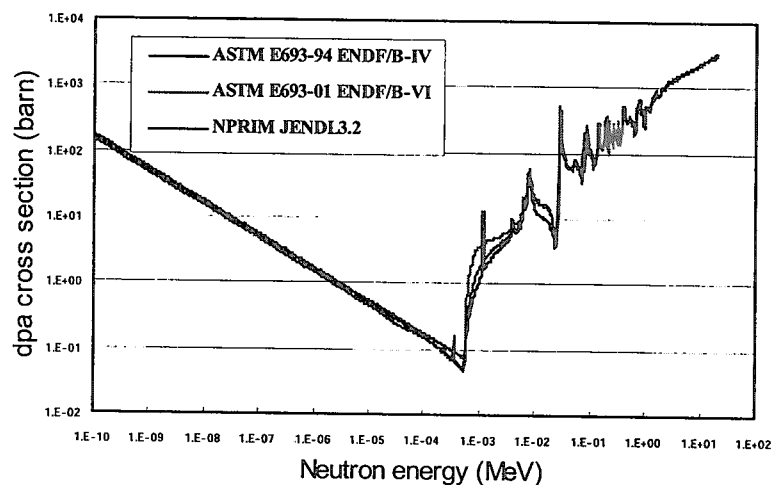


Fig. 3 Dpa cross-sections in iron

The neutron induced dpa in structural materials inside the reactor vessel was calculated using dpa cross-sections in iron derived from the three nuclear data. The dpa cross-section from JENDL3.2 was calculated using NPRIM code.<sup>8)</sup> The dpa cross-sections tabulated in the ASTM E693 standard (E693-94 and E693-01) were used for those from ENDF/B-IV and ENDF/B-VI, respectively. Fig. 3 compares the energy dependence of dpa cross-sections in iron. A small difference was observed in the energies from keV to 10keV. The gamma ray induced dpa cross-section in iron has not been standardized while several dpa cross-sections were proposed.<sup>1, 9, 10)</sup> In this study a gamma ray induced dpa cross-section was calculated taking into account Compton scattering, photoelectric effect and pair production, using the McKinley-Feshbach approximation for the electron and positron displacement cross-section, the NRT model<sup>11)</sup> for the displacement function and 40eV for the displacement threshold energy. Both neutron-induced dpa and gamma-induced dpa at the surveillance position and the reactor vessel based on JENDL3.2 agreed within 15% with those based on ENDF/B-IV and ENDF/B-VI.

The results described above indicate that JENDL3.2 gives sufficiently accurate fluxes of neutrons and gamma rays and dpa inside the reactor vessel of PWRs for engineering purpose. JENDL3.2 gives almost the same estimations of neutron fluence and dpa as ENDF/B currently used for PWR application.

### 3. Helium generation

The amount of helium generation through  $(n, \alpha)$  reactions in stainless steel components in the PWR was estimated using cross-section data in ENDF/B-VI and neutron fluxes calculated with BUGLE-96. The ENDF/B-VI alone includes cross-section data of  $^{59}\text{Ni}$  isotope. Fig.4 shows the relative contribution of the isotopes to the total helium generation at a baffle plate. The composition of the plate was assumed Fe - 18Cr - 8Ni - 0.06N - 0.0009B in wt %. At the beginning of irradiation up to ten years the  $^{10}\text{B}(n, \alpha)$  reaction is the main source of helium. After ten years the  $^{58}\text{Ni}(n, p)^{59}\text{Ni}(n, \alpha)^{56}\text{Fe}$  reaction becomes dominant and its contribution reaches to 90% of the total helium generation. Fig.5 shows the comparison of calculated helium generation and measured helium content in a thimble tube made of type 316 stainless steel. The detailed data was described elsewhere.<sup>12)</sup> The thimble tube was installed in

a fuel bundle for 13 effective full power years. The calculated values were in good agreement with the measurements for the sample B, C, D and E. However no good agreement was observed for the samples A, G and H, which were located near the thermal flux peak positions outside the active fuel length. Precise estimation of helium generation needs accurate thermal neutron flux and cross-sections of  $^{59}\text{Ni}$  isotope.

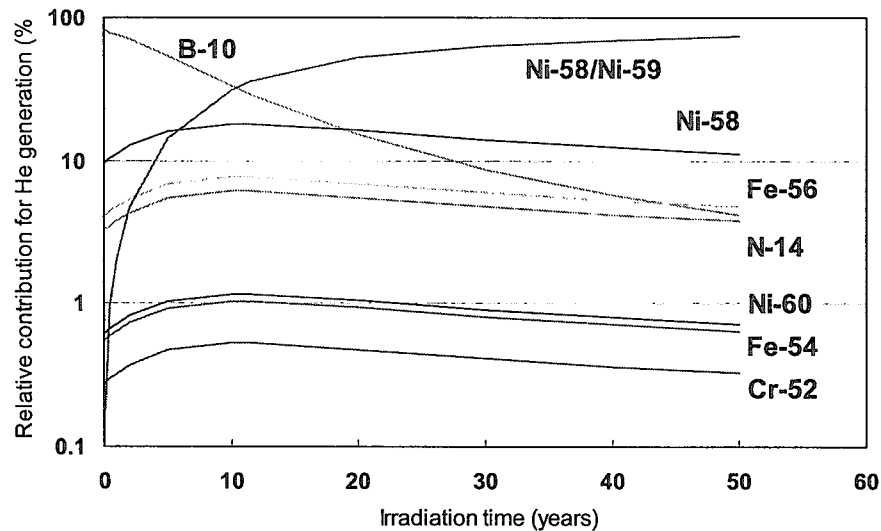


Fig.4 Relative contribution of isotopes to the total helium generation in in-core structural material.

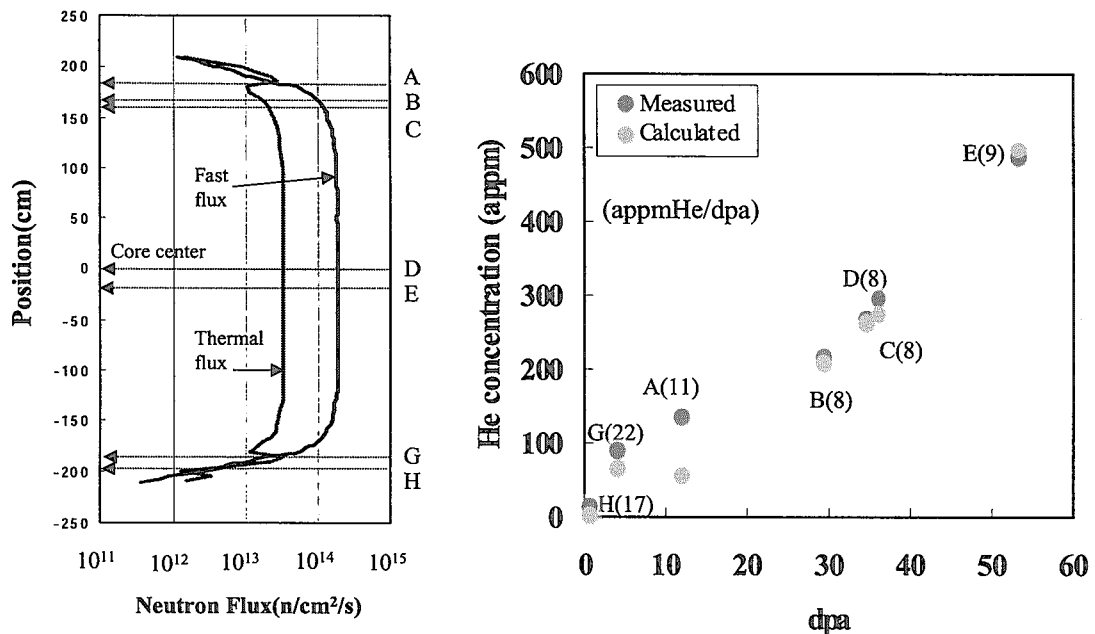


Fig.5 Comparison of measured helium content and calculated helium generation in in-core structural material (right) and specimen positions along the core height (left).



#### 4. Summary and requests to JENDL

The present calculations using JSSTD L and JENDL3.2 demonstrated that JENDL gives sufficiently accurate estimation of neutron flux and dpa rate in PWR. However JENDL is not suitable for calculations of helium generation because of the lack of  $^{59}\text{Ni}$  cross-section data. Requests to JENDL can be summarized as follows for accurate estimation of radiation field from a material viewpoint. First it is desirable to construct proper cross-section libraries that have an energy group structure suitable to material evaluation. The thermal region should contain several groups to improve the accuracy of thermal flux. The libraries examined in this paper contain one group (in JSSTD L and JSD-100) or two groups (in BUGLE-96). This probably is one of the reasons for a large difference in thermal flux between the three libraries. For the fast region the group division at 1 and 0.1 MeV is desirable. The division in JSSTD L and BUGLE-96 is 0.111 MeV and in JSD-100 is 0.1 MeV. Although the difference in fast flux between divisions at 0.1 MeV and 0.111 MeV may be small, factors causing data scattering in database analyses should be minimized. Secondly for evaluating generation of helium and hydrogen the cross-section data of  $^{59}\text{Ni}$  must be included as an indispensable element. Finally standard dpa cross-sections in iron and stainless steels derived from JENDL should be prepared, as the ASTM E693 has been standardized from ENDF/B.

#### Acknowledgements

The authors wish to thank Mr. H. KITAGAWA and M. OHMURA, Mitsubishi Heavy Industry Co, Ltd, for transport calculations and discussions. They also thank to Mr. T. ITO and late Associate Professor K. SHIN, Kyoto University, for MANP calculations and valuable comments, and thank to Dr. S. SIMAKAWA and Professor N. SEKIMURA, University of Tokyo, for use of NPRIM code.

#### References

- 1) For example, D. E. Alexander, *J.Nucl.Mater.*, **240**, 196 (1997).
- 2) For example, K. Asano et al., *Effects of Radiation on Materials: 19th International Symposium*, ASTM STP 1366, ASTM, p.944 (2000).
- 3) For example, F. A. Garner et al., *Proc. of 10th International Conference on Environmental Degradation of Materials in Nuclear Power Systems - Water Reactors*, NACE, 2002.
- 4) A. Hasegawa, *Nuclear Data News*, JAERI, No.62 (1999).
- 5) RSIC Code Package CCC-484 (ORNL, November 1989).
- 6) K. Koyama et al., JAERI-M 6928, JAERI (1977).
- 7) K. Fukuya et al., presented in *11th International Symposium on Reactor Dosimetry* held at Brussels, August 2002.
- 8) S. Shimakawa and N. Sekimura, *J. Nucl. Mater.*, in press.
- 9) J. K. Kwon and A. T. Motta, *Annals of Nuclear Energy*, **27**(2000)1627.
- 10) N. P. Bauman, *Proc. of 7th ASTM-EURATOM Symposium on Reactor Dosimetry*, ASTM, p.689 (1992).
- 11) M. J. Norgett et al., *Nucl. Eng. and Design*, **33**, 50 (1975).
- 12) K. Fujii et al, *Proc. of 10th International Conference on Environmental Degradation of Materials in Nuclear Power Systems - Water Reactors*, NACE, 2002.



## 2.12

### Calculation of $n+^{232}\text{Th}$ Reaction Cross Sections in the $E_n \leq 20$ MeV Energy Range

Han Yinlu

*China Institute of Atomic Energy, P.O. Box 275(41), Beijing 102413, China*

*\* e-mail: han@iris.ciae.ac.cn*

Consistent calculation and analysis of neutron scattering data of  $^{232}\text{Th}$  with optical model, semiclassical model includes both the Hauser-Feshbach theory and the exciton model, and the coupled channel theory is carried out in the  $E_n \leq 20$  MeV energy range based on the experimental data of total, nonelastic-scattering, fission, and other reaction cross section and elastic-scattering angular distributions. Especially, the analysis includes the elastic and inelastic scattering angular distribution, the inelastic scattering cross sections of discrete levels, the prompt fission neutron spectra, the double differential cross section and the angle-integrated spectra for neutron emission. Theoretical calculations are compared with recent experimental data and other evaluated data from ENDF/B6 and JENDL-3.

#### I. Introduction

The neutron interactions cross sections and prompt fission neutron spectrum in the energy range below 20 MeV are of fundamental importance for fission and accelerator-driven reactors because they dominate the neutron transport and neutron regeneration, respectively. Therefore, precise nuclear reaction data are required for the nuclear and shielding design of fission reactors and accelerator-based system such as accelerator-driven transmutation system. On the other hand, a careful analysis of certain nuclear cross section data file reveals either that various kinds of errors (even clerical ones) are indeed present in the evaluations for  $^{232}\text{Th}$ , or that these evaluations are not fully consistent with the most recent and accurate experimental data and results.

To meet needs, accurate nuclear reaction data of common cross sections, number of neutron per fission, the prompt fission neutron spectra, the angle-integrated spectra for neutron emission, neutron-induced double differential cross sections,  $\gamma$ -ray production cross sections and  $\gamma$ -ray production energy spectra for  $n+^{232}\text{Th}$  reaction are calculated in this work using recent experimental data, various models and methods for the neutron energy region  $E_n \leq 20$  MeV. The calculated results are analyzed and compared with experimental data and other evaluated data from ENDF/B6 and JENDL-3.

#### II. Theoretical Model and Parameters

The latest version of the UNF code<sup>1)</sup>, which calculates nuclear reaction cross sections at incident neutron energies below 20 MeV, is based on the optical model and the semi-classical model of multistep nuclear reaction processes, including the introduction of formation factors of composite particle in calculations of pick-up type composite particle emissions. Direct inelastic scattering to low-lying levels is calculated using the distorted wave Born approximation and it is included as input into the UNF calculations. The GNASH<sup>2)</sup> code does not have angular momentum conservation in the exciton component, and it uses a semiempirical method for calculating angular distributions in double differential cross sections.

The optical model is used to describe measured total, reaction, elastic scattering cross sections and elastic scattering angular distributions, and to calculate the transmission coefficient of the compound nucleus and the pre-equilibrium emission process. The optical potentials considered here are

Woods-Saxon<sup>3)</sup> form for the real part, Woods-Saxon and derivative Woods-Saxon form for the imaginary parts corresponding to the volume and surface absorptions respectively, and the Thomas form for the spin-orbit part. In order to obtain a set of neutron optical potential parameters for  $^{232}\text{Th}$ , the optical model code APOM<sup>4)</sup> was used in this work. In this code the best neutron optical potential parameters are searched automatically to fit with the relevant experimental data of total cross sections, nonelastic-scattering cross sections, elastic-scattering cross sections, and elastic-scattering angular distributions. The adjustment of optical potential parameters is performed to minimize a quantity called  $\chi^2$ , which represents the deviation of the theoretical calculated results from the experimental values.

The energy dependencies of potential depths and optimum neutron optical potential parameters of Th are expressed as follows:

$$V=51.0445-0.3125E_n+0.008986E_n^2-24.0V_3(N-Z)/A.$$

$$W_s=7.2421+0.1119E_n-12.0(N-Z)/A.$$

$$U_{so}=6.2$$

$$r_r=1.2386, r_s=1.2499, r_{so}=1.2386,$$

$$a_r=0.5932, a_s=0.7548, a_{so}=0.5932.$$

Where  $Z$ ,  $N$  and  $A$  are charge, neutron and mass numbers of target, respectively,  $E_n$  is incident neutron energy. The units of the potential  $V$ ,  $W_s$ ,  $W_v$ ,  $U_{so}$  are in MeV, the lengths  $r_r$ ,  $r_s$ ,  $r_{so}$ ,  $a_r$ ,  $a_s$ ,  $a_{so}$  are in fermi units and energies  $E_n$  is in MeV.

The calculated results of neutron total, nonelastic, elastic scattering cross sections and elastic scattering angular distribution are compared with experimental data for  $n+^{232}\text{Th}$  reaction. The calculated results of total cross sections are in good agreement with recent experimental data measured at Los Alamos<sup>5)</sup> in Fig.1, and elastic scattering angular distribution are in agreement with experimental data, while the calculated results of nonelastic cross sections and elastic scattering cross sections pass through existing experimental data in Fig.2. Based on the above fitting, this set of neutron optical potential parameters is determined for  $n+^{232}\text{Th}$  reaction.

The direct inelastic scattering cross sections to low-lying states are important in nuclear data theoretical calculations. The code ECIS<sup>6)</sup> with a distorted wave Born approximation is used. The discrete levels of  $^{232}\text{Th}$  are taken into account from ground ( $0.0\ 0^+$ ) up to the twenty-third ( $1.0787\ 0^+$ ) excited state. Levels above 1.0787 MeV are assumed to be overlapping and level density formalism to be used. The direct inelastic scattering cross sections and angular distributions of the first four excited levels are calculated. The coupled channel optical model parameters and deformation parameters ( $\beta_2=0.1950$ ,  $\beta_4=0.0820$ ) used in ECIS are taken from Ref.7).

The semiclassical model of multistep nuclear reaction processes, in which the discrete level effect in multiparticle emissions is included as well as the preequilibrium phenomenon combining parity conservation and angular momentum conservation, is used to describe the nuclear reaction preequilibrium and equilibrium decay processes.

This semiclassical model<sup>8)</sup> includes both the Hauser-Feshbach theory and the exciton model<sup>9,10)</sup>, and the exact Pauli exclusion effect in the exciton state densities<sup>11)</sup> is taken into account. The pick-up mechanism<sup>12)</sup> is used to describe the composite particle emission processes. Based on the leading particle model, the double differential cross section for all kinds of particles is obtained. In order to keep energy conservation for the whole reaction process, the recoil effect is taken into account in the UNF code.

The fission cross section is an important in  $n+^{232}\text{Th}$  reactions. Fission is included as a decay channel in the UNF code, that is, a fission competitive width can be estimated at every step of the

cascades. Three uncoupled fission barriers are used to represent the fission system. At each barrier a series of transition states characterized by excitation energy above the barrier, spin and parity can be constructed. At higher energies the discrete transition states are replaced by a continuum of such states, using the Gilbert-Cameron level density prescription and appropriate level density enhancement factors. The Bohr-Wheeler theory<sup>13)</sup> is used in transmission coefficients computed at each barrier. According to the experimental data of fission cross sections, the adjustment of the height parameters,  $V_f$ , the curvature parameters,  $\hbar\omega$ , of fission barriers, and the saddle level density factors,  $K_1$ , is performed to minimize a quantity called  $\chi^2$ , which represents the deviation of the theoretical calculated fission cross sections from the experimental values. The fission parameters obtained, exciton model parameter  $K$  and level density parameters are given in Ref.14).

### III. Theoretical Results and Analysis

The comparisons of calculated results of  $(n,\gamma)$  reaction cross sections with experimental data are given in Fig.3. The calculated results are in good agreement with experimental data taken from Refs.15-20) in the entire energy region. The calculated results of  $(n,\gamma)$  reaction cross sections are contributions of compound nuclear reaction below 6 MeV, and the direct reaction above 6 MeV. The cross sections of  $(n,p)$ ,  $(n,d)$ ,  $(n,t)$  and  $(n,\alpha)$  reactions are less than 12 mb, and have no experimental data.

The calculated results of inelastic scattering cross sections and inelastic scattering angular distributions for the first and second excited level are compared with experimental data in Figs.4 to 6. The figures show the compound nuclear reaction is domination for energy below 1.5 MeV, and the direct reaction is domination above 1.5 MeV. The calculated results of inelastic scattering cross sections, and inelastic scattering angular distributions of the first excited level are in good agreement with experimental data<sup>21-23)</sup>. The calculated results of inelastic scattering angular distributions of the second excited level are in basically agreement with experimental data. The calculated results of inelastic scattering angular distributions and inelastic scattering cross sections for the first and second excited level are lower than the experimental data at energy 3.4 MeV, and since the experimental data of inelastic scattering angular distribution are high for small angular, the experimental data of inelastic scattering cross section deviates from the tendency of all experimental data.

Since the first, second and third excited state of  $^{232}\text{Th}$  are 0.0492, 0.1621 and 0.3332 MeV, it is difficult to distinguish between the elastic scattering and inelastic scattering in experimentally. The experimental data of angular distribution inclusion elastic scattering and inelastic scattering of the first, second and third excited states were given in Refs.23,24), respectively. The calculated results of elastic, inelastic scattering angular distribution of the first and second excited states as well as total angular distribution at energy 2.4 MeV and 5.7 MeV are given in Fig.7, the results show the contribution of inelastic scattering are important in total angular distribution. The calculated results are in good agreement with experimental data taken from Ref.23). Fig.8 give the comparisons of calculated results with experimental data for elastic, inelastic scattering angular distribution of the first, second and third excited states in energy from 4.5 to 10 MeV, the calculated results fit experimental data very well for all energy.

Fig.9 gives the comparisons of calculated results with experimental data for  $(n,n')$  reaction. The calculated curves pass through the experimental data within error bars. The calculated results for  $(n,2n)$  reaction cross sections are in good agreement with the experimental data taken from Refs.25-29). There is a single experimental datum<sup>30)</sup> for the  $(n,3n)$  reaction at  $E_n=14$  MeV, the calculated results are

basically in agreement with the experimental data as shown in Fig.10. The fission cross section obtained from theoretical calculations as shown in Fig.11 and the number of neutrons per fission obtained from the systematic formulism which is obtained according to the experimental data of fission cross sections are modified slightly to better agree with the experimental data. The present results of fission cross section are in good agreement with experimental data<sup>31)</sup>.

The present calculated results and our earlier data<sup>14)</sup> of reaction cross sections for all channels are similar to the evaluated results in ENDF/B6 and JENDL-3 in curve shapes, but fit the new experimental data much better, especially the total cross sections,  $(n, n')$ ,  $(n, f)$  and  $(n, 2n)$  reaction cross sections. Based on the agreement of calculated results with experimental data for all reaction cross section, the energy spectrum, double differential cross section,  $\gamma$ -ray production cross sections and  $\gamma$ -ray production energy spectrum are calculated.

The fission neutron spectra are compared with experimental data at 1.5, 2.0, 2.9, 4.1 and 14.7 MeV, the Fig12. shows the theoretical calculated results are in good agreement with experimental data<sup>32-35)</sup> for all energy point.

The neutron-induced double differential emission spectra measurement is that of Baba et al.<sup>36)</sup> for 1.2, 2.03, 4.25, 6.1, 14.05 MeV incident neutrons. Additionally, Matsuyama et al.<sup>37)</sup> gave measurement results at 18.0 MeV. Calculated results and experimental data for neutron double differential emission spectra at 1.2 MeV are shown in Fig.13. Agreement is good over the whole emission energy range. Figure 13 shows some fluctuations in the calculated results, which are from discrete level contribution in the region of 0.15 to 1.1 MeV. The calculated results are the contribution of the fission channel above neutron emission energy 1.35 MeV.

The calculated results have been analyzed and compared to the double differential experiment data in energy 2.03, 4.25, 6.1, 14.05 and 18.0 MeV at Ref.14).

The experimental data and calculated results of angle-integrated neutron emission spectra are compared for incident energy  $E_n=2.03, 2.6, 4.25, 6.1, 14.05$  and 18.0 MeV, respectively. Our results are in excellent agreement with experimental data<sup>36)</sup> of angle-integrated neutron emission spectra at 2.03, 4.25 and 14.05 MeV incident energies, and in reasonable agreement with the spectra at 6.1 MeV incident energies. The experimental data of the spectra at 2.6 MeV were also given in Ref.38), Fig.14 is the comparison of calculated results with experimental data at incident energy 2.03 and 2.6 MeV, the calculated results at energy 2.03 MeV are in good agreement with experimental data taken from Ref.36) for the position and height of the peak, and at energy 2.6 MeV, there are some difference between the calculated results and the experimental data taken from Ref.38) for the peak position. The comparison of calculated results with experimental data for energy  $E_n=4.25$  and 6.1 MeV are given in Fig.15. Figs.13 to 15 also show the calculated results are from the contribution of fission spectra above emission neutron energy 2.2, 3.0, 4.5 and 6.4 MeV, the experimental data taken from Ref.36) are in good agreement with calculated results. The comparison of calculated results with experimental data is given in Fig.16 at incident energy 14.05 and 18 MeV. The calculated results are not in agreement with experimental data for  $E_n>5$  MeV and  $E_n<14$  MeV, where the calculated results are from the contribution of inelastic scattering and  $(n, 2n)$  reaction cross sections. Fig.17 gives the contribution of inelastic scattering,  $(n, 2n)$ ,  $(n, 3n)$ ,  $(n, f)$  reaction cross sections to spectra, and the values of reaction cross sections are given in table 1 at energy 18 MeV, the cross sections of  $(n, n')$ ,  $(n, 3n)$  and  $(n, f)$  reactions are larger than these of  $(n, 2n)$  reaction. The calculated spectra for energy 5.0 to 11.0 MeV is reasonable. Figs. 15 and 16 show experimental data of double differential cross sections is inconsistent with those of angle-integrated neutron emission spectra around the elastic peak.

Because emission spectra experimental data of Baba et al. included prompt fission and scattering neutrons, Figs.13 to 16 also demonstrate that calculated results of fission neutron spectra are reasonable.

Since neutron emission spectra and double differential cross sections provide a complementary information on inelastic scattering for discrete and continuum levels, (n, 2n), (n, 3n) reaction and neutron fission reaction of target nucleus, the agreement of neutron emission spectra and double differential cross sections between calculated results and experimental data also shows present calculated results of reaction cross sections are reasonable.

The double differential cross sections for proton, deuteron, triton and alpha emission,  $\gamma$ -ray production cross sections and  $\gamma$ -ray production energy spectrum are also calculated and analyzed at incident neutron energies below 20 MeV. The calculated results are given in our evaluation data file.

All our calculated results have been put into ENDF/B6 format and are saved in the Chinese Evaluated Nuclear Data Library, CENDL.

#### IV. Conclusion

Based on experimental data of total, nonelastic, elastic scattering cross sections and elastic scattering angular distribution of  $^{232}\text{Th}$ , a set of optimal neutron optical potential parameter is obtained by code APOM. All cross sections of neutron induced reactions, angular distributions, double differential cross sections, the angle-integrated spectra, the prompt fission neutron spectra,  $\gamma$ -ray production cross sections and  $\gamma$ -ray production energy spectra are calculated using theoretical models for  $n + ^{232}\text{Th}$  at incident neutron energies from 0.05 to 20 MeV, and theoretical calculated results are in good agreement with recent experimental data. The calculated results are given in ENDF/B6 format. The evaluated data of JENDL-3 are recommended for energy  $E_n < 0.05$  MeV.

#### Acknowledgments

This work is one of the physical and technological researches of Accelerator-Driven clean nuclear Power System (ADS), and supported by the China Ministry of Science and Technology under Contract No. G1999022600. I appreciate greatly the supported of the Researcher Invitation Program to the International Meeting Hosted by the Japan Atomic Energy Research Institute in the Field of Nuclear Safety.

#### REFERENCES

- 1) ZHANG Jingshang, Nucl. Sci. Eng. 142,207(2002).
- 2) P.G. Young, E.D. Arthur, and M.B. Chadwick, Comprehensive Nuclear Model Calculations: Theory and Use of the GNASH Code, Proc. IAEA Workshop Nuclear Reaction Data and Nuclear Reactors-Physics, Design, and Safety, Trieste, Italy, April 15-May 17, 1996, p. 227. A.GANDINI and G. REFFO, Eds., World Scientific Publishing, Ltd., Singapore (1998).
- 3) F.D. Becchetti Jr and G.W. Greenlees, Phys. Rev. 182,1190(1969).
- 4) SHEN Qingbiao, Commun. Nucl. Data Prog., 7,43(1992).
- 5) W.P. Abfalterer, F.B. Bateman, et al., Phys. Rev. C, 63,044608(2001).
- 6) J. Raynal, "Notes on ECIS94", CEA-N-2772, p.1, Commissariat a l'Energie Atomique, Saclay, France (1994).
- 7) G. Vladuca, A. Tudora, M. Sin, Regional Phenomenological Deformed Optical Potential for Neutron Interactions with Actinides, Rom. J. Phys., tome 41, no. 7-8(1996)515-526.

- 8) ZHANG Jingshang, Nucl. Data Prog., 7,15(1992).
- 9) G. Mantzouranis, H. Weidenmuller, and D. Agassi, Z. Phys. A, 276,145(1976).
- 10) Z. Sun, S. Wang, J. Zhang, and Y. Zhou, Z. Phys. A, 305,61(1982).
- 11) J. Zhang, and X. Yang, Z. Phys. A, 329,69(1988).
- 12) A. Iwamoto, and K. Harada, Phys. Rev. C, 26,1821(1982).
- 13) D.L. Hill and J.A. Wheeler, Phys. Rev., 89,1102(1953).
- 14) Han Yinlu, Shen Qingbiao, et al., Nucl. Sci. Eng., to be published.
- 15) M. Lindner, R.J. Nagle, and J.H. Landrum, Nucl. Sci. Eng. 59,381(1976).
- 16) W.P. Poenitz and D.L. Smith, Fast Neutron Radioactive Capture Cross Sections. ANL-NDM-42, (1978).
- 17) K. Kobayashi, Y. Fujita, and N. Yamamuro, Measurement of the Cross Section for the Th-232(n,g) Reaction From 1 KeV to 450 KeV. NEANDC(J)-56/U, (1978).
- 18) R.P. Anaand, H.M. Jain, et al., Neutron Capture Cross Section of Th-232. BARC-1239, 1984.
- 19) A.N. Davletshin, E.V. Teplov, et al., Yadernaye Konstanty, 14(1992).
- 20) A.N. Davletshin, E.V. Teplov, et al., Yadernaye Konstanty, 13(1993)
- 21) N.P. Glazkov, AE, 14,400(1963).
- 22) G. Haouat, J. Lachkar, et al., Nuc. Sci. Eng., 81,491(1982).
- 23) T. Iwasaki, M. Baba, et al., Contribution to the Specialists' Meeting on Fast Neutron Scattering on Actinide Nuclei, IWASAKI (1981).
- 24) A.B. Smith, S. Chiba, Annals of Nuclear Energy, 23,459(1996).
- 25) R.J. Prestwood, B.P. Bayhurst, Phys. Rev. 121,1438(1961).
- 26) H. Karius, A. Ackermann, W. Scobel, J. Phys. G, 5,715(1979).
- 27) H. Chatani, I. Kimura, Measurement of Th-232(n, 2n)Th-231 Reaction Cross Section With 14 MeV Neutrons. JAERI-M-91-032, p.245, 1991.
- 28) H. Chatani, I. Kimura, Annals of Nuclear Energy, 19,477(1992).
- 29) P. Paics, S. Daroczy, J. Csikai, et al., Phys. Rev. C, 32,87(1985).
- 30) M.H.MC Taggart, H. Goodfellow, J. Nuclear Energy, Parts A&B, Reactor Sci. Technology, AB, 17,437(1963).
- 31) Oleg Shcherbakov, Andrei Donets, et al., J. Nucl. Sci. Tech., Supplement, 2,230(2002).
- 32) S.E. Sukhikh, G.N. Lovchikova, et al., Yadernaye Konstanty, 3,34(1986).
- 33) M. Baba, H. Wakabayashi, et al., INDC(NDS)-220, 1989.
- 34) G.S. Boykov, V.D. Dmitriev, et al., Yadernaye Konstanty, 53,628(1993).
- 35) M. Baba, M. Ibaraki, et al., J. Nucl. Sci. Tech., Supplement, 2,204(2002).
- 36) M. Baba, H. Wakabayashi, T. Ito, et al., Measurements of Prompt Fission Neutron Spectra and Double-Differential Neutron Inelastic Scattering Cross Sections for 238-U and 232-Th. JAERI-M-89-143, 1989.
- 37) S. Matsuyama, M. Baba, T. Ito, et al., Nucl. Sci. Tech., 27,601(1990).
- 38) T. Miura, M. Baba, et al., Ann. Nucl. Energy, 28,937(2001).

Table 1 The calculated reaction cross sections at  $E_n=18$  MeV

(n, n')	(n,2n)	(n, 3n)	(n, f)
0.49035	0.27165	1.72164	0.50407

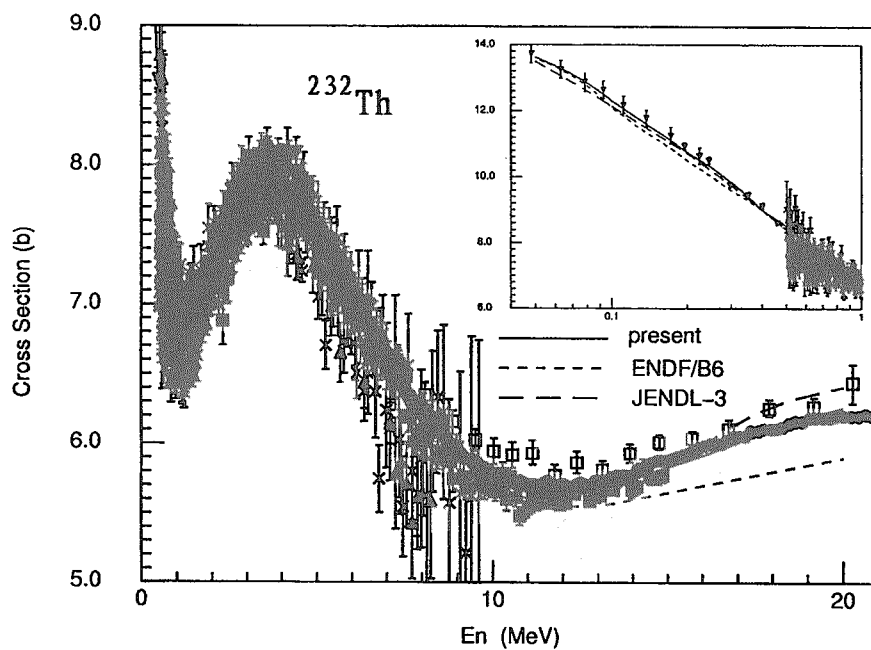


Fig.1 Calculated neutron total cross sections compared with experimental data.

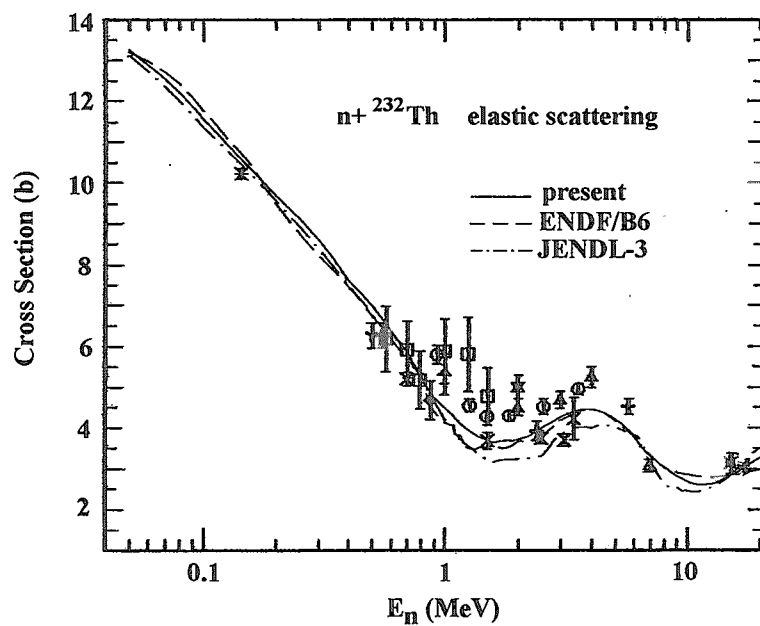


Fig.2 Calculated neutron elastic scattering cross section compared with experimental data.



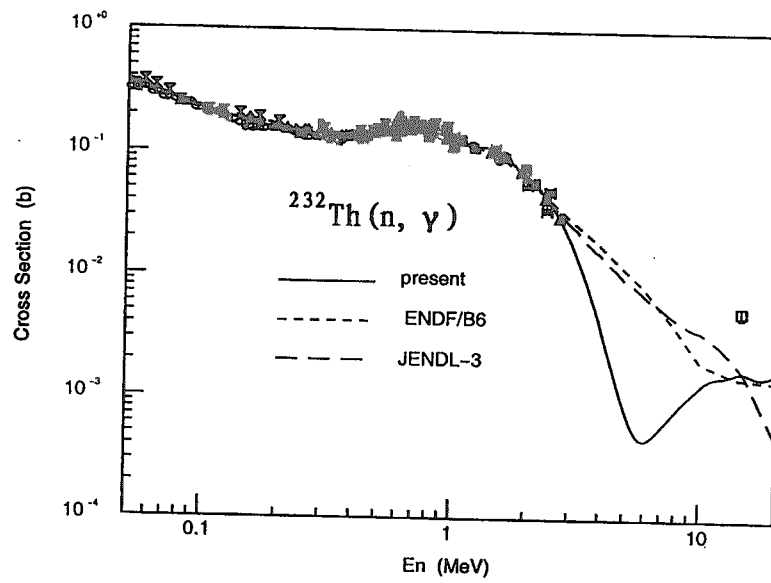


Fig.3 Calculated neutron captures cross section compared with experimental data.

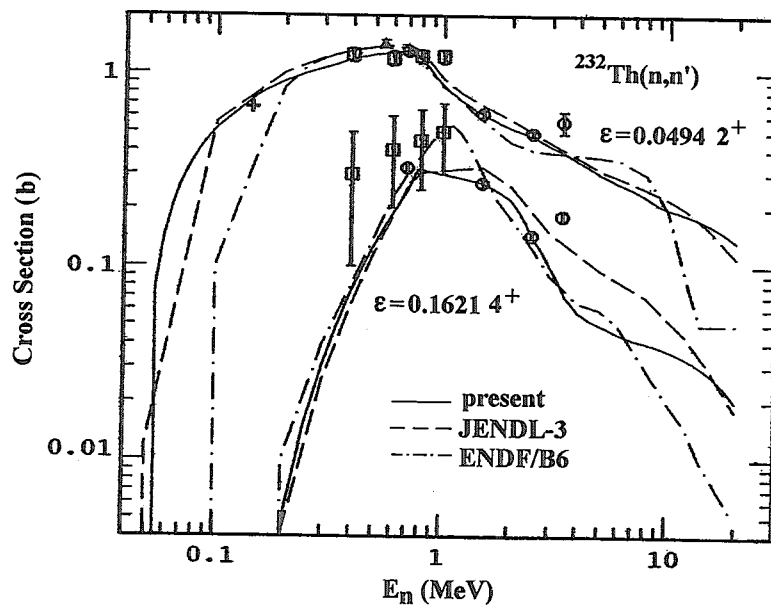


Fig.4 Calculated neutron inelastic cross section for the first and second excited levels compared with experimental data.

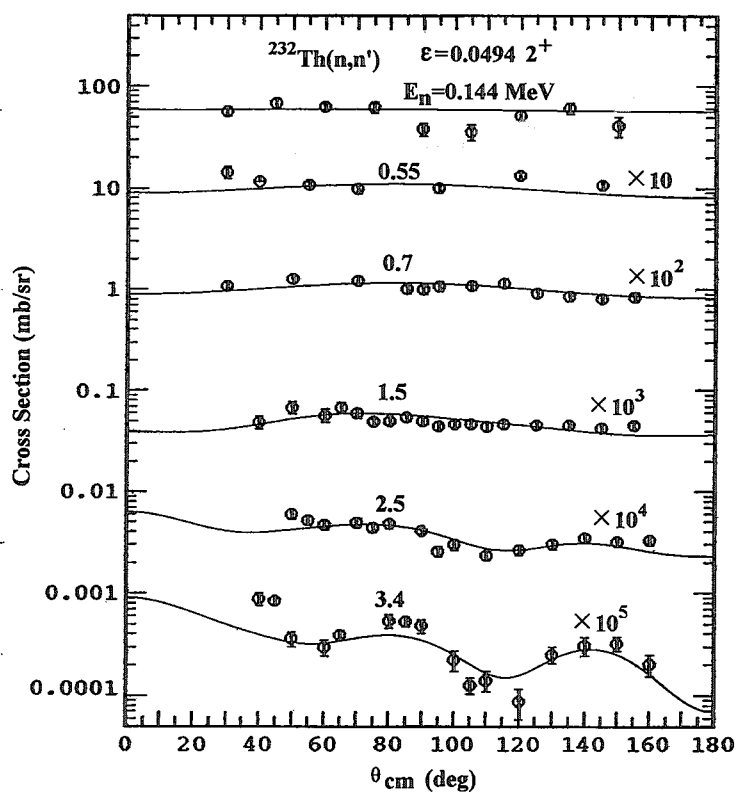


Fig.5 Calculated neutron inelastic scattering angular distribution for the first excited level compared with experimental data.

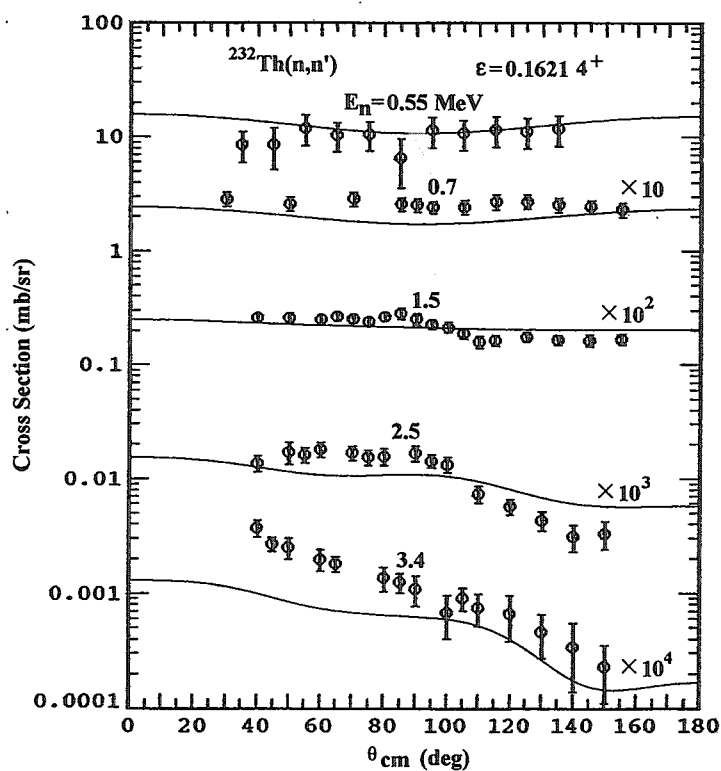


Fig.6 Calculated neutron inelastic scattering angular distribution for the second excited level compared with experimental data.

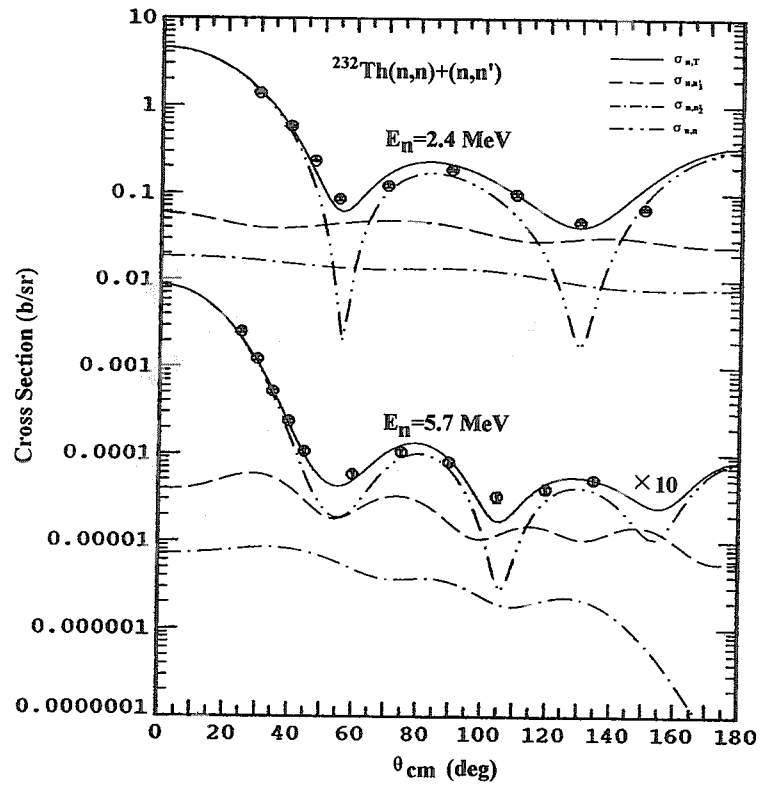


Fig.7 Calculated neutron elastic and inelastic scattering angular distribution of the first and second excited levels compared with experimental data at energy 2.4 and 5.7 MeV.

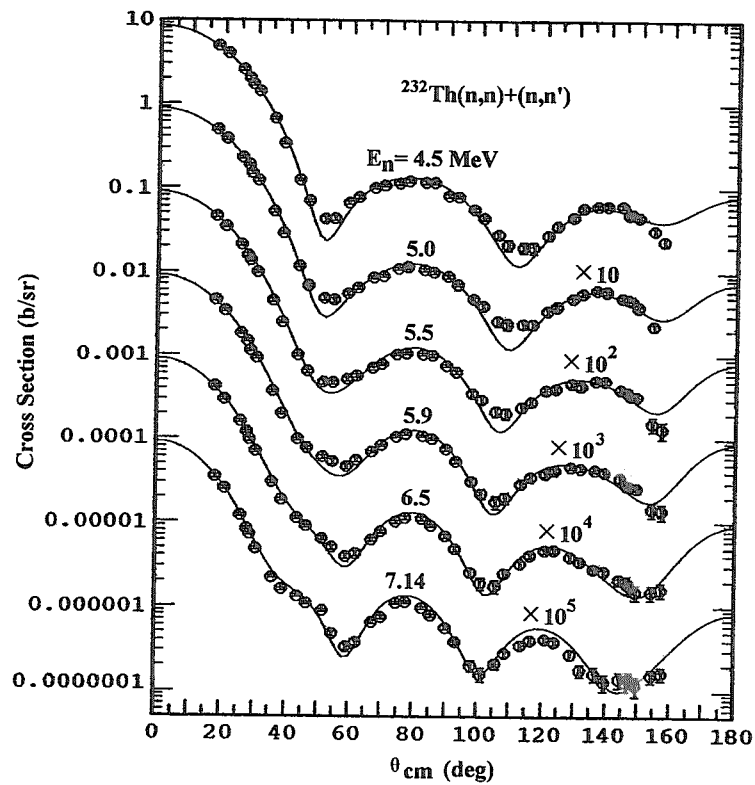


Fig.8(a) Calculated neutron elastic and inelastic scattering angular distribution of the first, second and third excited levels compared with experimental data.

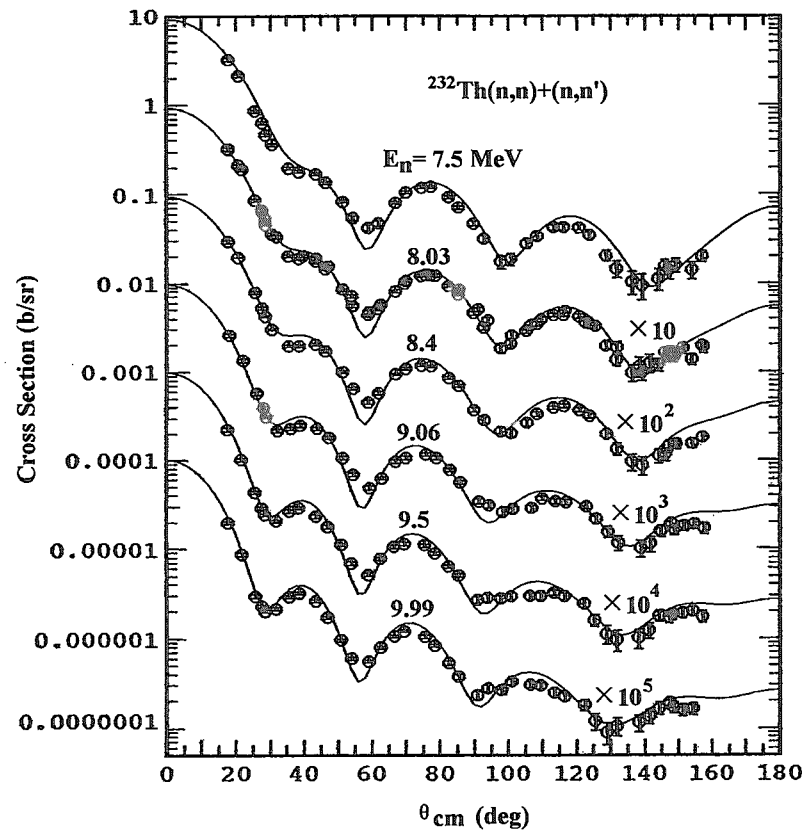


Fig.8(b) Calculated neutron elastic and inelastic scattering angular distribution of the first, second and third excited levels compared with experimental data.

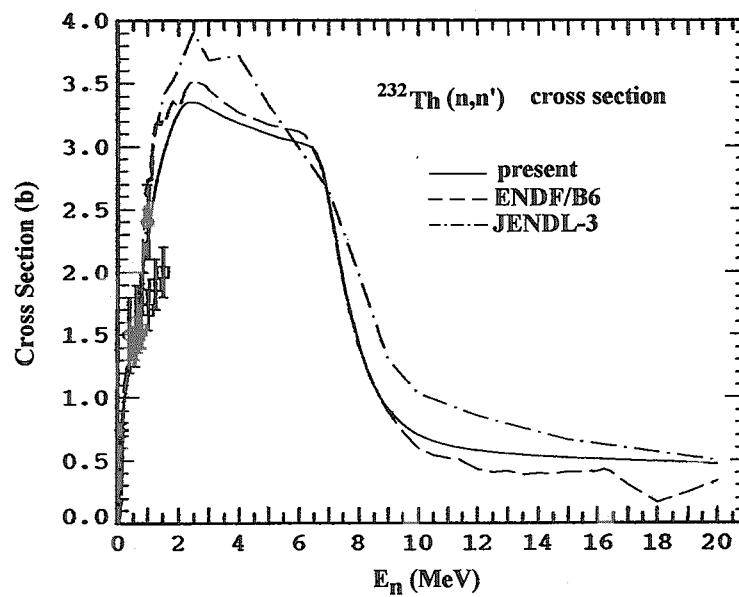


Fig.9 Calculated neutron inelastic cross sections compared with experimental data.

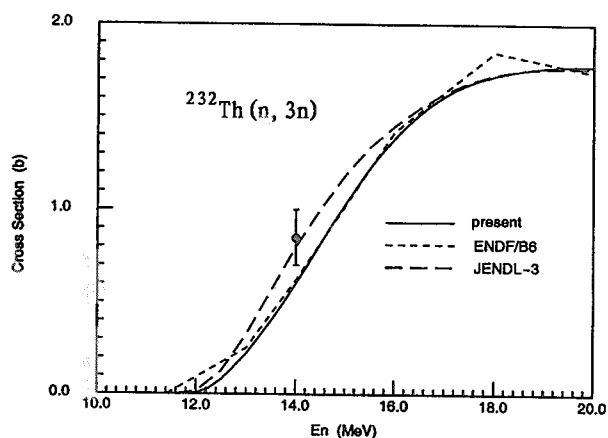


Fig.10 Calculated (n, 3n) reaction cross sections compared with experimental data.

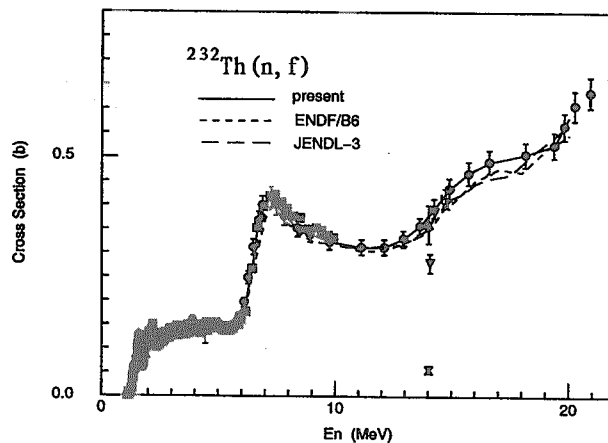


Fig.11 Calculated neutron fission cross sections compared with experimental data.

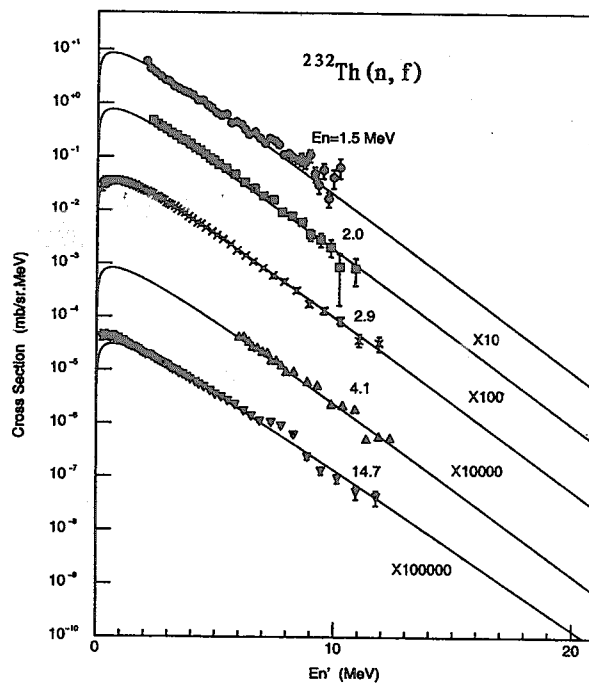


Fig.12 Calculated neutron fission spectra compared with experimental data at 1.5, 2.0, 2.9, 4.1 and 14.7 MeV incident neutron energy.

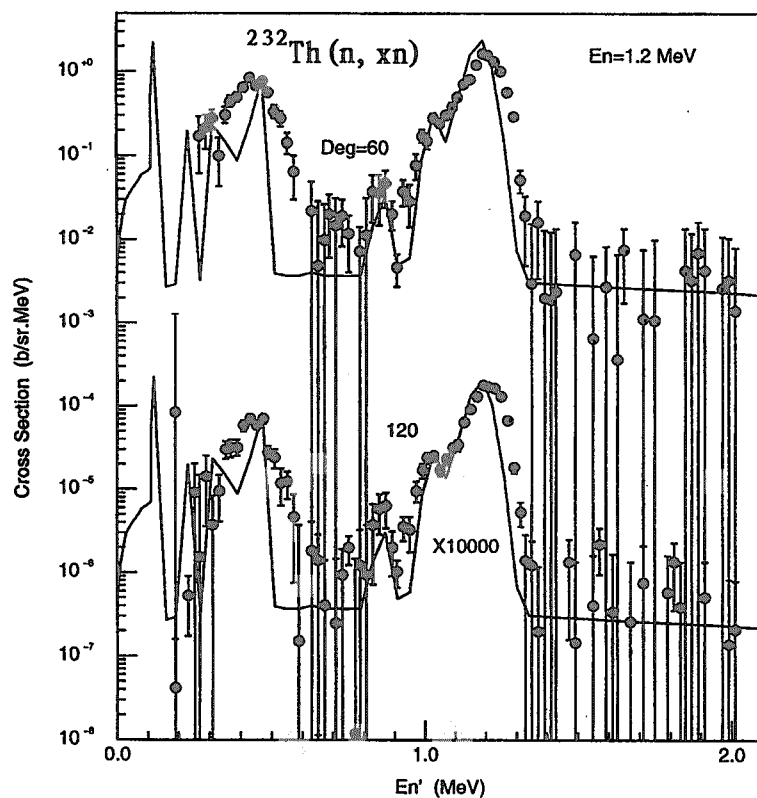


Fig. 13 Calculated double differential neutron emission spectra compared with experimental data at 1.2 MeV incident energy.

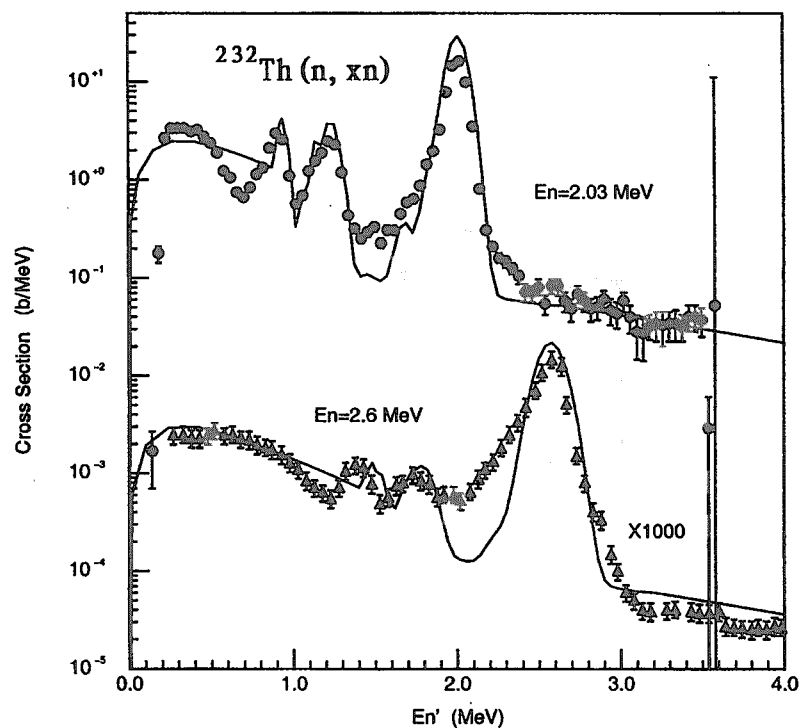


Fig.14 Calculated angle-integrated neutron emission spectra compared with experimental data at 2.03 and 2.6 MeV incident energy.

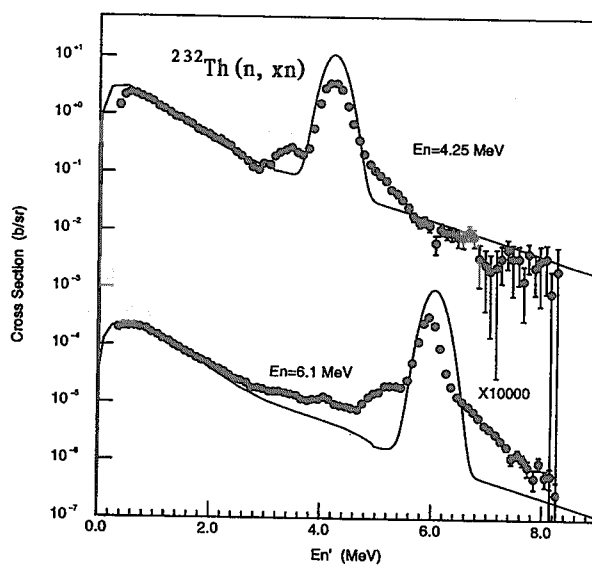


Fig.15 Calculated angle-integrated neutron emission spectra compared with experimental data at 4.25 and 6.1 MeV incident energy.

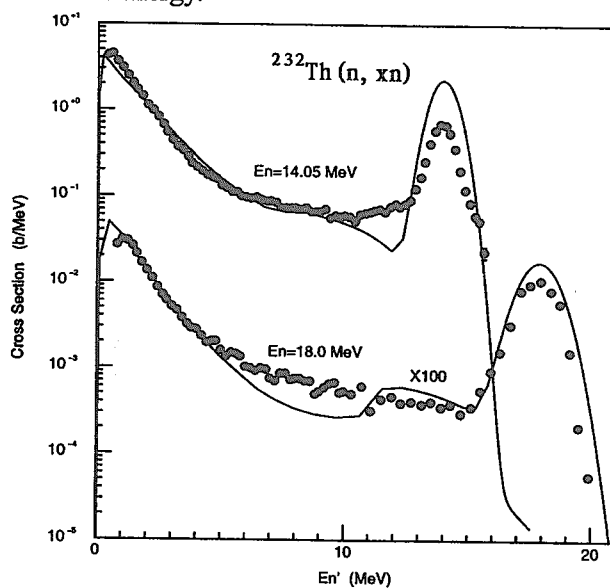


Fig.16 Calculated angle-integrated neutron emission spectra compared with experimental data at 14.05 and 18.0 MeV incident energy.

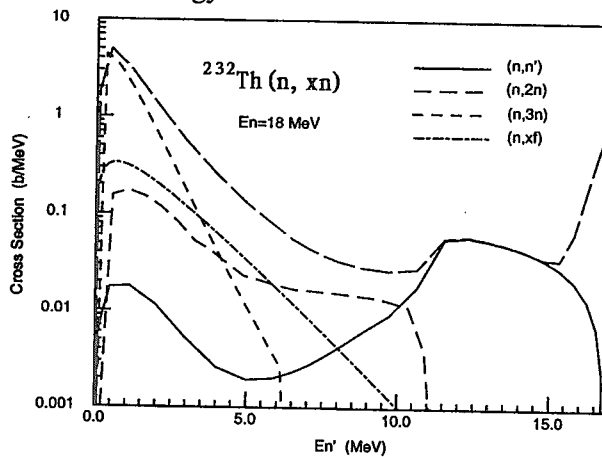


Fig.17 Calculated angle-integrated neutron emission spectra at 18.0 MeV incident energy.



## 2.13

**Progress in the KAERI High Energy Nuclear Data Library :  
Proton-induced Neutron Emission Spectra**

Young-Ouk Lee and Jonghwa Chang

*Korea Atomic Energy Research Institute, Korea  
P.O. Box 105 Yusong, Taejeon 305-600, Korea  
e-mail: yolee@kaeri.re.kr*

Proton-induced neutron yields and emission spectra up to a few hundreds MeV are important nuclear data in the particle transport of the accelerator-driven system (ADS) and in the space shielding for trapped protons and solar energetic particle events. Within the framework of KAERI high energy nuclear data library evaluation, energy-angle spectra of secondary neutrons produced from the proton-induced neutron production reaction, (p,xn), of C-12, Al-27, Fe-56, and Pb-208 for energies below 400 MeV are evaluated based upon model calculations, guided and benchmarked by existing experimental data. Theoretical calculations were performed with the optical model analysis for the direct reactions and transmission coefficients, Hauser-Feshbach model for the equilibrium emission, and the exciton model for the preequilibrium emission, using the ECIS-GNASH code system.

## 1. Introduction

In the particle transport analysis of the target system of ADS, proton-induced nuclear data, especially neutron yields and neutron emission spectra, play a key role [1].

Calculation of space system shielding is complicated due to the production of secondary products. A large fraction of the neutrons produced through the whole shield may be transported to the dose point. Thus, neutron contribution is an important component of the secondary radiation field, especially for astronauts protected by thick shielding on lunar or Martian bases.

The present work extends previous proton-nucleus non-elastic cross sections [2]. Energy-angle spectra of secondary neutrons produced from the proton-induced neutron production reaction of C-12 Al-27, Fe-56 and Pb-208 for energies below 400 MeV are evaluated based upon model calculations guided and benchmarked by existing experimental data. Since nuclear interactions are more sensitive to specific details of nuclear structure along with quantum effects for energies below few hundred MeV, our theoretical evaluation uses the optical model for the direct reactions, Hauser-Feshbach model for the equilibrium emission, and the exciton model for the preequilibrium emission.

## 2. Reference Measurements

Most of the measurements for energies below 150 MeV referenced in the LA150 library evaluation were also adopted in the present evaluation, and details are found in [3, 2].



Table 1: Reference measurements of neutron double-differential emission spectra for incident proton energy above 100 MeV

Reaction	Principal Author	$E_p$ [MeV]	Emission Angles [deg]	EXFOR entry
$^{12}\text{C}(p, xn)$	Meier (1989)	113.0	7.5, 30, 60, 150	O0100
	Meier (1992)	256.0	7.5, 30, 60, 150	C0168
$^{27}\text{Al}(p, xn)$	Meier (1989)	113.0	7.5, 30, 60, 150	O0100
	Scobel (1990)	160.3	0 - 145 (14 angles)	O0181
	Stamer (1993)	256.0	7.5, 30, 60, 150	C0511
	Meier (1992)	256.0	7.5, 30, 60, 150	C0168
$^{56}\text{Fe}(p, xn)$	Meier (1989)	113.0	7.5, 30, 60, 150	O0100
	Meier (1992)	256.0	7.5, 30, 60, 150	C0168
$^{208}\text{Pb}(p, xn)$	Scobel (1990)	120.0	0 - 145 (14 angles)	O0181
	Scobel (1990)	160.3	0 - 145 (14 angles)	O0181
	Stamer (1993)	256.0	7.5, 30, 60, 150	C0511
	Meier (1992)	256.0	7.5, 30, 60, 150	C0168

Additionally, important measurements of neutron emission spectra above 100 MeV of incident proton energy are referenced in Meier [4, 5], Scobel [6], and Stamer [7]. These four sets of measurements, listed in Table 1, provided important guidances in evaluating energy-angle spectra of emitted neutron for energies above 150 MeV.

### 3. Theoretical Models

#### 3.1 Optical Models

The optical model supplies not only the non-elastic cross section and the angular distribution of elastic scattering, but also the particle transmission coefficients for emission model calculations, such as equilibrium and preequilibrium decay models. In this work, the energy dependent potential wells for neutrons and protons were adopted from the previous work of Korea Atomic Energy Research Institute (KAERI) high energy library evaluation task [3, 2] for particle energies up to 400 MeV.

#### 3.2 Emission Models

For the emission reaction the latest version of the GNASH code [8] has been used. Several models and parameters are needed such as optical model transmission coefficients, gamma-ray transmission coefficients, level density models, preequilibrium components, and direct reaction effects.

The GNASH code has the exciton model in combination with the Kalbach angular-distribution systematics [9] to describe the processes of preequilibrium emission, and damping to equilibrium, during the evolution of the reaction. In the GNASH code, a simplified preequilibrium expression based upon the exciton model has been used for

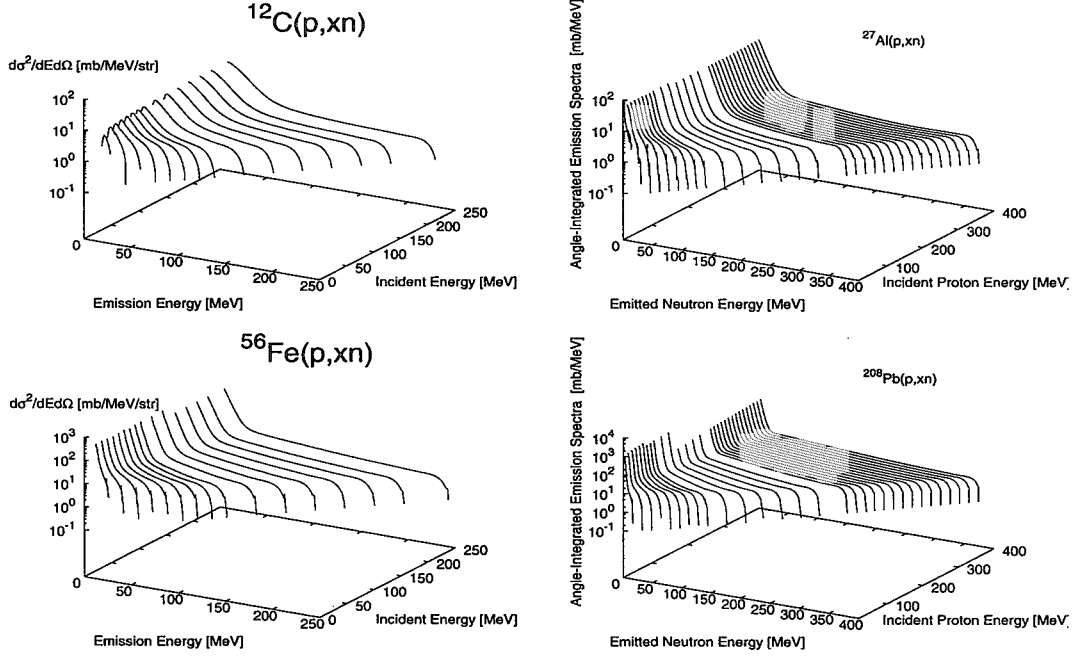


Figure 1: Evaluated angle-integrated neutron emission spectra for proton-induced reactions

correct reaction and level-excitation cross sections as well as spectra for preequilibrium effects :

$$\left(\frac{d\sigma}{d\epsilon}\right)_{preq} \propto \frac{\sigma_{inv}(\epsilon)m\epsilon\sigma_R}{|M|^2g^4E^3} \sum_{n=3}^{\bar{n}} (U/E)^{n-2}(n+1)^2(n-1), \quad (1)$$

where  $E$  and  $U$  are the excitation energies of the compound and residual nuclei, respectively;  $\sigma_R$  is the incident particle non-elastic cross section;  $m$ ,  $\epsilon$ , and  $\sigma_{inv}(\epsilon)$  are the mass, kinetic energy, and inverse cross section for the outgoing particle;  $g$  is the average single-particle level spacing from the Fermi-gas model; and  $n$  is the number of particles and holes ( $n = p+h$ ) in the compound nucleus. The sum extends from the initial exciton number 3 to  $\bar{n}$ , the limiting value attained when equilibrium is reached. To achieve a global agreement with the emission spectra measurements, the absolute square of the damping matrix  $|M|^2$  has been tuned as a phenomenological fudge factor.

The pion production channel opens at its production threshold energy (around 150 MeV), but the present model calculation does not include the pion channel, because its emission fraction to that of neutrons is at most 1 % at the higher emission energies for the energy range of our interest (see [10]).

## 4. Results and Comparisons

In order to give an overview of our evaluation results, Fig. 1 provides 3-dimensional plots of the angle-integrated emission spectra information of neutrons.

#### 4.1 $^{12}\text{C}$

For 113 MeV of incident proton, The first row of Fig. 2 compares our evaluation of double-differential neutron emission spectra at 7.5, 30, 60, and 150 degrees with the measurements of Meier et al. [4], together with the LA150 evaluation. Evaluated energy-angle spectra of emitted neutrons for 256 MeV of incident proton are compared with the Meier et al.'s data measured in 1992 [5], giving overall agreements.

#### 4.2 $^{27}\text{Al}$

The second row of Fig. 2 shows a comparison of our evaluation, the LA150 library, and the measurements of Meier [4] for double-differential neutron emission spectra at 7.4, 30, 60 and 150 degrees for incident protons of 113 MeV. Agreement is fairly good over the whole range of emission energies and angles except for slight overestimations for neutron energies below 20 MeV.

For incident proton energies above 150 MeV, our evaluations are compared with the measurements of Scobel [6] for 160.3 MeV and with the measurements of Stamer [7] for 256 MeV. Good agreements are shown for the 160.3 MeV case except at 145 degree, where our model calculations underestimate the measured neutron spectra. However, these discrepancies do not appear to be systematic in our model calculations since we have good agreements at 150 degree of 113 MeV and 256 MeV protons.

The 256 MeV case gives reasonable agreements except for slight overestimations at higher emission energies (preequilibrium emission) at 7.5 degree. The magnitude of the calculated pre-equilibrium emission spectra is determined by the Kalbach angular-distribution systematics in the GNASH code, and its accuracy is within that of the Kalbach systematics.

#### 4.3 $^{56}\text{Fe}$

For 113 MeV of incident proton, the third row of Fig. 2 shows excellent agreements among our evaluation, LA150, and the measurements [4] for double-differential neutron emission spectra at 7.5, 30, 60, and 150 degrees. Evaluated energy-angle spectra of emitted neutrons for 256 MeV of incident proton are compared with the measurements [5], providing quite good agreements for the entire energies and angles of emitting neutrons.

#### 4.4 $^{208}\text{Pb}$

The last row of Fig. 2 shows a comparison of our evaluation, the LA150 library, and the measurements of Scobel. [4] for double-differential neutron emission spectra at 11, 45, 95 and 145 degrees for incident protons of 120 MeV. Agreement is fairly good over the whole emission energies and angles except at 145 degree, where our model calculations as well as the LA150 library are smaller than the measured data. Again, these discrepancies do not appear to be systematic in our model calculations since we have good agreements at 145 degree of 160 MeV and at 150 degree of 256 MeV protons.

For incident proton energies above 150 MeV, our evaluations are compared with the measurements of Scobel [6] for 160.3 MeV, and in Fig. 2 with the measurements of

Meier [5] and Stamer [7] for 256 MeV. While good agreements are shown for the 160.3 MeV case, the 256 MeV case gives reasonable agreements except for slight overestimations at emission energies between 15 and 50 MeV, which is due to the limitation of Kalbach angular-distribution systematics.

## 5. Conclusion

Below 150 MeV of incident protons, no significant differences are noticed between our evaluation and the LA150 library, giving a good consistency with the measurements. This is mainly because the reference measurements, theoretical models, and model parameters are nearly the same for our evaluation and the LA150 library except the transmission coefficients of neutrons and protons, whose effects are minimal in the inclusive emission spectra.

For energies between 150 and 400 MeV, our evaluations are made on the same reaction models as the LA150 library, but with

- utilization of the optical model parameters of neutrons and protons validated for incident energies up to 400 MeV,
- benchmark with appropriate reference measurements for energies above 150 MeV, and
- adjustment of absolute square of the damping matrix to have a global agreement with emission spectra.

As a result, fairly good agreement has been achieved in the neutron double differential emission spectra for the entire emission energy and angle range. Slight discrepancies are observed at the preequilibrium emission energies between 15 and 50 MeV for 256 MeV protons incident on  $^{208}\text{Pb}$ , which come from the limitation of the Kalbach angular-distribution systematics.

## – References –

- [1] Lee, Y. O., *et al.*: In *Proc. of the International Conference on Nuclear Data for Science and Technology*. Oct., Tsukuba, Japan (2001).
- [2] Lee, Y. O., *et al.*: *IEEE Transactions on Nuclear Science*, **47**(6), 2435 (2000).
- [3] Lee, Y. O., *et al.*: In *Proc. of PHYSOR 2000: ANS International Topical Meeting on Advances in Reactor Physics and Mathematics and Computation into the Next Millenium*. Pittsburgh, Pennsylvania, U.S.A, May 7-12 (2000).
- [4] Meier, M., *et al.*: *Nucl. Sci. Eng.*, **102**, 310 (1989). EXFOR O0100.
- [5] Meier, M., *et al.*: *Nucl. Sci. Eng.*, **110**, 289 (1992). EXFOR C0168.
- [6] Scobel, W., *et al.*: *Phys. Rev. C*, **41**, 2010 (1990). EXFOR O0181.
- [7] Stamer, S., *et al.*: *Phys. Rev. C*, **47**, 1647 (1993). EXFOR C0511.
- [8] Young, P. G., *et al.*: In A. Gandini, G. Reffo, eds., *Proc. of the IAEA Workshop on Nuclear Reaction Data and Nuclear Reactors - Physics, Design, and Safety*, 227–404, Singapore (in press). Trieste, Italy, April 15 - May 17, 1996, World Scientific Publishing, Ltd.
- [9] Kalbach, C.: *Phys. Rev. C*, **37**, 2350 (1988).
- [10] Lee, Y. O., *et al.*: *J. of Nucl. Sci. and Tech.*, **36**(12), 1125 (1999).

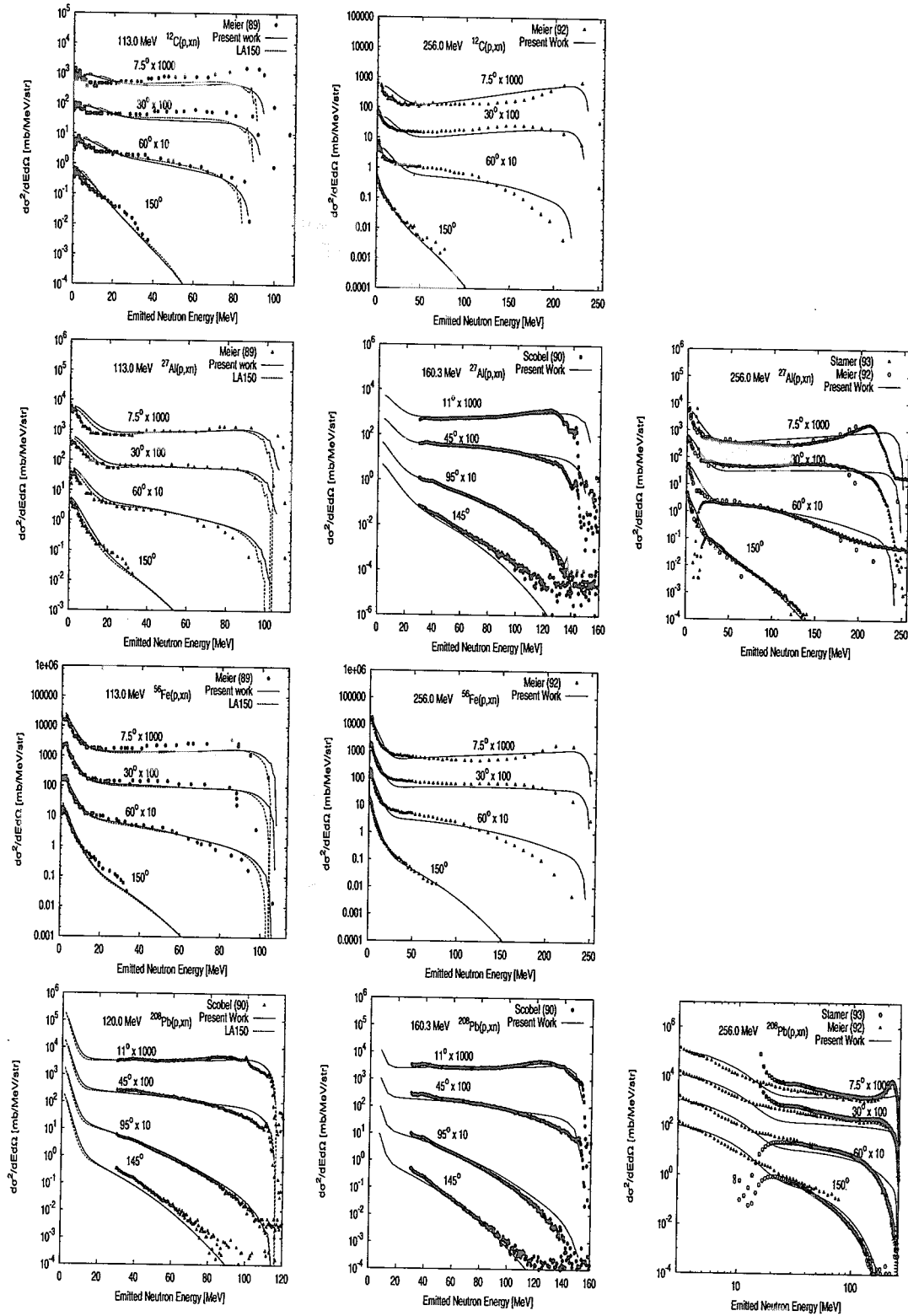


Figure 2: Evaluated double-differential neutron emission spectra compared with experimental data and the LA150 library



## 2.14

# BENCHMARK TESTS OF JENDL-3.3 AND ENDF/B-VI DATA FILES USING MONTE CARLO SIMULATION OF THE 3 MW TRIGA MARK II RESEARCH REACTOR

M.Q. Huda, T.K. Chakroborty, M.J.H. Khan and M.M. Sarker

Institute of Nuclear Science & Technology  
Atomic Energy Research Establishment  
Ganakbari, Savar, GPO Box 3787  
Dhaka-1000, Bangladesh.  
E-mail: quamrul@dhaka.net

The three-dimensional continuous-energy Monte Carlo code MCNP4C was used to develop a versatile and accurate full-core model of the 3 MW TRIGA MARK II research reactor at Atomic Energy Research Establishment, Savar, Dhaka, Bangladesh. The model represents in detail all components of the core with literally no physical approximation. All fresh fuel and control elements as well as the vicinity of the core were precisely described. Validation of the newly generated continuous energy cross section data from JENDL-3.3 was performed against some well-known benchmark lattices using MCNP4C and the results were found to be in very good agreement with the experiment and other evaluations. For TRIGA analysis continuous energy cross section data from JENDL-3.3 and ENDF/B-VI in combination with the JENDL-3.2 and ENDF/B-V data files (for  $^{nat}\text{Zr}$ ,  $^{nat}\text{Mo}$ ,  $^{nat}\text{Cr}$ ,  $^{nat}\text{Fe}$ ,  $^{nat}\text{Ni}$ ,  $^{nat}\text{Si}$ , and  $^{nat}\text{Mg}$ ) at 300K evaluations were used. Full  $S(\alpha,\beta)$  scattering functions from ENDF/B-V for Zr in ZrH, H in ZrH and water molecule, and for graphite were used in both cases. The validation of the model was performed against the criticality and reactivity benchmark experiments of the reactor. The MCNP calculated values for effective multiplication factor  $k_{eff}$  underestimated 0.0250% $\Delta k/k$  and 0.2510% $\Delta k/k$  for control rods critical positions and overestimated 0.2098% $\Delta k/k$  and 0.0966% $\Delta k/k$  for all control rods withdrawn positions using JENDL-3.3 and ENDF/B-VI, respectively. The core multiplication factor differs appreciably (~3.3%) between the no  $S(\alpha,\beta)$  (when temperature representation for free gas treatment is about 300K) and 300K  $S(\alpha,\beta)$  case. However, there is ~20.0% decrease of thermal neutron flux occurs when the thermal library is removed. Effect of erbium isotope that is present in the TRIGA fuel over the criticality analysis of the reactor was also studied. In addition to the  $k_{eff}$  values, the well known integral parameters:  $\delta^{28}$ ,  $\delta^{25}$ ,  $\rho^{25}$ , and  $C^*$  were calculated and compared for both JENDL3.3 and ENDF/B-VI libraries using the Monte Carlo simulation of the TRIGA reactor and found very close agreement among the two libraries. Results are also reported for most of the analyses performed by JENDL-3.2 and ENDF/B-V data libraries.

## 1. Introduction

A 3 MW TRIGA MARK II research reactor was commissioned at the Atomic Energy Research Establishment, Savar, Dhaka in 1986 and it went critical on 14<sup>th</sup> September, 1986. The diffusion theory model using multigroup cross section libraries analyzed some of the reactor experimental data. <sup>1</sup> In most cases, it was not possible to make valid comparisons due to various geometric and analytical approximations (e.g. homogenization, multigroup cross section treatment, etc.) commonly associated with these codes. So, applications of these codes for reactor analysis require qualification from other independent codes, which to some extent are free from the above-mentioned shortcomings. Because of this need for independent assessment, the Monte Carlo technique can be beneficial. For the purpose of modeling the TRIGA MARK II reactor, the general-purpose 3-D Monte Carlo *N*-Particle code MCNP4C <sup>2</sup> was chosen because of its general geometry modeling capability, correct representation of transport effects. The MCNP has the advantage of using a continuous energy cross section treatment as opposed to a multigroup approach thereby eliminating the errors in formulating few group cross sections. Continuous energy cross-section data from JENDL-3.3 and ENDF/B-VI in combination with JENDL-3.2 and ENDF/B-V data libraries (for  $^{nat}\text{Zr}$ ,  $^{nat}\text{Mo}$ ,  $^{nat}\text{Cr}$ ,  $^{nat}\text{Fe}$ ,

$^{nat}\text{Ni}$ ,  $^{nat}\text{Si}$ , and  $^{nat}\text{Mg}$ ) at 300K evaluations were used. Full  $S(\alpha,\beta)$  scattering functions from the ENDF/B-V library were used in both cases. An essential aspect of developing an accurate reactor physics model is validation. The accuracy of both the neutron transport physics as represented in MCNP and the user-defined model must be assessed. However, even though MCNP has been proven to simulate the physical interactions correctly, that does not mean that the model of TRIGA will provide accurate answers. Therefore, to build confidence, all the neutronic parameters including effective multiplication factor, in-core and ex-core neutron flux and benchmarking of reactivity experiments were performed for the fresh core to supplement and compare MCNP predicted values with the experiments. It may be mentioned that this benchmarking of Monte Carlo simulation of TRIGA reactor is one of very few low-enrichment benchmarks available.

## 2. MCNP Modeling of TRIGA

The TRIGA core consists of 100 fuel elements arranged in a concentric hexagonal array within the core shroud. The reactor is a light water cooled, graphite-reflected one, designed for continuous operation at a steady-state power level of 3000 kW (thermal). Figure 1 shows the cross sectional view of the present core arrangement of the reactor. The spaces between the rods are filled with waters that act as coolant and moderator. The repeated structure capability of MCNP was used to create a full core, three-dimensional model of TRIGA.<sup>2</sup> The fuel elements were modeled explicitly specifying the detailed structure of the rod to eliminate any homogenization effects. All the control rods were explicitly modeled along the active length with the exception of the drive mechanism. The central thimble was considered to be filled with water in the model and the pneumatic tube was assumed to be void. The graphite dummy elements are of the same general dimensions and construction as the fuel-moderator elements, except these elements are filled entirely with graphite. The model was extended up to ~100 cm radially containing the graphite reflector and lead shield and ~110 cm above and below the core centerline, which was more than sufficient to account for the neutron returning from the H<sub>2</sub>O coolant above and below the core. An annular well on the inside diameter in the top of the graphite reflector that provides for the rotary specimen rack Lazy Susan was also modeled along with the radial and tangential beam ports. Thus, it has been possible to describe the geometry of the TRIGA reactor explicitly without resorting to any approximation at all. The MCNP4C input was prepared in such a way that a very quick setup of any desired core configuration with an adequate position of all control rods is possible. A summary of the principal design parameters, material composition data and details of the modeling of the reactor can be found in Ref. 3. All geometric and material data are taken from the fabrication and shipment documentation, provided by the reactor vendor General Atomics.

## 3. Generation of Cross Section Library

Continuous energy cross-section data for all the materials present in the Monte Carlo simulation of the TRIGA reactor were generated from JENDL-3.3 using the NJOY nuclear data processing system. The Japanese Evaluated Nuclear Data Libraries (JENDL) has progressed through a number of versions; the latest version JENDL-3.3 has been tentatively released to test the validation in early 2000.<sup>4</sup> The cross section set at 300K was generated using NJOY99.0,<sup>5</sup> the latest version of NJOY, which constructs, broadens and formats the data into the appropriate form for MCNP. For heavier isotopes, resonance cross section formulae are used to calculate the elastic, capture, and fission cross sections over a defined "resonance range." Comparison of resonance integrals and thermal cross sections for  $^{235}\text{U}$  and  $^{238}\text{U}$  from JENDL and ENDF data libraries is shown in Table I. At higher energies in heavier nuclei, the resonances get so close together that they cannot be given separately. Instead of giving individual resonances with their energies and characteristic widths, ENDF-format evaluations give average values for the resonance spacing and the various characteristic widths, together with the probability distributions needed to describe the quantities. The self-shielded cross sections are computed by UNRESR and the probability tables are computed by PURR. The probability tables from PURR are usually processed by the ACER module and made available to the Monte Carlo code MCNP. Some modifications are required in MODER module of NJOY99.0 to process JENDL-

3.3 data of  $^{238}\text{U}$  nuclei comprised of covariance data. <sup>6</sup> Comparison of resolved and unresolved resonance energy regions for  $^{235}\text{U}$  and  $^{238}\text{U}$  isotopes from JENDL and ENDF is tabulated in Table II.

Validation of the newly generated continuous energy cross section data from JENDL-3.3 was performed against some well-known benchmark lattices using MCNP4C code and the results were found to be very good agreement with the experiment and other evaluations. Small fast reactor cores like GODIVA with hard neutron spectrum and thermal reactor core like TRX with water-moderated lattice of uranium fuel were selected. <sup>7</sup> Results are also reported from the analyses of these benchmark lattices based on JENDL-3.2, ENDF/B-V and ENDF/B-VI data libraries. Calculated lattice parameters are obtained from reaction rates edited for the central, asymptotic portion of the lattice. These are (with a thermal-cut energy of 0.625 eV):

$\delta^{28}$  = ratio of  $^{238}\text{U}$  fissions to  $^{235}\text{U}$  fissions.

$\delta^{25}$  = ratio of epithermal-to-thermal  $^{235}\text{U}$  fissions.

$\rho^{25}$  = ratio of epithermal-to-thermal  $^{238}\text{U}$  captures.

$C^*$  = ratio of  $^{238}\text{U}$  captures to  $^{235}\text{U}$  fissions.

These lattices directly test the  $^{235}\text{U}$  resonance fission integral and thermal fission cross section. They also test  $^{238}\text{U}$  shielded resonance capture and the thermal capture cross section. The integral parameters after leakage corrections for different lattices along with the  $k_{eff}$  values are summarized in Table III. <sup>7</sup> The eigenvalue predictions by MCNP4C using different versions of JENDL and ENDF libraries for all three lattices are excellent. For TRX-1, the  $\delta^{28}$  and  $\rho^{25}$  values for JENDL-3.3 are slightly overpredicting the experimental values, but much more closely than those of ENDF/B-VI. Excellent agreement are observed for  $\delta^{25}$  and  $C^*$  values for both the libraries. In case of TRX-2, once again, all the integral parameters are in good agreement with the experiment. TRX-2 is a more thermal system than TRX-1 and, as a rule, evaluations agree better with the experiment, reflecting the slight overprediction of  $^{238}\text{U}$  resonance capture. Comparing the calculated integral parameters based on the latest version of JENDL-3.3 with the measured values and results from other evaluations for three light water benchmark lattices, it can be concluded that the performance of the newly generated continuous energy cross section library from JENDL-3.3 is quite satisfactory and offers a significant improvement compared to the other libraries. Almost all the parameters are within the experimental uncertainty limits of the measurements. So the generated continuous energy cross section data files from JENDL-3.3 library can be used for the TRIGA benchmark analysis with confident.

#### 4. Results and Discussions

The neutronic analysis of the 3 MW TRIGA MARK II benchmark experiments at AERE, Savar was performed by the three-dimensional Monte Carlo code MCNP4C using the JENDL-3.3 and ENDF/B-VI data libraries and the results are summarized in the following sections.

##### A. Effective Multiplication Factor

The calculation of effective multiplication factor  $k_{eff}$  was performed for the core both with and without control rods. The control rods in the former were in the critical positions and in the latter were completely withdrawn positions. The initial critical core configuration ( $k_{eff}$  equal to 1.0) was obtained with critical rod height of all control rod bank positions to 37.1309% equivalent to a length of 14.146875 cm, i.e., all control rods were 23.953125 cm inserted to the active core. The estimated statistical error ( $1\sigma$ ) was reduced below 0.03% upon 3000 cycles of iteration on a nominal source size of 3,000 particles per cycle. The comparison between the MCNP calculated  $k_{eff}$  and the experimental one is shown in Table IV. The MCNP calculated values of  $k_{eff}$  underestimated 0.0250% $\Delta k/k$  and 0.2510% $\Delta k/k$  for control rods critical positions and overestimated 0.2098% $\Delta k/k$  and 0.0966% $\Delta k/k$  for all control rods withdrawn positions using JENDL-3.3 and ENDF/B-VI data libraries, respectively.



## B. Neutron Flux Analysis

A comparison was made between the experimentally measured peak neutron flux at the water filled central thimble (CT) and at the rotary specimen rack Lazy Susan (LS) of the reactor with the MCNP calculations and tabulated in Table V. The neutron flux, normalized to 3 MW (thermal), was calculated in MCNP that tallied the integrated neutron flux above the appropriate energy in the irradiated volume. The thermal energy range was chosen from 0 to 0.41 eV and epithermal energy range was 0.41 eV to 9.118 keV. The peak thermal neutron flux calculated by MCNP is under predicting the experimental one by ~8.46% and ~11.3% for JENDL-3.3 and ENDF/B-VI, respectively. It is also found that the MCNP predicted values for the epithermal neutron flux agree more closely with experimental values.

## C. Power Distribution and Peaking Factor

The total power produced within the fuel and fuel-follower elements of the core was calculated through MCNP4C using JENDL-3.3 and ENDF/B-VI and is shown in Fig. 2. The fuel and fuel-follower element numbers are such that the fuel number 1 in the Fig. 2 represents the C1 fuel element of TRIGA core arrangement (Fig. 1) and similarly 2 & 3 represents C2 & C4 fuel elements and so on. The maximum power production of  $5.6791 \times 10^4$  kW and  $5.5619 \times 10^4$  kW are observed for JENDL-3.3 and ENDF/B-VI, respectively, within the fuel element designated by C4 (Fig. 2) and is assumed to be the hottest rod in the TRIGA core. Now the hot-rod factor is determined in MCNP using the following component values:

$$\begin{aligned} \left[ \frac{\overline{P_{rod}}}{P_{core}} \right]_{\max} &= \frac{\text{Average Power Produced in the hottest Fuel Element}}{\text{Average Power in the Core}} \\ &= 1.8930 \text{ [obtained with JENDL-3.3]} \\ &= 1.8540 \text{ [obtained with ENDF/B-VI]} \end{aligned}$$

This value for C4 fuel element (hot rod) is found to be in very good agreement with the calculated value of 1.8746 obtained from CITATION calculation.<sup>1</sup>

## D. Effect of S( $\alpha,\beta$ ) Library

The initial critical eigenvalue predicted by the model were 0.99975 and 0.99749 for JENDL-3.3 and ENDF/B-VI, respectively and compared well with the measured value of 1.00. For a few low-z materials, thermal scattering S( $\alpha,\beta$ ) cross sections at certain temperatures are available that account for the effects of chemical binding and crystalline structure and is used in order to accurately model the neutron interactions at energies below ~4eV. Results of the effects of thermal library for Zr/H, H/Zr, light water and graphite are given in Table VI. The core multiplication factor differs appreciably (~3.3%) between the no S( $\alpha,\beta$ ) (when temperature representation for free gas treatment is about 300K) and 300K S( $\alpha,\beta$ ) case using both JENDL-3.3 and ENDF/B-VI libraries. However, there is ~20.0% decrease of thermal neutron flux occurs when the thermal library is removed, but no significant changes occur in case of epithermal neutron flux.

## E. Effect of Erbium Isotope over TRIGA LEU fuel

In the U-ZrH TRIGA fuel, the temperature-hardened spectrum is used to decrease reactivity through its interaction with a low energy-resonance material. Thus, erbium, with its double resonance at ~0.5 eV, is used in the TRIGA LEU fuel as both a burnable poison and a material to enhance the prompt negative temperature coefficient. When the fuel-moderator material is heated, the neutron spectrum is hardened, and the neutrons have an increasing probability of being captured by the low-energy resonances in erbium. This increased parasitic absorption with temperature causes the reactivity to

decrease as the fuel temperature increases. The neutron spectrum shift, pushing more of the thermal neutrons into the  $^{167}\text{Er}$  resonance as the fuel temperature increases, is illustrated in Fig. 3, where cold and hot neutron spectra are plotted along with the energy-dependent absorption cross section for  $^{167}\text{Er}$  from JENDL-3.3 and ENDF/B-VI. It may be mentioned that the isotopes of erbium have been incorporated for the first time in both JENDL-3.3 and ENDF/B-VI library. A study has also been performed regarding the effectiveness of  $^{166}\text{Er}$  and  $^{167}\text{Er}$  isotopes over the criticality calculation of TRIGA reactor using JENDL-3.3 and ENDF/B-VI and is summarized in Table VII. The MCNP calculated  $k_{\text{eff}}$  value overestimated 9.48% $\Delta k/k$  and 9.58% $\Delta k/k$  for JENDL-3.3 and ENDF/B-VI, respectively, when erbium is absent in the TRIGA LEU fuel; whereas ~99.05% and ~96.66% of this increment is because of  $^{167}\text{Er}$ .

#### F. Study of Integral Parameters

The eigenvalue predictions by MCNP4C using different versions of JENDL and ENDF libraries for TRIGA reactor are excellent. Calculation has also been performed to study the integral parameters using the Monte Carlo Simulation of TRIGA reactor based on JENDL and ENDF data libraries and tabulated in Table VIII. All the integral parameters are found to be very close.

#### G. Control Rod Worth

Adequate treatment of control rods is very important in the simulation of any specific core configuration. Even small deviations of the model could eventually lead to large systematic errors of the calculated  $k_{\text{eff}}$ . Detailed methods and formulations used to calculate the control rod worths can be found in Ref. 3. Total control rod worths together with the experimental data are summarized in Table IX. The agreement between the MCNP predicted values and the experimentally determined values are consistent within the estimated experimental error of 10%.<sup>3</sup>

### 5. Conclusions

MCNP has been used to develop a versatile and accurate reactor physics model of the TRIGA MARK II research reactor. To minimize errors due to an inexact geometry model, the reactor was very thoroughly modeled. Validation of the newly generated continuous energy cross section data from JENDL-3.3 using NJOY99.0 data processing system was performed against some well-known benchmark lattices using MCNP4C code and the results were found to be in very good agreement with the experiment and other evaluations. The consistency and accuracy of the MCNP4C model of the TRIGA reactor core was established by comparing calculations to the experimental results of the benchmark experiments and found to be in good agreement.

#### Acknowledgements

The authors wish to thank Dr. Makoto Takano of the Department of Fuel Cycle Safety Research, Tokai Research Establishment, JAERI, Japan for his valuable suggestions and assistance in modeling the various portions of the TRIGA reactor during his stay at AERE as a visiting scientist.

#### References

1. Bhuiyan S.I. et al.: *Nucl. Tech.*, **130**, 111 (2000).
2. "MCNP – Monte Carlo N-Particle Transport Code (Version 4C)," RSICC#:CCC-700 (2000).
3. Huda M.Q. et al.: *Proc. Int. Conf. Physor2002: New Frontiers of Nucl. Tech.*, Paper No.: 9E-19, Korea, Oct. 7-10, 2002.
4. "JENDL-3.3 - The Japanese Evaluated Nuclear Data Library, version 3.3," JAERI (2000).
5. "NJOY - The Nuclear Data Processing System (Version 99.0)," RSICC#: PSR-480 (2000).
6. Nakamura N. and Kosako K. et al.: Private Communication.
7. Sitaraman S. "MCNP: Light Water Reactor Critical Benchmarks", GE Nuclear Energy, NEDO-32028 (1992).

Table I: Comparison of resonance integrals and thermal cross sections in JENDL and ENDF (barn)

Material	Library	Resonance Integrals		Thermal Cross sections at 2200 m/s	
		Fission	Capture	Fission	capture
$^{235}\text{U}$	JENDL3.3	585.1	98.69	276	141
	ENDF/B-VI	584.88	98.66	276.04	140.49
	JENDL3.2	584.4	98.81	279	134
$^{238}\text{U}$	JENDL3.3	11.8E-06	2.717	1.72	277
	ENDF/B-VI	6.46E-05	2.72	1.7E-03	278
	JENDL3.2	11.8E-06	2.717	1.72	277

Table II: Comparison of resolved and unresolved resonance energy regions in JENDL and ENDF (eV)

Material	Library	Resolved Resonance Region	Unresolved Resonance Region
$^{235}\text{U}$	JENDL3.3	< 2250	2250 – 30000
	ENDF/B-VI	< 2250	< 100000
	JENDL3.2	< 500	500 – 30000
	ENDF/B-V	< 82	82 – 25000
$^{238}\text{U}$	JENDL3.3	1.0E-05 – 10000	10000 – 150000
	ENDF/B-VI	1.0E-05 – 10000	10000 – 149000
	JENDL3.2	1.0E-05 – 10000	10000 – 150000
	ENDF/B-V	1.0E-05 – 4000	4000 – 149000

Table III: Summary of the MCNP4C results to the reference one for selected benchmark lattice analysis

Lattice	Methods	$k_{eff}$	$\delta^{28}$	$\delta^{25}$	$\rho^{25}$	C*
GODIVA	Experiment	1.00000 ( $\pm 0.30$ )	-	-	-	-
	JENDL3.3	1.00329 (+0.33)	-	-	-	-
	ENDF/B-VI	0.99669 (-0.33)	-	-	-	-
	JENDL3.2	1.00156 (+0.16)	-	-	-	-
	ENDF/B-V	0.99814 (-0.19)	-	-	-	-
TRX-1	Experiment	1.00000 ( $\pm 0.20$ )	0.0946 ( $\pm 0.41$ )	0.0987 ( $\pm 0.10$ )	1.320 ( $\pm 2.10$ )	0.797 ( $\pm 0.80$ )
	JENDL3.3	1.00134 (+0.13)	0.09688 (+2.41)	0.09835 (-0.35)	1.352 (+2.42)	0.790 (-0.88)
	ENDF/B-VI	0.99930 (-0.07)	0.09874 (+4.38)	0.09943 (+0.74)	1.382 (+4.70)	0.796 (-0.13)
	JENDL3.2	1.00262 (+0.26)	0.09464 (+0.04)	0.09857 (-0.13)	1.355 (+2.65)	0.858 (+7.65)
	ENDF/B-V	1.00071 (+0.07)	0.09835 (+3.96)	0.10006 (+3.96)	1.379 (+4.47)	0.796 (-0.13)
TRX-2	Experiment	1.00000 ( $\pm 0.20$ )	0.0693 ( $\pm 0.35$ )	0.0614 ( $\pm 0.08$ )	0.837 ( $\pm 1.60$ )	0.647 ( $\pm 0.60$ )
	JENDL3.3	1.00095 (+0.10)	0.06915 (-0.22)	0.06037 (-0.22)	0.842 (+0.60)	0.639 (-1.24)
	ENDF/B-VI	0.99887 (-0.11)	0.06968 (+0.55)	0.06092 (+0.55)	0.857 (+2.39)	0.642 (-0.77)
	JENDL3.2	1.00169 (+0.17)	0.06726 (-2.94)	0.06054 (-2.94)	0.846 (+1.08)	0.638 (-1.39)
	ENDF/B-V	1.00007 (+0.007)	0.06965 (+0.51)	0.06168 (+0.51)	0.858 (+2.51)	0.642 (0.77)

Table IV: Comparison of criticality calculations to the experiment at different control rod positions

Control Rods Positions	Method	Core Multiplication Factor $k_{eff}$	C/E
Critical	Experiment	1.00000	-
	JENDL3.3	0.99975 $\pm$ 0.00027	0.999
	ENDF/B-VI	0.99749 $\pm$ 0.00029	0.997
	JENDL3.2	1.00457 $\pm$ 0.00027	1.004
	ENDF/B-V	0.99599 $\pm$ 0.00027	0.995
Withdrawn	Experiment	1.077459	-
	JENDL3.3	1.07972 $\pm$ 0.00028	1.002
	ENDF/B-VI	1.07850 $\pm$ 0.00028	1.000
	JENDL3.2	1.08072 $\pm$ 0.00028	1.003
	ENDF/B-V	1.07646 $\pm$ 0.00029	0.999

Table V: Comparison of the MCNP4C TRIGA reactor peak neutron flux calculations to the experiment

Method	Peak Neutron Flux ( $\times 10^{13}$ n/cm <sup>2</sup> .s)				C/E			
	CT		LS		CT		LS	
	Thermal	Epithermal	Thermal	Epithermal	Thermal	Epithermal	Thermal	Epithermal
Experiment	8.3034	1.8842	0.7721	0.2132	-	-	-	-
JENDL3.3	7.6007	1.8489	0.6277	0.2626	0.915	0.981	0.812	1.231
ENDF/B-VI	7.3631	1.8278	0.6285	0.2593	0.886	0.970	0.814	1.216
JENDL3.2	7.5127	1.8835	0.6202	0.2607	0.904	0.999	0.803	1.222
ENDF/B-V	7.3978	1.7937	0.6287	0.2606	0.890	0.951	0.814	1.222

Table VI: Effect of thermal library (Zr/H, H/Zr, lwtr &amp; grph) over the criticality and peak neutron flux calculation at different positions of the TRIGA reactor through MCNP4C using JENDL and ENDF

Condition	Library	Core Multiplication Factor $k_{eff}$	Peak Neutron Flux ( $\times 10^{13}$ n/cm <sup>2</sup> .s)			
			CT		LS	
			Thermal	Epithermal	Thermal	Epithermal
300K	JENDL3.3	$0.99975 \pm 0.00027$	7.6007	1.8489	0.6277	0.2626
S( $\alpha, \beta$ )	ENDF/B-VI	$0.99749 \pm 0.00029$	7.3631	1.8278	0.6285	0.2623
No	JENDL3.3	$1.03259 \pm 0.00030$	6.0971	1.7652	0.6325	0.2601
S( $\alpha, \beta$ )	ENDF/B-VI	$1.03125 \pm 0.00027$	5.8799	1.8194	0.6218	0.2653

Table VII: Effect of Erbium Isotope over the criticality calculation of the TRIGA reactor through MCNP4C using JENDL-3.3 and ENDF/B-VI data libraries

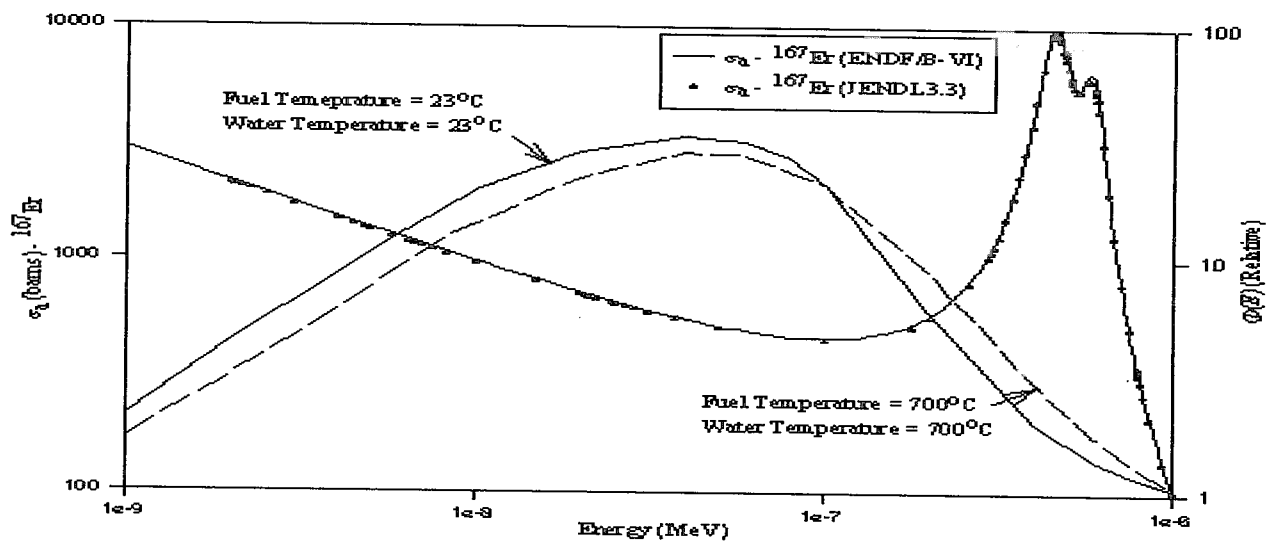
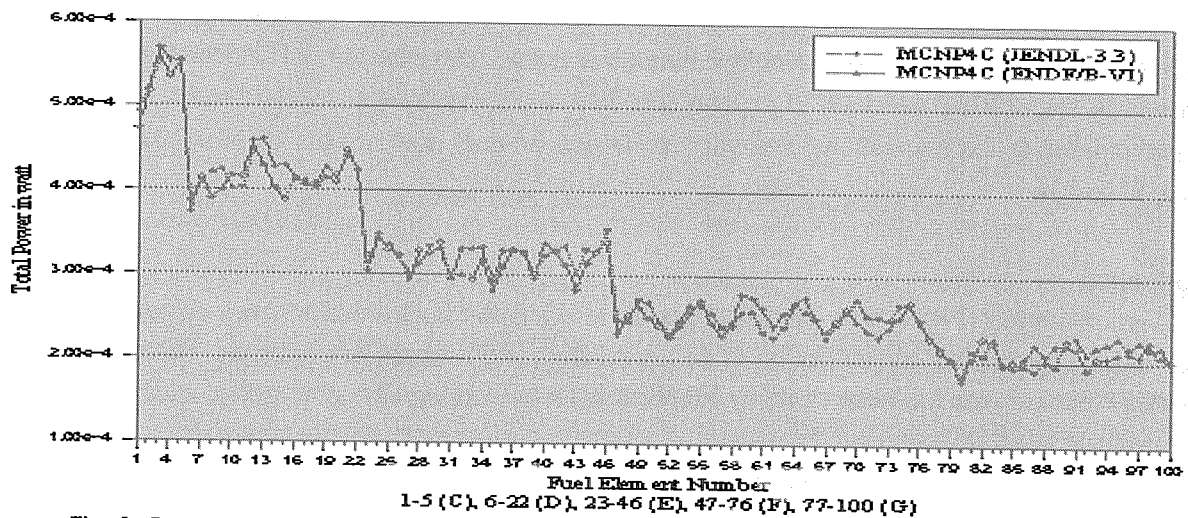
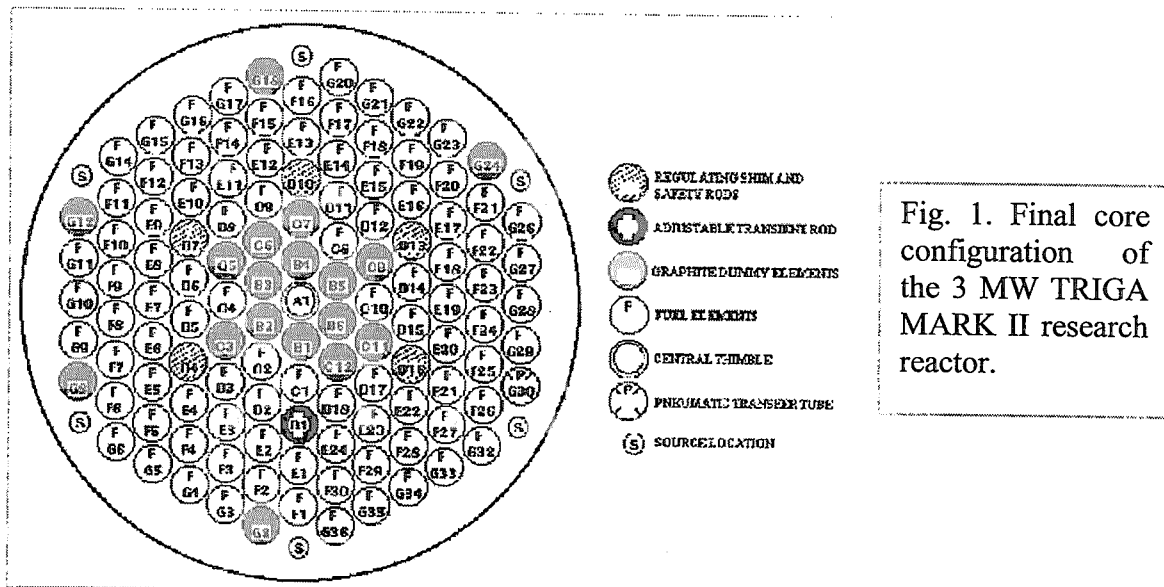
Condition	Library	Core Multiplication Factor $k_{eff}$	% $\Delta k/k$
With <sup>166</sup> Er & <sup>167</sup> Er	JENDL3.3	$1.07972 \pm 0.00028$	-
	ENDF/B-VI	$1.07850 \pm 0.00028$	-
Without <sup>166</sup> Er & <sup>167</sup> Er	JENDL3.3	$1.18209 \pm 0.00029$	9.48
	ENDF/B-VI	$1.18186 \pm 0.00027$	9.58
Without <sup>167</sup> Er	JENDL3.3	$1.18109 \pm 0.00030$	9.39
	ENDF/B-VI	$1.17836 \pm 0.00027$	9.26

Table VIII: Study of integral parameters using Monte Carlo simulation of TRIGA reactor based on JENDL and ENDF data libraries

Library	$k_{eff}$	$\delta^8$	$\delta^{25}$	$\rho^{25}$	C*
JENDL3.3	0.99975	7.50564E-03	0.13892	6.53831	0.13415
ENDF/B-VI	0.99749	7.60809E-03	0.14099	6.66915	0.13548
JENDL3.2	1.00457	7.28454E-03	0.13967	6.57643	0.13388
ENDF/B-V	0.99599	7.59845E-03	0.14272	6.55506	0.13366

Table IX: Comparison between the MCNP calculated control rod worths of TRIGA to the experiment

Control Rod Worth (\$)	Experiment (E)	JENDL3.3		ENDF/B-VI	
		C	C/E	C	C/E
SAFETY	$2.73 \pm 0.10$	$2.6324 \pm 0.0541$	0.9642	$2.6163 \pm 0.0530$	0.9584
SHIM I	$3.06 \pm 0.10$	$2.8519 \pm 0.0537$	0.9320	$2.8031 \pm 0.0521$	0.9160
SHIM II	$2.82 \pm 0.10$	$2.7634 \pm 0.0530$	0.9799	$2.7455 \pm 0.0536$	0.9736
SHIM III	$3.12 \pm 0.10$	$2.8941 \pm 0.0528$	0.9276	$2.8684 \pm 0.0526$	0.9194
REGULATING	$2.78 \pm 0.10$	$2.6821 \pm 0.0539$	0.9648	$2.6738 \pm 0.0536$	0.9618
TRANSIENT	$2.24 \pm 0.10$	$2.2832 \pm 0.0543$	1.0193	$2.3145 \pm 0.0545$	1.0333
TOTAL WORTH	16.75	16.1071	0.9616	16.0216	0.9565





## 2.15 History of FP Nuclear Data Evaluation

Masayoshi Kawai

High Energy Accelerator Research Organization,

1-1 Oho, Tsukuba-shi, 305-0801, Japan

*e-mail: masayoshi.kawai@kek.jp*

### Abstract

The fission product (FP) nuclear data of the JENDL library has been evaluated by FP Nuclear Data Working Group of JNDC for 172 nuclides from As-75 ( $Z=35$ ) to Tb-159 ( $Z=65$ ) for about 30 years since 1971. The working group was organized by total 29 members and initially lead by late Dr. Shungo Iijima. The fission product data were updated in the following sequence: JENDL-1 (28 nuclides) in 1975, JENDL-1.5 (34 nuclides) in 1977 (not released), JENDL-2 (100 nuclides) in 1985, JENDL-3.1 (172 nuclides) in 1990, JENDL-3.2 (172 nuclides) in 1995. The latest version JENDL-3.3 was released in 2002 contains total 337 nuclides. The 172 FP nuclides among them were evaluated by the Working Group with an assistance of the Nuclear Data Center of JAERI. The working group made a validation of the evaluated cross sections through integral tests for the STEK reactivity worth experiments, the CFRMF and EBR-II experiments for capture reactions in standard spectra. We have also participated in the international activities on fission product nuclear data of NEANSC/WPEC: SG-10, 17 and 21.

### Introduction

Fission product (FP) nuclear data are important to evaluate a nuclear reactor burn-up performance, reactor dosimetry, nuclear transmutation in fusion reactors and astrophysics research. The evaluation work of FP nuclear data has been made by FP Nuclear Data Working Group<sup>a)</sup> together with validation of the evaluated data by analyzing the integral experiments performed in reactor core spectra. The latest JENDL library, JENDL-3.3/1/ contains the data for 172 FP nuclides from As-75 to Tb-159. The brief history of the FP nuclear data of JENDL is summarized as follows:

- FPND WG was organized (1971),
- 28 FP nuclides for JENDL-1 FP (completed in 1975),
- Additional 34 FP nuclides for JENDL-1.5 FP (1977) (not released),
- 100 FP nuclides for JENDL-2 (1985),
- 172 FP nuclides for JENDL-3.1 (1990),
- 172 FP nuclides for JENDL-3.2 (1994).

In each stage, the integral tests were made to validate the evaluated data.

N.B. a) Members of Fission Product Nuclear Data (29 members)

JAERI: S. Igarasi, Y. Kikuchi, T. Sugi, K. Tasaka, S. Tanaka, T. Nakagawa,  
Y. Nakajima K. Nishimura, H. Nishimura, J. Matsumoto  
Toshiba (NAIG): S. Iijima, M. Kawai, T. Murata  
T. Yoshida  
Hitachi: A. Zukeran, K. Maki  
SAEI: H. Matsunobu  
KHI: T. Watanabe

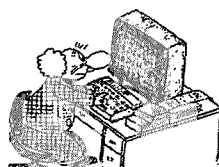


図 1 核データセンターの風景

MHI (MAPI): M. Sasaki, A. Hotta  
Fuji Electric: T. Aoki, I. Otake, H. Nakamura  
Univ. Tokyo: T. Obata  
Hosei Univ.: R. Nakasima  
Osaka Univ.: T. Nishigori  
NFI: T. Kawamoto  
Kyushu Univ.: T. Kawano, Y. Watanabe

## History of Evaluation of FP Nuclear Data for JENDL

Evaluation of FP nuclear data for JENDL-1 was started for 27 nuclides important to fast breeder reactor burn up calculations in 1971. They contribute 80% of capture by FP nuclides in a fast breeder reactor. The number of nuclides was increased to 28 soon after. Initially, we had nuclear model codes: statistical model code, RACY/2/, optical model codes: ELIESE-3/3/ and TOTAL. At that time, evaluated data were available only for capture cross sections by Benzi et al./4/ in Italy and AAEC library/5/ in Australia. We aimed at giving all quantities needed for evaluated data file. Accordingly, systematics of nuclear model parameters such as optical model parameters, level density parameters, gamma-ray strength functions were investigated together with level scheme data for the 28 nuclides. The preliminary data for 28 FP were evaluated in the energy range between 100 eV and 15 MeV in 1972/6/. Immediately after a new statistical model code CASTHY was developed by Igarasi/7/, reevaluation was made in the wide energy range from  $10^{-5}$  eV and 20 MeV for the 28 nuclides: Sr-90, Zr-93, Mo-95, Mo-97, Tc-99, Ru-101, Ru-102, Rh-103, Ru-104, Pd-105, Ru-106, Pd-107, Ag-109, I-129, Xe-131, Cs-133, Cs-135, Cs-137, Nd-143, Ce-144, Nd-144, Nd-145, Pm-147, Sm-147, Sm-149, Sm-151, Eu-153, Eu-155. Resonance parameters were taken from the BNL-325 third edition. The results were compiled into JENDL-1 FP data file/8, 9/ in 1975 prior to release of JENDL-1/10/ in 1977. Figure 1 compares the JENDL-1 data with other evaluations and experimental data for Tc-99 and Ag-109.

Since the 28 nuclides were not enough to compose mixed samples used for integral tests, additively the data of 34 nuclides were evaluated. The integral test results/11/ showed large discrepancies between the calculated and measured reaction rates and reactivity worth for several nuclides.

On the other hand, ENDF/B-V was released in 1979. They contained about 200 FP nuclides from Ge-72 to Dy-163/12/. In the Netherlands, RCN-2 files were developed by Gruppelaar/13/. We considered that such a number of FP nuclides as about 200 were not always necessary to analyze reactor burn-up performance. Accordingly, we selected 100 nuclides that gave 99.6% of capture contributions and about 195.4% cumulative fission yields in FBR for JENDL-2/14/. Figure 2 shows the 30 keV neutron capture contributions of the most important 30 nuclides in FBR. The resonance parameters were also evaluated/15/. The JENDL-2 FP data file was completed in 1985 after the general purpose file of JENDL-2 released in 1982/16/. Level density parameters were evaluated from observed resonance level spacings, Dobs, and level scheme data/17/. Optical model parameters/18/ were improved by considering the local systematics of total cross sections, the s- and p-wave neutron strength functions and scattering radii as shown in Fig. 3. This evaluation scheme is called the SPRT method. As for gamma-ray strength functions, we checked consistency between the measured capture cross sections and the integral tests. Figure 4 shows the evaluated capture cross sections of Eu-155. JENDL-2 shows resonance structure, while ENDF/B-V does not.

Integral test of JENDL-2 was made/19/ in 1985 - 1990 for the reactivity worth experiments at the STEK cores/20/ and the capture rate measurements in the standard spectra of CFRMF/21/ and EBR-II/22/. Cross section adjustment tools based on the Bayesian theorem were also developed. Covariance matrixes were calculated taking into account of nuclear model parameter errors, Poter-Thomas distribution for neutron widths, Dyson-Mehta statistics of levels and neutron flux errors. The reliability of the cross section adjustment based on the integral tests was clarified in the case of Zr-93: JENDL-1 cross sections overestimated the reactivity worths by about a factor of 2. Thus, new

evaluation of Zr-93 capture cross sections for JENDL-2 was made by reducing cross section by the factor of 2. Macklin's measurements/23/ reported after the evaluation supported the JENDL-2 as shown in Fig. 5.

Next, evaluation work for JENDL-3 was made aiming at wider applications to thermal reactors, fusion neutronics, reactor dosimetry and astrophysics as well as FBR calculations. In order to save man power, we developed evaluation tools/24/ such as JOBSETTER and its data file of nuclear model parameters to prepare input data for statistical model calculation with CASTHY. Multi-step evaporation and pre-equilibrium code PEGASUS/25/ was effectively used for evaluation of threshold reaction cross sections. Direct inelastic scattering cross sections were calculated with the DWBA code DWUCK-4. Figure 6 shows the evaluation scheme for JENDL-3 by using the various evaluation tools mentioned above. Evaluation of resonance /26/ was accelerated with the REPSTOR and its auxiliary codes developed by Nakawaga/ 27,28/: XTREP, ETREP, JCONV and PASSIN etc. New systematics of level density parameters evaluated on the basis of the level scheme data is shown in Fig. 7. Direct inelastic scattering cross sections were considered for even-even nuclides which were belong to nuclides around fission yield peaks and weak absorbing FP nuclides. Figure 8 shows the excitation function of inelastic scattering to the first excited state of Nd-144. The Bayesian adjustment method was adopted to evaluation for capture cross sections of Xe-132, 134 and Eu-152 and 154 for which no experimental data were available. The evaluation of FP nuclear data for JENDL-3.1 was completed in 1990 /29/.

Revision of JENDL-3.1 data was made for JENDL-3.2/30/ by considering new experimental data for 63 nuclides: thermal and resonance parameters for 33 nuclides, capture cross sections for 16 nuclides, direct inelastic scattering cross sections for 8 nuclides, and threshold reaction cross sections calculated with GNASH code for 16 nuclides (which were adopted from JENDL Fusion File) in 1994/31/. Figure 9 shows the typical results of capture cross sections for Cs-137, Sm-144, Sm-148 and Ru-101. For JENDL-3.2, a part of the resonance parameters were improved. As for Ru-101, level scheme data were revised and anomalous behavior of JENDL-3.1 capture cross section around 3 MeV diminished.

Integral tests of JENDL-3.1 and -3.2 showed the C/E values of sample reactivity worths were generally around unity for nuclides lighter than 130 and about 0.9 for heavier nuclides, except for several weakly absorbing nuclides/32,33/ as shown in Fig. 10.

For JENDL-3.3, obvious errors of compilation in JENDL-3.2 were corrected and new evaluations for Tc-99 and Ce-140 were adopted/1/. The data of Zr, Mo, Cd and Sb isotopes and Nb-93 were also revised by adopting the data of the JENDL Fusion File 99.

### Activities in WPEC of NEANSC

In 1990's, we participated the activities of Subgroup(SG)10/34/ and SG17/35/ in WPEC of NEANSC. In the SG10 activity investigating evaluation method of inelastic scattering cross sections for FP nuclides and the source of discrepancies of sample reactivity worths for weak absorbing nuclei of the STEK experiments between the measurements and the calculations, in order to answer to Gruppelaar's question/36/, we made the inter-comparison of the evaluated cross sections of JENDL-3.1, ENDF/B-VI and JEF-2/37/. Figure 11 shows an example of the level excitation functions of Mo-96. DEUCK-4 code calculation denoted with a dashed line shows a slightly anomalous behavior for 2.2193 MeV and 2.2345 MeV levels. Further investigation showed that anomalous behavior of the inelastic scattering of nuclides around A=100 came from abnormal p-wave strength functions due to improper optical model



parameters/38/. Figure 12 shows the inelastic scattering cross sections to 535.6 keV level of Mo-100. JENDL-3.2 which shows overestimation was calculated with the DWUCK-4 code using optical model parameters derived from the global fit. On the other hand, Smith's optical model parameters /39/ which were determined by reproducing elastic angular distributions and p-wave neutron strength functions for Zr, Mo, Pd etc. give a good agreement with the experimental data/40/ as shown in the figure. Interpretation of the discrepancies between the differential and integral data for nuclides around the nuclear mass of 100 was made with the rigorous transport calculations /33,41, 42/. Finally, we found probable evidence by the sensitivity study/43/ that the discrepancies came from the adjoint spectrum errors. Figure 13 shows the sensitivity profiles to adjoint spectrum errors (difference between transport calculation spectra /42/ and the ECN ones/20/) in cases of Mo-98 and Ce-140. Sensitivity profile of Mo-98 has a high peak in the high energy region: The effect of the adjoint spectrum error appears as like influence of inelastic scattering uncertainty on reactivity. This result is an answer to Gruppelaar's question. The sensitivity profile of Ce-140 is distributed in the wide energy region. This trend is observed for most weak absorbing FP nuclides except for nuclides around  $A=100$  and standard scattering samples such as oxygen and lead. These nuclides also showed similar discrepancies of reactivity worths as Zr and Mo isotopes. Thus, it has been concluded that poor adjoint spectrum produced the discrepancies of reactivity worth for weak absorbing FP nuclides.

In the SG17, comparison of the integral values such as one-group cross sections and reactivity worth of pseudo FP in a typical FBR core spectrum did not show so large differences between various evaluated data files compared to individual FP nuclides. We found some systematic differences of capture cross sections for important FP nuclides between JENDL-3.2 and JEF-2.2 came from adoption of adjusted cross section: JEF-2.2 adopted adjusted one, but JENDL-3.2 didn't/35/. Accordingly, it was found that there was strong correlation between the C/E values of reactivity worth calculated with JENDL-3.2 and one-group cross section ratios of JENDL-3.2 to JEF-2.2.

Recently, ENDF/B-VI was revised for 19 nuclides by considering new evaluated data of resonance parameters. CENDL-3 for 101 FP nuclides/44/ was compiled in China. SG-21 has been established in 2002 to review the evaluated data stored in JENDL-3.2, ENDF/B-VI.8, JEF-2.2, BROND-2, CENDL-3/45/.

## Conclusion

Previous Working Group of FP Nuclear Data continued very long term activity until completion of SG10 activity, although the WG formally finished in 1997 when the integral test of JENDL-3.2 was completed. Recently, partial revision of JENDL-3.2 was made for JENDL-3.3 by the Nuclear Data Center of JAERI. JENDL-3.3 seems to be good, but some parts are worse than CENDL-3 or ENDF/B-VI.8. Therefore, we are going to evaluate FP nuclear data for JENDL-4 by reorganizing the FP Nuclear Data Working Group in JNDC.

## References:

- 1) K. Shibata, et al.: J. Nucl. Sci. Technol., 39, 1125 (2002).
- 2) H. Nakamura and M. Hachya: JAERI-memo 3300 (1968)
- 3) S. Igarasi: JAERI 1224 (1972)
- 4) V. Benzi et al: "Fast neutron radiative capture cross sections of stable nuclei  $29 \leq A \leq 79$ ," CNEN-

- report RTFI (72) 6 (1972)
- 5) E.K. Rose: "The AAEC fission product cross section libraries FISPROD.POINTXSL and FISPROD.GROUPXSL," AAEC/TM-587 (1971).
  - 6) S. Iijima et al.: JAERI-M 5752 (1974).
  - 7) S. Igarasi and T. Fukahori: JAERI 1321 (1991)
  - 8) S. Iijima et al.: J. Nucl. Sci. Technol. 14, 161 (1977).
  - 9) Y. Kikuchi et al.: JAERI 1268 (1981)
  - 10) S. Igarasi et al.: JAERI 1261 (1979)
  - 11) S. Iijima et al.: NEANDC(E)-209"L", p.317 (1980)
  - 12) R.E. Schenter and T.R. England: NEANDC(E)209"L", p.253 (1980).
  - 13) H. Gruppelaar: ECN-13, ECN-33 (1977) and ECN-65 (1979)
  - 14) T. Aoki et al.: Proc. Int. Conf. on Nuclear Data for Basic and Applied Science, Santa Fe, Vol. 2, p.1627 (1985).
  - 15) For example, Y. Kikuchi et al.: JAERI M-86-030 (1986).
  - 16) T. Nakagawa (Ed.), JAERI-M 84-103 (1984).
  - 17) S. Iijima and M. Kawai: J. Nucl. Sci. Technol., 20, 77 (1983).
  - 18) S. Iijima et al.: J. Nucl. Sci. Technol., 21, 10 (1984).
  - 19) T. Watanabe et al.: JAERI-M 88-065, p. 148 (1988).
  - 20) J. J. Veenema and A.J. Jansen: ECN-10 (1976).
  - 21) Y. D. Harker and R. A. Anderl: NEANDC(E)-209"L" p.5 (1980).
  - 22) R.A. Anderl: EGG-PHYS-5182 (1981)
  - 23) R. L. Macklin: Astrophysics and Space Science, 115, 71 (1985)
  - 24) T. Nakagawa et al.: JAERI-Data/Code 97-050 (1997).
  - 25) T. Nakagawa et al.: JAERI-Data/Code 99-031 (1999)
  - 26) For example, Y. Nakajima: JAERI-Data/Code96-027 (1996).
  - 27) T. Nakagawa: JAERI-Data/Code 97-015 (1997).
  - 28) T. Nakagawa et al.: JAERI-Data/Code 99-030 (1999).
  - 29) M. Kawai et al.: J. Nucl. Sci. Technol., 29, 195 (1992).
  - 30) T. Nakagawa et al.: J. Nucl. Sci. Technol., 32, 1259 (1995)
  - 31) M. Kawai et al.: J. Nucl. Sci. Technol., 38, 261 (2001).
  - 32) T. Watanabe et al: Proc. IAEA Specialists' Meet. on Fission Product Nuclear Data, May, 1992, Tokai, NEA/NSC/DOC (92)9, p.411 (1992).
  - 33) T. Watanabe et al.: JAERI-Conf 96-008, p.140 (1996).
  - 34) M. Kawai et al: Evaluation Method of Inelastic Scattering Cross Sections for Weakly Absorbing Fission-Product Nuclides, NEA/WPEC-10 (2001).
  - 35) H. Gruppelaar et al.: Status of Pseudo-Fission-Product Cross Sections for Fast Reactor, NEA/WPEC-17 (1998).
  - 36) H. Gruppelaar et al.: Proc. Int. Conf. on Nuclear Data for Basic and Applied Science, Santa Fe, May 1985, Vol. 2, p.1537 (1986).
  - 37) M. Kawai et al.: Proc. IAEA Specialists' Meet. on Fission Product Nuclear Data, May, 1992, Tokai, NEA/NSC/DOC (92)9, p.39 (1992).
  - 38) T. Kawano et al.: J. Nucl. Sci. Technol., 35, pp 519 -526 (1998).

- 39) A.B. Smith et al.: Nucl. Phys. A415, 1 (1984).
- 40) I.G. Birm et al.: Proc. Int. Conf. on Nuclear Data for Science and Technology, Trieste, Italy, 19-24 May 1997, Part 1 p.526 (1997) .
- 41) M.Kawai et al.: Proc. Int. Conf. on Nuclear Data for Science and Application, Gatlinburg, May 1994, p.795 (1995).
- 42) K. Dietze: "Integral Test of JENDL-3.2 Data by Re-analysis of Sample Reactivity Measurements at Fast Critical Facilities," JNC TN9400 2001-043 (2001).
- 43) M. Kawai et al.: J. Nucl. Sci. Technol., Supplement 2, Vol.2, p. 982 (2002).
- 44) Zhuang Youxiang et al.: J. Nucl. Sci. Technol., Supplement 2, Vol. 1, 37 (2002).
- 45) P. Oblozinsky et al: "WPEC Subgroup 21", Report to the WPEC Meeting, Geel, May 23-24, 2002

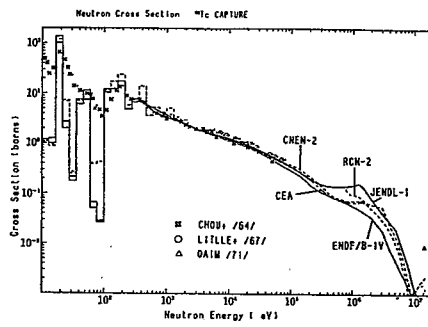
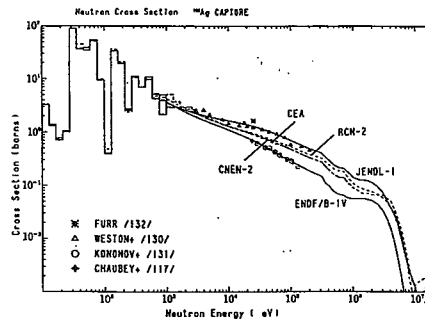
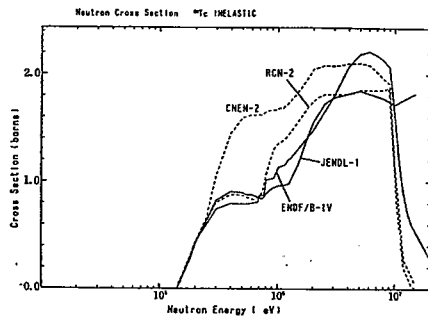
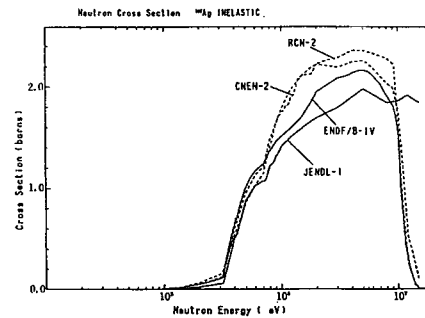
Fig. 3.5.2 Capture cross sections of  $^{99}\text{Tc}$ .Fig. 3.13.2 Capture cross section of  $^{109}\text{Ag}$ .Fig. 3.5.3 Inelastic scattering cross sections of  $^{99}\text{Tc}$ .Fig. 3.13.3 Inelastic scattering cross sections of  $^{109}\text{Ag}$ .

Fig. 1 Comparison of JENDL-1 capture and inelastic scattering cross sections for Tc-99 and Ag-109 with the other evaluation and experimental data.[Ref. 9]

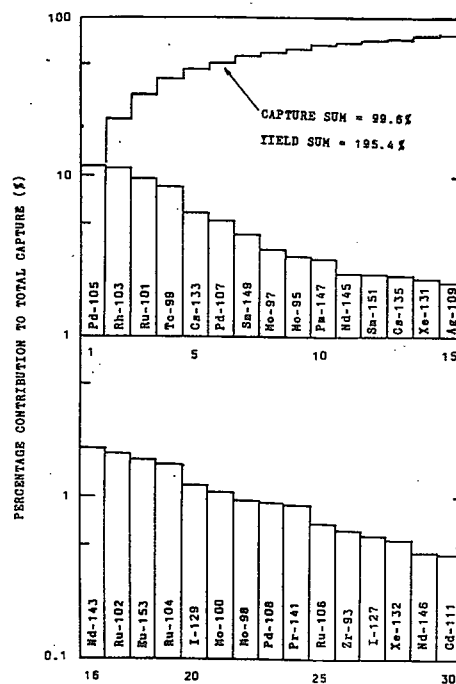


Fig. 2 30 keV neutron capture contributions of most important 30 nuclides. [Ref. 14]

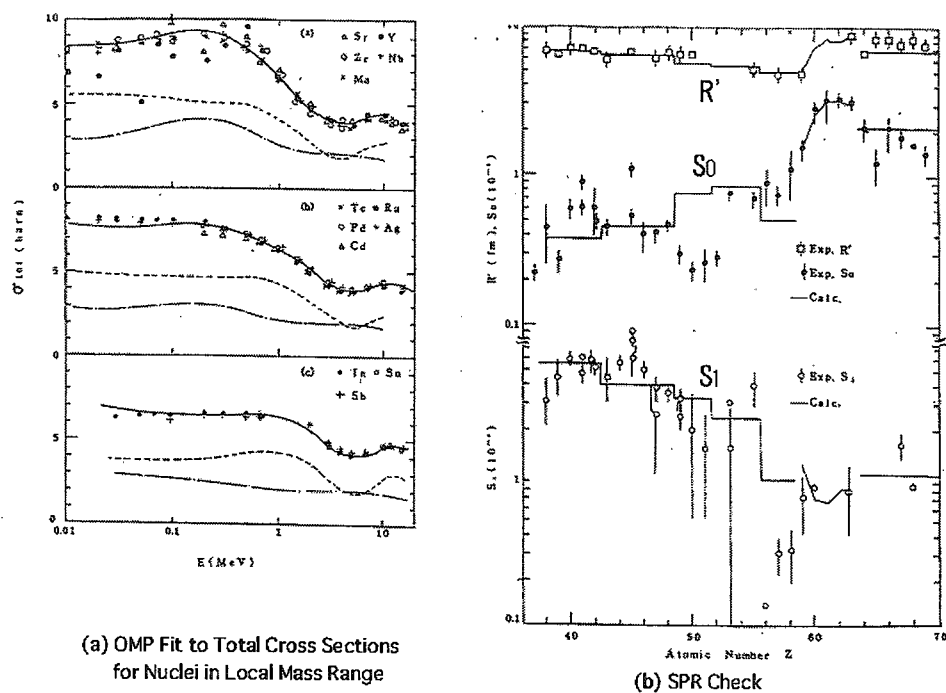


Fig. 3 Determination of optical model parameters with SPRT method[Ref.17]

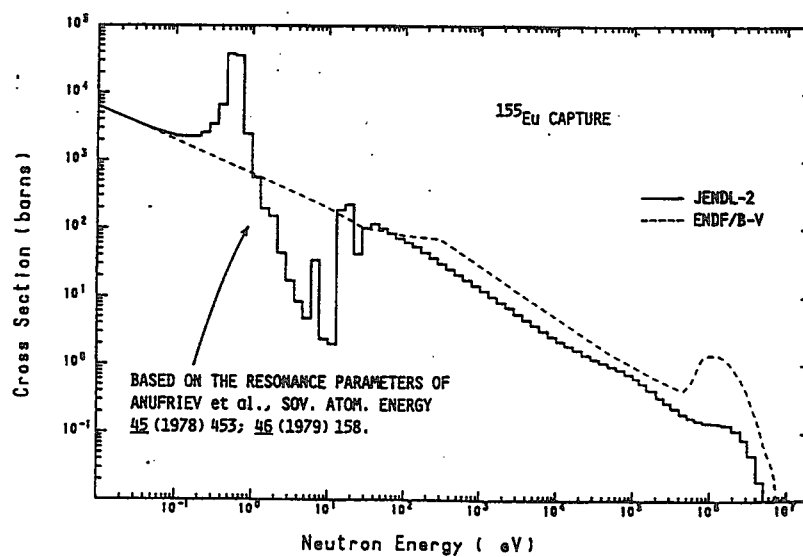
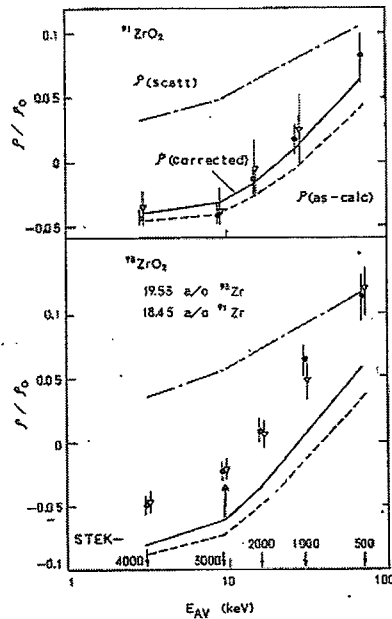
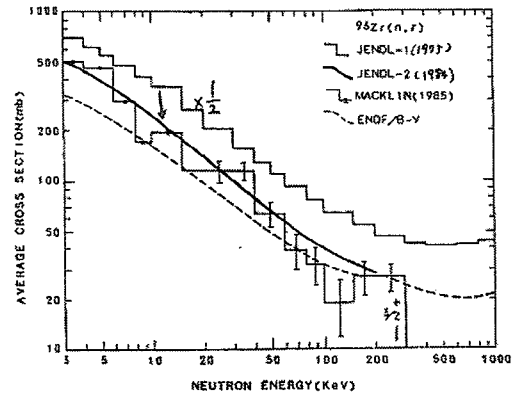


Fig. 4 Comparison of capture cross section for Eu-155[Ref. 14]



(a) Reactivity Worth of Zr-91 and Zr-93



(b) Capture Cross Section of Zr-93

Fig. 5 Integral test results and evaluation of capture crss sections of Zr-93.[Ref.14]

- (a) Calculated reactivity worth with JENDL-1 was corrected for oxygen contributoin. Agreement is good for Zr-91 while systematic overestimation of capture contribution is observed for Zr-93.
- (b) JENDL-2 was evaluated by reducing JENDI-1 by a factor of 2 and is agree with the Macklin's data that were reported after JENDL-2.

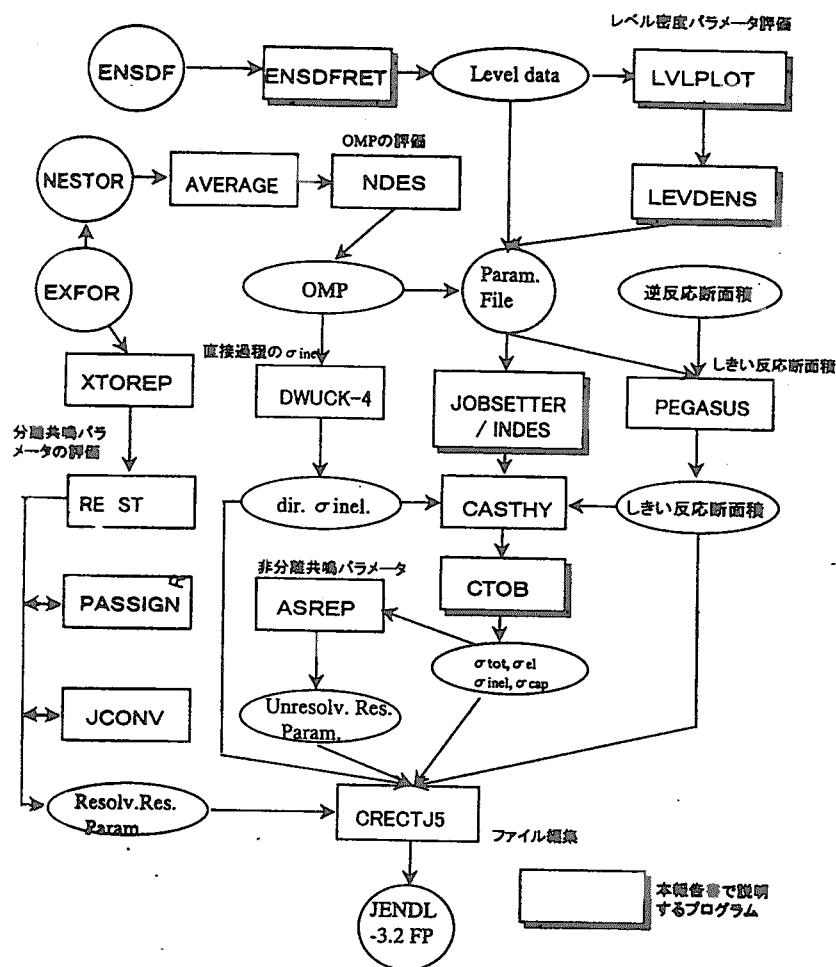
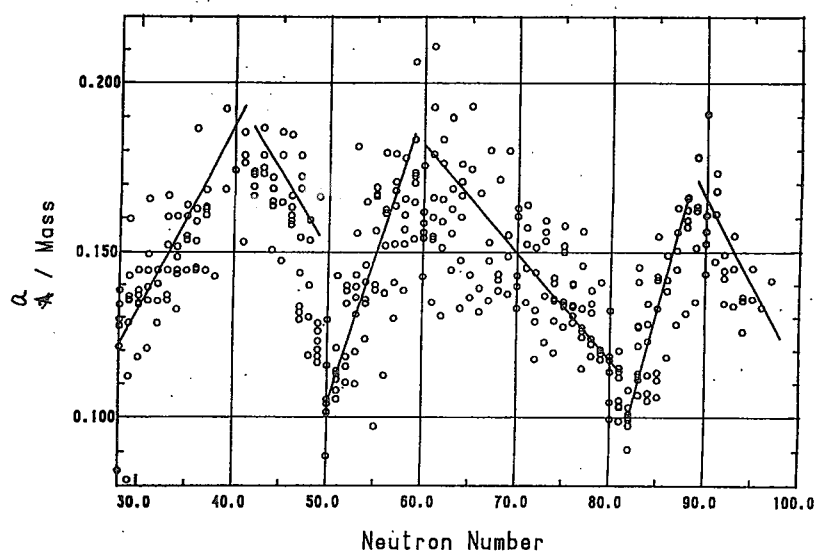


Fig. 6 Evaluation scheme[Re. 24]

Fig. 7 New systematics of level density parameter,  $a$ . [Ref. 29]

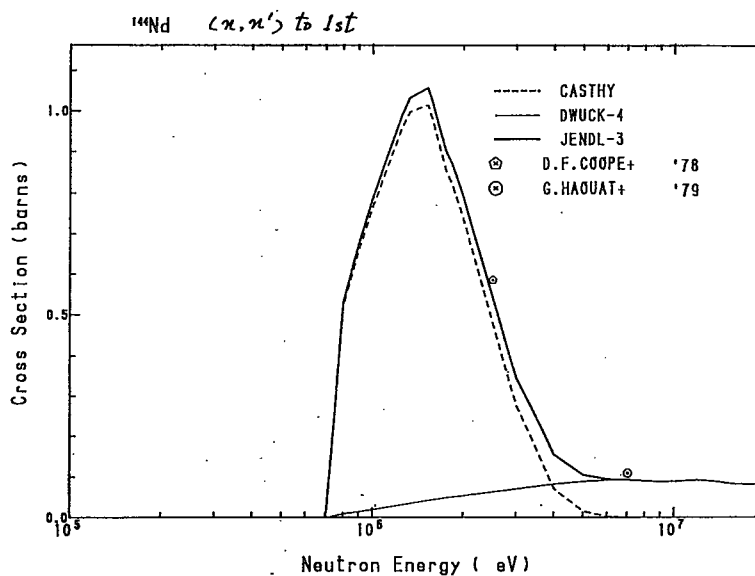


Fig. 8 Comparison of excitation function of inelastic scattering to the first excited state of Nd-144. [Ref. 29]

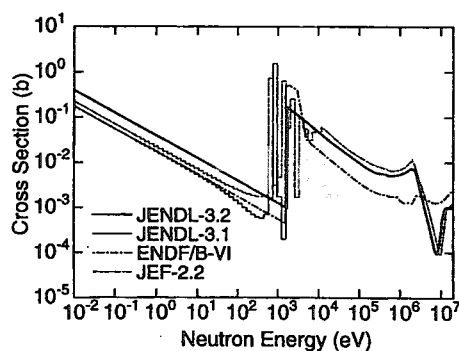


Fig. 1 Capture cross section of  $^{137}\text{Cs}$

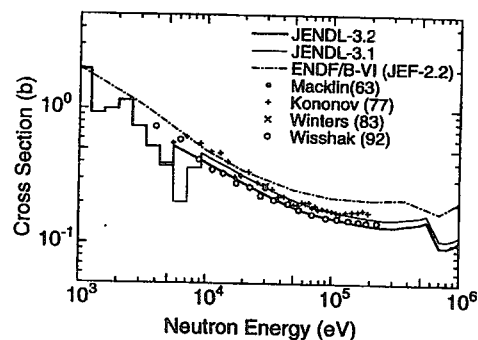


Fig. 3 Capture cross section of  $^{148}\text{Sm}$

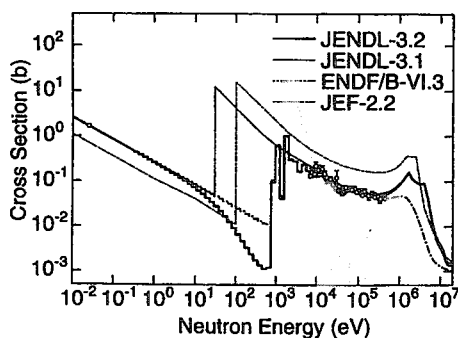


Fig. 2 Capture cross section of  $^{144}\text{Sm}$

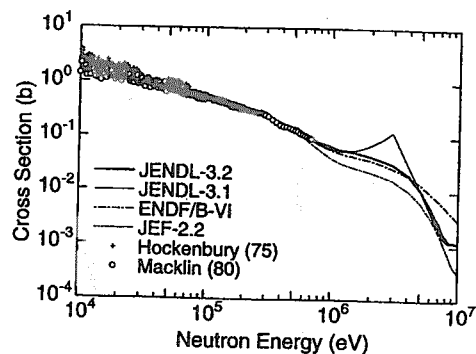


Fig. 4 Capture cross section of  $^{101}\text{Ru}$

Fig. 9 Typical results of evaluated capture cross sections for JENDL-3.2[Ref. 31]



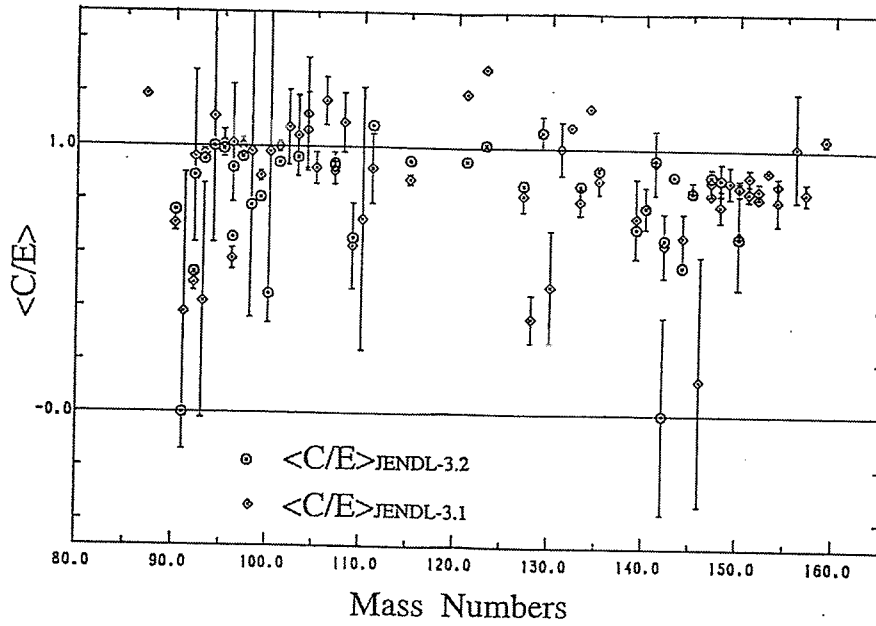


Fig. 10 Comparison of C/E values of sample reactivity worth measured at the STEK Experiments analyzed with JENDL-3.1 and -3.2. [Ref. 33]

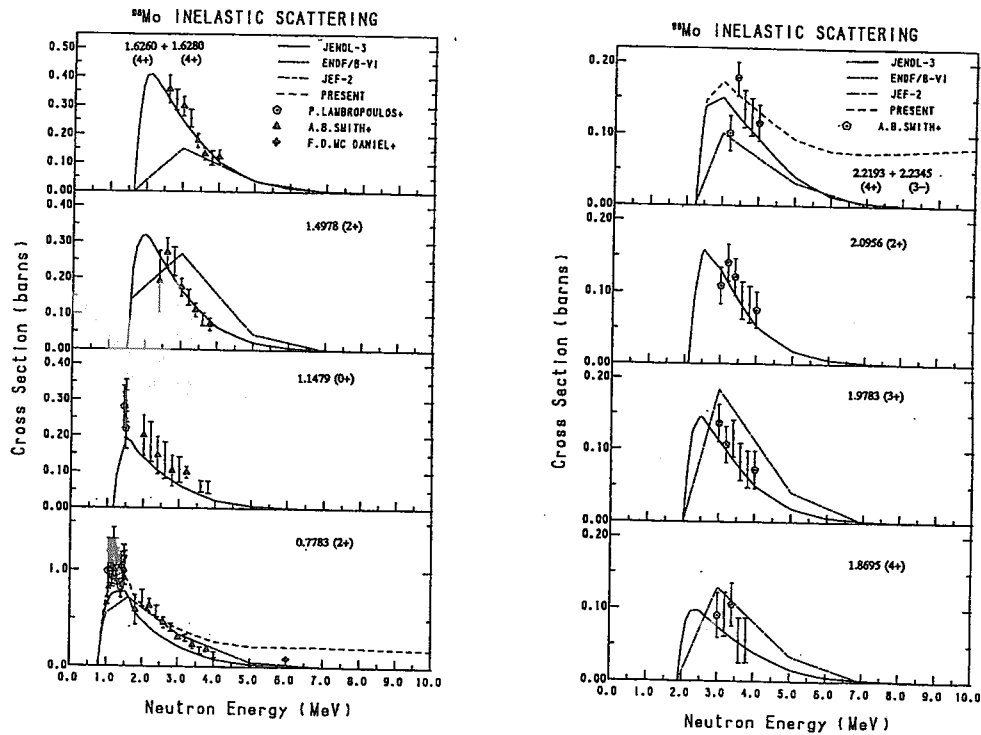


Fig. 11 Comparison of evaluated level excitation functions for Mo-96 with the experimental data. [Ref. 37] PRESENT is calculated with the DWUCK-4 code.

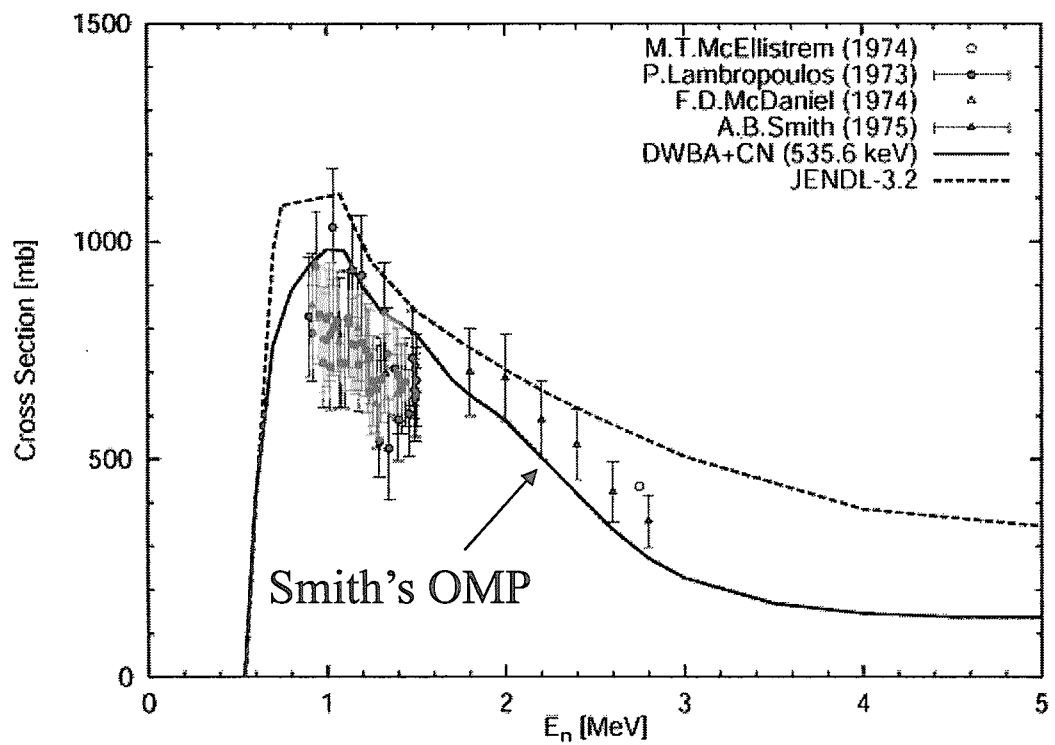


Fig. 12 Inelastic scattering cross section for Mo-100.[Ref. 38]

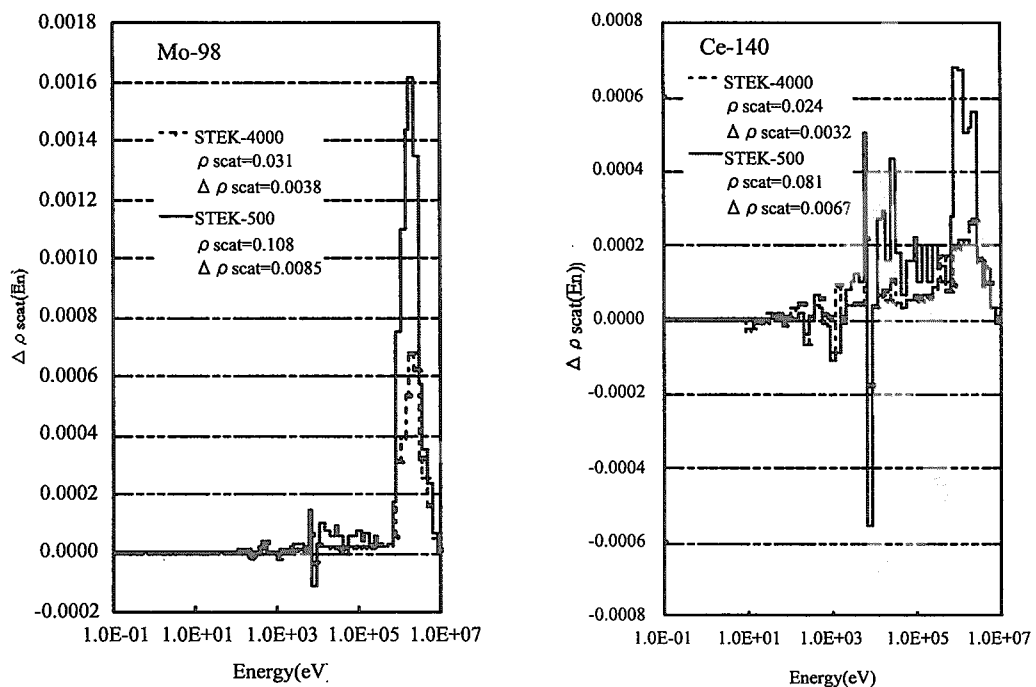


Fig. 13 Sensitivity profile of Mo-98 and Ce-140 against adjoint spectrum difference[Ref. 43]



## 2.16 Recent Experimental Data

Masayuki IGASHIRA and Kazuya OHGAMA

Research Laboratory for Nuclear Reactors, Tokyo Institute of Technology

2-12-1 O-okayama, Meguro-ku, Tokyo 152-8550

e-mail: [iga@nr.titech.ac.jp](mailto:iga@nr.titech.ac.jp)

Recent experimental data were reviewed for the neutron reaction cross sections of fission products. Some of our recent results on keV-neutron capture cross sections were compared with other experiments and the quality of recent experimental data was discussed.

### 1. Introduction

New experimental data are important for the re-evaluation of neutron reaction cross sections of fission products because the accuracy of calculations with nuclear reaction models is not enough at present. Therefore, it is valuable to investigate the new experimental data before starting the re-evaluation work. From this viewpoint, first, we reviewed the quantitative status of recent experimental data for the neutron cross sections of fission products, using the Computer Index of Neutron Data (CINDA)[1]. Secondly, we reviewed the experimental procedures of main laboratories. Finally, we compared some of our recent results on keV-neutron capture cross sections with other experiments and discussed the quality of recent experimental data.

### 2. Quantitative Review of Recent Experimental Data

The experimental data reported on and after 1994 were retrieved for the nuclides with the mass number from 66 to 172. Table 1 shows statistics for the total, capture, and inelastic-scattering cross section data. The number of nuclides for the capture cross section data is 2 to 10 times larger than the others, which is thought to reflect the importance of capture cross sections for many research fields such as nuclear engineering and nuclear astrophysics. However, the number (107) is only 60 % of that of fission products contained in JENDL-3.3[2]. Main laboratories which provided the capture cross section data are shown in Fig. 1, where the laboratory codes in CINDA are adopted. The activities of KFK and FEI are excellent. The total activity of Japanese laboratories is comparable to that of US laboratories. Similarly, the laboratories that provided the total and inelastic-scattering cross section data are shown in Figs. 2 and 3, respectively. As for the total cross sections, the activities of KFK, ORL, and IJI are excellent.

Table 1 Statistics for the total, capture, and inelastic scattering cross section data

Cross sections	Number of nuclides	Number of data sets	Number of references
Total	43	102	174
Capture	107	290	580
Inelastic scat.	10	18	45

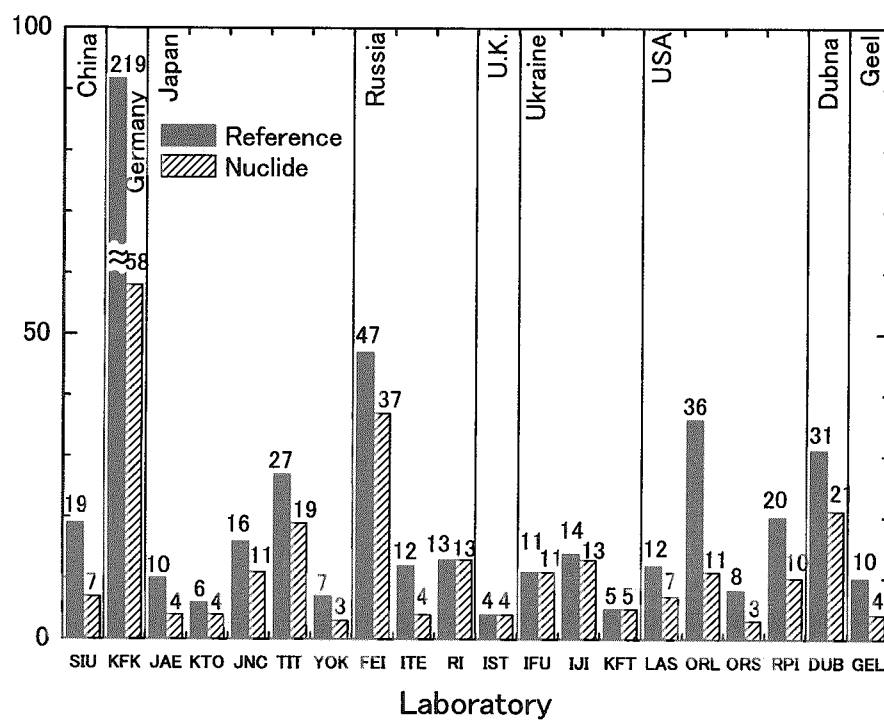


Fig. 1 Main laboratories which provided the capture cross section data

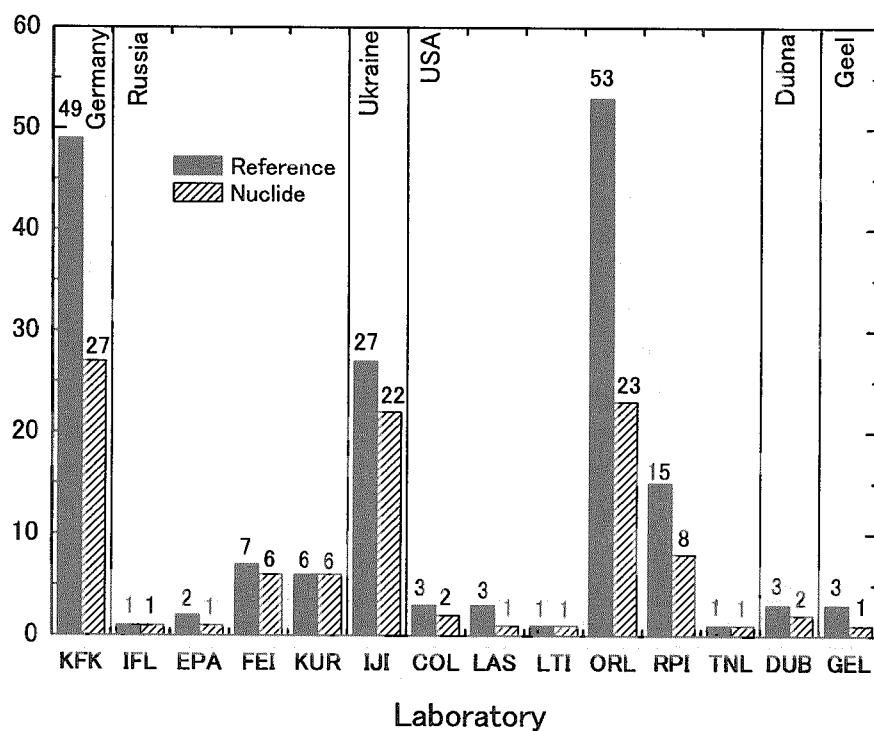


Fig. 2 Laboratories that provided the total cross section data

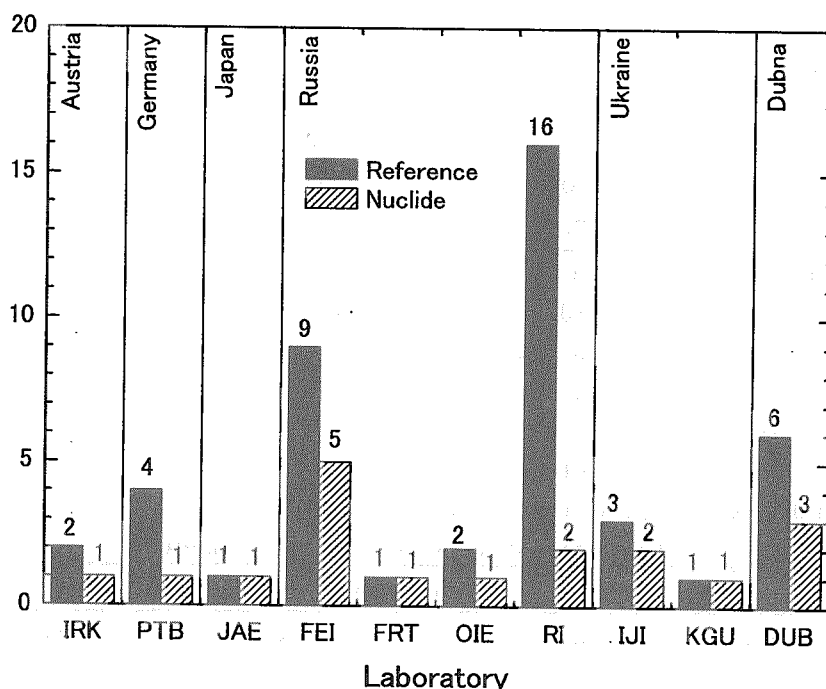


Fig. 3 Laboratories that provided the inelastic scattering cross section data

### 3. Experimental Procedures of Main Laboratories

The experimental procedures of main laboratories are summarized in Table 2, where the laboratories are categorized by their neutron sources. In the capture experiment, KFK, RPI, and KTO employed a segmented  $4\pi$ -spectrometer, and ORL, GEL, and KTO employed a pair of  $C_6D_6$  scintillation detectors. On the other hand, TIT employed an anti-Compton NaI(Tl) spectrometer together with a very-short neutron flight path (FP). JNC, JAE, and YOK adopted an activation method and provided the thermal capture cross sections and resonance integrals of radioactive fission products. As for the total experiment, all laboratories except for IJI employed a  $^6Li$ -glass scintillation detector.

### 4. Comparisons of keV-Neutron Capture Cross Section Data

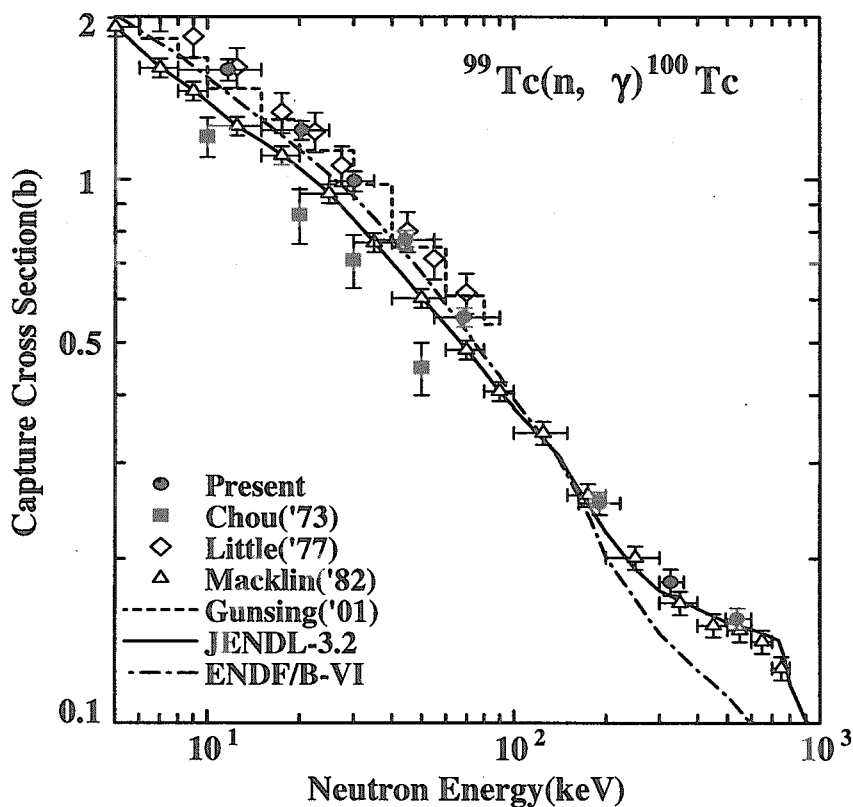
In order to investigate the qualitative status of recent experimental data on keV-neutron capture cross sections, the comparisons of data sets were made for some fission products. The comparisons for  $^{99}Tc$ ,  $^{140}Ce$ , and  $^{146}Nd$  are shown in Figs. 4-6, respectively, where "Present" means the results of TIT.

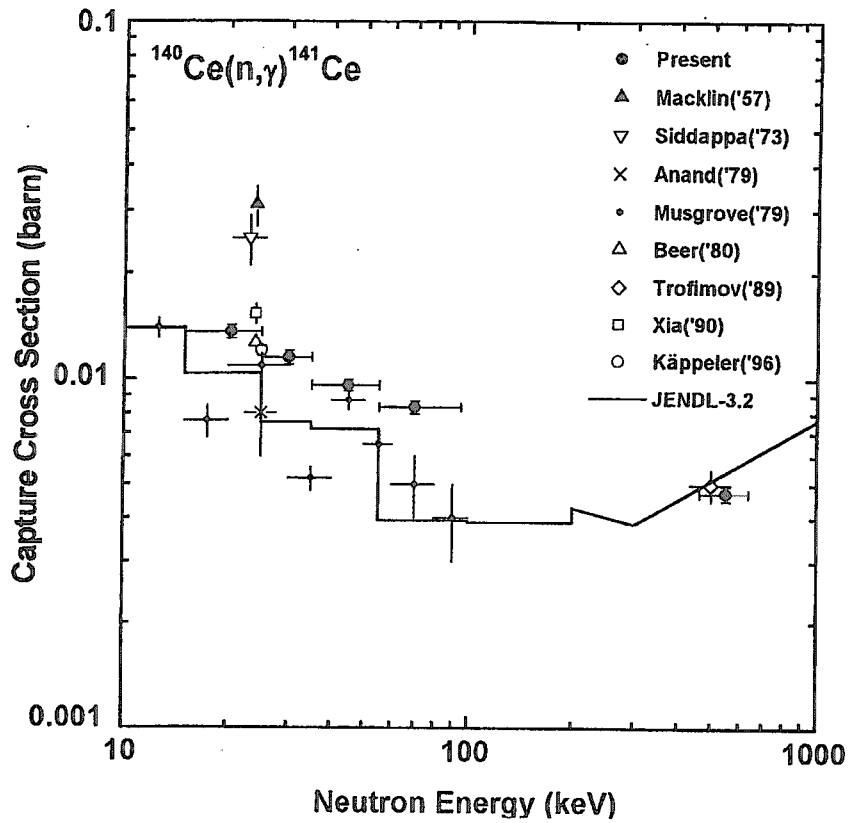
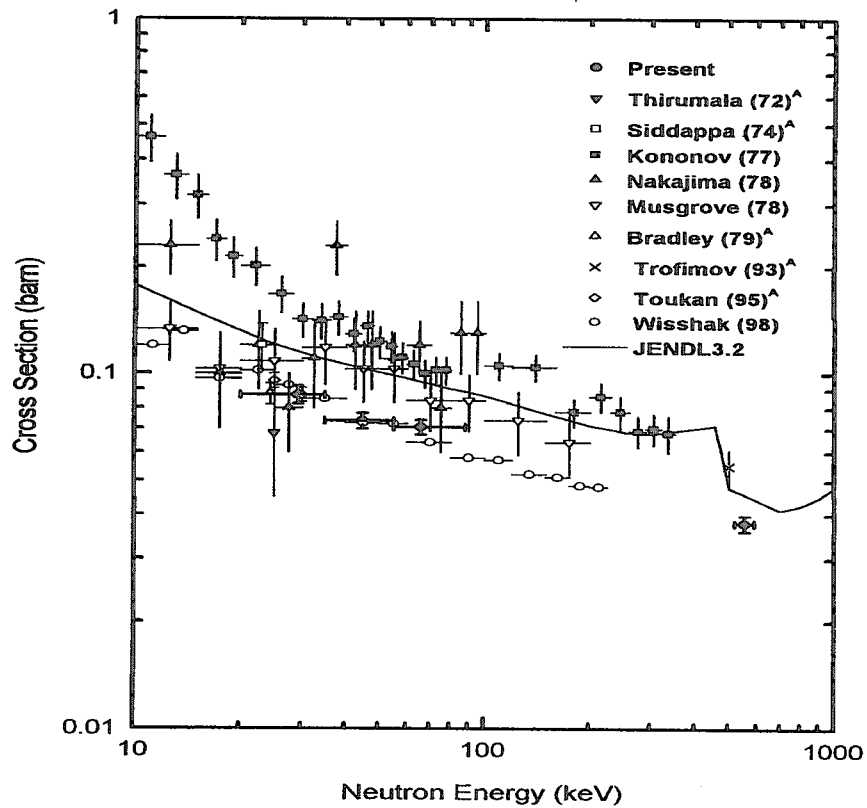
The recent results of TIT[3] and Günsing *et al.* (GEL)[4] for the long-lived radioactive nuclide of  $^{99}Tc$  agree with each other, as shown in Fig. 4, though they did not give the experimental errors. Below 100 keV, the recent results support the old results of Little and Block[5] rather than the results of Macklin[6]. However, above 200 keV, the results of TIT support those of Macklin.

Table 2 Experimental procedure of main laboratories

Group 1: Time-of-flight method with the ${}^7\text{Li}(p,n){}^7\text{Be}$ neutron source	
KFK: $E_n=3\text{-}230$ keV; Capture: 0.79 m FP + $4\pi\text{BaF}_2$ ; Total: 2.6 m FP + ${}^6\text{Li-galss}$	
FEI: $E_n=20\text{-}450, 1400$ keV; Capture: 2.4 m FP + 17 l tank; Total: 2.1 m FP + ${}^6\text{Li-glass}$	
TIT: $E_n=10\text{-}600$ keV; Capture: 0.12-0.20 m FP + Anti-Compton NaI(Tl)	
Group 2: Time-of-flight method with the photo-neutron source	
ORL: $E_n=\text{eV}\text{-}700$ keV; Capture: 40 m FP + 2 $\text{C}_6\text{D}_6$ ; Total: 80 or 200 m FP + ${}^6\text{Li-glass}$	
RPI: $E_n=\text{thermal}\text{-}3$ keV; Capture: 26 m FP + 16 NaI(Tl); Total: 26 m FP + ${}^6\text{Li-glass}$	
GEL: $E_n=\text{eV}\text{-}200$ keV; Capture: 28 m FP + 2 $\text{C}_6\text{D}_6$ ; Total: 49 m FP + ${}^6\text{Li-glass}$	
KTO: $E_n=\text{thermal}\text{-}40$ keV; Capture 1: 12 m FP + 2 $\text{C}_6\text{D}_6$ or 12 BGO Capture 2: Pb slowing-down spectrometer	
Group 3: Reactor neutron source	
IJI: $E_n=\text{thermal}\text{-}600$ keV; Time-of-flight method with a chopper, or Filtered beam; Total: ${}^3\text{He}$ or ${}^1\text{H}$ counter	
JNC, JAE, YOK: $E_n=\text{thermal}$ , resonance integral; Capture: Activation method	

FP: Flight Path

Fig. 4 keV-neutron capture cross sections of  ${}^{99}\text{Tc}$

Fig. 5 keV-neutron capture cross sections of  $^{140}\text{Ce}$ Fig. 6 keV-neutron capture cross sections of  $^{146}\text{Nd}$

As for  $^{140}\text{Ce}$  that has very small capture cross sections in the fission product region, an activation method was adopted in all previous measurements except for that of Musgrove *et al.*[7]. The recent activation result of Kaeppler *et al.* (KFK)[8] at 24 keV is in good agreement with those of TIT[9]. Musgrove *et al.*[7] performed their experiment at ORL, using a pair of  $\text{C}_6\text{F}_6$  scintillation detectors, not  $\text{C}_6\text{D}_6$ . Their results are smaller than those of TIT by about 40 %.

As for  $^{146}\text{Nd}$  that has rather small capture cross sections, both of activation and prompt  $\gamma$ -ray detection methods were adopted in the previous measurements, as shown in Fig. 6, where the superscript "A" on the references indicates the activation results. The recent results of Wisshak *et al.* (KFK)[10] and TIT[11] agree with each other within the experimental errors. Moreover, the recent activation result of Toukan *et al.* (KFK)[12] at 24 keV is in good agreement with those of Wisshak *et al.* and TIT.

From the above comparisons, no serious discrepancy was found among the recent experimental data on the keV-neutron capture cross sections of fission products.

## 5. Conclusion

After the evaluation work for JENDL-3.2 released in April 1994, new experimental data on capture cross sections were reported for about 60 % of fission product nuclides contained in JENDL-3.3. As for total and inelastic-scattering cross sections, however, new data were poor in comparison with the capture cross section data. The comparisons of recent experimental data showed that the quality of keV-neutron capture cross section data was good.

## References

- [1] URL address: <http://www.nea.fr/cinda/cindaora.cgi/>
- [2] K. Shibata *et al.*, *J. Nucl. Sci. Technol.*, **39**, 1125 (2002).
- [3] T. Matsumoto *et al.*, to be published in *J. Nucl. Sci. Technol.*
- [4] F. Gunsing *et al.*, *Nucl. Phys.*, **A688**, 496c (2001).
- [5] R.C. Little and R.C. Block, *Trans. Am. Nucl. Soc.*, **26**, 574 (1977).
- [6] R.L. Macklin, *Nucl. Sci. Eng.*, **81**, 520 (1982).
- [7] A.R. de L. Musgrove *et al.*, *Aust. J. Phys.*, **32**, 213 (1979).
- [8] F. Kaeppler *et al.*, *Phys. Rev. C*, **53**, 1397 (1996).
- [9] S. Harnood *et al.*, *J. Nucl. Sci. Technol.*, **37**, 740 (2000).
- [10] K. Wisshak *et al.*, *Phys. Rev. C*, **57**, 391 (1998).
- [11] T. Veerapasong *et al.*, *J. Nucl. Sci. Technol.*, **36**, 855 (1999).
- [12] K. A. Toukan *et al.*, *Phys. Rev. C*, **51**, 1540 (1995).



## 2.17 Present Status and Plans of JENDL FP Data Evaluation Project

KAWANO Toshihiko<sup>†</sup>

and

FP Nuclear Data Evaluation Working Group<sup>1</sup>

<sup>†</sup>*Interdisciplinary Graduate School of Engineering Sciences, Kyushu University  
6-1 Kasuga-kouen, Kasuga 816-8580, Japan*

e-mail: kawano@aees.kyushu-u.ac.jp

The Fission Product (FP) data evaluation is one of the key issues for the next revision of JENDL, since many data were carried over from JENDL-3.2 to 3.3. The new FP Working Group (FPWG) was organized in the Japanese Nuclear Data Committee (JNDC) to perform new evaluations of FP data for JENDL. In the present review of FP data evaluation, we show the history and current status of FP nuclear data, requirements of FP data, new measurements, the international cooperation, and the future plans toward the new JENDL.

### 1. Introduction

Although nuclear data of fission products (FP) are essential for various reactor calculations such as burn-up, gas production, decay heat, radiation damage etc., to meet of this requirement is very hard because there exists a large number of FP nuclides/isotopes, and the experimental data for many isotopes and reactions in a specific energy range are scarce. For example, 185 nuclides (from Ga to Eu) are stored in JENDL-3.3. Figure 1 shows a chart of nuclides compiled in JENDL-2, 3.2, and 3.3. To evaluate such a large number of nuclear data, nuclear model calculations get more important nowadays, and reliability and accuracy of the evaluated nuclear data depend on the quality of input variables. FP Working Group (FPWG) in the Japanese Nuclear Data Committee (JNDC) had continuously developed evaluation tools for resonance and smooth regions, as well as methods to validate the evaluated nuclear data.

During the last decade, the FP data evaluation became one of the key issues in the international cooperation. Subgroup 10, 17, and 21 in WPEC (Working Party on International Nuclear Data Evaluation Cooperation)[1, 2] were organized under OECD/NEA, some resonance parameters of FP were evaluated at BNL and KAERI for ENDF/B-VI, a series of FP cross section measurements were performed at several institutes, and an evaluation work for CENDL was also made at CIAE. In this good circumstances we restarted FP Working Group in 2002 to update the FP data in JENDL. We aim to brush up the old evaluations in the current JENDL, and hopefully we shall complete our new evaluation within several years. This FP data file will be a part of the next JENDL general purpose file. In order to complete this we need to survey new resonance parameters available, to inspect input parameters used, and to replace them by more reliable ones. This report summarizes current status of FP nuclear data and the future plans toward the new JENDL.

---

<sup>1</sup>S. Chiba, M. Igashira, M. Ishikawa, M. Kawai, T. Kawano, M. Matsunobu, T. Murata, T. Nakagawa, K. Shibata, T. Sugi, T. Watanabe, and A. Zukeran

## 2. International Activities

There are several international cooperative projects relating to the FP data evaluation. OECD/NEA organized the following three subworking groups:

Subgroup	Coordinator	Project Name	status
10	M. Kawai	Inelastic scattering cross sections for weakly absorbing FP nuclides	published[1]
17	H. Gruppelaar	Pseudo-fission-product cross sections for fast reactors	published[2]
21	P. Oblozinsky	Assessment of neutron cross sections for the bulk of fission products	new, 2001

and the subgroup 21 (SG21) is now working on an inter-comparison of FP data those are selected randomly. Quantities to be reviewed are the total, capture, elastic, inelastic,  $(n, 2n)$ ,  $(n, p)$ , and  $(n, \alpha)$  cross sections, resonance parameters, and thermal values. The results are open to public at the BNL web site (<http://www.nndc.bnl.gov/sg21/>).

Reference Input Parameter Library (RIPL)[3] was compiled at IAEA, which is a library containing nuclear model parameters mainly for the statistical Hauser-Feshbach model calculation. Nuclear masses, excited levels, optical potential parameters, level densities, GDR parameters, fission barriers are stored in RIPL. In 2002 they finalized the second edition, and a new task (phase III) was initiated. This library has an apparent benefit of FP data evaluations, since model calculations are essential in the FP region, and we need reliable global parameters and systematics in order for automatic input parameter setting and a cost-effective method to generate bulk data.

Figures 2, 3, and 4 show some examples in which RIPL was used to calculate the optical and Hauser-Feshbach-Moldauer models. Those calculations were made without any parameter adjustments in order to see adaptability of RIPL in the FP region.

A comparison of calculated total cross section of  $^{90}\text{Zr}$  with the experimental data is shown in Fig. 2. The optical potential used is the global potential parameter of Koning and Delaroche[4], which is adequate in the energy range from a few keV up to 200 MeV. The calculated cross section with the well-known Walter-Guss potential is also shown by the dotted line in this figure. In the case of  $^{90}\text{Zr}$  the global potential of Koning-Delaroche gives better fit to the data than JENDL-3.3. Of course the quality of fitting may depend on the target nuclide and we need a quantification study of adaptability of such global parameterization. However it is apparent that this global potential becomes a powerful tool to evaluate the FP nuclear data.

Figure 3 shows an example of calculated inelastic scattering to the first (1.761 MeV,  $0^+$ ) and second (2.186 MeV,  $2^+$ ) levels of  $^{90}\text{Zr}$ . The Koning-Delaroche global potential was used to generate the neutron transmission coefficients, and the level density parameters were taken from RIPL (phase I). The direct inelastic scattering was not included since its contribution is not so large below 4 MeV. In this case the calculated cross section underestimates the experimental data of Guenther *et al.*[5]

The comparison of capture cross section is shown in Fig. 4. Resonance parameters are given below 0.17 MeV, and the cross sections in the resonance region were averaged to compare with the statistical model calculations. The  $\gamma$ -ray transmission is often re-normalized to the experimental strength function  $2\pi\langle\Gamma_\gamma\rangle/D_0$  if available. RIPL also contains this strength function, and the solid line is the calculated cross section with this re-normalization. The dotted line shows the calculation without re-normalization, which is about three-times larger than the experimental data.

### 3. Resonance Region

There are some activities of FP cross section measurements at low energies. The major contributions from our country is, Tokyo Institute of Technology, Kyoto University Research Reactor, Japan Nuclear Cycle Development Institute, and so on. Accelerator facilities in abroad such as GELINA at IRMM or ORELA at ORNL also produce transmission data of FP nuclides, though they are not mass production of nuclear data, but sometimes they are related to fundamental physics.

In general FP resonance parameters in JENDL-3.3 are the same as those in JENDL-3.2, however the parameters of  $^{99}\text{Tc}$ ,  $^{140}\text{Ce}$ [6], and  $^{106}\text{Cd}$  were replaced by new sets. Gunsing *et al.*[7] carried out a transmission measurement of  $^{99}\text{Tc}$  from 3 eV to 150 keV and they analyzed their experimental data to obtain the resonance parameters up to 10 keV. Those parameters (up to 6 keV) were adopted for JENDL-3.3. Notable improvements between two parameter sets are the thermal cross section  $\sigma_{\gamma}^0$  and the resonance integral  $I_{\gamma}$ . The new resonance parameter set was evaluated so as to reproduce the experimental data  $\sigma_{\gamma}^0$  of Harada *et al.*[8] which is larger than the evaluation of Mughabghab *et al.*[9]. The following table compares  $\sigma_{\gamma}^0$  and  $I_{\gamma}$  values.

Library	$\sigma_{\gamma}^0$ [b]	$I_{\gamma}$ [b]	notes
JEF-2	19.1	304	same as Mughabghab
ENDF/B-VI	20.0	312	Ref. [10]
JENDL-3.2	19.6	311	
JENDL-3.3	22.8	323	almost the same as Gunsing
Gunsing <i>et al.</i>	23.1	323	Ref. [7]
Mughabghab <i>et al.</i>	$20.0 \pm 1.0$	$340 \pm 20$	Ref. [9]
Harada <i>et al.</i>	$22.9 \pm 1.3$	$398 \pm 38$	Ref. [8]

The resonance parameter of  $^{99}\text{Tc}$  was also revised for ENDF/B-VI by Oh *et al.*[10]. Recently Kobayashi *et al.*[11] measured the neutron capture cross section of this important FP up to about 3 keV. Those information may also make it possible to update the resonance parameters in the next revision.

### 4. Conclusion

We have reviewed the current status of FP nuclear data evaluation in Japan, as well as some international activities relating to the FP data. WPEC Subgroup 21 is making some inter-comparison of FP data in the nuclear data libraries. There are some activities of nuclear data production, but the experimental data are still insufficient for many FP nuclides.

In the resonance region, some new evaluations of resonance parameters are available, and it is also possible to derive a new parameter set by new measurements, like the  $^{99}\text{Tc}$  capture cross section measurement at KUR.

In the smooth region, we have a nuclear model parameter library, RIPL, which enables us to calculate various cross sections even though the experimental data are inaccessible. We have shown some simple examples of use of RIPL. This is the starting point, and we need some quantification study of adaptability of such global parameterization.

## References

- [1] M. Kawai, H. Gruppelaar, "Evaluation Method of Inelastic Scattering Cross Sections for Weakly Absorbing Fission-Product Nuclides," KEK Preprint 2002-54, NEA/WPEC-10 (2002).
- [2] H. Gruppelaar, "Status of Pseudo-Fission-Product Cross-Sections for Fast Reactors," NEA/WPEC-17, ECN-R-98-014 (1998).
- [3] "Handbook for Calculations of Nuclear Reaction Data — Reference Input Parameter Library —," IAEA-TECDOC-1034, International Atomic Energy Agency (1998).
- [4] A.J. Koning, J.-P. Delaroche, *Nucl. Phys. A*, **713**, 231 (2003).
- [5] P. Guenther, A. Smith, J. Whalen, *Phys. Rev. C*, **12**, 1797 (1975).
- [6] T. Nakagawa, O. Iwamoto, A. Hasegawa, "Re-evaluation of Neutron Nuclear Data for  $^{242m}\text{Am}$ ,  $^{243}\text{Am}$ ,  $^{99}\text{Tc}$  and  $^{140}\text{Ce}$ ," JAERI-Research 2002-035, Japan Atomic Energy Research Institute (2002).
- [7] F. Gunsing, A. Leprêtre, C. Mounier, C. Raepsaet, *Phys. Rev. C*, **61**, 054608 (2000).
- [8] H. Harada, S. Nakamura, T. Katoh, Y. Ogata, *J. Nucl. Sci. Technol.*, **32**, 395 (1995).
- [9] S.F. Mughabghab, M. Divadeenam, N.E. Holden, "Neutron Cross Sections" Vol.1: "Neutron Resonance Parameters and Thermal Cross Sections", Academic Press, New York (1981).
- [10] S.Y. Oh, J.H. Chang, S. Mughabghab, "Neutron Cross Section Evaluations of Fission Products Below the Fast Energy Region," BNL-NCS-67469, ENDF-362, KAERI/TR-1511/2000, Brookhaven National Laboratory (2000).
- [11] K. Kobayashi, private communication (2003).

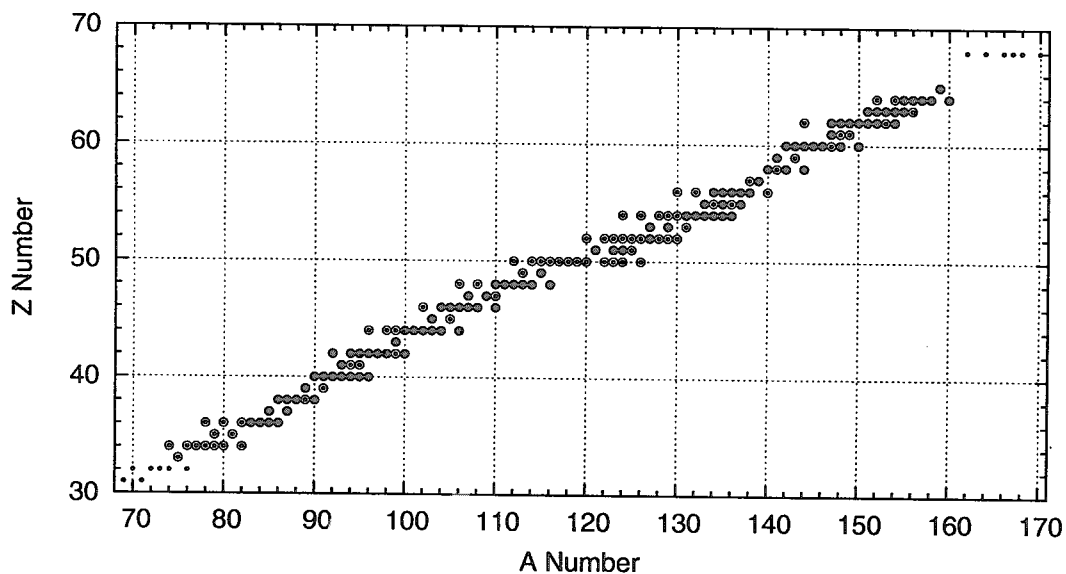


Fig. 1: Nuclides compiled in JENDL-2 (closed circle), JENDL-3.2 (open circle), and JENDL-3.3 (dot).

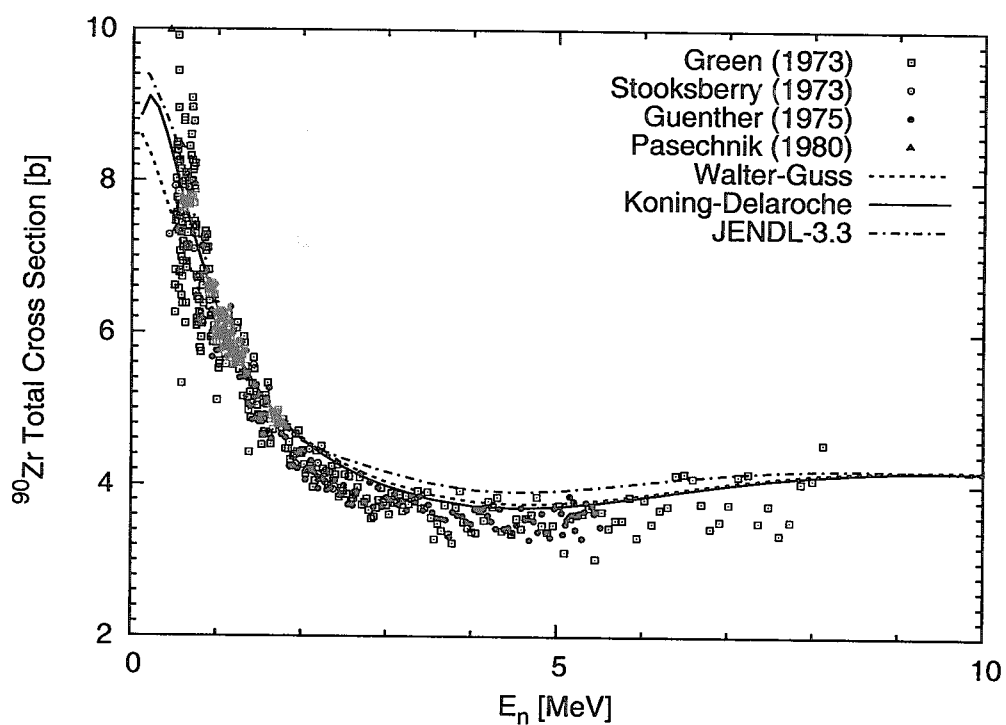


Fig. 2: Comparison of calculated total cross section for  $^{90}\text{Zr}$  with some global optical potential with the experimental data.

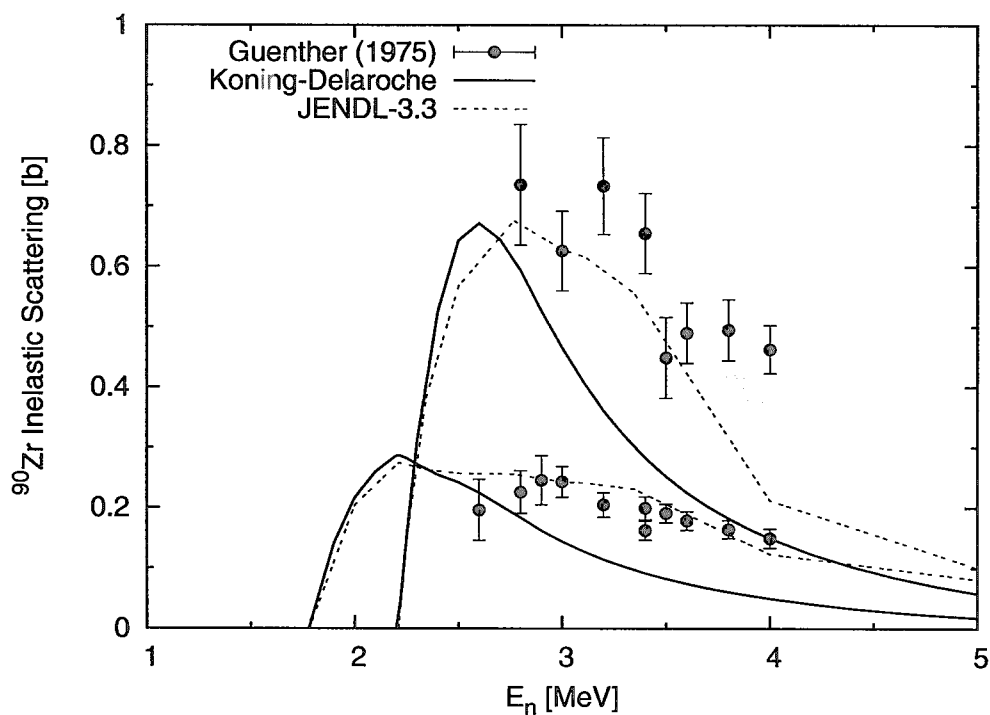


Fig. 3: Comparison of calculated inelastic scattering cross sections for  $^{90}\text{Zr}$  to the 1.761 and 2.186 MeV levels with the experimental data.

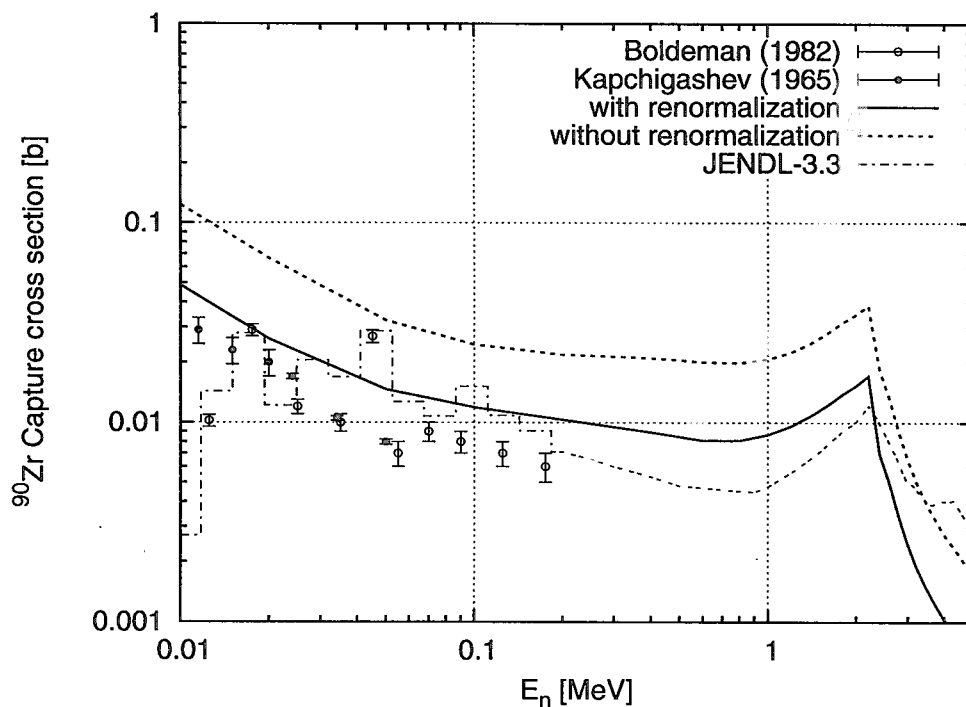


Fig. 4: Comparison of calculated neutron capture cross sections for  $^{90}\text{Zr}$  with the experimental data.

### **3. Papers Presented at Poster Sessions**







### 3.1 Neutron Capture Cross Section Measurement of Pr in the Energy Region from 0.003 eV to 140 keV by Linac Time-of-Flight Method

Samyol Lee<sup>a</sup>, Shuji Yamamoto<sup>a</sup>, Katsuhei Kobayashi<sup>a</sup>, Jungran Yoon<sup>b</sup>, and Taeik Ro<sup>b</sup>

<sup>a</sup>Research Reactor Institute, Kyoto University, Kumatori-cho, Sennan-gun, Osaka, 590-0494, Japan  
koba@rri.kyoto-u.ac.jp

<sup>b</sup>Dong-A University, 840 Hadan 2-dong, Saha-gu, Pusan, 604-714, Korea

*The cross section of the  $\text{Pr}(n, \gamma)$  reaction has been measured in the energy region from 0.003 eV to 140 keV by the neutron time-of-flight (TOF) method with a 46-MeV electron linear accelerator (linac) of the Research Reactor Institute, Kyoto University (KURRI). An assembly of  $\text{Bi}_4\text{Ge}_3\text{O}_{12}$  (BGO) scintillators was employed as a total energy absorption detector for the prompt capture  $\gamma$ -ray measurement from the sample. In order to determine the neutron flux impinging on the capture sample, a plug of  $^{10}\text{B}$  powder sample was used. The measured result was compared with the previous experimental and the evaluated data.*

#### 1. Introduction

Praseodymium-141 ( $^{141}\text{Pr}$ ) is a kind of fission products (FPs) which are produced in Light Water Reactors (LWRs) and Liquid-Metal-Cooled Fast Breeders Reactors (LMFBRs). The cumulative fission yields of the thermal neutron-induced fission of  $^{235}\text{U}$  is 5.8 % [1]. The yield value is pretty large in the fission products and  $^{141}\text{Pr}$  may be apt to accumulate in the spent-fuels. Therefore, accurate measurement of the nuclear data, especially the neutron capture cross section, is necessary for the assessment of reactor safety and for the investigation of high-burn-up core characteristics [2,3]. According to the evaluated data in ENDF/B-VI [4], the capture cross sections in the thermal and the keV energy regions are 11.5 and about 0.1 b, respectively. Since the  $^{141}\text{Pr}$  nuclide has the neutron magic number ( $N=82$ ) and excess proton on the  $2d_{5/2}$  sub-shell, the capture cross section may not be so large as expected. However, the accurate nuclear data of  $^{141}\text{Pr}$  is thought to be needed for evaluating the nuclear-transmutation performance in reactors. In the keV energy region, moreover, the capture cross section is also important for the study on the s-process for nucleosynthesis in stars [5,6,7].

Although the energy dependent cross section for the  $^{141}\text{Pr}(n, \gamma)$  reaction has been measured before, no data has been experimentally obtained below 22 eV, except for the thermal neutron capture cross section. Konks et al. [8] measured the cross section at energies from 22 eV to 40 keV with a lead slowing-down spectrometer, which gave poor energy resolution of about 30 to 35 % at full-width at half-maximum (FWHM). Gibbons et al. [9] obtained the data in the energy range of 7 to 170 keV using a Van de Graaff accelerator and a liquid scintillation tank detector. Taylor et al. [10] measured the cross section between 3 and 200 keV by the neutron time-of-flight (TOF) method using an electron linear accelerator (linac) and a pair of non-hydrogenous liquid scintillators. Very recently, the experimental group of Igashira et al. [11] measured the capture cross sections at energies of 10 to 100 keV making use of a 3-MV Pelletron accelerator and a large anti-Compton NaI(Tl)  $\gamma$ -ray spectrometer. The capture cross section has been compiled in JENDL-3.2 [12], ENDF/B-VI [4], and JEF-2.2 [13].

As mentioned above, the current situation of the experimental data is not always satisfied in quality and quantity. In the current study, the relative energy dependent cross section of the  $^{141}\text{Pr}(n, \gamma)$  reaction has been measured by the neutron time-of-flight (TOF) method with a 46-MeV electron linear accelerator (linac) of the Research Reactor Institute, Kyoto University (KURRI). Twelve pieces of  $\text{Bi}_4\text{Ge}_3\text{O}_{12}$  (BGO) scintillators were employed to measure capture gamma-rays from the sample as a total energy absorption detector [14]. The energy dependent neutron flux was obtained with the boron-10 ( $^{10}\text{B}$ ) sample and the  $^{10}\text{B}(n, \alpha \gamma)$  standard cross section. The result has been normalized to the thermal neutron capture cross section value of ENDF/B-VI data, and the result has been compared with the previous experimental data and the evaluated

cross sections in JENDL-3.2, ENDF/B-VI, and JEF-2.2.

## 2. Experimental procedure

The experimental arrangement is shown in Fig. 1. Bursts of fast neutrons were produced from the water-cooled photoneutron target, which was made of twelve sheets of Ta plate, 5 cm in diameter and the effective thickness is  $\sim 3$  cm[15]. This target was set at the center of a water tank, 30 cm in diameter and 35 cm high with wall thickness of 0.8 cm, to moderate the pulsed fast neutrons. A Pb block, 5 cm  $\times$  5 cm and 10 cm long, was placed in front of the Ta target to reduce the  $\gamma$ -flash generated by the electron burst from the target. The capture sample was placed at a distance of  $12.7 \pm 0.02$  m from the Ta target. The neutron and  $\gamma$ -ray collimation system was mainly composed of  $B_4C$ , Pb,  $Li_2CO_3$  and borated paraffin, and tapered from  $\sim 12$  cm in diameter at the entrance of the flight tube to 1.8 cm at the BGO assembly. In the experiment above 1 eV, a Cd sheet of 0.5 mm in thickness has placed in the neutron beam to suppress overlap of thermal neutrons from the previous pulses due to the high frequency operation.

In the background measurement, we measured the  $\gamma$ -ray from the blank sample (without Pr sample). The neutron beam intensity during the measurement was monitored with a  $BF_3$  counter inserted into the neutron beam.

The linac was operated with two different modes; One is for that below 20 eV with the repetition rate of 50 Hz, the pulse width of 3.0  $\mu$ s, the peak current of 0.5 A, and the electron energy of  $\sim 30$  MeV. The other is for that above 1 eV with the repetition rate of 300 Hz, the pulse width of 0.010  $\mu$ s, the peak current of 6 A, and the electron energy of  $\sim 30$  MeV, respectively.

In the measurement, we have employed three kinds of sample, as shown in Table 1. We have paid attention to the sample thickness of Pr not to be so large for the multiple-scattering and self-shielding corrections in the sample. The  $^{10}B$  sample in the form of powder packed in a thin aluminum case was used to measure the relative neutron flux. The graphite sample was also utilized for the experimental investigation of background due to neutrons scattered by the Pr sample. Because although the inside of the through-hole in the BGO assembly was covered with  $^6LiF$  tiles of 3 mm in thickness to absorb neutrons scattered by the capture sample, the tiles were not always enough to shield against higher energy neutrons above 10 eV[14]. The background to the scattered neutrons were corrected by considering the graphite thickness equivalent to the scattering cross section of the capture sample.

The BGO assembly, which is used for the capture  $\gamma$ -ray spectrometer, consists of twelve scintillation bricks of  $5 \times 5 \times 7.5$  cm<sup>3</sup>, and the total volume of the BGO scintillators is 2.25 liters[14]. Each BGO scintillators is equipped with a photo-multiplier tube of 3.8 cm in diameter. A through-hole of  $1.8 \times 1.8$  cm<sup>2</sup> in section is made in the BGO assembly. A collimated neutron beam is led through the hole to the capture sample that is placed at the center of the BGO assembly. Moreover, the BGO assembly installed in a house made of lead bricks of 5 to 10 cm in thickness to shield against background radiation from the surroundings.

Two kinds of signals were stored in the FAST ComTec's MPA/PC-multi-parameter system linked to a

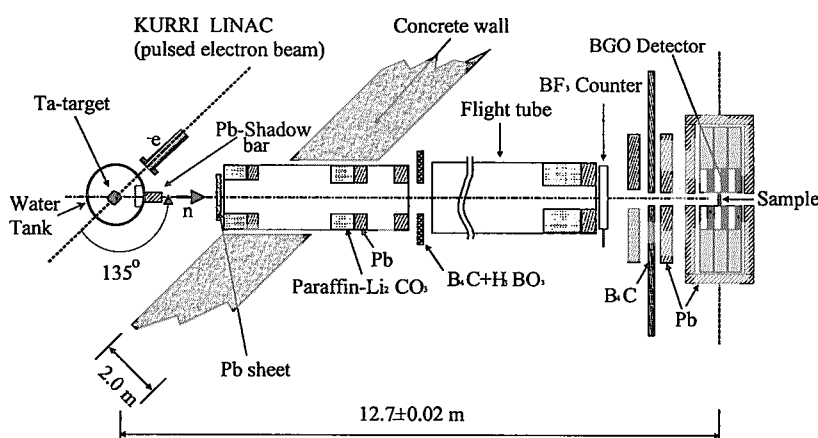


Fig. 1. Experimental arrangement for the capture cross section measurement.

personal computer. One is for the capture event measurement from the BGO detection system, and the other is for the  $\text{BF}_3$  counter to monitor the neutron beam intensity among the experimental runs. Output signals from the BGO detection system were fed into the time digitizer, which was initiated by the electron burst through the fast amplifier and the discriminator, and were stored in the multi-channel analyzer. The signals from the  $\text{BF}_3$  counter were also fed into the time digitizer through the linear amplifier and the timing-single channel analyzer. The data obtained were all stored in the multi-parameter system.

Table 1. Physical parameters of the samples used in the current measurements.

Sample	Physical form	Purity (%)	Isotopic Composition (%)	Thickness		Size
				(g/cm <sup>2</sup> )	(mm)	
<sup>141</sup> Pr	Foil	99.9	100	1.609	3.0	1.27 cm in diam.
<sup>10</sup> B <sup>†1</sup>	<sup>10</sup> B Powder	99.999	<sup>10</sup> B: 96.98 <sup>11</sup> B: 3.02	0.872	8.0	1.8 × 1.8 cm <sup>2</sup>
Graphite	Plate	99.99	100	1.892	10.0	1.8 × 1.8 cm <sup>2</sup>

<sup>†1</sup> Each sample (powder) was packed into a thin aluminum case (0.1 mm in thickness).

### 3. Data processing

#### 3.1. Derivation of the neutron capture cross section

A <sup>10</sup>B sample was used to determine the incident neutron flux on the sample. Since the thermal neutron cross section of the <sup>10</sup>B(n,  $\alpha$ ) reaction is  $3837 \pm 9$  b[16], the <sup>10</sup>B sample (0.872 g/cm<sup>2</sup>) is black for neutrons below several hundreds of keV as well as thermal neutrons. In addition, the energy dependent cross section ratio  $^{10}\text{B}(n, \alpha\gamma) / \{^{10}\text{B}(n, \alpha\gamma) + ^{10}\text{B}(n, \alpha)\}$  is almost constant in the relevant energy region[17]. Then, the capture counting rate of the <sup>10</sup>B sample at energy  $E$ ,  $C_B(E)$ , is given by the following relation:

$$C_B(E) = \varepsilon_B Y_B(E) \phi(E) = \varepsilon_B \phi(E), \quad (1)$$

where the subscript “B” means <sup>10</sup>B.  $Y_B(E)$  is the capture yield and unity in the relevant energy, because the <sup>10</sup>B sample can be black.  $\varepsilon_B$  is the detection efficiency for the <sup>10</sup>B(n,  $\alpha\gamma$ ) reaction. The neutron flux  $\phi(E)$  at a certain energy  $E$  can be obtained from the following relation:

$$\phi(E) = C_B(E) / \varepsilon_B / Y_B(E). \quad (2)$$

The capture counting rate for the <sup>141</sup>Pr sample at energy  $E$ ,  $C_{Pr}(E)$ , can be obtained from the following relation:

$$C_{Pr}(E) = \varepsilon_{Pr} Y_{Pr}(E) \phi(E), \quad (3)$$

where the subscript “Pr” means the sample of <sup>141</sup>Pr. Since the BGO detection system is a total energy absorption detector, the detection efficiency  $\varepsilon_{Pr}$  may be independent of neutron energy  $E$ . Finally, the capture yield  $Y_{Pr}(E)$  can be obtained using Eqs. (2) and (3) as

$$Y_{Pr}(E) = \varepsilon \frac{C_{Pr}(E)}{C_B(E)} Y_B(E), \quad (4)$$

where  $\varepsilon$  is a relative detection efficiency obtained from  $\varepsilon_B/\varepsilon_{Pr}$ . In the case of the  $^{10}\text{B}$  sample used in the current measurement, the capture yield  $Y_B(E)$  is unity in the relevant energy region, as mentioned above.

#### 4. Corrections and uncertainties

The capture yield,  $Y(E)$  is a primary value to be determined from the number of capture events occurring in the sample. The neutron capture yield for the sample is given by [18]

$$Y(E) = \{1 - \exp(-N\sigma_t(E)t)\} \frac{\sigma_c(E)}{f_c(E)\sigma_t(E)}, \quad (5)$$

where  $N$  is the atomic density of the sample,  $\sigma_t(E)$  is the neutron total cross section,  $t$  is the sample thickness,  $\sigma_c(E)$  is the neutron capture cross section, and  $f_c(E)$  is the correction function for the neutron scattering and/or self-shielding in the sample. Instead of the calculation with Eq. (5), we have employed the Monte Carlo code MCNP [19] and the cross sections in JENDL-3.2 to perform the detailed calculations considering the neutron transport in the sample. In the calculation, we have assumed that the capture sample is irradiated by the collimated parallel neutron beam. The random history number of the Monte Carlo calculation was 5,000,000. The correction function for the  $^{10}\text{B}$  sample has been calculated by using Eq. (5), because the  $^{10}\text{B}(n,\alpha\gamma)$  cross section has no resonance structure in the relevant energy region. After the neutron scattering and/or self-shielding correction, the capture cross section was derived in the low energy region of 0.003 to 20 eV. The result obtained was normalized to the reference thermal neutron cross section value at 0.0253 eV. For the high energy experiment in the energy range of 0.7 eV to 140 keV, the cross section was normalized to that in the low energy region by integrating the respective data in the overlapped energy region from 0.7 to 3 eV, after the correction.

The experimental uncertainties for the current measurement are 4.3 to 220 %, which are mainly due to the statistical errors (1.1 ~ 220 %) and uncertainties in the deviation of the  $^{10}\text{B}(n,\alpha\gamma)$  cross section curve (2.4 %) and the reference cross section value (3.0 %). We had poor counting statistics in the cross section minimum energy region between the resonance peaks. The uncertainty of the  $\gamma$ -ray detection efficiency for the BGO assembly is about 0.45 % [20]. In addition, we have considered the uncertainties due to the background subtraction of about 1 % and the corrections for neutron self-shielding and/or neutron scattering effects of 1.3 %.

#### 5. Results

The neutron capture cross section of  $^{141}\text{Pr}$  has been measured from 0.003 eV to 140 keV by the linac TOF method and the result has been normalized at 0.0253 eV to the reference value ( $11.6 \pm 0.35$  b), which was obtained very recently by Yoon et al [21].

The previous measurements and the evaluated data of JENDL-3.2 [12], ENDF/B-VI [4] and JEF-2.2 [13] are shown in Fig. 2. Most of the cross sections have been measured at energies more than keV. In the lower energy range, no experimental data has been reported before except for the thermal neutron cross sections and the data obtained by Konks et al. [8]. The data of Konks et al. are energy-broadened by the lead slowing-down spectrometer at the major resonance peak region. The data by Konks et al. are lower by about 18 % in average at energies from 1 to 40 keV, although their data tend to be in agreement with the current measurement from 5 to 40 keV within the experimental error. The data obtained by Taylor et al. [10] are in good agreement with the current measurement within the uncertainty. Very recently, the data by Harnood et al. [11] are in better agreement with the current result in the energy region from 12 to 70 keV. The data by Gibbons et al. [9] are in good agreement with the measurement and higher by 3.5 % in the energy region from 11.5 to 140 keV than the current measurement. We have observed a small resonance peak at about 5 eV. The peak structure has been also found in the neutron total cross section

measurements[22,23]. Their results may support that there exists the small peak which we have observed at about 5 eV for the first time in the capture cross section measurement.

The evaluated data of JENDL-3.2, ENDF/B-VI and JEF-2.2 show general agreement with the current measurement in the relevant energy region. However, in the cross section minimum region of about 10 to 500 eV, the evaluated data of JENDL-3.2 and JEF-2.2 are considerably lower than the measurement, although the ENDF/B-VI is in good agreement within the error.

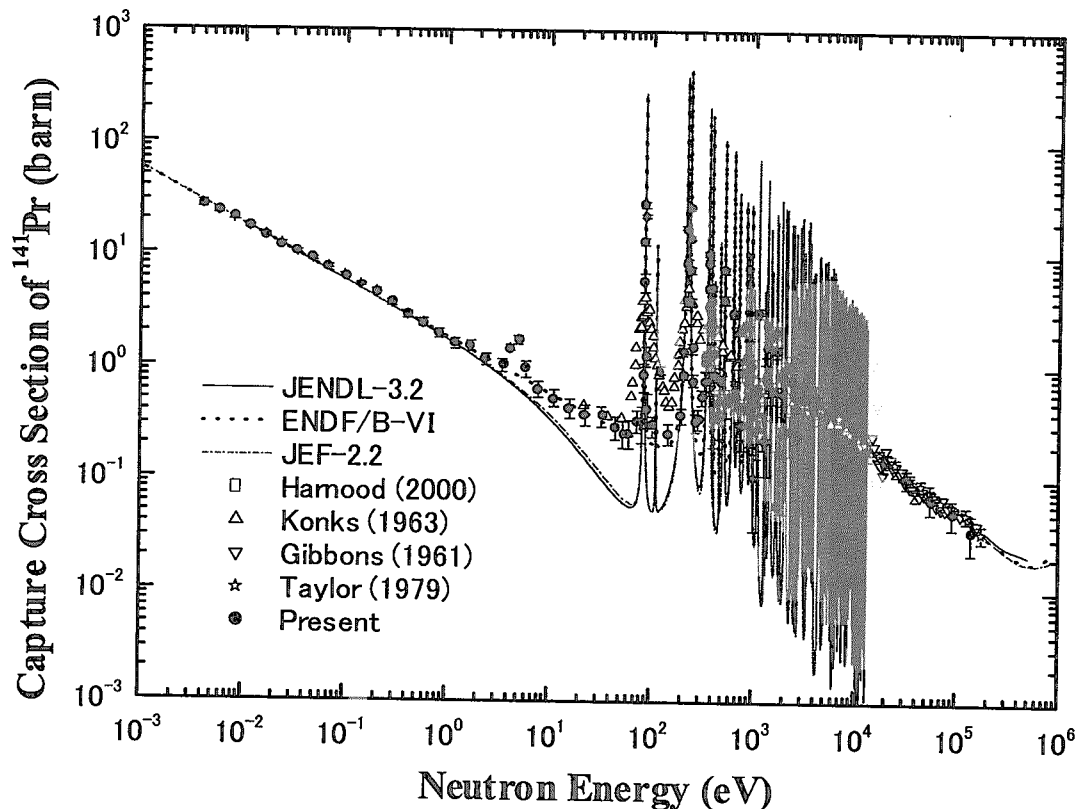


Fig. 2. Comparison of the previous experimental data and the evaluated cross sections with the present measurement for the  $\text{Pr}(n,\gamma)$  reaction.

## 6. Conclusion

The relative measurement of the  $^{141}\text{Pr}(n,\gamma)$  cross section has been performed from 0.003 eV to 140 keV, and the result has been normalized at 0.0253 eV to the reference value ( $11.6 \pm 0.35$  b), which was obtained very recently by Yoon et al[21]. The previous measurements and the evaluated data from ENDF/B-VI, JENDL-3.2 and JEF-2.2 are compared with the current measurement in Fig. 2. No experimental data have been reported before below 22 eV except for the thermal neutron cross section. As can be seen in Fig. 2, we have observed a small resonance peak at about 5 eV, whose peak structure has been found in the neutron total cross section measurements[22,23]. This fact may support the existence of the small resonance peak in the capture cross section curve. The data by Konks et al. have been measured with the lead slowing-down spectrometer[8]. In the non-resolved region from 5 to 40 keV, their data are close to the current measurement. The data by Gibbons et al.[9] and Taylor et al.[10] are in good agreement with the measurement. Very recently Harnood et al.[11] measured the cross section, which agreed well with the measurement at energies from 12 to 70 keV. The evaluated data from ENDF/B-VI, JENDL-3.2 and JEF-2.2 show good agreement with the current measurement in the relevant energy region, although the JENDL-3.2 and the JEF-2.2 data are considerably lower than the measurement and the ENDF/B-VI data in the cross section minimum region from 10 to 500 eV.

### Acknowledgment

The authors would like to express their thanks to the linac staff of the Research Reactor Institute, Kyoto University (KURRI) for making it possible to operate the accelerator steadily. One of the authors (Samyol Lee) performed this study by the Grant-in-Aid (No.: 02122) for Scientific Research (Tokubetsu Kenkyuin Shorei-hi) of Japan Society for the Promotion of Science. A part of this study was supported by the Grant-in-Aid (No.: 13680588) for Scientific Research from the Ministry of Education, Culture, Sports, Science and Technology of Japan.

### References

- [1] H. Ihara (Ed.), JAERI-M 89-204 Tables and Figures from JNDC Nuclear Data Library of Fission Products Version 2 (1989) 157.
- [2] R. L. Macklin and J. Halperin, Nucl. Sci. Eng. 73 (1980) 174.
- [3] S. Mizuno, M. Igashira, and K. Masuda, J. Nucl. Sci. Tec. 36 (1999) 493.
- [4] "ENDF-201, ENDF/B-VI Summary Documentation", BNL-NCS-17541, MOD1 New Evaluation (ENDF/B-VI) 4<sup>th</sup> ed., P. F. ROSE, Ed., Brookhaven National Laboratory (1991); see also V. McLane and Members of The Cross Section Working Group "ENDF-201 ENDF/B-VI Summary Documentation Supplement 1 ENDF/HE-VI Summary Documentation", BNL NCS-17541, MOD3 Rev. 2 (ENDF/B-VI), Suppl. 1, 4<sup>th</sup> ed., Brookhaven National Laboratory (1996).
- [5] D. D. Clayton, "Principles of stellar evolution and nucleosynthesis", Univ. of Chicago Press, Chicago (1968).
- [6] M. Busso and R. Gallino, Nucl. Phys. A621 (1997) 431c.
- [7] C. Arlandini, M. Heil, R. Reifarth, F. Käppeler, and P. V. Sedyshev, Nucl. Phys. A688 (2001) 487c.
- [8] V. A. Konks, Yu. P. PoPov, and F. L. Shapiro, Soviet Phys. JETP 19 (1964) 59.
- [9] J. H. Gibbons, R. L. Macklin, P. D. Miller, and J. H. Neiler, Phys. Rev. 122 (1961) 182.
- [10] R.B. Taylor, B. J. Allen, A. R. Del. Musgrove, and R. L. Macklin, Aus. J. Phys. 32 (1979) 551.
- [11] S. Harnood, M. Igashira, T. Matsumoto, S. Mizuno, and T. Ohsaki, J. Nucl. Sci. Tech. 37 (2000) 740.
- [12] "Descriptive Data of JENDL-3.2", JAERI-Data/ Code 98-006 (part II), K. Shibata, and T. Narita, Eds., Japan Atomic Energy Research Institute (1998).
- [13] C. Nordborg, and M. Salvatores, "Status of the JEF Evaluated Data Library", Proc. Intl. Conf. Nuclear Data for Science and Technology, Gatlinberg, Tennessee, May 9-13, Vol. 2, p. 680, American Nuclear Society (1994).
- [14] S. Yamamoto, K. Kobayashi, and Y. Fujita, J. Nucl. Sci. Tech. 33 (1996) 815.
- [15] K. Kobayashi, G. Jin, S. Yamamoto, K. Takami, Y. Kimura, T. Kozuka, and Y. Fujita, Annu. Rep. Res. Reactor Inst., Kyoto Univ. 22 (1987) 142.
- [16] S. F. Mughabghab, M. Divadeenam, and N. E. Holden, "Neutron Cross Sections", Neutron Resonance Parameters and Thermal Cross Sections, Vol. 1, part A: Z=1-60, Academic Press, New York (1984).
- [17] IAEA Technical Series No. 227, Nuclear Data Standards for Nuclear Measurement, IAEA, Vienna (1983).
- [18] H. W. Schmitt, ORNL-2883, 1-28-60 (1960).
- [19] F. J. Briesmeister (Ed.), MCNP-A General Monte Carlo Code for Neutron and Photon Transport, Version 4B, LA-12625-M, Los Alamos National Laboratory (1997).
- [20] S. Yamamoto, Y. Fujita, T. Shibata, and S. Selvi, Nucl. Instrum. Methods Phys Res. A249 (1986) 484.
- [21] J. Yoon, Nuclear Physics in print.
- [22] G. D. Hickman, Bull. American Phys. Soc. 10 (1965) 12.
- [23] V. McLane et al., Neutron Cross Sections, Vol. 2, Neutron Cross Section Curves, Academic Press (1988).

## 3.2

## Measurement of Cross Sections of the $^{210}\text{Po}$ Production Reaction by keV-Neutron Capture of $^{209}\text{Bi}$

Kosuke SAITO, Masayuki IGASHIRA, Toshiro OHSAKI,  
Toru OBARA and Hiroshi SEKIMOTO

*Research Laboratory for Nuclear Reactors, Tokyo Institute of Technology*

*Meguro-ku, Tokyo 152-8550*

*e-mail: kosuke@nr.titech.ac.jp*

The cross sections of the  $^{209}\text{Bi}(n,\gamma)^{210\text{g}}\text{Bi}$  reaction were measured in the keV-neutron region, using an activation method with the detection of  $\alpha$  rays from  $^{210}\text{Po}$ . Pulsed keV neutrons were generated from the  $^7\text{Li}(p,n)^7\text{Be}$  reaction by a 1.5-ns bunched proton beam from the 3-MV Pelletron accelerator of the Research Laboratory for Nuclear Reactors at the Tokyo Institute of Technology. The  $^{209}\text{Bi}$  samples were metallic bismuth evaporated on a gold backing. After sample irradiation, the 412-keV  $\gamma$  rays from the gold backing were measured with an HPGe detector, and then the  $\alpha$  rays from  $^{210}\text{Po}$  nuclei in the bismuth sample were measured with a Si surface barrier detector. The derived cross sections were  $1.9 \pm 0.4$  mb and  $0.62 \pm 0.14$  mb at the average neutron energies of 30 keV and 534 keV, respectively. The present value at 30 keV is in agreement with the previous measurement at 24 keV of Booth *et al.*, but about a quarter of the evaluation of JENDL Activation cross section File. The present result at 534 keV is the first experimental one around 500 keV, and is about a half of the evaluation of JENDL Activation cross section File.

### 1. Introduction

The Lead-Bismuth Eutectic Coolant (LBEC) attracts a great deal of attention in the research fields of fast breeder reactors and accelerator driven systems because of its advantages such as chemical inertness, high boiling point, low neutron moderation, etc. However, the  $\alpha$ -emitter of  $^{210}\text{Po}$  with the half-life of 138 d is produced in LBEC through the  $^{209}\text{Bi}(n,\gamma)^{210\text{g}}\text{Bi}$

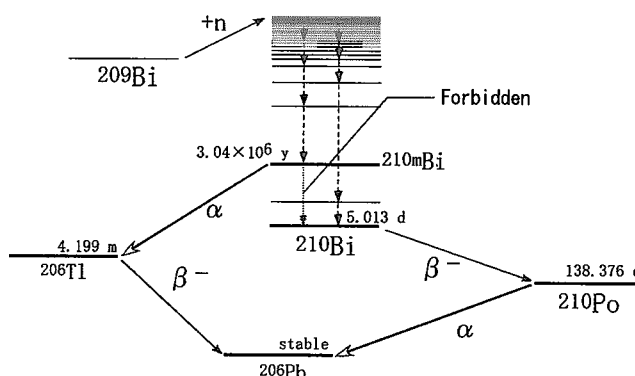


Fig. 1 Simplified decay scheme after neutron capture of  $^{209}\text{Bi}$

reaction and the following  $\beta^-$  decay of  $^{210}\text{gBi}$  with the half-life of 5.01 d. Figure 1 shows a simplified decay scheme after the neutron capture of  $^{209}\text{Bi}$ . The radioactivity of  $^{210}\text{Po}$  causes a problem when maintaining a system with LBEC. Moreover, as seen from Fig. 1,  $^{210\text{m}}\text{Bi}$  with the half-life of  $3.04 \times 10^6$  y is produced through the competitive neutron capture reaction of  $^{209}\text{Bi}(n,\gamma)^{210\text{m}}\text{Bi}$ . Such a long-live nuclide continuously accumulates in proportion to neutron irradiation time, which will bring about an important problem on nuclear wastes. Therefore, the  $^{210}\text{Po}$  and  $^{210\text{m}}\text{Bi}$  production cross sections, *i.e.* the  $^{209}\text{Bi}(n,\gamma)^{210\text{g}}\text{Bi}$  and  $^{209}\text{Bi}(n,\gamma)^{210\text{m}}\text{Bi}$  reaction cross sections, are very important to evaluate the radioactivity of  $^{210}\text{Po}$  and  $^{210\text{m}}\text{Bi}$  in a system with LBEC.

In astrophysics,  $^{209}\text{Bi}$  is the end point of S-process nucleosynthesis in stars and its keV neutron capture cross sections are important for the study on the nucleosynthesis. In nuclear physics, the cross sections are important for understanding the keV-neutron capture reaction mechanism.

In the present study, from the above viewpoints, the  $^{210}\text{Po}$  production cross sections in the keV-neutron region were measured with an activation method, and then the  $^{210\text{m}}\text{Bi}$  production cross sections were determined from the differences between the total capture cross sections of  $^{209}\text{Bi}$  and the  $^{210}\text{Po}$  production cross sections.

## 2. Experimental Procedure

The experiments were performed, using the 3-MV Pelletron accelerator of the Research Laboratory for Nuclear Reactors at the Tokyo Institute of Technology. Pulsed keV neutrons were generated from the  $^7\text{Li}(p,n)^7\text{Be}$  reaction by a 1.5-ns bunched proton beam from the Pelletron accelerator. The incident neutron spectrum on a  $^{209}\text{Bi}$  sample was measured by means of a Time-Of-Flight (TOF) method with a  $^6\text{Li}$ -glass scintillation detector. Each  $^{209}\text{Bi}$  sample was metallic bismuth evaporated on a gold backing whose diameter and thickness were 15 mm and 0.1 mm, respectively. The thickness of the bismuth layer is about 5  $\mu\text{m}$ . The sample was located at a distance of 2 or 5 cm from the neutron source and at an angle of  $0^\circ$  with respect to the proton beam axis. The irradiation time was 40 to 60 h. After each irradiation, the 412-keV  $\gamma$  rays from the gold backing were measured for 3 d with an HPGe detector with the relative efficiency of 100 %, and then the  $\alpha$  rays from  $^{210}\text{Po}$  nuclei in the bismuth sample were measured with a Si surface barrier detector for several months.

## 3. Data Processing

Figure 2 shows a normalized incident neutron energy spectrum,  $\eta(E_n)$ , which was derived from a TOF spectrum observed with the  $^6\text{Li}$ -glass detector. An average capture cross section of  $^{197}\text{Au}$ ,  $\langle\sigma_{\text{Au}}\rangle$ , was defined as follows, using  $\eta(E_n)$ :



$$\langle \sigma_{Au} \rangle = \int \sigma_{Au}(E_n) \eta(E_n) dE_n, \quad (1)$$

where  $\sigma_{Au}(E_n)$  is the standard capture cross section of  $^{197}\text{Au}$  taken from ENDF/B-VI[1] and is shown in Fig. 2. The decay curve of radioactivity of  $^{198}\text{Au}$  was obtained from the measurement of 412-keV  $\gamma$  rays, and the radioactivity,  $A$ , at the end ( $t' = 0$ ) of neutron irradiation was determined from the decay curve. Then, the neutron flux,  $\phi$ , was obtained from the following relation:

$$A = N \langle \sigma_{Au} \rangle \phi (1 - e^{-\lambda T_{irr}}), \quad (2)$$

where  $\lambda$  is the decay constant of  $^{198}\text{Au}$ ,

$N$  the number of  $^{197}\text{Au}$  nuclei, and  $T_{irr}$  the irradiation time.

The number of  $^{210}\text{Po}$  nuclei was obtained by solving the following differential equations:

$$\frac{dN_{Bi}(t)}{dt} = n \langle \sigma \rangle \phi - \lambda_\beta N_{Bi}(t), \quad (3)$$

$$\frac{dN_{Po}(t)}{dt} = \lambda_\beta N_{Bi}(t) - \lambda_\alpha N_{Po}(t), \quad (4)$$

in the period of irradiation, and after irradiation,

$$\frac{dN_{Bi}(t')}{dt'} = -\lambda_\beta N_{Bi}(t'), \quad (5)$$

$$\frac{dN_{Po}(t')}{dt'} = \lambda_\beta N_{Bi}(t') - \lambda_\alpha N_{Po}(t'), \quad (6)$$

where  $N_{Bi}$  and  $N_{Po}$  are the numbers of  $^{210}\text{gBi}$  and  $^{210}\text{Po}$  nuclei, respectively,  $n$  the number of  $^{209}\text{Bi}$  nuclei,  $\lambda_\beta$  and  $\lambda_\alpha$  the decay constants of  $^{210}\text{gBi}$  and  $^{210}\text{Po}$ , respectively, and  $\langle \sigma \rangle$  the average cross section for the  $^{210}\text{Po}$  production. Assuming that  $\phi$  and  $n$  were constant, these equations were solved and the  $\alpha$  activity of  $^{210}\text{Po}$  after irradiation,  $A_{Po}(t') = \lambda_\alpha N_{Po}(t')$ , was obtained as follows:

$$A_{Po}(t') = n \langle \sigma \rangle \phi \frac{\lambda_\alpha}{\lambda_\alpha - \lambda_\beta} \left\{ (1 - e^{-\lambda_\beta T_{irr}}) e^{-\lambda_\beta t'} - \frac{\lambda_\beta}{\lambda_\alpha} (1 - e^{-\lambda_\alpha T_{irr}}) e^{-\lambda_\alpha t'} \right\}. \quad (7)$$

By comparing Eq.(7) with the growing and decaying curve of the  $\alpha$  activity of  $^{210}\text{Po}$  obtained from the measurement of  $\alpha$  rays, the cross section,  $\langle \sigma \rangle$ , was derived with the  $\alpha$ -ray detection efficiency,  $\varepsilon$ , described below.

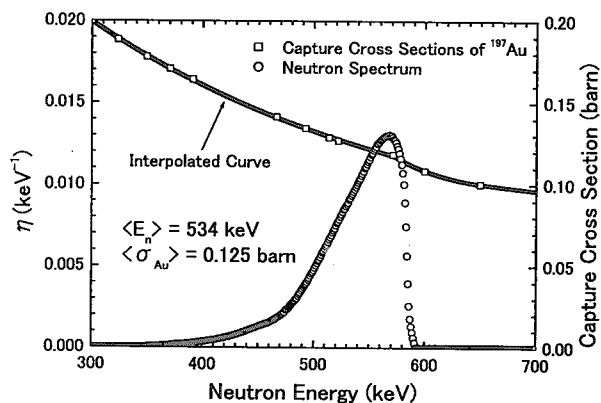


Fig. 2 Normalized incident neutron spectrum at the 534 keV experiment and the standard capture cross sections of  $^{197}\text{Au}$

The  $^{209}\text{Bi}$  samples had medium thickness (about  $5\text{ }\mu\text{m}$ ) in comparison with the range (about  $15\text{ }\mu\text{m}$ ) of  $5.3\text{-MeV}$   $\alpha$  rays from  $^{210}\text{Po}$ . A thin sample might be better than the present medium sample to make  $\alpha$ -ray spectroscopy with good energy resolution, but it must have the disadvantage of poor statistics. In contrast, a thick sample might have the advantage of good statistics, but it must cause continuous  $\alpha$ -ray spectra whose shapes depend on the surface condition of thick sample. From the above

consideration, the medium thickness was chosen in the present study. Monte-Carlo simulation was performed to check the sample thickness and determine the  $\alpha$ -ray detection efficiency. Figure 3 shows the simulated and measured  $\alpha$ -ray spectra at the  $534\text{-keV}$  experiment. The simulated spectrum is in good agreement with the measured one.

The  $^{210\text{m}}\text{Bi}$  production cross sections were determined as the differences between the  $^{210}\text{Po}$  production cross sections and the corresponding total capture cross sections which were previously measured by a prompt  $\gamma$ -ray detection method in our laboratory.

#### 4. Results and Discussion

The derived  $^{210}\text{Po}$  and  $^{210\text{m}}\text{Bi}$  production cross sections are listed in Table 1, and are compared with a previous measurement[2] and the evaluation of JENDL Activation cross section File (JENDL/A-96)[3] in Fig. 4. The present result of the  $^{210}\text{Po}$  production cross section at  $30\text{ keV}$  is in agreement with the previous measurement at  $24\text{ keV}$  of Booth *et al.*[2], but is about a quarter of the evaluation of JENDL/A-96. Booth *et al.* adopted a double ratio-comparison method with the standard of  $^{127}\text{I}$ , using a Sb-Be photoneutron source for the  $24\text{-keV}$  neutrons and a reactor neutron source for the thermal neutrons. They detected the  $\beta$ -rays from  $^{210\text{g}}\text{Bi}$  and  $^{128}\text{I}$ , separately. The present result of the  $^{210}\text{Po}$  production cross section at  $534\text{ keV}$  is the first experimental one around  $500\text{ keV}$ , and is about a half of the evaluation

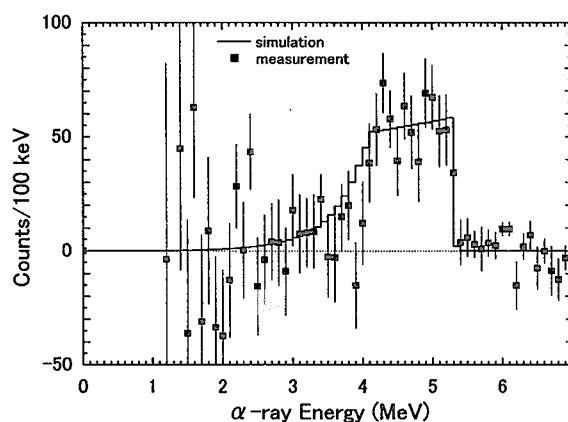


Fig. 3 Comparison between simulated and measured  $\alpha$ -ray spectra

Table 1 $^{210}\text{Po}$ and $^{210\text{m}}\text{Bi}$ production cross sections		
Neutron Energy (keV)	Cross Sections (mb)	
	$^{210}\text{Po}$	$^{210\text{m}}\text{Bi}$
30	$1.94 \pm 0.39$ (20%)	$0.65 \pm 0.40$ (61%)
534	$0.62 \pm 0.14$ (22%)	$0.76 \pm 0.16$ (21%)

of JENDL/A-96. As for the  $^{210\text{m}}\text{Bi}$  production cross section, the present result at 30 keV is about one third of the evaluation of JENDL/A-96. The present result at 534 keV is in agreement with the evaluation of JENDL/A-96 within the error, but this agreement seems to be accidental. Figure 5 shows the branching ratios derived from the present results and the evaluations of JENDL/A-96. The branching ratios derived from the present results are smaller than those from the evaluations by about 30 to 50 %, but both the neutron-energy dependences seem to agree with each other.

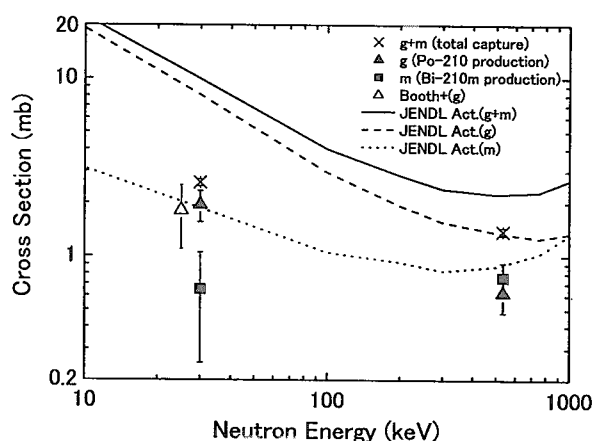


Fig. 4  $^{210}\text{Po}$  and  $^{210\text{m}}\text{Bi}$  production and total capture cross sections in the keV region

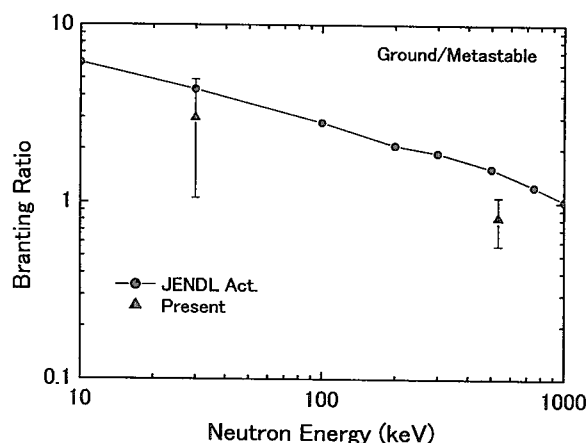


Fig.5 Branching ratios derived from the present results and the JENDL/A-96

## 5. Conclusion

The  $^{210}\text{Po}$  and  $^{210\text{m}}\text{Bi}$  production cross sections were derived at the average incident neutron energies of 30 and 534 keV. The derived cross sections were a half to a quarter of the evaluated values of JENDL/A-96 except for the  $^{210\text{m}}\text{Bi}$  production cross section at 534 keV. The branching ratios derived from the present cross sections were smaller than those from the JENDL/A-96 by about 30 to 50 %, but both the neutron-energy dependences were similar.

The present results are important for the evaluation of radioactivity of  $^{210}\text{Po}$  and  $^{210\text{m}}\text{Bi}$  produced in a system with LBEC. The present small values for the  $^{210}\text{Po}$  production cross sections might relieve the  $^{210}\text{Po}$  problem of LBEC.

## References

- [1] "ENDF/B-VI data file for  $^{197}\text{Au}$ (MAT=7925)," evaluated by Young, P.G. (1984).
- [2] Booth, R., Ball, W.P., MacGregor, M.H.: *Phys. Rev.*, 112, 226 (1958).
- [3] JENDL Activation cross section File 96(JENDL/A-96) for  $^{209}\text{Bi}$ , evaluated by Yamamuro, N. (1989).



### 3.3

#### Measurements of activation cross sections producing short-lived nuclei in the energy range of 2 - 3 MeV with pulsed neutron beam.

Toshiaki Shimizu<sup>1</sup>, Hironori Yamamoto<sup>2</sup>, Masafumi Kasaishi<sup>1</sup>, Itaru Miyazaki<sup>2</sup>  
Michihiro Shibata<sup>1</sup>, Kiyoshi Kawade<sup>1</sup>, Jun-ichi Hori<sup>3</sup> and Takeo Nishitani<sup>3</sup>

<sup>1</sup>*Department of Energy Engineering and Science, Nagoya University  
Furo-cho, Chikusa-ku, Nagoya 464-8603*

<sup>2</sup>*Department of Nuclear Engineering, Nagoya University  
Furo-cho, Chikusa-ku, Nagoya 464-8603*

<sup>3</sup>*Department of Fusion Engineering, Naka Fusion Research Establishment  
Japan Atomic Energy Research Institute, Tokai-mura, Naka-gun, Ibaraki-ken 319-1195  
e-mail: t-shimizu@ees.nagoya-u.ac.jp*

To measure activation cross sections producing short-lived nuclei with half-lives less than 10 s, pulsed neutron beam were used. A HPGe detector was properly shielded from neutrons, because it was set on the irradiation room.

By using the d-D neutron source of the Fusion Neutronics Source in Japan Atomic Energy Research Institute. Four (n, n') reaction cross sections for <sup>89</sup>Y, <sup>90</sup>Zr, <sup>137</sup>Ba and <sup>197</sup>Au with half-lives between 0.8 s and 2.6 min were obtained in the energy range of 2 - 3 MeV. The cross section for <sup>90</sup>Zr (n, n') <sup>90m</sup>Zr reaction was obtained for the first time. Present results were compared with the evaluated data JENDL-3.3 and FENDL.

#### 1. Introduction

In a D-T fusion reactor design, evaluated data libraries of neutron activation cross sections such as JENDL [1] are needed in the energy range up to about 20 MeV. They are used for estimation of the activities, gas productions, neutron damages and neutron dosimetry of the construction materials. The data of the libraries are evaluated on the basis of experimental data and theoretical calculations. Experimental data are also used to normalization of calculated excitation function, and improve the accuracy and reliability of the calculations.

When activation cross sections producing short-lived nuclei are measured, a pneumatic sample transport system which sends samples to the irradiating position and pulls them back

to the measuring position about 2 - 3 s is usually used. Using this system, good statistics have been attained for the measurements of activation cross section with half-lives longer than several seconds. However, measurements of short-lived nuclei with half-lives less than several seconds are difficult to get enough statistics because radioisotopes decay out during the sample transfer.

The in-beam measurement is also useful for measurements of short-lived nuclei. However, there is a problem of high gamma-ray backgrounds, which would give some limitations to measurements of weak induced activities.

In this work, with pulsed neutron, neutron shielding is required for protection of a HPGe detector from d-D neutrons. Neutrons cause both the degradation of detector and the activation of detector. To irradiate samples with pulsed neutron beam, the operation of the accelerator was synchronized to activity measurements.

As test measurements, the activation cross sections of  $^{89}\text{Y} (n, n') ^{89\text{m}}\text{Y}$ ,  $^{90}\text{Zr} (n, n') ^{90\text{m}}\text{Zr}$ ,  $^{137}\text{Ba} (n, n') ^{137\text{m}}\text{Ba}$  and  $^{197}\text{Au} (n, n') ^{197\text{m}}\text{Au}$  reactions whose half-lives were between 0.8 s and 2.6 min were measured.

## 2. Experiment

### 2.1. Experimental procedure and apparatus

The d-D neutrons were produced via  $\text{D} (d, n) ^3\text{He}$  reaction by bombarding a deuterated titanium (Ti-D) target on a copper backing with a  $d^+$  beam of 350 kV using the Fusion Neutronics Source (FNS) at Japan Atomic Energy Research Institute (JAERI). The durations of irradiation and measurement were chose to be the same, which is about two half-lives of the induced activity.

Figure 1 shows the experimental arrangement 1. We used the 0-degree beam line of the FNS to produce d-D neutrons. The sample was irradiated at the end of the collimator as a neutron shield, which was installed at angle of 80 degree with respect to the deuteron beam direction. The energy of emission neutron was 2.65 MeV. The diameter of collimator was 5 cm. The thickness of collimator was 200 cm. The distance between the neutron source and the sample was 390 cm. The induced activities were measured with the 10% HPGe detector. The distance between the sample and the detector was 5 cm.

The experimental arrangement 2 at the 80-degree beam line of the FNS is shown in Fig. 2. The sample was located at an angle of 0 degree with respect to the deuteron beam direction, the energy of emission neutron was 3.1 MeV. The distance between the neutron source and the sample was about 70 cm. The distance between the sample and detector was 2 cm. The HPGe detector was shielded against neutrons from the source by using polyethylene blocks with 60 cm thick and lead blocks 5 cm thick. Determination the optimum position of HPGe detector was done by the Monte-Carlo simulation code MCNP-4C [2]. The main cause of

neutron leak was neutrons scattered from samples.

The neutron fluence rate was measured with use of the  $^{115}\text{In} (n, n') ^{115\text{m}}\text{In}$  reaction ( $T_{1/2} = 4.486 \text{ h}$ ), whose cross section data were taken from JENDL Dosimetry File 99 [3]. The measured fluence rates at sample position of each arrangement were  $1 \times 10^4$  and  $1 \times 10^5 \text{ n/cm}^2/\text{s}$ , respectively. The mean neutron energy at the irradiation position was determined by the ratio of induced activity by the  $^{64}\text{Zn} (n, p) ^{64}\text{Cu}$  ( $T_{1/2} = 12.701 \text{ h}$ ) to  $^{115}\text{In} (n, n') ^{115\text{m}}\text{In}$  reactions.

## 2.2. Measurements of activation cross sections

Activation cross sections were measured by the activation method. All cross section values were determined by referring to the standard reaction cross section of  $^{115}\text{In} (n, n') ^{115\text{m}}\text{In}$ . The samples were set on the irradiating position together with the indium foil as a monitor of neutron fluence rate. The indium foils were set behind the sample. The samples were 20 mm x 20 mm and 0.05 - 2 mm in thickness. The weights of samples were 0.4 - 10 g. In Table 1, the chemical form, the isotopic abundance and the weight of samples are listed.

Gamma rays emitted from the irradiated samples were measured with the HPGe detector. Gamma-ray spectra of  $^{90}\text{Zr} (n, n') ^{90\text{m}}\text{Zr}$  reaction obtained by pulsed and continuous neutron beam are shown in Fig. 3-(a) and (b), respectively. The 2319 keV gamma-ray peak of interest is clearly seen in Fig. 3-(a). On the other hand, the gamma-ray peak of 2319 keV is not clearly observed owing to high room backgrounds as shown in Fig. 3-(b). The gamma rays emitted from indium and zinc were measured with a 115% HPGe detector after neutron irradiation.

## 2.3. Decay data

In Table 2, the decay data of half-lives,  $\gamma$ -ray energies and  $\gamma$ -ray emission probabilities are listed together with the measured reactions and the Q-values.

## 3. Results

The cross section data of four  $(n, n')$  reactions for  $^{89}\text{Y}$  (neutron energy:  $E_n = 3.1 \text{ MeV}$ ),  $^{90}\text{Zr}$  ( $E_n = 3.1 \text{ MeV}$ ),  $^{137}\text{Ba}$  ( $E_n = 2.65 \text{ MeV}$ ) and  $^{197}\text{Au}$  ( $E_n = 2.65, 3.1 \text{ MeV}$ ) were obtained. The present cross section values are shown in Fig. 4 together with the previous data measured with a pneumatic sample transport system, and the evaluated data in JENDL-3.3 and FENDL/A-2.0 [5]. These cross sections are in agreement with the previous data within the experimental uncertainties. The evaluated data for  $^{137}\text{Ba}$  are overestimated. The data for  $^{90}\text{Zr}$  in FENDL/A-2.0 are underestimated. Re-evaluations for those reactions are strongly recommended.

#### 4. Conclusion

The method for measurement of activation cross sections with pulsed neutron beam is useful for producing nuclei with half-lives less than several seconds. In this method, activation cross sections down to about 300 mb could be measured.

#### Acknowledgments

The authors would like to thank to Messrs. C. Kutsukake, S. Tanaka, Y. Abe, M. Seki and Y. Oginuma for the operation of the accelerator at FNS. We are also grateful to Dr. H. Sakane of Radioisotope Research Center in Nagoya University for his valuable discussion.

#### References

- [1] T. Nakagawa, K. Shibata, S. Chiba, T. Fukahori, Y. Nakajima, Y. Kikuchi, T. Kawano, Y. Kanda, T. Ohsawa, H. Matsunobu, M. Kawai, A. Zukeran, T. Watanabe, S. Igarashi, K. Kosako and T. Asami; J. Nucl. Sci. Technol. 32, 1259 (1995).
- [2] J. F. Briesmeister, Ed, "MCNP-A General Monte Carlo N-Particle Transport Code, Version 4C" LA-13709-M, 2000.
- [3] K. Kobayashi, T. Iguchi, S. Iwasaki, T. Aoyama, S. Shimakawa, Y. Ikeda, N. Odano, K. Sakurai, K. Shibata, T. Nakagawa and M. Nakazawa, JAERI 1344 2002.
- [4] E. Browne, R. B. Firestone, "Table of Radioactive Isotopes". John Wiley & Sons, New York (1986).
- [5] A. B. Pashchenko, Summary Report for IAEA Consultants' Meeting on Selection of Evaluations for the FENDL/A-2.0 Activation Cross Section Library. INDC (NDS)-341, International Atomic Energy Agency (1996).

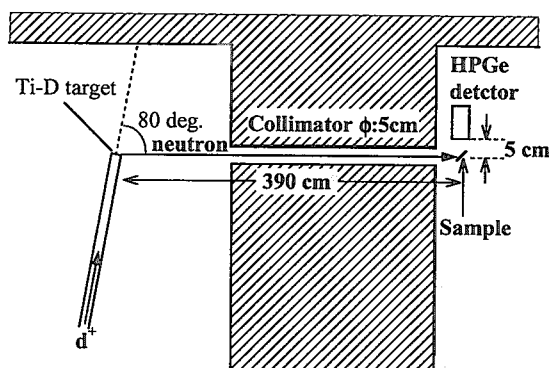


Fig. 1. The schematic view of the present experimental arrangement 1.

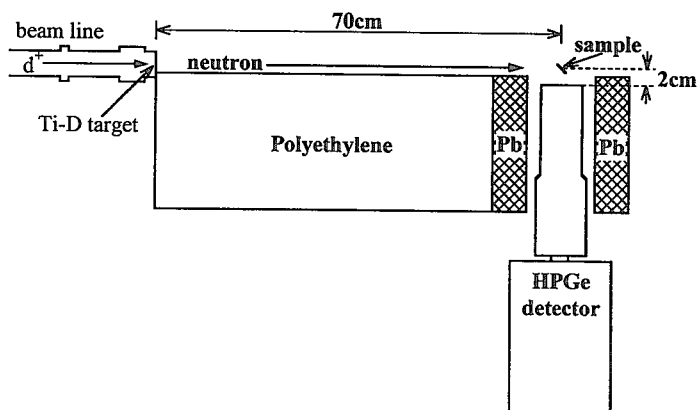


Fig. 2. The schematic view of the present experimental arrangement 2.

Table 1. Chemical form, weight and abundance of the samples

Target nuclei (isotopic composition)	Chemical form	Arrangement 1 Weight [g]	Arrangement 2 Weight [g]	Abundance [%]
$^{89}\text{Y}$ (natural)	Y	3.2	1.1	100
$^{90}\text{Zr}$ (natural)	Zr	10	2.5	51.45
$^{137}\text{Ba}$ (enriched)	$\text{BaCO}_3$	0.4	---	64.04(137), 0.02(130), 0.02(132), 0.06(134), 0.23(135), 1.55(136), 34.12(138)
$^{197}\text{Au}$ (natural)	Au	3.2	0.4	100

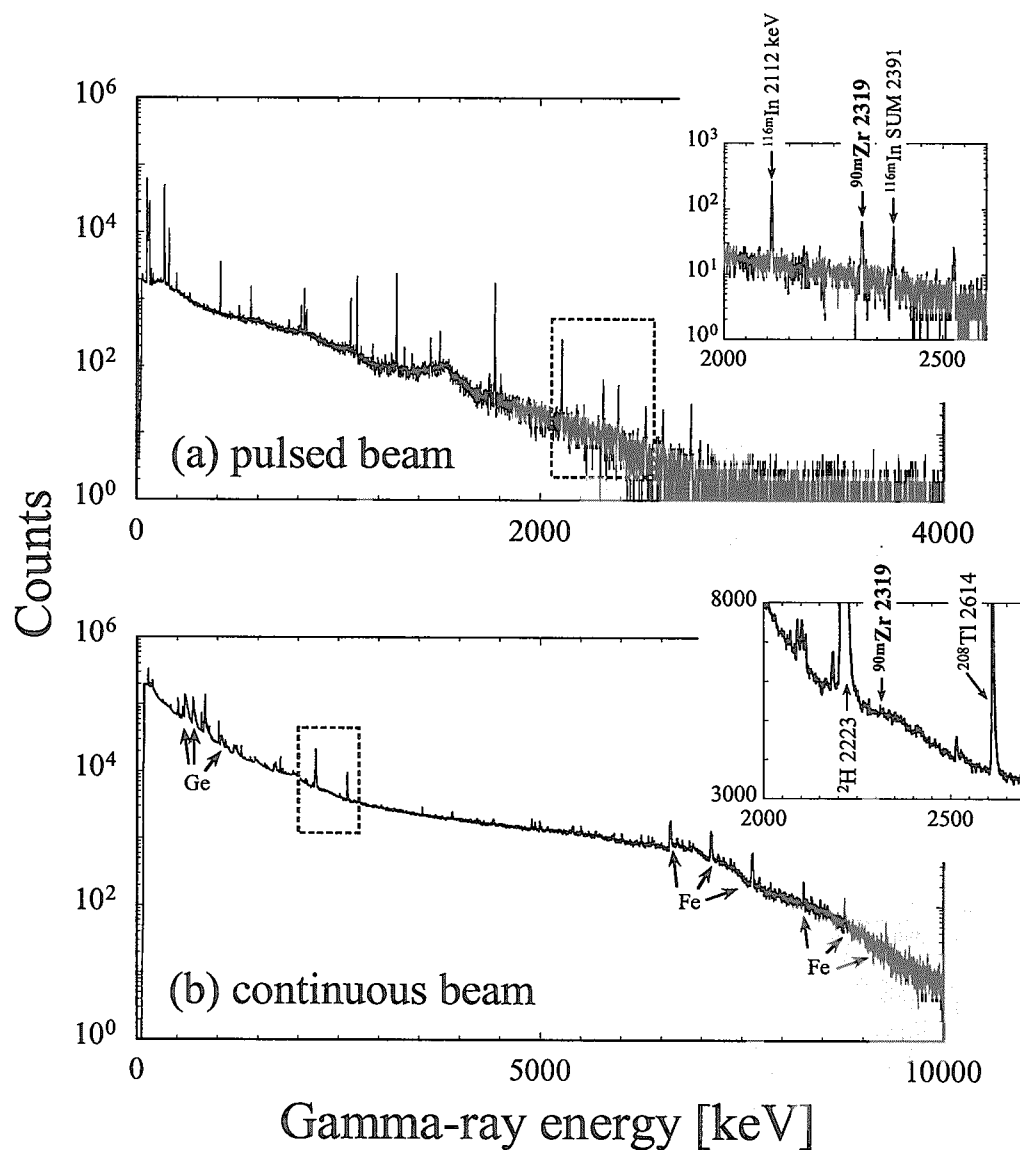


Fig. 3. Gamma-ray spectra of  $^{90}\text{Zr} (n, n') ^{90\text{m}}\text{Zr}$  reaction measured with the pulsed neutron beam (a) and the continuous neutron beam (b).



Table 2. Measured reactions and associated decay data<sup>a)</sup>

Reaction	Half-life	$\gamma$ -ray energy [keV]	$\gamma$ -ray emission probability [%]	Q-value [keV]
$^{89}\text{Y} (n, n') ^{89\text{m}}\text{Y}$	16.06 <sub>4</sub> s	909.15 <sub>7</sub>	99.14 <sub>10</sub>	909.15
$^{90}\text{Zr} (n, n') ^{90\text{m}}\text{Zr}$	809.2 <sub>20</sub> ms	2318.900 <sub>5</sub>	84 <sub>1</sub>	2319.000
$^{137}\text{Ba} (n, n') ^{137\text{m}}\text{Ba}$	2.552 <sub>1</sub> min	661.660 <sub>3</sub>	90.1 <sub>1</sub>	661.660
$^{197}\text{Au} (n, n') ^{197\text{m}}\text{Au}$	7.8 <sub>1</sub> s	279.11 <sub>6</sub>	73 <sub>11</sub>	409.15
$^{115}\text{In} (n, n') ^{115\text{m}}\text{In}^{\text{b)}$	4.486 <sub>4</sub> h	336.258 <sub>18</sub>	45.8 <sub>22</sub>	336.258

a) Taken from ref. 4.

b) Standard reaction used for neutron fluence rate monitor.

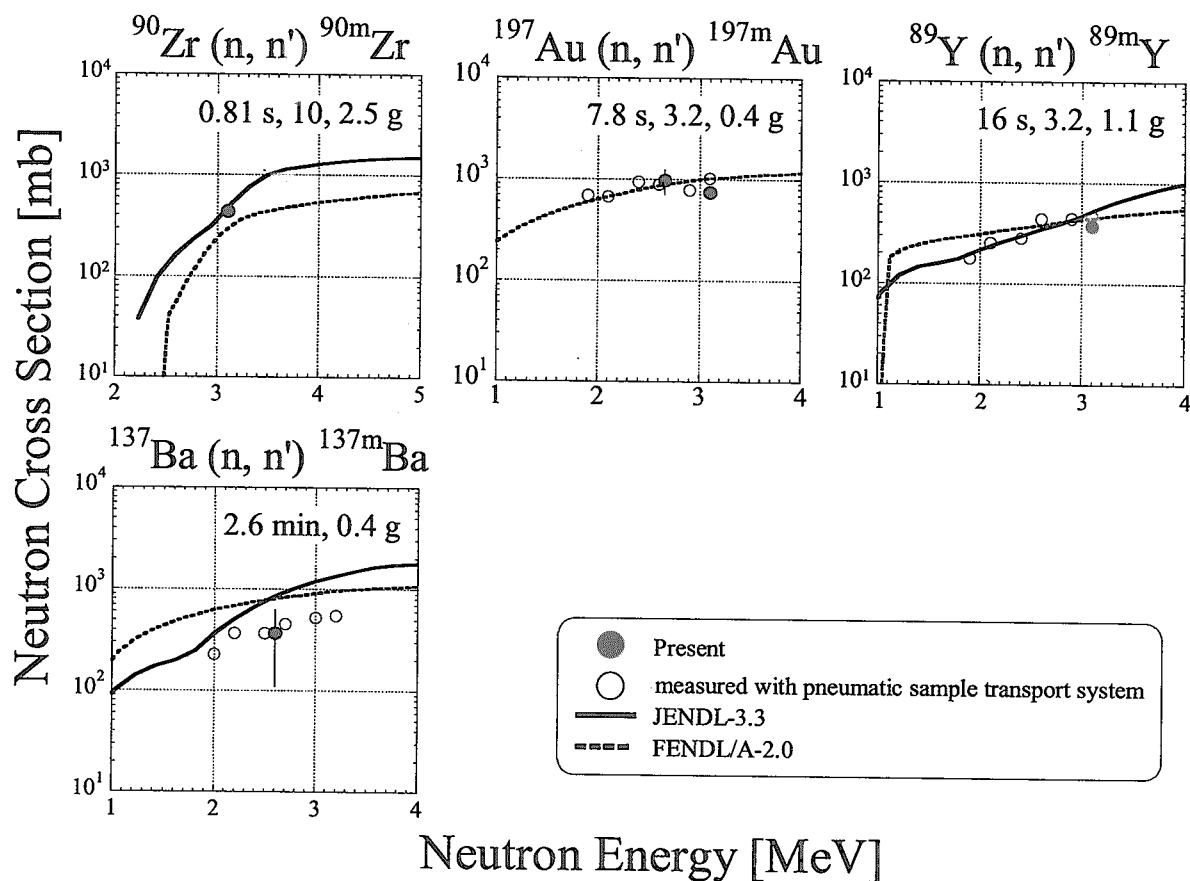


Fig. 4. The experimental cross section data for (n, n') reaction compared with the previous experimental data and the evaluated data in JENDL-3.3 and FENDL/A-2.0.



### 3.4 Measurement of (n,2n) reaction cross section using a 14MeV pencil beam source

Motoyuki Mitsuda<sup>1)</sup>, Ryohei Tanaka<sup>1)</sup>, Yasushi Yamamoto<sup>1)</sup>, Norimasa Mori<sup>1)</sup>,  
Isao Murata<sup>1)</sup>, Akito Takahashi<sup>1)</sup>, Kentaro Ochiai<sup>2)</sup>, Takeo Nishitani<sup>2)</sup>

<sup>1)</sup> *Department of Nuclear Engineering, Osaka University*

*Yamada-oka 2-1, Suita, Osaka 565-0871, Japan*

e-mail : mitsuda@stu.ncul.eng.osaka-u.ac.jp

<sup>2)</sup> *Japan Atomic Energy Research Institute*

*Tokai-mura, Ibaraki 319-1195, Japan*

The method has been established to measure (n,2n) reaction cross section with the coincidence detection technique using a pencil beam DT neutron source at FNS, JAERI. Using a cylindrical manganese, the (n,2n) cross section was measured precisely with the foil activation method, was used to check the experimental method. It was confirmed from the experimental results that this method has been generally established. It is expected that complete (n,2n) reaction cross section measurements for elements producing stable-isotope by (n,2n) reaction are possible in combination with the coincidence detection and TOF methods.

#### 1. Introduction

The (n,2n) reaction is of primary interest in the application for fusion reactors, because it is a neutron multiplication reaction and has a large cross section value for light and heavy nuclides in the energy range of several MeV to 14MeV. Number of elements, which (n,2n) cross sections were measured for, is less than half of the total number of stable isotopes, because in the past (n,2n) reaction cross section measurements, the foil activation method was generally used. This means that the measurement became difficult unless appropriate radioisotopes were produced by the reaction. In other words, by using the foil activation method, the (n,2n) reaction cross section of a certain nuclide can be measured. This means that if a sample element has two isotopes, the total measurement for the element is impossible in principle by the foil activation method.

On the other hand, there exist some other methods to obtain (n,2n) reaction cross section values<sup>1)</sup>; that is nuclide-dependent special methods such as the detection of charged-particles emitted following the (n,2n) reaction. For example, light elements such as beryllium, neutron multiplication measurements were done using a very large tank type scintillator to catch two neutrons by the (n,2n) reaction. The accuracy of those methods is however not so high compared with the activation method. Consequently, it seems that there is no method to accurately measure (n,2n) reaction cross sections available to every natural element. In

addition, especially for light elements such as beryllium, a little complicated neutron correlation between angular and energy distributions are expected. An appropriate method to measure such differential spectrum data was not reported so far. Such double differential cross sections of angle-energy correlation data are also very important for the fusion reactor design.

In the present study, using a beam-type DT neutron source at fusion neutronics source (FNS) of JAERI, the method was established to accurately measure  $(n,2n)$  reaction cross sections and its energy and angular distributions of simultaneously emitted two neutrons with the coincidence detection technique for all the existing elements, especially applying to elements having no experimental data.

## 2. Experimental

As well known, measurement of  $(n,2n)$  reaction cross section is possible in principle with the coincidence detection technique for two neutrons emitted simultaneously. However one must shield detectors to prevent direct neutrons from the source entering the detectors, the pencil beam DT neutrons was developed by making a narrow hole through a very thick shield between the target room and the measurement room as shown in Fig.1. The average neutron intensity is  $1 \times 10^6$  neutrons/sec/cm<sup>2</sup> at the exit of the collimator. The neutron flux rapidly decreases outside the 2cm  $\phi$  beam region, therefore neutron detectors can be arranged near the sample without any material assemblies radiation shield. On the beam line at 60cm from the collimator, a small sample was positioned, that means the sample was placed at 350cm from the neutron source. At this sample position, neutron flux is about  $0.9 \times 10^6$  neutrons/sec/cm<sup>2</sup>. The dimension of the sample are 1.5cm  $\phi \times 3$ cm long. Two spherical NE213 (40mm  $\phi$ ) detectors were arranged, the distance between sample and detector was equally 10cm for two neutron detectors. ( Fig.2 )

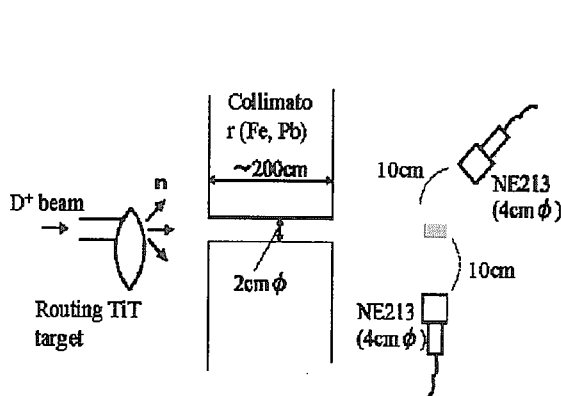


Fig.1 Experimental arrangement

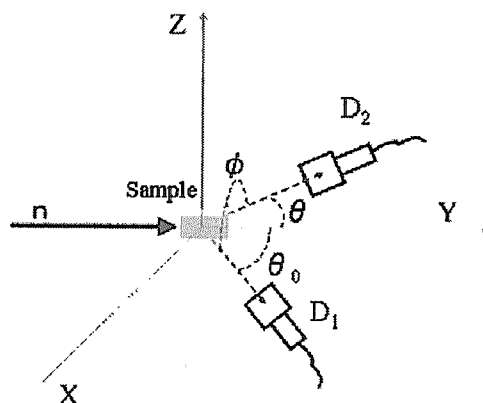


Fig.2 Arrangement of detectors and sample

The measurement was carried out with the coincidence detection technique and  $n/\gamma$  pulse shape discrimination technique to measure only two neutrons from  $(n,2n)$  reaction. The

former is a technique to selectively measure two particles emitted simultaneously such as two neutrons from  $(n,2n)$  reaction by coincidence detection. The  $(n,3n)$  reaction is also detected by this method, but it can be neglected because the threshold energy is mostly larger than 14MeV as shown in Fig.3. The latter technique was employed to exclude coincident signals of  $n\gamma$  and  $\gamma\gamma$  pairs through nuclear reactions such as  $(n,n'\gamma)$ ,  $(n,2n\gamma)$  etc by discriminating  $\gamma$ -ray signals with

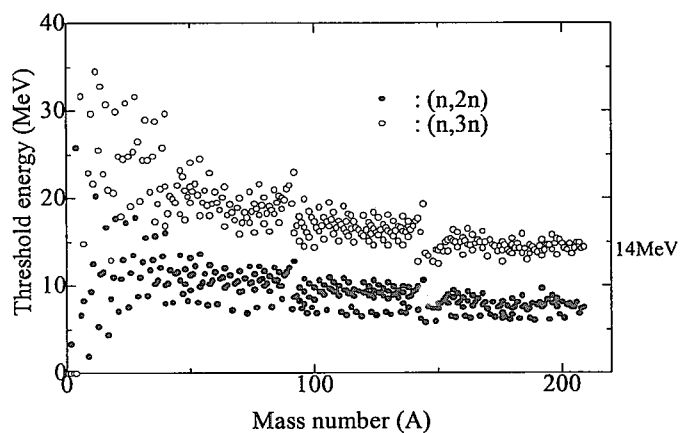


Fig.3 Threshold energy of  $(n,2n)$  and  $(n,3n)$  reaction

the rise-time spectrum of dynode signals. Two delay amplifiers with different gain were used to extend the dynamic range of the detector and to cover the range from 100keV to 10MeV. The electronic circuit used in the present experiment is shown in Fig.4.

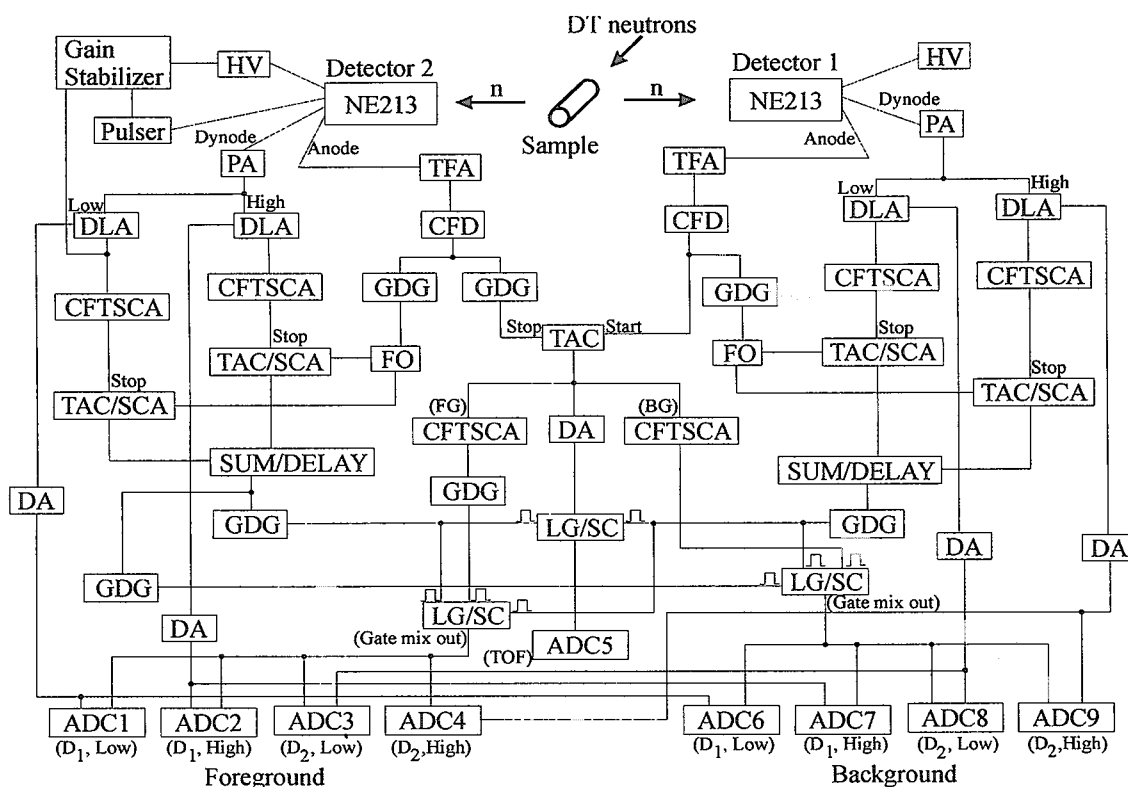


Fig.4 Electronic circuit of the  $(n,2n)$  reaction cross section measurement

Foreground (FG) and background (BG) indicated in the figure correspond to coincident and time-independent signals, respectively, as shown in Fig.5, which shows the time difference distribution between anode signals of the two NE213 detectors. A large peak

corresponding to the FG signals is found as coincident events of two of (n,2n) neutrons detected. Since the correlated neutrons are emitted simultaneously and so that their signals are of course detected almost simultaneously, a 250ns delay is added to one anode signal. The BG counts are successfully suppressed and a good S/N ratio was achieved. In the coincidence measurement, the time spectrum of anode signals of both detectors was measured with time-to-amplitude-converter

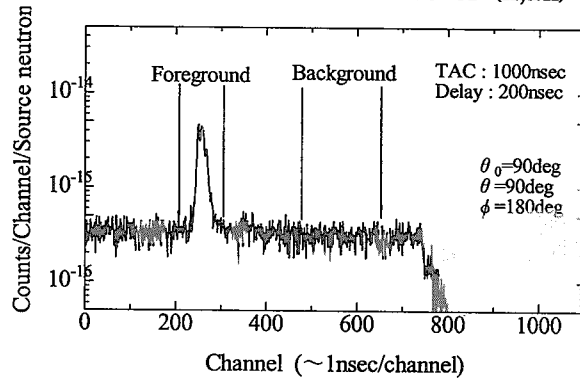


Fig.5 Time difference spectrum between anode signals of the two detectors

(TAC). And the correlated spectrum region was gated to detect only coincident signals. The dynode signals were fed to the pulse shape discrimination circuit including delay line amplifier, timing single channel analyzer and TAC, to exclude gamma-ray signals.

### 3. Data processing

The net raw neutron spectrum is deduced by the following equation:

$$y = y_{FG} - \alpha y_{BG}$$

where,  $y_{FG}$  and  $y_{BG}$  represent net raw foreground and background respectively,  $\alpha$  is the ratio of the gate widths between FG and BG in the time difference spectrum of the two anode signals. The cross section can be obtained by the next equations:

$$N\sigma\phi\eta(d\Omega_1/4\pi)(d\Omega_2/4\pi)f_1f_2R_1 = y_1$$

$$N\sigma\phi\eta(d\Omega_2/4\pi)(d\Omega_1/4\pi)f_2f_1R_2 = y_2$$

where,  $N$  is the number of manganese atoms,  $\sigma$  is the (n,2n) reaction cross section,  $\phi$  is the neutron flux at the sample,  $\eta$  is the neutron multiplicity of (n,2n) reaction, that is  $\eta=2$ ,  $d\Omega_1$ ,  $d\Omega_2$  are solid angles of the detector1 and detector2,  $f_1$ ,  $f_2$  are the efficiencies of the detector1 and detector2,  $R_1$ ,  $R_2$  are the response functions of the detector1 and detector2,  $y_1$ ,  $y_2$  are the pulse height spectrum of the detectors, respectively.

The terms,  $y_1R_1^{-1}$  and  $y_2R_2^{-1}$  were calculated by the FORIST<sup>2)</sup> unfolding code, and the detector efficiency and response functions were evaluated by the SCINFUL<sup>3)</sup> code.

### 4. Results and discussion

Fig.6 and Fig.7 show raw neutron pulse height spectra in low gain and high gain respectively. It is confirmed that the FG spectrum was sufficiently larger than that of BG by over one order of magnitude considering that the ratio was 1.8 times of the gate width difference between FG and BG.

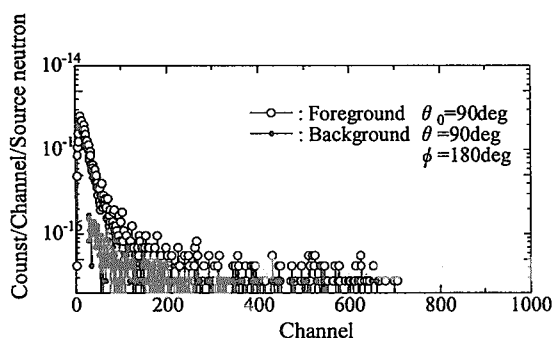


Fig.6 Raw neutron pulse height spectrum of low gain

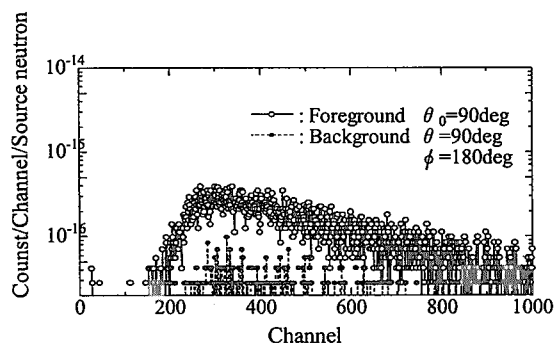


Fig.7 Raw neutron pulse height spectrum of high gain

Fig.8 shows neutron energy spectrum obtained by unfolding the pulse height spectrum with FORIST. In the figure, the error bars are not specified because the error bars are such large that the spectrum become not legible if specified. The one- $\sigma$  values are found several tens percentages. However a fairly good agreement between experiment and JENDL fusion file is seen except for low energy region. The detector response matrix causes large discrepancies in the low energy region. Extrapolating the spectrum derived the cross section.

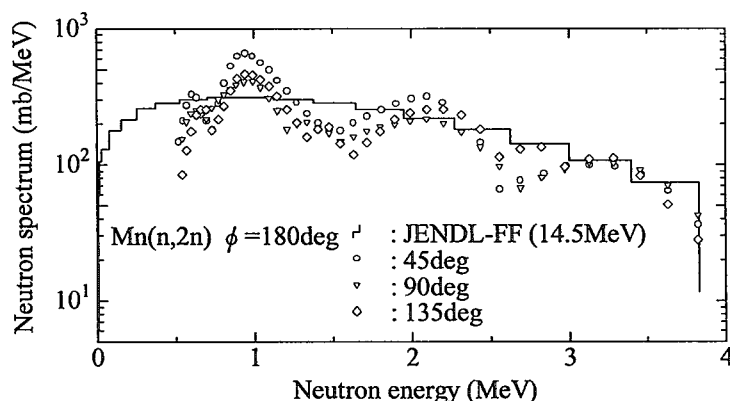


Fig.8 The energy spectrum of Mn(n,2n) reaction cross section

Fig.9 shows angular distribution for axial direction compared with the nuclear data of JENDL Fusion File. It seems that one can see a slightly forward oriented distribution. However, the accuracy is not so good as to conclude it. Nevertheless, the integral value, that is (n,2n) reaction cross section was obtained as  $0.6 \pm 0.1$  barn.

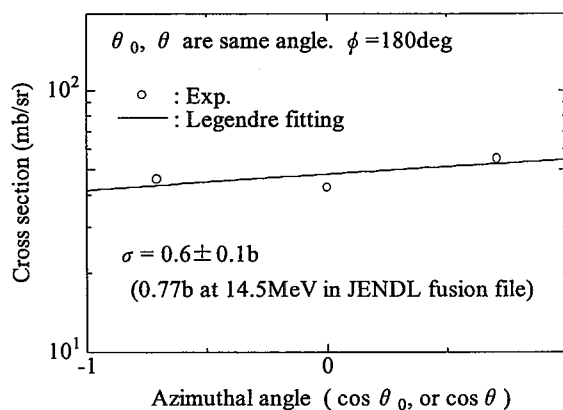


Fig.9 The angular distribution of Mn(n,2n) reaction cross section

## 5. Conclusion

Using a developed pencil beam DT neutron source at FNS of JAERI, the method has been established to measure (n,2n) reaction cross section and its energy and angular distributions of simultaneously emitted two neutrons with the coincidence detection technique. In the present measurement, the (n,2n) reaction cross section of manganese which is well known as measured repeatedly with the foil activation method was measured to check the experimental method. From the results, it was confirmed that the present method was basically successful to measure energy spectrum of two neutrons emitted through (n,2n) reaction, however one problem was found that the statistical accuracy was not sufficient to cover the whole angular correlation.

## Reference

- 1) for example, see compiled data in EXFOR
- 2) R.H. Johnson et al., ORNL/RISC-40 (1976)
- 3) J.K.Dickens, ORNL-6462 (1988)



### 3.5 Neutron Production by 0.8 and 1.5 GeV Protons on Fe and Pb Targets at the Most-Forward Region

Daiki SATOH<sup>1</sup>\*, Nobuhiro SHIGYO<sup>1</sup>, Kenji ISHIBASHI<sup>1</sup>, Yasushi TAKAYAMA<sup>1</sup>,  
Shunsuke ISHIMOTO<sup>1</sup>, Yosuke IWAMOTO<sup>1</sup>, Hideki TENZOU<sup>1</sup>, Tatsushi NAKAMOTO<sup>2</sup>,  
Masaharu NUMAJIRI<sup>3</sup> and Shin-ichiro MEIGO<sup>2</sup>

<sup>1</sup>Department of Applied Quantum Physics and Nuclear Engineering, Kyushu University,  
6-10-1 Hakozaki, Higashi-ku, Fukuoka 812-8581, Japan  
email: sato@meteor.nucl.kyushu-u.ac.jp

<sup>2</sup>High Energy Accelerator Research Organization, 1-1 Oho, Tsukuba 305-0801, Japan

<sup>3</sup>Japan Atomic Energy Research Institute, Tokai-mura, Ibaraki 319-1195, Japan

Neutron-production double-differential cross-sections for 0.8 and 1.5 GeV protons incident on Fe and Pb targets were measured at the most-forward region. Neutrons were measured by the time-of-flight (TOF) method. An NE213 liquid organic scintillator was set at 0-degree as neutron detector. Neutron detection efficiencies are calculated by a Monte Carlo simulation code SCINFUL-QMD. Experimental data were compared with other experimental data and the results of calculation codes based on Intranuclear-Cascade-Evaporation (INC/E) and Quantum Molecular Dynamics (QMD) models. Disagreement with the codes is discussed.

#### 1. Introduction

Studies on spallation reaction have recently been made for various applications, such as spallation neutron source and Accelerator-Driven-System (ADS) for transmutation of nuclear waste or energy-production. For example, projects for intense neutron sources based on the proton-incident spallation reaction have been proposed in Japan (Japan Proton Accelerator Research Complex; J-PARC[1]), USA (National Spallation Neutron Source; SNS[2]) and Europe (European Spallation Source; ESS[3]).

For the design of these facilities, evaluated nuclear data in the energy region up to a few GeV are required. Compilation of the high energy nuclear data files is carrying out in the world, for instance, JENDL High Energy File[4] (JENDL-HE, Japan), LANL High Energy File[5] (LA-150, USA), Medium Energy Nuclear Data Library[6] (MENDL-2, Russia). Nuclear data evaluation is generally performed on the basis of experimental data and theoretical model calculations. However, the experimental data are sparse and unsatisfied. Theoretical model calculations play, therefore, an important role. Intranuclear-Cascade-Evaporation (INC/E) model[7] and Quantum Molecular Dynamics (QMD) model[8] have often been utilized in the energy region above a few hundred MeV. Although improvement of the calculation codes have been performed, some discrepancies still remain between experimental data and model predictions. In general, calculation codes tend to fail to reproduce the neutron-production double-differential cross-sections in the most-forward region. Theoretical models employed in these codes cannot treat correctly a collective-effect such as the analog of a giant resonance accompanied with the isospin flip. Experimental data are required to improve the model precision in this region.

Measurement of neutron-production double-differential cross-sections in the most-forward direction has been carried out by the time-of-flight (TOF) method at the  $\pi 2$  beam line of 12-GeV proton synchrotron (12-



GeV PS) in the High Energy Accelerator Research Organization (KEK). At KEK, we have already measured neutron-production double-differential cross-sections by the TOF method, except for 0-degree measurement. The detail of those experiments was written in our previous reports[9,10].

The recoil proton method combined with a magnetic spectrometer has been often utilized for 0° neutron spectrum measurement[11,12], because TOF technique has a poor energy resolution for high energy neutrons. The TOF method, however, owns a higher detection efficiency and simpler data analysis than the recoil proton method. Since the beam intensity at the  $\pi^2$  beam line is very weak, we adopted TOF technique as the neutron detection method. For obtaining the better experimental data, the improvement of energy resolution in the measurement is essential. A high-resolution TOF method was devised to meet this demand: three rapid-rise-time photomultipliers were connected with a neutron detector.

In this work, we report the results of 0-degree measurement by the high-resolution TOF method. Cross sections were obtained on targets of Fe and Pb at incident proton energies of 0.8 and 1.5 GeV. We aimed at measuring the emitted neutrons above a few hundred MeV because of the experimental constraint. Comparisons are made between the experimental data and the results of calculation codes, NMTC/JAM[13] based on INC/E model and IQMD[14] on QMD model.

## 2. Experimental method

The experiment was carried out at the  $\pi^2$  beam line of 12-GeV PS at KEK. Schematic view of the experimental arrangement is shown in Fig. 1. NE102A plastic scintillators were set in front of the target to define the incident proton beam area. The coincidence of signals from these scintillators was counted to determine the number of incident particles. The incident beam was deflected at the downstream of the target with electric bending magnet in order to prevent it from being incident on the 0° detector. Since the vertical gap between the magnetic poles was narrow (30 cm), secondary scattering of emitted particles takes place on the magnet pole piece. It was difficult to set the shielding between the electric bending magnet and the neutron detector, without giving influence to neutrons of interest. Therefore, the measurement was made without the shielding.

The Fe and Pb targets were bombarded by the proton beam. Targets were cylindrical disk with a diameter of 50 mm. The thickness of Fe and Pb targets was 30 and 20 mm, respectively. NE213 liquid organic scintillator was employed as neutron detector. The shape was cylinder 12.7 cm in diameter and 12.7 cm thick. The neutron detector was placed at 0°. For improvement of the energy resolution, photomultipliers of fast rise time (Hamamatsu H2431, rise time 0.7 ns) were adopted. Three H2431s 5.1 cm in diameter were connected with the NE213 scintillator. The neutron arrival time was obtained by time-average of three photomultipliers to give the best time resolution. Flight path length was 3.5 and 5.0 m for 0.8 and 1.5 GeV proton incidence, respectively. In front of the neutron detector, NE102A scintillator was mounted as a veto detector to reject the charged particle events. Background measurements were performed without target to subtract the neutrons produced from the beam scintillators.

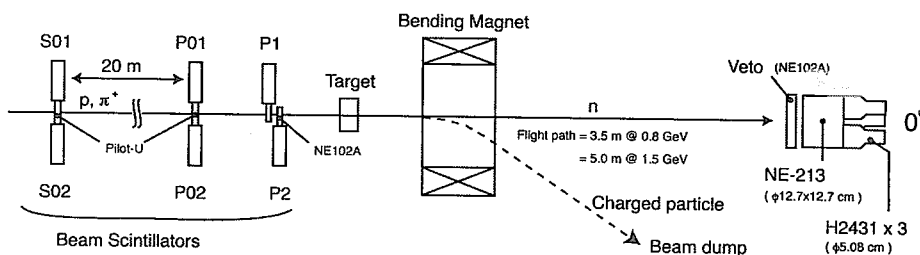


Fig. 1 Illustration of experimental arrangement.

### 3. Data analysis

Neutron spectra were obtained by subtracting the results of the target-out measurement from those of the target-in, after normalization with the number of incident protons. An example of the TOF spectra of the target-in and -out measurements by 0.8 GeV protons on Fe target is shown in Fig. 2, where the spectrum includes events of both neutrons and gamma-rays. The horizontal axis of the TOF spectrum was reversed, because the start signal for the TOF measurement was made at neutron detector. A sharp peak due to prompt gamma-rays was utilized as the time standard for converting TOF to emitted neutron energy. Prompt gamma peak is also presented in the results of target-out. The latter prompt gamma-rays came from the beam scintillators located at the upstream of the target, and were generated slightly prior to those from the target.

In usual TOF experiments using high-intensity pulsed beam, the time resolution is determined by the pulse width of the beam. However, the beam intensity at  $\pi 2$  beam line was very weak in a level of about  $10^5$  particles/2.5 s, and incident protons were individually counted in this measurement. Hence, the uncertainty of TOF came from the resolution of the detectors. The energy resolution for this experiment is shown in Fig. 3. In this figure, solid and dashed curves stand for the energy resolution of the NE213 scintillator with three H2431s and that with a Hamamatsu R1250 (rise time 2.5 ns) whose diameter is 12.7 cm, respectively. The energy resolution was obtained from the FWHM of the prompt gamma peak. The energy resolution of the NE213 scintillator with three H2431s is 100 MeV at 0.8 GeV and 55 % better than that with R1250. This resolution is better than other experiments[10] performed by NE213 scintillator with R1250, but about twice the value for the recoil proton spectrometer[15].

For high energy neutron incidence into NE213 scintillator, neutron events tend to overlap gamma ones, and then the pulse-shape discrimination (PSD) characteristics are deteriorated[16]. For this reason, the PSD technique was unusable for neutrons of interest in this measurement. Fortunately, most of gamma-rays have energies below several MeV. Then, we employed the higher-level bias setting, which is twice of the gamma-ray energy from Am-Be source (4.33 MeVee) to reduce the affect of the gamma-rays. Neutron detection efficiencies were calculated by the Monte Carlo code SCINFUL-QMD[17,18].

### 4. Results and discussion

Neutron-production double-differential cross-sections by 0.8 and 1.5 GeV protons on Fe and Pb targets are presented in Figs. 4 to 7. The bias level was set at twice the Am-Be threshold, 8.66 MeVee, because the main purpose of the experiment was the measurement of the neutrons above 100 MeV. Error-bars includes both

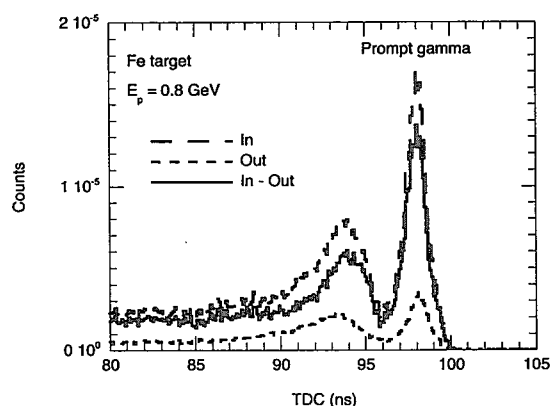


Fig. 2 Time-of-flight (TOF) spectrum for neutrons and gamma-rays obtained by 0.8 GeV protons on iron target. Dashed and dotted lines indicate the results with target and without target, respectively. Solid line shows the difference between target-in and target-out events.

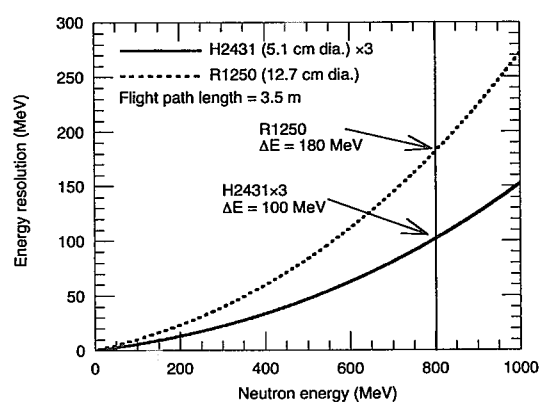


Fig. 3 Energy resolution by two type of photomultipliers. Signals of three photomultipliers of H2431 were time-averaged for evaluating neutron arrival time.

statistical uncertainties and contiguity of neutron detection efficiency of 15 %. Experimental data are compared with other experimental data[11,12] measured by recoil proton spectrometers and the results of model calculation codes. The results of other experiments and calculation codes were broadened by Gaussian to fit to our energy resolution. The solid and dashed lines in Figs. 4(a) to 7(a) indicate the original values and the modified results, respectively. Our data were compared with the modified results in Figs. 4(b) to 7(b). Solid lines show the calculation results of the NMTC/JAM[13]. NMTC of this version adopts the inmedium nucleon-nucleon elastic scattering cross-sections of Cugnon[19,20]. Dashed lines indicate the calculation results of JQMD[14], which incorporates QMD with Statistical Decay Model (SDM) model. The experimental data obtained by Leray et al.[12] are exhibited in Figs. 4(b) and 5(b) with chain lines. The data by Bonner et al.[11] are also shown in Fig. 5(b) with dotted line. The cross-sections consist of two main components. The peak close to the energy of incident protons corresponds to quasi-elastic (charge exchange; CEX) nucleon-nucleon collisions. The lower broad peak positioning around 3/4 of incident energy is ascribed to pion-associated neutrons via the  $\Delta$ -resonance excitation in inelastic nucleon-nucleon collisions.

In Figs. 4(b) and 5(b) for the 0.8 GeV proton incidence, the experimental data exhibit both the CEX and pion-associated peak. For the Fe target, our data show good agreement with the experimental results of Leray et al. in the pion-associated region, although slightly smaller in the CEX region. For the Pb target, in the CEX region, the experimental data agree with the predictions of NMTC/JAM well. On the contrary, the absolute values of other experiments are 45 % larger than the results of our experiment. Below 250 MeV, the experimental data tend to include the neutrons scattered from the bending magnet pole piece. The effect is clear for Fe which has relatively low cross section in this energy region. In Figs. 6(b) and 7(b) for the 1.5 GeV proton incidence, the experimental data exhibit the pion-associated peak. However, the CEX peak does not appear due to the deterioration of the energy resolution. The absolute values at the pion-associated region are larger than JQMD and smaller than NMTC/JAM. Below 500 MeV, the experimental data tend to give larger values than code predictions. There is a possibility that the experimental data indicated with open circles contain the affection caused by the scattering at the bending magnet. For both 0.8 and 1.5 GeV proton incidence, the calculation results of NMTC/JAM show the remarkable overestimation at the pion-associated peak. This overestimation may be explained by an excessive forward angular distribution of  $\Delta$  particles adopted in the INC code. In contrast, the results of JQMD are in better agreement with experimental data at the pion-associated peak. However, JQMD does not exhibit the CEX peak.

## 5. Conclusion

The neutron-production double-differential cross sections were measured for 0.8 and 1.5 GeV protons incident on Fe and Pb targets. The high-resolution TOF method was adopted to determine the neutron energy. Three rapid-rise-time photomultipliers were connected with an NE213 scintillator to improve energy resolution in the measurement. For 0.8 GeV proton incidence, the CEX peak was identified by the high-resolution TOF method. Our experimental data agree with the results of NMTC/JAM in the CEX region. The discrepancy between the experimental data and those obtained by Leray et al. are less than 30 % in the pion-associated regions. For 1.5 GeV proton incidence, the results give middle values between NMTC/JAM and JQMD predictions in the pion-associated region. Present data exhibit the predictive capability of these models is not yet sufficient. NMTC/JAM show the abnormal pion-associated peak due to the inappropriate angular distribution of  $\Delta$  particle.

## Acknowledgement

The authors express their gratitude to Prof. Y. Yoshimura, Mr. M. Taino and the beam channel staff of KEK for their continuous encouragement and generous support of the experiment.

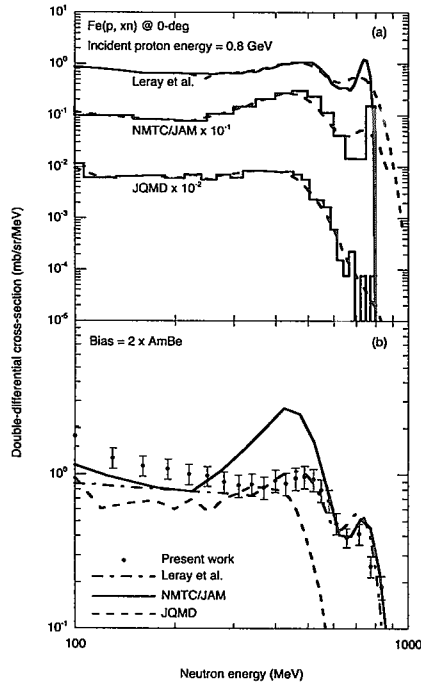


Fig. 4 Neutron-production double-differential cross-sections for 0.8 GeV protons on iron target. The upper figure of (a) shows original values and modified results adjusted to fit to the present experimental energy resolution. Comparison between our experimental data and modified results is shown in the lower figure of (b). Marks exhibit our experimental data. Solid and dashed lines present the results by NMTC/JAM and JQMD, respectively. Chain line indicates the experimental data by Leray et al.

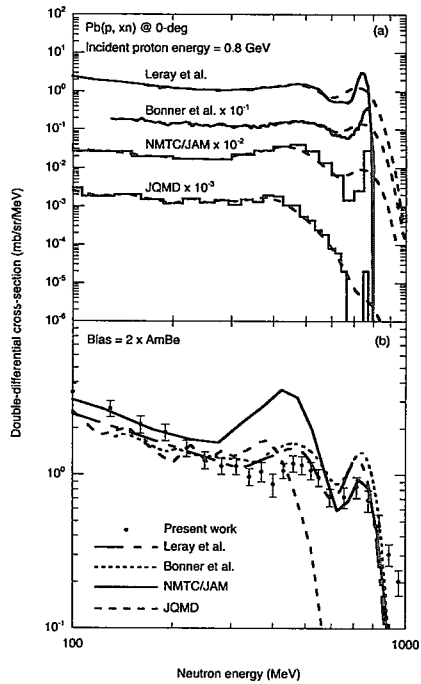


Fig. 5 Same as for Fig. 4, except for lead target. Dotted line indicates the experimental data by Bonner et al.

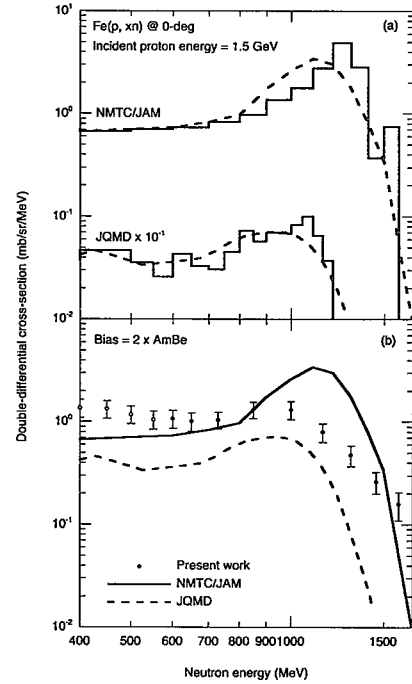


Fig. 6 Neutron-production double-differential cross-sections for 1.5 GeV protons on Fe target. Marks indicates experimental data. Solid and dashed lines present the results by NMTC/JAM and JQMD, respectively.

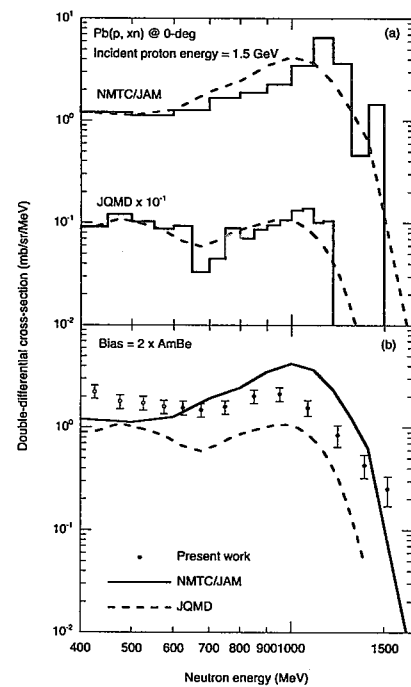


Fig. 7 Same as for Fig. 6, except for Pb target.

## References

- [1] The Joint Project Team of JAERI and KEK, *The Joint Project for High-Intensity Proton Accelerators*, JAERI-Tech 99-056, Japan Atomic Energy Research Institute (JAERI), (1999).
- [2] *Conceptual Design Report, National Spallation Neutron Source*, NSNS/CDR-2/V1 and NSNS/CDR-2/V2, vols. 1 and 2, Oak Ridge National Laboratory (ORNL), (1997).
- [3] G. Bauer, *The ESS Target Station Concept*, ESS-96-60T (1996).
- [4] T. Fukahori, Y. Watanabe, N. Yoshizawa, et al., "JENDL High Energy File," *J. Nucl. Sci. Technol.*, Supplement 2, 25 (2002).
- [5] M. B. Chadwick, P. G. Young, R. E. MacFarlane, et al., *LA150 Documentation of Cross Sections, Heating, and Damage*, Los Alamos National Laboratory Report LA-UR-99-1222, Los Alamos National Laboratory (LANL), (1999).
- [6] Yu. N. Shubin, V. P. Lunev, A. Yu. Konobeyev, et al., *Cross section data library MENDL-2 to study activation as transmutation of materials irradiated by nucleons of intermediate energies*, report INDC(CCP)-385, International Atomic Energy Agency, (1995).
- [7] H. W. Bertini, "Intranuclear-cascade calculation of the secondary nucleon spectra from nucleon-nucleus interactions in the energy range 340 to 2900 MeV and comparisons with experiment," *Phys. Rev.*, **188**, 1711 (1969).
- [8] J. Aichelin, "Quantum molecular dynamics - A dynamical microscopic  $n$ -body approach to investigate fragment formation and the nuclear equation of state in heavy ion collisions," *Phys. Rep.*, **202**, 233 (1991).
- [9] T. Nakamoto, K. Ishibashi, N. Matsufuji, et al., "Spallation neutron measurement by the time-of-flight method with a short flight path," *J. Nucl. Sci. Technol.*, **32**, 827 (1995).
- [10] K. Ishibashi, H. Takada, T. Nakamoto, et al., "Measurement of neutron-production double-differential cross sections for nuclear spallation reaction induced by 0.8, 1.5 and 3.0 GeV protons," *J. Nucl. Sci. Technol.*, **34**, 529 (1997).
- [11] B. E. Bonner, J. E. Simmons, C. R. Newsom, et al., "Systematics of  $0^\circ$  neutron production by 800 MeV protons on targets with  $27 < A < 238$ ," *Phys. Rev.*, **18** (1978).
- [12] S. Leray, F. Borne, S. Crespin, et al., "Spallation neutron production by 0.8, 1.2, and 1.6 GeV protons on various targets," *Phys. Rev.*, **C65** (2002).
- [13] K. Niita, S. Meigo, H. Takada, et al., *High Energy Particle Transport Code NMTC/JAM*, JAERI-Data/Code 2001-007, Japan Atomic Energy Research Institute (JAERI), (2001).
- [14] K. Niita, T. Maruyama, Y. Nara, et al., *Development of JQMD (Jaeri Quantum Molecular Dynamics) Code*, JAERI-Data/Code 99-042, Japan Atomic Energy Research Institute (JAERI), (1999).
- [15] E. Martinez, J. Thun, Y. Patin, et al., "Spallation neutron spectra measurements Part II: Proton recoil spectrometer," *Nucl. Instrum. Method*, **A385**, 345 (1997).
- [16] Y. Iwamoto, D. Satoh, H. Kitsuki, et al., "Deterioration of pulse-shape discrimination in liquid organic scintillator at high energies," *2000 IEEE Nuclear Science Symposium Conference Record*, 6-215, (2001).
- [17] D. Satoh, N. Shigyo, Y. Iwamoto, et al., "Study of neutron detection efficiencies for liquid organic scintillator up to 3 GeV," *IEEE Trans. Nucl. Sci.*, **48**, 1165 (2001).
- [18] D. Satoh, S. Kunieda, Y. Iwamoto, et al., "Development of SCINFUL-QMD code to calculate the neutron detection efficiencies for liquid organic scintillator up to 3 GeV," *J. Nucl. Sci. Technol.*, Supplement 2, 657 (2002).
- [19] J. Cugnon, "Monte carlo calculation of high-energy heavy-ion interactions," *Phys. Rev.*, **C22**, 1885 (1980).
- [20] J. Cugnon, T. Mizutani, J. Vandermeulen, "Equilibration in relativistic nuclear collisions. A monte carlo calculation," *Nucl. Phys.*, **A352**, 505 (1981).



## 3.6

The Measurement of Energy Spectra for  $^9\text{Be}(p,p'x)$  Reaction at 392 MeV

Tadahiro KIN<sup>1,\*</sup>, Fuminobu SAIHO<sup>1</sup>, Shinya HOHARA<sup>1</sup>, Katsuhiko IKEDA<sup>1</sup>,  
 Fumiaki KONDO<sup>1</sup>, Ikuo FUKUCHI<sup>1</sup>, Kiyohisa ICHIKAWA<sup>1</sup>,  
 Genichiro WAKABAYASHI<sup>1</sup>, Yusuke UOZUMI<sup>1</sup>, Nobuo IKEDA<sup>1</sup>,  
 Masaru MATOBA<sup>1</sup>, and Norihiko KOORI<sup>2</sup>

<sup>1</sup>Department of Applied Quantum Physics and Nuclear Engineering, Kyushu University, Fukuoka 812-8581, Japan

<sup>2</sup>Faculty of Integrated Arts and Sciences, University of Tokushima, Tokushima 770-8502, Japan

Multistep direct processes in proton production reaction was investigated with proton beam of 392 MeV bombarding  $^9\text{Be}$  target nuclei. Energy spectra were measured at ten laboratory angles from 20 to 105 degrees and compared with two theoretical models, the quantum molecular dynamics (QMD) and the intranuclear cascade (INC) model. Additionally, we modified the former model with improving the ground state in the code.

**KEYWORDS:** intermediate energy, proton, beryllium 9, double differential cross section, QMD, INC

## I. Introduction

Recently, nuclear data which have been measured by using intermediate energy accelerators have been needed in many fields; science, engineering, medicine and so on. For example, they are cancer therapy with proton beam, the study of transmutation of nuclear waste and estimating the expose dose of spacemen etc.

A number of data were measured and studied for  $(p,p'x)$  and  $(p,nx)$  reactions at incident energies from several tens of MeV to 200 MeV. At around GeV region, systematic studies of  $(p,nx)$  reactions were made at some laboratories. However, only few studies have so far been made at the region from 200 MeV to 400 MeV on  $(p,p'x)$  reaction.

We investigate double differential cross section energy spectra of  $(p,p'x)$  reactions at 392 MeV with target nuclei of  $^9\text{Be}$ . We compare the data with two classical theories: QMD model + statistics decay model (SDM)<sup>1)</sup> and INC model.<sup>2-4)</sup> And we try to modify the former model with improving the ground state in the code.

## II. Experiment

Measurements of proton production reactions were carried out at RCNP. Proton beams were accelerated by the ring-cyclotron. Proton beam of 392 MeV bombarded  $^9\text{Be}$  target located at the center of a one-meter-diameter chamber. Energy spectra of emitted protons were measured by using stacked scintillators detectors<sup>5,6)</sup> placed out the chamber. A sketch of detectors is given in Fig. 1. The arrangement of them is shown in Fig. 2. Each detector size is shown in Table. 1.

The detectors are most suitable for investigating gross structures of energy spectra. Measurements were made at ten laboratory angles from 20 deg. to 105 deg. Energy calibrations were made with pp scatterings with a target of polyester foil. The particle identification was successfully done by a  $\Delta E$ -E prescription in off-line analyses.

Table 1 The Size of Detectors of stacked scintillators detectors

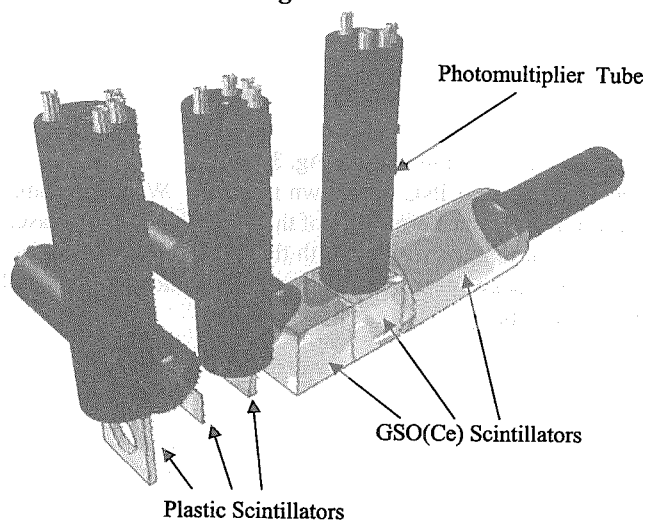
Detector	Size	Number
Plastic	$44 \times 44 \times 5 \text{ mm}^3$	2
Plastic	$20 \times 30 \times 0.5 \text{ mm}^3$	2
Plastic	$20 \times 30 \times 2 \text{ mm}^3$	2
GSO(Ce)	$43 \times 43 \times 43 \text{ mm}^3$	5
GSO(Ce)	$\phi 62 \times 120 \text{ mm}$	1

## III. Results and discussion

The measured energy spectra were compared with the QMD and the INC models. In this work, we employed the JQMD code for the QMD model calculation. The INC code used presently was developed in our laboratory.

\* Corresponding author, Tel. +81-92-642-3764, Fax. +81- 92-642-3800, E-mail: kinnya@nucl.kyushu-u.ac.jp

▪ For FORWARD Angle



▪ For BACKWARD Angle

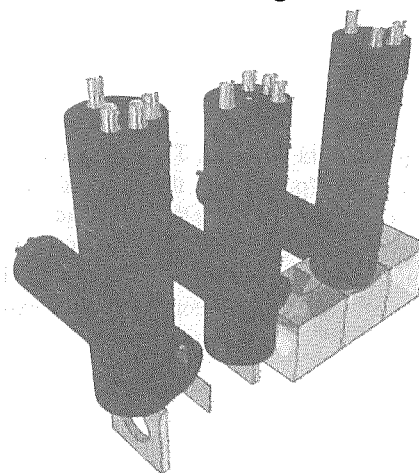


Fig. 1 A sketch of detectors

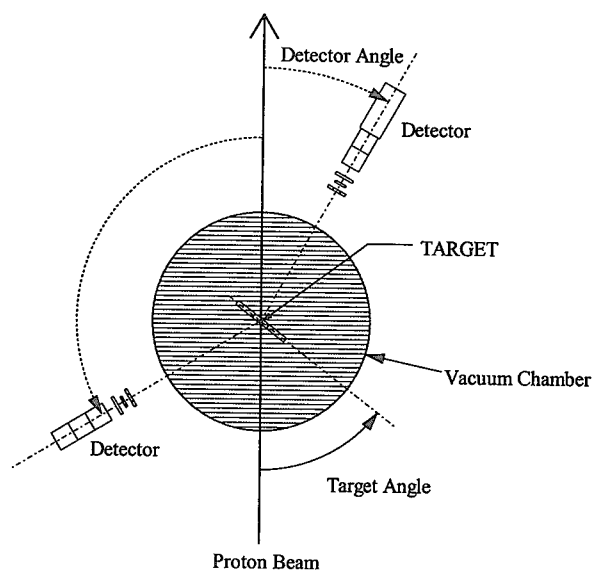


Fig. 2 Placement of the target, the chamber and detectors

At first, we compared the measured spectra with the QMD model but the shapes of them by the QMD do not have good reproducibility at each angles. At forward angles, the width of a quasi-free peak is narrower than that of experiment. At 50 and 45 degrees there are quasi-free peaks around 200 MeV and 150 MeV respectively but the measured spectra are smooth.

Then, we studied distributions of the momentum and the nucleon density of the target nuclear ground state generated by the QMD model. Fig. 3 shows distributions for  $^9\text{Be}$  ground state. With the standard JQMD which is shown by the dotted line, both of momentum and density distribute within narrower regions than that of local Fermi gas model.<sup>7)</sup>

To enlarge the distributions of QMD, we changed parameters of the density dependent potential for nucleon interactions. The code uses the local Skyrme type potential:

$$U_{Sky}(r) = A \frac{\rho(r)}{\rho_0} + \frac{B}{1+\tau} \left( \frac{\rho(r)}{\rho_0} \right)^\tau$$

We adjusted the parameters  $A$  and  $B$ . The resultant distributions are shown by solid lines in Fig. 3.

Energy spectra of  ${}^9\text{Be}(p,p'x)$  with the standard and modified QMD and the INC are shown in Fig. 4. With the modified QMD, the shapes of spectra are better than standard one in all angles. But the absolute values of them are bigger than measured one. Especially the spectra of 50 and 60 degrees show good experiment reproducibility. With the INC, at forward angles in lower energy range the cross sections are close to experiment value. At backward angles they resemble to modified the QMD. In particular the spectrum of 25 degrees shows good experiment reproducibility.

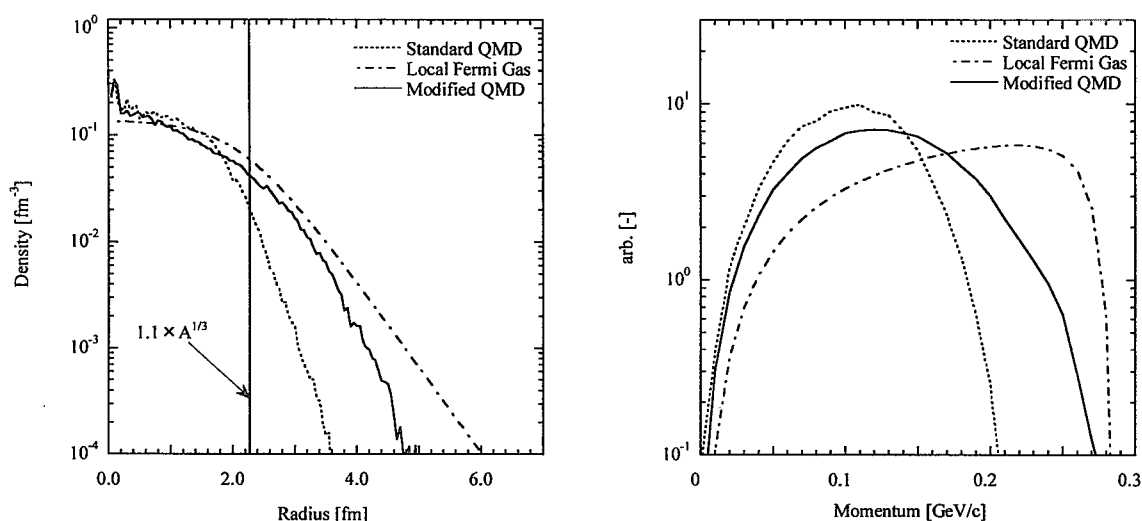


Fig. 3 Distributions of nucleon density(top) and momentum(bottom) for the  ${}^9\text{Be}$  ground state

#### IV. Conclusion

We investigated energy spectra of  $(p,p'x)$  reactions at 392 MeV with  ${}^9\text{Be}$  target. Experiment was carried out at the RCNP ring-cyclotron facility. The measured spectra were compared with the QMD and the INC models. In addition we modified the ground state in the QMD. It is found that the theoretical spectra are sensitive to ground state parameters of the target nucleus. And with the INC code that we developed the experiment reproducibility is better than the standard QMD.



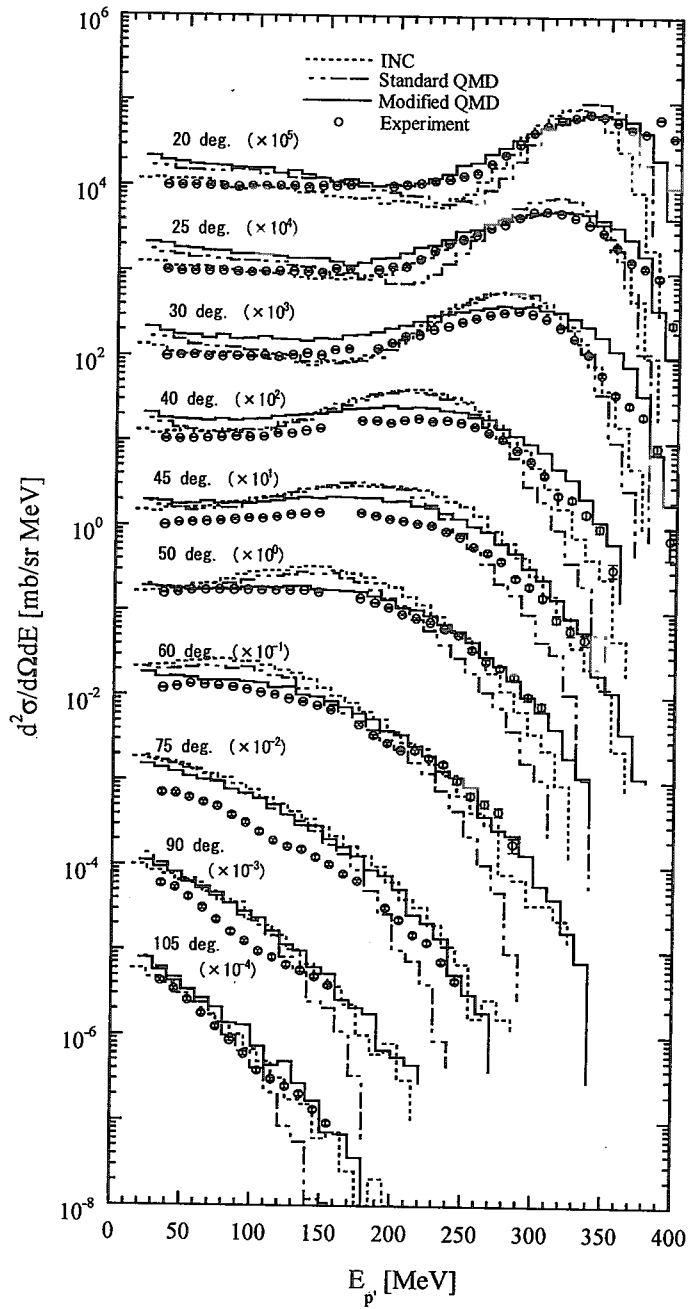


Fig. 4 Double Differential Cross Section of  ${}^9\text{Be}(p,p'x)$

#### References

- 1) K. Niita, S. Chiba, T. Maruyama, H. Takada, T. Fukahori, Y. Nakahara, and A. Iwamoto *Phys. Rev. C* **52**, 2620 (1995).
- 2) H. W. Bertini *et al.*, *Phys. Rev.* **131**, 1801 (1963).
- 3) Y. Yariv and Z. Fraenkel, *Phys. Rev. C* **20**, 2227 (1979).
- 4) J. Cugnon, *ibid.* **22**, 1885 (1980).
- 5) K. Anami, *et al.*, *J. Nucl. Instrum. Methods Phys. Res. A* **404**, 327 (1998).
- 6) H. Yosida, *et al.*, *J. Nucl. Instrum. Methods Phys. Res. A* **411**, 46 (1998).
- 7) J. W. Negele, *et al.*, *Phys. Rev. C* **1**, 1260 (1970).



### 3.7 Measurements of Differential Thick Target yield for C, Al, Ta, W, Pb(p,xn) reactions at 50 and 70 MeV

Naoki KAWATA, Mamoru BABA, Takao AOKI, Masayuki HAGIWARA,  
Toshiro ITOGA, Naoya HIRABAYASHI, Shunsuke YONAI, Takashi NAKAMURA  
Cyclotron and Radioisotope Center (CYRIC), Tohoku University  
Aoba01, Aramaki, Aoba-ku, Sendai-shi, Miyagi-ken, Japan  
email: nkawata@cyric.tohoku.ac.jp

2002/1/3

Differential thick target neutron yields (TTY) for C, Al, Ta, W, Pb(p,xn) reaction were measured at 50 and 70 MeV at several laboratory angles between 0- and 110-deg. with the time-of-flight method. We determined neutron energy spectra from ~0.6 MeV to highest secondary neutron energy.

## 1 Introduction

By the development of accelerator technology, the performance and the reliability of accelerators were greatly improved in recent years. High intensity and high energy accelerators are now available. Use of the accelerators are expended to material studies, medical treatment, radiobiology studies and environment science as well as nuclear physics. Now some accelerators with high energy and intensity are under construction or in e.g., Japan Proton Accelerator Research Complex (JAERI, KEK), SNS (Spallation Neutron Source, United States), and ESS (European Spallation Source).

However, nuclear data required for radiation shielding and safety design are not good enough in quality to the high energy accelerators. In particular, experimental data covering wide range of secondary neutron energies are very few. (Meigo's experimental data for C(p, xn) at 68 MeV[10], LANL experimental data for Al, Fe, Pb(p,xn) at 113 MeV[1]) Therefore, the data for secondary neutrons spectra from the accelerator components are required.

We have started experiments on the neutron emission spectrum of the  $^{nat}\text{C}(\text{p},\text{xn})$ ,  $^{nat}\text{Al}(\text{p},\text{xn})$ ,  $^{nat}\text{Ta}(\text{p},\text{xn})$ ,  $^{nat}\text{W}(\text{p},\text{xn})$ , and  $^{nat}\text{Pb}(\text{p},\text{xn})$  reactions for tens of MeV region using the AVF cyclotron (K=110) at CYRIC[2], Tohoku University. This paper reports neutron emission spectra at 50 and 70 MeV for several laboratory angles between 0- and 110-deg.

## 2 Experiment

The experimental setup is shown in figure 1. A proton beam accelerated by the AVF cyclotron was transported to the target room NO.5 of CYRIC equipped with a beam-swinger system and a neutron TOF channel[3]. The beam swinger system changes the incident angle of the beam onto the target from 0-deg to 110-deg and enables to measure angular distributions with fixed detector setup.

The targets (C, Al, Ta, W, Pb) were plate of natural elements. Their sizes were shown in figure 2.

The target chamber was shielded with a 2.5 m thick concrete wall having a beam channel for collimeters. Emitted neutrons were detected by a NE213 scintillation detector, 14cm-diam  $\times$  10 cm-thick or 2 inch-diam  $\times$  2 inch-thick equipped with pulse-shape-discriminator (PSD). The larger and smaller detectors were placed around ~ 11 m and ~ 3.5 m from the target (figure ??), respectively. The shorter flight path was adopted to measure the low energy part (~ 0.6-5 MeV) of the neutron spectrum by low pulse-height bias (~ 0.6 MeV). The TOF, PSD and pulse-height data were collected event by event as three parameter list data for off-line analysis.[4]

Table 1: Present measurement and target size

Proton energy [MeV]	Target	use	angle [deg.]	proton range [mm]	target thickness [mm]
50	C	beam dump, degrader	0, 15, 30, 45, 60, 90	11	15
	Al	beam line		11	10
	Ta	neutron source		3	3
	W	neutron source		2	3
70	C	beam dump, degrader	0, 30, 60, 90, 110	29	31
	Al	beam line		20	20
	W	neutron source		4	5
	Pb	neutron source		8	8

### 3 Experimental procedure

The pulse width of proton beam was generally less than 1 ns in FWHM, and the beam current on the target was around 5 ~ 10 nA. The beam current was digitized and recorded by a scaler for normalization of the neutron TOF spectrum. The TOF data for 50 MeV were obtained at six laboratory angles (0, 15, 30, 45, 60, 90), for 70 MeV at six laboratory angles (0, 30, 60, 90, 110).

### 4 Data analysis

Neutron TOF spectra gated by the PSD signal and the lower pulse-height bias were converted into energy spectra. The efficiency vs energy curves of the detectors were obtained by calculation with a revised version of the Monte Carlo code SCINFUL [5] that was verified to be accurate with in  $\pm 5\%$  up to 80 MeV [6]. The spectra were normalized by the integrated beam current and corrected for the effect of the attenuation in the target and air using the data of LA150[6][7][8].

### 5 Results and discussion

In the following, experimental data are compared with the TTY data derived from LA150 except for  $^{nat}\text{Ta}(p, xn)$ . The TTY from LA150 was obtained by using the following equation. [9]

$$\frac{d^2Y(E_0)}{dEd\Omega} = N \int_0^T \frac{d^2\sigma(E_0 - \int_0^t (\frac{dE}{dt}) dt)}{dEd\Omega} \times e^{-N\sigma_{\text{nonel}}(E_0 - \int_0^t (\frac{dE}{dt}) dt)Y} dt \quad (n \cdot \text{MeV}^{-1} \cdot \text{sr}^{-1} \cdot \text{projectile}^{-1}) \quad (1)$$

where,  $E_0$ : incident particle energy [MeV],  $N$ : density of target nuclide [ $1/\text{cm}^3$ ],  $T$ : thickness of the target [cm],  $\sigma_{\text{nonel}}$ : nonelastic cross section [ $\text{cm}^2$ ],  $dE/dt$ : stopping power of incident particles [MeV/cm]

C data at 70 MeV, experimental data were compared also with Meigo's data at 68 MeV. [10]

#### 5.1 $^{nat}\text{C}(p, xn)$

Figure 2 and figure 4 show neutron spectra from  $^{nat}\text{C}(p, xn)$  at 50 and 70 MeV respectively. Because the  $Q$  value for main component  $^{12}\text{C}(p, n)$  is -18.1 MeV, the energy of emitted neutron is not so high. The high energy neutron component caused from  $^{13}\text{C}$  which is included about 1.1 % naturally. Since C is light nuclide, its spectra have no evaporation peak, then neutron generation rate is low. Therefore C is suitable for beam dump, beam stopper, and the energy degrader and so on.

Figure 3 and figure 5 show the comparison with LA150 and Meigo's experimental data. As you see, agreement between experimental data are very good, but the data of LA150 trace general trend but underestimate experimental data for high energy region at 50 and 70 MeV. Therefore, LA150 should be improved more to estimate neutron yield from beam dump and so on.

#### 5.2 $^{nat}\text{Al}(p, xn)$

Figure 6 and figure 8 show neutron yields from  $^{nat}\text{Al}(p, xn)$  at 50 and 70 MeV. Because  $Q$  value of the reaction is -5.59 MeV (is not so large), the spectra have high energy neutrons. Besides, small evaporation peaks exist around low energy region.

Figure 7 and figure 9 show the results for the Al(p,n) reaction. For 70 MeV, a result of MCNPX calculation using LA150 as a nuclear data is also shown. The yield from equation(1) is in good agreement with the results of MCNPX underestimate experimental data in high energy region, but similar experimental spectrum in the shape and angular distribution for all region.

### 5.3 $^{nat}\text{Ta}(p,xn)$ , $^{nat}\text{W}(p,xn)$ , $^{nat}\text{Pb}(p,xn)$

Figure 10, 12, 14, and 16 show the results for  $^{nat}\text{Ta}$ ,  $^{nat}\text{W}$ ,  $^{nat}\text{Pb}(p,xn)$ , respectively. These neutron spectra emitted from heavy nuclides have large evaporation peak with low energy. This evaporation peak is suitable for neutron source with high intensity. Figure 11 shows angular distribution of  $^{nat}\text{Ta}$ . From this figure, the yields of low energy neutron is isotropic. The angular distribution of  $^{nat}\text{W}(p,xn)$  and  $^{nat}\text{Pb}$  are very similar each other.

Figure 13, 15, 17 show the comparison of experimental data with the LA150 data. The data of LA150 trace generally well the experimental data although there are still marked differences in high energy parts.

## References

- [1] C. A. GOULDING J. B. McCLELLAND G. L. MORGAN C. E. MOSS M. M. MEIER, D. A. CLARK and W. B. AMIAN. Differential neutron production cross sections and neutron yields from stopping-length targets for 113-mev protons. *Nucl. Sci. Eng.*, Vol. 102, p. 310, 1989.
- [2] Cyric web page. <http://www.cyric.tohoku.ac.jp>.
- [3] K. Kumagaik Y. Kikuchi T. Uekusa T. Uemori H. Fujisawa N. Sugimoto K. Itoh M. Baba et al. A. Terakawa, H. Suzuki. New fast-neutron time-of-flight facilities at cyric. *Nucl. Instr. and Meth.*, Vol. 491, pp. 419–425, 2002.
- [4] M. Ibaraki et al. *Nucl. Sci. Eng.*, Vol. 35, p. 843, 1998.
- [5] J. K. Dickens. *ORNL-6463*. Oak Ridge National Laboratory, 1988.
- [6] S. Meigo. Measurements of the response function and the detection efficiency of an ne213 scintillator for neutrons between 20 and 65 mev. *Nucl. Instr. and Meth. in Phys. Res. A*, Vol. 401, pp. 356 – 378, 1997.
- [7] M. B. Chadwick, P. G. Young, R. E. MacFarlane, P. Moller, G. M. Hale, R. C. Little, A. J. Koning, S. Chiba. *LA150 Documentation of Cross Sections, Heating, and Damage: Part A (Incident Neutrons)*. LANL Accelerator Production of Tritium Program, 1999.
- [8] M. B. Chadwick, P. G. Young, R. E. MacFarlane, P. Moller, G. M. Hale, R. C. Little, A. J. Koning, S. Chiba. *LA150 Documentation of Cross Sections, Heating, and Damage: Part B (Incident Protons)*. LANL Accelerator Production of Tritium Program, 1999.
- [9] Takashi Nakamura. *Radiation Physics and Accelerator safety Engineering*. Chijin Shokan, 2001.
- [10] Shinichiro Meigo. In *Proc. Int. Conf. on Nuclear Data*, p. 413, Trieste, 1997.

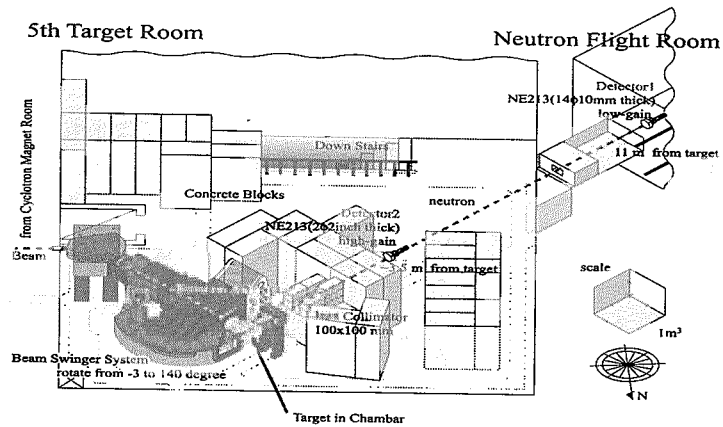


Figure 1: schematic view of 5th target room of CYRIC

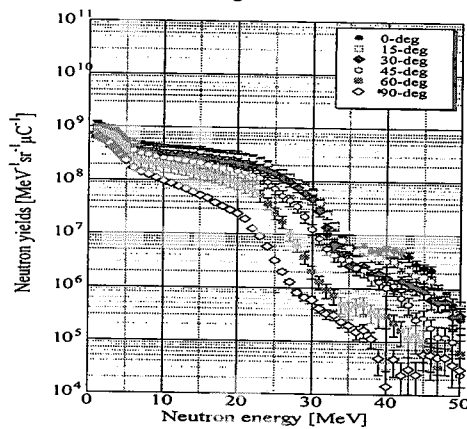


Figure 2: thick target yield for C(p,xn) at 50 MeV

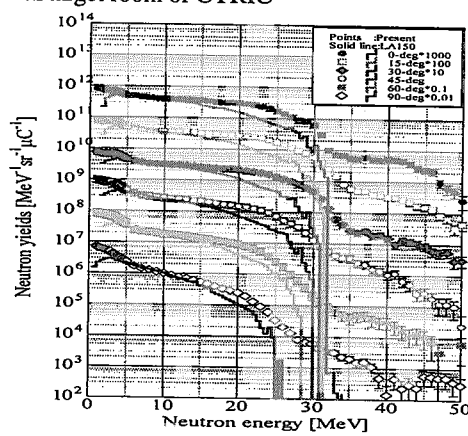


Figure 3: comparison with La150 for C(p,xn) at 50 MeV

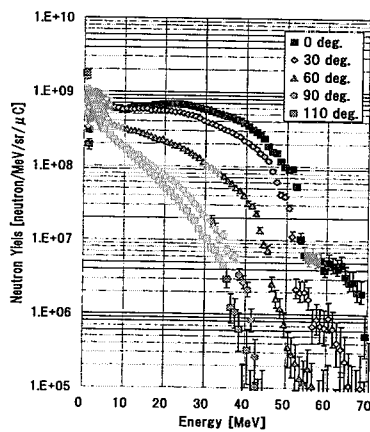


Figure 4: Thick target yield for C(p,xn) at 70 MeV

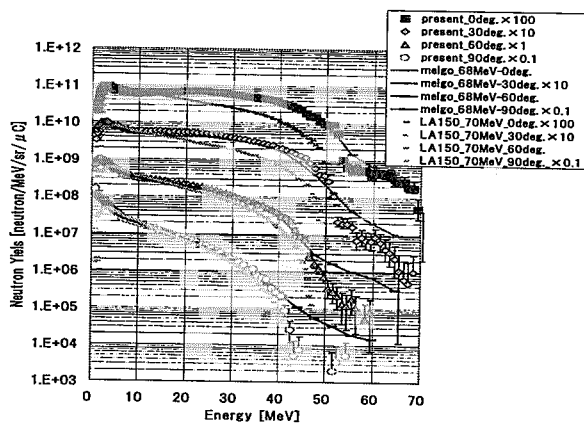


Figure 5: Comparison with La150 & Meigo's data

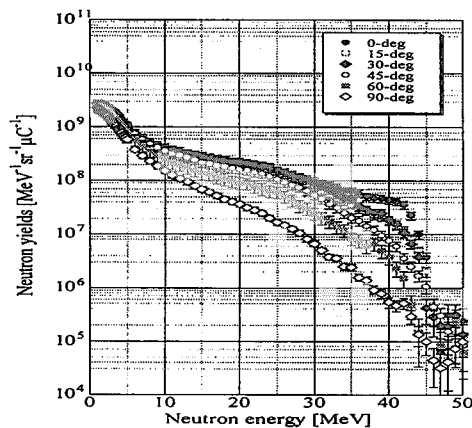


Figure 6: Thick target yield for Al(p,xn) at 50 MeV

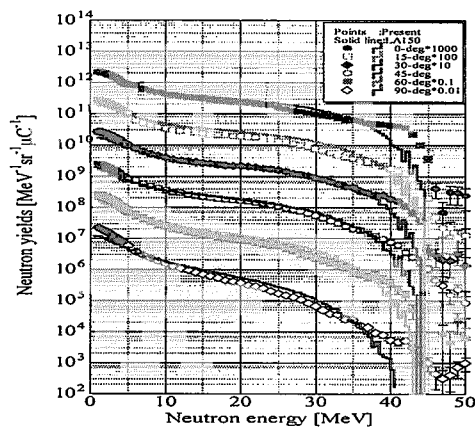


Figure 7: Comparison with La150 for Al(p,xn) at 50 MeV

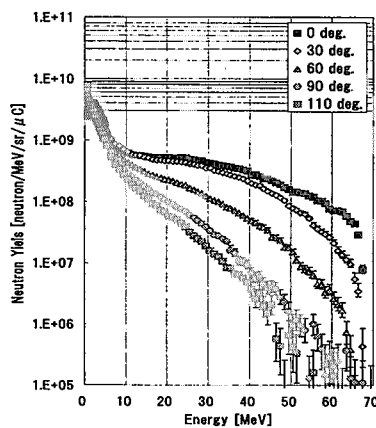


Figure 8: thick target yield for Al(p,xn) at 70 MeV

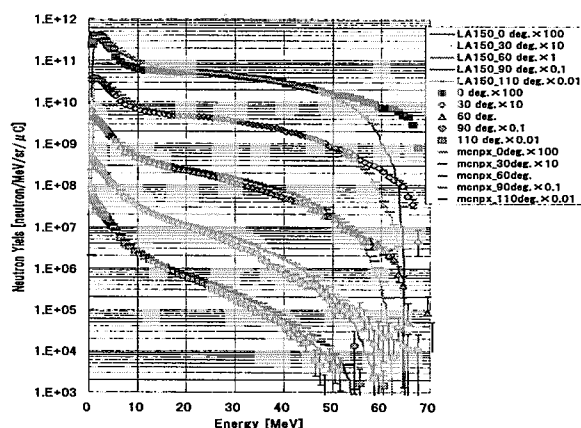


Figure 9: comparison with La150 &amp; MCNPX for Al(p,xn) at 70 MeV

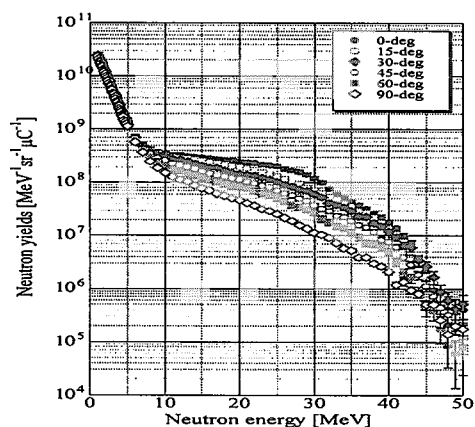


Figure 10: Thick target yield for Ta(p,xn) at 50 MeV

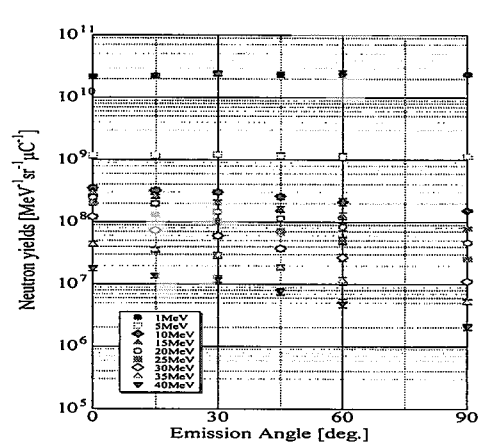


Figure 11: Angular distribution of Ta(p,xn)

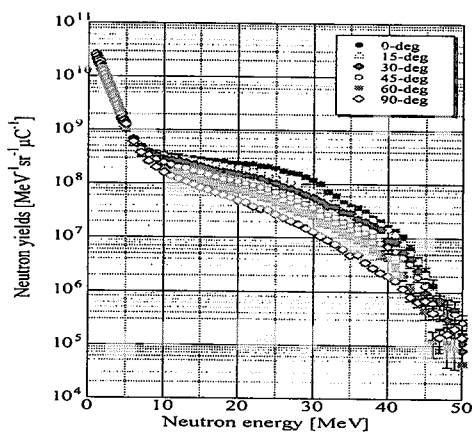


Figure 12: Thick target yield for W(p,xn) at 50 MeV

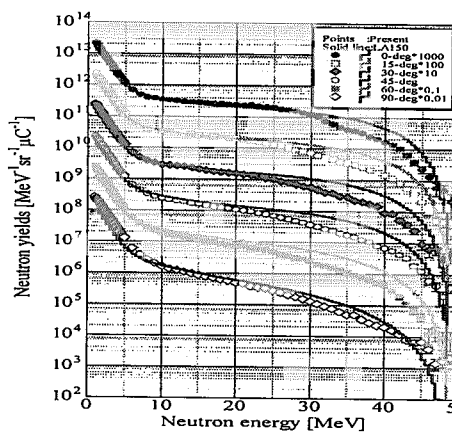


Figure 13: Comparison with La150 for W(p,xn) at 50 MeV

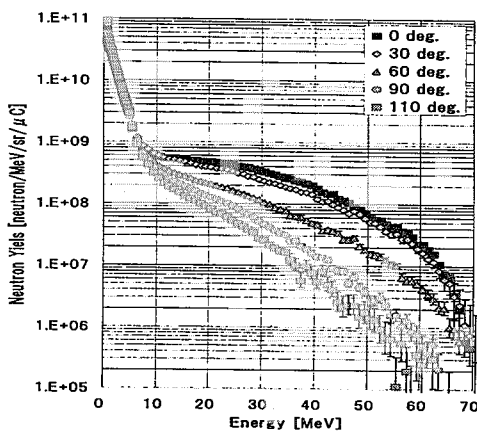


Figure 14: Thick target yield for W(p,xn) at 70 MeV

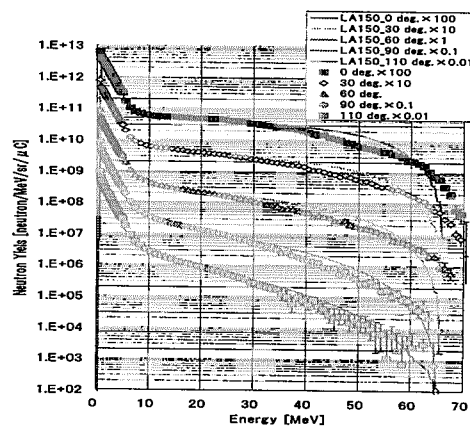


Figure 15: Comparison with La150 for W(p,xn) at 70 MeV

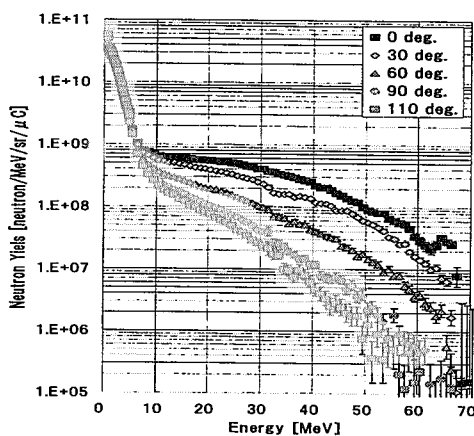


Figure 16: Thick target yield for Pb(p,xn) at 70 MeV

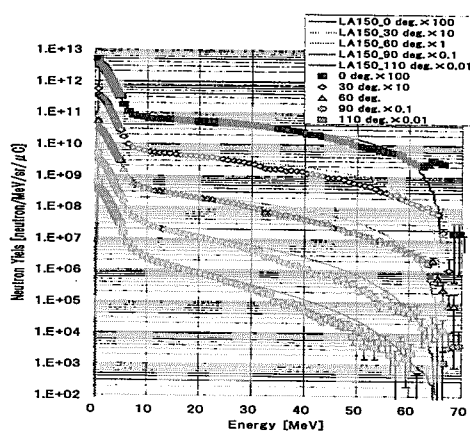


Figure 17: Comparison with La150 for Pb(p,xn) at 70 MeV



### 3.8 Measurements of Neutron Emission Spectra and $^7\text{Be}$ Production in $\text{Li(d,n)}$ and $\text{Be(d,n)}$ Reactions for 25 and 40 MeV deuterons

Masayuki HAGIWARA, Mamoru BABA, Takao AOKI\*, Naoki KAWATA, Naoya HIRABAYASHI  
and Toshiro ITOGA

Cyclotron and Radioisotope Center (CYRIC), Tohoku University  
Aoba01, Aramaki, Aoba-ku, Sendai-shi, Miyagi-ken, Japan  
Email: [hagi@cyric.tohoku.ac.jp](mailto:hagi@cyric.tohoku.ac.jp)

The neutron spectra in  $\text{Li(d,n)}$  and  $\text{Be(d,n)}$  reactions for  $E_d = 25, 40$  MeV were measured from  $\sim 1$  MeV to highest energy of secondary neutrons at ten laboratory angles between 0- and 110-deg with the time-of-flight (TOF) method. In addition, the number of  $^7\text{Be}$  accumulated in the targets was also measured by counting the  $\gamma$ -rays from  $^7\text{Be}$  using a pure Ge detector to obtain  $^7\text{Be}$  production cross-section and yields.

#### 1. Introduction

The  $\text{Li(d,n)}$ ,  $\text{Be(d,n)}$  reactions are expected as high-intensity neutron production reactions, in particular the  $^{\text{nat}}\text{Li(d,n)}$  reaction using a liquid lithium target will be adopted in IFMIF (International Fusion Materials Irradiation Facility) [1]. For the design and operation of the neutron source, detailed knowledge is required on the energy-angular neutron emission spectra of the  $^{\text{nat}}\text{Li(d,n)}$  and  $^9\text{Be(d,n)}$  reactions, and the radioactivity ( $^7\text{Be}$ ,  $^3\text{H}$  etc.) accumulated in the targets. The neutron flux and spectral data are indispensable for precise estimation of the neutron irradiation effects and radiation shielding, and the radioactivity accumulation is of great concern for the management of the targets. However the data status is not good enough as shown by marked differences among experimental data [2]. We have started experiments on the neutron emission spectrum of the  $^{\text{nat}}\text{Li(d,n)}$  and  $^9\text{Be(d,n)}$  reaction and the radioactivity induced in the target using the AVF cyclotron ( $K=110$ ) at CYRIC, Tohoku University [3].

This paper presents the experiments on the 1) neutron emission spectra and the 2) production of radioactive nuclide,  $^7\text{Be}$ , for the  $^{\text{nat}}\text{Li(d,n)}$  and  $^9\text{Be(d,n)}$  reaction with thick target for 25,40 MeV deuterons. The neutron spectra were measured for almost entire range of secondary neutrons at ten laboratory angles between 0- and 110-deg with the time-of-flight (TOF) method using a beam swinger system. The number of  $^7\text{Be}$  accumulated in the targets was measured by counting the  $\gamma$ -rays from  $^7\text{Be}$  using a pure Ge detector. Besides, to improve the data accuracy of the thick target yields of neutrons and the radioactivity accumulated in the target, we have also measured the data for a thin lithium target at 40 MeV and the excitation function of the  $^{\text{nat}}\text{Li(d,x)}^7\text{Be}$  reaction below 40 MeV by applying a stacked target method. Experimental results are compared with other experimental data and calculations. A part of results for 25 MeV were reported in ref. 3.

#### 2. Experimental apparatus

The experimental setup is presented in Fig.1. A deuteron beam accelerated by the AVF cyclotron was transported to the target room No.5 equipped with a beam-swing system and a neutron TOF channel [4]. The beam swinger system changes the incident angle of the beam onto the target from 0- deg to 110-deg and enables to measure angular distributions with fixed detector setup.

The targets (Li,Be) were metallic plate of natural elements. The lithium target was prepared by mechanical pressing of a lithium ingot under argon atmosphere to avoid oxygen contaminant and the lithium ingot was cleaned up thoroughly prior to the pressing to avoid carbon contamination. The lithium and beryllium targets were  $\sim 8$  mm and  $\sim 3$  mm thick for 25 MeV, respectively to stop the incident beam within the targets. For 40 MeV, We prepared a thin lithium target ( $\sim 0.85$  mm) and a stacked targets that consists of eight lithium plates with different thickness ( $\sim 1.3, \sim 6.7, \sim 1, \sim 4.7, \sim 0.9, \sim 2.7, \sim 0.7, \sim 3.4$  mm, total thickness  $\sim 21.4$  mm) to measure not only thick target neutron spectra but also excitation function of the  $^{\text{nat}}\text{Li(d,x)}^7\text{Be}$  reaction. They were set on a remotely-controllable target changer together with a beam viewer of aluminum oxide. The support frame of the target was isolated from the ground to read beam current on the target and was surrounded with a copper mesh biased about  $-600$  V to suppress secondary electron emission.

The target chamber was shielded with a 2.5 m thick concrete wall having a beam channel for collimators. Iron collimators, 10-cm-diam, were inserted into the beam channel to collimate neutrons from the target. Emitted neutrons were detected by NE213 scintillation detectors, 14 cm-diam  $\times$  10 cm-thick or 5 cm-diam  $\times$  5 cm-thick equipped with pulse-shape-discrimination (PSD). The larger and smaller detectors were placed around  $\sim 11$  m

\*Present address: Tokyo Electric Power Company (TEPCO)



and ~3.5 m from the target (fig.1), respectively. The shorter flight path was adopted to measure the low energy part (~1-5 MeV) of the neutron spectrum by low pulse-height bias (~600 keV). The TOF, PSD and pulse-height data were collected event by event as three parameter list data for off-line analysis [5].

### 3. Experimental procedure

The pulse width was generally less than 1 ns in FWHM, and the beam current on the target was around 5 nA. The beam current was digitized and recorded by a multi-channel scaler for normalization of the neutron TOF spectrum and the  $^7\text{Be}$  production measurement. The TOF data for 25 MeV were obtained at ten laboratory angles (0, 5, 10, 15, 20, 25, 30, 40, 60 and 90 deg), for 40 MeV at nine laboratory angles (0, 10, 15, 20, 30, 40, 60, 90 and 110 deg), respectively.

The activities of  $^7\text{Be}$  accumulated in the lithium and beryllium target were measured by detecting 477 keV  $\gamma$ -rays due to the decay of  $^7\text{Be}$  in the targets bombarded by a deuteron beam during the neutron spectrum measurement with a pure Ge detector (EURICIS MESURESE GPC50-195-R) and a multi-channel analyzer.

### 4. Data analysis

#### 4.1. Neutron spectrum

Neutron TOF spectra gated by a PSD signal and lower pulse-height bias were converted into energy spectra. The efficiency vs energy curves of the detectors were calculated by a revised version of the Monte Carlo code SCINFUL [6] that was verified to be accurate within  $\pm 5\%$  up to 80 MeV [7]. The spectra were normalized by the integrated beam current and the corrected for the effect of the attenuation in the sample and air using the data of W. P. Abfalterer et al. [17] and LA150 [18].

#### 4.2. $^7\text{Be}$ activity

The induced  $^7\text{Be}$  activity was determined from the  $\gamma$ -ray counts by the pure Ge detector, and corrected for the decay, the peak efficiency of the Ge detector, the self-absorption effect in the samples and the beam current fluctuation during irradiation. The efficiency of the Ge detector was determined by the calculation using the Monte Carlo code EGS 4 [8]. The calculated results were confirmed at several energy points with standard  $\gamma$ -ray sources. In the case of the stacked samples, we took into account the energy degradation and the attenuation of projectiles through the targets. In each stacked sample, the energy of projectile deuteron was calculated by the TRIM code [15] and the number of projectile deuterons were corrected for the attenuation using the total cross-section calculated by Shen's formula [16].

### 5. Results and discussion

#### 5.1. (d+Li, d+Be) neutron spectra

For 25 MeV, the present results for the  $^{\text{nat}}\text{Li}(d,n)$  and  $^9\text{Be}(d,n)$  neutron spectrum at ten laboratory angles are shown in Fig.2 and Fig.3, respectively. The low limit is as low as around 1 MeV. The error bars of the spectra represent the statistical errors mainly. In Fig.4, the present data at 0, 20, 60, 90 deg are compared with the experimental data by Lone et al at 23 MeV [2] and the calculation by the M<sup>c</sup>Delicious code [14]. The data of Lone et al are reported only for 0-deg.

The experimental spectra are divided into two parts; a high-energy tail region (only for  $^{\text{nat}}\text{Li}(d,n)$ ) due to direct stripping reactions and a main peak region centered around 10 MeV which is a main neutron source in IFMIF. The data by Lone et al. are in good agreement with the present one in the 10-23 MeV region while they are much larger in the low energy region. Such a high yields of low energy neutrons as seen in the other data is unlikely for the reaction of light element like Li which has a very strong recoil effect. For the high energy tail region, the data by Sugimoto [9] at 32 MeV are closer to the present one rather than those by Lone et al. and calculation. It is necessary to clarify the spectrum in this energy region because high-energy neutrons cause much more damage due to large helium production cross-sections and larger energy of primary-knock-on atoms.

The intensity of high-energy tail is highest around 15-deg while total neutron yields are highest at 0-deg. The former conclusion is in agreement with Sugimoto [9] and can be interpreted by the angular momentum effect in the  $^7\text{L}(d,n_0)^8\text{Be}$  reaction. Therefore, to reduce the influence of high-energy neutrons and obtain higher intensity irradiation field, neutrons to angles close to 0-deg will be preferable. The present data can be used to assess the applicability of calculation codes and models for the neutron emission spectrum of the reaction [10].

For 40 MeV, the present results with the thick and thin target of  ${}^{\text{nat}}\text{Li}(\text{d},\text{n})$  neutron spectrum at nine or seven laboratory angles are shown in Fig.5 and Fig.6, respectively. In Fig.7, the present data at 0, 20, 60, 90 110 deg are compared with the other data collected by Simakov et al [14]. Similarly as the spectra at 25 MeV, the experimental spectra are in good agreement with the other data around 6-25 MeV region, but different at both low energy region (<5 MeV) and high energy region (>30 MeV).

## 5.2. ${}^7\text{Be}$ activity

The measured  ${}^7\text{Be}$  activity was compared with other experimental data and the calculation by the code IRAC [11] used for activity assessment of accelerator components. Figures 8 and 9 show the comparison of the present results, the IRAC code and other experimental data [12,13] for Li and Be, respectively. For the lithium data, the present results at 25 MeV look to be consistent with the data around 22 MeV [11] and at 40 MeV [12], but are substantially higher than the IRAC calculation. The production of  ${}^7\text{Be}$  via the (d,n) reaction on elemental lithium will be due to the  ${}^7\text{Li}(\text{d},\text{n})$  and the  ${}^6\text{Li}(\text{d},\text{n})$  reactions mainly. Figure 10 shows the comparison of the experimental data and the IRAC calculation for the  ${}^{\text{nat}}\text{Li}(\text{d},\text{n})$  reaction cross-section. The present data is in good agreement with other ones at low energy region (6.8, 9.3 MeV). The IRAC code underestimates the  ${}^7\text{Li}(\text{d},\text{n})$  cross-sections and this may be a principal reason of the underestimation of the IRAC code for the  ${}^7\text{Be}$  production rate. For the beryllium data, similar underestimation is observed and reported even for the new code [10].

## Acknowledgement

The present was supported by Japan Atomic Energy Research Institute (JAERI) and National Institute for Fusion Science (NIFS). The authors express their thanks to Dr. M. Sugimoto (JAERI), S. Simakov, U. Fischer for providing with data and the operation crew of the CYRIC, Tohoku university for their cooperation.

## References

- [1] IFMIF CDA TEAM, IFMIF Conceptual Design Activity Final Report edited by Marcello Martone, Report 96.11, Enea, Dipartimento Energia, Frascati (1996)
- [2] M.A.Lone et al., Nucl. Instrum. Methods, 143 (1977) 331
- [3] M. Baba, T. Aoki, M. Hagiwara et al., J. Nucl. Materials 307-311 (2002) 1715-1718.
- [4] A.Terakawa et al., Nucl. Instrum. Methods A 491 (2002) 419.
- [5] M. Ibaraki et al., Nucl. Sci. Technol., 35. (No.12) (1998) 843
- [6] J. K. Dickens, ORNL-6436, Oak Ridge National Laboratory, 1988
- [7] S.Meigo Nucl. Instrum. Methods in Physics Research A 401 (1997) 365
- [8] W.Nelson, H.Hirayama, D.W.O.Rogers, "The EGS4 Code System" SLAC-265, Stanford University, Stanford (1985)
- [9] M.Sugimoto (Japan Atomic Energy Research Institute), Private communication
- [10] A.Yu.Konobeyev, Yu.A.Korovin, P.E.Pereslavytsev, U. Fischer, U.Möllendorff, Nucl. Sci.Eng.,139 (2001) 1
- [11] S.Tanaka et al. Proc. of 8<sup>th</sup> Int. Conf. On Radiation Shielding, Arlington, Apr. 1994, Vol.2, (American Nuclear Society, 1994) pp965
- [12] EXFOR system: OECD/NEA <http://www.nea.fr>
- [13] U.Von Möllendorff, H.Feuerstein and H.Giese, Proc. 20<sup>th</sup> Symp., on Fusion Technology (Marseille, France, 7-11 Sept.1998) pp.1445
- [14] S.P. Simakov, U. Fischer et al.: Pre-print of paper contributed to 10<sup>th</sup> International Conference on Fusion Reactor Materials (ICFRM-10), Baden-Baden, Germany, 14-19 October 2001
- [15] J. F. Ziegler, J. P. Biersack, U. Littmark, "The Stopping and Range of Ions in Solids," vol. 1 of series "Stopping and Ranges of Ions in Matter," Pergamon Press, New York (1984).
- [16] W. Q. Shen, B. Wang, J. Feng, W. L. Zhan, Y. T. Zhu and E. P. Feng, "Total Reaction Cross section for Heavy Ion Collisions and Its Relation to the Neutron Excess Degree of Freedom" Nucl. Phys. A, 491, 130 (1989)
- [17] W. P. Abfalterer, F. B. Bateman, F. S. Dietrich, R. W. Finlay, R. C. Haight and G. L. Morgan "Measurement of neutron total cross sections up to 560 MeV" Phy. Rev. C, 63, 044608 (200104)
- [18] M. B. Chadwick, P. G. Young et al., Nucl. Sci. Eng. 131, 293, 1999

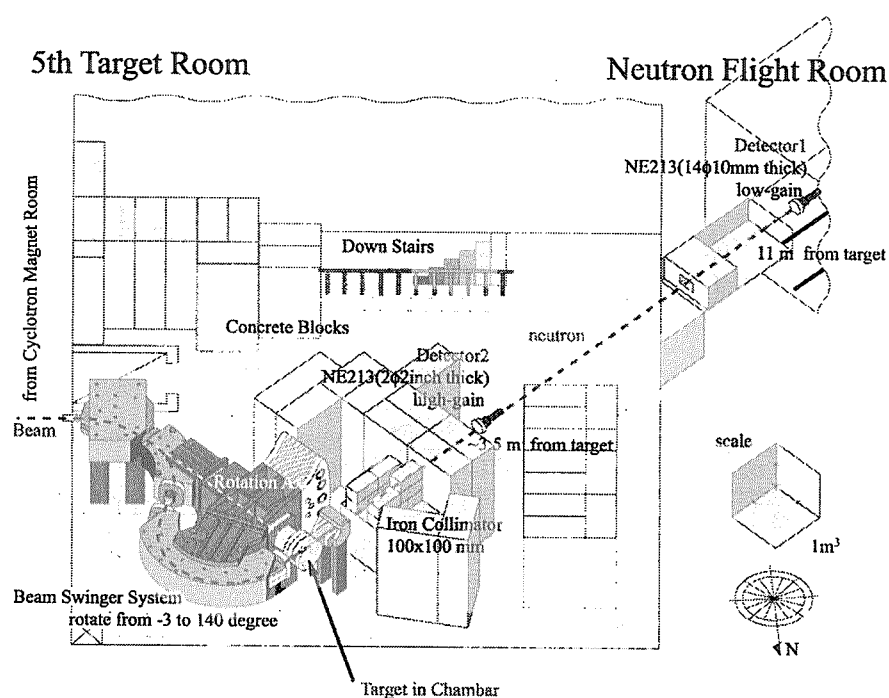


Fig.1: The layout of TR 5 at CYRIC, Tohoku University

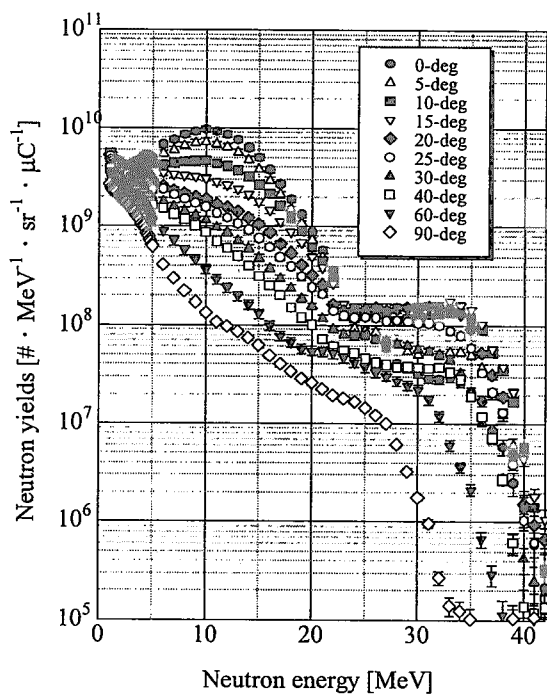


Fig.2: The neutron spectra of thick lithium for incident deuteron energy of 25 MeV

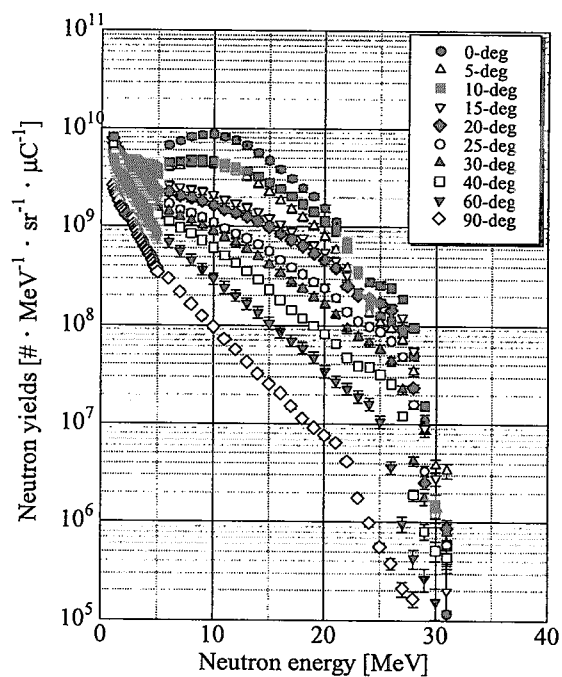


Fig.3: The neutron spectra of thick beryllium for incident deuteron energy of 25 MeV

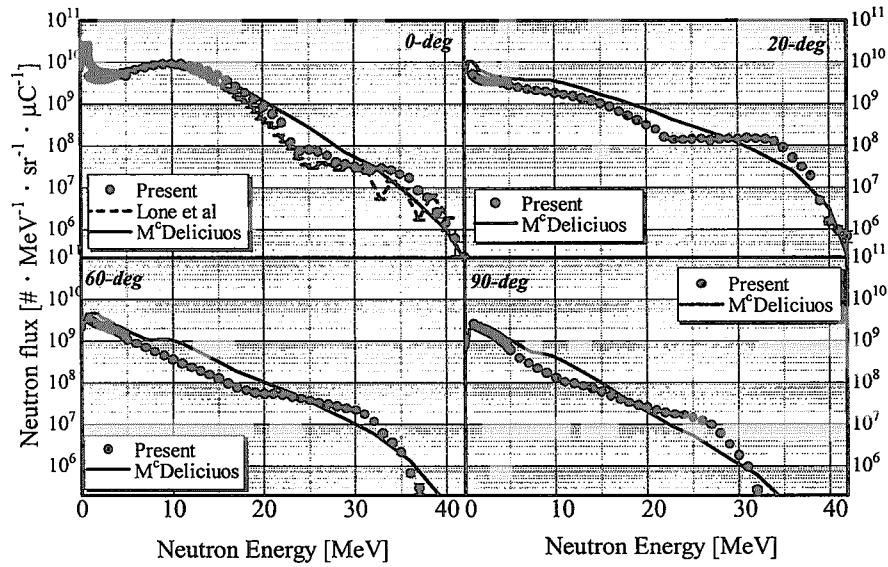


Fig.4: Comparison of the present Li(d,n) neutron spectrum with the data by Lone et al [2] and M<sup>c</sup>Delicious calculation [14].

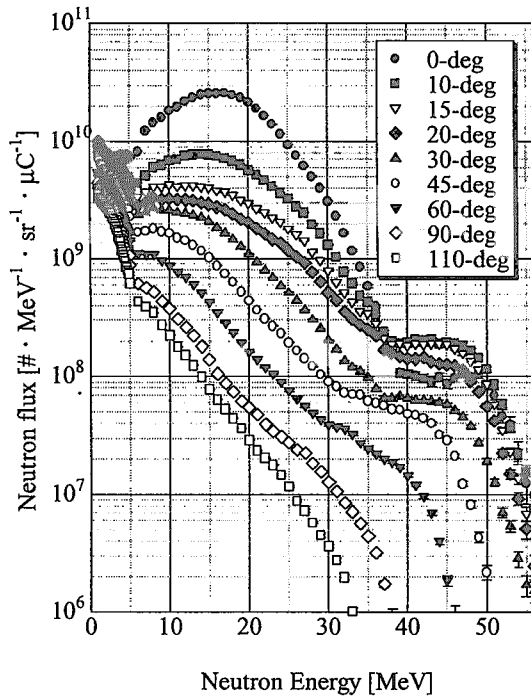


Fig.5: The neutron spectra of the thick lithium for incident deuteron energy of 40 MeV

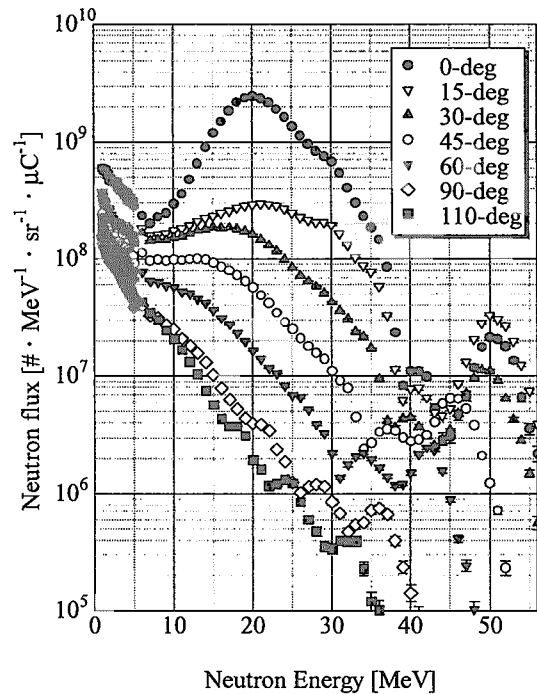


Fig.6: The neutron spectra of the thin lithium for incident deuteron energy of 40 MeV

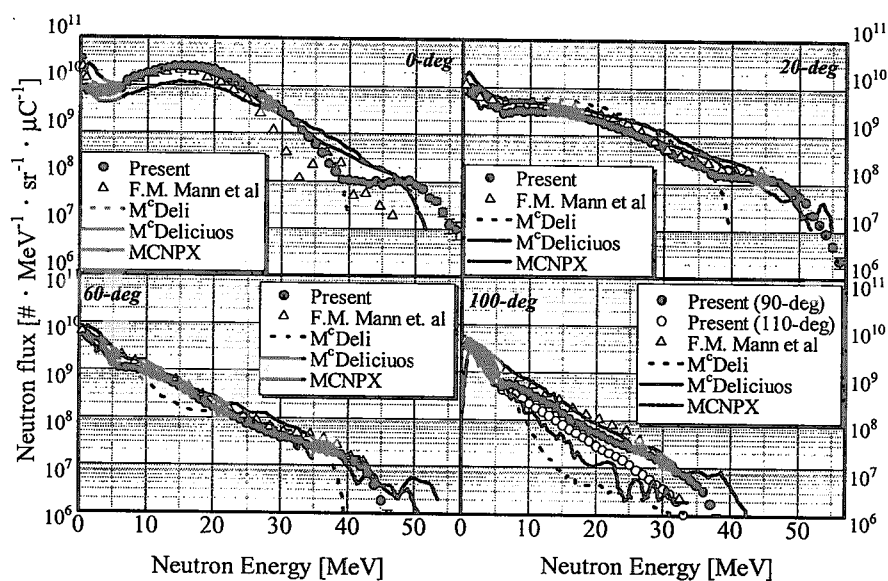


Fig.7: Comparison of the present  ${}^{\text{nat}}\text{Li}(\text{d},\text{n})$  neutron spectrum with the other experimental data and calculation collected by Simakov et al [14].

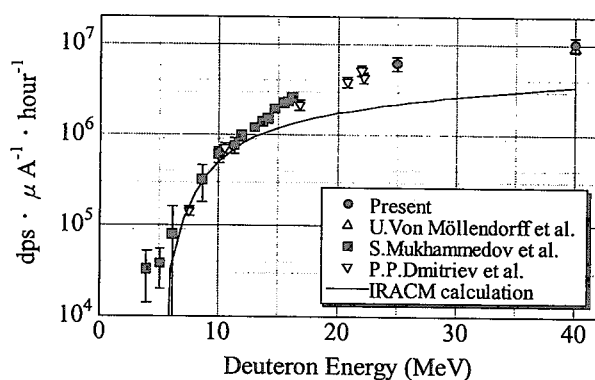


Fig.8:  ${}^7\text{Be}$  production rate via the  ${}^{\text{nat}}\text{Li}(\text{d},\text{x})$  reaction

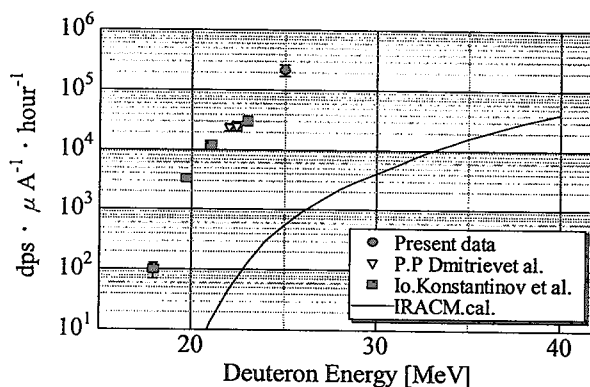


Fig.9:  ${}^7\text{Be}$  production rate via the  ${}^9\text{Be}(\text{d},\text{x})$  reaction

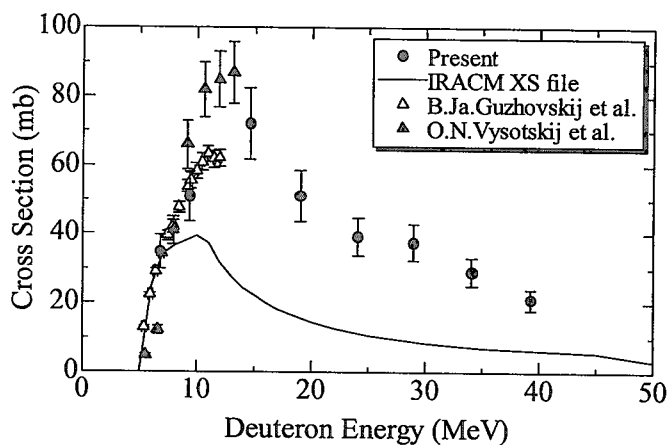


Fig.10:  ${}^{\text{nat}}\text{Li}(\text{d},2\text{n}){}^7\text{Be}$  reaction cross-section



## 3.9

**Method of Measurement of Cross Sections of Heavy Nuclei Fission Induced by Intermediate Energy Protons**

Alexander KOTOV<sup>1</sup>, Alexander CHTCHETKOVSKI<sup>1</sup>, Oleg FEDOROV<sup>1</sup>,  
Tokio FUKAHORI<sup>2</sup>, Yuri GAVRIKOV<sup>1</sup>, Yuri CHESTNOV<sup>1</sup>,  
Vladimir POLIAKOV<sup>1</sup>, Larissa VAISHNENE<sup>1</sup> and Vil VOVCHENKO<sup>1</sup>

<sup>1</sup>*Petersburg Nuclear Physics Institute, Gatchina,  
Leningrad district, Orlova roscha 1, 188300, Russia*

<sup>2</sup>*Japan Atomic Energy Research Institute,  
Tokai-mura, Naka-gun, Ibaraki-ken, 319-1195 Japan*  
e-mail: kotov@mail.pnpi.spb.ru

The purpose of this work is experimental studies of the energy dependence of the fission cross sections of heavy nuclei, <sup>nat</sup>Pb, <sup>209</sup>Bi, <sup>232</sup>Th, <sup>233</sup>U, <sup>235</sup>U, <sup>238</sup>U, <sup>237</sup>Np and <sup>239</sup>Pu, by protons at the energies from 200 to 1000 MeV. At present experiment the method based on use of the gas parallel plate avalanche counters (PPACs) for registration of complementary fission fragments in coincidence and the telescope of scintillation counters for direct counting of the incident protons on the target has been used. First preliminary results of the energy dependences of proton induced fission cross sections for <sup>nat</sup>Pb, <sup>209</sup>Bi, <sup>235</sup>U and <sup>238</sup>U are reported.

**1. Introduction**

The interest in fission cross section measurements is coming both from fundamental (nuclear properties of highly excited nuclei, such as temperature dependence of level density and fission barriers) and applied nuclear physics (new energy production concepts based on accelerator driven systems, for nuclear waste transmutation technologies). All existing experimental data on total cross sections of fission process induced in heavy nuclei by protons are dispersed in the range which exceeds the declared accuracy of measurements. For some nuclei total fission cross sections are absent in the chosen energy range.

The purpose of this work is experimental studies of the energy dependence of the fission cross sections of heavy nuclei, <sup>nat</sup>Pb, <sup>209</sup>Bi, <sup>232</sup>Th, <sup>233</sup>U, <sup>235</sup>U, <sup>238</sup>U, <sup>237</sup>Np and <sup>239</sup>Pu, by protons at the energies from 200 to 1000 MeV. At present experiment the method based on use of gas parallel plate avalanche counters (PPACs) for registration of complementary fission fragments in coincidence and the telescope of scintillation counters for direct counting of the incident protons on the target has been used. The PPACs for detection of fission events together with target are placed on the way of the proton beam providing very large solid angle acceptance. This allowed to provide high precision measurements at the intensity of proton beam about 10<sup>5</sup>-10<sup>7</sup> p/s that is important for precise monitoring of the proton flux by scintillation counters. First preliminary results of the energy dependences of proton induced fission cross sections for <sup>nat</sup>Pb, <sup>209</sup>Bi, <sup>235</sup>U and <sup>238</sup>U are reported.

**2. Experiment**

The experiment was carried out at the 1 GeV proton synchrocyclotron of Petersburg Nuclear Physics Institute (Gatchina, PNPI). The targets were irradiated with protons and two resulting fission fragments were detected for each fission event. Having the number of fission

events as well as the number of protons passed through the target, solid angle of registration and thickness of the target, the total fission cross sections have been determined.

## 2.1 Proton Beams

The synchrocyclotron of PNPI provides the external proton beam with the fixed energy of 1000 MeV and the intensity up to 1  $\mu$ A. To obtain the proton beams with energies from 900 MeV to 200 MeV at intervals 100 MeV the method of degrading of the initial 1000 MeV proton beam has been chosen. It is based on the direct beam dumping on the appropriate set of copper degraders. The appropriate system of beam transportation from the degrader (installed at the accelerator outlet) to the experimental setup has been created. The system of the beam transportation and focusing consisting of two doublets of magnetic quadrupole and a bending magnet represents a magnetic spectrometer with a high momentum resolution  $\Delta p/p \sim 0.008$  (FWHM). The measurements of the intensity at all energies showed that the beam intensities up to  $10^7$  p/s on the area  $2 \times 2 \text{ cm}^2$  can be reached even for 200 MeV proton beam that is more than enough for purpose of our experiment. The energies of the proton beams were determined by the time-of-flight method. The analysis of TOF spectra enabled us to conclude that an admixture of  $\pi^+$  mesons in proton beams is practically absent. Maximum admixture does not exceed 1% for 200 MeV proton beam.

## 2.2 Registration of Fission Events

In this experiment, the detectors of choice were gas parallel plate avalanche counters since they are known to be very efficient in registering fission fragments. They are also ideal for experiments at accelerators because they have good timing properties (time resolution is better than 300 ps), and they are practically insensitive to neutrons, photons and light charged particles with minimum specific energy losses.

The detector for registration coincident fission fragments represents an assemblage consisting of two identical PPACs and the target to be studied. The electrodes of PPAC were made of thin stretched aluminized Mylar foils ( $300 \mu\text{g}/\text{cm}^2$ ) and spaced at 1 mm. The assemblage was placed in the reaction chamber filled by saturated heptane gas at the pressure 6-10 Torr. The schematic drawing of the assemblage and related electronics is shown in Fig.1. Both fission fragments produced in the target are detected in coincidence by two PPACs with active areas of 80 mm in diameter located at a short distance at opposite sides of investigated target, providing a large solid angle acceptance of nearly 10 sr.

The pulse height from PPAC depends on specific energy losses of registered particles and gas amplification which can be changed by proper choice of applied anode-cathode potential. Thus at the fixed threshold of the discriminator the registration efficiency of PPAC can be modified by changing applied high voltage. The possibility to discriminate light particles with low specific energy losses and the good timing properties of PPACs[1] allowed us to use this assemblage directly in the incident proton beam, providing a large solid angle acceptance at 100% detection efficiency of fission fragments. However, in real beam conditions the use of the threshold criterion is not enough. The amplitude spectra derived from single PPAC show some contribution of the background events with low amplitude. These events come from the products of other nuclear reactions mainly induced by protons in the electrodes of PPACs, backing and different media on the way of the beam. If the coincidence condition is turned on, this component is strongly suppressed.

It should also be pointed out that the assemblage is quite transparent to intermediate energy protons, allowing the location of the several assemblages one after another on the way of the proton beam. This is very important in order to increase the statistics of the

measurements. In our experiment we placed five similar assemblages with the investigated targets in reaction chamber. Schematic view of the experimental setup together with the set of scintillation counters is given in Fig.2.

### 2.3 Targets

The investigated target represents the thin layer of fissioning material laid by vacuum evaporation method of on thin backing foil ( $50\text{--}80 \text{ mkg/cm}^2$ ) made of alumina- $\text{Al}_2\text{O}_3$ . The diameter of backing foils is equal to 50 mm while the diameter of target spot in the center of backing is 40 mm. The thicknesses of targets were in the range from 100 to  $450 \mu\text{g/cm}^2$ .

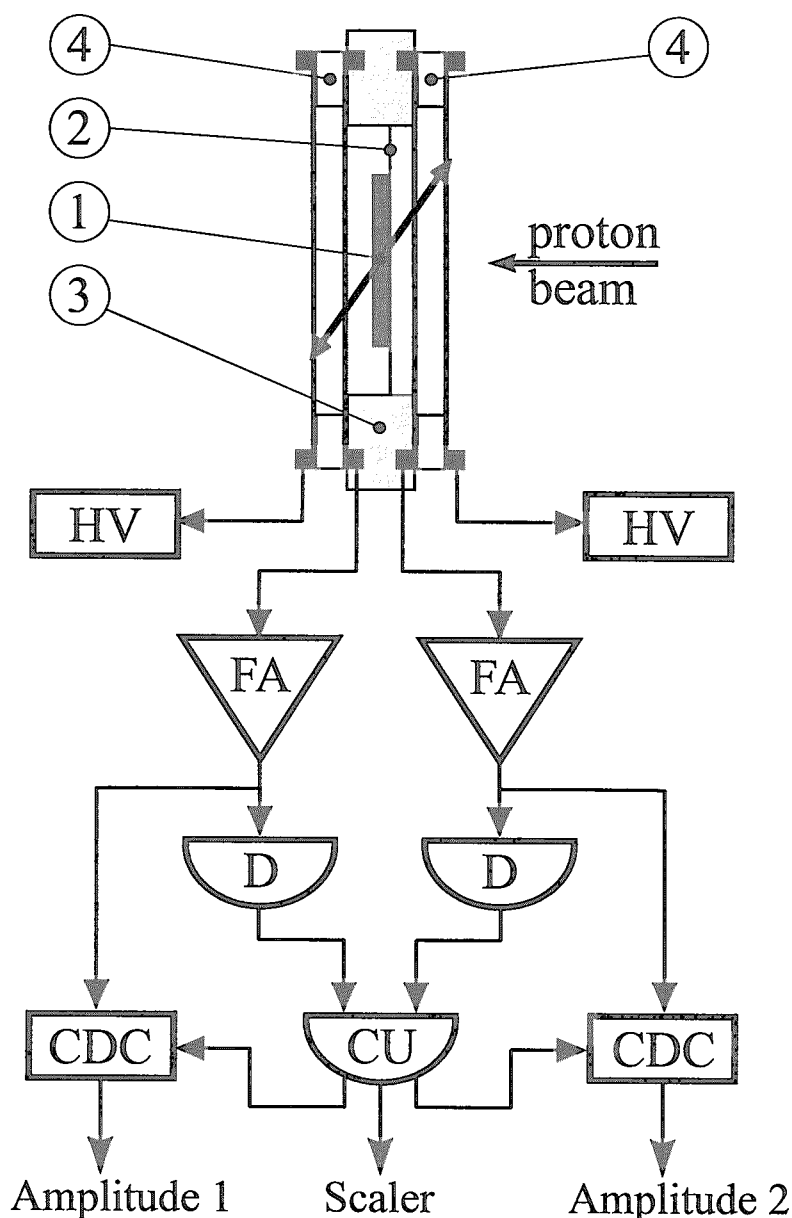


Fig.1. Schematic drawing of the fission fragment registration method

1. target; 2. target backing; 3. target support; 4. PPACs; HV- high voltage; FA- fast amplifier; D- discriminator; CDC- charge to digital converter; CU- coincidence unit;



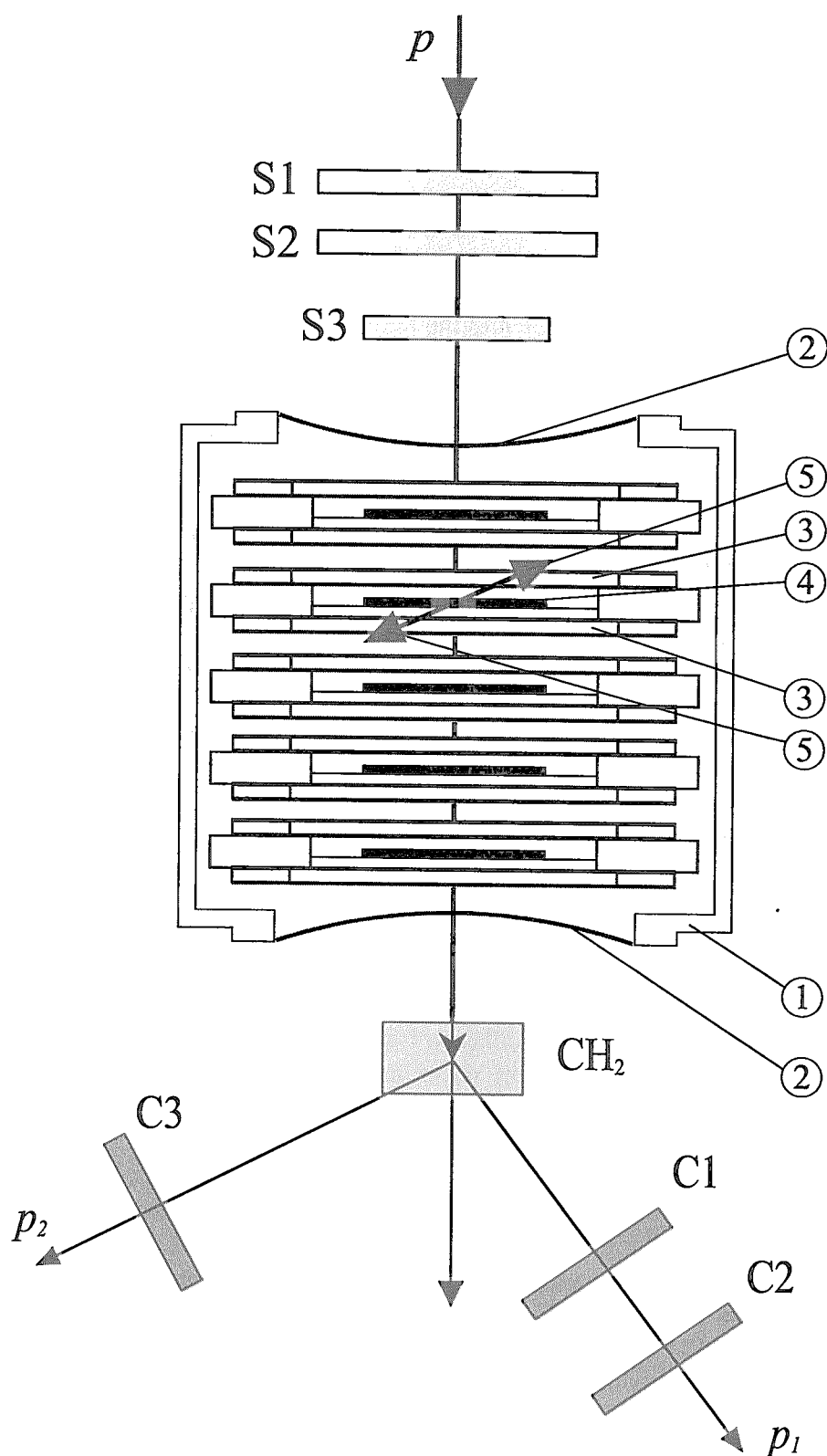


Fig.2. Schematic view of the setup for fission cross section measurements

1. chamber filled by heptane; 2. thin entrance window (Kapton); 3. parallel plate avalanche counters; 4. target on thin supporting foil; 5. registered fission fragments; S1,S2,S3- scintillation counters; C1,C2,C3- scintillation counters for registration pp-elastic scattering.

## 2.4 Monitoring System

The monitoring system (see Fig.2) consists of the set of scintillation counters. It intends for measurement of the incident proton flux on a working part of the target. The number of incident protons has been determined by direct counting. The monitoring was performed by telescope of three scintillation counters S1, S2 and S3 which was located just before an entrance window of the reaction chamber. All counters together with the assemblages of PPACs have been carefully aligned. However the recorded number of proton hits for each investigated target is somewhat less than the actual number because of the inefficiency of the telescope. The value of the efficiency can be estimated by measuring the ratio of the number of fission events in coincidence with the telescope and the number of fission events registered by PPAC assemblages. This ratio gives the reliable estimation of the monitor efficiency because the registration efficiency of PPAC for fission fragments is 100% and the diameter of the scintillation counter S3 is equal to the diameter of target spot. The value of inefficiency was maximum at 1000 MeV energy proton beam and did not exceed 8%.

Another source of the inefficiency of monitor is connected with a probability of appearance over than one proton in the single bunch which increases with proton intensity. The experimental estimation of the probability has been obtained by measuring the number of events corresponding to appearance at least two protons in two neighboring bunches. This value has been used for correction of monitor counting. This correction value amounts to several percent at the intensity about  $10^5$  p/s. All measurements have been performed at the intensities about  $10^5 - 10^7$  p/s.

The total proton flux has been obtained by two methods. First one is based on measurement of the sum of fission events for all targets and second one – on registration *pp* elastic scattering (see Fig.2). Both methods have been calibrated by means of direct proton counting with scintillation telescope at low intensity.

## 3. Preliminary Results

The number of fission events (having subtracted the background events using– threshold, coincidence and amplitude correlation as criteria of selection) has been corrected for a solid angle acceptance. To determine the geometrical acceptance of the target-PPACs system, Monte Carlo calculation was performed. This calculation takes into account the proton beam spot size, an effect of any collimators between the target and PPACs, anisotropy of fission fragments in the lab. system caused by a longitudinal component of the momentum of the fissioning nuclei and the energy losses of fission fragments in target, backing and electrode of PPAC. Our preliminary results for proton-induced fission cross sections for  $^{238}\text{U}$ ,  $^{235}\text{U}$ ,  $^{209}\text{Bi}$  and  $^{\text{nat}}\text{Pb}$  at energy range from 200 MeV to 1000 MeV are presented in Fig. 3-6. The previously existing proton-induced fission cross sections data for these nuclei taken from a review[2] are also shown. As one can see in Fig. 3 our results for uranium disagree with the most of early obtained data. The energy dependence of fission cross sections after slight increasing demonstrates some plateau in the energy range from 400 to 1000 MeV. Approximately the same energy dependence for  $^{235}\text{U}$  can be seen in Fig.4 although the values of fission cross sections are slightly less than for  $^{238}\text{U}$ . Our findings for  $^{209}\text{Bi}$  in Fig.5 are somewhat different from the most data obtained in other experiments and show increasing of fission cross section with increasing energy from 200 MeV to 400 MeV. Our data at energies above 400 MeV have quite similar values (in the error limits), demonstrating, in all probability, a plateau in the energy dependence of fission cross sections in this energy range. The same behavior of energy dependence of fission cross sections is observed for  $^{\text{nat}}\text{Pb}$  (Fig.6).

However, in contrast to data for  $^{209}\text{Bi}$ , the increase of fission cross sections at energies from 200 to 500 MeV is steeper than for  $^{209}\text{Bi}$ .

#### 4. Summary

The method of experimental study for proton induced fission cross sections in the 200-1000 MeV energy region and preliminary results for  $^{\text{nat}}\text{Pb}$ ,  $^{209}\text{Bi}$ ,  $^{235}\text{U}$  and  $^{238}\text{U}$  are reported. The efficiency, accuracy and reliability of the method for obtaining the energy dependence of fission cross sections is shown. The method will be used for further measurements for  $^{232}\text{Th}$ ,  $^{233}\text{U}$ ,  $^{237}\text{Np}$  and  $^{239}\text{Pu}$  target nuclei.

#### References

- [1] A.A. Kotov *et al.*, *Nucl. Instr. Meth.*, **178**, 55 (1980).
- [2] A.I. Obuchov, *J. Part. and Nuclei*, **32**, 162 (2001).  
A.V. Prokofiev, *Nucl. Instr. Meth.*, **A463**, 557 (2001).

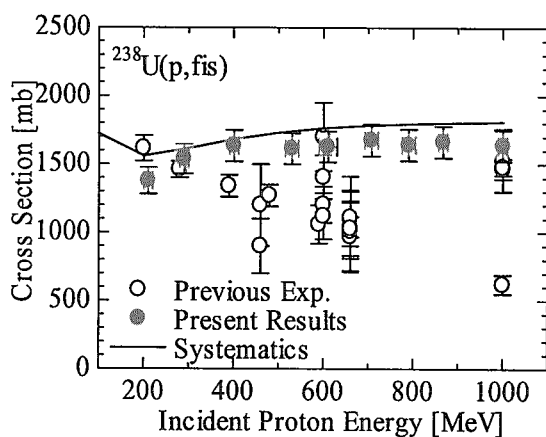


Fig.3. Energy dependence of fission cross section for  $^{238}\text{U}$

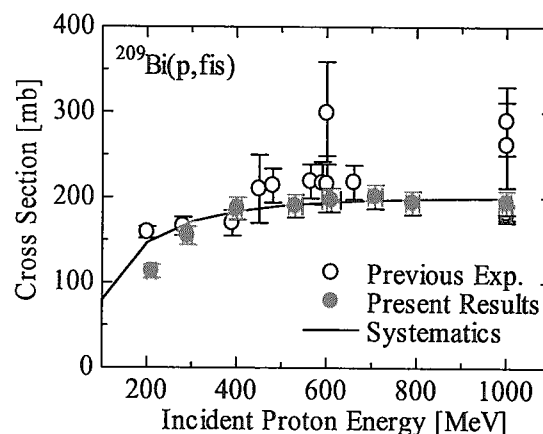


Fig.5. Energy dependence of fission cross section for  $^{209}\text{Bi}$

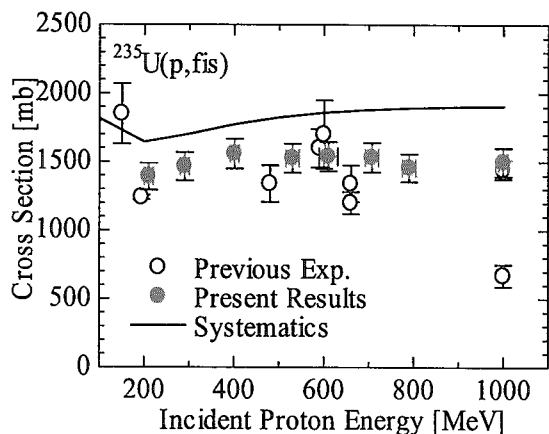


Fig.4. Energy dependence of fission cross section for  $^{235}\text{U}$

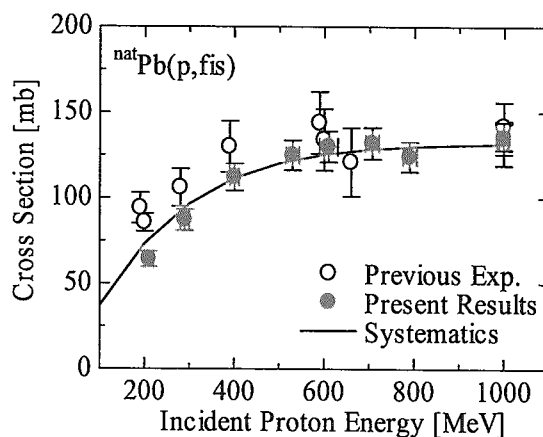


Fig.6. Energy dependence of fission cross section for  $^{\text{nat}}\text{Pb}$



## 3.10

 $^{100}\text{Mo}(p,d)^{99}\text{Mo}$  reaction at 50 MeV and direct reaction analysis

F. Aramaki<sup>a</sup>, Syafarudin<sup>b</sup>, G. Wakabayashi<sup>b</sup>, Y. Uozumi<sup>b</sup>, N. Ikeda<sup>b</sup>  
M. Matoba<sup>b</sup>, T. Sakae<sup>c</sup>, N. Koori<sup>d</sup>

<sup>a</sup> Kyushu Institute of Information Science

<sup>b</sup> Dept. of Nuclear Engineering, Kyushu University

<sup>c</sup> Proton Medical Research Center, Tsukuba University

<sup>d</sup> College of General Education, University of Tokushima

The  $^{100}\text{Mo}(\vec{p},d)^{99}\text{Mo}$  reaction has been studied with 50 MeV polarized protons. Angular distribution of the differential cross section and the analyzing power have been measured for neutron hole states in the  $^{99}\text{Mo}$  up to the excitation energy of 6 MeV. The data analysis with a standard distorted-wave Born Approximation (DWBA) theory provides transferred angular momenta ( $l$  and  $j$ ) and spectroscopic factors of neutron hole states for 40 excited states from the ground states up to the excitation energy of 3 MeV. The direct reaction model and the continuous strength functions were used to analyze spectrum regions from discrete levels to continuum.

## 1. Introduction

By means of medium-weight mass target nuclei and moderate bombarding energy, one can observe many discrete excitation levels and just above them a continuum spectrum in the one-nucleon transfer reactions. As shown in Figure 1, the spectrum is structured discretely and gradually becomes structureless in the higher area, and finally forms a plateau.[1, 2, 3] As for the discrete region, experimental data for assigning  $lj$ -values for excitation levels are scarce, and assignment results are not in good agreement, especially above 2MeV. In this paper, we describe the new results in assigning  $lj$ -values using  $^{100}\text{Mo}(\vec{p},d)^{99}\text{Mo}$  reaction at 50MeV.

Continuum spectrum is understood as a reflection of the phenomena occurred in shell-orbit, e.g. nuclear dumping, shell-orbit fragmentation, nuclear surface vibration. The effect of nucleon pickup and direct reaction plays an important role more contributive than other effects. An approach proposed by Lewis[4] is employed based on DWBA and asymmetrical Lorentzian form strength function having energy dependent spreading width.[5, 6]

This paper describes results of studies on  $^{100}\text{Mo}(\vec{p},d)^{99}\text{Mo}$  reaction with 50MeV polarized protons. Assignment of excitation levels below 4MeV region was carried out and compared the derived value with previously observed values, and spectrum was analyzed using a continuous strength function and DWBA-based cross sections of the correlated neutron hole states.

## II. Experiment

The experiment was carried out at the AVF cyclotron facility of the Research Center for Nuclear Physics, Osaka University, using the enriched (97.27%)  $^{100}\text{Mo}$  target foil. The beams of high energy resolution ( $\sim 30\text{keV}$ ) and a polarized proton beam with the polarization of about 80% accelerated to the energy of 50MeV was used. Polarized beam data determined the spin parity values more definitely. Emitted deuterons from  $^{100}\text{Mo}(\vec{p},d)^{99}\text{Mo}$  reaction were detected and momentum analyzed by the focal plane of a RAIDEN spectrograph with a position sensitive proportional counter detector system. Angular distributions of cross sections and analyzing powers were detected at  $8^\circ \sim 43^\circ$  laboratory angles. The measured

energy range corresponds to the excitation energy region from the ground state to about 6.5 MeV. Details of the experiment procedure are described in the previous papers.[5, 7]

Forty one levels were analyzed in the excitation energy below 4 MeV. From comparisons between the experimental angular distribution of the cross sections and the predictions of the DWBA theory using the optical potential parameters, the  $lj$ -angular momentum transfer were assigned. The normalization of the cross section was performed by the scaling the measured  $^{100}\text{Mo}(p,p)$  elastic scattering cross section to an optical model predictions using the parameters of global potential.

Figure 1 shows a typical double differential cross section for the  $^{100}\text{Mo}(\bar{p},d)^{99}\text{Mo}$  reaction at the  $8^\circ$  laboratory angle. From the comparisons between the experimental and theoretical angular distributions of cross sections and analyzing powers, the  $lj$ -angular momentum transfers were assigned. Thirty six levels were analyzed in the excitation energy region below 3.5 MeV and the  $lj$ -transfers were assigned for 36 levels.

For the continuum area, double differential cross sections are predicted by the DWBA using global optical potential. The double differential cross section-energy spectra were reproduced fairly well using the DWBA-based cross sections and the asymmetrical Lorentzian form strength response function having energy-dependent spreading width. The absolute values are in good agreement and very close order to the experimental data.

### III. Theoretical Analysis

Double differential cross sections are analyzed with the direct reaction model composed by an incoherent sum of the DWBA predictions from all the constituent shell-orbits, as expressed by,

$$\frac{d\sigma}{d\Omega}(E) = 2.30 \sum_{l,j} \frac{C^2 S_{l,j}(E)}{2j+1} \times \frac{d\sigma}{d\Omega}_{l,j}^{\text{DW}}(E) \quad (1)$$

where  $d\sigma/d\Omega|_{l,j}^{\text{DW}}(E)$  is the DWBA cross section,  $C^2 S_{l,j}(E)$  is the strength function of spectroscopic factor for the  $lj$ -transfer, given as follows,

$$C^2 S_{l,j}(E) = \left( \sum_{l,j} C^2 S_{l,j} \right) \times f_{l,j}(E) \quad (2)$$

The degrees of continuum strength is estimated by the Breit-Wigner form,

$$f_{l,j}(E) = \frac{n_0}{2\pi} \frac{\Gamma(E)}{(|E - E_F| - E_{l,j})^2 + \Gamma^2(E)/4} \quad (3)$$

where  $E_{l,j}$  is the calculated energy of the single-particle state which varies with the spreading width  $\Gamma(E)$ , and  $n_0$  is the renormalization constant and  $E_F$  the resonance energy. The spreading widths  $\Gamma(E)$  are expressed with the function proposed by Mahaux and Sartor [8] and Brown and Rho as follows[9]

$$\Gamma(E) = \frac{\epsilon_0(E - E_F)^2}{(E - E_F)^2 + E_0^2} + \frac{\epsilon_1(E - E_F)^2}{(E - E_F)^2 + E_1^2} \quad (4)$$

where  $\epsilon_0$ ,  $\epsilon_1$ ,  $E_0$ , and  $E_1$  are constants used to express the effect of nuclear damping. The used parameter values are as follows,

$$\begin{aligned} \epsilon_0 &= 19.4 \text{ (MeV)}, & E_0 &= 18.4 \text{ (MeV)}, \\ \epsilon_1 &= 1.40 \text{ (MeV)}, & E_1 &= 1.60 \text{ (MeV)} \end{aligned} \quad (5)$$

The sum-rules of the spectroscopic factors of neutron orbits for  $T \pm \frac{1}{2}$  isospin states above the closed shell core are estimated with a simple shell model prescription as described in the following equation[10]

$$\sum C^2 S = \begin{cases} \frac{n_n - \frac{n_p}{2T+1}}{2T+1} & \text{for } T < T - \frac{1}{2} \\ \frac{n_p}{2T+1} & \text{for } T > T + \frac{1}{2} \end{cases} \quad (6)$$

where  $n_n$  and  $n_p$  are the numbers of neutrons and protons, respectively, above the closed shell core and  $T$  is the target isospin.

The differential cross section and analyzing power data were analyzed with the DWBA code DWUCK[11] based on the zero-range and local energy approximation model.

**IV. Discussion** Angular distributions of cross sections and analyzing powers for 36 levels assigned for laboratory angles from  $8^\circ \sim 43^\circ$ . Results are

shown in table 1 along with DWBA prediction at  $8^\circ$  laboratory angle. The measured energy spectrum of double differential cross section and analyzing powers were converted to 500keV wide energy spectra. In Figures 2 and 3, solid lines represents theoretical differential cross section and analyzing powers, and histograms the experimental ones. Not only for  $8^\circ$ , the theory predicts differential cross section in discrete region ( $\sim 3$ MeV) fairly well, but in the region above 4MeV it does not and differential cross sections are small. Compared to other analysis results[12], experimental cross section values are too small. The shape of angular distributions of analyzing power are generally well produced.

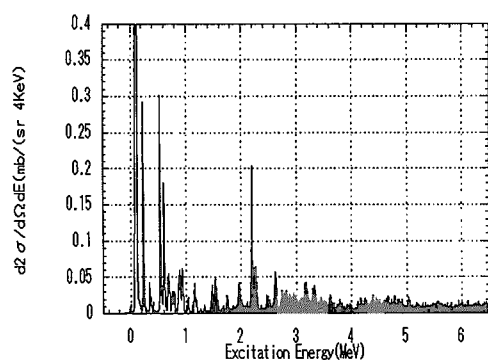


Figure 1: Typical energy spectrum of deuterons emitted from the  $^{100}\text{Mo}(p,d)^{99}\text{Mo}$  reaction at 50 MeV.

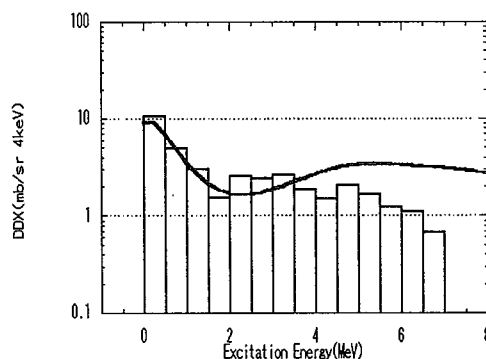


Figure 2: Comparison of theoretical and experimental double differential cross section.  $^{100}\text{Mo}(p,d)^{99}\text{Mo}$  reaction at 50 MeV,  $\theta = 8^\circ$  laboratory angle.

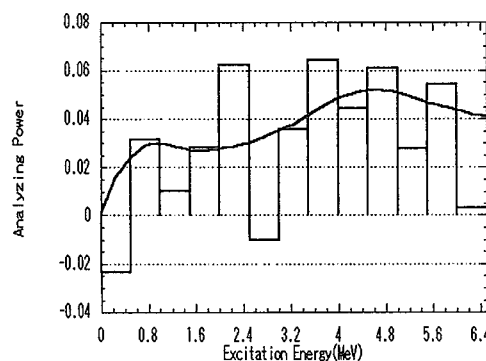


Figure 3: Comparison of theoretical and experimental analyzing power.  $^{100}\text{Mo}(p,d)^{99}\text{Mo}$  reaction at 50 MeV,  $\theta = 8^\circ$  laboratory angle.

## V. Conclusions

The use of a polarized beam improved the results of spin parity assignments. Several new assignments are added to the previous results, especially in the relatively high excitation energy region (3~4MeV). Overall predictions of angular distributions are in good agreement with experimental data for analyzing power distribution. This analysis gives a new possibility to distribution pattern of the continuum spectra for large scope of nuclei.

We are grateful to the staff of RCNP, Osaka University for their supports during the experiment.

## References

- [1] S.Hirowatari, Syafarudin, F.Aramaki, A.Nohtomi, G.Wakabayashi, Y.Uozumi, N.Ikeda, M.Matoba, Y.Aoki, K.Hirota, N.Okumura, and T.Joh, Nucl. Phys. A714 (2003) 3
- [2] Syafarudin, F.Aramaki, G.Wakabayashi, Y.Uozumi, N.Ikeda, M.Matoba, K.Yamaguchi, T.Sakae, N.Koori, and T.Maki, International Conference on Nuclear Data for Science and Technology(ND2001-conf. 8-11 October 2001); J. Nucl. Sci. Technol., supplement. 2,(2002) 377.

- [3] P.K.Bindal, D.H.Youngblood, R.L.Kozub, and P.H.Hoffmann-Pinther, Phys. Rev. C12 (1975) 1826.
- [4] M.B.Lewis, Phys. Rev. C11(1975) 145.
- [5] M.Matoba, O.Iwamoto, T.Sakae, N.Koori, H.Ohgaki, H.Kugimiya, H.Ijiri, T.Maki, and M.Nakano, Nucl. Phys. A581 (1995) 21.
- [6] M.Matoba, K.Kuromaru, O.Iwamoto, A.Nohtomi, Y.Uozumi, T.Sakae, N.Koori, H.Ohgaki, H.Ijiri, T.Maki, M.Nakano, and H.M.Sen Gupta, Phys. Rev. C53 (1996) 1792.
- [7] M.Matoba, O.Iwamoto, Y.Uozumi, T.Sakae, N.Koori, H.Ohgaki, H.Kugimiya, H.Ijiri, T.Maki, and M.Nakano, Nucl. Phys. A581 (1995) 21.
- [8] C.Mahaux and R.Sartor, Nucl. Phys. A528 (1991) 253.
- [9] G.E.Brown and M.Rho, Nucl. Phys. A372 (1981) 397.
- [10] H.Langevin-Joliot, J.van de Wiele, J.Guillot, E.Gerlic, L.H.Rosier, A.Willis, M.Morlet, G.Duhamel-Chretien, E.Tomasi-Gustafsson, N.Biasi, S.Micheletti, and S.Y.van der Werf, Phys. Rev. C47 (1993) 1571
- [11] P.D.Kunz, code DWUCK, University of Colorado (unpublished)
- [12] R.B.Firestone, V.S.Shirley, C.M.Baglin, S.Y.Frank Chu, and J.Zipkin, Table of Isotopes 8th ed., New York, John Wiley (1996)

Table 1: Spectroscopic results from neutron pickup reactions on  $^{100}\text{Mo}$ .

Present work				Ref.[3]				Ref.[12]	
$E_x$ (MeV)	$l$	$j^\pi$	$C^2S$ ( $p,d$ )	$E_x$ (MeV)	$l$	$j^\pi$	$C^2S$ ( $p,d$ ) ( $d,t$ )	$E_x$ (MeV)	$j^\pi$
0.000	0	$\frac{1}{2}^+$	0.202	0.000	0	$\frac{1}{2}^+$	(0.30) 0.14	0.000	$\frac{1}{2}^+$
0.096	2	$\frac{5}{2}^+$	1.691	0.098	2	$\frac{5}{2}^+$	1.84 1.80	0.098	$\frac{5}{2}^+$
0.235	4	$\frac{7}{2}^+$	1.358	0.231	4	$\frac{7}{2}^+$	1.39 1.75	0.236	$\frac{7}{2}^+$
0.352	2	$\frac{3}{2}^+$	0.082	0.345	2	$\frac{3}{2}^+$	0.06 0.16	0.351	$\frac{3}{2}^+$
0.525	0	$\frac{1}{2}^+$	0.680	0.531	0	$\frac{1}{2}^+$		0.525	$\frac{1}{2}^+$
0.547	2	$\frac{5}{2}^+$	0.253		2	$\frac{5}{2}^+$	0.33 0.55	0.547	$\frac{5}{2}^+$
0.610	2	$\frac{5}{2}^+$	(0.253)	0.604	2	$\frac{5}{2}^+$	0.24 0.32	0.615	$\frac{5}{2}^+$
0.683	5	$\frac{11}{2}^-$	0.705	0.675	5	$\frac{11}{2}^-$	0.50 (1.20)	0.698	$(\frac{7}{2}^+)$
0.750	4	$\frac{7}{2}^+$	0.237	0.747	2	$\frac{5}{2}^+$	0.07 0.10	0.754	$\frac{7}{2}^+$
0.790	2	$\frac{3}{2}^+$	0.070	0.788	(2)	$(\frac{3}{2}^+)$	0.06 0.08	0.793	$(\frac{3}{2}, \frac{5}{2})^+$
				0.878	(2)	$(\frac{3}{2}^+)$	0.07 0.06	0.890	$\frac{3}{2}^+$
0.897	4	$\frac{9}{2}^+$	0.412		(4)	$(\frac{9}{2}^+)$	0.59 0.30	0.906	$\frac{1}{2}^+$
0.938	2	$\frac{5}{2}^+$	0.131	0.924	2	$\frac{5}{2}^+$	0.15 0.22	0.945	$\frac{5}{2}^+$
1.037	3	$\frac{5}{2}^-$	0.205	1.022	(3)	$(\frac{5}{2}^-)$	0.26	1.026	$(\frac{3}{2}, \frac{5}{2})^+$
1.157	2	$\frac{5}{2}^+$	0.125	1.165	2	$\frac{5}{2}^+$	0.10 0.08	1.167	$\frac{5}{2}^+$
1.262	0	$\frac{1}{2}^+$	0.041					1.280	
1.337	4	$\frac{7}{2}^+$	0.121	1.320	4	$\frac{7}{2}^+$	0.10		
1.471	2	$\frac{5}{2}^+$	0.084	1.455	2	$\frac{3}{2}^+$	0.10 0.10	1.494	$\frac{5}{2}^+$
1.532	2	$\frac{3}{2}^+$	0.129	1.516	2	$\frac{3}{2}^+$	0.13 0.15	1.561	$\frac{1}{2}^+, \frac{3}{2}, \frac{5}{2}^+$
1.575	2	$\frac{5}{2}^+$	0.042					1.571	$\frac{1}{2}, \frac{3}{2}, \frac{5}{2}^+$
1.674	5	$\frac{11}{2}^-$	0.155	1.637	5	$\frac{11}{2}^-$	0.07		
								1.682	$(\frac{3}{2}, \frac{5}{2})^+$
1.749	2	$\frac{5}{2}^+$	0.063	1.714	2	$\frac{3}{2}^+$	0.05 0.05		
				1.793	4	$\frac{7}{2}^+$	0.17 0.10		
1.847	5	$\frac{11}{2}^-$	0.156	1.891	1	$\frac{1}{2}^-$	0.12 0.11	1.893	$(\frac{1}{2}^-, \frac{3}{2}^-)$
1.967	1	$\frac{1}{2}^-$	0.201	1.910	1	$\frac{1}{2}^-$	0.27		
				1.934	4	$\frac{9}{2}^+$	0.19		
2.020									
2.119	4	$\frac{9}{2}^+$	0.844	2.103	4	$\frac{9}{2}^+$	1.02 1.00		
2.260	1	$\frac{1}{2}^-$	0.294	2.155	1	$\frac{1}{2}^-$	0.28 0.26		
2.383	1	$\frac{1}{2}^-$	0.062	2.330	2	$\frac{3}{2}^+$	0.063 1.00		
2.481				2.436	1	$\frac{1}{2}^-$	0.24 0.20		
				2.531	1	$\frac{1}{2}^-$	0.10		
2.622	1	$\frac{3}{2}^-$	0.252	2.591	1	$\frac{1}{2}^-$	0.09		
2.741	1	$\frac{1}{2}^-$	0.080	2.632	1	$\frac{1}{2}^-$	0.13		
2.820	1	$\frac{1}{2}^-$		2.702	1	$\frac{1}{2}^-$	0.10		
2.887	2	$\frac{5}{2}^+$	0.111	2.797	2	$\frac{5}{2}^+$	0.04		
2.970	2	$\frac{3}{2}^+$	0.120	2.870	1	$\frac{1}{2}^-$	0.17		
3.062	1	$(\frac{3}{2}^-)$	0.134						
3.170	2	$\frac{3}{2}^+$	0.221						
3.326	1	$\frac{1}{2}^-$	0.251						
3.497	4	$(\frac{7}{2}, \frac{9}{2})^+$	0.251						
3.622	3	$\frac{7}{2}^+$	0.959						
3.731	2	$\frac{5}{2}^+$	0.078						
3.812	2	$\frac{5}{2}^+$	0.117						
4.174	1	$(\frac{3}{2}^-)$							



### 3.11 Evaluation of cross sections for nucleons up to 3 GeV on $^{12}\text{C}$

Y. Watanabe, O. Iwamoto<sup>†</sup>, T. Fukahori<sup>†</sup>, S. Chiba<sup>‡</sup>, and E.Sh. Sukhovitskii<sup>¶</sup>  
*Department of Advanced Energy Engineering Science, Kyushu University,*

*Kasuga, Fukuoka 816-8580, Japan*

<sup>†</sup>*Nuclear Data Center, JAERI, Japan*

<sup>‡</sup>*Advanced Science Research Center, JAERI, Japan*

<sup>¶</sup>*Radiation Physics and Chemistry Problems Institute, 220109, Minsk-Sosny, Belarus*

Corresponding e-mail: watanabe@aees.kyushu-u.ac.jp

We have performed an evaluation of cross sections on  $^{12}\text{C}$  for both neutron and proton with energies between 20 MeV and 3 GeV. The evaluation is based on measured data as well as predictions from nuclear model calculations and some systematics. The results are compared with available experimental data and the LA150 evaluation. Thick target neutron production spectra for proton incident on carbon are analyzed using the evaluated double-differential (p,xn) cross sections.

#### 1. Introduction

High-energy neutron and proton nuclear data for  $^{12}\text{C}$  are requested with high priority in various applications, such as shielding design of accelerator facilities, dose evaluation in cancer therapy with neutron and proton beams, efficiency calculation of neutron detectors, and nucleosynthesis prediction of light elements, Li, Be, and B. The LA150 library developed in LANL[1,2] as a high-energy nuclear database is currently used for computer code simulations of accelerator-driven systems[3], which treats the nuclear interaction of neutrons and protons with energies up to 150 MeV with materials. In such the simulations, the Monte Carlo codes based on microscopic simulation approach such as the intranuclear cascade model are built-in to deal with the nuclear processes at energies above 150 MeV, instead of the nuclear data library. Because of saving the computation time, however, the nuclear data above 150 MeV is also required for calculations of the transport of high-energy nucleons in medium and estimations of isotope production. In the present work, the cross sections of  $^{12}\text{C}$  have been evaluated for both neutrons and protons with energies between 20 MeV and 3 GeV, in order to meet the requirement and contribute to a development project of the JENDL High-Energy File in the Japanese Nuclear Data Committee (JNDC) [4].

In Sec.2, an outline of evaluation method is described, and several results are shown with experimental data and the LA150 evaluation in Sec. 3. A summary is given in Sec. 4.

#### 2. Evaluation method

The evaluation of cross sections on  $^{12}\text{C}$  has been performed using experimental data as well as predictions from nuclear model calculations and systematics. The cross sections evaluated for both neutrons and protons with energies between 20 MeV and 3 GeV are as follows: total cross sections, elastic scattering cross sections and their angular distributions, light-particle and gamma-ray production cross sections and double-differential cross sections, and isotope production cross sections.

A theoretical model calculation system developed in the present work is illustrated in Fig.1. The calculation codes are divided into two groups, depending upon the incident energy.

A major code used for intermediate energies up to 150 MeV was the GNASH code[5] based on statistical Hauser-Feshbach plus preequilibrium models. Optical model calculations were carried out using the OPTMAN code[6] based on the coupled-channels method with the nuclear Hamiltonian parameters determined by the soft-rotator model[7]. Transmission coefficients obtained by the CC calculation were used in GNASH calculations of particle and gamma ray emission cross sections and isotope production cross sections up to 150 MeV. We have partially revised the GNASH code so as to take into account the surface effect in two nucleons emission in the preequilibrium process and level widths in the statistical decay between discrete levels in residual nuclei. The DDXs in c.m. system were finally converted into the DDXs in laboratory system in an empirical way that the moving source model[8] and the Kalbach systematics[9] are applied to the evaporation and preequilibrium components, respectively. The DWUCK4 code[10] was used for calculations of the following two direct transitions to discrete states: the  $^{12}\text{C}(p,d)$  and  $(n,d)$  pick-up processes for the ground state transition and the  $^{12}\text{C}(p,n)$  charge-exchange reaction for the ground and first excited states. Note that the latter calculation is based on the microscopic DWBA with a Yukawa-type effective interaction of range 1 fm whose depth was determined by normalizing some experimental data.

In the energy range above 150 MeV, the code JQMD[11] based on Quantum Molecular Dynamics (QMD) plus statistical decay model (GEM[12]) was employed. Also, the code TOTELA[4] based on systematics was employed as a tool for evaluation of total, elastic, and proton reaction cross-sections. The Niita systematics[13] was used in TOTELA with partial modification for the empirical formula of elastic angular distributions in which a fitting with experimental data is improved around the first minimum of the angular distributions.

Several isotope production cross sections were evaluated by fitting their available experimental data:  $^7\text{Be}$ ,  $^{10}\text{Be}$ , and  $^{11}\text{C}$  in the  $p+^{12}\text{C}$  reaction. In addition, the JQMD/GEM calculations were applied for energies below 150 MeV for some isotope production reactions in order to obtain rather smooth connection between GNASH and JQMD results as mentioned below.

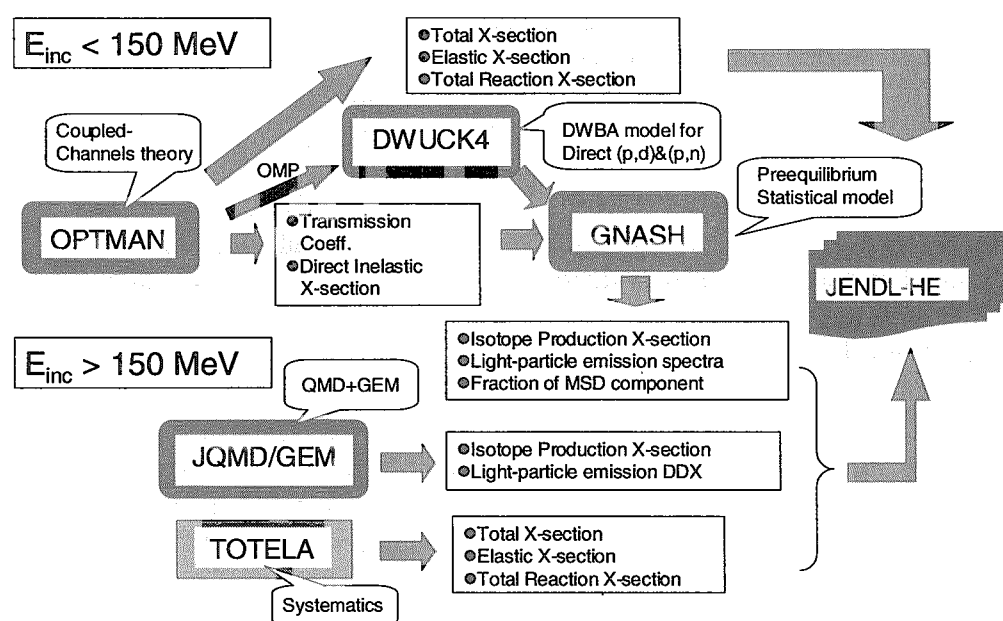


Fig.1 Model calculation code system used in the present evaluation.

### 3. Results and discussions

The evaluated neutron total, elastic, and reaction cross sections are shown in Fig. 2, and compared with available experimental data and the LA150 evaluation[2]. The total cross sections were evaluated by fitting measured data at energies up to 600 MeV with the GMA code[14] and using the Niita systematics at energies above 600 MeV. The neutron elastic cross section was obtained by subtraction of the reaction cross section from the total cross section at each incident energy. The OPTMAN calculation with the parameters determined in ref.[7] was made for evaluation of angular distributions of nucleon elastic scattering from  $^{12}\text{C}$ .

Figure 3 shows light particle production cross sections for the  $n+^{12}\text{C}$  reaction. The evaluated cross sections are compared with the LA150 evaluation and experimental data[15,16,17]. The GNASH prediction for the proton production was multiplied by a factor of 1.3 in order to reproduce the measured data of Slypen et al.[17]. It should be noted that the present evaluation includes the production of triton and  $^3\text{He}$ , while there is no data in the LA150.

In Fig. 4, excitation functions for the  $A=6$  to 11 isobars produced from the  $p+^{12}\text{C}$  reaction are compared with a compilation of measured data by Read and Viola[18] and the LA150 data. The present evaluation shows better agreement with the measured data than the LA150 at energies below 100 MeV. The QMD/GEM calculation for each isotope was normalized to a few experimental data[18] at energies above 1 GeV. The same normalization factor was used for the QMD/GEM prediction for the neutron-induced reactions. Fig. 5 shows a comparison of evaluated excitation function of  $^{11}\text{C}$  production in  $n+^{12}\text{C}$  with experimental data and the LA150 evaluation. The evaluated cross sections are larger than the LA150 data over the whole energy range, and are in good agreement with the measured data[19,20], but underestimate the data of Kim et al.[21] at energies above 40 MeV.

Evaluated double-differential cross sections (DDXs) are compared with measured ones and the LA150 evaluation for  $^{12}\text{C}(p,xp)$  at 68 MeV[22] and  $^{12}\text{C}(p,xn)$  at 3 GeV[23] in Figs. 6 and 7, respectively, showing overall good agreement with the measured data. For the  $^{12}\text{C}(p,xn)$  reaction, the evaluated DDXs for 113 MeV are compared with experimental ones[24] in Fig. 8. Fairly good agreement is obtained except for the high-energy end at 7.5 and 30 degrees. The transformation was made of the equilibrium component of DDXs from the c.m. into the laboratory system based on the moving source model[8]. We emphasize that this led to the agreement seen at low emission energies. Note that the LA150 result reported in ref.[25] overestimates the measurement remarkably at emission energies below 30 MeV.

We have analyzed thick target neutron production spectra for proton incident on carbon using a simple calculation method[26] that involves an integration of the evaluated double differential (p,xn) cross sections with a stopping-power weighting. The result for an incident energy of 68 MeV is compared with measurement[26] in Fig. 9. The calculation shows good agreement with the measured data, except for the high-energy end of the spectra. The disagreement may be partly because we neglect a contribution from (p,xn) on  $^{13}\text{C}$  and the energy resolution of the detector used.

### 4. Summary and conclusion

We have evaluated the cross sections for nucleons up to 3 GeV on  $^{12}\text{C}$ , using available experimental data, model calculations, and systematics. The present evaluation was compared with the LA150 evaluation and the experimental data. In addition, several thick target neutron production data were analyzed using the present DDX data and the satisfactory agreement was obtained except for the high emission energy region where the contribution from  $^{13}\text{C}(p,n)$

is expected. Finally the cross sections evaluated in the present work will be accepted into the JENDL High-Energy File.

### Acknowledgements

The authors are grateful to the member of the JNDC high-energy nuclear data evaluation working group for their valuable comments on this work. A part of this work was supported by International Science and Technology Center under Project B-521 (Funding Party is Japan).

### References

- [1] M.B. Chadwick et al., Nucl. Sci. Eng. **123**, 17 (1996).
- [2] M.B. Chadwick et al., Nucl. Sci. Eng. **131**, 293 (1999).
- [3] M.B. Chadwick et al., Prog. in Nucl. Energy, **38**, 179 (2001).
- [4] T. Fukahori et al., J. Nucl. Sci. and Technol. Suppl. **2**, 25 (2002).
- [5] P.G. Young et al., LA-12343-MS, Los Alamos National Laboratory (1992).
- [6] E.Sh. Sukhovitskii et al., OPTMAN and SHEMMAN codes, JAERI-Data/Code 98-019 (1988).
- [7] S. Chiba et al., J. Nucl. Sci. and Technol. **37**, 498 (2000).
- [8] H. Kitsuki et al., J. Nucl. Sci. and Technol. **38**, 1 (2001).
- [9] C. Kalbach, Phys. Rev. C **37**, 2350 (1988).
- [10] P.D. Kunz and E. Rost, DWUCK4 code, *Computational Nuclear Physics 2: Nuclear Reactions*, (Springer-Verlag, Berlin, 1993, Eds. K. Langanke et al.), p. 88.
- [11] K. Niita et al., Phys. Rev. C, **52**, 2620 (1995); JAERI-Data/Code 99-042 (1999).
- [12] S. Furihata, Nucl. Inst. Method in Phys. Res. B **171**, 251 (2000); S. Furihata and T. Nakamura, J. Nucl. Sci. and Technol. Suppl. **2**, 758 (2002).
- [13] K. Niita, Proc. of the 1999 Nuclear Data Symp.; JAERI-Conf 2000-005 (2000), p.98.
- [14] S. Chiba et al., Proc. 1993 Nuclear Data Symp., JAERI-M 94-019, p.300 (1994).
- [15] T.S. Subramanian et al., Phys. Rev. C **34**, 1580 (1986).
- [16] I. Slypen et al., Phys. Rev. C **53**, 1309 (1996).
- [17] I. Slypen et al., Nucl. Phys. A **671**, 3 (2000).
- [18] S.M. Read and V.E. Viola, Jr., At. Data Nucl. Data Table, **31**, 359 (1984).
- [19] O.D. Brill et al., Sov. Phys. Dokl. **6**, 24 (1961).
- [20] T.S. Soewarsono et al., JAERI-M-92-027 (1992), p.354.
- [21] E. Kim et al., Nucl. Sci. and Eng., **129**, 209 (1998).
- [22] M. Harada et al., J. of Nucl. Sci. and Technol., Suppl. **1**, 687 (2000); J. Nucl. Sci. and Technol. Suppl. **2**, 393 (2002).
- [23] K. Ishibashi et al., J. Nucl. Sci. Technol. **34**, 529 (1997).
- [24] M.M. Meier et al., Nucl. Sci. Eng. **102**, 310 (1989).
- [25] M.B. Chadwick et al., Proc. of Int. Conf. on Nuclear Data for Science and Technology, Trieste (1997), p.1683.
- [26] S. Meigo et al., Proc. of Int. Conf. on Nuclear Data for Science and Technology, Trieste (1997), p.413.

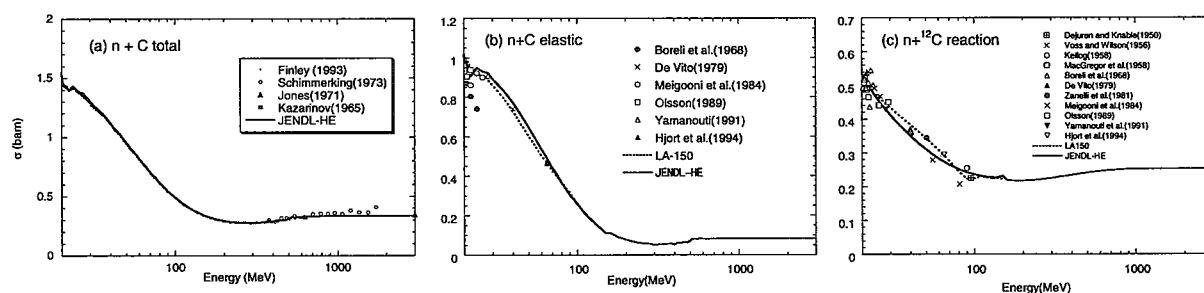


Fig.2 Total, elastic and reaction cross sections for  $n+^{12}\text{C}$ . The solid curves (JENDL-HE) are the present evaluation and the dotted ones are the LA150 evaluation.

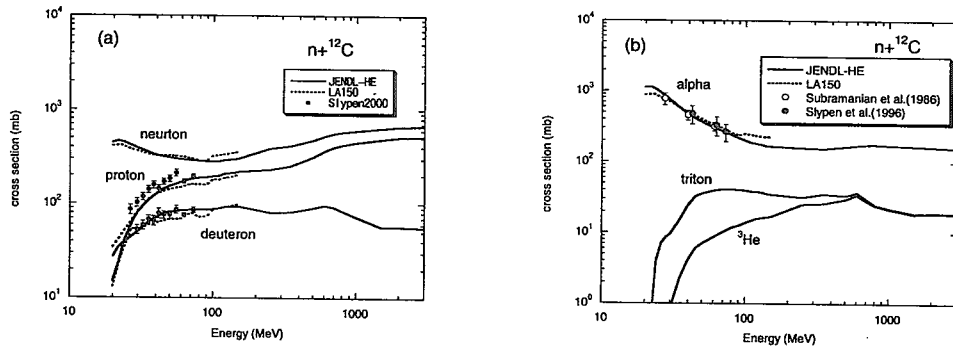


Fig.3 Light particle production cross-sections for  $n+^{12}\text{C}$ . The solid curves (JENDL-HE) are the present evaluation and the dotted ones are the LA150 evaluation.

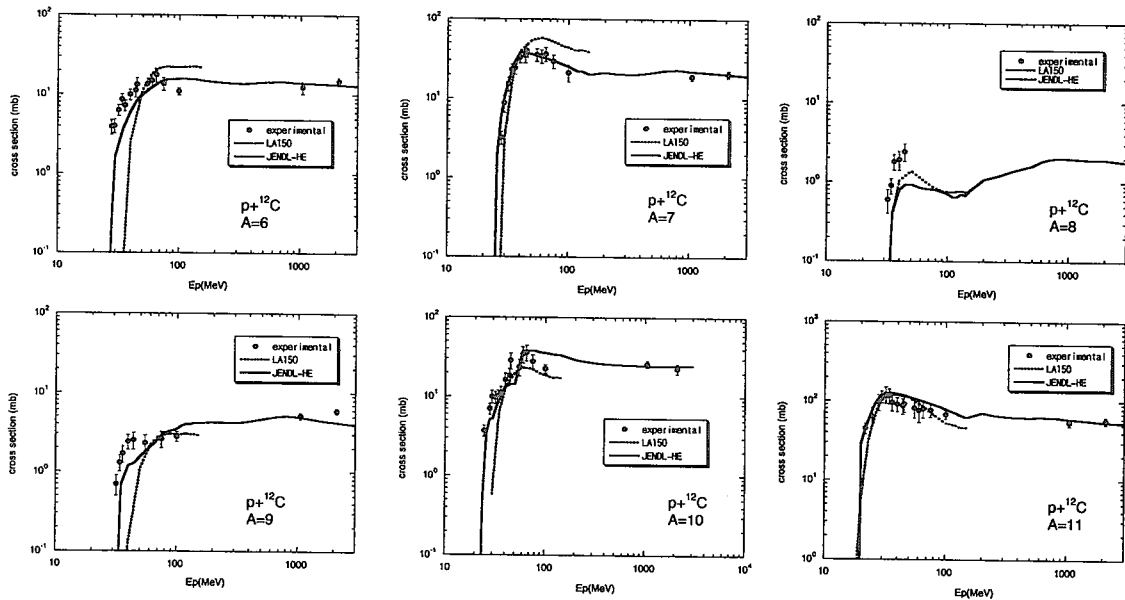


Fig.4 Excitation functions for the A=6 to 11 isobars produced from the  $p+^{12}\text{C}$  reaction. The solid curves (JENDL-HE) are the present evaluation and the dotted ones are the LA150 evaluation.

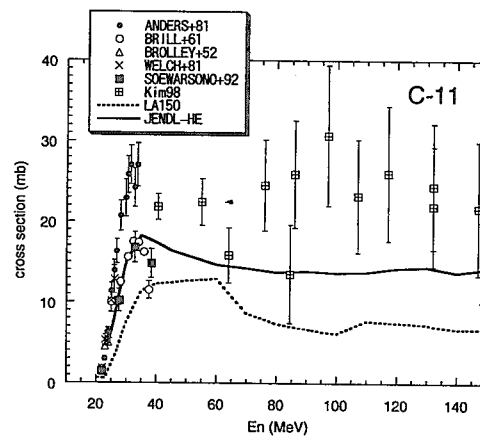


Fig.5 Excitation function of the  $^{12}\text{C}(n,2n)^{11}\text{C}$  reaction. The solid curves (JENDL-HE) are the present evaluation and the dotted ones are the LA150 evaluation.

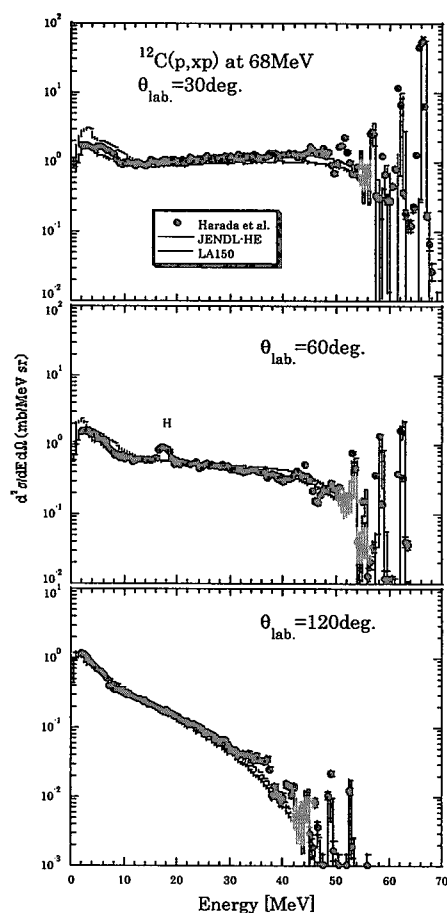


Fig.6 Double-differential (p,xp) cross sections at 68 MeV. The solid histograms are the present evaluation and the dotted ones are the LA150 evaluation. The experimental data are taken from [22].

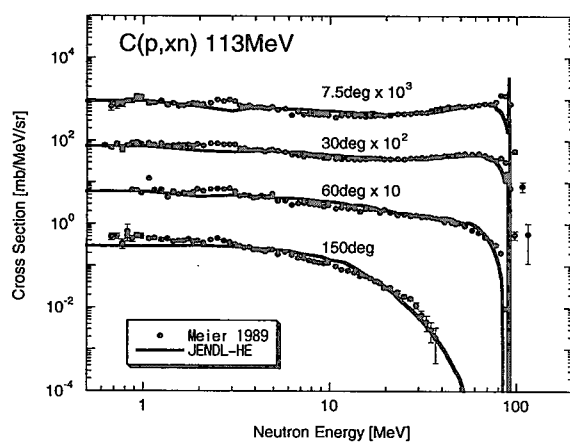


Fig.8 Double-differential (p,xn) cross sections for 113 MeV. The experimental data are taken from [24].

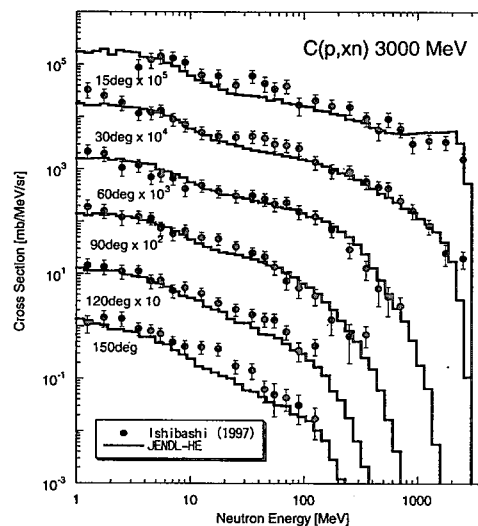


Fig.7 Double-differential (p,xn) cross sections at 3 GeV. The experimental data are taken from [23].

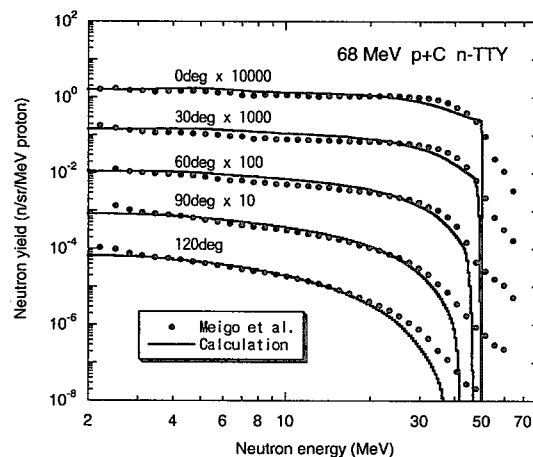


Fig.9 Thick target neutron production spectra for 68-MeV proton incident on carbon. The experimental data are taken from [26].



### 3.12 Brief Note on the Statistical Calculation of Final Continuum Reaction Cross Sections of Light Nuclides

Toru Murata

AITEL Corporation

4-1 Ukishima-cho Kawasakiku, Kawasaki, 210-0862, Japan

murat@green.ocn.ne.jp

#### 1. Introduction

Statistical models are usually adopted for the calculation and evaluation of reaction cross sections to the final continuum state using the level density formula such as given by Gilbert and Cameron<sup>1)</sup>. The level density parameters are determined to reproduce level structure and/or resonance level spacing of the nucleus. In the statistical compound nucleus model, cross sections to discrete levels decrease abruptly, and continuum level cross section increase strongly above the energy point where the continuum levels switched on. In the present study, for the nucleus which level scheme were well determined up to higher excitation energy more than 10 MeV, discrete level cross sections were calculated and summed up and compared with the cross section to the assumed continuum level corresponding to the discrete levels above several MeV excitation energy. Calculation of the (n,n') cross sections were made with CASTHY code<sup>2)</sup> of Moldauer model option using level density parameters determined with former method<sup>3)</sup>. It is shown that the assumed continuum cross section is fairly large compared with the summed up cross section. Origins of the discrepancy were discussed.

#### 2. Calculation

##### 1) Level Density Formula and Parameters

The level density formulae of Fermi gas type and constant temperature model given in CASTHY code are adopted. The level density parameters are determined to reproduce the stair-case plot of level schemes of target nucleus;  $^7\text{Li}$  and  $^{16}\text{O}$ . The stair-case plots are shown in Fig.1 for  $^7\text{Li}$  and Fig.2 for  $^{16}\text{O}$  comparing with integrated values of level density. The level density parameters are given in the figures. The parameters are T; nuclear temperature, a; Fermi gas constant,  $E_c$ ; connection energy of constant temperature model and Fermi gas model, PE; pairing energy, Co; Fermi gas model normalization factor, SPC; spin cutoff factor and  $U_c = E_c - \text{PE}$ .

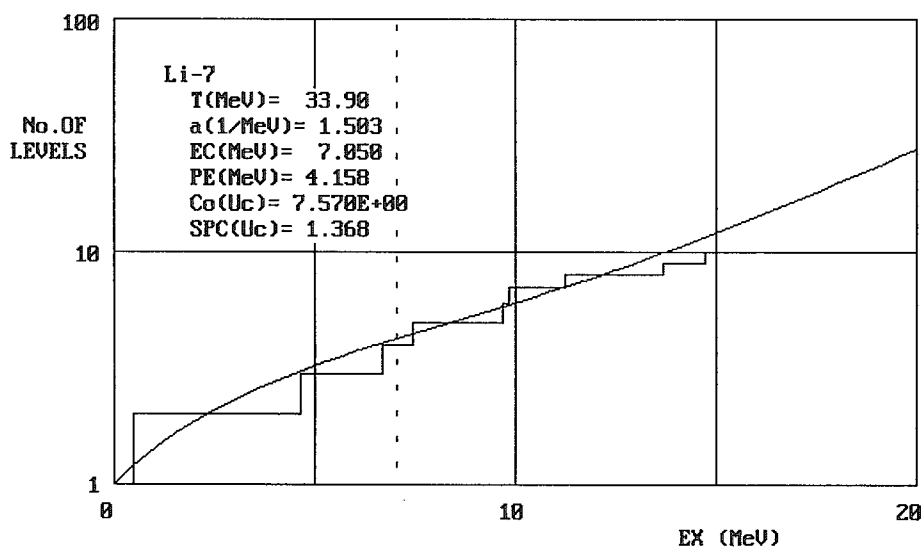


Fig.1. Staircase plot of  ${}^7\text{Li}$  excited levels and determination of level density parameters of  ${}^7\text{Li}$ .

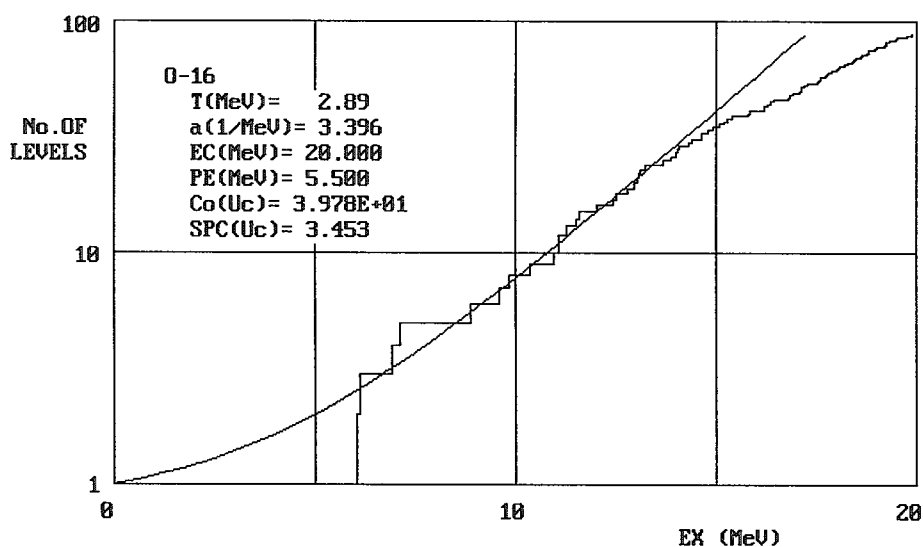


Fig. 2. Staircase plot of  ${}^{16}\text{O}$  excited levels and determination of level density parameters of  ${}^{16}\text{O}$ .

## 2) Cross Section Calculation

Neutron inelastic scattering cross sections to continuum state above some excitation energy ( $Ex \geq 6.50\text{ MeV}$  for  ${}^7\text{Li}$  and  $Ex \geq 6.92\text{ MeV}$  for  ${}^{16}\text{O}$ ) were calculated at first using level density parameters determined in section 2.1. Then the inelastic scattering cross sections to discrete levels corresponding to the same excitation energy range were



calculated and summed up. Comparison between the continuum cross section and the summed up cross section is made in Fig.3 for  ${}^7\text{Li}$  and in Fig.4 for  ${}^{16}\text{O}$ . In the figures, dashed curve 1) is the cross section of final continuum state calculated with the level density parameters given in the above figures, dashed curve 2), same cross section calculated with spin cutoff factor 3 times as large as that of curve 1) and solid line represent the summed up discrete cross section.

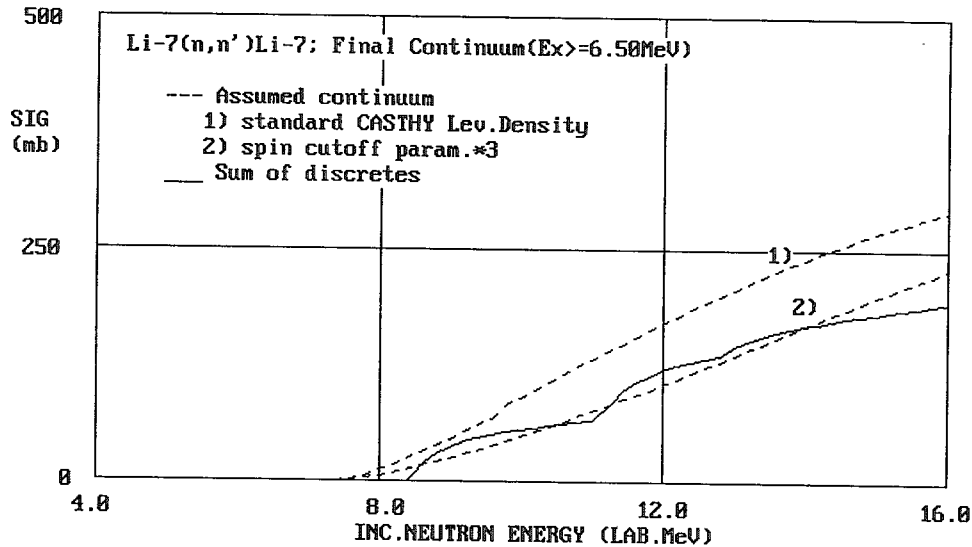


Fig.3. Calculated  ${}^7\text{Li}(n,n')$  final continuum cross section comparison between sum of discrete levels (solid line) and assumed continuum state(dashed line).

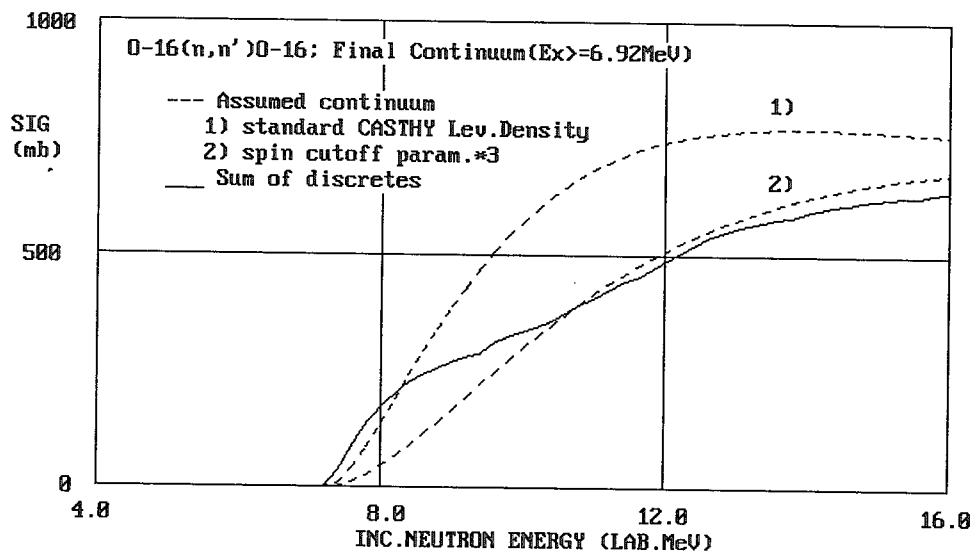


Fig.4. Calculated  ${}^{16}\text{O}(n,n')$  final continuum cross section comparison between sum of discrete levels (solid line) and assumed continuum state(dashed line).

### 3. Discussion

As is shown in Fig.3 and Fig.4, the cross section to the assumed continuum state is larger about 1.5 times than the summed up cross sections. In each case, the 3 times larger spin cutoff factor (dashed curve 2) gives rather good agreement with the summed up cross sections. Larger spin cutoff factor suppresses number of low spin state, and will reduce the continuum cross section. So, there will be possibility that the formula of spin cutoff factor is inadequate. To check the calculated spin cutoff factor, spin distribution of  $^{17}\text{O}$  was examined. The result is shown in Fig.5 and adequacy of the value is confirmed.

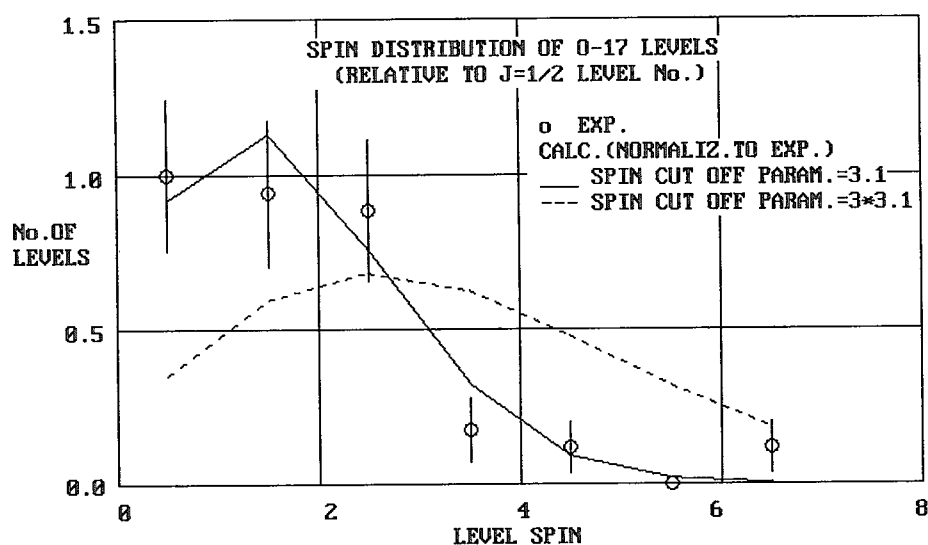


Fig.5. Spin distribution of  $^{17}\text{O}$  excited levels and determination of the spin-cutoff parameter. Solid line is calculated with formula of spin cutoff factor given in CASTHY code. Dashed line shows the result with 3 times large factor.

There is possibility that the small differences in the stair-case plot between level scheme plot and level density integral values will cause large difference of the cross section. To check this, dummy level scheme easy to be reproduced by level density formulae was made for dummy  $^{16}\text{O}$  nucleus. Spin-parity distribution was also made artificially to reproduce theoretical distribution. Stair-case plot of the dummy  $^{16}\text{O}$  is shown in Fig.6 and cross section plot in Fig.7. The difference of the cross section was somewhat reduced but still remain same extent.

Other origins of the cross section discrepancy are

- 1) Some level density formula was applied to determine level density parameters inconsistent with that of cross section calculation. (Application error)
- 2) Spin parity distribution of the level scheme can not be described well by the

present level density formula.

- 3) The present discrepancy is in the range of statistical fluctuation, which is caused by spin-parity distribution fluctuation.
- 4) Present statistical model can not deal properly the competition between continuum state and discrete levels.

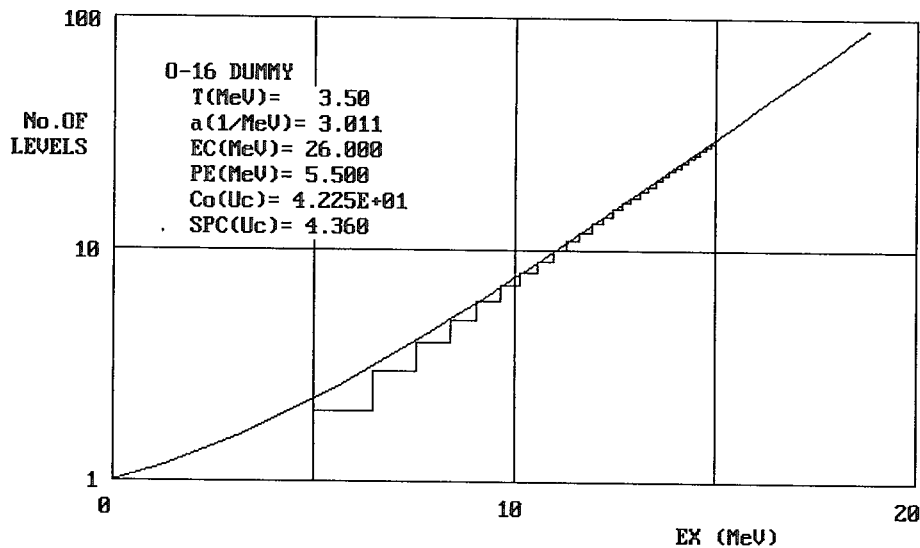


Fig.6. Staircase plot of dummy  $^{16}\text{O}$  excited levels and determination of level density parameters of  $^{16}\text{O}$

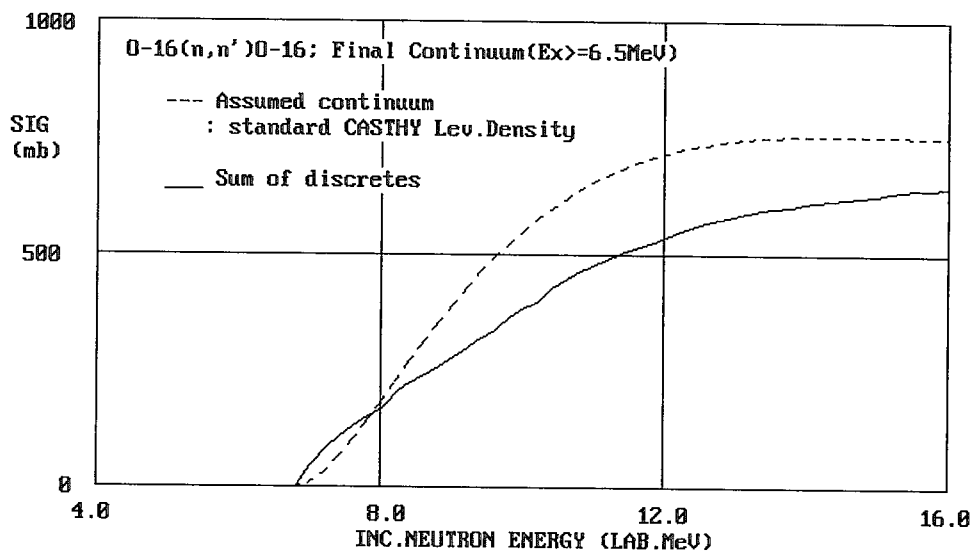


Fig.7. Calculated dummy  $^{16}\text{O}(n,n')$  final continuum cross section comparison between sum of discrete levels (solid line) and assumed continuum state(dashed line).

#### 4. Conclusions

The number of excited levels may be reproduced by level density formula, though the cross section depends on the spin-parity of the levels and the dependence on low spin states is rather large. The spin cutoff parameter calculated with a rigid body model gives large component of low spin states.

Present study was restricted in the framework of the statistical compound nucleus model. In the case of inclusion of pre-compound process, discrete level cross sections increase so much and continuum cross sections decrease.

For excited states of light nuclei, excitation energy below about 10 MeV or more, may not be treated as continuum state with simple level density parameter set.

Thanks are due to Dr. Y. Watanabe (Kyushu Univ.) for valuable discussion and Dr. T. Nakagawa (JNDC) for preparation of CASTHY code and helpful support.

#### References

- [1] Gilbert, A., Cameron, A. G.W. : Can.J.Phys.43,1446(1965)
- [2] Igarasi, S., Fukahori, T. : JAERI 1321 (1991)
- [3] Murata, T. : JAERI-Conf 2001-006 (2001), p.289

### 3.13 Evaluation of Cross Sections of $^{63}\text{Cu}$ and $^{65}\text{Cu}$ for JENDL High Energy File

N. Yamano, T. Fukahori\*, and S. Chiba\*\*

*Department of Nuclear Design, Sumitomo Atomic Energy Industries, Ltd.,  
2-10-14 Ryogoku, Sumida-ku, Tokyo 130-0026 Japan*

*\*Nuclear Data Center, Department of Nuclear Energy System, JAERI, Japan*

*\*\*Advanced Science Research Center, JAERI, Japan*

*e-mail: yamano@sae.co.jp*

Cross sections of  $^{63}\text{Cu}$  and  $^{65}\text{Cu}$  for neutron and proton induced reactions have been evaluated up to 3 GeV for the High Energy File of Japanese Evaluated Nuclear Data Library (JENDL-HE). Different theoretical model codes were employed in this evaluation. For intermediate energy region between 20 and 150 MeV, GNASH based on statistical Hauser-Feshbach and preequilibrium models was used. Transmission coefficients calculated with DWUCK were used in the GNASH calculations of particle and photon emission cross sections and isotope production cross sections up to 150 MeV. The input parameters for the model codes were determined through analysis of experimental data in this energy region. For high-energy region between 150 MeV and 3 GeV, the JQMD-GEM code based on Quantum Molecular Dynamics (QMD) with statistical decay model (GEM) was employed. For energy region below 20 MeV, the existing JENDL-3.3 data were adopted. Several isotope production cross sections above 20 MeV were analyzed using the GMA code based on the generalized least-squares method or empirical fits in which experimental data were available. The results were compared with available experimental data as well as integral experiments such as thick target neutron yields.

#### 1. Introduction

The high-energy nuclear data are important for nuclear design and safety analysis in accelerator applications such as the J-PARK project jointly conducted by JAERI and KEK. The High Energy Nuclear Data Evaluation Working Group in the Japanese Nuclear Data Committee (JNDC) continues nuclear data evaluation for neutron and proton induced reactions for energies up to 3 GeV towards completion of JENDL High Energy File (JENDL-HE).<sup>1)</sup> Copper is one of the first priority nuclides requested by user's community in JNDC. Guided by experimental data, we have performed a comprehensive set of nuclear model calculations for neutron and proton reactions on  $^{63}\text{Cu}$  and  $^{65}\text{Cu}$  for incident energies between 20 MeV and 3 GeV.

Several theoretical model codes were employed in this evaluation. For intermediate energies between 20 and 150 MeV, The GNASH code<sup>2)</sup> based on statistical Hauser-Feshbach and preequilibrium models was used. The Distorted Wave Born Approximation (DWBA) code DWUCK<sup>3)</sup> was used to determine direct-interaction cross sections needed as input for the GNASH calculations of particle and photon emission cross sections and isotope production cross sections up to 150 MeV. For high energies between 150 MeV and 3 GeV, the JQMD-GEM code<sup>4)</sup> based on Quantum Molecular Dynamics (QMD) with statistical decay model (GEM) was employed. For energies below 20 MeV, the existing JENDL-3.3<sup>5)</sup> data were adopted. Several isotope production cross sections above 20 MeV were analyzed using the GMA code<sup>6)</sup> based on the generalized least-squares method or empirical fits in which experimental data were available. This evaluation scheme is shown in Fig. 1. The optical-model parameters, discrete energy levels, and other parameters needed in the GNASH calculations were determined through analysis of experimental data in this energy region, and are discussed in Chapter 2. Comparison of calculated results to measured data including integral experiments such as thick target neutron yields (TTY) is given in Chapter 3.

#### 2. Parameter Determination

##### 2.1 Optical-model parameters

For high-energy data evaluation, the optical-model parameters are essential input for the nuclear model calculations, much effort was spent to determine good sets of neutron optical-model parameters for  $n + ^{63,65}\text{Cu}$  and proton optical-model parameters for  $p + ^{63,65}\text{Cu}$  so as to reproduce the elastic scattering angular-distribution data available, as well as the nonelastic, elastic and total cross sections. To obtain the neutron optical-model parameters, the experimental natural total cross-section data sets selected for fitting were those of Guenther et

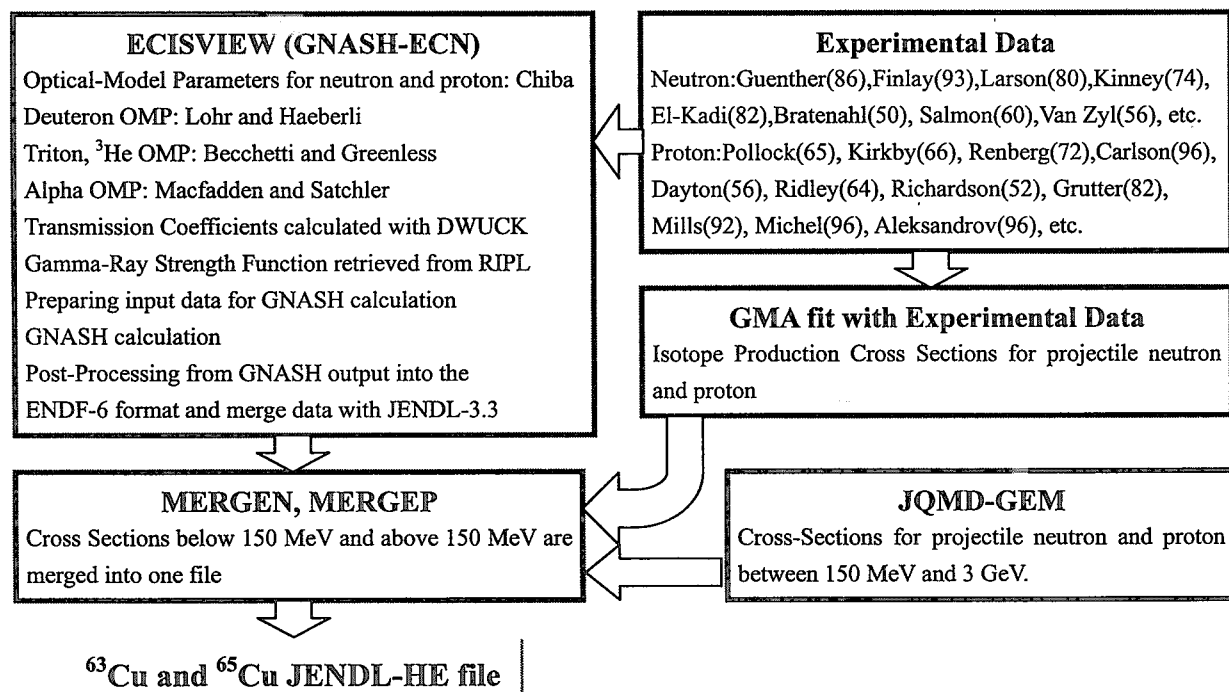


Fig. 1 Evaluation scheme of nuclear data evaluation for Cu

al.<sup>7)</sup> from 1.2 to 4.5 MeV; Larson et al.<sup>8)</sup> from 4.5 to 5.3 MeV; Finlay et al.<sup>9)</sup> from 5.3 to 600 MeV; and Schimmerling et al.<sup>10)</sup> from 379 to 1731 MeV. The experimental angular-distribution data were taken from those of Guenther et al. at 2.0, 2.5, 3.0, and 3.9 MeV; Kinney and Perey<sup>11)</sup> at 5.5, 7.0, and 8.5 MeV; El-Kadi et al.<sup>12)</sup> at 7.96, 9.94, 11.93, and 13.92 MeV; Bratenahl et al.<sup>13)</sup> at 84 MeV; Salmon<sup>14)</sup> at 96 MeV; and Van Zyl et al.<sup>15)</sup> at 136 MeV. Kinney and Perey, and El-Kadi measured data for both <sup>63</sup>Cu and <sup>65</sup>Cu at each energy; the other data sets are for natural Cu. The angular distributions for <sup>63</sup>Cu and <sup>65</sup>Cu were similar to each other, and did not show significant isotopic dependence, so that all of the above data sets were used simultaneously to find out one set of optical-model parameters for both <sup>63</sup>Cu and <sup>65</sup>Cu. The isotopic cross sections were obtained using a  $A^{2/3}$  dependence. For proton incident reactions, the experimental natural total reaction cross-section data sets selected for fitting were those of Pollock and Schrank<sup>16)</sup> at 16.37 MeV; Kirkby and Link<sup>17)</sup> at 99 MeV; and Renberg et al.<sup>18)</sup> from 225 to 548 MeV. The other data were retrieved from compilation by Carlson.<sup>19)</sup> The experimental angular-distribution data were taken from those of Dayton and Schrank<sup>20)</sup> at 17 MeV; Ridley and Turner<sup>21)</sup> at 30.3 MeV; and Richardson et al.<sup>22)</sup> at 340 MeV. These measured data are for natural Cu. The isotopic cross sections were obtained using a  $(1+A^{1/3})^2$  dependence.

To obtain the neutron and proton optical-model parameters, we employed ECISVIEW<sup>23)</sup> based on a modified optical-model formula developed by Chiba to fit the above selected sets of elastic scattering angular-distribution data as well as the total cross sections. The best-fit parameter set was then used for the rest of the model calculations to generate required transmission coefficients. For the other outgoing channels we used global potentials, i.e. the deuteron potential of Lohr and Haeberli,<sup>24)</sup> the triton and <sup>3</sup>He potentials of Becchetti and Greenless,<sup>25)</sup> and the alpha potential of Macfadden and Satchler.<sup>26)</sup> Figures 2(a) and (b) show comparisons of calculated results with measured elastic scattering angular-distribution data for neutrons. Figures 3(a) and (b) indicate comparisons of calculated results with measured total cross sections. Figures 4(a) and (b) also show comparisons of calculated results with measured elastic scattering angular-distribution data for protons. Figures 5(a) and (b) also indicate comparisons of calculated results with measured total reaction cross sections for protons.

## 2.2 The direct reaction model and parameters

The DWBA code DWUCK was employed to calculate the direct-interaction component of the inelastic scattering cross sections to a number of levels in <sup>63,65</sup>Cu for which information was available. The deformation parameters and the energy levels for the several MeV were taken from McCarthy and Crawley,<sup>27)</sup> and the other values were determined by considering measured data of neutron emission spectra for (n,xn) and (p,xn) reactions.

### 2.3 Gamma-ray strength functions, Level-density parameters and the other parameters

The gamma-ray strength function model of Uhl and Kopecky<sup>28)</sup> was employed, and the parameters given by Jianfeng<sup>29)</sup> compiled in the RIPL library were adopted. We used the standard level density options of the GNASH code. For the preequilibrium part, the particle-hole level density of Williams was used. For compound nucleus reactions, the Ignatyuk formula<sup>30)</sup> was adopted, and the partial level density parameters for (p, xn) and (p, xnp) reactions were slightly modified to reproduce measured neutron emission spectra from (p, xn) reactions.

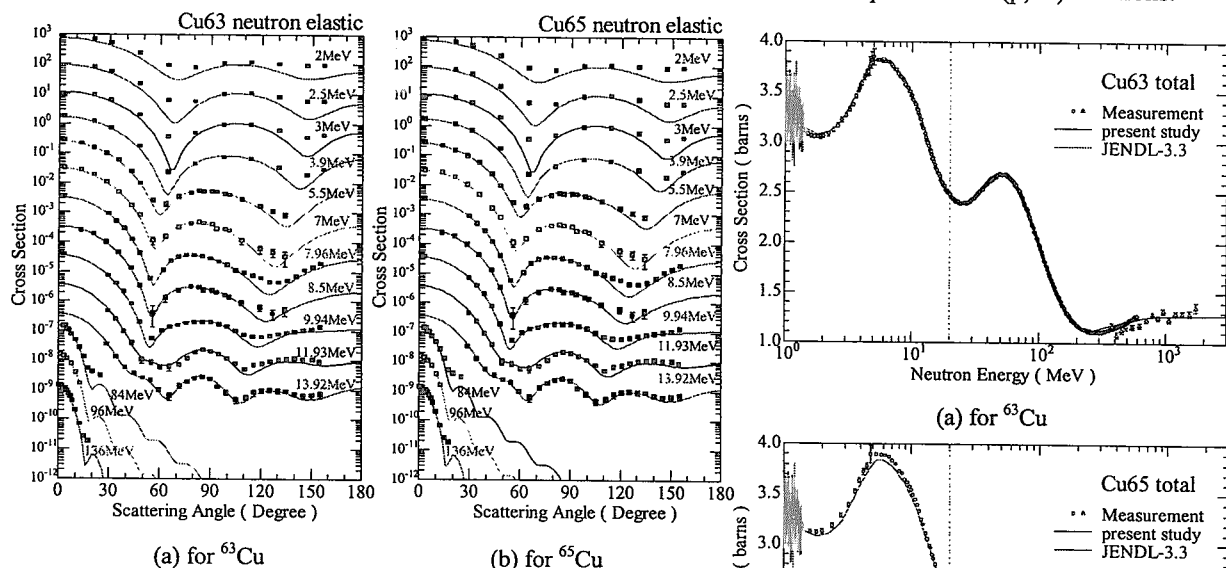


Fig. 2 Results of elastic scattering angular distribution for Cu

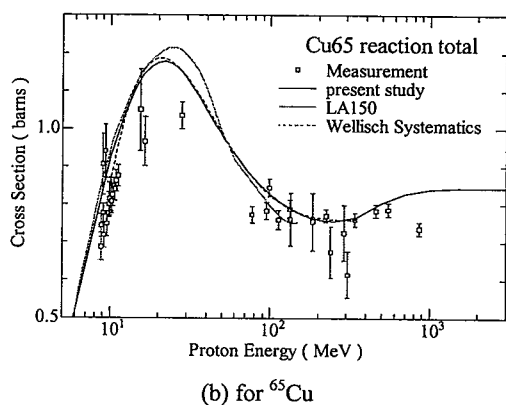
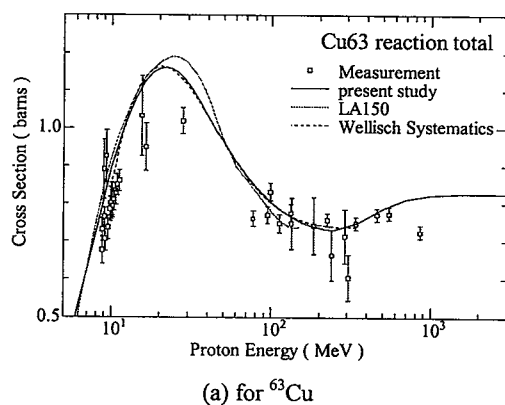


Fig. 5 Results of total reaction cross sections for Cu

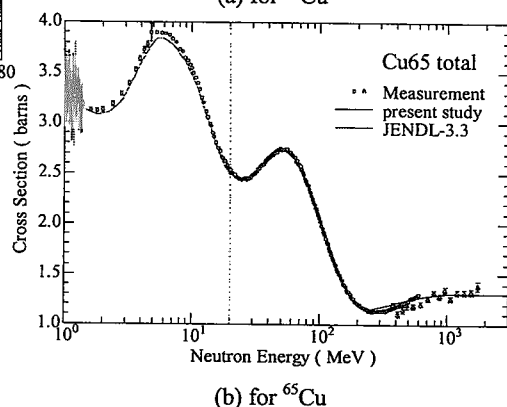


Fig. 3 Results of total cross sections for Cu

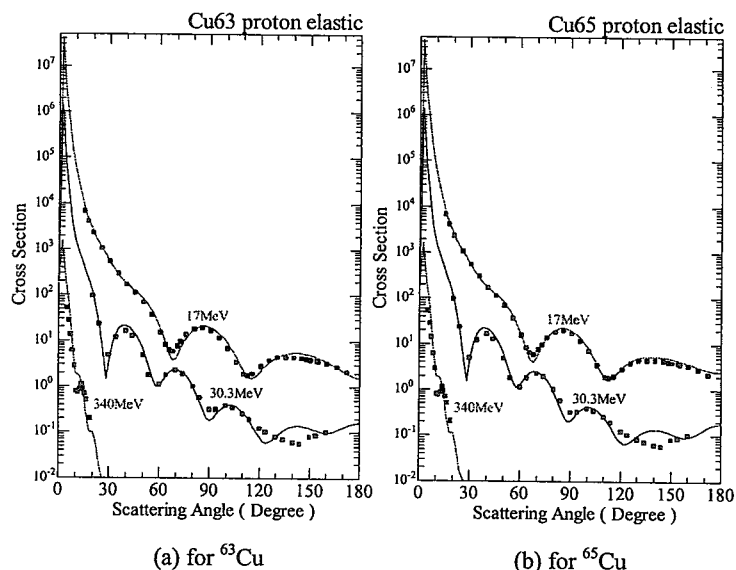


Fig. 4 Results of elastic scattering angular distribution for Cu

### 3. Comparison of calculations with experiments

#### 3.1 Neutron emission spectra

A few measurements exist for neutron emission spectra above 20 MeV for Cu. Figure 6 shows a comparison for 25.7 MeV  $^{65}\text{Cu}(n, xn)$  reaction data by Marcinkowski et al.<sup>31)</sup> A comparison of calculated energy-angle double differential cross sections (DDX) with the measurement is presented in Fig. 7. The calculated results are in good agreement with measurements.

For projectile proton reactions, measurements of  $^{63}\text{Cu}(p, xn)$  reaction at 25 MeV and  $^{65}\text{Cu}(p, xn)$  reaction at 26 MeV are shown Figs. 8 and 9, respectively. The DDX measurement for 26 MeV  $^{65}\text{Cu}(p, xn)$  reaction by Scobel et al.<sup>32)</sup> is presented in Fig. 10. The calculated results are in good agreement with experiments.

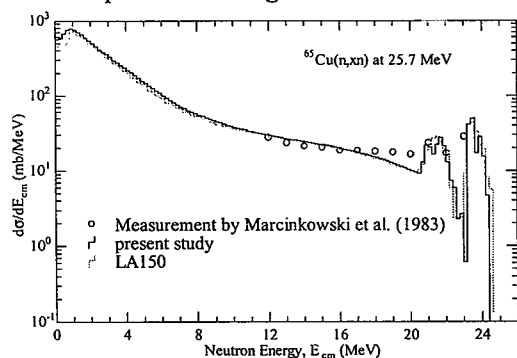


Fig. 6 Results of neutron emission spectrum for  $^{65}\text{Cu}$

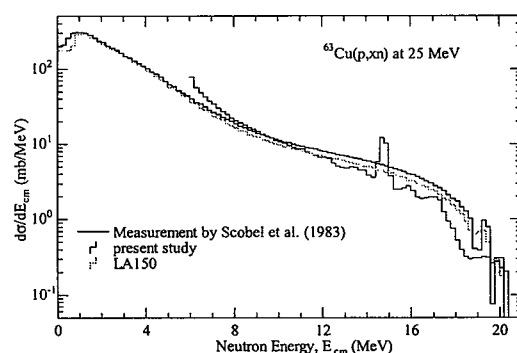


Fig. 8 Results of neutron emission spectrum for  $^{63}\text{Cu}$

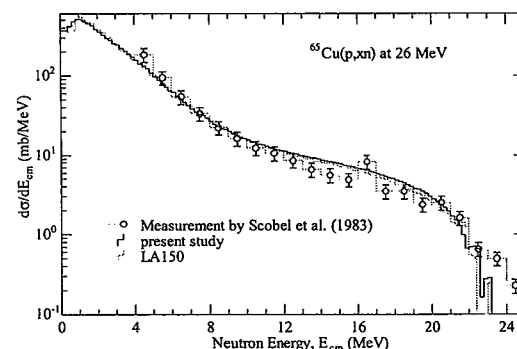


Fig. 9 Results of neutron emission spectrum for  $^{65}\text{Cu}$

#### 3.2 Isotope production cross sections

Isotope production cross sections for  $^{63}\text{Cu}$  and  $^{65}\text{Cu}$  were simultaneously evaluated by using the GMA code in order to satisfy measured data for natural Copper in which measured data were available. Figure 11 shows the isotope production cross sections for  $^{63}\text{Cu}(p, x)^{63}\text{Zn}$  reaction. In this case,  $^{63}\text{Zn}$  isotope is mainly produced by  $^{63}\text{Cu}(p, n)^{63}\text{Zn}$  and  $^{65}\text{Cu}(p, 3n)^{63}\text{Zn}$  reactions. These cross sections were simultaneously evaluated by using GMA or empirical fits,

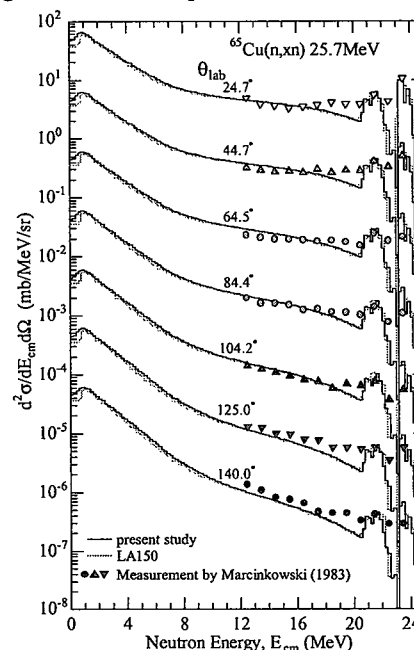


Fig. 7 Results of neutron emission spectrum for  $^{65}\text{Cu}$

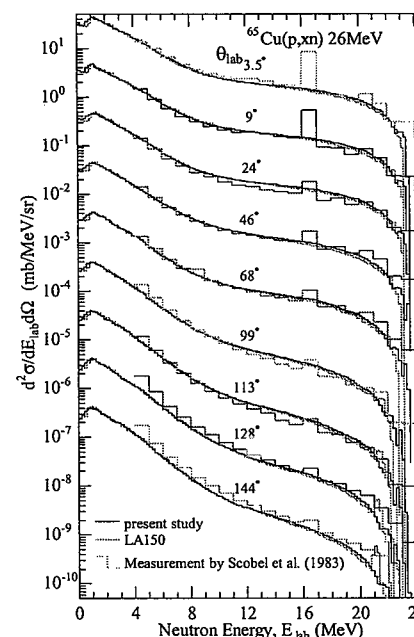


Fig. 10 Results of neutron emission spectrum for  $^{65}\text{Cu}$



and are presented in Figs. 12 and 13, respectively.

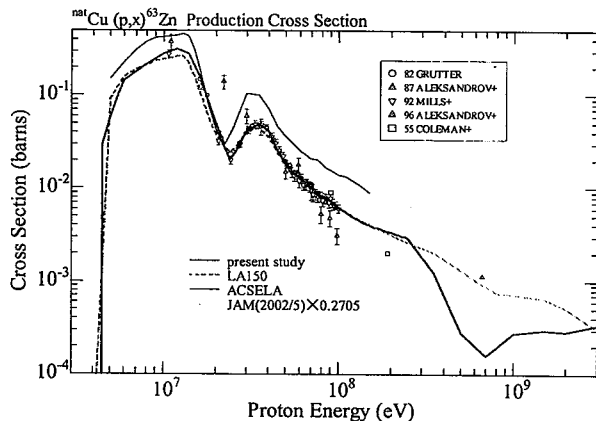


Fig. 11 Cross sections for  $^{nat}\text{Cu}(p, x)^{63}\text{Zn}$  reaction

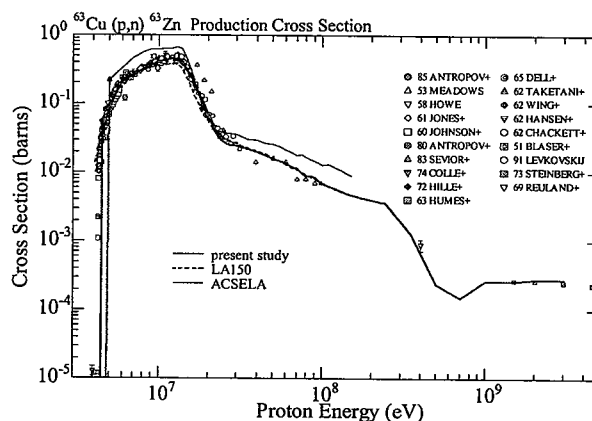


Fig. 12 Cross sections for  $^{63}\text{Cu}(p, n)^{63}\text{Zn}$  reaction

### 3.3 Thick target neutron yields

Neutron spectrum measurement from thick target bombarded by protons is one of good benchmarks for integral test of nuclear data. Since high energy cross-section measurements were not available, we compared thick target neutron yields (TTY) calculated with the QMDPROD code developed by Meigo using energy-angle double differential cross section compiled in this study. Comparisons of calculated TTY with measurements for 30, 52 and 67 MeV projectile protons are shown in Figs. 14(a) to (c), respectively. Calculated neutron emission spectra show in good agreement with measurements.

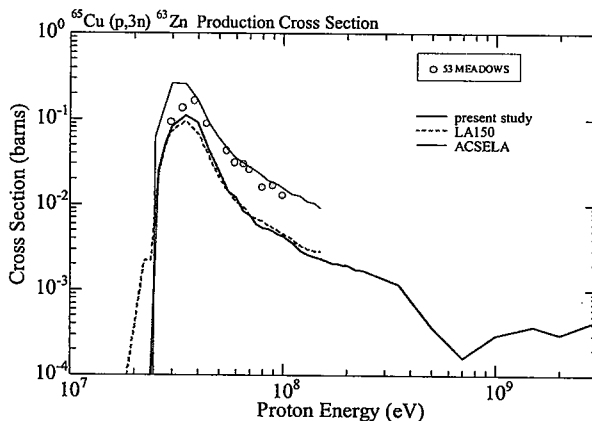
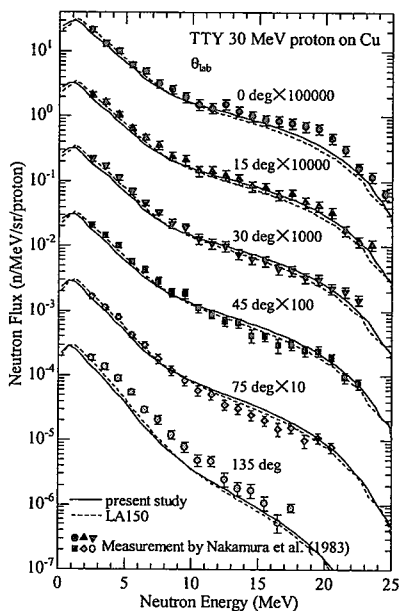
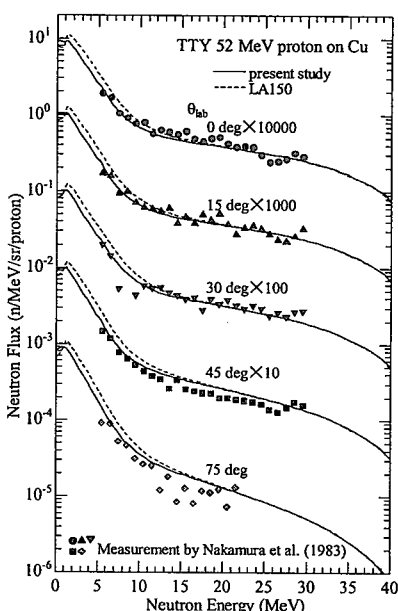


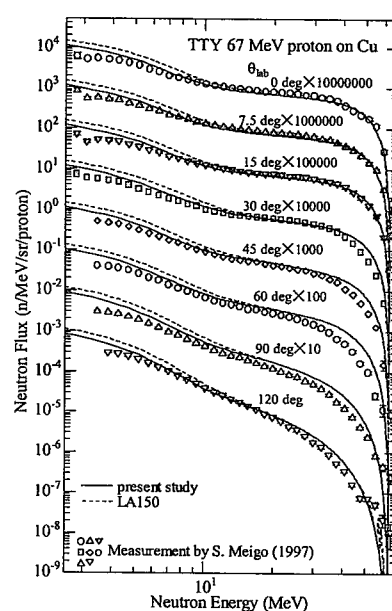
Fig. 13 Cross sections for  $^{65}\text{Cu}(p, 3n)^{63}\text{Zn}$  reaction



(a) for 30 MeV



(b) for 52 MeV



(c) for 67 MeV

Fig. 14 Results of thick target neutron yields for natural Cu bombarded by protons.

#### 4. Conclusion

Neutron and proton induced cross-section data for  $^{63}\text{Cu}$  and  $^{65}\text{Cu}$  have been evaluated up to 3 GeV for the High Energy File of Japanese Evaluated Nuclear Data Library (JENDL-HE). The results were compared with available experimental data and other evaluations as well as integral experiments such as thick target neutron yields, and a good agreement was obtained with measurement. However, number of energy-angle double differential cross-section measurements above 100 MeV is quite few, so that the accuracy of evaluated data is not clear in this energy region. We need cross-section measurements including DDX data in order to evaluate accurate nuclear data for high-energy accelerator applications. Integral measurement such as thick target neutron yield is valuable to validate nuclear data for projectile proton.

#### References

- 1) T. Fukahori, et al., *J. Nucl. Sci. Technol.*, Supplement 2, pp. 25-30 (2002).
- 2) P.G. Young, E.D. Arthur, M.B. Chadwick, "Comprehensive nuclear model calculations: Introduction to the theory and use of the GNASH code," *Workshop on nuclear reaction data and nuclear reactors*, April 15-May 17, 1996, Trieste, Italy.
- 3) P.D. Kunz, "DWUCK4 - Distorted Waves (1 July 1978), U. Colorado-Version," unpublished (1992).
- 4) K. Niita, et al., "Development of JQMD (Jaeri Quantum Molecular Dynamics) Code," JAERI-Data/Code 99-042 (1999).
- 5) K. Shibata, et al., *J. Nucl. Sci. Technol.*, **39**, 1125 (2002).
- 6) S. Chiba, private communication (1999).
- 7) P. Guenther, D.L. Smith, A.B. Smith, J.F. Whalen, *Nucl. Phys.*, **A448**, 280 (1986).
- 8) D.C. Larson, J.A. Harvey, N.W. Hill, ORNL-5787 (1981).
- 9) R.W. Finlay et al., *Phys. Rev. C* **47**, 237 (1993).
- 10) W. Schimmerling, T.J. Devlin, W.W. Johnson, *Phys. Rev. C* **7**, 248 (1973).
- 11) W.E. Kinney, F.G. Perey, ORNL-4908 (1974).
- 12) S.M. El-Kadi, et al., *Nucl. Phys.*, **A390**, 509 (1982).
- 13) A. Bratenahl, S. Fernbach, R.H. Hildebrand, C.E. Leith, B.J. Moyer, *Phys. Rev.*, **77**, 597 (1950).
- 14) G.L. Salmon, *Nucl. Phys.*, **21**, 15 (1960).
- 15) C.P. Van Zyl, R.G.P. Voss, R. Wilson, *Philosophical Magazine*, **1**, 1003 (1956).
- 16) R.E. Pollock, G. Schrank, *Phys. Rev.*, **B140**, 575 (1965).
- 17) P. Kirkby, W.T. Link, *Canadian J. Phys.*, **44**, 1847 (1966).
- 18) P.U. Renberg et al., *Nucl. Phys.*, **A183**, 81 (1972).
- 19) D.C. Carlson, *At. Data and Nucl. Data Tables*, **63**, 94 (1996).
- 20) I.E. Dayton, G. Schrank, *Phys. Rev.*, **101**, 1358 (1956).
- 21) B.W. Ridley, J.F. Turner, *Nucl. Phys.*, **58**, 497 (1964).
- 22) R.E. Richardson, W.P. Ball, C.E. Leith, B.J. Moyer, *Phys. Rev.*, **86**, 29 (1952).
- 23) A.J. Koning, J.J. van Wijk, J.P. Delaroche, "ECISVIEW: A Graphical Interface for ECIS95," Proc. of the NEA Specialists' Meeting on the Nucleon Nucleous Optical Model up to 200 MeV," Bruyères-le-Châtel, Nov. 13-15, 1996.
- 24) J.M. Lohr, W. Haeberli, *Nucl. Phys.*, **A232**, 381 (1974).
- 25) F.D. Becchetti, Jr., G.W. Greenlees, *Phys. Rev.*, **182**, 1190 (1969).
- 26) L. Macfadden, G.R. Satchler, *Nucl. Phys.*, **84**, 177 (1966).
- 27) A.L. McCarthy, G.M. Crawley, *Phys. Rev.*, **150**, 935 (1966).
- 28) J. Kopecky, M. Uhl, *Phys. Rev. C* **41**, 1941 (1990).
- 29) L. Jianfeng, Su Zongdi, Zuo Yixin, IAEA-TECDOC-1034 (1998).
- 30) A.V. Ignatyuk, G.N. Smirenkin, A.S. Tishin, *Sov. J. Nucl. Phys.*, **21**, 255 (1975).
- 31) A. Marcinkowski, et al., *Nucl. Phys.*, **A402**, 220 (1983).
- 32) W. Scobel, *Z. Phys.*, **A311**, 323 (1983).



### 3.14 Nuclear Data Evaluations of Neutron and Proton Incidence on Zr, Nb, and W for Energy up to 200 MeV

Satoshi KUNIEDA, Nobuhiro SHIGYO, Kenji ISHIBASHI

*Department of Applied Quantum Physics and Nuclear Engineering, Kyushu University  
6-10-1 Hakozaki, Higashi-ku, Fukuoka 812-8581, Japan  
e-mail: kuni@meteor.nucl.kyushu-u.ac.jp*

Neutron and proton nuclear data were evaluated on Zr, Nb, and W for energy up to 200 MeV. To execute optical model calculations, spherical optical potentials were developed to reproduce experimental data for many elements. The GNASH nuclear model code was used to evaluate light-particle production cross sections. For neutron emission, giant resonance correction came to be performed in the code system.

#### 1. Introduction

High energy (up to several GeV) evaluated nuclear data are required for many elements to implement transport simulations, for such applications as the high-intensity neutron source and the accelerator-driven transmutation system of nuclear wastes. Evaluations are now being performed by JNDC working groups, and evaluated data files will be released as JENDL High Energy File.

Zirconium is important element because it has been applied in field of the nuclear technology, and its data are not included in LA150 evaluated data library [1]. Niobium is also important element because it has the merit as the superconductor component that will be used in the accelerator systems. And for the sake of the design of the spallation neutron source, tungsten is one of the quiet important elements as the target material. Nb, and W are included in LA150. To evaluate nuclear reaction data on these elements is relevant to the recent and future nuclear technologies.

It is efficient to evaluate nuclear reaction data by use of the Quantum Molecular Dynamics (QMD) [2] for energy up to several GeV, but QMD can not reproduce experimental data in intermediate energy region where the pre-equilibrium effect appear eminently. On the contrary, the GNASH nuclear model code [3] is based on Hauser-Feshbach statistical model for particle evaporations, and the exciton model for pre-equilibrium emissions, and it reproduce experimental data well in intermediate energy region.

For the aforementioned reasons, neutron and proton nuclear reaction data were evaluated on Zr, Nb, and W for energy up to 200 MeV. To begin with, optical model potential parameters were developed based on experimental data for medium and heavy nuclei as phenomenological approach. And light-particle production cross sections were evaluated by the GNASH code with transmission coefficients derived from the optical model analysis. All low-lying inelastic direct reaction cross sections were evaluated by Distorted Wave Born Approximation (DWBA). In addition to these model calculations, the correction of neutron scattered via excitations of giant resonance are also made with the Energy-Weighted Sum Rule (EWSR) [4] and DWBA in this work.

#### 2. Optical model analysis

The optical model is very efficient method not only for cross section evaluations that include elastic angular distributions and total or non-elastic components, but also for derivations of transmission coefficients required in Hauser-Feshbach statistical model calculations for particle evaporations from compound nuclei. In the model, optical potential is

important parameter that must be adjusted to give good reproductions of experimental data. Problems are that the potential parameter must have energy and atomic mass number dependence, because there are not enough experimental data but for neutron total cross sections, on Zr, Nb and W, in wide energy range (above  $\sim 20$  MeV). There are some global potentials, for example, neutron and proton potentials by Becchetti and Greenlees [5], neutron potential by Walter and Guss [6], nucleon potential by Young and Madland [7]. But their energy regions are limited, and accuracies on each nucleus are insufficient for use in nuclear data evaluations.

Spherical neutron optical potential was developed based on Fe, Ni, Cu, Y, Zr, Nb, Sn, W, and Pb experimental data [8] or data from systematics with the TOTELA [9] for energy up to 200 MeV. To obtain their energy dependences, parameters were searched by eye guidance with the ECIS-96 [10] calculations and graphical tool. Neutron potential parameter set obtained in this analysis is shown in table 1. Symbols of potential depths in the table are of the standard form, and  $E$ ,  $A$ , and  $\eta$  mean the incident neutron energy, the atomic mass number and the nuclear symmetry  $(N-Z)/A$ . For the depth of the imaginary surface term, Woods-Saxon function form was used to describe the smooth decrease, and also to be included the mass number dependence in half decrease energy point  $E'$  to describe the neutron penetration at about nuclear surface into different nuclei.

For neutron evaluations, potential parameters were slightly modified to reproduce experimental data, especially for neutron total cross sections exactly. For proton evaluations, neutron potential parameters that were added Coulomb term and changed the sign of symmetric term were also used with slight modification to reproduce experimental data.

Neutron total cross sections for  $^{90}\text{Zr}$  are shown in Fig 1. Evaluated values (solid line) reproduce experimental data [11][12] exactly. Proton non-elastic cross sections for W are shown in Fig 2. Because there aren't experimental data except one at about 100 MeV [13] for W,  $^{181}\text{Ta}$  experimental data [13][14] and data from systematics were used in the evaluation. Present evaluation is compared with calculations used global potentials in the figure, and the comparison with LA150 was also performed. The evaluation was based on data from systematics rather than Kirkby's data above  $\sim 80$  MeV. Neutron and proton elastic angular distribution cross sections are shown in Fig 3 and Fig 4 with experimental data [15-24] for  $^{90}\text{Zr}$ . Evaluated values reproduce experimental data successfully in the wide energy range for neutron incidence. For proton incidence, the reproductions are reasonably well though over estimations for back angles are seen in some energy points.

### 3. Particle production cross sections

To evaluate light-particle production cross sections, the GNASH nuclear model code was used for energy up to 200 MeV. Transmission coefficients required in the Hauser-Feshbach statistical model were derived from the optical model. Neutron and proton potentials described above section are used in incident and outgoing channels. In outgoing channels of composite particles, Lohr and Haeberli's potential [25] was used for deuteron, Becchetti and Greenlees's for triton and helium-3, Avrigeanu's [26] was used for alpha particle. Ignatyuk's parameter [27] was used in Fermi gas level density. Low-lying in-elastic direct reaction cross sections were obtained by DWBA with the DUWCK-4 code. Deformation parameters for each nuclear level were taken from Reference Input Parameter Library (RIPL) [28].

An example angle-integrated cross section is shown in Fig 5 for  $^{90}\text{Zr}(p,xn)$ . The evaluated values reproduce experimental data at 90 MeV [29] well. For double differential cross section evaluations, the Kalbach's systematics [30] was used with result of the GNASH calculations. Examples of double differential cross section are shown in Fig 6 for  $(p,xn)$  on

$^{90}\text{Zr}$  at 90 MeV, and Fig 7 for  $(p, xp)$  on  $^{93}\text{Nb}$  at 65 MeV. Evaluated values reproduce 90 MeV experimental data [29] and 65 MeV experimental data [31] on each element reasonably well.

In Addition to these model calculations, corrections of neutron emission via excitations of the giant resonance (GR) were performed with Lorentzian shaped function, as follow equation [32].

$$\left(\frac{d\sigma}{dE}\right)_{GR} = \sum_l \sigma_l^{DWBA} \frac{\Gamma^2}{\pi \{(E - \hbar\omega_l)^2 + \Gamma^2/4\}}$$

Where,  $E$  is outgoing neutron energy, and  $(d\sigma/dE)_{GR}$  means the angle-integrated cross section for GR contribution.  $\Gamma$  is the width of resonances, and was adopted about 5 MeV.  $\hbar\omega_l$  are the adjustable parameters which means the average excitation energies of GR state having multipolarity  $l$ .  $\sigma_l^{DWBA}$  are neutron emission cross sections via excitation of GR, and were calculated by DWBA with deformation parameters derived from Energy-Weighted Sum Rule (EWSR). Giant dipole, quadrupole and low-energy octupole resonances (GDR, GQR, and LEOR) were taken into account as well as Reference 32.

In the GNASH code, final neutron angle-integrated spectra were calculated to sum compound (CN), pre-equilibrium (PE), in-elastic (IE) and giant resonance (GR) contributions as follow equations.

$$\frac{d\sigma}{dE} = F \left(\frac{d\sigma}{dE}\right)_{CN} + \sum_i \left(\frac{d\sigma}{dE}\right)^i \quad F = 1 - \frac{1}{\sigma_{CN}} \sum_i \left[ \int dE \left(\frac{d\sigma}{dE}\right)^i \right]$$

$i$  denotes CN, PE, IE and GR.  $F$  is the reduction factor for CN contribution to preserve reaction cross sections. GR contribution was added in this work. Angle-integrated cross section for  $(n, xn)$  on  $^{184}\text{W}$  is shown in Fig 8. These evaluated vales with the correction reproduce 26 MeV experimental data [33] very well. In Fig 9, results of differential cross sections were shown with experimental data [34]. The Kalbach's systematics was also used in evaluation, and it reproduces experimental data considerably.

#### 4. Conclusion

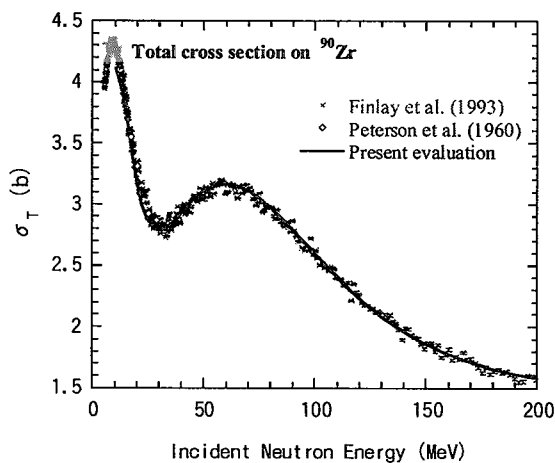
Neutron and proton reaction data were evaluated on Zr, Nb, and W for energy up to 200MeV. For the evaluations, the optical model and the GNASH code was used. The giant resonance correction was also made for  $(n, xn)$  reaction. These data were connected with JENDL-3.3, compiled into ENDF format files for each element and incident particle, and will be released as low energy parts of JENDL High Energy File.

#### References

- [1] M. B. Chadwick, P. G. Young, S. Chiba, *et al* : *J. Nucl. Sci. Eng.*, **131**, 293-328 (1999).
- [2] K. Niita, S. Chiba, T. Maruyama, *et al.* : *J. Phys. Rev.* **C37**, 2350 (1988).
- [3] P. G. Young, *et al.* : LA-6947 (1977) ; LAUR-88-382 (1988).
- [4] G. R. Satchler : *J. Nucl. Phys.* **A195**, 1 (1972).
- [5] F. D. Becchetti Jr. and G. W. Greenlees : *J. Phys. Rev.* **182**, 1190 (1969).
- [6] R. L. WALTER and P. P. Guss : *Proc. Int. Conf. Nuclear Basis and Applied Science, Santa Fe, New Mexico*, 1985, ed. P. G. Young (Gordon and Breach, New York, 1986).
- [7] P. G. Young and D. G. Madland : IAEA, INDC(NDS)-335, 109 (1995).
- [8] OECD NEA DATA BANK (<http://www.nea.fr/html/dbdata/>).
- [9] T. Fukahori and K. Niita : "Program TOTELA Calculating Basic Cross Sections in Intermediate Energy Region by Using Systematics," INDC(NDS)-416.
- [10] J. Raynal : "Optical Model and Coupled-Channel Calculation in Nuclear Physics," International

- Atomic Energy Agency report, IAEA SMR-9/8 (1970), p. 281.
- [11] R. W. Finlay, W. P. Abfalterer, G. Fink, E. Monte, T. Adami, P. W. Lisowski, G. L. Morgan, R. C. Haight : *J. Phys. Rev. C* **47**, 237 (1993).
- [12] J. M. Peterson, A. Bratenahl, J. P. Stoering : *J. Phys. Rev.* **120**, 521 (1960).
- [13] P. Kirkby, and W. T. Link : *Can. J. Phys.*, **44**, 1847 (1966).
- [14] R. Abegg, J. Birchall, N. E. Davison, M. S. De Jong, *et al.* : *J. Nucl. Phys.* **A324**, 109 (1979).
- [15] Y. Wang, J. Rapaport : *J. Nucl. Phys.*, **A517**, 301 (1990).
- [16] M. Ibaraki, M. Baba, *et al.* : *J. Nucl. Instrum. Methods.*, **A446/3**, 536 (2000).
- [17] K. Matsuda, H. Nakamura, *et al.* : *J. Phys. Soc. Jap.*, **22**, 1311 (1967).
- [18] W. Makofske, G. W. Greenlees, *et al.* : *J. Phys. Rev. C* **5**, 780 (1972).
- [19] J. B. Ball, C. B. Fulmer, R. H. Bassel : *J. Phys. Rev. B* **135**, 706 (1964).
- [20] L. N. Blumberg, E. E. Gross, A. Van Der Woude, A. Zucker, R. H. Bassel : *J. Phys. Rev.* **147**, 812 (1966).
- [21] C. B. Fulmer, J. B. Ball, A. Scott, M. L. Whiten : *J. Phys. Rev.* **181**, 1565 (1969).
- [22] H. Sakaguchi, M. Nakamura, K. Hatanaka, A. Goto, T. Noro, F. Ohtani, H. Sakamoto, H. Ogawa, S. Kobayashi : *J. Phys. Rev. C* **26**, 944 (1982).
- [23] V. Comparat, R. Frascaria, N. Marty, M. Morlet, A. Willis : *J. Nucl. Phys.* **A221**, 403 (1974).
- [24] A. Nadasen, P. Schwandt, P. P. Singh, W. W. Jacobs, A. D. Bacher, P. T. Debevec, M. D. Kaitchuck, J. T. Meek : *J. Phys. Rev. C* **23**, 1023 (1981).
- [25] J. Lohr and W. Haeberli : *J. Nucl. Phys.* **A232**, 381 (1974).
- [26] V. Avrigeanu, *et al.* : *J. Phys. Rev. C* **49**, 2136 (1994).
- [27] A. V. Ignatyuk, G. N. Smirenkin, and A. S. Tishin : *Sov. J. Nucl. Phys.*, **21**, 255 (1975).
- [28] Reference Input Parameter Library (<http://www-nds.iaea.org/ripl/>).
- [29] A. M. Kalend, B. D. Anderson, *et al.* : *J. Phys. Rev. C* **28**, 105 (1983).
- [30] C. Kalbach : *J. Phys. Rev. C* **37**, 2350 (1988).
- [31] H. Sakai, K. Hosono, N. Matsuoka, *et al.* : *J. Nucl. Phys.* **A344**, 41 (1980).
- [32] P. Demetriou, A. Marcinkowski, P. E. Hodgson : *J. Nucl. Phys.* **A596** (1996).
- [33] A. Marcinkowski, R. W. Finlay, *et al.* : *J. Nucl. Phys.* **A501**, 1 (1989).
- [34] A. Marcinkowski, R. W. Finlay, *et al.* : *J. Nucl. Phys.* **A402**, 220 (1983).

Table 1. Neutron optical potential parameters.

Fig 1. Neutron total cross section on  $^{90}\text{Zr}$ .

$$V = 44.314 \exp(-0.01022E) + 0.0132E - 8.9465\eta + 5.27$$

$$r_v = 1.277 - 0.000151E + 0.01E^1$$

$$a_v = 0.5856 + 0.001E - 0.1E^1$$

$$W = 0.005E + 14.0 / (1.0 + (130 / (E + 5.65))^1.5)$$

$$r_w = r_v$$

$$a_w = a_v$$

$$W_d = W'_d / (1.0 + \exp((E - E') / 20.0))$$

$$W'_d = 11.398 - 7.858\eta$$

$$E' = -501.33 + 2.7059A - 48.472A^{2/3} + 291.42A^{1/3}$$

$$r_{wd} = 1.085 - 0.000139E$$

$$a_{wd} = 0.49646 + 9.3028 \times 10^{-5}A - 0.00027E$$

$$V_{so} = 6.0 \exp(-0.005E)$$

$$r_{vso} = 1.017$$

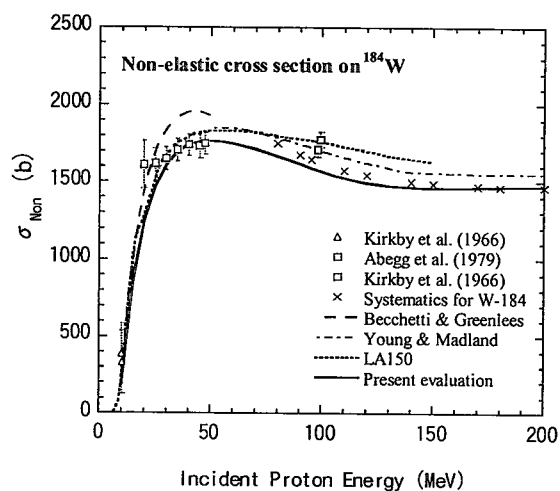
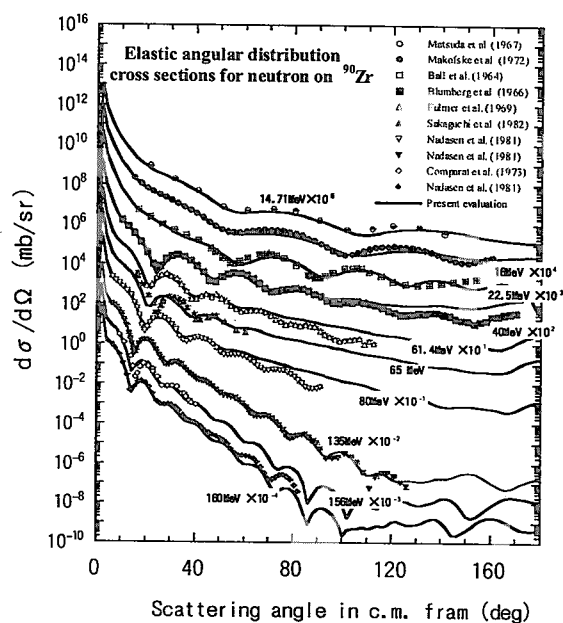
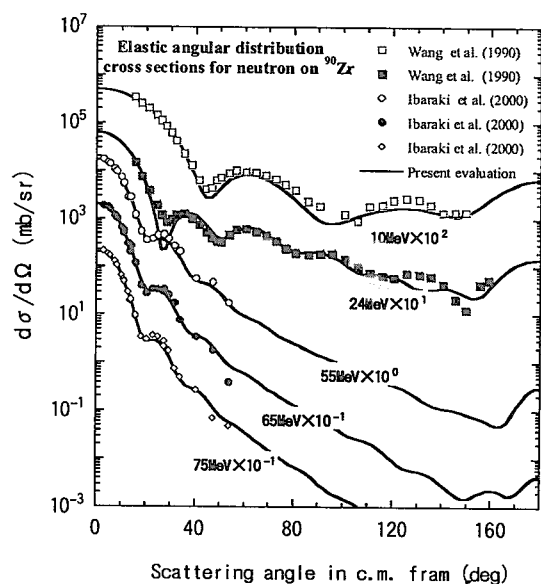
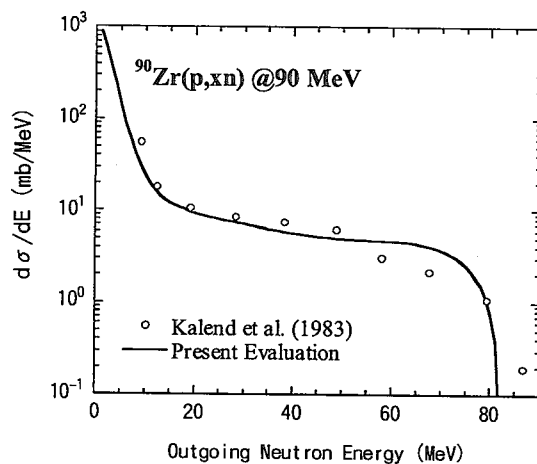
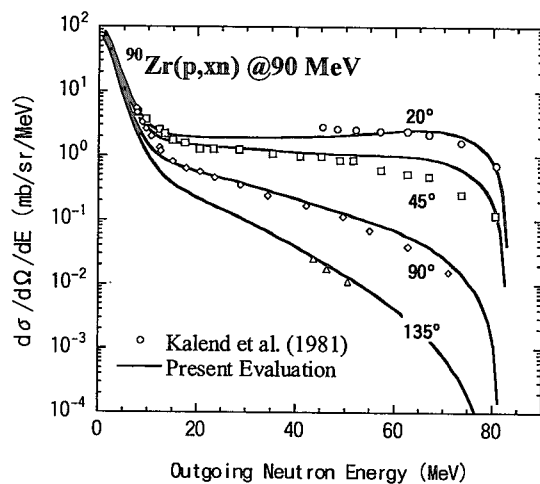
$$a_{vso} = 0.6$$

$$W_{so} = 7.0 / (1.0 + \exp((E - 10.0) / 20.0))$$

$$r_{wso} = r_{vso}$$

$$a_{wso} = a_{vso}$$

( $E$  is in MeV, and  $r, a$  are in fm)

Fig 2. Proton non-elastic cross section on  $^{184}\text{W}$ .Fig 4. Proton elastic angular distribution cross sections on  $^{90}\text{Zr}$ .Fig 3. Neutron elastic angular distribution cross sections on  $^{90}\text{Zr}$ .Fig 5. Angle-integrated cross section for  $^{90}\text{Zr}(p,xn)$  at 90 MeV.Fig 6. Double differential cross sections for  $^{90}\text{Zr}(p,xn)$  at 90 MeV.

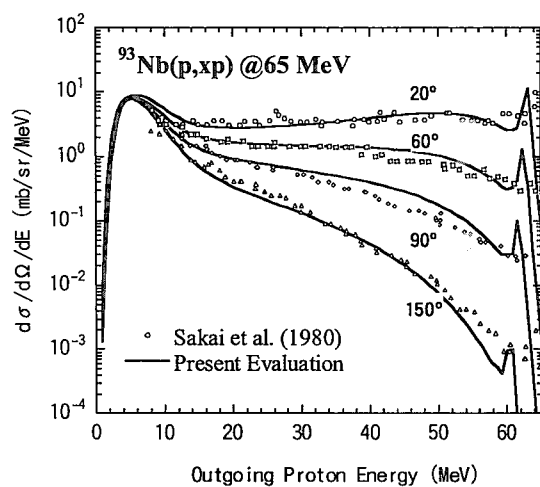


Fig 7. Double differential cross sections for  $^{93}\text{Nb}(p,xp)$  at 65 MeV.

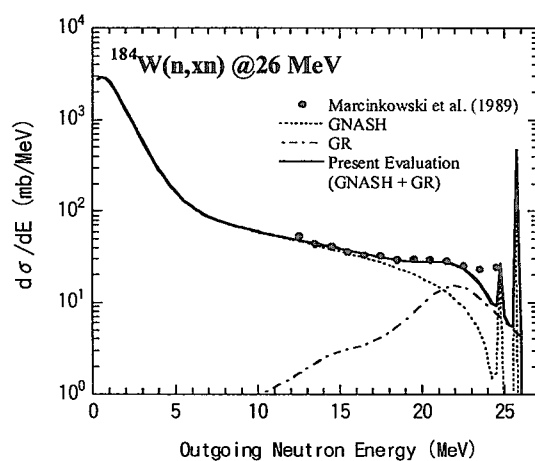


Fig 8. Angle-integrated cross section for  $^{184}\text{W}(n,xn)$  at 26 MeV.

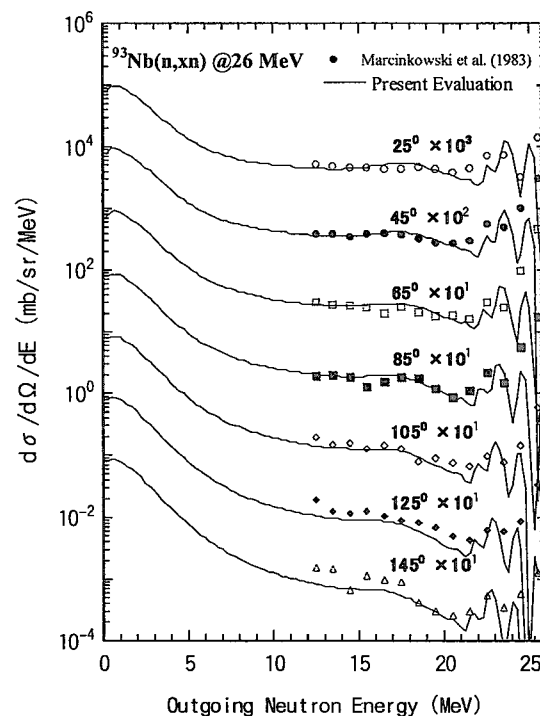


Fig 9. Double differential cross sections for  $^{184}\text{W}(n,xn)$  at 26 MeV.





### 3.15 Thick Target Benchmark Test for the Code Used in the Design of High Intensity Proton Accelerator Project

Shin-ichirō MEIGO<sup>1</sup>, Masatoshi HARADA

Tokai Establishment, Japan Atomic Energy Research Institute, Tokai-mura 319-11

<sup>1</sup>email: meigo@linac.tokai.jaeri.go.jp

In the neutronics design for the JAERI and KEK Joint high intensity accelerator facilities, transport codes of NMTC/JAM, MCNPX and MARS are used. In order to confirm the predict ability for these code, it is important to compare with the experiment result. For the validation of the source term of neutron, the calculations are compared with the experimental spectrum of neutrons produced from thick target, which are carried out at LANL and KEK. As for validation of low energy incident case, the calculations are compared with experiment carried out at LANL, in which target of C, Al, Fe, and <sup>238</sup>U are irradiated with 256-MeV protons. By the comparison, it is found that both NMTC/JAM and MCNPX show good agreement with the experiment within by a factor of 2. MARS shows good agreement for C and Al target. MARS, however, gives rather underestimation for all targets in the neutron energy region higher than 30 MeV. For the validation high incident energy case, the codes are compared with the experiment carried out at KEK. In this experiment, W and Pb targets are bombarded with 0.5- and 1.5-GeV protons. Although slightly disagreement exists, NMTC/JAM, MCNPX and MARS are in good agreement with the experiment within by a factor of 2.

#### 1. Introduction

In the design of facility for Japan Proton Accelerator Research Complex (J-PARC), which is driven by the corporation between JAERI and KEK, transport calculation codes are used in order to obtain neutronic properties such as neutron flux, shielding, radiation dose and heat. In the design of J-PARC facilities, which consists of LINAC and synchrotron accelerators and experimental facilities of spallation pulse neutron source, accelerator driven transmutation system (ADS), and nuclear and particle physics, calculation codes of NMTC/JAM[1], MCNP-X[2] and MARS[3] are used to predict neutronic properties.

In general it is important to know predict ability of the calculation code used in the actual neutronic design. In this study, calculation results are compared with the experimental results. As for the validation of the source term of neutron, the calculations are compared with the experimental spectrum of neutrons produced from thick target, which were carried out at LANL and KEK.

#### 2. Experiment

##### 2.1 LANL Experiment

Thick target experiments[4, 5] were carried out at the target 2 area of Weapon Neutron Research Facility (WNR), which is shown in Fig. 1. The proton beam with energies between 113 and 800 MeV from the Los Alamos Clinton P. Anderson Meson Physics Facility (LAMPF) bombards the target at the center of the room. The experimental area is a circular of 12 m in diameter at beam elevation, which is surrounded by a compacted tuff of 10 m and a concrete wall of 0.4 m on the inside the room. Several radial penetrations view the center of the room at beam elevation, forming neutron flight paths with line of sight to the target. The flight paths were chosen from 29 to 67 m, which were valid according to the observed angles.

The time-of-flight method was applied for measuring the neutron spectra. The neutron detectors for 60 and 120 degree were BC-418 plastic scintillators of 5.08 cm in diameter and 5.08 cm long. For the shorter flight paths, scintillators of 5.08 cm in diameter and 2.54 cm long were used.

The absolute intensity of proton beam was determined by monitoring the secondary electron produced by the proton beam through a gold-plated aluminum foil with linearity to proton current within 1 % and absolute uncertainty of 5 %.

The target materials were carbon, aluminum, and iron, all in their natural isotopic abundance, and <sup>238</sup>U. Targets for each element are longer than the stopping length for 256-MeV-proton. The diameters of the targets were comparable to the lengths to minimize the escape probability of secondary proton with energy near that of the primary beam. The physical characteristics of the targets are listed in Table 1. The absolute neutron

spectrum are corrected for background, dead time and attenuation of air. Uncertainties for the measurements up to 20 MeV are assigned as 20 %, and those above 20 MeV are 33 %.

## 2.2 KEK Experiment

Thick target experiments[6, 7] were performed at the  $\pi^2$  beam line of the 12-GeV proton synchrotrons at KEK. A schematic view of the experiment for lead target is shown in Fig. 2. The incident proton was supplied as the secondary particle generated by an internal target, which was placed in the 12-GeV proton beam by using slow extraction mode. After passing the bending magnet of beam channel, the secondary beam having a unique momentum was introduced to the thick target. The intensity of the incident particles was so weak (less than  $10^5$  particles/spill) that incident protons were counted one by one with beam scintillators. The protons were identified from  $\pi$  mesons produced at the internal target by the time-of-flight (TOF) technique with a pair of scintillators (Pilot U) located at a separation distance of 20 m. In order to subtract the neutrons produced from the beam scintillators, background measurements were performed without target. A beam dump consisted of a carbon block pile of 0.5x0.5 m in the area and 1 m in thickness was located at 8.5 m distance from the target.

The time-of-flight method was applied for measuring the neutron spectra. The flight paths for each detector are approximately 1.2m. The neutron detectors were NE213 liquid scintillators of 12.7 cm in diameter and 12.7 cm in length. In order to reject the detection of the charged particles, NE102A scintillators were used as veto counters. They were placed at a distance of 2 cm from the surface of the NE213 scintillators. The absolute intensity of proton beam was determined by monitoring the pair of plastic scintillators(Pilot U).

The physical characteristics of the targets are summarized in Table 2. The target was a rectangular parallelepiped 15x15x20 cm whose purity was 99.95% and 94.8% for lead and tungsten, respectively. Those targets had 20 cm in length for the beam direction, which was enough thick to stop 0.5-GeV protons completely, while it caused the partial energy loss for 1.5-GeV protons. The size of the beams had Gaussian shape with 2.0 and 1.6 cm in FWHM on the perpendicular and horizontal plains, respectively. The interval between and duration of the proton pulses were 4 and 2.5 s, respectively. The absolute neutron spectrum is corrected for background neutrons, dead time, and the attenuation at the veto counter.

## 3. Calculation Code

Spectrum of neutron produced from thick target was calculated with the following calculation code having the calculation option, which was exactly the same as used in the neutronics design for the J-PARC facilities.

NMTC/JAM ver 2.1[1] was employed. Default options for the calculation were used for the analysis, which are specified as 1) Bertini cascade model, 2) with in-medium nucleon-nucleon cross section (NNCS), 3) with angular distribution of 50 % isotropic and 50% at forward direction for  $\Delta$  decay, 4) without pre-equilibrium process, 5) GEM evaporation model with Igunatyuk level density parameter and 6) with elastic scattering of nucleon in the transport calculation. For the analysis of the KEK experiment, also NNCS in free space was used. For the transport calculation of the neutron having the energy lower than 20 MeV, MCNP-4A was used. In the calculation of MCNP-4A, JENDL-3.2 library was employed.

MCNPX ver 2.2.6[2] was employed. Default options for the calculation are used for the analysis, which is specified as 1) Bertini model for nucleons and  $\pi$  mesons and with ISABEL model for other particles, 2) with pre-equilibrium model, and 3) with elastic scattering of nucleon. As for neutron library except for U-238, LA150 was employed, which is available up to 150 MeV. For U-238 case, the file is not available, so that JENDL-3.2 was employed. Also calculations by using the library for the proton of LA150 were performed.

MARS ver 14.00[3] was employed. In the calculation, whole energy spectrum was obtained without using MCNP.

## 4. Comparison with LANL Experiment

### 4-1 Carbon Target

The results for carbon target bombarded with 256-MeV protons are compared in Fig. 3. It is found that NMTC/JAM gives good agreement with the experiment for all energy and angular regions. Slight overestimation by a factor of 2 is found at 60 degree in the energy higher than 20 MeV.

The calculation results with MCNPX are also shown in this figure. MCNPX is in good agreement with the experiment in general. At backward in the angular region larger than 120 degree, MCNPX, however, overestimates by a factor of  $\sim 5$ . This overestimation is thought to be caused by emphasis of pre-equilibrium

process after cascade model for light target nuclide.

In Fig. 3, the calculation results with MARS are shown. It is found that MARS shows good agreement with the experiment in general. At 150 degree, MARS, however, underestimates the experiment by a factor of 2 in the energy region above 15 MeV.

#### 4-2 Aluminum Target

In Fig. 4, comparison for aluminum target bombarded with 256-MeV protons is shown. It is recognized that NMTC/JAM gives good agreement with the experiment. As well as the result for C target, slight overestimation by a factor of 2 is found at 30 degree in the energy region between 10 and 30 MeV. At 60 degree in the energy range above 15 MeV, NMTC/JAM gives slight overestimation by a factor of 2. On the other hand, NMTC/JAM at 150 degree gives underestimation by a factor of 2. This fact is mainly caused by the lack of pre-equilibrium process in this calculation.

MCNPX is in good agreement with the experiment in general. Although MCNPX for C target gives overestimation at backward angles, MCNPX for Al target shows good agreement with the experiment. MCNPX overestimates by a factor of 2 at 60 degree in the energy range above 15 MeV.

In Fig. 4, the calculation results with MARS are shown. In the energy region below 15 MeV, MARS shows good agreement with the experiment. At 60 degree in the energy range above 15 MeV, MARS overestimates by a factor of 2.

#### 4-3 Iron Target

Figure 5 shows comparison for iron target bombarded with 256-MeV protons. NMTC/JAM are in significantly good agreement with the experiment. At 60 degree in the energy region above 20 MeV, NMTC/JAM is in good agreement with the experiment, whereas overestimates the results for C and Al target. On the contrary, in energy region below 5 MeV, NMTC/JAM gives underestimation by a factor of 2. At 150 degree, NMTC/JAM underestimates the experiment by a factor of 2, which is mainly caused by the lack of pre-equilibrium process. On the other hand for lower energy region lower than 10 MeV, it is found NMTC/JAM at backward angles gives remarkably good agreement with the experiment.

MCNPX also gives remarkably good agreement with the experiment. Even for fine spectrum structure due to the resonance of neutron capture, MCNPX results at backward angles reproduce the experimental data very well. At 60 degree, MCNPX gives underestimation by a factor of 2 in the energy region below 5 MeV.

In Fig. 5, MARS results are also compared. It is found that MARS shows good agreement with the experiment. At 60 degree in the energy region below 3 MeV, MARS shows underestimation by a factor of 2.

#### 4-4 U-238 Target

In Fig. 6, comparisons for U-238 target bombarded with 256-MeV protons are shown. NMTC/JAM shows good agreement with the experiment. At 30 and 60 degree, although NMTC/JAM gives slight overestimation by a factor of 2 in the energy region between 5 and 10 MeV, NMTC/JAM shows remarkably good agreement with the experiment in the energy region above 20 MeV. At 150 degree, NMTC/JAM underestimates the experiment by a factor of 2 mainly due to the lack of pre-equilibrium.

MCNPX also gives good agreement with the experiment. Around at 20 MeV, MCNPX gives a slight overestimation by a factor of 2 except for 150 degree. At 150 degree in the higher energy than 40 MeV, MCNPX overestimates by a factor of 2. This overestimation is thought to be caused by the emphasis of pre-equilibrium process.

By comparison of MARS with the experiment, it is found that MARS underestimates by a factor of 3 in the energy region around 5 MeV at whole angles. This underestimation is probably caused by the fission model used in MARS. Around at 10 MeV, MARS reproduces the experiment fairly well. However, in the energy region above 15 MeV at forward angular region, MARS overestimates the experiment by a factor of 2.

### 5. Comparison with KEK experiment

#### 5-1 Tungsten Target Irradiated by 0.5- and 1.5-GeV Protons

Figures 7 and 8 show the comparison for W target bombarded with 0.5- and 1.5- GeV protons, respectively. In these figures, NMTC/JAM, MCNPX and MARS are compared with the experiment. It is found that

NMTC/JAM shows good agreement with the experiment. In Figs 7 and 8, NMTC/JAM with free NNCS is also shown, which gives considerable underestimation by a factor of 4 in the energy region between 20 and 100 MeV. However, this disagreement is eliminated by using the in-medium NNCS, which is used as option of default calculation. Even by using in-medium NNCS, the underestimation is found by a factor of 2 at 150 degree. This underestimation is mainly affected by lack of the pre-equilibrium process.

The calculations with MCNPX are also compared in Figs 7 and 8. It is found that MCNPX is in good agreement with the experiment at whole energy and angular regions. At backward angles, MCNPX shows remarkably good agreement with the experiment.

The results with MARS are also shown in Figs. 7 and 8. By comparison, it is found that MARS gives good agreement with the experiment. However, it is found MARS gives under estimation by a factor of 2 around 6 MeV at 150 degree for 0.5-GeV protons

### 5-3 Lead Target Irradiated by 0.5- and 1.5-GeV Protons

Results for Pb target irradiated by 0.5- and 1.5- GeV protons are compared in Figs. 9 and 10, respectively. It is recognized that NMTC/JAM with in-medium NNCS shows good agreement with the experiment. However, NMTC/JAM with free NNCS gives considerable underestimation in the energy region between 20 and 100 MeV. At 150 degree, NMTC/JAM with in-medium NNCS shows underestimation by a factor of 2 at 150 degree mainly due to lack of the pre-equilibrium process.

The calculations with MCNPX give remarkably good agreement with the experiment. However, around at 2 MeV except for 150 degree, MCNPX overestimates by a factor of 2. At backward angles, MCNPX shows remarkably good agreement with the experiment.

The results with MARS are also shown in Figs. 9 and 10. MARS gives good agreement with the experiment. In the energy region between 2 and 10 MeV at 150 degree, MARS underestimates the experiment by a factor of 2.

## 5. Concluding Remarks

Comparison of spectra of neutron produced from thick target between the calculation code and the experiment are made. Although some discrepancies are found, it can be concluded that NMTC/JAM, MCNPX and MARS can predict neutron spectra within a factor of 2 except for U-238 target with MARS code.

## References

- [1] K. Niita, et al., *Nucl. Instr. Meth B* **184**, 406 (2001)
- [2] L. S. Waters, ed., "*MCNPX User's Manual, Version 2.3.0*", LA-UR-02-2607 (2002)
- [3] N.V. Mokhov, "*The Mars Code System User's Guide*", Fermilab-FN-628 (1995)
- [4] M. M. Meier, et al., *Nucl. Sci. Eng.*, **104**, 339-363 (1990)
- [5] M. M. Meier, et al., "*Differential Neutron Production Cross Sections and Neutron Yields from Stopping-Length Targets for 256-MeV Protons*", LA-11518-MS, Los Alamos National Laboratory (1989)
- [6] S. Meigo, et al., *Nucl. Instr. Meth A* **431**, 521 (1999)
- [7] S. Meigo, et al., *J. Nucl. Sci. and Technol. Suppl.* **2**, 1252 (2002)

Table 1 Physical characteristics of the targets used in LANL experiment

Element	Radius (cm)	Length in beam direction (cm)	Density (g/cm <sup>3</sup> )
Carbon	8.00	30.00	1.646
Aluminum	8.00	20.00	2.715
Iron	8.00	8.00	7.86
<sup>238</sup> U	4.00	5.00	18.98

Table 2 Physical characteristics of the targets used in KEK experiment

Element	Cross section (cm)	Length in beam direction (cm)	Density (g/cm <sup>3</sup> )	Purity (wt%)
Tungsten	15x15	20.00	18.05	W 94.8, Cu 2.1, Ni 3.1
Lead	15x15	20.00	11.33	Pb 95.5

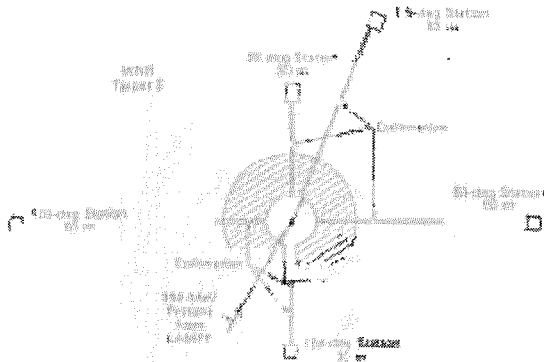


Fig. 1. Schematic view of LANL experiment set up.

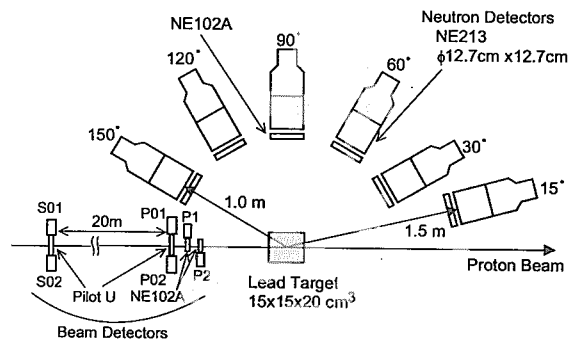


Fig. 2. Schematic view of KEK experiment set up.

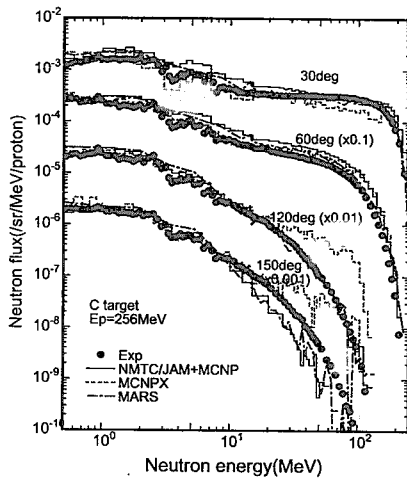


Fig. 3 Comparison of C target irradiated by 256-MeV protons

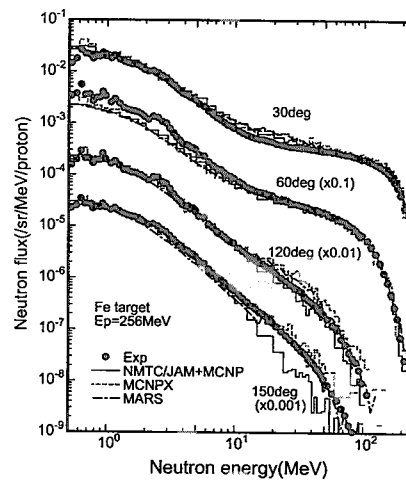


Fig. 5 Comparison Fe target irradiated by 256-MeV protons

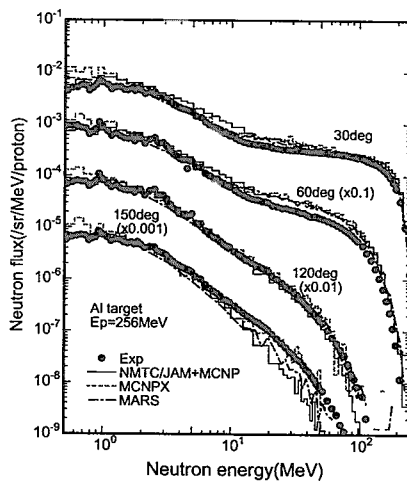


Fig. 4 Comparison of Al target irradiated by 256-MeV protons

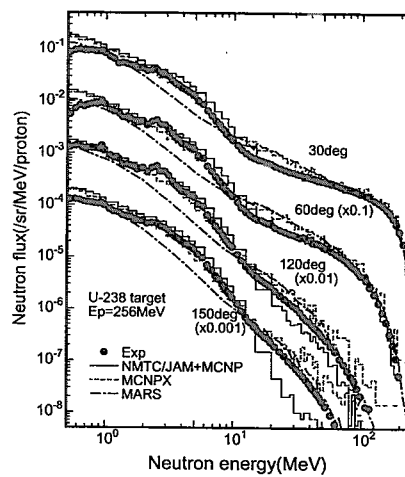


Fig. 6 Comparison of U-238 target irradiated by 256-MeV protons

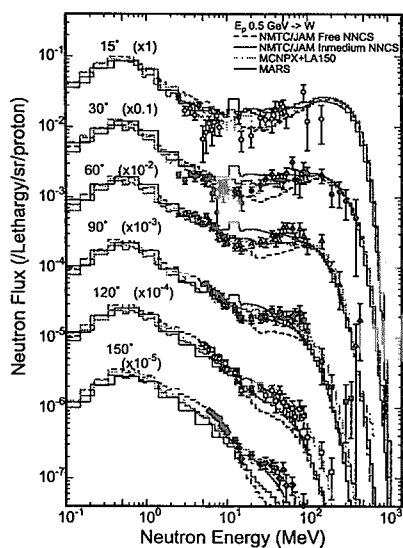


Fig. 7 Comparison of W target irradiated by 0.5 GeV protons

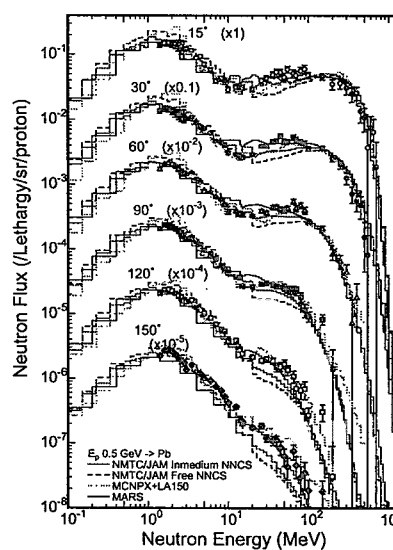


Fig. 9 Comparison of Pb target irradiated by 0.5 GeV protons

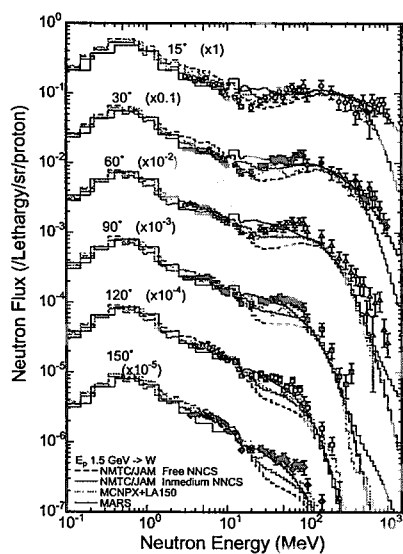


Fig. 8 Comparison of W target irradiated by 1.5 GeV protons

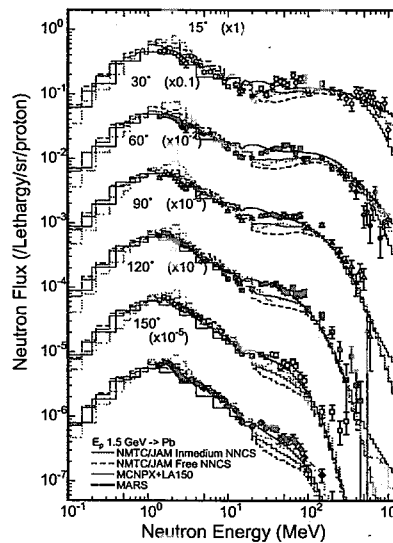


Fig. 10 Comparison of Pb target irradiated by 1.5 GeV protons



### 3.16 Comment to VITAMIN-B6

Chikara KONNO

Center for Proton Accelerator Facilities, Japan Atomic Energy Research Institute  
Tokai-mura, Naka-gun, Ibaraki-ken 319-1195 JAPAN  
e-mail: konno@cens.tokai.jaeri.go.jp

Hiroshi NAKASHIMA

Center for Proton Accelerator Facilities, Japan Atomic Energy Research Institute  
Tokai-mura, Naka-gun, Ibaraki-ken 319-1195 JAPAN  
e-mail: nakasima@shield4.tokai.jaeri.go.jp

Richard A. Lillie

Oak Ridge National Laboratory  
P.O. Box 2008, Oak Ridge, TN 37831-6363 US  
e-mail: lilliera@ornl.gov

HILO2K is a new multigroup cross-section library for neutron and gamma energies to 2 GeV and 20 MeV, respectively. We performed a simple benchmark test in order to validate HILO2K. This benchmark test suggested that HILO2K has some problem. We investigated the problem and pointed out that the problem comes from insufficient self-shielding correction and inadequate scattering matrices in VITAMIN-B6, which provided much of the low energy data in HILO2K.

#### 1. Introduction

Recently Oak Ridge National Laboratory prepared a new multigroup cross-section library, HILO2K [1], for neutron energy to 2 GeV and adopted it for neutronics calculations of the SNS project [2]. In this paper a simple benchmark test with HILO2K will be performed in order to validate HILO2K. Through this benchmark test, it is pointed out that the self-shielding correction in VITAMIN-B6 [3], which provided many of the low energy data in HILO2K, is insufficient and the scattering matrices in VITAMIN-B6 is inadequate.

#### 2. Overview of HILO2K

HILO2K is an ANISN formatted multigroup cross-section library for neutron and gamma energies to 2 GeV (83 groups) and 20 MeV (22 groups), respectively. The nuclides included in HILO2K are  $^1\text{H}$ ,  $^2\text{H}$ , He, Be,  $^{10}\text{B}$ ,  $^{11}\text{B}$ , C, N, O, Na, Mg, Al, Si, S, K, Ca, Cr, Mn, Fe, Ni, Cu, Zr, Nb, Cd, Ba, Gd, Ta, W, Hg, Pb,  $^{235}\text{U}$  and  $^{238}\text{U}$ . The neutron ( $> 20$  MeV) cross sections [42 groups] are based on data calculated with MCNPX [4]. The nonelastic scattering cross sections of  $^2\text{H}$ , C,

N, O, Al, Si, Ca, Cr, Fe, Ni, Cu, Nb, W, and Pb are normalized to those in LA150 [5]. On the contrary, the neutron ( $< 20$  MeV) [41 groups] and gamma cross sections are obtained by collapsing VITAMIN-B6 (neutron 199 groups, gamma 42 groups, generated from ENDF/B-VI [6]), which has self-shielding correction with the Bondarenko method [7].

HILO2K has two versions with  $P_0$  Legendre expansion; one is a standard version where all reaction data are taken into account, while the other is a modified version where a neutron collision with scattering angle cosines greater than 0.99 and with more than 95 % of the incident neutron energy was ignored in order to represent strongly forward peaked angular distributions in high energy region. Here we used the modified version.

### 3. Simple Benchmark Test

We performed a simple benchmark test to validate HILO2K. This benchmark test consisted of a concrete sphere or an iron sphere of 5 m in radius with an isotropic 2 GeV neutron source in the center. Neutron dose rates and neutron spectra in the sphere were calculated with the Sn code ANISN [8] and HILO2K. Calculations with MCNPX (neutron only mode. ENDF/B-VI was adopted for neutron cross section library below 20 MeV.), which is used to obtain neutron ( $> 20$  MeV) cross sections of HILO2K, were carried out as a reference. It was judged through comparison between the ANISN and MCNPX calculations whether HILO2K has any problems.

The calculated neutron dose rates and neutron spectra in the spheres are shown in Figs. 1 - 5. In the concrete sphere the neutron dose rates are almost the same between the ANISN and MCNPX calculations and the discrepancy between the neutron spectra of the ANISN and MCNPX calculations was at most within 50 %, even on the sphere surface, 5 m from the center. This was not the case in the iron sphere, particularly at positions far from the center. The dose rate with ANISN was around 3 orders of magnitude smaller than that obtained with MCNPX at 4 m from the center. The calculated neutron spectra suggest that the large discrepancy in the dose rate mainly comes from the differences in the neutron flux below 1 MeV.

### 4. Problem in VITAMIN-B6 (1)

In order to investigate causes for the discrepancy in the neutron flux below 1 MeV, we examined VITAMIN-B6, which provided many of the low energy data in HILO2K. At first we found out the following problem; the smallest background cross section of  $^{56}\text{Fe}$  in VITAMIN-B6 is 1, but natural iron requires a smaller background cross section of  $^{56}\text{Fe}$ , around 0.2. It is considered that this problem leads to insufficient self-shielding correction and wrong neutron flux.

Then we performed a new ANISN calculation for the iron benchmark with two revised HILO2K libraries, HILO2K-r1 and HILO2K-r2, where neutron cross sections below 20 MeV were replaced with those of the smallest background cross section of  $^{56}\text{Fe}$  is  $10^{-5}$  and 1 b, respectively, processed by using NJOY99.67 [9] and TRANSX2.15 [10] from ENDF/B-VI. Figures 6 and 7 show the result. The ANISN calculation with HILO2K-r2 agrees with the MCNPX calcu-



lation best, but there is still difference. It is considered that this difference is due to the coarse group structure of HILO2K and limitation of the simple self-shielding correction.

Figures 6 and 7 also indicate that the ANISN calculation with HILO2K-r1 agrees with MCNPX calculation better than that with the original HILO2K. This result appears very strange since the smallest background cross section of HILO2K-r1 is the same as that of the original HILO2K. Next we investigate this phenomenon.

## 5. Problem in VITAMIN-B6 (2)

We still more comb through VITAMIN-B6 and found out that the ingroup scattering matrices of Legendre order  $l \geq 1$  in HILO2K-r1 is different from those in VITAMIN-B6 or the original HILO2K as shown in Fig. 8. This difference causes from whether the transport approximation (consistent-P approximation) [9] is applied. The consistent-P approximation for a group  $g$  is the following approximation;

$$\sigma_{l \leftarrow g}^{SN} = \sigma_{l \leftarrow g}^{PN} - (\sigma_{lg}^{PN} - \sigma_{0lg}^{PN}), \quad (1)$$

$$\sigma_g^{SN} = \sigma_{0lg}^{PN}, \quad (2)$$

$$\sigma_{lg}^{PN} = \frac{\int_g \sigma_t(E) W_l(E) dE}{\int_g W_l(E) dE}, \quad (3)$$

$$\sigma_{l \leftarrow g}^{PN} = \frac{\int_g dE \int_g dE \sigma_t(E \rightarrow E) W_l(E)}{\int_g dE W_l(E)}, \quad (4)$$

$$W_l(E) = \frac{C(E)}{[\sigma_0 + \sigma_t(E)]^{l+1}}, \quad (5)$$

where  $PN$  means  $PN$  cross sections,  $SN$  means  $SN$  cross sections,  $l$  is Legendre order,  $\sigma_t$  is the total cross section,  $W_l(E)$  is a weight function,  $C(E)$  is a smooth function of neutron energy  $E$ , and  $\sigma_0$  is the background cross section. HILO2K-r1 has the consistent-P approximation. On the contrary, no transport approximation seems to be applied to VITAMIN-B6 or the original HILO2K since the term in parentheses in the right side of Eq. (1) is neglected. Therefore the ingroup scattering matrices of Legendre order  $l \geq 1$  in VITAMIN-B6 or the original HILO2K is not adequate. We also confirmed that the ANISN calculation by using HILO2K-r1 without the consistent-P approximation agreed with that by using the original HILO2K. It is concluded that this is the reason of the ANISN calculation with HILO2K-r1 agrees with MCNPX calculation better than that with the original HILO2K in the iron sphere benchmark test.

The term in parentheses in the right side of Eq. (1) is very small since  $W_l(E)$  is a smooth function of neutron energy  $E$  and  $\sigma_{lg}^{PN}$  is almost the same as  $\sigma_{0lg}^{PN}$  if the self-shielding effect is

small. Thus the effect of no transport approximation in VITAMIN-B6 or the original HILO2K does not appear in the concrete sphere benchmark test, where the self-shielding effect is small.

It should be noted that multigroup libraries for shielding, such as JSSTD [11], often have no transport approximation and that they cause the same problem as VITAMIN-B6.

## 6. Conclusion

We investigated the validity of the multigroup library HILO2K for neutron energy to 2 GeV through the simple benchmark tests, which consisted of a concrete sphere or an iron sphere of 5 m in radius with an isotropic 2 GeV neutron source in the center, with ANISN and MCNPX. The benchmark tests indicated that ANISN with HILO2K gave similar results as MCNPX in the concrete sphere, while the ANISN calculation with HILO2K was very different from the MCNPX one in the iron sphere.

We examined VITAMIN-B6, from which the low energy data in HILO2K come, since this discrepancy appeared in neutron flux below 1 MeV. It was concluded that the discrepancy between the ANISN and MCNPX calculations for the iron sphere was due to the smallest background cross section 1 of  $^{56}\text{Fe}$  in VITAMIN-B6 and no transport approximation (consistent-P approximation), which produced inadequate multigroup cross sections for materials with large self-shielding effect.

We generated a natural iron multigroup library below 20 MeV without the above two defects by using ENDF/B-VI, NJOY and TRANSX and replaced the natural iron multigroup library below 20 MeV in HILO2K by the new one. This new natural iron multigroup library improved the discrepancy between the ANISN and MCNPX calculations in the iron sphere. The next version of HILO2K will contain this newly generated natural iron multigroup library below 20 MeV.

## References

- [1] Lillie R.A. and Gallmeier F.X. : Proc. 4th Int. Top. Meet. Nucl. Applicat. Accel. Tech., p.302 (2000).
- [2] Appleton B.R. : ORNL/TM-6063 (1997).
- [3] White J.E., et al. : ORNL/TM-6795/R1 (2000).
- [4] Hughes H.G., et al.: Proc. of Int. Conf. on Mathematics & Computation, Reactor Physics & Environmental, Analysis in Nuclear Applications, p. 939 (1999).
- [5] Chadwick M.B., et al. : Nucl. Sci. Eng., 131, 293 (1999).
- [6] Rose P.F. : BNL-NCS-17541 (ENDF-201) (1991).
- [7] Bondarenko I.I. (Ed.) : Group Constants for Nuclear Reactor Calculations, Consultants Bureau, New York, (1964).
- [8] DOORS3.2 : One, Two- and Three-Dimensional Discrete Ordinates Neutron/Photon Transport Code System, RSICC CODE PACKAGE CCC-650 (1998).
- [9] MacFarlane R.E. and Muir D.W. : LA-12740-M (1994).
- [10] MacFarlane R.E. : LA-12312-MS (1993).
- [11] Hasegawa A. and Yamano N. : J. Nucl. Sci. Technol., Supplement 1, 723 (2000).

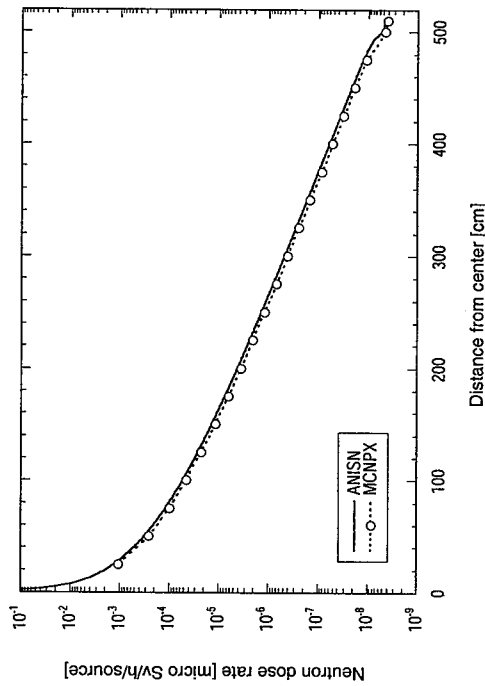


Fig. 1 Calculated neutron dose rates in the concrete sphere.

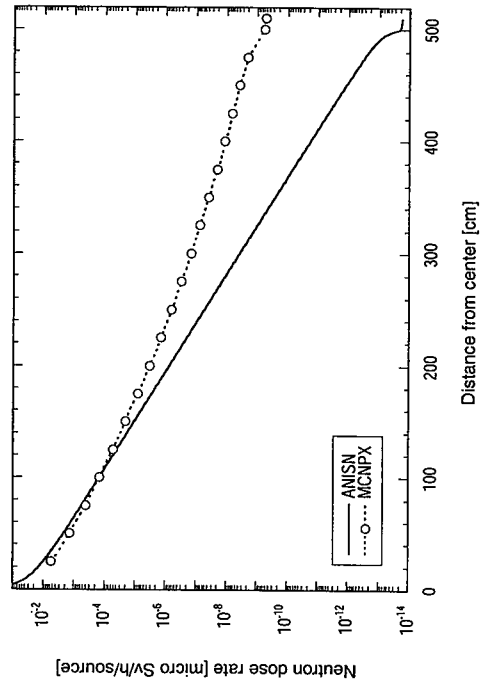


Fig. 3 Calculated neutron dose rates in the iron sphere.

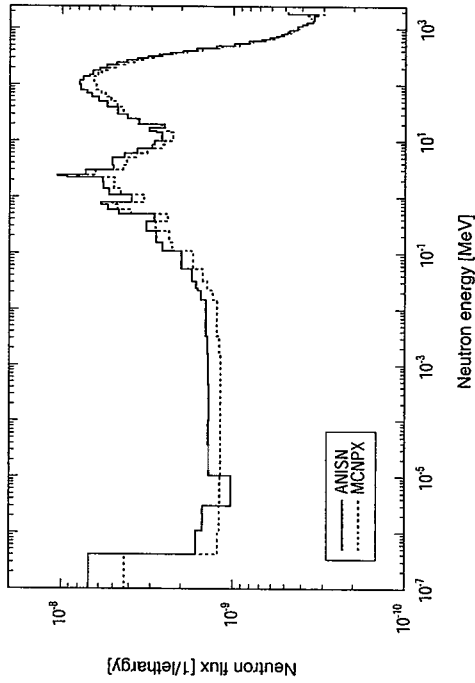


Fig. 2 Calculated neutron spectra at 4 m from the center in the concrete sphere.

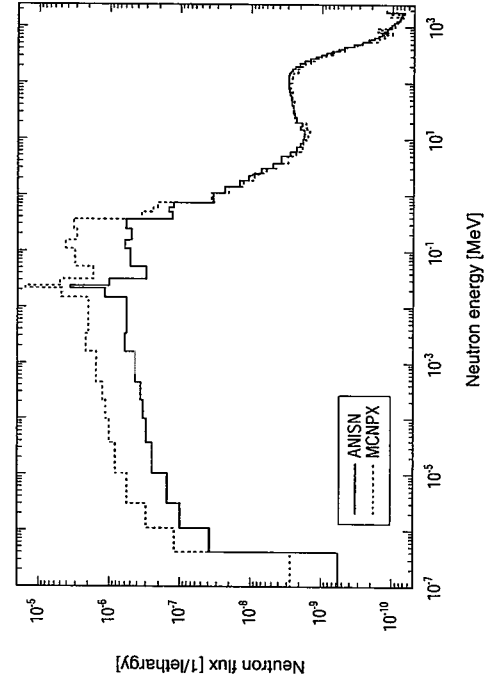


Fig. 4 Calculated neutron spectra at 2 m from the center in the iron sphere.

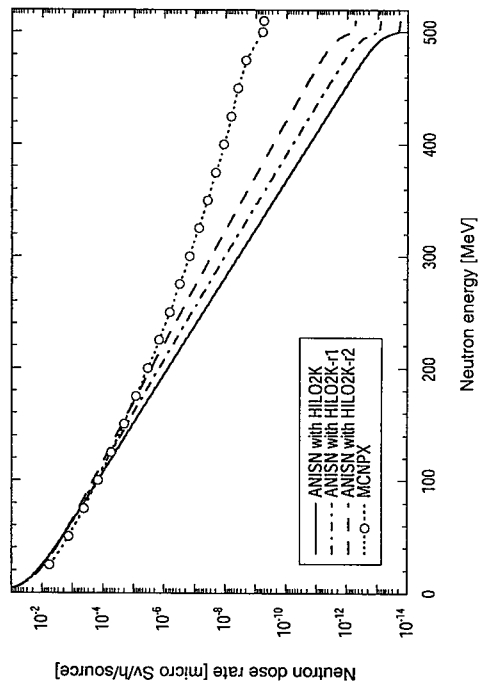


Fig. 6 Calculated neutron dose rates in the iron sphere.

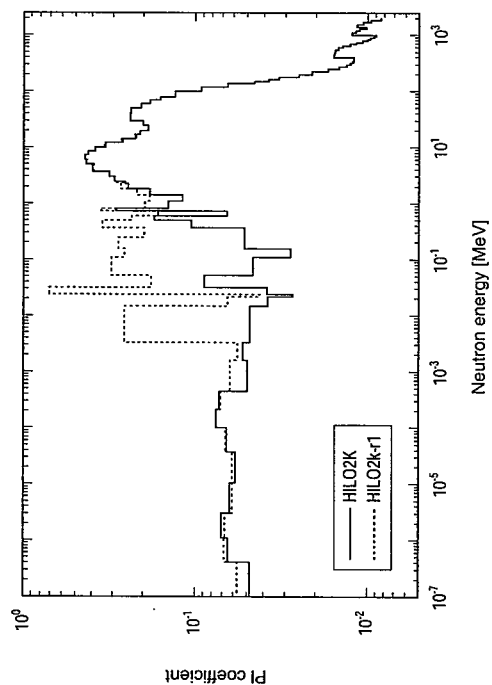


Fig. 8 Legendre coefficient of  $l=1$  of ingroup scattering matrices for natural iron.

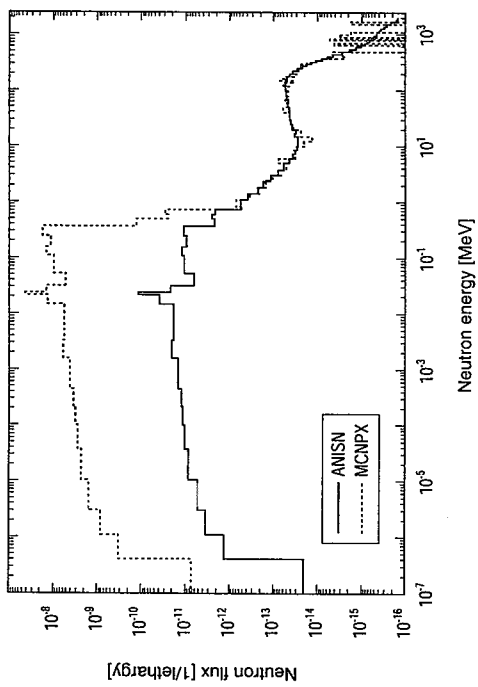


Fig. 5 Calculated neutron spectra at 4 m from the center in the iron sphere.

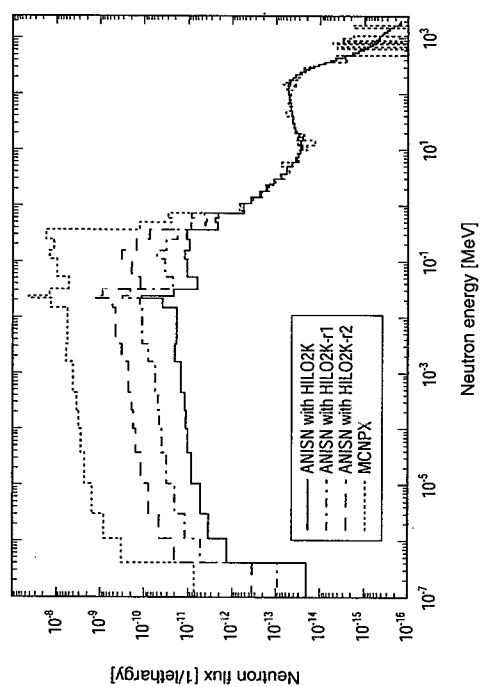


Fig. 7 Calculated neutron spectra at 4 m from the center in the iron sphere.



### 3.17 NMLIB

Chikara KONNO

Center for Proton Accelerator Facilities, Japan Atomic Energy Research Institute  
Tokai-mura, Naka-gun, Ibaraki-ken 319-1195 JAPAN  
e-mail: konno@cens.tokai.jaeri.go.jp

Yujiro IKEDA

Center for Proton Accelerator Facilities, Japan Atomic Energy Research Institute  
Tokai-mura, Naka-gun, Ibaraki-ken 319-1195 JAPAN  
e-mail: ikeda@cens.tokai.jaeri.go.jp

Koji NIITA

Research Organization for Information Science & Technology  
Tokai-mura, Naka-gun, Ibaraki-ken 319-1106 JAPAN  
e-mail: niita@hadron03.tokai.jaeri.go.jp

A new general purpose neutron incident nuclear data library, NMLIB, for neutron energy up to 3 GeV is generated by using NMTC/JAM for neutron cross sections above 20 MeV and JENDL-3.2 or -3.3 for neutron cross sections below 20 MeV. MATXS files (NMLIB/MG) and ACE files (NMLIB/MC) of NMLIB are also produced from NMLIB with the NJOY code. A simple test calculation suggests that NMLIB, NMLIB/MG and NMLIB/MC have no problem except for self-shielding.

#### 1. Introduction

Various shielding designs have been underway in JAERI-KEK Joint (JKJ) project [1]. Simple methods (Moyer's model [2] and DUCT-III [3]) and Monte Carlo codes (NMTC/JAM [4] and MCNPX [5]) were used in the designs. The calculation time of the simple methods is very short, while that of Monte Carlo calculations is very long for deep penetration. In the SNS project [6] the HILO2K [7] multigroup library for neutron energy up to 2 GeV is widely used in order to reduce calculation time. At first we hoped to generate a multigroup library for neutron energy up to 3 GeV, which is an energy of proton incident to neutron source in JKJ project, from JENDL High Energy File [8]. But the release of JENDL High Energy File is too delayed. Then we planned to generate a general purpose neutron incident nuclear data library, NMLIB, for neutron energy up to 3 GeV separately and produce MATXS files (NMLIB/MG) and ACE files (NMLIB/MC) from NMLIB. An overview and a simple test calculation of NMLIB, NMLIB/MG and NMLIB/MC will be described in this paper.

## 2. Overview of NMLIB

NMLIB is a general purpose neutron incident nuclear data library for neutron energy up to 3 GeV of the ENDF format [9]. The high energy neutron cross section data ( $> 20$  MeV) in NMLIB were calculated with the modified NMTC/JAM code (default option parameter), which outputs neutron cross section data, and were stored as (n,x) reaction, except for elastic scattering. The low energy neutron cross section data ( $< 20$  MeV) in NMLIB were JENDL-3.2 [10] or JENDL-3.3 [11]. NMLIB includes hydrogen, carbon, nitrogen, oxygen, aluminum, silicon, calcium, iron and copper at this time for concrete and iron shields and beam dump.

MATXS files (neutron 195 groups up to 3 GeV, gamma 35 groups up to 3 GeV,  $P_{14}$  expansion), NMLIB/MG, of NMLIB were produced with the NJOY99.67 [12] code modified for neutrons up to 3 GeV and Legendre order higher than 7. The energy boundary of the group structure is shown in Table 1. The photo-atomic data file, EPDL97 [13], for gamma energy up to 10 GeV was used for this processing. The specifications of the NJOY processing are the following; 1) the temperature is 300 K, 2) weight functions are a thermal Maxwellian at low energies +  $1/E$  for neutron and  $1/E$  for gamma, 3) background cross sections are  $10^6$ ,  $10^4$ ,  $10^3$ , 300, 100, 30, 10, 1, 0.1,  $10^{-5}$  for neutron. A multigroup library for Sn calculations was prepared with the TRANSX2.15 [14] code from NMLIB/MG. New format ACE files, NMLIB/MC, of NMLIB were also produced with the modified NJOY code. The temperature is 300 K.

## 3. Test Calculation

We performed a simple test calculation to validate NMLIB. The model of this test consisted of a concrete sphere or an iron sphere of 5 m in radius with an isotropic 3 GeV neutron source in the center. Neutron dose rates and neutron spectra in the sphere were calculated. The codes and libraries used are the following;

- 1) Monte Carlo code PHITS [15] with JENDL-3.2 or -3.3 (neutron only mode),
- 2) Monte Carlo code PHITS with NMLIB/MC (neutron only mode),
- 3) Sn code ANISN [16] with NMLIB/MG  
(Bondarenko's self-shielding correction [17],  $P_9$  expansion,  
Extended transport approximation [14]),

where PHITS is a successor of NMTC/JAM, which is used to obtain neutron ( $> 20$  MeV) cross sections of NMLIB. It was judged through comparison with the PHITS calculation with JENDL-3.2 or -3.3 whether NMLIB/MC and NMLIB/MG have any problems.

The calculated neutron dose rates and neutron spectra in the spheres are shown in Figs. 1 - 8. In the concrete sphere all the calculated neutron dose rates and neutron spectra are almost the same together. On the other hand, in the iron sphere the PHITS calculation with NMLIB/MC agrees with the PHITS calculation with JENDL, while a discrepancy between the ANISN calculation with NMLIB/MG and the PHITS calculations increases with the distance from the center. The calculated neutron spectra suggest that the discrepancy between the ANISN calculation with NMLIB/MG and the PHITS calculations mainly comes from the difference in the neutron flux below 1 MeV, where the resonance peaks of iron cause self-shielding. Although the Bondarenko's self-shielding correction was performed in the ANISN calculation, it is considered that the correction is not enough for the iron assembly thicker than 2 m in the case of the

neutron group structure shown in Table 1. Thus it is concluded that the discrepancy between the ANISN calculation with NMLIB/MG and the PHITS calculations comes from limitation of the Bondarenko's self-shielding correction rather than a proper problem in NMLIB/MG.

#### 4. Conclusion

A general purpose neutron incident nuclear data library, NMLIB, for neutron energy up to 3 GeV was prepared for JKJ project. MATXS (NMLIB/MG) and ACE (NMLIB/MC) files are produced from NMLIB with NJOY modified for NMLIB. Test calculations with NMLIB suggested the followings;

- 1) The calculations with NMLIB agree well with PHITS calculations with JENDL-3.2 or -3.3 in the concrete sphere case.
- 2) In the iron sphere case the calculations with NMLIB/MC agree well with PHITS calculations with JENDL-3.2 or -3.3, while those with NMLIB/MG do not in the deep positions. Simple self-shielding correction in NMLIB/MG is considered to be not enough for very thick iron assembly.

It is concluded that NMLIB/MC and NMLIB have no problem. The self-shielding correction of NMLIB/MG is not adequate for very thick iron assembly. It is noted that this is not a defect of only NMLIB/MG but limitation of the Bondarenko's self-shielding correction.

#### References

- [1] The Joint Project team of JAERI and KEK : JAERI-Tech 2000-003 (2000) [in Japanese].
- [2] Moyer B.J. : Proc. 1st Int. Conf. Shielding around High Energy Accelerators, p. 65 (1962).
- [3] Tayama R., et al. : KEK Internal 2001-8 (2001) [in Japanese].
- [4] Niita K., et al. : JAERI-Data/Code 2001-007 (2001).
- [5] Hughes H.G., et al. : Proc. of Int. Conf. on Mathematics & Computation, Reactor Physics & Environmental, Analysis in Nuclear Applications, p. 939 (1999).
- [6] Appleton B.R. : ORNL/TM-6063 (1997).
- [7] Lillie R.A. and Gallmeier F.X. : Proc. 4th Int. Top. Meet. Nucl. Applicat. Accel. Tech., p.302 (2000).
- [8] Fukahori T., et al. : J. Nucl. Sci. Technol., Supplement 2, 25 (2002).
- [9] McLane V. (Ed.) : BNL-NCS-44945-01/04-Rev (1998).
- [10] Nakagawa T., et al. : J. Nucl. Sci. Technol., 32, 1259 (1995).
- [11] Nakagawa T. and Shibata K. : JAERI-Conf 2001-006, p. 27 (2001).
- [12] MacFarlane R.E. and Muir D.W. : LA-12740-M (1994).
- [13] Cullen D.E., et al. : UCRL-ID-50400, Vol. 6, Rev 5 (1997).
- [14] MacFarlane R.E. : LA-12312-MS (1993).
- [15] Iwase H., et al. : J. Nucl. Sci. Technol., 39, 1142 (2002).
- [16] DOORS3.2 : One, Two- and Three-Dimensional Discrete Ordinates Neutron/Photon Transport Code System, RSICC CODE PACKAGE CCC-650 (1998).
- [17] Bondarenko I.I. (Ed.) : Group Constants for Nuclear Reactor Calculations, Consultants Bureau, New York, (1964).

Table 1 Energy boundary of group structure.

Neutron 195 group								Gamma 35 group	
Group	Upper energy [eV]	Group	Upper energy [eV]	Group	Upper energy [eV]	Group	Upper energy [eV]	Group	Upper energy [eV]
1	3.0000e+09	51	5.2205e+06	101	3.6883e+05	151	5.5308e+03	1	3.0000e+09
2	2.0000e+09	52	4.9658e+06	102	3.3373e+05	152	4.3074e+03	2	2.0000e+09
3	1.5000e+09	53	4.7237e+06	103	3.0197e+05	153	3.7074e+03	3	1.5000e+09
4	1.0000e+09	54	4.4933e+06	104	2.9849e+05	154	3.3546e+03	4	1.0000e+09
5	7.0000e+08	55	4.0657e+06	105	2.9721e+05	155	3.0354e+03	5	7.5000e+08
6	5.0000e+08	56	3.6788e+06	106	2.9452e+05	156	2.7465e+03	6	5.0000e+08
7	3.5000e+08	57	3.3287e+06	107	2.8725e+05	157	2.6126e+03	7	3.0000e+08
8	2.5000e+08	58	3.1664e+06	108	2.7324e+05	158	2.4852e+03	8	2.0000e+08
9	2.2500e+08	59	3.0119e+06	109	2.4724e+05	159	2.2487e+03	9	1.5000e+08
10	2.0000e+08	60	2.8651e+06	110	2.3518e+05	160	2.0347e+03	10	1.0000e+08
11	1.8000e+08	61	2.7253e+06	111	2.2371e+05	161	1.5846e+03	11	7.5000e+07
12	1.6000e+08	62	2.5924e+06	112	2.1280e+05	162	1.2341e+03	12	5.0000e+07
13	1.4000e+08	63	2.4660e+06	113	2.0242e+05	163	9.6112e+02	13	3.0000e+07
14	1.3000e+08	64	2.3852e+06	114	1.9255e+05	164	7.4852e+02	14	2.0000e+07
15	1.2000e+08	65	2.3653e+06	115	1.8316e+05	165	5.8295e+02	15	1.4000e+07
16	1.1000e+08	66	2.3457e+06	116	1.7422e+05	166	4.5400e+02	16	1.2000e+07
17	1.0000e+08	67	2.3069e+06	117	1.6573e+05	167	3.5358e+02	17	1.0000e+07
18	9.0000e+07	68	2.2313e+06	118	1.5764e+05	168	2.7536e+02	18	8.0000e+06
19	8.0000e+07	69	2.1225e+06	119	1.4996e+05	169	2.1445e+02	19	7.5000e+06
20	7.0000e+07	70	2.0190e+06	120	1.4264e+05	170	1.6702e+02	20	7.0000e+06
21	6.5000e+07	71	1.9205e+06	121	1.3569e+05	171	1.3007e+02	21	6.5000e+06
22	6.0000e+07	72	1.8268e+06	122	1.2907e+05	172	1.0130e+02	22	6.0000e+06
23	5.5000e+07	73	1.7377e+06	123	1.2277e+05	173	7.8893e+01	23	5.5000e+06
24	5.0000e+07	74	1.6530e+06	124	1.1679e+05	174	6.1442e+01	24	5.0000e+06
25	4.5000e+07	75	1.5724e+06	125	1.1109e+05	175	4.7851e+01	25	4.5000e+06
26	4.0000e+07	76	1.4957e+06	126	9.8037e+04	176	3.7267e+01	26	4.0000e+06
27	3.5000e+07	77	1.4227e+06	127	8.6517e+04	177	2.9023e+01	27	3.5000e+06
28	3.0000e+07	78	1.3534e+06	128	8.2503e+04	178	2.2603e+01	28	3.0000e+06
29	2.7500e+07	79	1.2873e+06	129	7.9499e+04	179	1.7604e+01	29	2.5000e+06
30	2.5000e+07	80	1.2246e+06	130	7.1998e+04	180	1.3710e+01	30	2.0000e+06
31	2.2500e+07	81	1.1648e+06	131	6.7379e+04	181	1.0677e+01	31	1.5000e+06
32	1.9600e+07	82	1.1080e+06	132	5.6562e+04	182	8.3153e+00	32	1.0000e+06
33	1.7500e+07	83	1.0026e+06	133	5.2475e+04	183	6.4760e+00	33	4.0000e+05
34	1.4900e+07	84	9.6164e+05	134	4.6309e+04	184	5.0435e+00	34	2.0000e+05
35	1.3500e+07	85	9.0718e+05	135	4.0868e+04	185	3.9279e+00	35	1.0000e+05
36	1.2200e+07	86	8.6294e+05	136	3.4307e+04	186	3.0590e+00		1.0000e+04
37	1.0000e+07	87	8.2085e+05	137	3.1828e+04	187	2.3824e+00		
38	9.5123e+06	88	7.8082e+05	138	2.8501e+04	188	1.8554e+00		
39	9.0484e+06	89	7.4274e+05	139	2.7000e+04	189	1.4450e+00		
40	8.6071e+06	90	7.0651e+05	140	2.6058e+04	190	1.1254e+00		
41	8.1873e+06	91	6.7205e+05	141	2.4788e+04	191	8.7643e-01		
42	7.7880e+06	92	6.3928e+05	142	2.4176e+04	192	6.8256e-01		
43	7.4082e+06	93	6.0810e+05	143	2.3579e+04	193	5.3158e-01		
44	7.0469e+06	94	5.7844e+05	144	2.1875e+04	194	4.1399e-01		
45	6.7032e+06	95	5.5023e+05	145	1.9305e+04	195	1.0000e-01		
46	6.5924e+06	96	5.2340e+05	146	1.5034e+04		1.0000e-05		
47	6.3763e+06	97	4.9787e+05	147	1.1709e+04				
48	6.0653e+06	98	4.5049e+05	148	1.0595e+04				
49	5.7695e+06	99	4.0762e+05	149	9.1188e+03				
50	5.4881e+06	100	3.8774e+05	150	7.1017e+03				



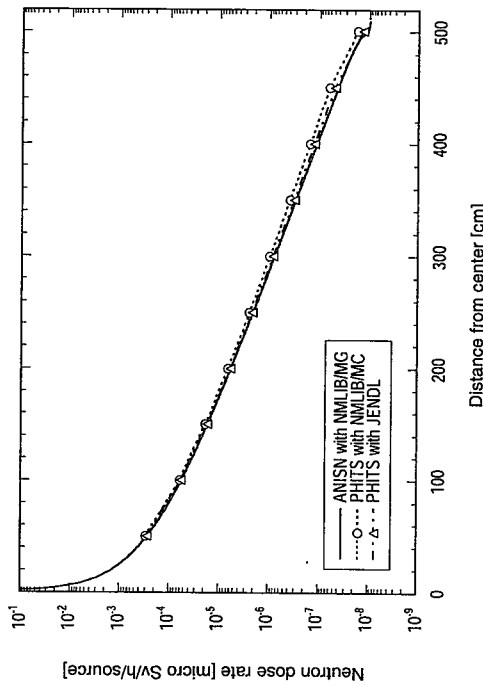


Fig. 1 Calculated neutron dose rates in the concrete sphere.

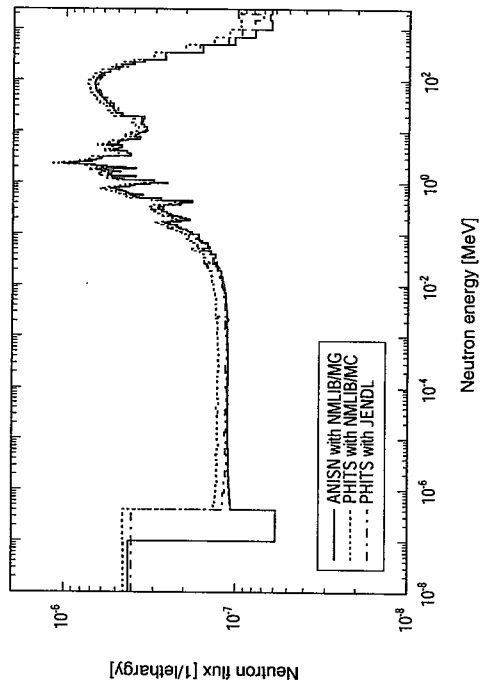


Fig. 3 Calculated neutron spectra at 2 m from the center in the concrete sphere.

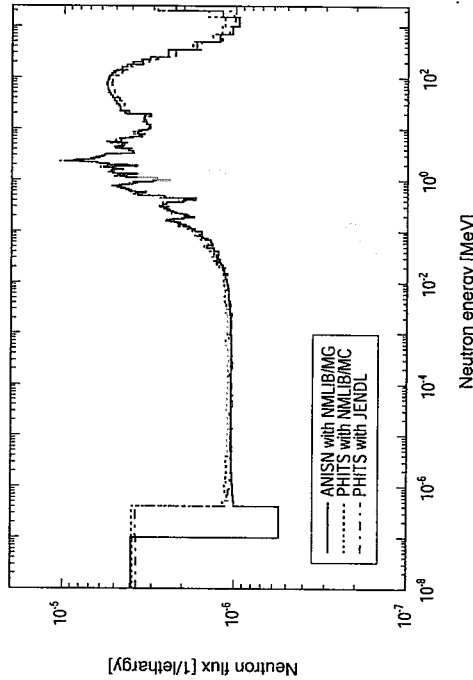


Fig. 2 Calculated neutron spectra at 1 m from the center in the concrete sphere.

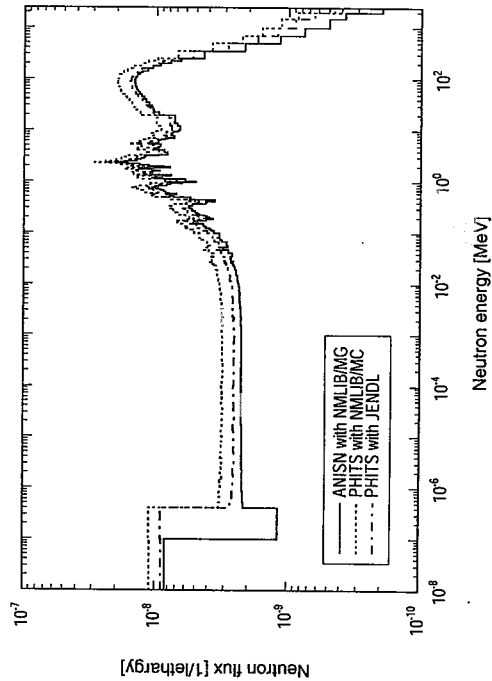


Fig. 4 Calculated neutron spectra at 4 m from the center in the concrete sphere.

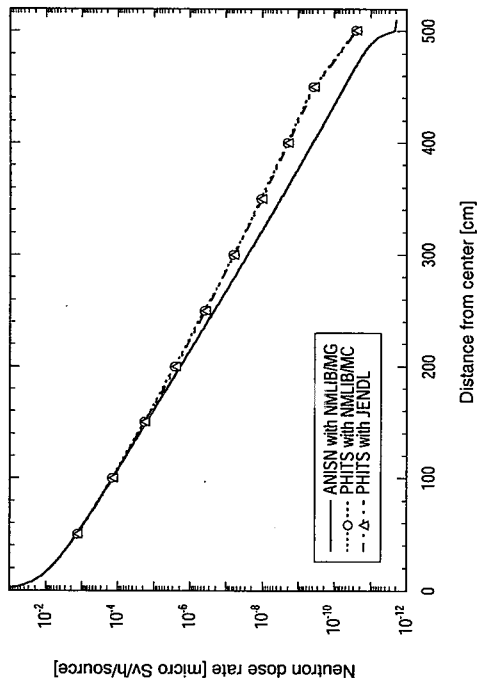


Fig. 5 Calculated neutron dose rates in the iron sphere.

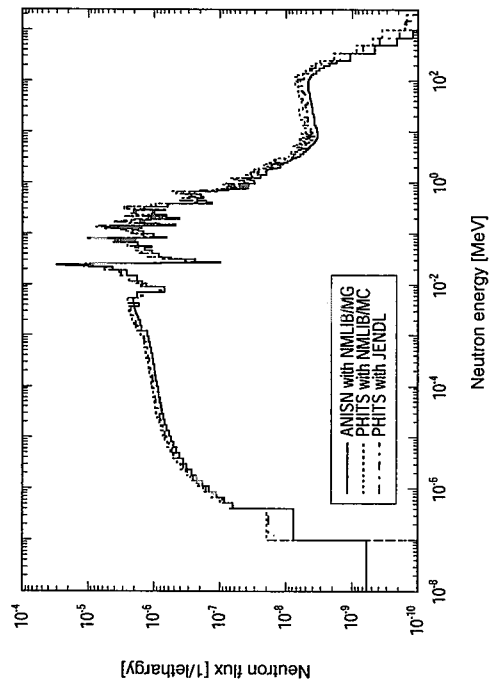


Fig. 7 Calculated neutron spectra at 2 m from the center in the iron sphere.

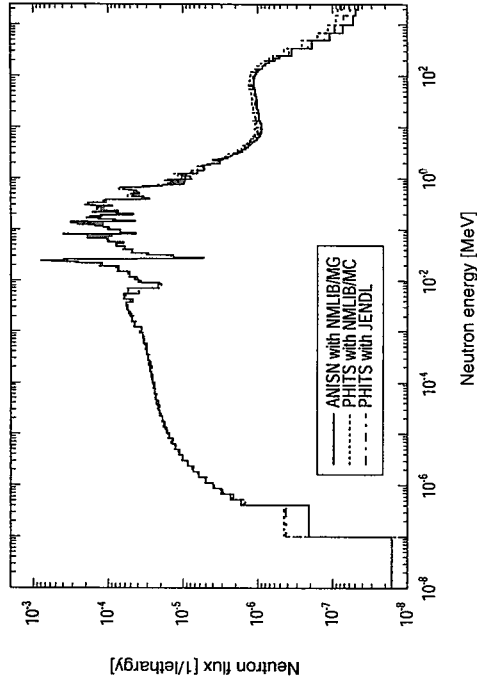


Fig. 6 Calculated neutron spectra at 1 m from the center in the iron sphere.

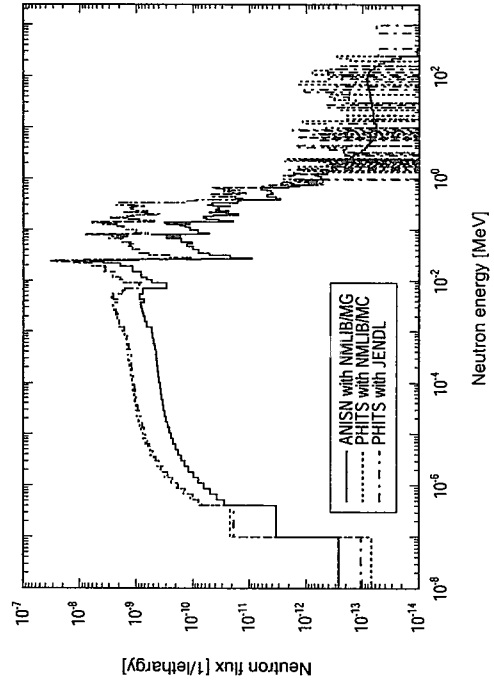


Fig. 8 Calculated neutron spectra at 4 m from the center in the iron sphere.



### 3.18 Neutron Optical Potentials in Unstable Nuclei and the Equation of State of Asymmetric Nuclear Matter

K. Oyamatsu<sup>1,2)</sup>, K. Iida<sup>2)</sup>

<sup>1)</sup>Aichi Shukutoku University, <sup>2)</sup>RIKEN

Neutron single particle potential is one of the basic macroscopic properties to describe structure and reactions of nuclei in nuclear reactors and in the universe. However, the potential is quite uncertain for unstable nuclei primarily because the equation of state (EOS) of asymmetric nuclear matter is not known well. The present authors studied systematically the empirical EOS of asymmetric nuclear matter using a macroscopic nuclear model; about two hundred EOS's having empirically allowed values of  $L$  (symmetry energy density derivative coefficient) and  $K_0$  (incompressibility) were obtained from the fittings to masses and radii of stable nuclei. It was suggested that the  $L$  value could be determined from global ( $Z$ ,  $A$ ) dependence of nuclear radii. In the present study, the single particle potential is examined assuming kinetic energies of non-interacting Fermi gases. The potential in a nucleus can be calculated easily, once the density distribution is solved using the effective nuclear interaction (EOS). Neutron and proton single particle potentials are calculated systematically for  $^{80}\text{Ni}$  using the two hundred EOS's. It is found that the neutron-proton potential difference has clear and appreciable  $L$  dependence, while the potential for each species does not show such simple dependence on  $L$ .

#### 1. Introduction

In the past, the present authors independently studied extremely neutron-rich nuclei in neutron star matter and supernova matter. The key for the description is found the equation of state (EOS) of asymmetric nuclear matter, which determines the bulk property of neutron rich nuclei. The empirical EOS of symmetric nuclear matter is determined well from stable nuclei. While the asymmetric matter EOS should be, in principle, determined from neutron rich nuclei, it has not been possible because experiments using sufficiently neutron rich nuclei has been prohibitively difficult.

Now the progress of experimental technique is opening the door to experimental study of neutron rich nuclei, the authors have studied possibility of empirical determination of the EOS using a macroscopic nuclear model. Firstly, about 200 empirically allowed EOS's are constructed systematically by fitting masses and radii of stable nuclei. Secondly, properties of neutron rich nuclei are calculated using the EOS's. It is found that masses and radii of unstable nuclei has appreciable dependence on the EOS. The key parameter is found  $L$  (symmetry energy density derivative coefficient), which can not be determined from stable nuclei.

Now we turn to the EOS dependence of optical potential parameters. In the present study, the potential depth of the neutron and proton single particle potentials is studied using the 200 EOS's.

#### 2. Key EOS parameters

In this paper, we deal with the energy per nucleon of nuclear matter,  $w$ , as a function of nucleon number density  $n$  and proton fraction  $x$ . The empirical EOS is characterized by a limited number of parameters. It is useful to consider Taylor expansion of the energy per nucleon, which is given by

$$w(n, x) \approx w_0 + \frac{K_0}{18n_0^2}(n - n_0)^2 + (1 - 2x)^2 \left[ S_0 + \frac{L}{3n_0}(n - n_0) \right] \quad (1)$$

Here,  $n_0$  and  $w_0$  are saturation density and energy of symmetric nuclear matter, respectively. They are well determined from stable nuclei. The incompressibility of symmetric matter,  $K_0$ , should also be determined from stable nuclei but its values is somewhat uncertain even at present. The parameters of interest here are  $S_0$ , the symmetry energy, and the symmetry energy density derivative coefficient,  $L$ . In terms of the density dependent symmetry energy  $S(n)$ , these parameters are defined as  $S_0 = S(n_0)$  and

$$L = 3n_0 \left. \frac{dS}{dn} \right|_{n=n_0}. \quad (2)$$

The saturation point (density and energy) of asymmetric nuclear matter mainly determines nuclear masses and radii of neutron rich nuclei. A useful and intuitive EOS parameter to characterize the saturation point of asymmetric nuclear matter is the slope of the saturation line (the line joining the saturation points) at  $n=n_0$ , which is given by

$$y = - \frac{S_0 K_0}{3L n_0} \quad (3)$$

In the followings, this parameter,  $y$ , will be used to empirically constrain the symmetry energy.

### 3. Empirically allowed EOS of asymmetric nuclear matter

In this study, a macroscopic nuclear model is used to derive the empirical EOS of asymmetric nuclear matter because the EOS is nothing but a macroscopic property of nuclei. We begin with a model for the bulk energy density of uniform nuclear matter. The energy density,  $w(n, x) \times n$  is written as the sum of kinetic and potential energy densities as a function of the neutron density  $n_n$  and the proton density  $n_p$ ; and total nucleon density  $n = n_n + n_p$ ;

$$\varepsilon_0(n_n, n_p) = \frac{3}{5} \left( \frac{3\pi^2}{2} \right)^{2/3} \left[ \frac{\hbar^2}{2m_n} n_n^{5/3} + \frac{\hbar^2}{2m_p} n_p^{5/3} \right] + \left[ 1 - (1 - 2x)^2 \right] v_s(n) + (1 - 2x)^2 v_n(n) \quad (4)$$

Here,  $n = n_n + n_p$  and  $x = n_p/n$ . The first term in Eq. (4) is the Fermi kinetic energies of neutrons and protons. The functions  $v_s(n)$  and  $v_n(n)$  denote potential energy densities for  $x=1/2$  (symmetric nuclear matter) and  $x=0$  (pure neutron matter), respectively.

$$v_s(n) = a_1 n^2 + \frac{a_2 n^3}{1 + a_3 n}, \quad v_n(n) = b_1 n^2 + \frac{b_2 n^3}{1 + b_3 n} \quad (5)$$

These functions have desirable limiting behavior; two body interactions are dominant at low densities while, at high densities, the sound speed does not exceed the speed of light thanks to the denominators. The present model (Eqs. (4) and (5)) is flexible enough to fit various effective interactions of contemporary use such as Skyrme type interactions in the non-relativistic theory and Lagrangeans of relativistic mean field theory.

In the Thomas-Fermi approximation, the binding energy of a nucleus is written, using the local neutron (proton) density  $n_n(r)$  ( $n_p(r)$ ), as

$$-B = \int dr \varepsilon_0(n_n, n_p) + \int dr F_0 |\nabla n(r)|^2 + \frac{e^2}{2} \int dr \int dr' \frac{n_p(r) n_p(r')}{|r - r'|}, \quad (6)$$

with  $n = n_n + n_p$ . Here  $\varepsilon_0(n_n, n_p)$  in the first term in Eq. (6) denotes the energy density, namely the EOS. The first term in Eq. (6) is the bulk energy, the second term is the gradient energy

with an adjustable constant  $F_0$ , and the third term is the Coulomb energy. In this paper, we assume, for simplicity, that the nucleon distributions  $n_i(r)$  ( $i=n,p$ ) are parametrized as

$$n_i(r) = \begin{cases} n_i^{\text{in}} \left[ 1 - \left( \frac{r}{R_i} \right)^{t_i} \right] & r \leq R_i \\ 0 & r > R_i \end{cases} \quad (7)$$

Here,  $R_i$  and  $t_i$  are the radius and surface diffuseness parameters, respectively with  $n_i^{\text{in}}$  being the central density.

For a given nucleus, the binding energy  $B$  is calculated by minimizing the Eq. (6) with respect to the variation of  $R_i$  and  $t_i$ . Consequently, the nuclear mass and radius are functions of interaction parameters,  $a_1$ - $a_3$  and  $b_1$ - $b_3$  in Eq. (5), and  $F_0$  in Eq. (6). The six parameters,  $a_1$ - $a_3$  and  $b_1$ - $b_3$  directly determine the EOS in the present model while  $F_0$  represents finite range effects of nuclear interactions.

The values of the interaction parameters are determined empirically to fit masses and radii of stable nuclei. The fitting procedure together with input data for the fitting are described in Ref. [1] and [2]. In the present study, the value of  $b_3$  is fixed as a typical value  $b_3 \approx 1.6$ . This particular choice does not affect the conclusion of the present study.

It is noted that various interaction parameter sets can reproduce the masses and radii of stable nuclei almost equally because the neutron-proton asymmetry is not large enough in stable nuclei to determine the symmetry energy. To generate empirically allowed EOS systematically, the fittings were performed for fixed values of empirically allowed values of  $(\gamma, K_0)$ . The obtained parameter sets cover essentially all possible EOS's as shown in Fig. 1.

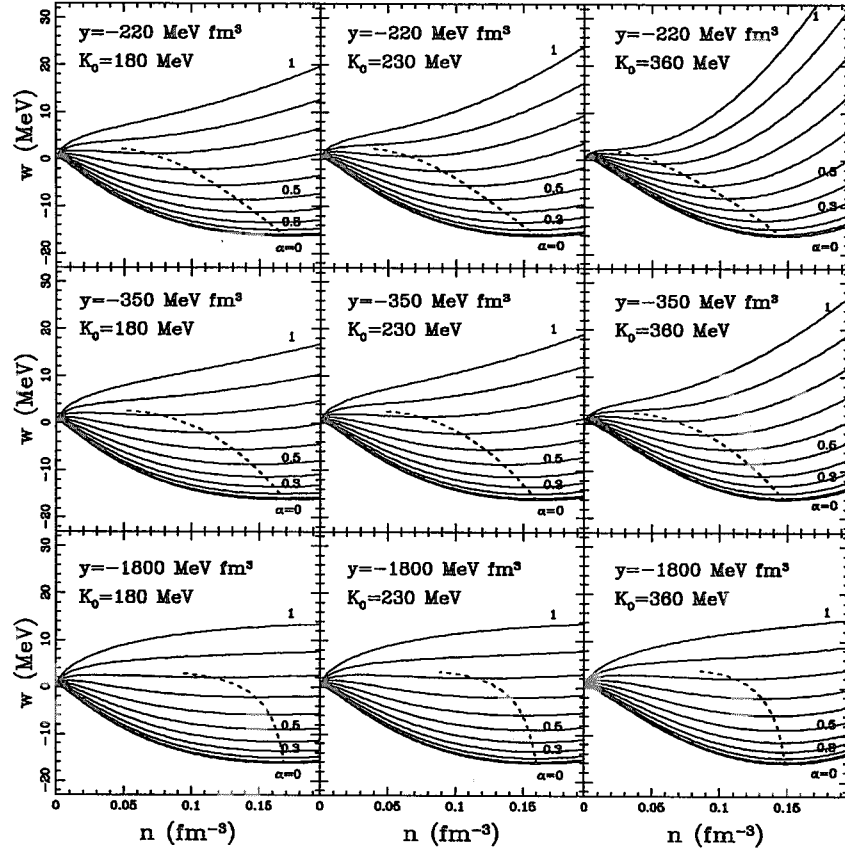


Fig. 1. Empirically allowed EOS's obtained from the fitting to stable nuclei.

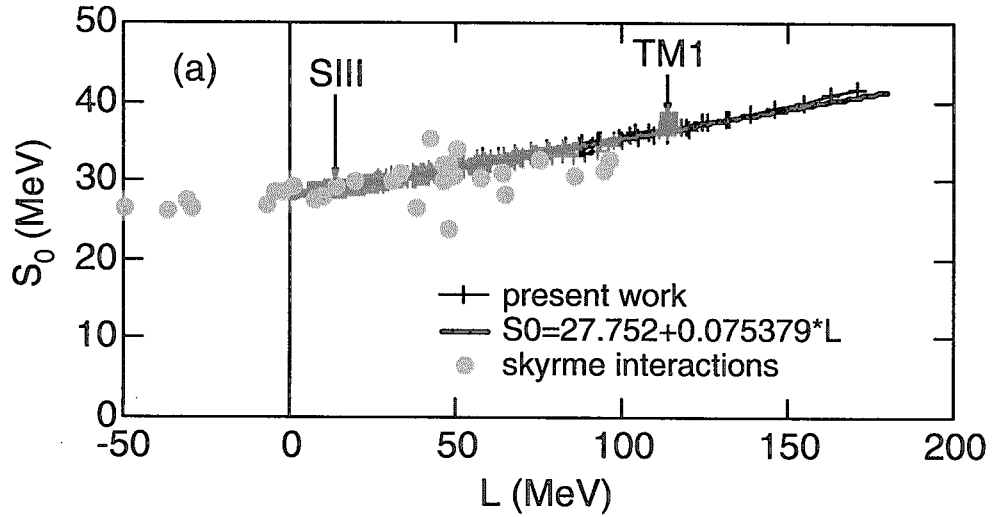
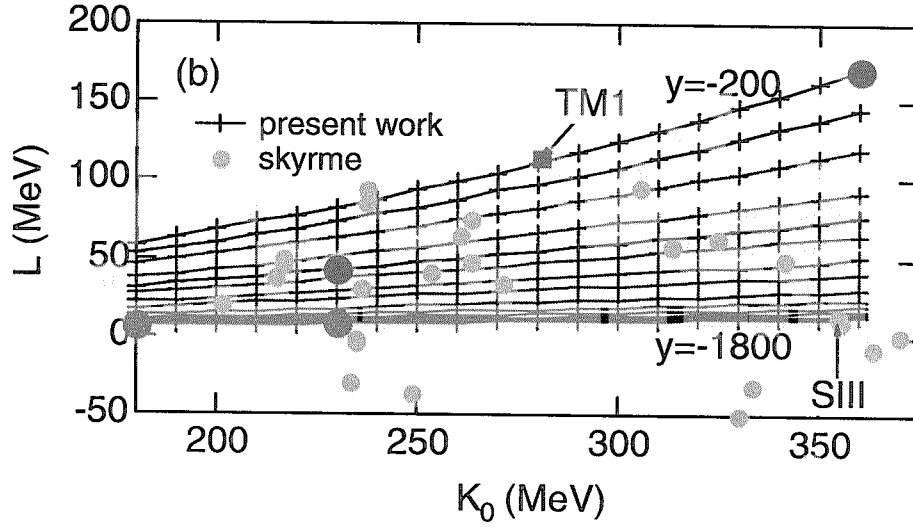
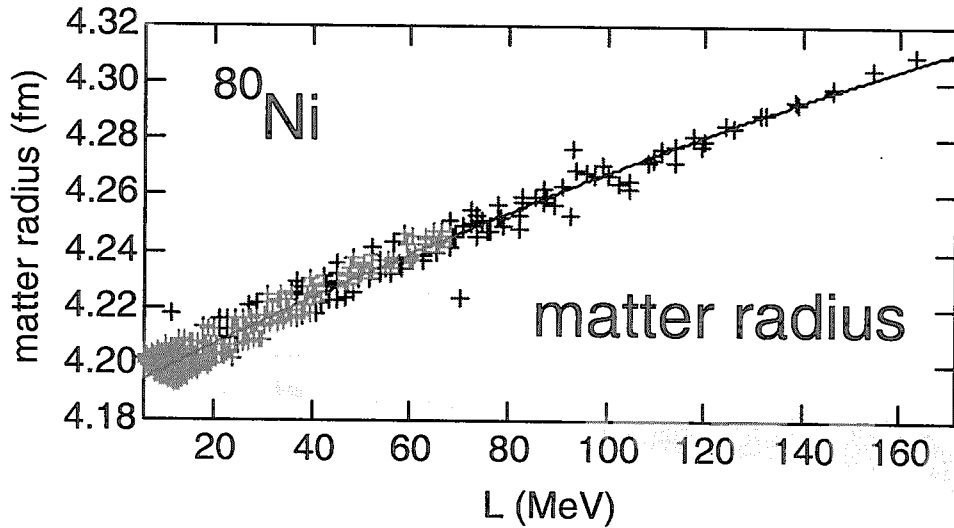


Fig. 2. Strong correlation between  $S_0$  and  $L$ .

Fig. 3. Empirically allowed region of  $(K_0, L)$ .Fig. 4. Matter radius of  $^{80}\text{Ni}$  as a function of  $L$ .

From this systematic study, it is found, for empirically allowed EOS's, that  $S_0$  and  $L$  are strongly correlated as shown in Fig. 2. It is also found that there is an empirical allowed region of  $(K_0, L)$  shown in Fig. 3.

In Ref. [2], it is concluded that nuclear radii of neutron rich nuclei strongly depend on  $L$  as shown in Fig. 4. This feature together with the  $S_0$ - $L$  correlation opens the door to determine the asymmetric matter EOS from measurements of nuclear radii in laboratories.

#### 4. Single particle potential of neutron-rich nuclei

It is interesting to investigate neutron and proton single particle potentials of unstable nuclei from the viewpoints of both nuclear structure and reaction studies. As a key potential parameter, we focus on the depth of the neutron (proton) single particle potential. The single particle potentials are given by

$$U_n = \frac{\partial v(n_n, n_p)}{\partial n_n}, \quad U_p = \frac{\partial v(n_n, n_p)}{\partial n_p} + (\text{Coulomb}) \quad (8)$$

where  $v(n_n, n_p)$  is the potential energy density given by

$$v(n_n, n_p) = \varepsilon_0(n_n, n_p) - (\text{kinetic part}) = \left[ 1 - (1 - 2x)^2 \right] v_s(n) + (1 - 2x)^2 v_n(n) \quad (9)$$

The potential depth is given by the  $U_n$  (or  $U_p$ ) value at  $r=0$ . In the present model (Eqs.(4) and (9)), the effective nucleon mass is taken to be one.

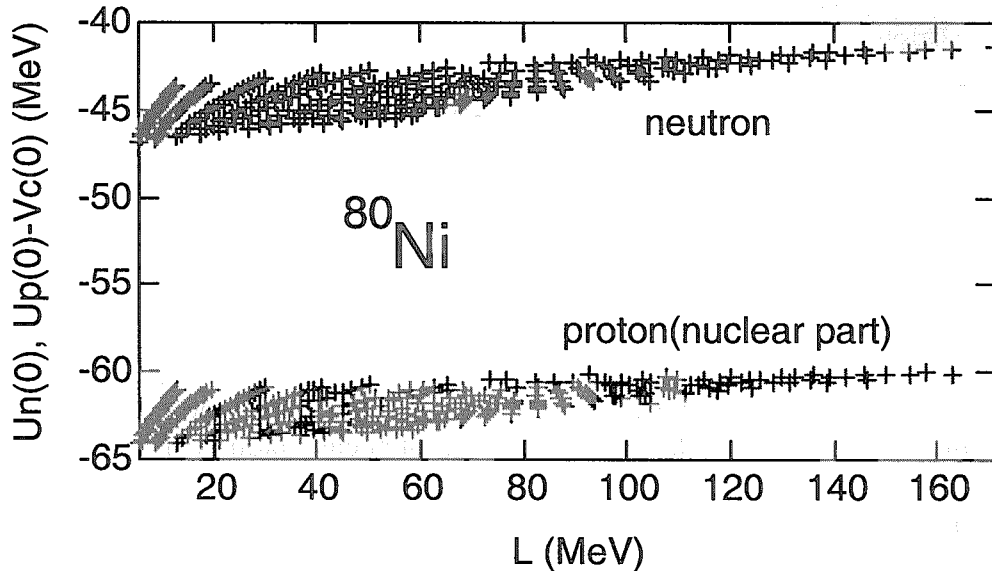
In Fig. 5, the potential depth is shown for neutrons and protons as well as its difference between neutrons and protons. For proton potential  $U_p$ , the Coulomb potential is subtracted to examine effects which directly reflect nuclear interactions. It is seen that the neutron-proton potential difference depends obviously on  $L$  while such simple  $L$  dependence is not seen for the neutron (or proton) potential depth. The  $L$  dependence of the potential difference is only 1 MeV, which is relatively small but appreciable compared with its absolute value (about 18 MeV).

### 5. Summary

In the Thomas-Fermi model, single particle potential can be directly calculated from the EOS, once nuclear distributions are solved using an effective nuclear interaction. The present study shows, similarly to nuclear masses and radii, the neutron-proton potential difference has clear and appreciable  $L$  dependence. The  $L$  dependence reflects that fact that neutron and proton densities at the center are sensitive to  $L$ . Hence it seems interesting to examine this feature in relation to nuclear radii and formation of neutron skins of neutron rich nuclei.

[1] K.Oyamatsu and K.Iida, Proc. The fourth symposium on Science of Hadrons under Extreme Conditions, JAERI-CONF 2002-011, pp.36-49 (in Japanese).

[2] K. Oyamatsu and K.Iida, nucl-th/0204033.





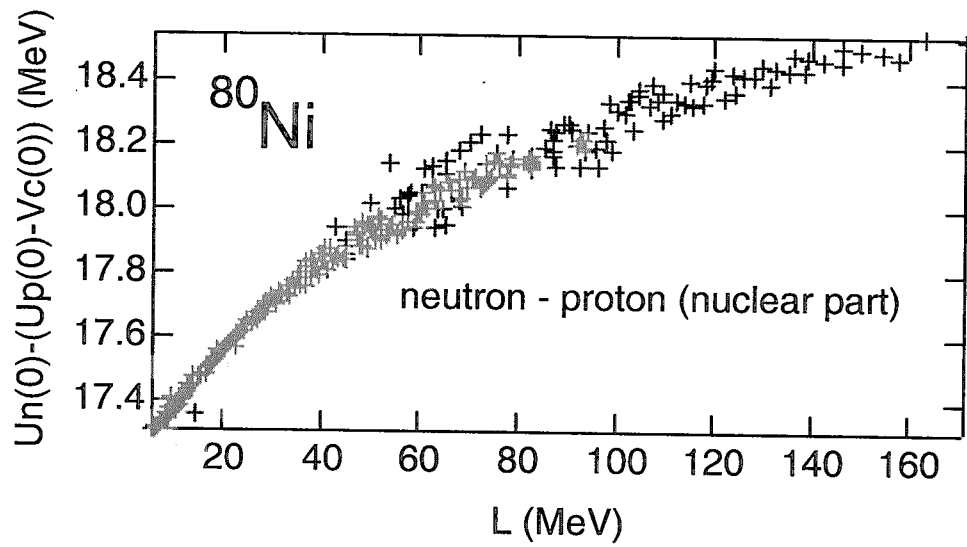


Fig. 5. The potential of the single particle potential of  $^{80}\text{Ni}$  (upper box) and its difference between neutrons and protons (lower box). For the proton potential, the Coulomb potential is subtracted to examine its nuclear part only.



### 3.19 Light Output Response of GSO(Ce) Scintillator to Deuterons

Fuminobu SAIHO<sup>†</sup>, Tadahiro KIN, Shinya HOHARA, Katsuhiko IKEDA

Fumiaki KONDO, Kiyohisa ICHIKAWA, Ikuo FUKUCHI

Yusuke UOZUMI, Nobuo IKEDA, Genichiro WAKABAYASHI, Masaru MATOBA

Department of Applied Quantum Physics and Nuclear Engineering, Kyushu University

Hakozaki, Higashi-ku, Fukuoka 812-8185

e-mail: <sup>†</sup>saiho@nucl.kyushu-u.ac.jp

We have measured the preequilibrium reaction process by (p,dx) reaction in intermediate energy region using the cerium-doped gadolinium orthosilicate,  $\text{Gd}_2\text{SiO}_5$ -GSO(Ce) scintillation detector. In order to carry out energy calibration of the measured deuteron spectra at 300- and 392 MeV, the light output response of the GSO(Ce) scintillator to deuterons was investigated by using pp, pd and  $\alpha$ d elastic scattering. And the results of calculation by Birks' formula show the overall agreement with experimental data.

#### 1.Introduction

GSO(Ce) has various advantages compared with other typical crystal scintillators: remarkably high radiation hardness, comparatively large density, higher light output, and no hygroscopic. From these reasons, GSO(Ce) has the characteristic which was excellent to the nuclear reaction experiment.

In order to obtain the experiment data to double differential cross section (DDX), it is necessary to carry out energy calibration from the relation between a channel obtained by ADC and the energy lost within the scintillator.

Until now, the light output response to protons was studied by Anami et al.[2] up to maximum energy 161MeV and by Avdeichikov et al.[1] up to 30 MeV. And the light output response to deuterons was studied by Avdeichikov et al.[1] up to 40 MeV. It is valuable to extend the investigated energy range up to several hundreds of MeV. Furthermore, in measurements of deuteron energy by stacked spectrometers, one must pay attention to the pulse height difference between the stopping and the penetrating protons and deuterons even if they would deposit the same energies in the crystal.

In this paper, we describe an experimental study of light output response of GSO(Ce) to protons up to 161 MeV and to deuterons up to 215 MeV. Furthermore, the obtained data was compared with the formula which Birks[3] proposed for organic scintillators.

#### 2.Experimental

The beam experiment was performed at the Research Center for Nuclear Physics (RCNP), Osaka University. A sketch of the experimental setup is shown in Fig. 1. The proton beam of 392 MeV and the  $^4\text{He}$  beam of 400 MeV bombarded polyester target of  $17.5 \text{ mg/cm}^2$  and  $\text{CD}_2$  target of  $50 \text{ mg/cm}^2$ . The response of the stacked GSO(Ce) spectrometer was investigated with monoenergetic particles from elastic pp, pd and  $\alpha$ d scattering. In a target, nuclei other than a proton and a deuteron are also contained. Those nuclei react with an incidence particle. These reaction events have a continuum energy spectrum

and overlaps with a monoenergetic particles from pp, pd and  $\alpha$ d scattering. Therefore, they were removed by performing coincidence measurement.

A schematic diagram of the spectrometers was shown in Fig. 2. There were two types of spectrometer. One consisted of three plastic scintillators, two cubic GSO(Ce) crystals of  $43 \times 43 \times 43 \text{ mm}^3$  and a cylinderistical GSO(Ce) crystal of 62 mm diameter by 120 mm length. Another consisted of three plastics, three cubic GSO(Ce) crystals of  $43 \times 43 \times 43 \text{ mm}^3$ . One of plastics in each spectrometer had an aperture of 15 mm diameter and acted as an active slit to determined the solid angle of the spectrometer. To optimize the light collection of the plastics and GSO(Ce) crystals, five facets were lapped with aluminum tape. Shading sheet wrapped around the spectrometer.

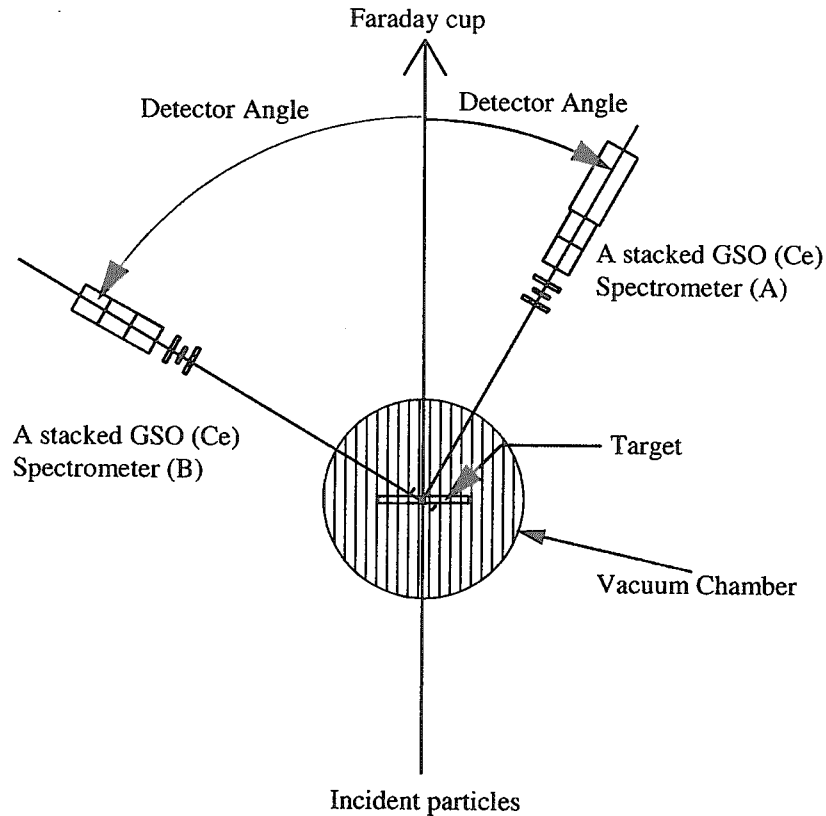


Figure 1: Experimental set up for the monoenergetic proton and deuteron measurement.

### 3. Results and Discussion

The energy dependence of the GSO(Ce) light output for protons and deuterons has been measured by using pp, pd and  $\alpha$ d scattering. Fig. 3 shows the measured light output, in arbitrary units, as a function of the energy for protons and deuterons. The error bars of the present data correspond to FWHM of the peaks in measured energy spectra. The curves are results of calculations proposed by Birks for inorganic scintillators. The light output per unit length,  $dL/dx$ , is defined as

$$\frac{dL}{dx} = \frac{S(dE/dx)}{1 + kB(dE/dx)} \quad (1)$$

where  $S$  is the absolute scintillation factor,  $BdE/dx$  represents the density of quenching centers per unit distance and  $k$  is a quenching parameter ( $kB$  is Birks parameter). The parameters,  $S$  and  $kB$ , are

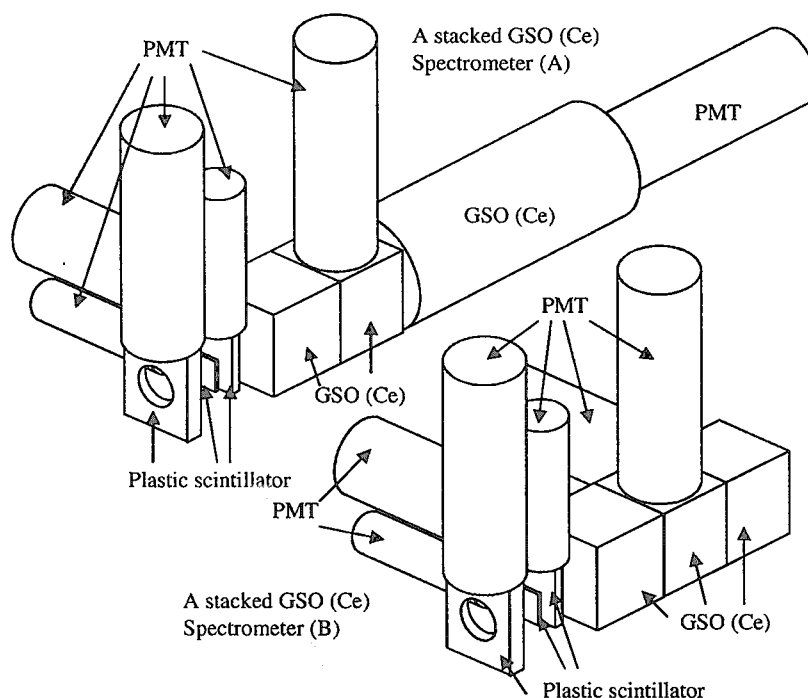


Figure 2: A schematic diagram of the stacked GSO(Ce) spectrometer.

determined by a best fit to the experimental data. The fitting result gives best fitted value  $S$  is 6.6 and  $kB$  is  $1.70 \times 10^{-5} \text{ (MeV/m)}^{-1}$ . The calculations provide an excellent description of the shape of relative light output. The maximum energy deposited in the cubic GSO(Ce) crystal of  $43 \times 43 \times 43 \text{ mm}^3$  are 161 MeV and 215 MeV at a proton and a deuteron, respectively. The response to protons and deuterons which penetrate 43 mm cubic GSO(Ce) is calculated by the use of Birks' formula. The calculated light outputs are shown in Fig. 4, and compared with the results of the present measurements. The measured data are well described by using the relation  $dL/dE$  versus  $E$  determined presently. Fig. 5 shows the energy spectra for 247 MeV monoenergetic protons and 256 MeV monoenergetic deuterons. A horizontal axis is the energy which changed the channel obtained by ADC by the relation between light output and energy in Fig. 4. The full energy peaks agree quite well with the energy calculated by two calculation codes (elastic scattering calculation and energy loss calculation).

#### 4. Conclusion

The light output response of GSO(Ce) to protons and deuterons was investigated by using  $pp$ ,  $pd$  and  $\alpha d$  scattering. The energy dependence of the light output response of GSO(Ce) was interpreted by Birks' formula. The light output difference between the stopping and the penetrating particles has been reasonably described by Birks' formula. The parameters were obtained  $S = 6.6$  (arbitrary unit) and  $kB = 1.70 \times 10^{-5} \text{ (MeV/m)}^{-1}$  for both protons and deuterons. The parameters,  $S$  and  $kB$ , were not dependent on a particle.

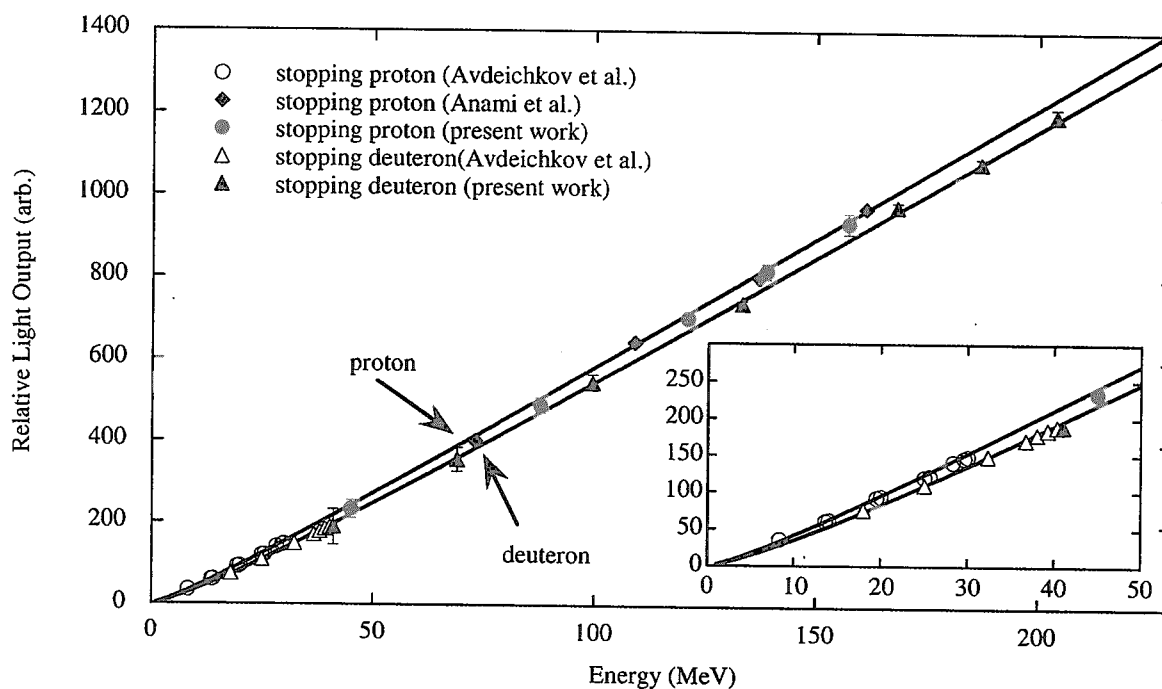


Figure 3: Light output of the GSO(Ce) as a function of energy for protons and deuterons.

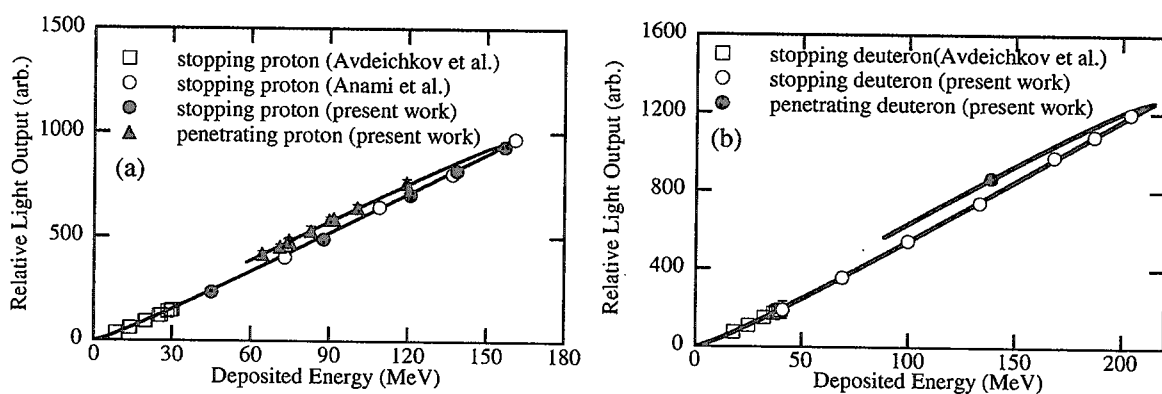


Figure 4: Light output of the GSO(Ce) to (a) penetrating protons as well as stopping protons and (b) penetrating deuterons as well as stopping deuterons.

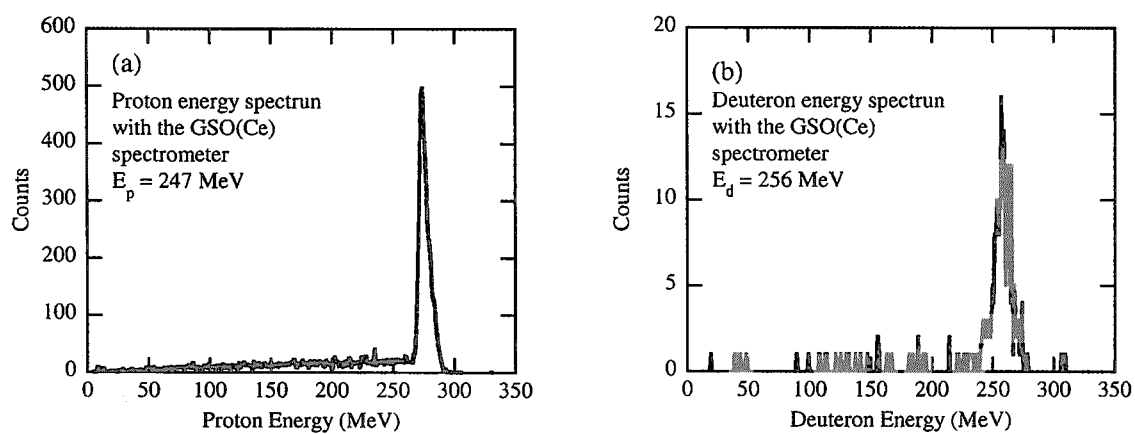


Figure 5: Energy spectra for (a) 274 MeV monoenergetic protons and (b) 256 MeV monoenergetic deuterons

## References

- [1] V.V. Avdeichikov, et al., J. Nucl. Instrum. Methods Phys. Res. A 349, 216 (1994).
- [2] K. Anami, et al., J. Nucl. Instrum. Methods Phys. Res. A 404, 327 (1998).
- [3] J. B. Birks, The Theory and Practice of Scintillation Counting, Pergamon Press, Oxford, 187 (1964).



### 3.20 The Development of melamine-D for the precise measurement of detection efficiencies of high energy $\gamma$ -rays

Shoji NAKAMURA<sup>1)</sup>, Hideo HARADA<sup>1)</sup>, Hirokazu TAKAYAMA<sup>2)</sup> and Kiyoshi KAWADE<sup>2)</sup>

1)Japan Nuclear Cycle Development Institute, Tokai Works, Tokai-mura, Naka-gun, Ibaraki-ken 319-1194

2)Nagoya University, Furo-cho, Tikusa-ku, Nagoya-city, Aichi-ken 464-8603

E-mail: rgm@tokai.jnc.go.jp

In order to obtain the precise detection efficiencies for high energy  $\gamma$ -rays in the prompt  $\gamma$ -ray spectroscopic measurement, the prompt  $\gamma$ -rays emitted from nitrogen contained in Melamine-D are utilized. This work shows the effectiveness of Melamine-D.

#### 1. Introduction

Since the high energy  $\gamma$ -rays up to about 10 MeV are emitted in the prompt  $\gamma$ -ray spectroscopic experiments, it is necessary to determine the  $\gamma$ -ray detection efficiencies in good accuracy for such high-energy regions. The neutron capture  $\gamma$ -rays from  $^{14}\text{N}$  ( $n,\gamma$ ) reaction have been often utilized. Figure 1 shows an example of a  $\gamma$ -ray spectrum obtained by the Liquid Nitrogen target. Many  $\gamma$ -ray peaks are observed up to the energy region of about 10 MeV. When melamine-H ( $\text{C}_6\text{H}_6\text{N}_6$ ) is used for the target, there is a problem of strong background caused by  $^1\text{H}$  ( $n,\gamma$ ) reaction. Recently liquid nitrogen target was developed for this purpose [1], however, there are still some problems, i.e., the difficulty of handling the low temperature liquid, strong background  $\gamma$ -rays from the container, and the uncertainty of the target geometry. The melamine-D was developed as a new calibration target, whose chemical form was  $\text{C}_6\text{D}_6\text{N}_6$ . The cross section of deuterium is 0.5mb[2] and much smaller than that of hydrogen (332mb[2]), therefore it is expected that deuterium-exchanged melamine contributes to the background reduction.

This work aims to examine the effectiveness of melamine-D for the calibration of the high energy  $\gamma$ -rays.

#### 2. Experiment

The melamine-D powder was compressed under the 2.0 t pressure power for 2 minutes by a compressor. The powder was shaped in tablets as shown in Figure 2, therefore the geometrical error was reduced. The tablet targets were irradiated by B-4 neutron guide facility in Kyoto University Research Reactor Institute. The neutron flux of the B-4 neutron guide is known as about  $5 \times 10^7 \text{ n/cm}^2\text{s}$ . The prompt  $\gamma$ -rays emitted from the targets were measured by a high purity Ge detector. The appearance of the measurement set-up is shown in Figure 3. The usual melamine-H powder was also shaped in the same tablet, and its measurements were performed in comparison with the measurements with the melamine-D target. The irradiation times were about 10 hours for each target.

#### 3. Results and Discussion

The  $\gamma$ -ray spectra are shown in Figure 4 in for melamine-H and melamine-D targets. The  $\gamma$ -ray intensity of 2.2 MeV  $\gamma$ -ray from  $^1\text{H}$  ( $n,\gamma$ ) reaction in the melamine-D target was 20 times smaller than that in melamine-H, therefore the background was decreased remarkably below 2.2MeV as shown in Figure 5. The  $\gamma$ -rays with small intensities were

also clearly observed. For example, the weak  $\gamma$ -ray peak of 1.999MeV is just located at the Compton edge of the 2.2 MeV  $\gamma$ -ray peak. By reducing the B.G. with melamine-D, this weak  $\gamma$ -ray peak was observed clearly.

#### 4. Conclusion

To calibrate the detector for the high energy  $\gamma$ -rays in the prompt  $\gamma$ -ray spectroscopic experiment, the use of the deuterium-exchanged melamine (melamine-D) was proposed as a target. The substantiation experiment shows the effectiveness of the melamine-D target, and the  $\gamma$ -rays with the small emission intensities were clearly observed.

#### Acknowledgement

This work has been carried out in part under the Visiting Researcher's Program of the Research Reactor Institute, Kyoto University.

#### Reference

- [1] H. Sakane *et al.*: KURRI Prog. Rep., p.37 (1999).
- [2] R. B. Firestone, V. S. Shirley, C. M. Baglin, S. Y. F. Chu, and J. Zipkin, Table of Isotopes, 8th edition, John Wiley and Sons, New York, (1995).

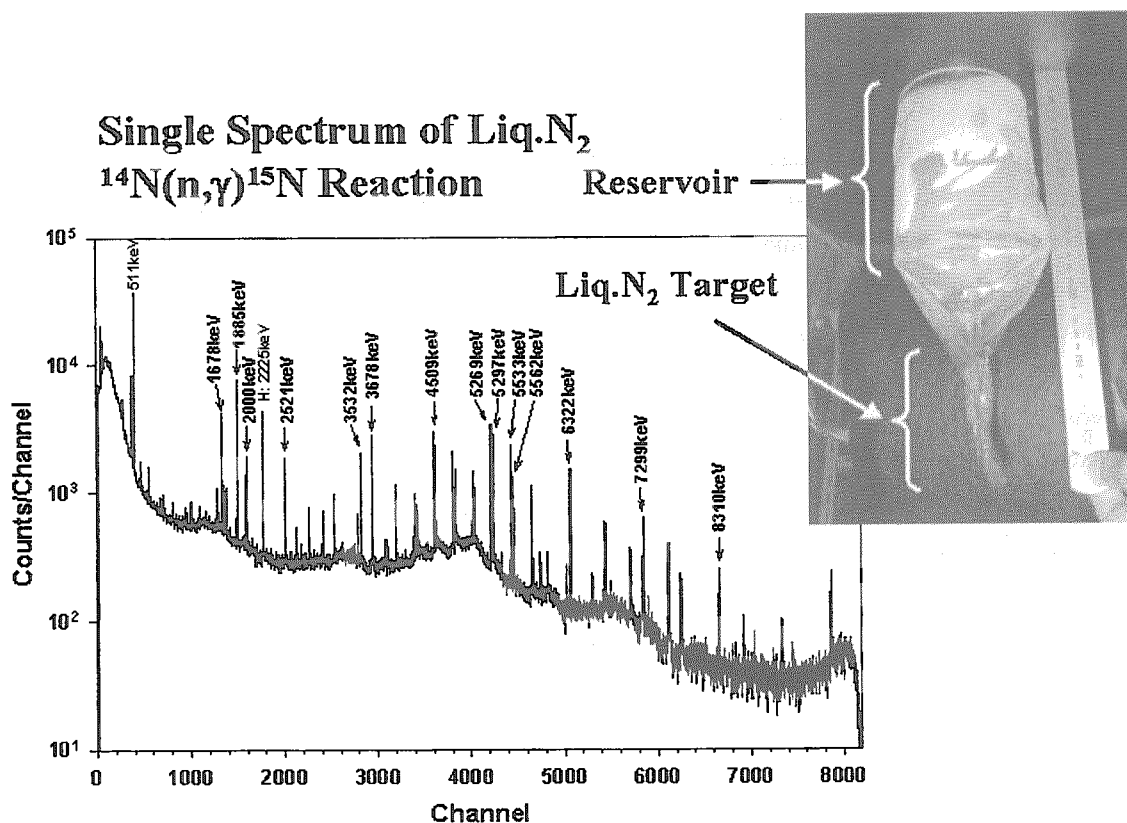
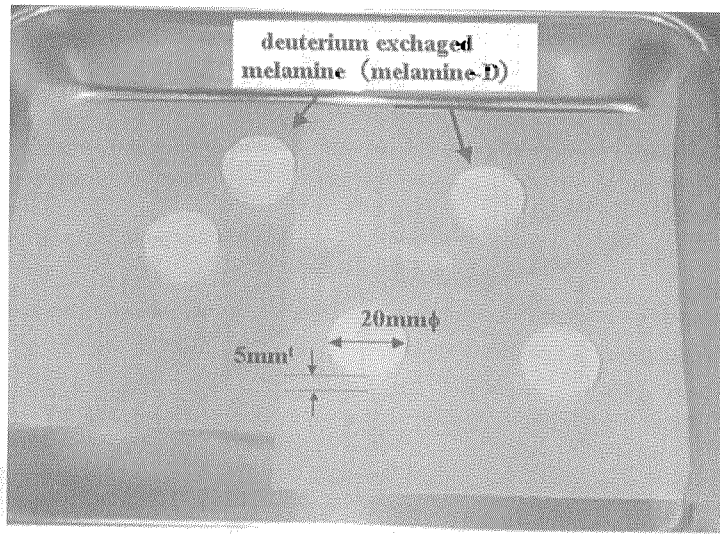
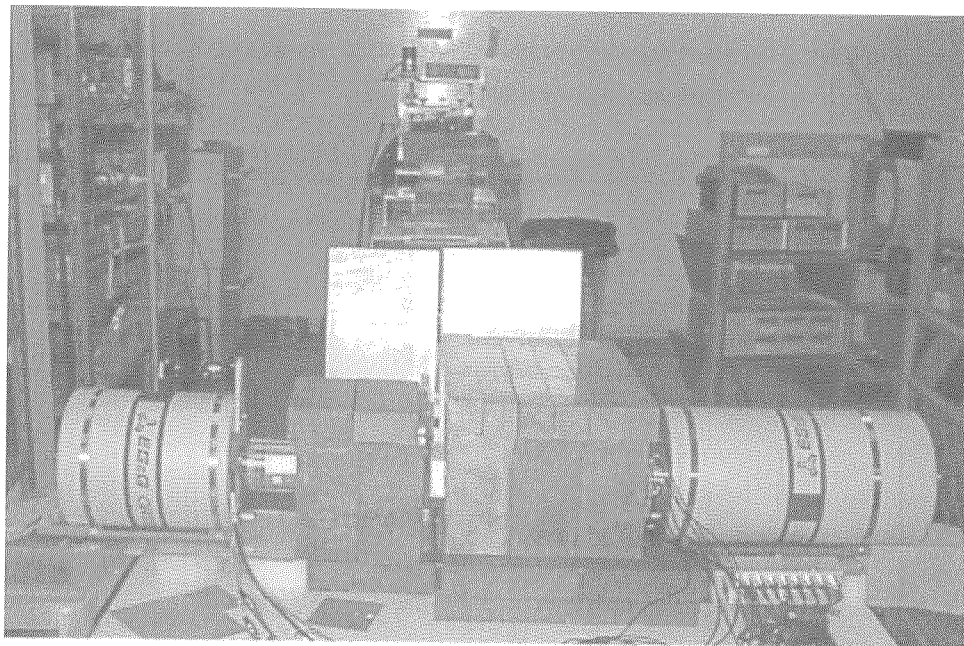


Figure 1 An example of the  $\gamma$ -ray spectrum obtained by the  $^{14}\text{N}(n,\gamma)^{15}\text{N}$  reaction and the  $\text{Liq.N}_2$  target





**Figure 2** Melamine-D target shaped in tablets by a compressor



**Figure 3** Appearance of the measurement set-up at B-4 neutron guide facility in Kyoto Research Reactor Institute

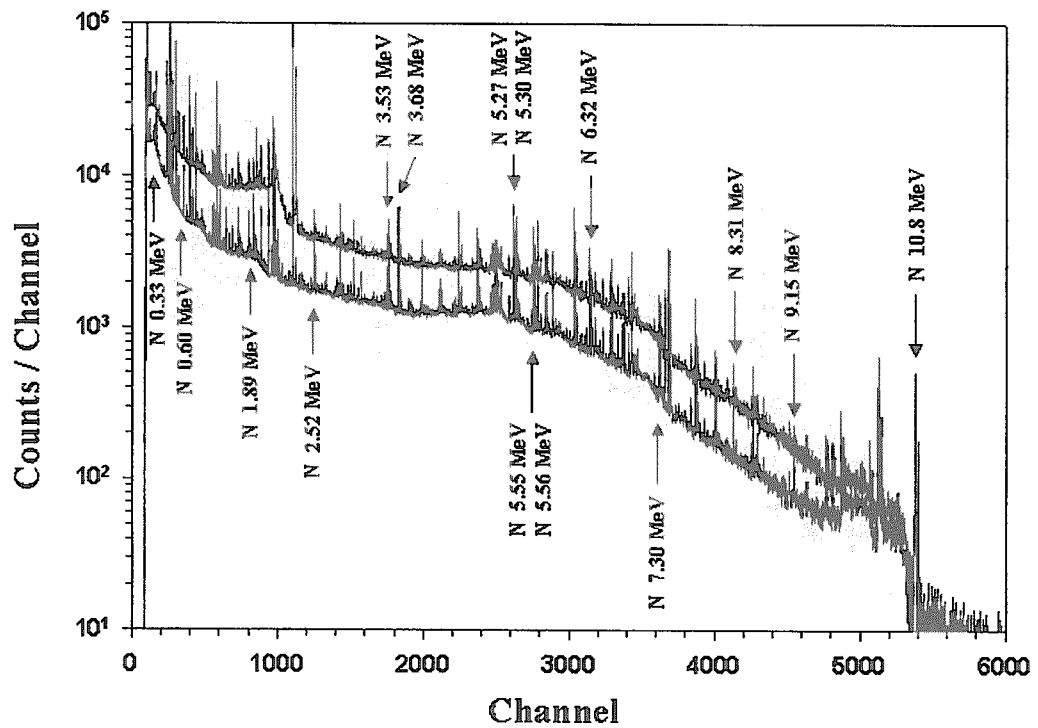


Figure 4 Gamma-ray spectrums obtained with melamine-H (upper) and melamine-D (lower) targets

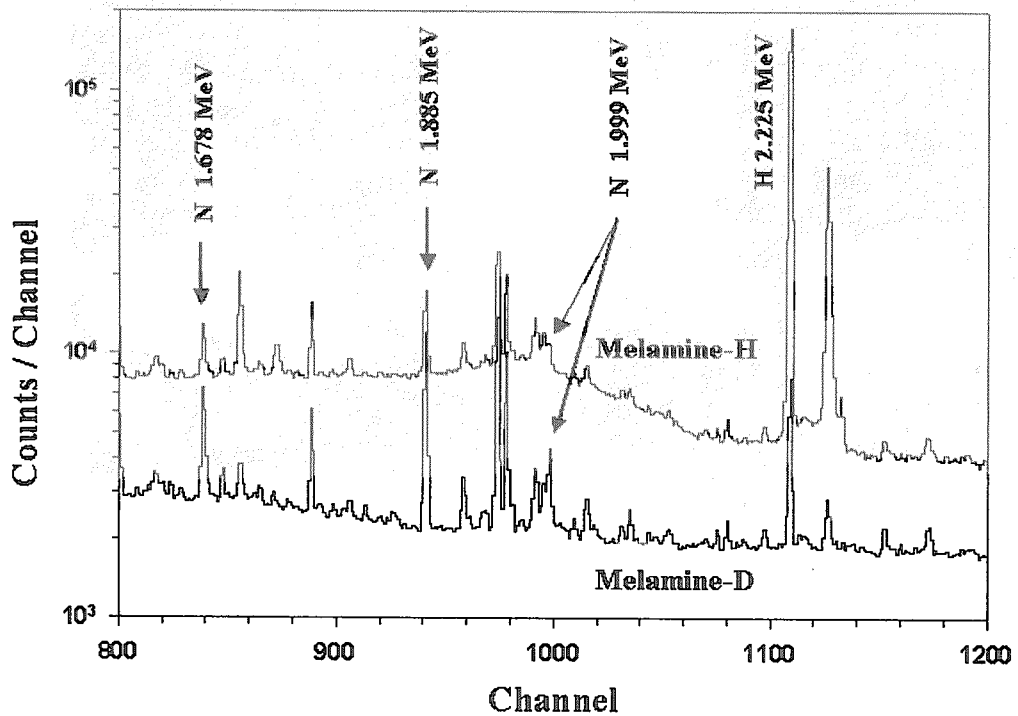


Figure 5 Gamma-ray spectrums around the 2MeV energy region extracted from Fig.4



### 3.21 Measurement of the Westcott Conventionality Thermal Neutron Flux and Suchlike at Irradiation Facilities of the KUR

Hiroshi CHATANI

*Research Reactor Institute, Kyoto University  
Kumatori-cho, Sennan-gun, Osaka 590-0494, Japan  
E-mail: chatani@rri.kyoto-u.ac.jp*

The thermal neutron flux and the epithermal index, i.e., the strength of the epithermal  $dE/E$  component relative to the neutron density including both thermal and epithermal neutrons, at the hydraulic conveyer (Hyd), pneumatic tube No. 2 (Pn-2) and slant exposure tube (Slant), i.e., principal exposure facilities of the Kyoto University Reactor (KUR), are measured by the multiple foil activation method using the  $\text{Au}(n, \gamma)\text{Au-198}$  and  $\text{Co}(n, \gamma)\text{Co-60}(g+m)$  reactions. Although neutron flux varies with core configuration et al., e.g., number of fuel elements, the available values at Hyd are that the thermal neutron flux is  $(1.07 \pm 0.03) \times 10^{14} \text{ cm}^{-2} \text{ sec}^{-1}$ , the epithermal index is  $0.0373 \pm 0.0009$  and the fast neutron flux is  $(3.8 \pm 0.2) \times 10^{13} \text{ cm}^{-2} \text{ sec}^{-1}$ . Moreover, thermal and fast neutron flux distributions are low at the top and high at the bottom of an Al irradiation capsule of Hyd. The gradient is 14 % / 8 cm in height. The distributions in the horizontal direction are flat with a 2.2 cm diam.

#### 1. Introduction

There are some experimental holes and irradiation facilities in the KUR for practicing various experiments. The irradiation facilities are used for the production of radioisotopes (RI), radioactive analysis, material testing, cross-section measurement and so forth. Therefore, determination of the neutron flux is of great importance for evaluating or predicting the activity or neutron fluence, i.e., flux time. Furthermore, recently, studies on nuclear transmutation management have been actively carried out. Concerning the experiments using reactors, measurement of the  $(n, \gamma)$  cross sections is required. In particular, when the  $(n, \gamma)$  reaction cross sections, normally listed values, are measured, it is necessary to determine the  $2200 \text{ m sec}^{-1}$  neutron flux. Accordingly, the Westcott conventionality thermal neutron flux [1], epithermal index and so forth are studied at Hyd: at the center of the KUR core, Pn-2: in the graphite reflectors and Slant: outside the reflectors; configurations of the facilities are illustrated in Figs. 1 and 2.

Furthermore, neutron flux distributions of thermal+epithermal (sum of thermal and epithermal) and fast in the irradiation capsules are measured. These distributions are useful for discussing the ununiformity of activation or setting up monitor foils for the measurement of the cross-sections.

#### 2. Westcott conventionality thermal neutron flux using multiple foil activation method

According to the convention proposed by Westcott et al.[1], the effective cross section  $\hat{\sigma}$  in the well-moderated thermal neutron reactors is expressed as

$$\hat{\sigma} = \sigma_0 (g + rs) , \quad (1)$$

where  $\sigma_0$  is a  $2200 \text{ m sec}^{-1}$  cross section,  $g$  and  $s$  are functions of the temperature  $T$  and are measures of the departure of the cross-section law from the  $1/\nu$  form in the thermal and epithermal regions, respectively. The former factor is the Westcott  $g$ -factor, which is tabulated by Westcott [2];  $r$  is the epithermal index. If the cross section obeys a  $1/\nu$  law,  $g = 1$  and  $s = 0$ . Furthermore,  $s$  is defined as

$$s = \frac{1}{\sigma_0} \sqrt{\frac{4}{\pi} \frac{T}{T_0}} I'_0 , \quad (2)$$

where  $T_0$  is the room temperature  $293.6 \text{ K}$ , and  $I'_0$  is a reduced resonance integral which is obtained by subtracting the  $1/\nu$ -term from an excess resonance integral  $I_0$ , which is given by  $I'_0 = I_0 - 0.45\sigma_0$ , if cadmium cutoff energy  $E_{Cd}$  is  $0.5 \text{ eV}$ .

Therefore, the reaction rate will have the form [3]

$$R = nv_0\sigma_0 (gG_{th} + r\sqrt{T/T_0}s_0G_{epi}) . \quad (3)$$

Here,  $n$  is the neutron density including both thermal and epithermal neutrons, and  $v_0$  is  $2200 \text{ m sec}^{-1}$ .  $G_{th}$  and  $G_{epi}$  are the corrections of self-shielding for thermal and epithermal neutrons, respectively, and these are described in the following.  $G_{th}$  is calculated using [4]

$$G_{th} = \frac{1 - 2E_3(\tau_0)}{2\tau_0} , \quad (\tau_0 = \Sigma_a t) , \quad (4)$$

where  $E_3$  is the exponential integral,  $\Sigma_a$  is the macroscopic absorption cross-section for  $2200 \text{ m sec}^{-1}$  neutrons, and  $t$  is the thickness of the detector. Moreover, Beckurts and Wirtz [5] propose a simple approximation for  $G_{epi}$  as

$$G_{epi} = \frac{1}{\sqrt{1 + 2\mu_{a0}\delta}} , \quad (5)$$

where  $\mu_{a0}$  is the mass absorption coefficient at the peak of a resonance and  $\delta$  is the surface mass loading.  $s_0$  is the invariant quantity of  $s$  and is expressed as  $s_0 = s\sqrt{T_0/T} = \frac{1}{\sigma_0} \sqrt{\frac{4}{\pi}} I'_0$  [6]. Furthermore, to divide Eq. (3) by  $\sigma_0 gG_{th}$ ,

$$\frac{R}{\sigma_0 gG_{th}} = nv_0 + nv_0 r \sqrt{T/T_0} \frac{s_0 G_{epi}}{gG_{th}} . \quad (6)$$

Equation (6) is a linear equation accompanied by an intercept  $nv_0$  (Westcott thermal neutron flux) and an inclination  $nv_0 r \sqrt{T/T_0}$  (epithermal neutron flux). Exactly the same equation having a common intercept and inclination will be formed for the  $\text{Au}(n, \gamma)\text{Au-198}$  and  $\text{Co}(n, \gamma)\text{Co-60}(g+m)$  reactions, if Au and Co are irradiated at the same time and at the same position [3].

Table 1 Nuclear data and parameters used

Reaction	$\sigma_0$ (barns) [7]	$I_0$ (barns) [7]	$g$ (at 40°C)	$G_{th}$	$G_{epi}$
Au(n, $\gamma$ )Au-198	$98.65 \pm 0.09$	$1550 \pm 28$	1.0064 [2]	0.999	0.992
Co(n, $\gamma$ )Co-60(g+m)	$37.18 \pm 0.06$	$74 \pm 2$	1	0.999	0.997

### 3. Experimental

The activation detectors used were 0.1143%Au-Al alloy foils, 0.0314%Au-Al alloy wires and 0.483%Co-Al alloy foils. Therefore,  $G_{th} \approx G_{epi} \approx 1$ , since these detectors can be approximated to infinite dilution. In the case of Hyd, several tens mg of Au-Al and Co-Al were hermetically enclosed in a 5-mm-diameter quart tube, set in an Al capsule, and then irradiated at 5000 kW for 10 min. Induced activities were measured using calibrated high-purity Ge detectors (HPGe). Moreover, fast neutron fluxes were measured using the Ti(n,p)Sc-47 or that of -48 reactions. Arrangements of the detectors in the capsules for all the cases have been shown elsewhere [8, 9].

### 4. Results and discussion

Appearances of Eq. (6) for these three facilities are shown in Fig. 3. Results of the thermal neutron fluxes and so forth are tabulated in Table 2. The epithermal index varies from 0.011 to 0.047 depending on the facilities. It is clarified that by making the most of the distinctive qualities of each facility, measurement of the (n,  $\gamma$ ) effective cross sections for various epithermal indexes is possible. Therefore, the effective cross section at  $r\sqrt{T/T_0} = 0$ , i.e., at the Maxwellian component only, on the extension line connecting two effective cross-sections measured at different facilities, will be available [10].

Relative distributions of the "thermal+epithermal" and the fast neutron fluxes in the irradiation capsules are shown in Figs. 4, 5 and 6. In these figures, thermal+epithermal distribution simply means the relative reaction rate of the Au(n,  $\gamma$ ); therefore, in the cases of Hyd, Pn-2 and Slant, respectively, approximately 60, 70 and 17 % of the reaction rates are caused by epithermal neutrons.

Difference of the thermal neutron fluxes of Hyd 1<sup>st</sup> exp. and Hyd 2<sup>nd</sup> exp. in Fig. 3 is considerably dependent on the number of the fuel elements, which were 24 and 21, respectively.

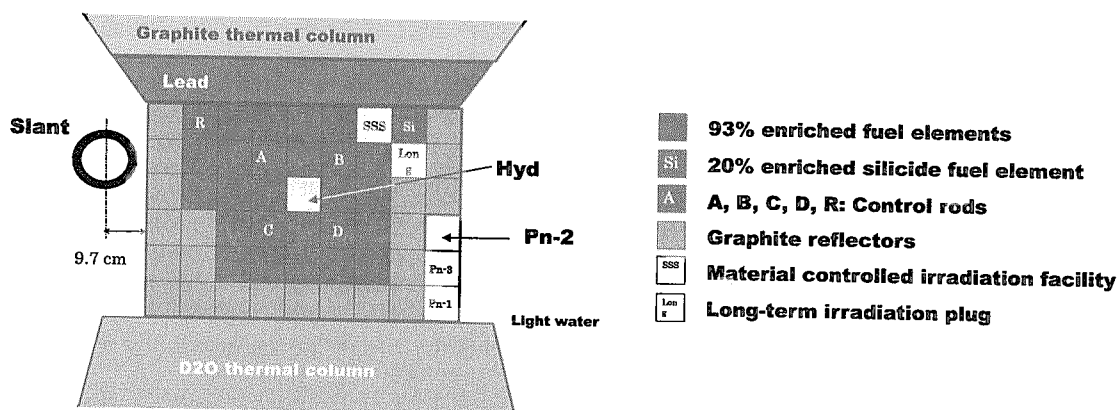


Fig.1 Horizontal core configuration

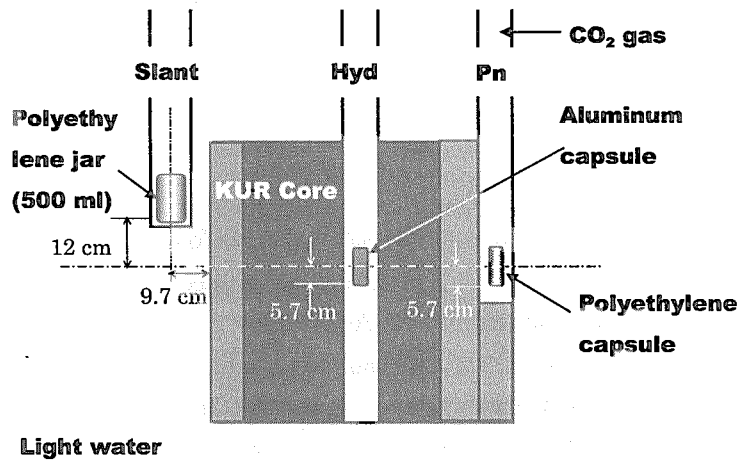


Fig. 2 Vertical configuration of the irradiation facilities

Table 2 Westcott thermal neutron flux and so forth at the irradiation facilities of the KUR

Facility: Detector position in a capsule:	Hyd (1 <sup>st</sup> exp.) 1 cm above the bottom	Pn-2 Near the center	Slant 2 cm above the bottom
$nv_0$ (cm <sup>-2</sup> sec <sup>-1</sup> )	$(1.07 \pm 0.03) \times 10^{14}$	$(1.76 \pm 0.04) \times 10^{13}$	$(1.09 \pm 0.03) \times 10^{13}$
$nv_0 r \sqrt{T/T_0}$ (cm <sup>-2</sup> sec <sup>-1</sup> )	$(4.00 \pm 0.10) \times 10^{12}$	$(8.21 \pm 0.21) \times 10^{11}$	$(1.18 \pm 0.03) \times 10^{11}$
$r \sqrt{T/T_0}$	$0.0373 \pm 0.0009$	$0.0466 \pm 0.0012$	$0.0108 \pm 0.0004$
Cd-ratio of Au ( $R_{Cd}$ ) <sup>a)</sup>	$2.53 \pm 0.06$	$2.22 \pm 0.06$	$6.3 \pm 0.3$
Fast neutron flux (cm <sup>-2</sup> sec <sup>-1</sup> )	$(3.8 \pm 0.2) \times 10^{13}$ <sup>b)</sup>	$(3.4 \pm 0.1) \times 10^{12}$ <sup>c)</sup>	$(1.05 \pm 0.40) \times 10^{12}$ <sup>b)</sup>

a) Calculated using  $R_{Cd} = \frac{g + s_0 r \sqrt{T/T_0}}{r \sqrt{T/T_0}} \left[ f_\delta s_0 + \frac{g}{K} \right]^{-1}$  where  $K$  is Westcott's  $K$ -factor which is

tabulated by Westcott et al. [1],  $f_\delta$  is transmission of the 4.9 eV neutrons through a Cd thickness  $\delta$ .

b) Determined using the averaged cross section  $\sigma = 17.7$  mb of the  $\text{Ti}(n,p)^{47}\text{Sc}$  reaction for the fission neutron spectrum of  $^{235}\text{U}$ .

c) Determined using the averaged cross section  $\sigma = 0.302$  mb of the  $\text{Ti}(n,p)^{48}\text{Sc}$  reaction.

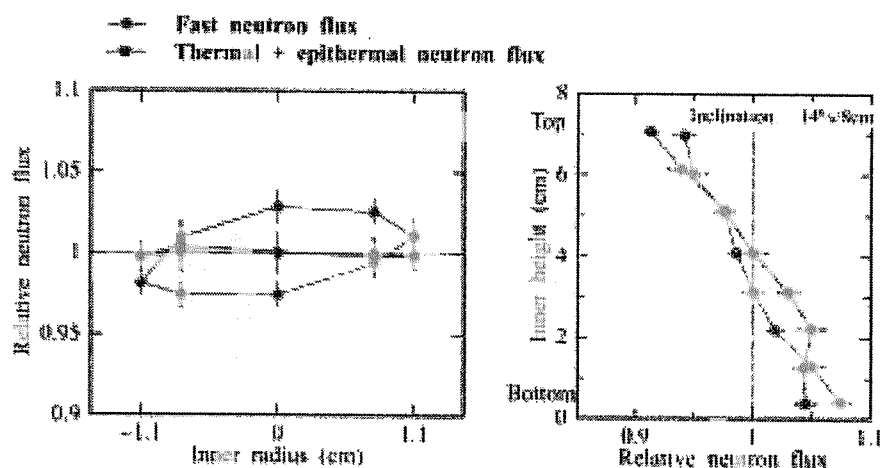


Fig. 4 Neutron flux distributions in an Al capsule of Hyd. Left: horizontal direction: along the inner wall of the capsule; Right: along the vertical axis

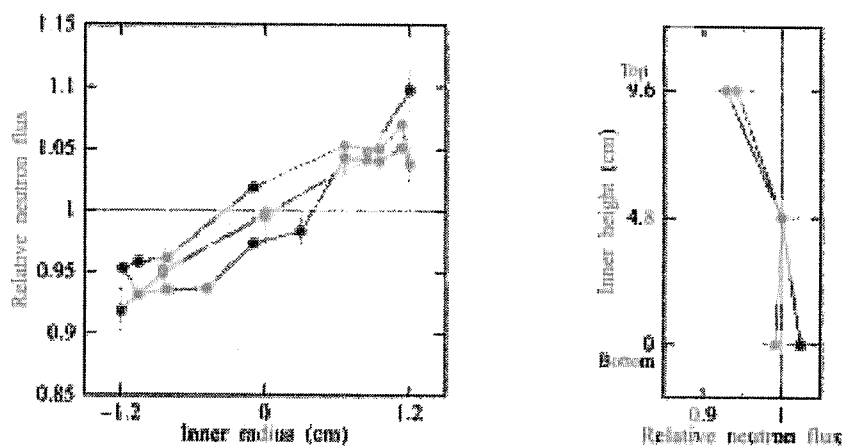


Fig. 5 Neutron flux distributions in a polyethylene capsule of Pn-2. Left: horizontal direction: along the inner wall of the capsule; Right: along the vertical axis

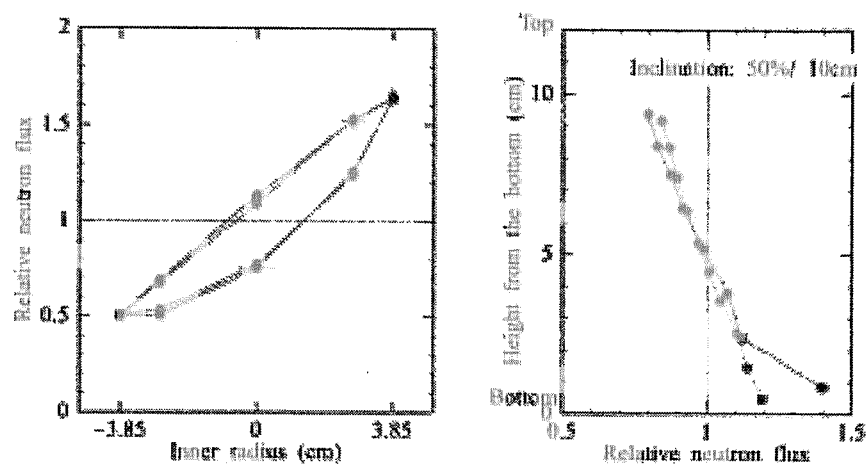


Fig. 6 Neutron flux distributions in a polyethylene jar of Slant. Left: horizontal direction: along the inner wall of the jar; Right: along the vertical axis

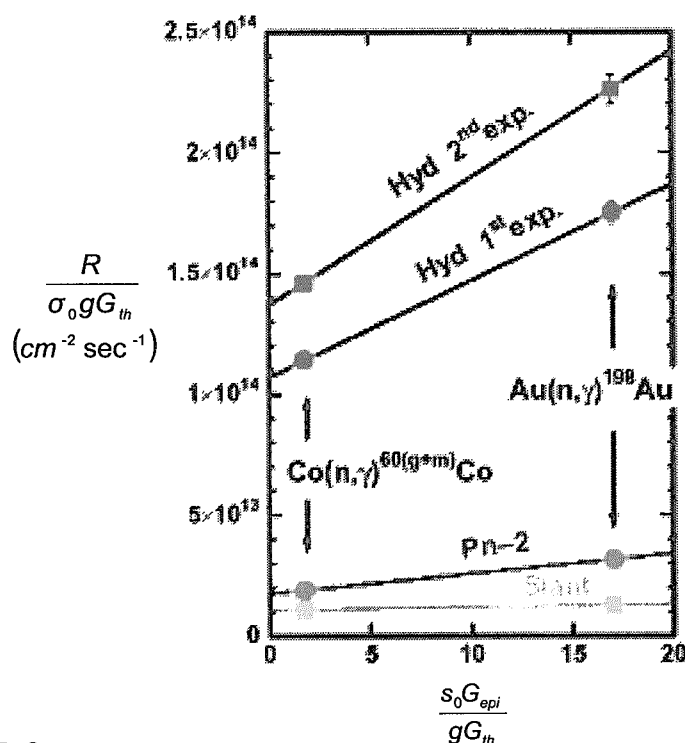


Fig. 3

Appearances of Eq. 4 for  
Hyd (1<sup>st</sup> and 2<sup>nd</sup> experiments),  
Pn-2 and Slant

Intercept: thermal neutron flux  
Inclination: epithermal neutron  
flux

## 5. References

- [1] C. H. Westcott, W. H. Walker and T. K. Alexander, "Effective cross sections and cadmium ratios for the neutron spectra of thermal reactors", Proc. 2<sup>nd</sup> Int. Conf. Peaceful Use of Atomic Energy, Geneva, New York, **16**, 70-76 (1958).
- [2] C. H. Westcott, "Effective cross section values for well-moderated thermal reactor spectra", AECL-1101 (1960).
- [3] H. Matsuoka and T. Sekine, "Reactor-neutron monitoring with multiple activation detectors", JAERI-M 9552 (1981) (in Japanese).
- [4] G. C. Hanna, "The neutron flux perturbation due to an absorbing foil; a comparison of theories and experiments", Nucl. Sci. Engineering, **15**, 325-337 (1963).
- [5] K. H. Beckurts and K. Wirtz, "Neutron Physics" Springer-Verlag, Berlin, 268 (1964).
- [6] W. H. Walker, C. H. Westcott and T. K. Alexander, "Measurement of radiative capture resonance integrals in a thermal reactor spectrum, and the thermal cross section of Pu-240", Can. J. Phys., **38**, 57-77 (1960)
- [7] S. F. Mughabghab, M. Divadeenam and N. E. Holden, "Neutron Cross Sections (Vol.1), Neutron Resonance Parameters and Thermal Cross Sections", Academic Press, New York (1981).
- [8] H. Chatani, "Measurement of the neutron flux distributions, epithermal index, Westcott thermal neutron flux in the irradiation capsules of Hydraulic conveyer (Hyd) and Pneumatic tubes (Pn) facilities of the KUR", KURRI-TR-432 (April, 2001) (in Japanese).
- [9] H. Chatani, "Measurement of the neutron flux of irradiation facilities of the KUR ( I ), Slant exposure tube", 36<sup>th</sup> Scientific Lecture Meeting, KURRI (Jan., 2002) (in Japanese).  
<http://www-j.rii.kyoto-u.ac.jp/KOUEN/kouen36/36houbun/P13.pdf> (in Japanese).
- [10] T. Sekine and H. Baba, "A study of reactor-neutron-induced reactions: Double neutron capture process and the systematics of the (n,2n) reaction", JAERI 1266 (1979).



## 3.22

Effects of nucleon correlations in  $(p, d)$ ,  $(e, e'p)$  and  $(\gamma, p)$  reactions

M.K. Gaidarov<sup>a</sup>, K.A. Pavlova<sup>a</sup>, A.N. Antonov<sup>a</sup>, M.V. Stoitsov<sup>a</sup>,  
 S.S. Dimitrova<sup>a</sup>, M.V. Ivanov<sup>a</sup>, C. Giusti<sup>b</sup>,  
 S.E. Massen<sup>c</sup>, Ch.C. Moustakidis<sup>c</sup>

<sup>a</sup>*Institute of Nuclear Research and Nuclear Energy,  
 Bulgarian Academy of Sciences, Sofia 1784, Bulgaria*

<sup>b</sup>*Dipartimento di Fisica Nucleare e Teorica, Università di Pavia,  
 Istituto Nazionale di Fisica Nucleare, Sezione di Pavia, Pavia, Italy*

<sup>c</sup>*Department of Theoretical Physics, Aristotle University of Thessaloniki,  
 GR-54006 Thessaloniki, Greece*

A study of the nucleon correlation effects on the one-nucleon removal reactions in closed- as well as open-shell nuclei is performed. We use correlated quasi-hole overlap functions extracted from the asymptotic behavior of the one-body density matrices containing different types of nucleon correlations. The corresponding spectroscopic factors calculated within this approach are reduced with respect to the shell model predictions in a way that reflects the role of the correlations included in different methods. The resulting bound-state overlap functions are applied to calculate the cross sections of  $(e, e'p)$ ,  $(\gamma, p)$  and  $(p, d)$  reactions on the same theoretical footing. The theoretical results are generally successful to reproduce the shape of the experimental cross sections. Thus this study clarifies the importance of various types of correlations, which are accounted for to a different extent in the theoretical methods considered, on the reaction cross sections.

## 1 Introduction

The strong short-range and tensor components of the nucleon-nucleon (NN) interactions induce correlations in the nuclear wave function which are going beyond the independent-particle approximation. Therefore, it has always been a point of experimental and theoretical interest to find observables which reflect these correlations in a unambiguous way. In this sense both, the overlap functions and single-nucleon spectroscopic factors, have attracted much attention in analyzing the empirical data from one-nucleon removal reactions, such as  $(e, e'p)$ ,  $(p, d)$ ,  $(d, {}^3\text{He})$ , and also in other domains of many-body physics, as e.g. atomic and molecular physics [1].

Recently, a general procedure has been adopted [2] to extract the bound-state overlap functions and the associated spectroscopic factors and separation energies on the base of the ground-state (g.s.) one-body density matrix (OBDM). The advantage of the procedure is that it avoids the complicated task for calculating the whole spectral function in nuclei [3]. Of course, the general success of the above procedure depends strongly on the availability of realistic OBDM's.

Initially, the method for extracting bound-state overlap functions (OF) has been applied in [4] to a model OBDM [5] accounting for the short-range nucleon correlations within the Jastrow correlation method. The resulting OF's have been used [6] to study one-nucleon removal processes in contrast to the mean-field approaches which account for the nucleon correlations by modifying the mean-field potentials. The results obtained for the differential cross sections

of  $^{16}\text{O}(p, d)$  and  $^{40}\text{Ca}(p, d)$  pick-up reactions at various incident energies demonstrated that the OF's can be applied as realistic form factors to evaluate absolute cross sections of such reactions. The analysis of single-particle (s.p.) OF's has been extended to more realistic OBDM's emerging from the correlated basis function (CBF) method [7, 8], the Green function method (GFM) [9] and the generator coordinate method (GCM) [1, 10]. In addition, OBDM's of open-shell nuclei deduced from Jastrow-type calculations have been used [11]. We have chosen the CBF theory since it is particularly suitable for the study of the short-range correlations (SRC) in nuclei. The CBF calculations have recently been extended to medium-heavy doubly-closed shell nuclei [7, 8] using various levels of the Fermi hypernetted chain approximation [7]. The GFM [9, 12] provides detailed information on the spectral functions and nucleon momentum distributions predicting the largest effects of the short-range and tensor correlations at high momentum and energy. The results on the one- and two-body density and momentum distributions, occupation probabilities and natural orbitals obtained within the GCM using various construction potentials [13] have shown that the NN correlations accounted for in this method are different from the short-range ones and are rather related to the collective motion of the nucleons.

The main aim of the present work is to study the effects of the NN correlations included in the correlation methods mentioned above on the behavior of the bound-state proton and neutron overlap functions in closed- as well as open-shell nuclei and of the related one-nucleon removal reaction cross sections. Such an investigation allows to examine the relationship between the OBDM and the associated overlap functions within the correlation methods used and also to clarify the importance of the effects of NN correlations on the overlap functions and the reaction cross sections.

## 2 Overlap functions and their relationship with the one-body density matrix

For a correct calculation of the cross section of nuclear reactions with one-neutron or one-proton removal from the target nucleus, the corresponding OF's for the neutron and proton bound states must be used in the reaction amplitudes. Here we would like to remind that the single-particle OF's are defined by the overlap integrals between eigenstates of the  $A$ -particle and the  $(A - 1)$ -particle systems:

$$\phi_\alpha(\mathbf{r}) = \langle \Psi_\alpha^{(A-1)} | a(\mathbf{r}) | \Psi^{(A)} \rangle, \quad (1)$$

where  $a(\mathbf{r})$  is the annihilation operator for a nucleon with spatial coordinate  $\mathbf{r}$  (spin and isospin operators are implied). In the mean-field approximation  $\Psi^{(A)}$  and  $\Psi_\alpha^{(A-1)}$  are single Slater determinants, and the overlap functions are identical with the mean-field s.p. wave functions, while in the presence of correlations both  $\Psi^{(A)}$  and  $\Psi_\alpha^{(A-1)}$  are complicated superpositions of Slater determinants. In general, the overlap functions (1) are not orthogonal. Their norm defines the spectroscopic factor

$$S_\alpha = \langle \phi_\alpha | \phi_\alpha \rangle. \quad (2)$$

The normalized OF associated with the state  $\alpha$  then reads

$$\tilde{\phi}_\alpha(\mathbf{r}) = S_\alpha^{-1/2} \phi_\alpha(\mathbf{r}). \quad (3)$$

The OBDM can be expressed in terms of the OF's in the form:

$$\rho(\mathbf{r}, \mathbf{r}') = \sum_\alpha \phi_\alpha^*(\mathbf{r}) \phi_\alpha(\mathbf{r}') = \sum_\alpha S_\alpha \tilde{\phi}_\alpha^*(\mathbf{r}) \tilde{\phi}_\alpha(\mathbf{r}'). \quad (4)$$

The asymptotic behavior of the radial part of the neutron OF for the bound states of the  $(A - 1)$ -system is given by [2]:

$$\phi_{nlj}(r) \rightarrow C_{nlj} \exp(-k_{nlj}r)/r, \quad (5)$$

where  $k_{nlj}$  is related to the neutron separation energy

$$k_{nlj} = \frac{\sqrt{2m\epsilon_{nlj}}}{\hbar}, \quad \epsilon_{nlj} = E_{nlj}^{(A-1)} - E_0^A. \quad (6)$$

For proton bound states, due to an additional long-range part originating from the Coulomb interaction, the asymptotic behavior of the radial part of the corresponding proton OF's reads

$$\phi_{nlj}(r) \rightarrow C_{nlj} \exp[-k_{nlj}r - \eta \ln(2k_{nlj}r)]/r, \quad (7)$$

where  $\eta$  is the Coulomb (or Sommerfeld) parameter and  $k_{nlj}$  in (6) contains in this case the mass of the proton and the proton separation energy.

Taking into account Eqs. (4) and (5), the lowest ( $n = n_0$ ) neutron bound-state  $lj$ -overlap function is determined by the asymptotic behavior of the associated partial radial contribution of the OBDM  $\rho_{lj}(r, r')$  ( $r' = a \rightarrow \infty$ ) as

$$\phi_{n_0lj}(r) = \frac{\rho_{lj}(r, a)}{C_{n_0lj} \exp(-k_{n_0lj}a)/a}, \quad (8)$$

where the constants  $C_{n_0lj}$  and  $k_{n_0lj}$  are completely determined by  $\rho_{lj}(a, a)$ . In this way the separation energy  $\epsilon_{n_0lj}$  and the spectroscopic factor  $S_{n_0lj}$  can be determined as well. Similar expression for the lowest proton bound-state OF can be obtained having in mind its proper asymptotic behavior (7).

### 3 Results for the cross sections of $(e, e'p)$ , $(\gamma, p)$ and $(p, d)$ reactions on closed-shell ( $^{16}\text{O}$ , $^{40}\text{Ca}$ ) and open-shell ( $^{24}\text{Mg}$ , $^{28}\text{Si}$ , $^{32}\text{S}$ ) nuclei

Figure 1 shows the ground state angular distribution of the reaction  $^{28}\text{Si}(p, d)^{27}\text{Si}$  representing pickup of  $1d_{5/2}$  neutrons induced by 185 MeV protons. In the figure three different theoretical curves are given in respect to deuteron optical potential parameters used in the calculations. Particularly, the effects of changing the radius of the real part of this potential  $R_d$  is shown. The best agreement with the experimental data is achieved with the value of  $R_d=0.8$  fm giving also the best fit in [14]. Apart from the shown sensitivity of the calculations to the deuteron optical potential, in general, we should mention that the  $(p, d)$  reaction is more sensitive to the reaction mechanism adopted than to the choice of the bound-state wave function. Nevertheless, it is seen from Fig. 1 that our theoretically calculated OF corresponding to the  $1d$  bound state is able to reproduce the absolute cross section.

It turned out from the previous analyses of one-nucleon removal reactions [15, 16] that quasifree nucleon knockout is more suitable to investigate the role of overlap functions as bound-state wave functions. An example of electron induced proton knockout from  $^{32}\text{S}$  for the transition to the ground  $2s_{1/2}$  state of  $^{31}\text{P}$  is illustrated in Figure 2. In the figure the result obtained with the proton OF for the  $2s$  state of  $^{32}\text{S}$  and the optical potential from [17] is compared with the NIKHEF data from [18]. A reasonable agreement with the experimental data for the reduced cross section is obtained. In the analysis of [18] the calculations are performed within the same distorted wave impulse approximation (DWIA) framework and with the same optical potential, but phenomenological s.p. wave function is used with a radius adjusted to the data. We emphasize that in the present work the OF theoretically calculated on the basis of the Jastrow-type OBDM of  $^{32}\text{S}$  does not contain free parameters. It can be seen from Fig. 2 that our spectroscopic factor of 0.5648 gives a good agreement with the size of the experimental cross section.

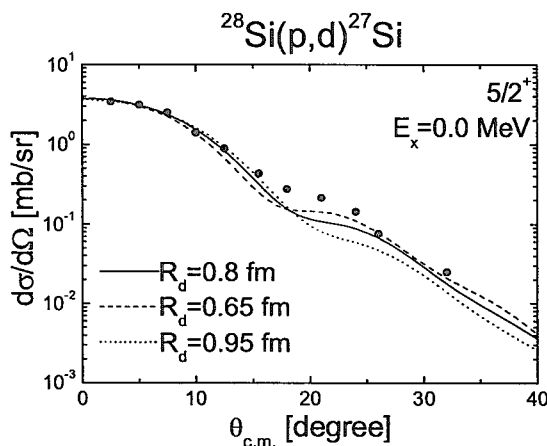


Figure 1: Differential cross-section for the  $^{28}\text{Si}(p,d)^{27}\text{Si}$  reaction at incident proton energy  $E_p=185$  MeV to the  $5/2^+$  ground state in  $^{27}\text{Si}$ . Line convention referring to different calculations with neutron OF derived from the OBDM is given (see also the text). The experimental data [14] are given by the full circles.

Apart from the effects of SRC studied in [16, 19] and discussed already in this Section, we looked into the role of correlations caused by the collective nucleon motion. Figure 3 shows the angular distribution of the  $^{40}\text{Ca}(\gamma,p)^{39}\text{K}_{g.s.}$  reaction at  $E_\gamma=60$  MeV. In the figure the results given by the sum of the one-body and of the two-body seagull currents are compared with the contribution given by the one-body current, which roughly corresponds to the DWIA treatment based on the direct knockout mechanism. The results obtained with the OF from GCM for the ground state transition and with the phenomenological Woods-Saxon (WS) wave function are compared in the figure. In order to check the consistency in the description of different one-proton removal reactions, the calculated cross sections have been multiplied by the same reduction factors obtained from the analysis of corresponding  $(e,e'p)$  data, i.e. 0.55 with GCM and 0.6625 with WS. The differences between the two curves are considerable and larger than in the  $(e,e'p)$  reaction [15]. A reasonable agreement with the size and the shape of the experimental cross section is obtained when meson-exchange currents (MEC) are added. Although both calculations with the GCM and WS wave functions are able to give a good description of the  $^{40}\text{Ca}(e,e'p)$  data for the transition to the  $3/2^+$  ground state of  $^{39}\text{K}$  [15], the  $(\gamma,p)$  results presented in Fig. 3 for the same transition show that the GCM overlap function leads to a better and more consistent description of data for the  $(e,e'p)$  and  $(\gamma,p)$  reactions. This result suggests proper accounting for the nucleon correlation effects in the framework of the GCM.

## 4 Conclusions

The s.p. overlap functions calculated on the basis of OBDM for the ground state of closed- and open-shell nuclei emerging from different correlation methods have been used to calculate the cross sections of the  $(p,d)$ ,  $(e,e'p)$  and  $(\gamma,p)$  reactions. The theoretical results for the cross sections show that they are sensitive to the shape of the different OF's and are generally able to reproduce the shape of the experimental cross sections. In order to reproduce the size of

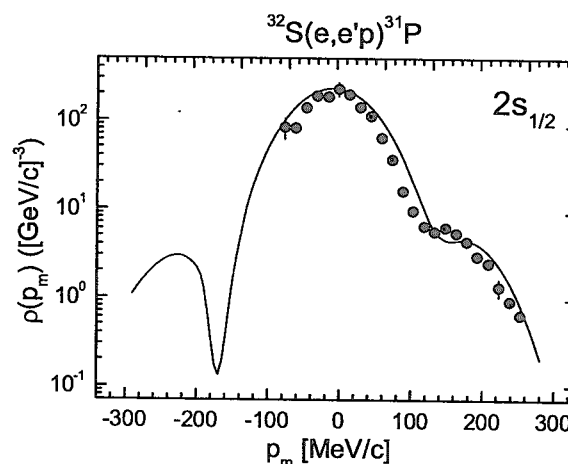


Figure 2: Reduced cross section of the  $^{32}\text{S}(e, e'p)^{31}\text{P}$  reaction as a function of the missing momentum  $p_m$  for the transition to the  $1/2^+$  ground state of  $^{31}\text{P}$ . The proton OF is derived from the OBDM (solid line). The experimental data (full circles) are taken from Ref. [18].

the experimental data a reduction factor must be applied to the calculated cross sections. The fact that it is consistent in different nucleon removal reactions gives a more profound theoretical meaning to this parameter. The results indicate that the effects of SRC correlations taken into account within CBF and GFM and of correlations accounted for in GCM which are of long-range type are of significant importance for the correct analysis of the processes considered.

The authors thank the Bulgarian National Science Foundation which partly supported this work under the Contract No.  $\Phi$ -905.

## References

- [1] A.N. Antonov, P.E. Hodgson, and I.Zh. Petkov, *Nucleon Correlations in Nuclei* (Springer-Verlag, Berlin, 1993).
- [2] D. Van Neck, M. Waroquier, and K. Heyde, *Phys. Lett. B* **314**, 255 (1993).
- [3] A.N. Antonov, M.V. Stoitsov, M.K. Gaidarov, S.S. Dimitrova, and P.E. Hodgson, *J. Phys. G* **21**, 1333 (1995).
- [4] M.V. Stoitsov, S.S. Dimitrova, and A.N. Antonov, *Phys. Rev. C* **53**, 1254 (1996).
- [5] M.V. Stoitsov, A.N. Antonov, and S.S. Dimitrova, *Phys. Rev. C* **47**, R455 (1993); *Phys. Rev. C* **48**, 74 (1993); *Z. Phys. A* **345**, 359 (1993).
- [6] S.S. Dimitrova, M.K. Gaidarov, A.N. Antonov, M.V. Stoitsov, P.E. Hodgson, V.K. Lukyanov, E.V. Zemlyanaya, and G.Z. Krumova, *J. Phys. G* **23**, 1685 (1997).
- [7] F. Arias de Saavedra, G. Co', A. Fabrocini, and S. Fantoni, *Nucl. Phys. A* **605**, 359 (1996).
- [8] F. Arias de Saavedra, G. Co', and M.M. Renis, *Phys. Rev. C* **55**, 673 (1997).

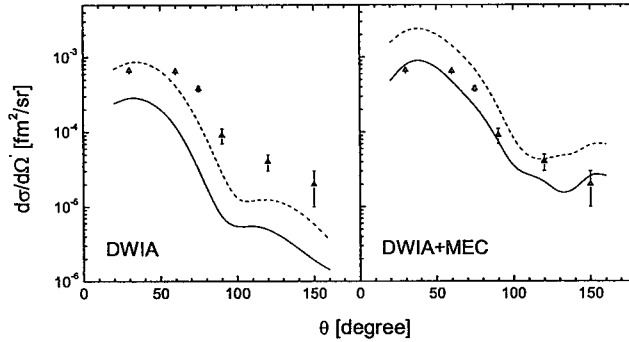


Figure 3: Angular distribution of the  $^{40}\text{Ca}(\gamma, p)$  reaction for the transition to the  $3/2^+$  ground state of  $^{39}\text{K}$  at  $E_\gamma = 60$  MeV. The optical potential is taken from Ref. [17]. The OF is derived from the OBDM of GCM (solid line). The dashed line is calculated with the WS wave function. The experimental data (triangles) are taken from Ref. [20].

- [9] A. Polls, H. Mütter and W.H. Dickhoff, *Proceedings of Conference on Perspectives in Nuclear Physics at Intermediate Energies*, Trieste, 1995, edited by S. Boffi, C. Ciofi degli Atti, and M.M. Giannini, p.308 (1996, World Scientific).
- [10] A.N. Antonov, P.E. Hodgson, and I.Zh. Petkov, *Nucleon Momentum and Density Distributions* (Clarendon Press, Oxford, 1988).
- [11] Ch.C. Moustakidis and S.E. Massen, *Phys. Rev. C* **62**, 034318 (2000).
- [12] W.H. Dickhoff and H. Mütter, *Rep. Prog. Phys.* **55**, 1947 (1992).
- [13] M.V. Ivanov, A.N. Antonov, and M.K. Gaidarov, *Int. J. Mod. Phys. E* **9**, No.4, 339 (2000).
- [14] O. Sundberg and J. Källne, *Arkiv Fysik* **39**, 323 (1969).
- [15] M.V. Ivanov, M.K. Gaidarov, A.N. Antonov, and C. Giusti, *Phys. Rev. C* **64**, 014605 (2001).
- [16] M.K. Gaidarov, K.A. Pavlova, A.N. Antonov, M.V. Stoitsov, S.S. Dimitrova, M.V. Ivanov, and C. Giusti, *Phys. Rev. C* **61**, 014306 (2000).
- [17] P. Schwandt, H.O. Meyer, W.W. Jacobs, A.D. Bacher, S.E. Vigdor, M.D. Kaitchuck, and T.R. Donoghue, *Phys. Rev. C* **26**, 55 (1982).
- [18] J. Wesseling, C.W. de Jager, L. Lapikás, H. de Vries, M.N. Harakeh, N. Kalantar-Nayestanaki, L.W. Fagg, R.A. Lindgren, and D. Van Neck, *Nucl. Phys.* **A547**, 519 (1992).
- [19] M.K. Gaidarov, K.A. Pavlova, S.S. Dimitrova, M.V. Stoitsov, A.N. Antonov, D. Van Neck, and H. Mütter, *Phys. Rev. C* **60**, 024312 (1999).
- [20] C. Van den Abeele, D. Ryckbosch, J. Ryckbosch, J. Dias, L. Van Hoorebeke, R. Van de Vyver, J.-O. Adler, B.-E. Andersson, L. Isaksson, H. Ruijter, and B. Schröder, *Phys. Lett. B* **296**, 302 (1992).



### 3.23 Energy Dependence of Microscopic Corrections for Nuclear Droplet Model

Hisashi Nakamura

Nishi-turuma, Yamato-city, Kanagawa-Ken 242-0005, Japan

e-mail: kyu-san@kc4.so-net.ne.jp

Unified description of microscopic corrections (shell, pairing and deformation) for the nuclear mass is performed based on the finite range Droplet model (*FRDM*) and on the shell-group-wise average (*SGWA*) method. The energy dependence of those corrections are described by using the statistical thermodynamic method and an analytical form of single-particle spectra.

#### 1. Introduction

Systematics of nuclear reactions depends strongly on the shell, pairing and deformation effects. The mass formulas have been used to determine those corrections from measured mass excess data, but the discrepancy between the estimated and measured values of those effects may amount up to 2 MeV. The most often used correction energies are those of Myers and Swiatecki (M&S, 1967). In the present work the macroscopic Droplet terms of *FRDM* (Möller *et al*, 1995) are taken as the starting point for a more detailed description of microscopic corrections based on a new model of single-particle state density model. The energy dependence of those corrections are described by using the statistical thermodynamic method and the analytical form of single-particle spectra.

#### 2. Model of single-particle spectrum

In the framework of statistical thermodynamics the single-particle spectrum plays an important role, it is written in terms of the anisotropic harmonic oscillator model, considering only fundamental harmonics for the main-shell with the subshell associated with pairing correlations. (Table.1)

#### 3. Results

Results of analyses and calculations are shown on the following figures (Table.2) Microscopic corrections & fitting errors of mass formulas.

[Fig.1] Shell-group-wise-average of microscopic corrections.

[Fig.2] Plot of polynomial expressions for corrections.

[Fig.3] Energy dependence of corrections for *FRDM*.

#### Acknowledgements

The author is grateful to members of a working group of Sigma-Committee in JAERI, for many useful discussions about the present works.

Table 1

## Model of Single-Particle Spectrum

*Anisotropic harmonic oscillator with quasi-particle spectrum*

$$g(\varepsilon) = \sum_X g_X \left\{ 1 + \frac{1}{3} f_X \sum_i \cos \omega_i (\varepsilon - \varepsilon_X) \right\} \{ 1 - \cos \omega_{PX} (\varepsilon - \lambda_X) \}, \quad (1)$$

$$\omega_1 = \omega_2 \equiv \omega_{\perp} \approx \varpi (1 + \frac{1}{3} \delta), \quad \omega_3 \equiv \omega_z \approx \varpi (1 - \frac{2}{3} \delta),$$

$$\omega_p = 2 / \Delta_0,$$

 $\varpi$  *average harmonic oscillator frequency* $\delta$  *quadratic deformation parameter*

$$= 3(R_3 - R_{\perp}) / (R_3 + 2R_{\perp})$$

 $g_X$  *single-particle density (two-fold degenerate)* $x = (z \text{ or } n)$  *particle orbit* $f_x$  *shell-structure amplitude* $\lambda_X$  *Fermi-level* $\Delta_0$  *quasi-particle gap energy at ground state.*



**Table 2**  
**Microscopic corrections & fitting errors of mass formula**

*Classification of measured mass excess (RIPLE, 1998):*

核種数	N20	N28	N50	N82	N126	N184	Total
Z20	24	33	7				57
Z28	7	54	53				107
Z50		6	192	267	2		459
Z82				179	418	9	597
Z126					62	232	294

(例) Z20 shell : Z=15~20, N20 shell : N=15~20 Total=1514 (31: not included)

Range of deformed nuclei : ( Z28-N50, Z50-N82, Z82-N126, Z126-N184 )

*Shell-Group-Wise Average (SGWA) corrections in mass excess data :*

Mass formula :  $E(Z, N : \delta) = E_{\text{mac}}(Z, N : 0) + E_{\text{s+p}}(Z, N : \delta)$

$E_{\text{mac}}(Z, N : 0)$  = Finite Range Droplet Model ( *FRDM* : 1998 ) = *Spherical components*.

● Droplet (1974) + Yukawa-plus-exponential model ( *LANL&Berkeley Group*, 1981 )

$E_{\text{s+p}}(Z, N : \delta)$  = Shell-Group-Wise-Average ,  $\delta$  : *deformation parameter*.

● Single-particle potential model = shell-, pairing- and deformation corrections.

*Fitting error of nuclear mass formula*

Shell-group		No. of Nuclei	[ $\sigma_{\text{th}}(\text{MeV})$ ]			
Z=	N=		M & S (1967)	Möller <i>et al</i> (1998)	Present model	
15~	15~				SGWA	New formula
20	20	24	6.625	1.477	0.191	0.203
	28	33	9.202	1.362	0.108	0.164
28	28	54	6.529	1.146	0.391	0.406
	50	53	3.969	0.384	0.122	0.271
50	50	192	2.367	0.607	0.304	0.391
	82	267	1.331	0.709	0.309	0.455
82	82	179	1.115	0.483	0.471	0.561
	126	418	0.971	0.485	0.447	0.624
126	126	62	1.125	0.392	0.238	0.526
	184	232	1.301	0.392	0.444	0.526
Total		151	2.521	0.621	0.387	0.514

<i>Root Mean Squares</i>	<b>2.522</b>	<b>0.626</b>	<b>0.408</b>	<b>0.530</b>
--------------------------	--------------	--------------	--------------	--------------

M&S(1967) : Myers W.D. and Swiatecki W.J., *Ark.Fys.* **36**, 343(1967).

Möller *et al* (1998) : Moller P., Nix J.R., Myers W.D. and Swiatecki W.J.,  
*Atom.Data and Nucl.Data Tbl.* **59**, 185(1995).

$$\sigma_{\text{th}}^2 = (1/\sum w_i) \sum w_i [(M_{\text{exp}}^i - M_{\text{th}}^i)^2 - \sigma_{\text{exp}}^i{}^2], \quad w_i = 1/(\sigma_{\text{exp}}^i{}^2 + \sigma_{\text{th}}^i{}^2)$$

$M_{\text{exp}}^i$  : measured mass,  $M_{\text{th}}^i$  : estimated mass,  $\sigma_{\text{exp}}^i$  : measured error.

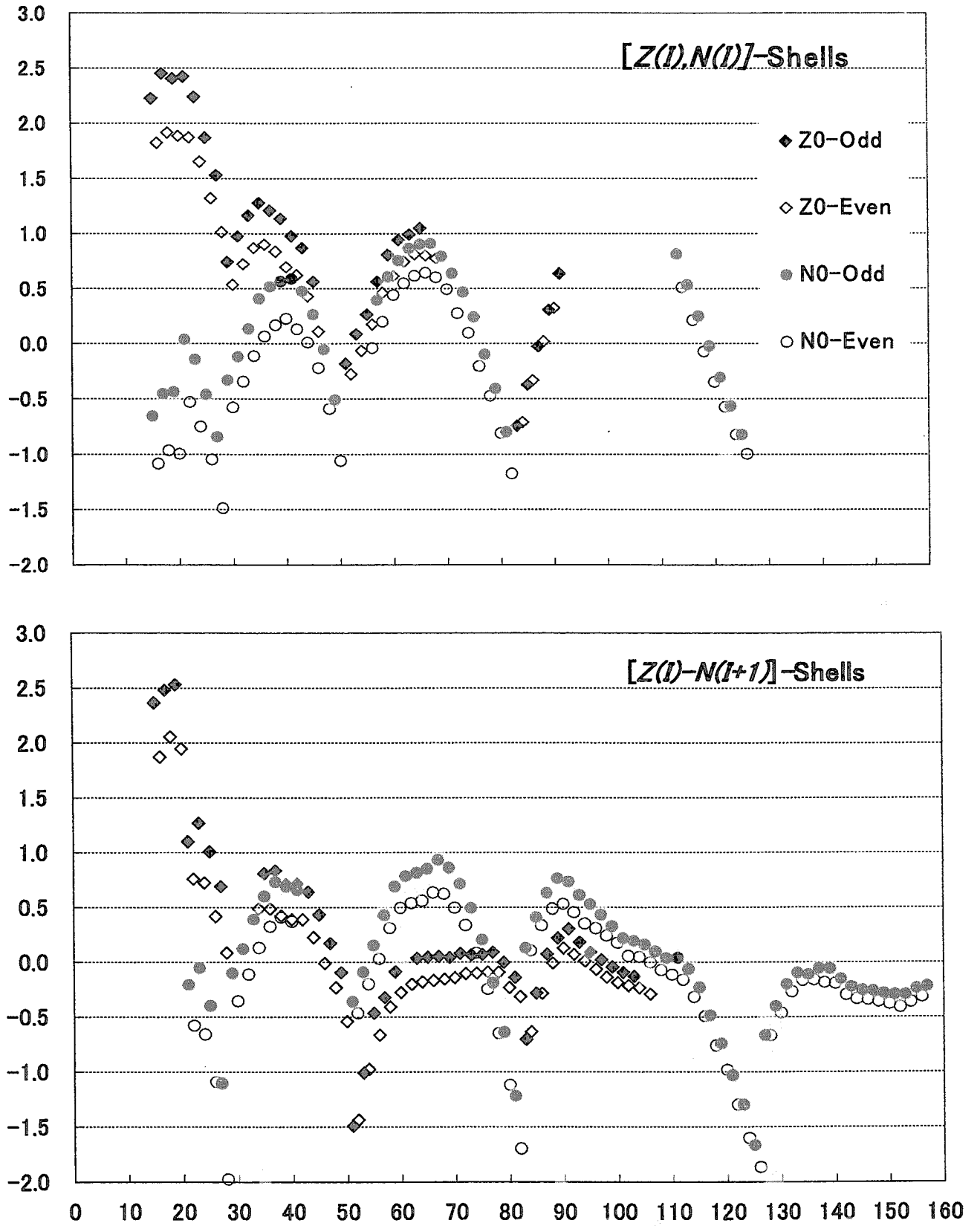


[Fig.1] Shell-group-wise average of microscopic corrections ( $\text{MeV}/A^{1/3}$ ) in measured mass excess data.  $\blacklozenge, \diamond$  for proton,  $\bullet, \circ$  for neutron.

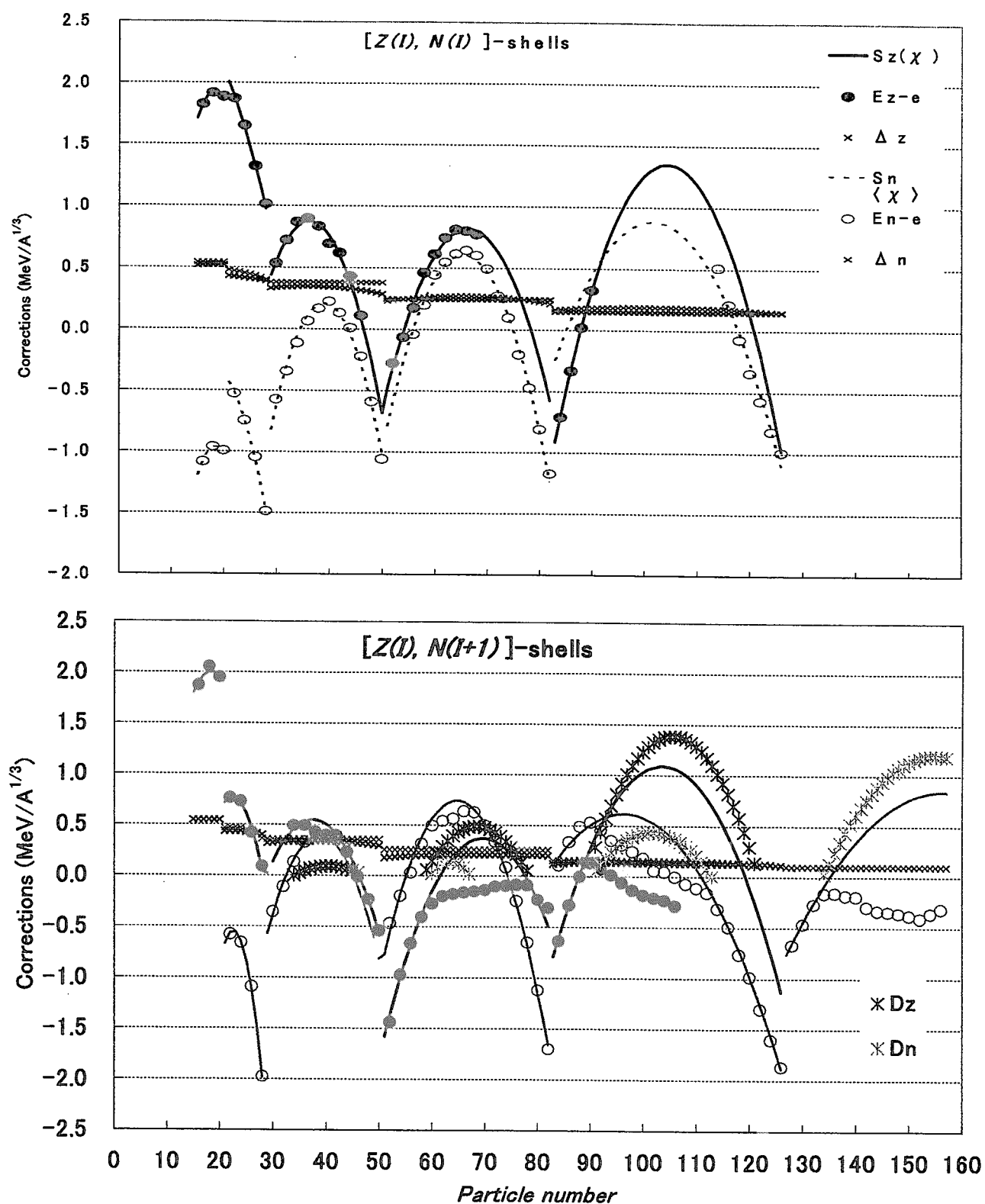


[Fig.2] Plot of polynomial expressions for microscopic corrections extracted from measured mass data. ●, ○ are extracted ones (for even-particles), — ..... polynomial fits to shell corrections, ×, × those of pairing gap parameters, ※, ※ deformation effects, which are obtained from (polynomial expression — extracted correction).

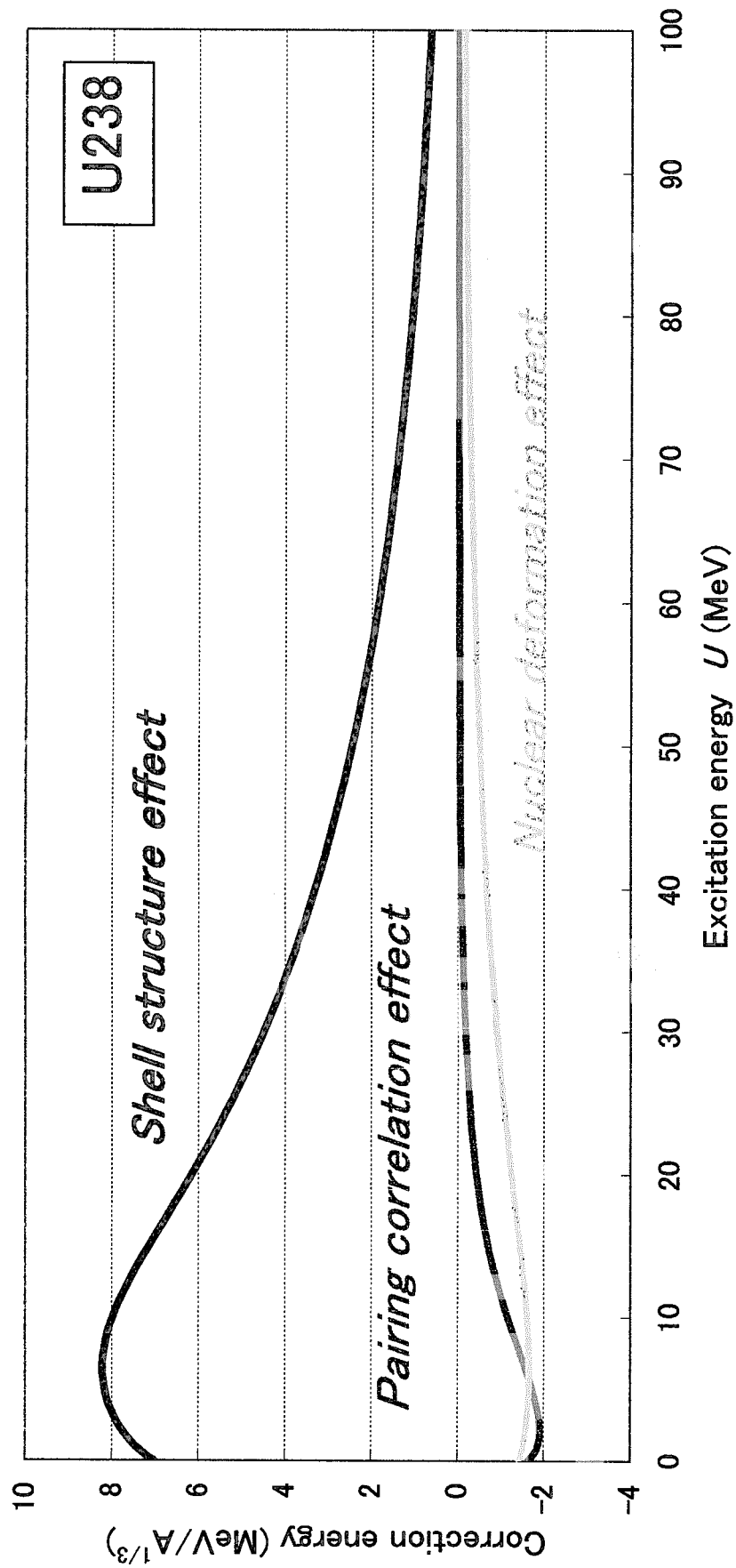


[Fig.3] Energy Dependence of Microscopic Corrections for FRDM

### 3.24 Recurrence of the excited states of nuclei and time coherency of the de Broglie wave in $^{16}\text{O}+n$ resonances

Makio OHKUBO

SOHONRR, 1663-39, Senba-cyo, Mito-shi, Ibaraki-ken 310-0851 Japan

#### Abstract

From the requirement of the time periodicity of a (quasi)stable state, frequencies of the normal modes, which compose the state, are commensurable (integer ratios) with each other, and the excitation energies  $E_x$  are written as a sum of inverse integers. We propose an expression:  $E_x = G \sum \frac{1}{n}$ , where  $n$ =integers and  $G=34.5\text{MeV}$ . Recurrence time is defined as  $\text{LCM}(n_j) \times \tau_0$ , where  $\tau_0 = 2\pi\hbar/G = 1.20 \times 10^{-22}\text{s}$ . LCM vs.  $E_x$  are illustrated for all possible  $n_j$  of 2 and 3 normal modes. In  $^{16}\text{O} + n$  resonances, integer ratios are found between the recurrence frequencies of  $^{17}\text{O}$  and the de Broglie wave frequencies of incident neutron, meaning time coherency between them. A simple branch pattern is found in  $^{16}\text{O} + n$  resonance levels.

#### 1. Introduction

In a compound nucleus(CN) formed by resonance reaction, it is surmised that many degrees of freedom will be excited and coupled to form chaotic mixture. Statistical properties of the observed resonances are well agreement with the predictions of random matrix theory (RMT) which is based on the random hypotheses on the CN. However, several non-statistical properties are reported more than 3 decades, which are analysed by methods based on self-similarity in level dispositions, which are always used to decode cryptogram. The results of analyses in the neutron resonance level dispositions/spacings are described in [1-5] and references therein. Through these analyses, special level spacings (we call dominant spacings) are found which appear frequently than in ensembles of levels by RMT. Two points became clear; (a) multiple integer ratios between dominant spacings for a nucleus; (b) integer ratios among dominant spacings of different nuclei. In order to grasp more basic furcation property of resonance levels, we have made level spacing analyses on s-wave resonances of 15 even-even light target nuclei up to several hundred keV neutron energy, where simple excitations are expected because of small number of degrees of freedom excited. Thirty dominant spacings are adopted in the 15 nuclides. Among these dominant spacings of different nuclei, there are multiple integer ratios, and it became clear that many of the dominant spacings  $D$  (under recoil energy correction) are written as  $D = G/mn$ , where  $G=34.5\text{ MeV}$ , and  $m, n$  :integers. From these, it is inferred that excitation energy  $E_x$  might be in a form  $E_x = G/k$  ( $k$ : integer) [6,7]. These analyses suggest following points.

(A) level furcation structures characteristic of each nucleus.

(B) a common energy constant  $G$  in many nuclei.

These features require a new view point on the compound nucleus which are diametrically different from the ordinary statistical descriptions of highly excited states.

In order to describe these regular structures in resonance levels, we are developing "Recurrence Model" of the CN [8,9], where time behaviors of CN are explicitly discussed. Assuming dynamic behaviors of the CN, mechanism of each resonance may be clarified.

In this article, are described S-matrix and the time response function, excitation energy as a sum of inverse integers, map of LCM vs.  $E_x$ , time coherence between compound nuclear recurrence and the de Broglie wave in  $^{16}\text{O}+n$  resonances, and a special level pattern.

#### 2. S-matrix and response function

As to the recurrence of the CN, a relation exists between S-matrix and a response function[10]. For the neutron-nucleus reaction, an S-matrix  $S(E)$  is defined from which cross section  $\sigma_s(E) = (\pi/k^2) |1 - S(E)|^2$ , etc. are determined. Consider incident wave  $\psi^-(r, t)$  and outgoing wave  $\psi^+(r, t)$  around interaction region of radius  $R$ . For s-wave, a response function  $F(r)$  is defined as,

$$\psi^+(r, t) = \int_0^\infty d\tau F(\tau) \psi^-(r, t - \tau) \dots (1).$$

The  $S(E)$  can be expressed as a Fourier integral of the response function  $F(\tau)$ ,

$$S(E)e^{2ikR} = \int_0^\infty d\tau F(\tau)e^{i\frac{E\tau}{\hbar}} \dots\dots\dots(2),$$

where  $\tau$  is previous time the response come back. For an isolated resonance at  $E_0$ ,  $S(E)$  has a peak at  $E_0$ , then  $F(\tau)$  must be a periodic function with a period  $\tau = 2\pi\hbar/E_0$  during life time  $\sim \hbar/\Gamma$ . For a large resonance,  $F(\tau)$  behaves like a pulse array with pulse separation  $\tau_{rec}$ , like an intermittent pulses, where  $\tau_{rec}$  is the recurrence time of the CN. At every recurrence time, phase of the CN recurred almost to the initial phase, and at the time neutron density will peaks on the compound nuclear surface. If  $F(\tau)$  is a non-periodic function (or  $\tau_{rec}$  becomes infinity), the recurrence is not realized, and only chaotic behaviors and continuum are expected.

$F(\tau)$  can be decomposed into Fourier series with periods  $\tau_j = \tau_{rec}/k_j$ , where  $k_j$  are integers, ( $j=1,2,.. M$ ).  $\tau_j$  is written as  $n_j\tau_0$ , where  $n_j$  is integer and  $\tau_0$  is a unit time.  $\tau_{rec}$  is the least common multiple(LCM) for ensemble ( $n_j$ ) multiplied by  $\tau_0$ . Frequency ratios as well as time periods among these normal modes are commensurable(in integer ratios) with each other. Frequency components  $\omega_j$  of  $F(\tau)$  is proportional to the inverse integers  $\omega_j = (2\pi/\tau_0)/n_j$ . Coherent sum of the Fourier components composes pulse array in  $F(\tau)$ , which describe a resonance scatterer for incident neutron wave. As to resonant reaction mechanism, neutron wave tunnels through the dynamical potential build up on nuclear surface with a time period  $\tau_{rec}$  which behaves like an array of "time slit", through which interference takes place between passing and trapped components of a incident neutron wave packet. If the recurrence is coherent with the incident de Broglie wave, constructive interference takes place, and induces resonance reactions. Otherwise, destructive interference induces no reactions except for the potential scattering. An illustration of time sequence of resonance reactions is shown in Fig.1.

### Time Evolution of Resonance Reaction

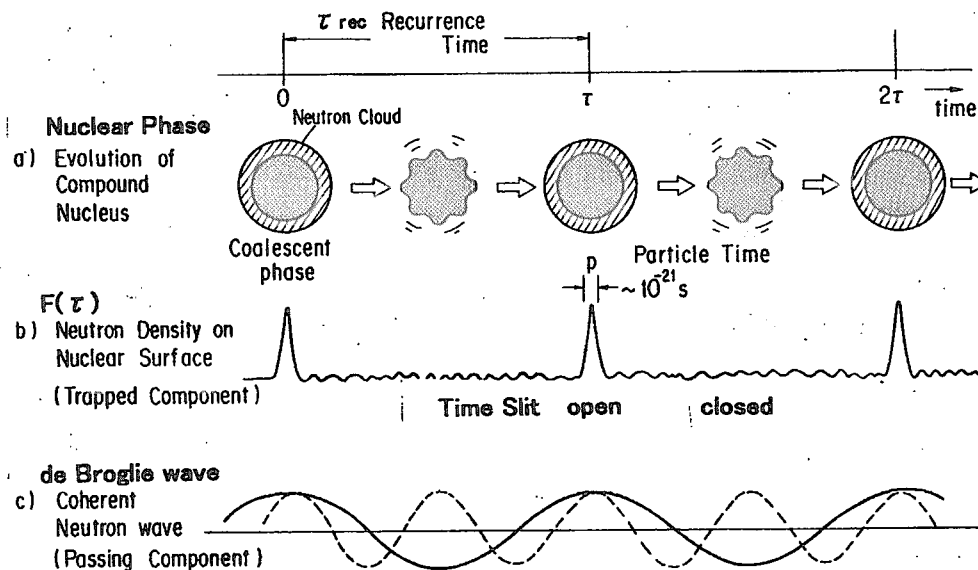


Fig.1 Time evolution of resonance reaction. a) Compound nuclear phase. b)  $F(\tau)$  or Neutron density on nuclear surface or Amplitude of the initial state. Time slit open at high amplitude. c) incident de Broglie wave.

It is considered that the response function  $F(\tau)$  is under the influence of an ensemble of normal modes of which total excitation energy is  $E_x = \hbar(\omega_1 + \omega_2 + .. + \omega_M)$ , written as a sum of inverse integers,

$$E_x = \frac{2\pi\hbar}{\tau_0} \sum_{j=1}^M \frac{1}{n_j} \quad (n_j \text{ integer}) \dots\dots(3)$$

Compound nucleus formed by neutron resonances can be approximately decomposed into  $M$  normal modes ( $M \leq 10$ ) of which frequencies are  $\omega_j$ . Total Hamiltonian is a sum of these normal modes.

$$H = H_1 + H_2 + \dots + H_M, \quad \dots\dots\dots(4)$$

The compound nuclear states  $\psi(x,t)$  are described as a direct products of these normal modes,

$$\psi(x, t) = \psi_1(x_1, t) \otimes \psi_2(x_2, t) \otimes \dots \psi_M(x_M, t) \dots (5)$$

Though the detailed structures of  $\psi_j(x_j, t)$  are not known, the requirement of time periodicity must be fulfilled.

$$\psi_j(x, t + \tau_j) = \psi_j(x, t) \quad (j=1, 2, \dots, M) \dots (6)$$

where  $\tau_j = \tau_0 \times n_j$ . Total recurrence is,

$$\psi(x, t + \tau_{rec}) = \psi(x, t) \dots (7)$$

where  $\tau_{rec} = \tau_0 \times \text{LCM}(n_1, n_2, \dots, n_M)$ .

A unit time is not necessary to be a constant for resonance to resonance. However, there are many cases where  $2\pi\hbar / \tau_0 = G (=34.5 \text{ MeV})$  are common for  $D_0$  and  $E_x$ . If  $G$  is a constant for a nucleus, level spacings  $D$  is, from Eq.(3), in a form,

$$D = G \sum \left( \frac{1}{m} \pm \frac{1}{n} \right) = G \frac{m'}{n'} \quad (m', n' : \text{integers}) \dots (8)$$

The above discussion can be applied to general (quasi) stable states because of time periodicity of the states. An example is ground state rotational band of  $^{50}\text{Cr}$ , where  $E_x$  are written in a form  $E_x = G'/n$ , where  $n=5, 6, 8, 12$ , and  $G'=(11/10)G$  [9].

### 3. Ensembles of the minimum LCM

For a (quasi) stable state of nucleus, there are many ensembles of normal modes possible to be excited which satisfy the energy relation in Eq.(3). However, we think that only a few ensembles of the minimum recurrence time or smallest LCM will be excited strongly. This means that ensembles of  $n_j$  ( $j=1, 2, \dots, M$ ) with simple integer ratios will be realized. This will be analogous to the Fermat's principle in optics, or Hamilton's principle in mechanics; the real path minimize the transit time from a point A to another point B. In our case of recurrence, phase point start from A to reach B, which is equal to A.

Using Eq.(3), we have searched for possible ensembles and their LCM for two and three normal modes where  $E_x$  is defined with  $G=34.5 \text{ MeV}$ .

$$\text{2-normal modes} \quad E_x = G \left( \frac{1}{n_1} + \frac{1}{n_2} \right) \dots (9)$$

$$\text{3-normal modes} \quad E_x = G \left( \frac{1}{n_1} + \frac{1}{n_2} + \frac{1}{n_3} \right) \dots (10)$$

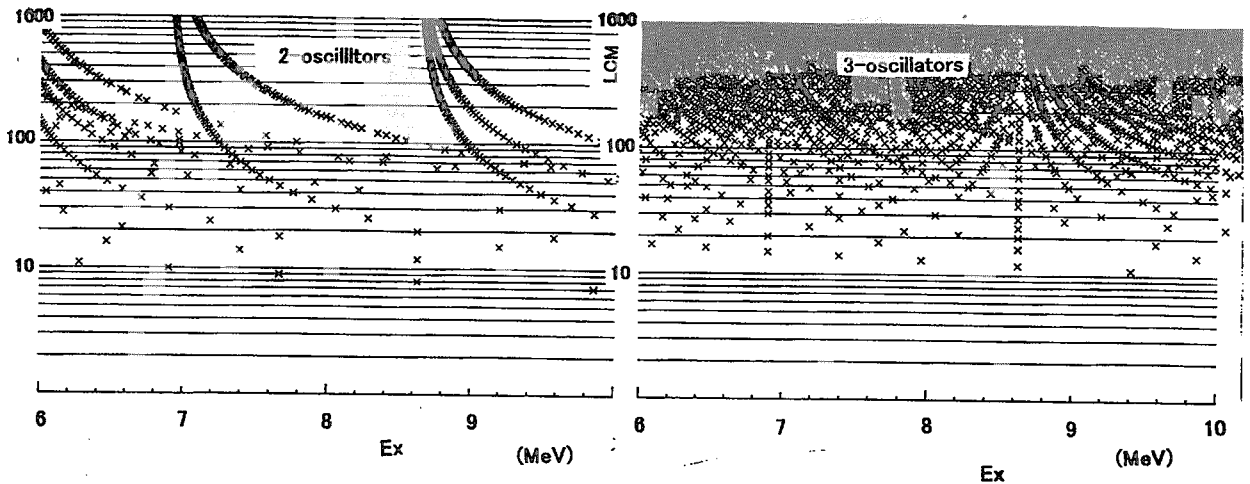


Fig.2 LCM vs.  $E_x$  for  $\text{LCM} \leq 1000$  and  $E_x$  from 6 to 10 MeV. a) 2-normal modes b) 3-normal modes.

As shown in Fig.2, there are many special  $E_x$  where LCM are small. At  $E_x = G/n$ , LCM make dips, and around them LCM become large. Among the points several bands are found, with simple meaning on the LCM. It is interesting that around  $E_x = G/n$  accompanying bands are found having asymptotes at  $E_x = G/n$  ( $n=2, 3, 4, \dots$ ). For 2-normal modes, a common band with the same curvature are found, with  $E_x$  and LCM written as

$$E_x = G(1/n + 1/nm) \quad (n=2, 3, 4, \dots; m=1, 2, 3, \dots) \dots (11)$$

$$\text{LCM} = nm. \dots (12)$$

For  $n=3$  band, the elements of the common band are at  $E_x/G = 2/3, 3/6, 4/9, 5/12, 6/15, 7/18, 8/21, \dots, (k+1)/3k$  : ( $k=1, 2, 3, \dots$ ). Also for  $n=5$  band,  $E_x/G = 2/5, 3/10, 4/15, 5/20, 6/25, 7/30, 8/35, \dots, (k+1)/5k$  : ( $k=1, 2, 3, \dots$ ). Between  $n=3$  and  $n=5$  bands, a spacing of  $(1/3 - 1/5)G = 4.6 \text{ MeV}$

appears many times. This will be related to the results of Sukhoruchkin[5] where level spacings  $D_{ij}$  distributions of real nuclei show a peak at  $\Delta = 4.6\text{MeV}$  for  $A \leq 50$  nuclei. Similarly, following spacings will be enhanced in level spacing distributions: between band 2 and 3,  $=5.75\text{MeV}$ ; between 2 and 4,  $=8.625\text{MeV}$ ; between 2 and 5,  $=10.35\text{MeV}$ ; between 3 and 4,  $=2.875\text{MeV}$ ; between 3 and 6,  $=5.75\text{MeV}$ ,...so on. For 3 normal modes, possible points of small LCM increase, and the similar bands as above are seen.

#### 4. Time Coherency of the de Broglie wave with the Recurrence in $^{16}\text{O}+n$ resonances

By an analogy of the quantum beat in laser physics, it is considered that recurrence frequency of a compound nucleus might be commensurable to the de Broglie wave frequency  $\omega_k = E_k^*/\hbar$  of the incident neutron wave. We have investigated integer ratios of  $E_x/E_n^*$  for the resonances of light nuclei, where  $E_n^*$  is recoil corrected neutron energy. For many of the resonances of  $^{16}\text{O}+n$ , simple integer ratios are found;  $E_x/E_n^* = n/m$  within an accuracy less than  $\sim 2 \times 10^{-3}$ . Newly evaluated data of 36 levels below  $E_x \leq 10\text{ MeV}$  [11] are used. Results are shown in Table 1.

For example, a sharp resonance at  $E_n = 1651.4\text{keV}$  ( $E_n^* = 1553.3\text{keV}$  using neutron mass  $= 1.0092$ , and  $^{16}\text{O} = 15.995$ ),  $E_x = 5696.7\text{ keV}$ , the ratio  $E_x/E_n^* = 11/3$ . As  $E_x = (33/200)G = (1/8 + 1/25)G$  and  $\text{LCM} = 200$ , the recurrence energy is  $E_{rec} = G/200 = 172.6\text{keV}$ . Neutron energy is  $E_n^* = (9/200)G = 9E_{rec}$ , and neutron separation energy is  $S_n = 4143.3\text{keV} = 24E_{rec} = (3/25)G$ . Difference  $\delta$  between  $E_n^* = 1553.3\text{keV}$  and  $9E_{rec}$  is,  $\delta = E_n^* - 9E_{rec} = -0.3\text{ keV}$  or ratio  $\delta/E_{rec} = 2 \times 10^{-3}$ . This means that in a recurrence time of  $^{17}\text{O}$   $200 \times \tau_0 = 2.40 \times 10^{-20}\text{ s}$ , incident de Broglie wave oscillate exactly 9 cycles. This coherency hold during life time ( $\hbar/\Gamma$ ,  $\Gamma \sim 4.1\text{keV}$ ) of this resonance  $\sim 1 \times 10^{-18}\text{ s}$ . This supports the resonance reaction mechanism described in section 2. In the 36 levels of  $^{16}\text{O}+n$  resonances, we found 15 cases of integer ratios with  $m \leq 11$  and  $n \leq 20$ , as shown in Table 1. The other resonances are excluded because the ratios  $E_x/E_n^*$  are between large integers.

Table 1 Ratios of de Broglie frequencies to the Recurrence frequencies in  $^{16}\text{O}+n$

j	$j\pi$	$E_x$ (keV)	$E_n$ (keV)	$E_x/E_n^*$	$E_x/G^\dagger$	LCM	$E_{rec}$ (keV)	R	$\delta$ (keV)	$\delta/E_{rec}$
1	7/2-	5696.7	1651.4	11/3	33/200	200	172.6	9	0.2	0.001
2	5/2-	5732.3	1689.1	18/5	18/108	108	318.4	5	-2.6	-0.008
3	3/2+	5868.7	1834.1	17/5	17/100	100	345.2	5	-0.6	-0.002
4	1/2-	5932.0	1901.4	10/3	10/58	58	593.2	3	7.0	0.012
5	1/2+	6380.2	2377.9	20/7	20/108	108	319.0	7	2.8	0.009
6	5/2-	7164.6	3211.7	19/8	19/91	91	377.1	8	3.2	0.008
7	3/2+	7239.1	3291	7/3	7/33	33	1034.1	3	-4.7	-0.005
8	5/2+	7378.2	3438.8	16/7	16/75	75	461.1	7	4.8	0.010
9	3/2-	7446.9	3511.9	9/4	9/42	42	827.4	4	-4.3	-0.005
10	7/2-	7686.9	3767	13/6	13/58	58	591.3	6	-2.9	-0.005
11	7/2-	8963.2	5123.7	13/7	13/50	50	689.5	7	-4.2	-0.006
12	5/2+	9194.1	5369.3	20/11	20/75	75	459.7	11	-3.9	-0.008
13	5/2-	9479.5	5672.6	16/9	16/58	58	592.5	9	2.5	0.004
14	7/2+	9710.9	5918.6	7/4	7/25	25	1387.3	4	11.7	0.008
15	9/2+	9859.1	6076.2	19/11	19/66	66	518.9	11	5.0	0.010

$\delta = E_n^* - R E_{rec}$   $S_n = 4143.3\text{keV}$   $^\dagger G$  varies within  $\pm 1\%$  from  $34500\text{keV}$ .

For two sharp resonances of No.8 and 12 in Table 1, they are same  $\text{LCM} = 75$  and same  $J\pi = 5/2+$ . Energy relations are shown in Fig.3. For No.8 resonance,  $E_x = 7378.2\text{keV} = (1/5 + 1/75)G = (3/25 + 7/75)G$  with  $\text{LCM} = 75$ , where  $(3/25)G$  is neutron separation energy. For No.12 resonance,  $E_x = 9194.1\text{keV} = (20/75)G = (1/5 + 1/15)G = (3/25 + 11/75)G$  with  $\text{LCM} = 75$ .

We would like to stress that the above analyses give evidence that the model of the compound nucleus composed of normal modes is really valid, with energies  $E_x = G \sum \frac{1}{n_j}$ ,  $\tau = \text{LCM}(n_j) \times \tau_0$  with almost correct value  $G = 34.5\text{MeV}$ .

#### 5. Level Patterns in $^{16}\text{O}+n$ resonances

In  $D_{ij}$  distributions of  $^{16}\text{O}+n$  resonances, shown in Fig.4, remarkable peaks appear at  $D_{ij}$  ( $D_{ij}^*$ ) = 550(517.6), 1609(1515), 1930(1816) keV, which are adopted as dominant spacings. The 1930keV peak corresponds to the spacing between the two levels No.8 and 12 in Table 1. We noticed that



the 1930keV spacings( we call a) frequently neighbor the another spacing 550 keV ( we call b) like a branch. Level patterns of outside branch /b/a/b/ and inside branch /b/a-2b/b/ are searched, where "/" means a real resonance level. The full patterns /b/b/a-2b/b/b/, shown in Fig.5, and partial ones where some levels except /a/ disappear, are recorded. In 37 levels in the region  $E_n \leq 6207$  keV, there are eight /a/ with an error  $a=1930 \pm 10$  keV, and  $b = 550 \pm 10$  keV. For clarity, two levels at both sides of /a/ we call stem levels.

Probability of appearance of the pattern is estimated assuming all the levels are disposed homogeneously without any correlation. In observed 37 resonance levels in the region, two pairs of closely separated levels( 3 and 9 keV) exist, and we regard as two single levels. Then, the average level spacing is 177 keV, and the average number of levels in 20keV channel width is 0.113. For 6 times appearance of stem levels /a/, 14 branch levels are placed at  $550 \pm 10$  keV separation from stem levels, where maximum possible levels is 24. Probability of appearance P of such case are estimated by binomial distribution, as,  $P = {}_{24}C_{14} \lambda^{14} (1-\lambda)^{10} \sim 1.7 \times 10^{-7}$ , where  $\lambda = 0.129$  is probability of appearance of a level in a channel of 20keV width. As the branch length b is arbitrary, number of channels  $n = (965/20 \sim 50)$  must be multiplied. Therefore the expected number of set is  $n \times P \sim 0.9 \times 10^{-5}$ , which is sufficiently small to deny the assumption of random (or RMT) distribution of the resonance levels. It is stressed that several patterns different from that in Fig.5 will be simultaneously found like another patterns in periodic lattice. Therefore, we can say that the resonance levels of  $^{16}\text{O}+n$  dispose with fairly simple structures a facet of which can be discovered by rather crude methods as above. Similar structures are found in nuclear levels of wide mass and energy region.

Average numbers of normal modes M excited in  $^{16}\text{O}+n$  are estimated to be  $\sim 2$ , by a formula  $M=1+\ln(E_x/D)/\ln(2\pi)$  [8], where D is for same  $J\pi$  levels. For two  $5/2^+$  levels of No.8 and 12 in Table 1, a simple configuration will be expected with recurrence energy 460keV. The time dependent descriptions of resonance reactions and non-statistical description of fine structure resonances will be a realm of nuclear research in 21 century, related to the multiphonon excitation, fine structures in giant resonances.

## References

- [1] S.Sukhoruchkin: *Proc.Conf.Nucl.Data for Reactors, Paris,1966,Vol 1, p159, Vienna,1967* ; S.Sukhoruchkin: *Proc. Int. Conf. on Statistical Properties of Nuclei* (Plenum, New York 1972) p.215
- [2] K.Ideno, M.Ohkubo: "Nonrandom distributions of neutron resonance levels" *J.Phys.Soc.Jap.* 30,620(1971); K.Ideno:"Nonstatistical behaviours of the level spacing distributions in neutron resonances" *ibid.* 37,581(1974)
- [3] C.Coceva, F.C.Corvi, P.Giacobbe, and M.Stefanon; *Proc. Int. Conf. on Statistical Properties of Nuclei* (Plenum, New York 1972) p.447
- [4] F.N.Belyaev, S.P.Borovlev: *Yad.Fiz.* 27.289(1978), transl.*Sov.J.Nucl.Phys.* 27(2),157(1978)
- [5] S.Sukhoruchkin: "Shell stabilization of excitations in odd odd nuclei" ISINN-4, E3-96-336 Dubna 1996, ISINN-5, Dubna 1997, ISINN-6, Dubna 1998, ISINN-7, Dubna 1999, ISINN-8, Dubna
- [6] M.Ohkubo: "Regular level structures in s-wave neutron resonances in light or magic e-e nuclei up to several hundred keV" *INDC(JPN)* -185/U, JAERI-Conf 2000-005, p325,
- [7] M.Ohkubo:"Quantum recurrence in neutron resonances and a unit time in nuclei" *INDC(JPN)* -188/U, JAERI-Conf 2001-006, p300
- [8] M.Ohkubo:"Recurrence of the compound nucleus in neutron resonance reactions" *Phys.Rev.C*, 53,1325(1996)
- [9] M.Ohkubo;" Non-statistical level disposition analysis in neutron resonances" *J.Nucl.Sci.Technol. Supplement 2, Proc. Int. Conf. ND2001* p508 (2002).
- [10] A.G. Sitenko: *Lecture in Scattering Theory*(Pergamon, New York 1971)
- [11] R.O.Sayer, L.C.Leal, L.M.Larson, R.R.Spencer, and R.Q.Wright: "R-Matrix Evaluation of  $^{16}\text{O}$  Neutron Cross Sections up to 6.3 MeV" *J.Nucl.Sci.Technol. Supplement 2, Proc. Int. Conf. ND2001* p88, (2002).

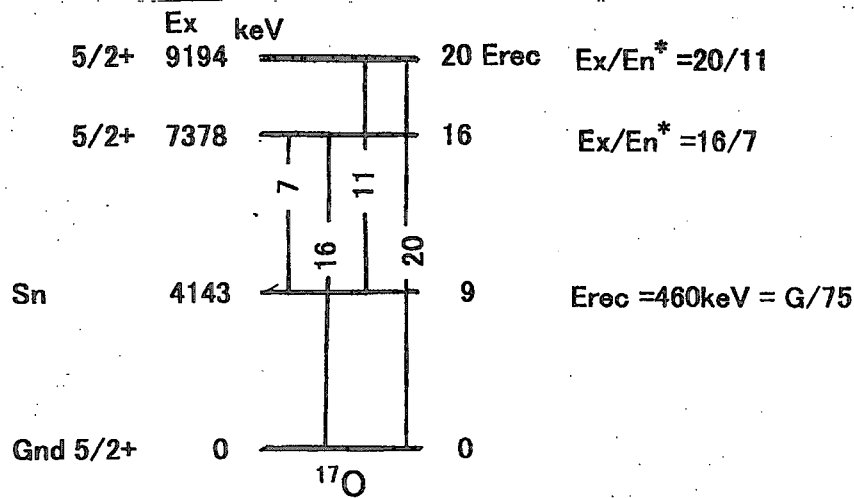


Fig.3 Levels scheme of  $5/2+$  with  $E_{rec} = 460\text{keV}$ .

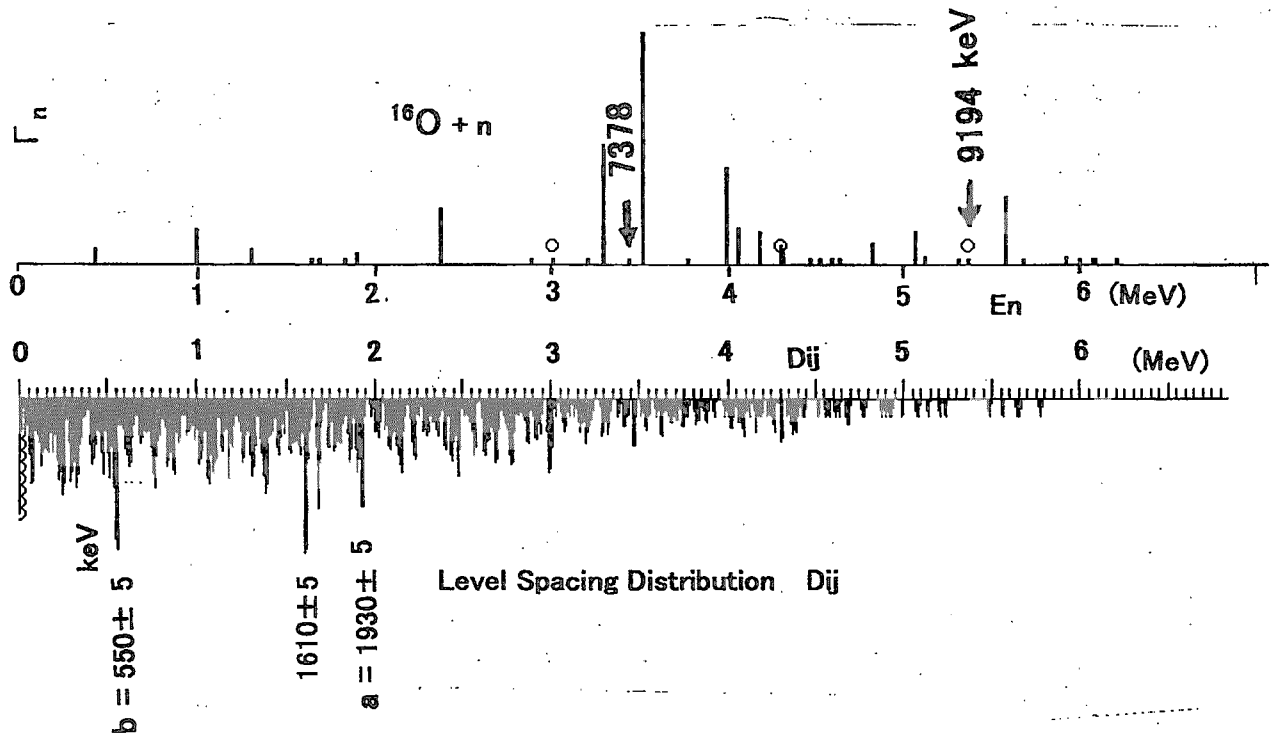


Fig.4 upper part: Neutron widths vs neutron energy for  $^{16}\text{O}+n$  resonances. lower part: Level spacing distribution for  $^{16}\text{O}+n$  resonances, where correlation of level spacing  $a=1930\text{ keV}$  and  $b=550\text{keV}$  are discussed in text. Spacing  $a=1930\text{keV}$  ( $a^*=1816\text{keV}$ ) correspond to the difference between  $5/2+$  levels of 7378 and 9194 keV shown in Fig.3.

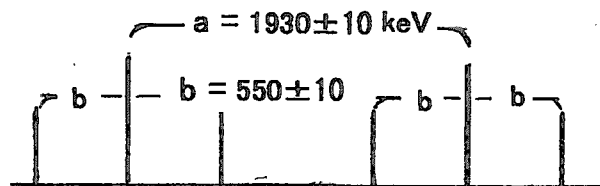


Fig.5 Level pattern searched for : stem levels  $a=1930\text{keV}$  and branch levels  $b$  free parameter. For 6 times appearance of stem levels, 14 levels are situated on branch positions at  $b=550\text{keV}$ .



### 3.25 Analysis of cosmic ray neutron-induced single-event phenomena

Yasuyuki TUKAMOTO, Yukinobu WATANABE, and Hideki NAKASHIMA

*Department of Advanced Energy Engineering Science, Kyushu University,*

*Kasuga, Fukuoka 816-8580, Japan*

Corresponding email: watanabe@aces.kyushu-u.ac.jp

We have developed a database of cross sections for the  $n+^{28}\text{Si}$  reaction in the energy range between 2 MeV and 3 GeV in order to analyze single-event upset (SEU) phenomena induced by cosmic-ray neutrons in semiconductor memory devices. The data are applied to calculations of SEU cross sections using the Burst Generation Rate (BGR) model including two parameters, critical charge and effective depth. The calculated results are compared with measured SEU cross-sections for energies up to 160 MeV, and the reaction products that provide important effects on SEU are mainly investigated.

#### 1. Introduction

In recent years, much concerns has been paid to cosmic-ray induced soft errors in semiconductor memory devices used on ground level[1]. Cosmic-rays on ground level consist of mainly neutrons with wide energy range from MeV to GeV. A microscopic picture of the cosmic ray induced soft errors is the following. Energetic neutrons interact with materials used in the devices, and light charged particles and heavy ions can be generated via a nuclear reaction with a silicon nucleus. They can give rise to local charge burst in a micron volume, which results in upsets of the memory cell information quantum that are called "single-event upsets (SEUs)". Therefore, quantitative estimation of the soft errors requires reliable nuclear reaction data for silicon in the high-energy range and modeling of charge transport in microelectronics devices.

So far, we have developed a database of cross sections for  $^{28}\text{Si}$  at neutron energies between 20 MeV and 3 GeV, which is necessary for soft error simulation[2]. The database was successfully applied to calculations of neutron-induced SEU cross sections using the Burst Generation Rate (BGR) model [2,3] and a neutron-induced soft-error simulation code system for semiconductor memory devices[4].

In the future, the size of memory devices will be reduced, and it is expected that the influence of low energy neutrons on SEUs cannot be ignored because a critical charge causing the SEU becomes smaller[5]. In the present work, therefore, we have extended the database so as to include the cross sections below 20 MeV. Double-differential cross sections for all recoils in the  $n+^{28}\text{Si}$  reaction are necessary for estimation of neutron-induced soft-errors. They were obtained using a kinematics calculation with the JENDL-3.3 library[6]. Finally, the cross section data were used to analyze some experimental data up to 160 MeV[7,8] by the BGR model calculation. In this report, we will discuss some results of the analysis, paying particular attention to SEUs for neutron energies below 20 MeV.

#### 2. Development of database for $n+^{28}\text{Si}$ reaction

##### 2.1 Outline

The JENDL-3.3 library[6] was used to obtain the double-differential cross sections (DDXs) for light charged particles (p and  $\alpha$ ) and all recoils ( $^{24,25}\text{Mg}$ ,  $^{27,28}\text{Al}$ , and  $^{27,28}\text{Si}$ ) in the  $n+^{28}\text{Si}$  reaction at energies between 2 and 20 MeV. A method of processing the JENDL-3.3

library will be described in the next subsection. The data for energies between 20 to 150 MeV were taken from the LA150 library[9] in which the DDXs of all recoils are included. We have calculated the cross sections for energies above 150 MeV using the QMD[10] plus statistical decay model (GEM[11]) calculation.

## 2.2 Calculation of double-differential cross sections for recoils with JENDL-3.3

For neutron elastic and inelastic scattering, the emission energy and angle of the recoiled nucleus  $^{28}\text{Si}$  can be easily obtained using the two-body kinematics [12], and the DDXs of  $^{28}\text{Si}$  in the laboratory system are also converted from the data of differential neutron elastic and inelastic scattering cross sections in the JENDL-3.3 library. The same kinematics calculation was also applied to two heavy recoils,  $^{28}\text{Al}$  and  $^{25}\text{Mg}$ , produced by (n,p) and (n, $\alpha$ ) reactions.

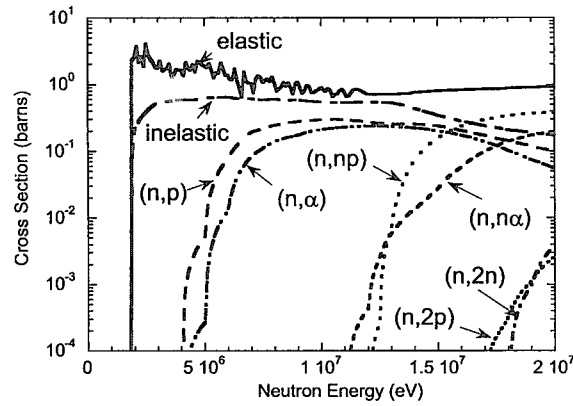
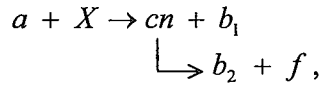


Fig.1 JENDL-3.3 cross sections for various reactions at neutron energies up to 20 MeV

As shown in Fig.1, two particle emission such as (n,np) and (n, $\alpha$ ) becomes dominant as the incident neutron energy increases and the influence on SEUs is expected to become crucial. However, it is not simple to obtain the DDXs of the recoils produced by the two-particle emission, because exclusive energy spectra for the second particle emission are not included in the JENDL-3.3. Note that the DDX spectra of the first neutron emission are included as MF=6, MT=16,22 and 28 in the JENDL-3.3. Hence, we assume that two-particle emission occurs via two-body sequential decay from the excited residual nucleus after the first particle emission:



where  $a$  and  $X$  are incident particle (neutron) and target nucleus ( $^{28}\text{Si}$ ), and  $cn$  is the residual nucleus,  $^{28}\text{Si}$ , after the first neutron ( $b_1$ ) emission, and  $b_2$  and  $f$  are the second emission particle and the recoil, respectively. The DDXs of the recoil nucleus,  $f$ , in the laboratory system are given by the following expression [13]:

$$\begin{aligned} \left( \frac{\partial^2 \sigma}{\partial \Omega_f \partial E_f} \right)^{\text{lab}} &= \int \left( \frac{\partial^2 \sigma}{\partial \Omega_{cn} \partial E_{cn}} \right) \frac{1}{\sigma_{dec}^{(i)}} \left( \frac{\partial^2 \sigma_{dec}}{\partial \Omega_f' \partial E_f'} \right) \left| \frac{\partial(\cos \theta_f', \phi_f', E_f')}{\partial(\cos \theta_f^{\text{lab}}, \phi_f^{\text{lab}}, E_f^{\text{lab}})} \right| d\Omega_{cn} dE_{cn} \\ &= \int \left( \frac{\partial^2 \sigma}{\partial \Omega_{cn} \partial E_{cn}} \right)^{\text{lab}} \frac{1}{\sigma_{dec}^{(i)}} \left( \frac{\partial^2 \sigma_{dec}}{\partial \Omega_f' \partial E_f'} \right) \left| \frac{\partial(\cos \theta_f', \phi_f', E_f')}{\partial(\cos \theta_f^{\text{lab}}, \phi_f^{\text{lab}}, E_f^{\text{lab}})} \right| d\Omega_{cn}^{\text{lab}} dE_{cn}^{\text{lab}}, \quad (1) \end{aligned}$$

where  $(\partial^2 \sigma / \partial \Omega_{cn} \partial E_{cn})^{ab}$  is calculated from the data of DDXs of the emitted particle,  $b_1$ , using the two-body kinematics, and  $(\partial^2 \sigma_{dec} / \partial \Omega'_f \partial E'_f)$  is the DDX of the final recoil,  $f$ , in the rest frame of the compound nucleus,  $cn$ , and  $\sigma_{dec}^{(i)}$  is the integrated cross section over  $\Omega'_f$  and  $E'_f$ .  $(\partial^2 \sigma_{dec} / \partial \Omega'_f \partial E'_f)$  is calculated by assuming the evaporation model for emission of  $b_2$  and its isotropic angular distribution. In the evaporation model calculation, empirical formulae given in ref.[14] were used for the inverse cross sections of proton,  $\alpha$ , and neutron, and the level density formula based on the Fermi-gas model was employed with the level density parameter  $a=A/8$ , where  $A$  is the mass number.

The DDXs for light-charged particles (proton and  $\alpha$ ) are included in the JENDL-3.3 library. Finally, a database of all DDXs for protons,  $\alpha$  and all recoils ( $^{24,25}\text{Mg}$ ,  $^{27,28}\text{Al}$ , and  $^{27,28}\text{Si}$ ) emitted in the  $n+^{28}\text{Si}$  reaction were prepared for energies between 2 and 20 MeV.

### 3. Modified Burst Generation Rate (BGR) model

The SEU rate is defined by

$$\text{SEU rate} = \int \sigma_{SEU}(E_n) \phi(E_n) dE_n, \quad (2)$$

where  $\sigma_{SEU}(E_n)$  is the SEU cross section for the neutron energy,  $E_n$ , and  $\phi(E_n)$  is the neutron flux. Using the BGR method[2,3],  $\sigma_{SEU}(E_n)$  is given by

$$\sigma_{SEU}(E_n) = C \cdot V \cdot BGR(E_n, Q_c, d), \quad (3)$$

where  $C$  is the charge collection efficiency and  $V$  is the sensitive volume per bit. It should be noted that the product of  $C$  and  $V$  is treated as a normalization parameter to be determined by fitting measured data of  $\sigma_{SEU}(E_n)$ . The BGR is defined as the probability that a nuclear reaction produces charged particles and ions which deposit the kinetic energy more than  $E_c$  in a sensitive volume, and is given as a function of incident neutron energy,  $E_n$  and critical charge,  $Q_c$  which can be converted into  $E_c$  using the relation  $E_c (\text{MeV}) = 22.5 Q_c (\text{pC})$ .

Since the energy deposit of the charged particles and ions in a small volume depends on the linear energy transfer (LET), we introduce an "effective depth  $d$ " as a parameter for BGR calculations. Thus,

$$\begin{aligned} BGR(E_n, Q_c, d) &= \sum_i BGR(E_n, Q_c, d, A_i, Z_i) \\ &= N_{Si} \sum_i \int_{E_{\min}^{(i)}(d)}^{E_{\max}^{(i)}(d)} \left( \frac{d^2 \sigma}{dE d\Omega} \right)^{(i)} d\Omega dE, \end{aligned} \quad (4)$$

where  $N_{Si}$  is the number density of silicon atoms, and the index  $i$  stands for the kind of reaction product with mass number  $A_i$  and atomic number  $Z_i$ .  $(d^2 \sigma / dE d\Omega)^{(i)}$  is the double-differential production cross section of the reaction product  $i$ . By taking into account the LET, the upper and lower limits of the integration,  $E_{\max}^{(i)}(d)$  and  $E_{\min}^{(i)}(d)$ , are estimated as the maximum and minimum energies of the reaction product  $i$  that deposits the energy above  $E_c$  within  $d$ . The SRIM code[15] is used for calculations of the LET. It should be noted that isotropic angular distribution is assumed for emission of the reaction products for simplicity.

### 4. Results and discussion

Figures 2 and 3 shows a comparison of the calculation with measured data [7,8] for SRAMs with 256Kb or 1Mb. The measured data are normalized to the data of Cypress. The

normalization constant  $C \cdot V$  in Eq.(3) was determined so that the BGR function calculated with  $Q_c=53$  fC and  $d=1.0$   $\mu\text{m}$  gives a best fit to the data of Cypress. The obtained result shows satisfactory agreement with the measured data over the whole neutron energy range.

The region below 20 MeV in Fig.2 is expanded in Fig.3. The calculated SEU cross-sections are decomposed into individual contribution from each recoil nucleus. The recoil,  $^{25}\text{Mg}$ , produced by the  $(n,\alpha)$  reaction shows the largest contribution at energies below 17 MeV. Also, the recoil,  $^{24}\text{Mg}$ , produced by the  $(n,n\alpha)$  reaction affects considerably the SEUs with increase in neutron energy. In Fig.4, the energy spectra of all recoils are plotted at an incident energy of 20 MeV in order to see why these Mg isotopes have significant contributions to SEUs. The critical charge  $Q_c=53$  fC corresponds to the energy deposit  $E_{\text{dep}}=1.2$  MeV. The minimum energy of the recoil that can provide this energy deposit within  $d=1.0$   $\mu\text{m}$  is about 1.8 MeV ( $E_{\text{min}}^{(i)}(d)$  in Eq.(4)). The energy spectra of Mg isotopes are distributed over the range above 1.8 MeV and have relatively large cross sections as can be seen in Fig.4. This is a possible reason why the Mg isotopes contribute significantly to SEUs.

Also, we have investigated the kind of reaction products that influence largely the SEUs for energies between 20 MeV and 150 MeV. The result is presented as a fraction of each recoil element to total SEUs in Fig.5. It is shown that production of heavy ions such as Al and Mg plays a major role in the SEUs at energies above 40 MeV, because such ions have large LET. It is also found that the contribution from Si is reduced with decrease in neutron energy. This trend can be explained by the fact that the elastic and inelastic cross sections become small and their angular distributions become steeper as the neutron energy increases.

Finally, the incident energy range having the most effect on the SEU rate has been examined by assuming a neutron flux distribution on the ground level given by IBM group[1]. The BGR functions are plotted for three different critical charges,  $Q_c=4.4$ , 13.3 and 30 fC in Fig.6. The effective depth  $d$  is assumed to be 0.35  $\mu\text{m}$  in the calculation. The product of the BGR and the neutron flux corresponding to the integrand in the right-hand side of Eq.(2) are shown in Fig.7 to examine the neutron sensitivity. It is found that the sensitivity increases remarkably at neutron energies below 20 MeV as  $Q_c$  decreases. This indicates that the nuclear data below 20 MeV will become important for estimation of soft-error rates as the size of memory devices is reduced because the reduction of the size leads to that of  $Q_c$ .

## 5. Conclusion

The database of cross sections for the  $n+^{28}\text{Si}$  reaction was developed in the energy range between 2 MeV and 3 GeV for evaluations of the soft-errors in semiconductor memory devices induced by cosmic-ray neutrons. The data were applied to calculations of SEU cross sections using the modified BGR model that takes into account the effective depth in the sensitive volume as a parameter. The calculated results reproduced well the energy dependence of the measured SEU cross-sections for energies up to 160 MeV. It was found that the reaction products that influence the SEUs mainly are the heavy ions such as Mg and Al having large LET, particularly, the Mg isotopes have significant contribution at energies below 20 MeV. The dependence of the neutron sensitivity on the critical charge  $Q_c$  was investigated over neutron energies up to 150 MeV, and it was found that the sensitivity increases remarkably at neutron energies below 20 MeV with decrease in  $Q_c$ .

## Acknowledgements

The authors are grateful to Mr. Y. Kawakami and Dr. M. Hane for valuable discussions on SER simulation calculation.

## References

- [1] J.F. Ziegler et al., IBM J. Res. Develop. **40**, No.1 (1996).
- [2] T. Ikeuchi et al., J. of Nucl. Sci. and Technol., Suppl. **2**, 1380 (2002).
- [3] J.F. Ziegler and W. Lanford, Science **206**, 776 (1979).
- [4] Y. Kawakami et al., NEC Research & Development, **43**(2), 146 (2002).
- [5] H. Ibe et al., Applied Physics, **70**, No.11, 1308 (2001) [in Japanese].
- [6] K. Shibata et al., J. of Nucl. Sci. and Technol. **39**, 1125 (2002).
- [7] K. Johansson et al., IEEE Trans. Nucl. Sci. **45**, 2519 (1998).
- [8] K. Johansson et al., *ibid.* **46**, 1427 (1999).
- [9] M.B. Chadwick et al., Nucl. Sci. Eng. **131**, 293 (1998).
- [10] K. Niita et al., JQMD code, JAERI-Data/Code 99-042 (1999).
- [11] S. Furihata, Nucl. Instr. Method in Phys. Res. B **171**, 251 (2000); S. Furihata and T. Nakamura, J. Nucl. Sci. and Technol. Suppl. **2**, 758 (2002).
- [12] G.G. Ohlsen, Nucl. Instr. Methods, **37**, 240 (1965).
- [13] M.D. Baker et al., Nucl. Sci. Eng. **96**, 39 (1987).
- [14] A. Chatterjee et al., Pramana **16**, 391 (1981).
- [15] J.F. Ziegler, SRIM code (1999).

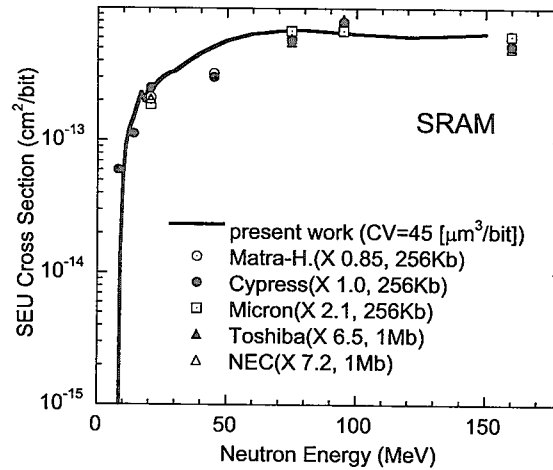


Fig.2 Comparison of the calculated SEU cross sections with the measured ones taken from Refs.[7,8]. The measured data are normalized to the data of Cypress.

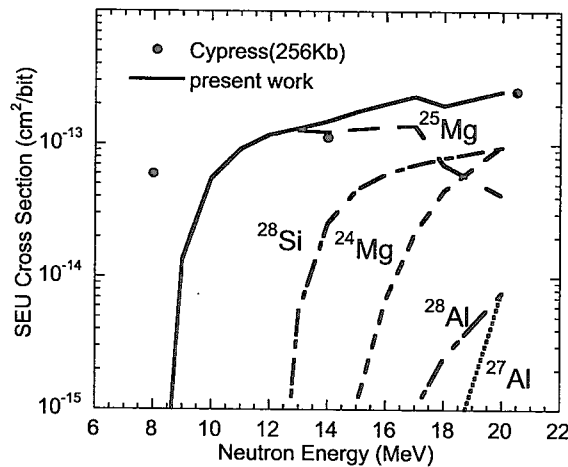


Fig.3 Same as in Fig.2, but the energy range below 20 MeV.

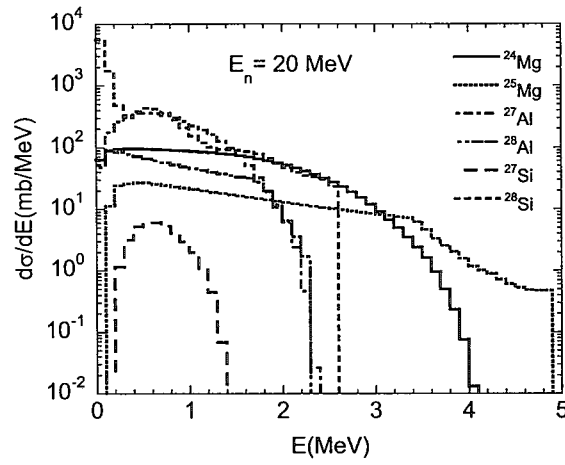


Fig.4 Energy spectra of all recoils for an incident energy of 20 MeV.

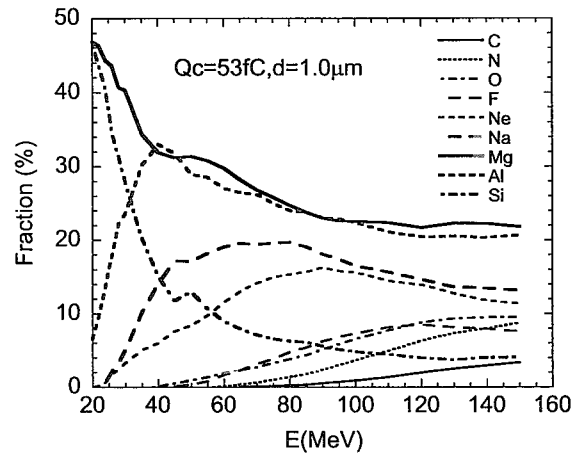


Fig.5 Fraction of each recoil element to total SEUs as a function of incident neutron energy.

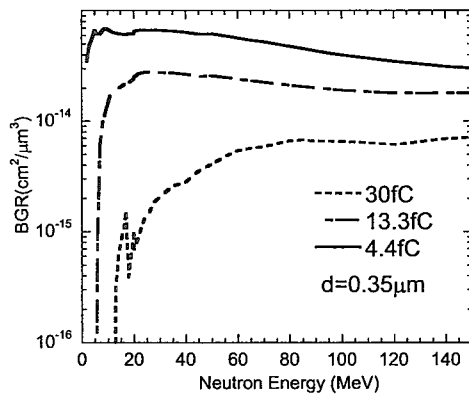


Fig.6 BGR functions for  $Q_c=4.4, 13.3$  and  $30$  fC and effective depth  $d=0.35 \mu\text{m}$ .

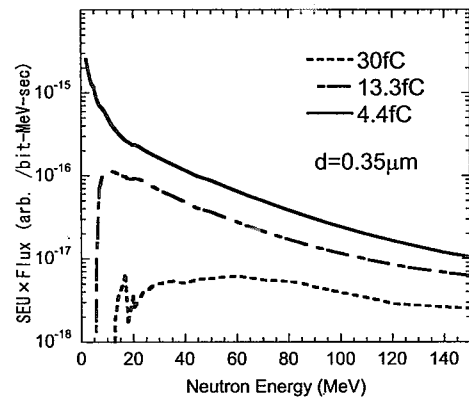


Fig.7 Sensitivity of the critical charge  $Q_c$  to SEUs for the cosmic-ray neutron flux given by IBM model[1].





### 3.26 Soft Errors of Semiconductors Caused by Secondary Cosmic-ray Neutrons

Hidehori SAWAMURA<sup>\*1&\*2</sup> Tetsuo IGUCHI<sup>+2</sup> Takanobu HANDA<sup>+1</sup>

<sup>\*1</sup> Computer Software Development Co., Ltd.  
Tomihisa-cho, Sinjyuku-ku, Tokyo, 162-0067  
e-mail: sawamura@csd.co.jp

<sup>\*2</sup> Department of Nuclear Engineering, Nagoya University  
Furo-cho, Chigusa-ku, Nagoya-shi, AICHI, 464-01  
e-mail: sawamura@avocet.nucl.nagoya-u.ac.jp

Cosmic-ray spallations in the atmosphere produce high energy neutrons, and these neutrons wake up an upset of bits on memory devices. This phenomenon is called 'soft error' or 'single-event upset'. The neutron originated soft errors are mainly caused by nuclear reactions between a silicon nucleus and a high energy neutrons, which produce  $\alpha$ -particles and Mg, Al and other fragments. A preliminary analysis have been made on the neutron induced soft errors by simulating behaviors on neutrons and  $\alpha$ -particles of their nuclear reaction product in Si with MCNP-X<sup>[1]</sup>(LANL) and LAHET150(LANL) datasets.

Key words: Semiconductor, Neutron, Cosmic-ray, Single event-upset, Soft error

#### 1. Introduction

Semiconductor soft errors on memory bits caused by secondary cosmic-ray neutrons were reported in 1979 by Ziegler<sup>[2][3]</sup>. In those days, attention was only paid to the soft error caused by  $\alpha$ -particles<sup>[4]</sup> from decay of a very small amount of radioactive impurities in semiconductors. The soft error by secondary cosmic-ray neutrons had not been remarked until 1990's. In 1994, however, O'Gorman, et al. reported that the contribution of neutrons to the soft error was almost equal to that of  $\alpha$ -particles from the radioactive impurities for 288Kbit DRAM<sup>[5]</sup> chips. In 1996, IBM, Boeing, Fujitsu, etc<sup>[6-11]</sup>, pointed out that the soft error rate increases with an increase of integration density of semiconductor devices. The neutron induced soft errors would be dominant for DRAM integrated with higher density than 4Mbits, comparing with  $\alpha$ -particle induced ones<sup>[11-13]</sup>. To estimate the neutron induced soft error rate, we have made a preliminary transport calculation on neutrons and  $\alpha$ -particles of their nuclear reaction product in Si with MCNP-X(LANL) and LAHET150(LANL) datasets.

---

+1: Computer Software Development Co., Ltd

+2: Nagoya University

## 2. Process

In this section, we will describe semiconductor soft error processes due to cosmic-ray neutrons. A. Neutrons produced in cosmic-ray spallations reach on the ground of the earth. Fig.1 shows the particle flight path. The rates of secondary cosmic-rays are summarized in Table 1. Muons consist about 60% of secondary cosmic-rays and neutrons consist about 40% of them. Electric charge in a semiconductor cell by a deposit energy from a cosmic-ray muon induced is negligible. However, heavy nuclei fragments produced by a nuclear reaction between a neutron and a silicon nucleus deposit huge amount of energy that brings about a single event upset. Thus, about 99% of soft-errors by secondary cosmic-rays are caused by cosmic-ray neutrons<sup>[14, 15]</sup>.

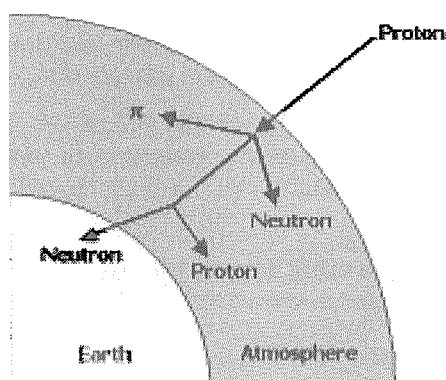


Fig.1 Secondary Cosmic-ray Neutrons

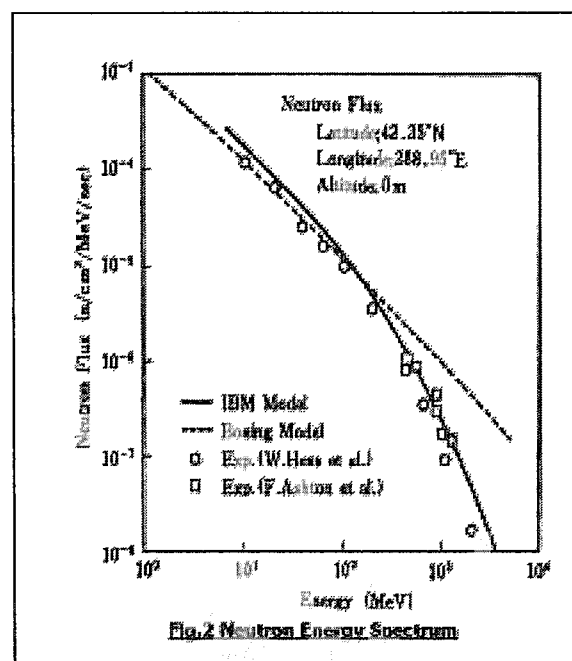


Fig.2 Neutron Energy Spectrum

Table1. A main component of Secondary Cosmic-ray [sea level]

Secondary Cosmic-ray	Rate [sea level]	Reaction on the Semiconductor	Electric Charge
Muon	59.1%	Electromagnetic Interaction	~0.5fc/μm
Neutron	40.5%	Nuclear Reaction	150fc/μm
Proton	0.325%	Electromagnetic Interaction (20%) Nuclear Reaction (80%)	1~3fc/μm 150fc/μm
Pion	0.044%	Electromagnetic Interaction + Nuclear Reaction	Low Charge

According to the IBM model, the cosmic-ray neutron spectrum<sup>[14, 15]</sup> on the ground is represented by the following Formula(1) and Fig.2. Table2 shows the neutron flux<sup>[14, 15]</sup>.

$$\text{FLUX} = 1.5 \exp \{f(\ln(E))\} \quad \dots \text{Formula (1)}$$

$$F(x) = -5.2752 - 2.6043x + 0.5985x^2 - 0.08915x^3 + 0.003694x^4 \quad (10\text{MeV} < E < 10\text{GeV})$$

Table 2. Neutron Flux ( $E > 10 \text{ MeV}$ )

New York;	20 n/cm <sup>2</sup> /hour
Tokyo;	12 n/cm <sup>2</sup> /hour
Denver;	97.6 n/cm <sup>2</sup> /hour
London;	22.8 n/cm <sup>2</sup> /hour

B. Formula (2) shows dominant processes producing  $\alpha$ -particles and other heavy ions in a silicon by an incident neutron. Fig.3 shows an example of images of the interactions.

Nuclear Reaction (Example) ... Formula (2)

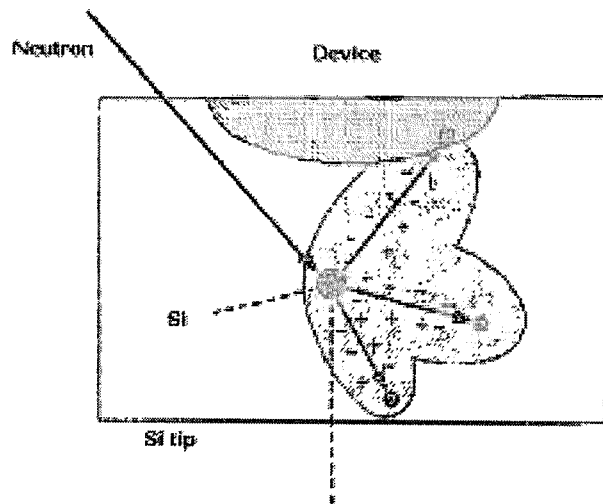
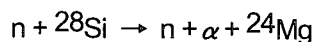
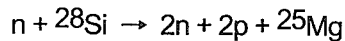
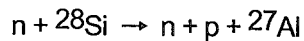
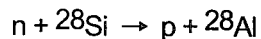


Fig.3 Nuclear Reaction

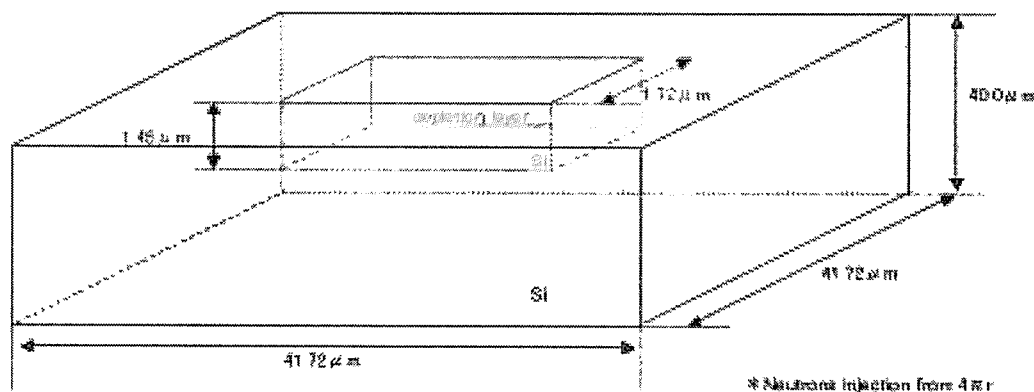
C. The  $\alpha$ -particle or the other heavy ion deposit some energy on a memory bit. If the generated charge by the deposit energy is greater than the threshold of a single-event upset, a soft error occurs. Unfortunately, the complete cross section list of the interactions is not publicly opened. Therefore, in this report, we have analyzed only the phenomena related to  $\alpha$ -particles.

D. An upset of a bit on memory devices has an energy threshold. For example, an upset of a bit on common SRAM devices occurs when a bit is given an electric charge around 10fC to 30fC. The energy of 3.6 eV is required to create an electron-hole pair in Silicon. Therefore, the 10fC and the 30 fC correspond to the deposit energy of 0.23 MeV and 0.68 MeV. Less than about 3000 Fit is preferable as for the soft error rate of a semiconductor (Fit = failure in time ; failure=upset of bit, time=1.0E+9hour).

### 3. Analysis

We calculated an expected soft error rate on a 1Mbit SRAM device caused by neutrons generated from cosmic rays. The soft error rate is calculated from the number of event that the energy deposition in the depletion layer is greater than the soft error threshold. Note that on this analysis, we only take into account the energy deposition by an  $\alpha$ -particle produced from a nuclear reaction between an incident neutron and a silicon nucleus. We used a neutron transport Monte Carlo code, MCNP-X on this simulation. Fig.4 shows the geometry of a SRAM cell used for the input of the simulation. In the simulation, neutrons are generated on the surfaces of the silicon substrate shown in Fig.4. The place of the neutron origin is randomly selected on the surfaces event-by-event and the direction of the neutron is also randomly selected but only directed to the inside of the substrate. The neutron spectrum is based on the IBM model shown in Fig.2 . We assumed that the injected neutron flux is  $12 \text{ n/cm}^2/\text{hour}$ , which is the experimentally measured neutron flux in Tokyo shown in Table 2.

Fig.4. Analyzed Model



### 4. Results and discussion

We generated  $1.04 \times 10^9$  neutrons in the Monte Carlo simulation. It corresponds to the real time of  $8.67\text{E}+11$  hours by using the generated area of  $1.0\text{E}-4\text{cm}^2$  and the flux of  $12 \text{ n/cm}^2/\text{hour}$ . The CPU time is about 20 hours on the 1.9GHz Pentium4 Linux PC. Assuming that the soft error threshold is 30fc (0.68MeV), 7 events are observed as an energy deposition greater than the threshold in the depletion layer by an  $\alpha$ -particle. From this result, the soft error rate is derived as  $8.4\text{E}-12$  errors/hour/cell. Therefore, the soft error rate of the 1Mbit SRAM device is expected to be  $8.4\text{E}-6$  errors/hour and it corresponds to 8400 Fit.

Fig.5 shows the deposit energy by an  $\alpha$ -particle in the depletion layer of the cell as a function of number of neutrons generated. This figure shows about 1/6 portion of the total generated neutrons with the histogram bin size of around 3000 event. In this plot, three events can be seen as an energy deposition greater than 30 fc ( 0.68 MeV). Note that this 1/6 portion is selected as an example of a statistical soft error rich region in this simulation.

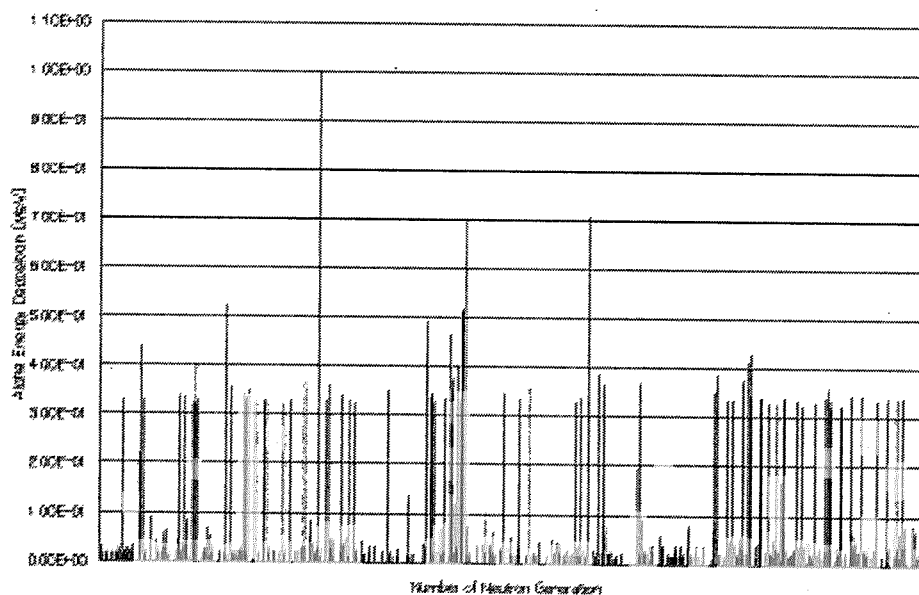


Fig.5. Alpha Particle Energy Deposition about 1 device

The result of  $8400 \pm 3200$  Fit (68% confidence level) is larger than a preferable upper limit of 3000 Fit. However, since this simulation result has a large statistical uncertainty, we need more statistics to improve the statistical precision. In addition to the statistics, we have to think of the following subjects.

- \* Heavy ion fragments effect other than  $\alpha$ -particles.
- \* Simulate more accurate geometry of the cell.
- \* Chemical properties other than silicon, like impurities doped to semiconductors, coating materials, and other layers like metal and  $\text{SiO}_2$ .
- \* Broader energy spectrum of neutrons outside of 10 MeV to 150 MeV.

## 5. Conclusion

In this study, we calculated the soft error rate of a 1Mbit SRAM cell caused by an  $\alpha$ -particle generated from cosmic-ray neutrons using a neutron transport and the interaction Monte Carlo code MCNP-X. The result shows the soft error rate of  $8400 \pm 3200$  Fit (68% confidence level, statistical error only). We will improve the analysis accuracy by simulating more detailed geometry and the chemical composition, and by improving the nuclear cross section file used for the simulation code.

## References

- [1] Laurie S. Waters, Editor : "MCNPX-TM USER'S MANUAL Version 2.4.0", LA-CP-02-408, August 2002
- [2] J.F.Ziegler and W. A. Lanford : "Effect of Cosmic Rays on Computer Memories," Science, vol. 206, p.776, 1979.
- [3] J.F.Ziegler and W. A. Lanford : "The Effect of Sea Level Cosmic Rays on Electric Devices," J. Appl. Phys., vol. 528, p.4305, 1981.
- [4] T. C. May and M. H. Wood : "Alpha-Particle-Induced Soft-Errors in Dynamic Memories," IEEE Trans. Electron Dev., vol. ED-26, p. 2, 1979.
- [5] T. J. O'Goman : "The Effect of Cosmic Rays on the Soft Error Rate of a DRAM at ground level," IEEE Trans. Electron Dev., vol. ED-41, p. 553, 1994.
- [6] J.F.Ziegler : "IBM Experiments in Soft Fails in Computer Electronics (1978-1994)," IBM J. Res. Develop., vol. 40, p.3, 1996.
- [7] T. J. O'Goman, J. M. Ross, A. H. Taber, J. F. Ziegler, H. P. Muhlfeld, C. J. Montrose, H. W. Curtis and J. L. Walshi, : "Field Testing for Cosmic Ray Soft Errors in Semiconductor Memories," IBM J. Res. Develop., vol. 40, p.41, 1996.
- [8] J.F.Ziegler, H. P. Muhlfeld, C. J. Montrose, H. W. Curtis, T. J. O'Goman and J. M. Ross : "Accelerated Testing for Cosmic Soft-Error Rate," IBM J. Res. Develop., vol. 40, p.51, 1996.
- [9] W. R. Mckee, H. P. McAdams, E. B. Smith, J. W. McPherson, J. W. Janzen, J. C. Ondrusek, A. E. Hyslop, D. E. Russell, R. A. Coy, D. W. Bergman, N. Q. Nguyen, T. J. Aton, L. W. Block and V. C. Huynh : "Cosmic Ray Neutron Induced Upsets as a Major Contributor to the Soft Error Rate of Current and Future Generation DRAMs," Interbational Releability Physics Symposium, Tech. Dig., p. 1, 1996.
- [10] E. Normand : "Single-Event Upset at Ground Level," IEEE Trans. Nucl. Sci., vol. NS-43, p.2742, 1996.
- [11] Y. Tosaka, S. Satoh, K. Suzuki, T. Sugii, H. Ehara, G. A. Woffinden and S. A. Wender : "Impact of Cosmic Ray Neutron Induced Soft Errors on Advanced CMOS Circuits," Symposium on VLSI Technology, Tech. Dig., p.148, 1996.
- [12] Y. Tosaka, S. Satoh, T. Itakura, K. Suzuki, T. Sugii, H. Ehara and G. A. Woffinden : "Cosmic Ray Neutron Induced Soft Errors in Sub-Half Micron CMOS Circuits," IEEE Electron Dev. Lett., vol. EDL-18, p.99, 1997.
- [13] Y. Tosaka, S. Satoh, T. Itakura, H. Ehara, T. Ueda G. A. Woffinden and S. A. Wender : "Measurements and Analysis of Neutron-Induced Soft Errors in Sub-Half Micron CMOS Circuits," IEEE Trans Dev., vol. ED-45, p.1453, 1998.
- [14] J.F.Ziegler : "Terrestrial Cosmic Rays," IBM J. Res. Develop., vol. 40, p.19, 1996.
- [15] J.F.Ziegler : "Terrestrial Cosmic Ray intensities," IBM J. Res. Develop., vol. 42, p.117, 1998.



### 3.27 PRA (Probabilistic Risk Assessment) for Spent Fuel Decommissioning of the Fugen Nuclear Power Station

D.T. SONY TIAHYANI

Nuclear Safety Technology Development Center  
National Nuclear Energy Agency of Indonesia – BATAN  
Serpong – Tangerang 15310, Indonesia

Y. IGUCHI, S. KIYOTA

Fugen Nuclear Power Station – Japan Nuclear Cycle Development Institute  
3 Myojin-cho, Tsuruga-shi, Fukui 914-8510, Japan

#### Abstract

Fugen Nuclear Power Station will be permanently shutdown in 2003 and immediate fuel unloading and fuel transportation is necessary. The spent fuel pool should be stored safely because the spent fuels are kept in the spent fuel pool. Loss of cooling in the spent fuel pool can lead to a serious condition. This paper is to calculate the risk of the spent fuel pool especially probability calculation of consequence during decommissioning. In this case, fuel uncover is as end state. Calculation is based on NUREG-1738. Analysis has been done for 4 initiating events that are loss of cooling, internal fire, loss of offsite power (LOPA) and loss of inventory. Initiating event frequency is adopted from Fugen condition and NUREG. More, calculation data is taken from the living PSA of Fugen and NUREG. Results of analysis showed that the spent fuel pool of Fugen is safe enough because the fuel uncover probability is  $4.438\text{E}-08$  per year. Moreover, the spent fuel pool cooling system of the Fugen NPS has high reliability because the failure probability is  $7.435\text{E}-04$  per year and will become  $2.794\text{E}-06$  per year if RHR (residual heat removal) system is included. Therefore, RHR system can be considered in the accident management during decommissioning. On the other hand, the maintenance cost increases by keeping the RHR system during decommissioning.

Keywords : PRA, Spent Fuel Pool, Decommissioning

#### 1. Introduction

Fugen is a heavy-water-moderated, boiling light water cooled, pressure tube type prototype reactor with electric output of 165 MWe. Fugen got a final license of commercial operation in March 1979. Since then, Fugen has been operating more than 23 years and achieved 21 TWh of power generation 130,000 hours of total operation time and 64% as an average load factor [1]. In this period, it has operated safely and reliably.

After the permanent shutdown in 2003, immediate fuel unloading and fuel transportation is necessary. This activity needs about several years because of capacity of the Tokai reprocessing plant. During this period, the plant especially the spent fuel pool should be stored safely because the spent fuels are kept in the spent fuel pool. Loss of cooling in this system or incident can lead to a serious condition, therefore it is necessary to analyze risk of the spent fuel pool during decommissioning.

The spent fuel assemblies are retained in the spent fuel pool (SFP) and submerged in water to cool the remaining decay heat and to shield the radioactive assemblies. Therefore, the most severe accident postulated of SFPs is loss of water from pool. In this case, decay heat for the fuel clad heats up and Zr clad will reach the point of rapid oxidation in air. More, Zr react with air or steam and this reaction is exothermic. The energy released from exothermic reaction and combined with the fuel decay heat, can cause the reaction to become self-sustaining and ignite the Zirconium. The increase in heat from the oxidation reaction can also raise the temperature in adjacent fuel assemblies and propagate the oxidation reaction. The zirconium fire would result in a significant release of the spent fuel fission products which would be dispersed from the reactor site in the thermal plume from the zirconium fire.

Purpose of this paper is to calculate probability or frequency of consequence during decommissioning of Fugen.

#### 2. Layout of Fugen System and Spent Fuel Pool Cooling System

The cooling system is to remove the heat generated in the core by boiling and to send the steam to turbine [2]. The coolant flows into the lower header from the outlet of the recirculation pumps through 2 check

valves and enters into the pressure tubes from the bottom. The heat from the fuels causes coolant to boil in the core, forming a two-phase flow of saturated steam and water, this then goes into the steam drums through the reactor outlet pipes. The two-phase flow entering the steam drums is separated into the saturated steam and water, the steam is then sent to turbine, while saturated water is mixed with the feed water and returned via the recirculation pumps through the downcomer and manifolds. Layout of Fugen is shown in Figure 1.

The reactor cooling system consists of 224 pressure tubes which are divided into two independent loops, each loop consists of a steam drum, 2 recirculation pumps, a manifold, a lower header and piping connecting these components. Four downcomers from the steam drum are combined into 2 before connected to each recirculation pump. In each loop, coolant (light water) is supplied into 112 inlet pipes in the reactor inlet header and flows into each pressure tube and then flows into the steam drum through 112 outlet pipes.

The spent fuel pool system is designed to make subcriticality condition of fuel, therefore design criteria is as follows. Temperature of pool water is kept between 20 °C and 70 °C. Also, condition of fuel assembly is arrangement, so that  $k_{\text{eff}}$  is less than 0.85. More, pool water temperature is adjusted less than 66 °C to make safety margin.

The block diagram of spent fuel pool cooling system is shown in Figure 2. Suction is taken from the spent fuel storage pool via recirculation pumps of pool cooling (A, B and C) and is passed through the heat exchanger (A, B and C). After cool down, the coolant goes through filter system or by-pass and is returned to the discharge line. Coolant flow in shell side of heat exchanger, therefore temperature outlet of heat exchanger is kept on less than 52 °C.

RHR (Residual Heat Removal) system is used for the abnormal condition of the SFP (Spent Fuel Pool). First condition, if amount of fuel is taken from core quickly with large decay heat after shut down when reactor troubles. Second condition, if recirculation pump of pool cooling is loss of function after loss of normal power.

## 2. Analysis Method

### 2.1. Event Tree for Initiating Event

Analysis has been done based on NUREG-1738 [3]. Analysis used event tree analysis and fault tree analysis. An event tree is a quantifiable logical network that begins with an initiating event or condition and progresses through a series of branches (usually binary) that represent expected system or operator performance that either succeeds or fails and arrives at either a success or failed condition at the end of the tree. There are 4 internal initiating events that lead to fuel uncover (endstate). The other way, a fault tree is a logic diagram that is used to determine the logical combination of failure or condition causes that will produce an undesired event.

In this case, to calculate risk of spent fuel pool especially probability calculation used 4 initiating events that are loss of cooling, internal fire, loss of power and loss of inventory. Event trees for each initiating event are developed as in Figure 3.

Initiating Event for Loss of Cooling (IE-LOC) includes conditioning arising from loss of coolant system flow because of the failure of the operating pumps or valves, from piping failures, from an ineffective heat sink (e.g., loss of heat exchanger). In this condition, there are 5 expected (mitigating) systems/operator performance to end state as follows: Control Room Alarms (LOC-CRA), Other Indications of Loss of Cooling (LOC-IND), Operator Recovery of Cooling System (LOC-OCS), Operator Recovery Using Onsite Sources (e.g.: fire water system) (LOC-OFD), Operator Recovery Using Offsite Sources (LOC-OFB).

Initiating event for Internal Fire (IE-FIR) is to assume fires of sufficient magnitude, therefore if not suppressed, would cause a loss of cooling to the spent fuel pool. Cause of loss of cooling is from damage of spent fuel pool cooling system or the offsite power feeder system. In this condition, there are 5 expected (mitigating) systems/operator performance to end state as follows: Control Room Alarms (FIR-CRA), Other Indications of Loss of Cooling due to Fire (FIR-IND), SFPC System Survive – Fire Suppression (FIR-OSP), Operator Recovery Using Onsite Sources (FIR-OMK), Operator Recovery Using Offsite Sources (FIR-OFD).

Initiating event for Loss of Offsite Power from Plant-centered and Grid-related (IE-LOPA) is to represent loss of spent fuel pool cooling resulting from losses of offsite power from plant centered and grid-related. These events include: hardware failures, design deficiencies, human error (in maintenance and switching), localized weather-induced faults (e.g. lightning) etc. In this condition, there are 4 expected systems/operator performance to end state, as follows: Offsite Power Recovery (LOPA-OPR), Cooling System Restart and Rerun (LOPA-OCS-REV), Operator Recovery Using Makeup Systems (LOPA-OMK), Operator Recovery Using Offsite Sources (LOPA-OFD).

Initiating event for Loss of Inventory (IE-LOI) includes loss of coolant inventory from events such as those resulting from configuration control errors, siphoning, piping failures, and gate and seal failures. In this condition, there are 7 expected systems/operator performance to end state, that are loss exceeds normal makeup capacity (LOI-NLL), Control Room Alarms (LOI-CRA), Other Indications of Inventory Loss (LOI-IND),



operator isolates leak and initiates SFP make-up (LOI-OIS), operator initiates SFP Makeup System (LOI-OIL), operator initiates make-up using fire pumps (LOI-OMK), recovery from offsite sources (LOI-OFD)

## 2.2. Frequency of initiating event and mitigating system

Initiating event frequency for loss of cooling system is calculated based on failure of the spent fuel pool cooling system of Fugen, therefore fault tree of SFP cooling system is arranged which top event is Spent Fuel Pool Cooling System Fail. Fire and loss of inventory initiating event frequency are adopted from NUREG. LOPA (Loss of Offsite Power) frequency is adopted from level 1 PSA of Fugen. Frequency or failure probability for each mitigating system is determined based on fault tree analysis.

## 3. Calculation and Result

Component failure data is adopted from living PSA of Fugen (<http://ftessn13.fugen.t-hq.inc.go.jp:8010>) [4]. Some data, especially human error data used NUREG data that is generic data. Also, generic data from the level PSA 1 of Fugen is used to calculate failure probability of the spent fuel pool system. Calculation is carried out by using Saphire Window ver. 6.14. The result of calculation is shown in Table 1.

Table 1. The result calculation for fuel uncover frequency

Initiating Event	Frequency, per year		End State (Fuel Uncovery) Frequency, per year	
	RHR not included, per year	RHR included, per year	RHR not included, per year	RHR included, per year
1. Loss of Cooling	7.435E-04	2.794E-06	3.494E-10	1.537E-12
2. Fire	3.000E-03	3.000E-03	3.999E-08	3.999E-08
3. LOPA	1.200E-03	1.200E-03	1.341E-09	1.341E-09
4. Loss of Inventory	1.000E-03	1.000E-03	2.695E-09	2.695E-09
TOTAL			4.438E-08	4.403E-08

## 4. Discussion

Based on event tree analysis, there are 11 sequences for loss of cooling initiating event, that are 3 sequences for fuel uncover condition and 8 sequences is safely. First worst condition, operators know that initiating event occurred but operators fail to recovery of cooling system or to run fire pumps. Moreover, operators fail to recovery using offsite sources. Frequency of this condition is 3.486E-10 per year. Second worst condition, if control room alarm fail after initiating event occurred, but operators know initiating event from other indications. The following sequences are as like first worst condition, so frequency of second worst condition is 7.743E-13 per year. Third worst condition is pessimistic condition which all mitigating systems fail and frequency of this condition is 4.561E-17 per year.

There are 8 sequences for fire initiating events, 3 sequences are worst condition (fuel uncover). First worst condition, operators know that initiating event occurred but spent fuel pool cooling system fail. Also, operators fail to recovery using diesel fire pumps and offsite sources. Frequency of this condition is 3.864E-08 per year. Second worst condition, if control room alarm fail but operators can detect initiating event because other indications, therefore spent fuel pool cooling system was damaged. More, operators fail to recovery using diesel fire pumps and offsite sources. Frequency of second condition is 1.128E-09 per year. Third worst condition is pessimistic condition which all mitigating systems fail and frequency of this condition is 2.190E-10 per year.

For loss of offsite power initiating event, there are 2 fuel uncover condition from 7 sequences. First worst condition, Operator used the other electric line after initiating event occurred, but cooling system fail to restart and rerun. Moreover, operators fail to recovery using makeup system and offsite sources. Frequency of first condition is 8.044E-11 per year. Third worst condition is pessimistic condition and has frequency of 1.261E-09 per year.

Loss of inventory initiating event has 19 sequences that are 6 sequences are worst condition. The first worst condition, leakage is within normal makeup capacity and can be detected from control room alarm. Moreover, operators fail to initiate spent fuel pool makeup also operators fail to recovery using fire pumps and offsite sources. Frequency of this condition is 2.198E-09 per year. The second worst condition like as the first condition but Initiating event detected from the other indication. Frequency of second worst condition is 5.037E-12 per year. The third worst condition is identical with second condition but initiating event can't be detected because control room alarm and the other indication fail. Frequency of third worst condition is 6.045E-11 per

year. The fourth worst condition, leakage is more than normal makeup capacity, so the spent fuel pool cooling system has not effect. Initiating event can be detected from control room alarm, but operator fail to isolate leak and to initiate spent fuel pool makeup. More, operator fail to recovery using fire pumps and offsite sources. Frequency of this condition is  $2.388\text{E-}10$  per year. The fifth worst condition is identical with the fourth worst condition but initiating event can detected from the other indications. Frequency of the fifth worst condition is  $1.891\text{E-}10$  per year. The sixth worst condition is pessimistic condition and has frequency of  $3.450\text{E-}12$  per year.

The result indicate fuel uncover frequency of about  $10^{-8}$  per year. This value is sufficiently below the upper limit of interval estimation for safety target as defined by NUREG-1738 (about  $5\text{E-}07$  per year).

Reliability of the spent fuel pool system is high because the failure probability is about  $7.435\text{E-}04$  per year and this value becomes about  $2.794\text{E-}06$  per year if residual heat removal system is included for analysis. Therefore, RHR system can be considered in the accident management during decommissioning. On the other hand, the maintenance cost increases by keeping the RHR system during decommissioning.

The largest contribution to fuel uncover is fire initiating event. This is because the fire initiating event is not caused of the system failure. More, the fuel uncover probability is slightly different if RHR included because the largest contribution is from the fire initiating event, but the fuel uncover probability is caused the loss of cooling initiating event can be reduced by more than 50%.

To complete this analysis, evaluation for the thermal-hydraulic characteristic of the spent fuel storage in SFP of decommissioning plants should be done. This result is to determine the time available for plant operators to take actions to prevent a Zr fire. The focus was the time available before fuel uncover and the time available before the Zr ignites after fuel uncover. Based-on NUREG, some events for example operator recover or pump repair is limited for 85 hours (recovery effort is not effective if when than this time). This value is determined based on safety analysis of NPP in US.

## 5. Conclusion

The spent fuel pool of Fugen NPS is safe enough during decommissioning because of the fuel uncover probability is below the upper limit from safety target as NUREG defined ( $5\text{E-}07$  per year). Moreover, the spent fuel pool cooling system has high reliability.

## Acknowledgements

Author acknowledge to JNC (Japan Nuclear Cycle Development Institute) that gives opportunity to make a research with PSA topic for Fugen NPS. Also, author acknowledge to MEXT (Ministry of Education, Culture, Sport, Science and Technology) that gives financial support to follow Scientist Exchange program for this research.

## References

- [1] Y. Iguchi et al., Preparatory Activities of the Fugen Decommissioning Project, Decontamination, Decommissioning and Disposal – WANO TC Workshop Tokai 2002.
- [2] Development of Advanced Thermal Reactor Fugen, Vol. 1,2, JNC TN3410 99-003, Fugen NPS-Japan Nuclear Cycle Development Institute, 1999.
- [3] Technical Study of Spent Fuel Pool Accident Risk at Decommissioning Nuclear Power Plant, NUREG-1738, October 2000.
- [4] Fugen System and Living PSA Data, Fugen intranet : (<http://ftessn13.fugen.t-hq.jnc.go.jp:8010>)

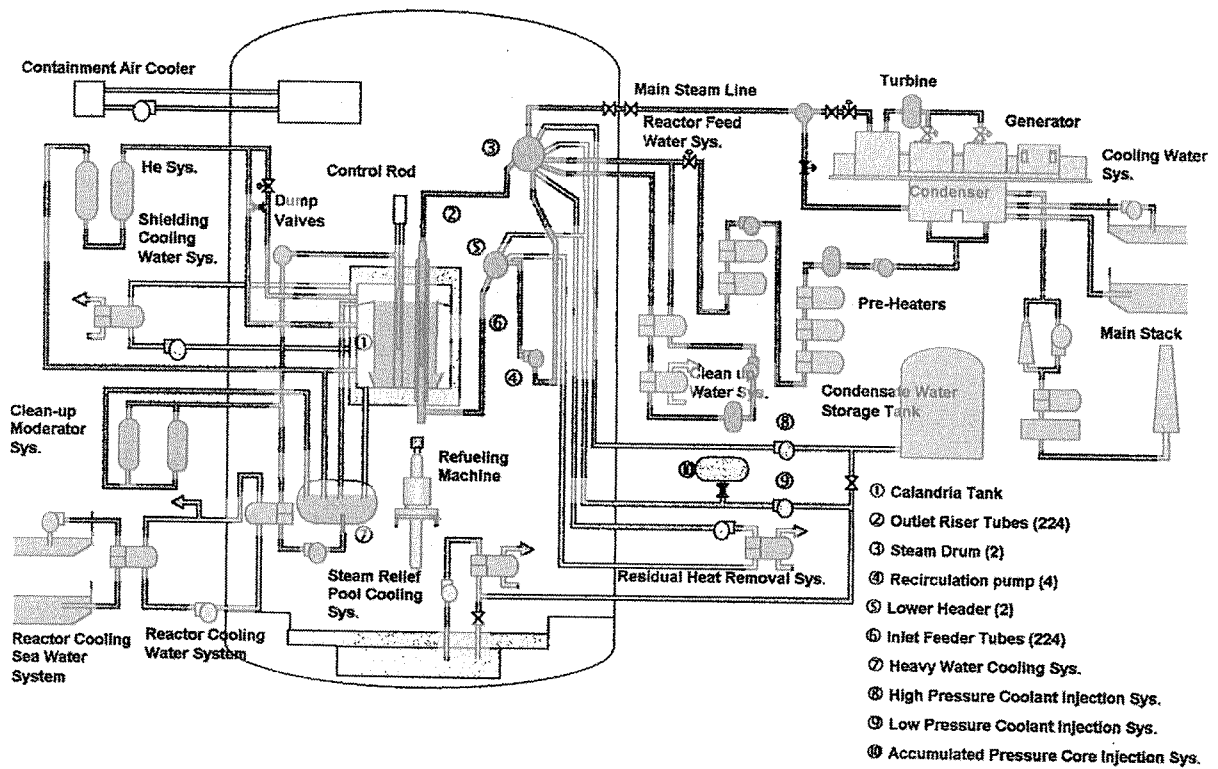


Figure 1. Layout of Fugen System

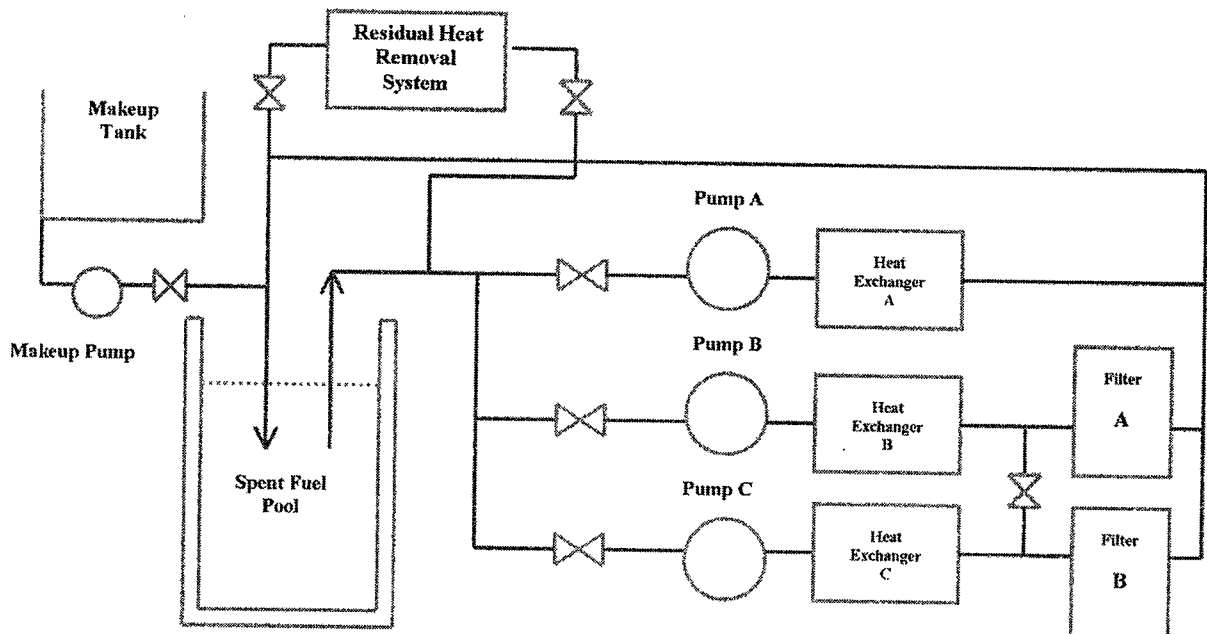


Figure 2. Block Diagram of Spent Fuel Pool Cooling System

Loss of Cooling	Control Room Alarms	Other Indications of Loss of Cooling	Operator Recovery of Cooling system	Operator Initiates Makeup Using Fire Pumps	Recovery Using Offsite Sources	#	SEQUENCE	END-STATE	FREQUENCY
IE-LOC	LOC-CRA	LOC-IND	LOC-OCS	LOC-OFD	LOC-OFB				
						1	LOC	OK	
						2	LOC*OCS	OK	
						3	LOC*OCS*OFD	OK	
						4	LOC*OCS*OFD*OFB	FUEL-UNCOVERY	1.534E-12
						5	LOC*OCS*OFD*OFB*OFB	OK	
						6	LOC*OCS*OFD*OFB*OFB*OFB	OK	
						7	LOC*OCS*OFD*OFB*OFB*OFB*OFB	OK	
						8	LOC*OCS*OFD*OFB*OFB*OFB*OFB*OFB	FUEL-UNCOVERY	3.331E-15
						9	LOC*OCS*OFD*OFB*OFB*OFB*OFB*OFB*OFB	OK	
						10	LOC*OCS*OFD*OFB*OFB*OFB*OFB*OFB*OFB*OFB	OK	
						11	LOC*OCS*OFD*OFB*OFB*OFB*OFB*OFB*OFB*OFB*OFB	FUEL-UNCOVERY	2.433E-19

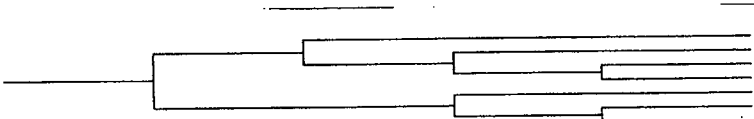
1LOSS-OF-COOLING - Loss of cooling for spent fuel storage pool

2002/04/04 Page 1

Fire Event in the Aux/Reactor Building	Control Room Alarms (Fire)	Other Indications of LSPC Due to Fire	SFPC System Survive	Operator Recovery Using Diesel Fire Pumps	Recovery Using Offsite Sources	#	SEQUENCE	END-STATE	FREQUENCY
IE-FIR	FIR-CRA	FIR-IND	FIR-OSP	FIR-OMK	FIR-OFD				
						1	FIR	OK	
						2	FIR*OSP	OK	
						3	FIR*OSP*OMK	OK	
						4	FIR*OSP*OMK*OFD	FUEL-UNCOVERY	3.864E-08
						5	FIR*OSP*OMK*OFD*OFB	OK	
						6	FIR*OSP*OMK*OFD*OFB*OFB	OK	
						7	FIR*OSP*OMK*OFD*OFB*OFB*OFB	FUEL-UNCOVERY	1.128E-09
						8	FIR*OSP*OMK*OFD*OFB*OFB*OFB*OFB	FUEL-UNCOVERY	2.190E-10

2FIRE-EVENT-IN-THE-A-R - Fire event in the auxiliary/reactor building

2002/04/04 Page 2

Loss of Offsite Power From Plant Centered and Grid	Offsite Power Recovery Prior to SFPC system loss	Cooling System Restart and Return	Operator Recovery Using Makeup system	Recovery from Offsite sources	#	SEQUENCE	END-STATE	FREQUENCY
IE-LOPA	LOPA-OPR	LOPA-OCS	LOPA-OMK	LOPA-OFD				
						1 LOPA 2 LOPA*OCS 3 LOPA*OCS*OMK 4 LOPA*OCS*OMK*OFD 5 LOPA*OPR 6 LOPA*OPR*OMK 7 LOPA*OPR*OMK*OFD	OK OK OK FUEL-UNCOVERY OK OK FUEL-UNCOVERY	8.04E-11     1.26E-09
LOSS-OF-OFFSITE-POWER - Loss of offsite power from plant centered and grid related								
2002/04/04 Page 3								

3LOSS-OF-OFFSITE-POWER - Loss of offsite power from plant centered and grid related

2002/04/04 Page 3

Loss of Coolant Inventory	Leak Within Normal Makeup Capacity	Control Room Alarms	Other Indications of Inventory Loss	Operator Isolates Leak and Initiates SFP Makeup	Operator Initiates SFP Makeup	Operator Initiates Makeup Using Fire Pumps	Recovery From Offsite Sources	#	SEQUENCE-NAMES	END-STATE-NAMES	FREQUENCY	
IE-LOI	LOI-NLL	LOI-CRA	LOI-IND	LOI-OIS	LOI-OIL	LOI-ONK	LOI-OFD					
									1	LOI	OK	
									2	LOI*OIS	OK	
									3	LOI*OIS*OMK	OK	
									4	LOI*OIS*OMK*OFD	FUEL-UNCOVERY	2.198E-09
									5	LOI*OIS*OMK*OFD*OFB	OK	
									6	LOI*OIS*OMK*OFD*OFB*OFB	OK	
									7	LOI*OIS*OMK*OFD*OFB*OFB*OFB	OK	
									8	LOI*OIS*OMK*OFD*OFB*OFB*OFB*OFB	FUEL-UNCOVERY	5.037E-12
									9	LOI*OIS*OMK*OFD*OFB*OFB*OFB*OFB*OFB	OK	
									10	LOI*OIS*OMK*OFD*OFB*OFB*OFB*OFB*OFB*OFB	OK	
									11	LOI*OIS*OMK*OFD*OFB*OFB*OFB*OFB*OFB*OFB*OFB	FUEL-UNCOVERY	6.045E-11
									12	LOI*NLL	OK	
									13	LOI*NLL*OIS	OK	
									14	LOI*NLL*OIS*OMK	OK	
									15	LOI*NLL*OIS*OMK*OFD	FUEL-UNCOVERY	2.388E-10
									16	LOI*NLL*OIS*OMK*OFD*OFB	OK	
									17	LOI*NLL*OIS*OMK*OFD*OFB*OFB	OK	
									18	LOI*NLL*OIS*OMK*OFD*OFB*OFB*OFB	FUEL-UNCOVERY	1.891E-10
									19	LOI*NLL*OIS*OMK*OFD*OFB*OFB*OFB*OFB	FUEL-UNCOVERY	3.450E-12

LOSS-OF-INVENTORY - Loss of Inventory in spent fuel pool

2002/04/05Page 4

4LOSS-OF-INVENTORY - Loss of Inventory in spent fuel pool

2002/04/05 Page 4

Figure 3. Event Tree for Spent Fuel Decommissioning of the Fugen NPS



### 3.28

#### Radiation Damage Calculation by NPRIM Computer Code with JENDL3.3

Satoshi SHIMAKAWA<sup>a,b</sup>, Naoto SEKIMURA<sup>b</sup> and Naoki NOJIRI<sup>a</sup>

<sup>a</sup> Department of HTTR Project, Japan Atomic Energy Research Institute,  
3607 Oarai-machi, Higashi-ibaraki-gun, Ibaraki-ken, 311-1394 Japan

E-mail: shim@oarai.jaeri.go.jp, nojiri@oarai.jaeri.go.jp

<sup>b</sup> Department of Quantum Engineering and Systems Science, University of Tokyo,  
7-3-1 Hongo, Bunkyo-ku, Tokyo, 113-8656 Japan

E-mail: sekimura@q.t.u-tokyo.ac.jp

The Neutron Damage Evaluation Group of the Atomic Energy Society of Japan starts an identification of neutron-induced radiation damage in materials for typical neutron fields. For this study, a computer code, NPRIM, has been developed to be free from a tedious computational effort, which has been devoted to the calculation of derived quantities such as dpa and helium production rate. Neutron cross sections concerning to damage reactions based on JENDL3.3 are given with 640-group-structure. The impact of cross sections based on JENDL3.3 to damage calculation results has been described in this paper.

#### 1. Introduction

Within the framework of the neutron damage evaluation group in the Atomic Energy Society of Japan a study is under way to evaluate neutron induced radiation damage under several neutron fields of power reactors, material testing reactors and future fusion reactors. Various types of neutron irradiation tests will be proposed and designed to solve materials issues and develop new materials using research and testing reactors. There is a strong requirement to have more reliable parameters for irradiation tests from materials research users; however, there is no convenient tool to provide guide for damage correlation between different neutron environments. A computer code NPRIM [1] has been developed to provide a convenient way to calculate damage parameters such as dpa. Several neutron spectra are prepared as typical neutron fields, such as the JMTR [2], HTTR [3], YAYOI [4], JOYO [5], HFIR [6], ATR [7] and DT fusion [8].

In this paper, the impact of cross sections based on JENDL3.3, JENDL3.2, JENDL3.1, ENDF/B-VI, ENDF/B-V and ENDF/B-IV, to damage calculation results has been described using NPRIM code.

#### 2. Specification of NPRIM

The NPRIM code, which can be obtained from the Internet site (<http://marie.q.t.u-tokyo.ac.jp/nprim/>), works with a graphical user interface (GUI) on PC platforms of Windows or Macintosh. Therefore, users do not need a lot of operation skills to use a workstation or mainframe computer. Calculation results of NPRIM code include energy-dependent and reaction-dependent dpa (displacement per atom), and gas productions, such as He appm (atomic parts per million of helium). The longstanding spectral indices, such as fast neutron fluence ( $E > 1.0$  or  $> 0.1$  MeV) and others, are also calculated. Cross section sets and sample neutron spectra are bundled in the code. To evaluate radiation damage, users are only required to specify a neutron spectrum with free energy structure.

Neutron spectrum input is allowed in free energy structure. The input energy structure is automatically transformed to 640 groups and the quantities concerning to neutron irradiation are calculated with the energy dependent cross sections. The output energy structure can be also selected from the bundled sets or a user defined structure.

### 3. Processing of neutron cross sections

Cross sections of damage energy production and helium gas production are generated from the nuclear data file of JENDL3.3 [9] by the nuclear processing code NJOY 99.32. In the NJOY code [10], point wise cross section is re-processed by the BROADR module to adopt a Doppler broadening effect. The HEATR module is used to calculate the cross sections of damage energy production and helium production. Robinson's numerical approximation to the Lindhard partition function is implemented in the HEATR module for displacement model. The GROUPE module is used to convert into a fine group structure (SAND-IIA: 640 group structure) with the weighting function of fission spectrum,  $1/E$  slow-down spectrum and Maxwellian thermal spectrum. The cross sections for the energy range from  $10^{-10}$  to 20 MeV are as the cross section sets in the NPRIM code.

A damage energy production cross section represents the probability that atoms are displaced from initial lattice positions by collisions initiated from a neutron of a specified energy. In the NPRIM calculation, the damage energy production cross section,  $\sigma_D$ , is converted to the dpa cross section,  $\sigma_{dpa}$ , as

$$\sigma_{dpa}(E) = \frac{0.8}{2Ed} \sigma_D(E) \quad (1)$$

where  $Ed$ , named displacement energy, is the threshold energy for knock-on atom displaced from its lattice position. The value of  $Ed$  in iron has been selected as 40eV. Four reaction types of damage energy production cross sections, the total, elastic scattering, inelastic scattering and disappearance, are stored into the cross section set. The disappearance reaction is represented as summation of  $(n,\gamma)$ ,  $(n,\alpha)$ ,  $(n,p)$  and other charged particle production cross sections.

The helium production cross section,  $\sigma_{He}$ , is generated from a total alpha production cross section (MT number=207 in the JENDL3.3) and also stored into the cross section set. Therefore,  $\sigma_{He}$  is a summation of the cross sections of  $(n,\alpha)$ ,  $(n,n\alpha)$ ,  $(n,2\alpha)$ ,  $(n,3\alpha)$  and other alpha production reaction, as follows.

$$\sigma_{He}(E) = \sigma_{n,\alpha}(E) + \sigma_{n,n\alpha}(E) + 2\sigma_{n,2\alpha}(E) + 3\sigma_{n,3\alpha}(E) + \dots \quad (2)$$

To compare the calculation results, other cross section sets such as the ASTM E693-94 [11], ENDF/B-V of the SPECTER [12], JENDL3.1 of the TENJIN [13], JENDL3.2 of the NPRIM and the new standard of ASTM E693-01 [14] based on ENDF/B-VI are also prepared.

### 4. Impact of cross sections

#### 4.1. dpa of iron

Trial dpa calculations for a pure iron under neutron irradiation in several reactors are performed with various cross section sets. Table 1 compares the calculated results by the NPRIM code for 100 effective full power days in fission reactors, at the irradiation holes in the HTTR, JMTR, JOYO, at the core region in the PWR and BWR, and at the first wall for the DT fusion reactor (design phase of ITER).

For all the listed reactors, the dpa values using JENDL3.3 (NPRIM code) are good agreement with those using ENDF/B-V (SPECTER code), ENDF/B-IV (ASTM Standard E693-94) and ENDF/B-VI (new ASTM Standard E693-01). The difference of dpa shows slight overestimation by about 0 – 3% in the fission reactors. The values based on JENDL3.3 show good agreement within 2% compared with those of ENDF/B-V in the fission reactors. In the DT fusion reactor, the difference shows slight underestimation by about 1 – 3%. The calculated dpa values based on JENDL3.3 code, ENDF/B-V and ENDF/B-VI show reasonable agreement within 3%. On the other hands, dpa based on the JENDL3.3 is about 0 – 4% overestimation compared with the JENDL3.2-based one. Fig. 1 shows differences between the JENDL3.3 and JENDL3.2 dpa cross sections for natural iron. The resonance parameters of iron in the JENDL3.3 have been modified from JENDL3.2. Therefore, the dpa discrepancy in the fission reactors is mainly caused by the values of elastic cross section in the energy range from 1.5 to 800 keV.

Table 1. Calculation results of iron dpa compared with other codes.

Library (Code or Standard)	HTTR hole	JMTR hole	JOYO hole	PWR* core	BWR* core	DT first wall
JENDL3.3 (NPRIM)	0.0433	2.35	11.0	0.128	0.126	10.2
JENDL3.2 (NPRIM)	0.0419	2.29	10.6	0.125	0.123	10.2
-----	-----	-----	-----	-----	-----	-----
ENDF/B-V (SPECTER)	0.0433	2.32	10.9	0.126	0.125	10.5
ENDF/B-IV (ASTM E693-94)	0.0428	2.31	10.7	0.126	0.125	10.4
ENDF/B-VI (ASTM E693-01)	0.0427	2.29	10.8	0.125	0.123	10.3

(unit in dpa; for 100 effective full power days)

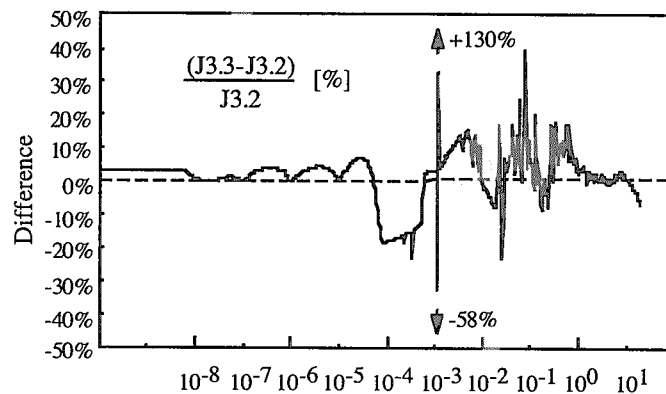
\* Normalized to  $1 \times 10^{17} \text{ m}^{-2} \text{ s}^{-1}$  ( $E > 1.0 \text{ MeV}$ )

Fig. 1. Differences between the JENDL3.3 and JENDL3.2 dpa cross sections for natural iron

#### 4.2. dpa rate and helium production rate of stainless steel

The dpa cross section for an austenitic stainless steel type 304 (304SS) is represented as atom-weighted summation of major elements. Chemical composition of the 304SS is assumed as iron of 71.8 wt-%, nickel of 9.3 wt-% and chromium of 18.9 wt-%, and other minor elements and impurities, such as C, Si, Mn, P, Cu, Nb, V, N, Co and B, are ignored in this calculation. Fig.2 shows dpa cross section of stainless steel type 304 using NPRIM code with JENDL3.3, comparing with one of natural iron using ASTM E693-94.

Table 2 shows the results of dpa rate (dpa/s) using JENDL3.3 for 304SS in several reactors, comparing with those using ENDF/B-V in the SPECTER code. The dpa rate using JENDL3.3 differs by -3% from those using ENDF/B-V. Especially, concerning to the dpa rates of the listed fission reactors, it is found that the values using JENDL3.3 show in excellent agreement with those using ENDF/B-V, within 0.6%.

Helium production rates in the 304SS are summarized in Table 2. With aging of power reactors, degradation of weldability caused by helium bubble formation on grain boundaries in austenitic steels has become one of the problems to maintain the irradiated structure materials [15]. Therefore, it is important to evaluate of helium production as accurate as possible. In Table 2, these values do not include the two-step helium productions through  $^{58}\text{Ni}(n,\gamma)^{59}\text{Ni}(n,\alpha)^{56}\text{Fe}$  reaction by low energy neutrons. The value of helium production rate using JENDL3.3 in the material testing reactors, i.e. the JMTR and JOYO, differs by about 10% from those using ENDF/B-V.

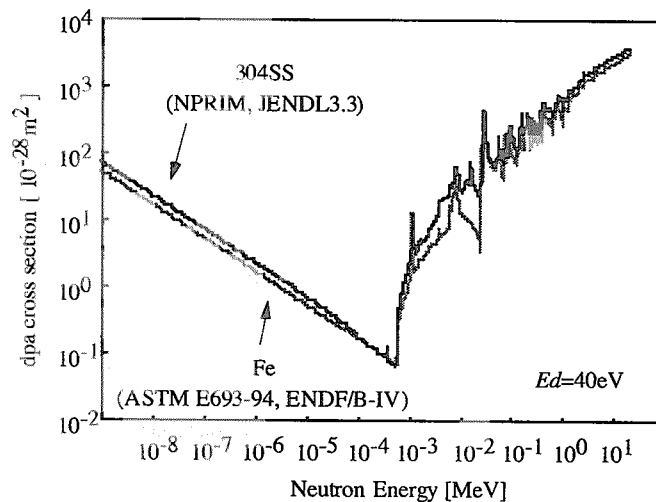


Fig. 2. dpa cross section for 304SS (JENDL3.3,NPRIM) and iron (ENDF/B-IV,ASTM)

Table 2. Calculation results of dpa and He production rate for 304SS in several reactors.

Library (Code)	HTTR hole	JMTR hole	JOYO hole	PWR* core	BWR* core	DT first wall
dpa rate (unit in $\times 10^{-7}$ dpa/s)						
JENDL3.3 (NPRIM)	0.0523	2.76	13.1	0.150	0.148	11.9
ENDF/B-V (SPECTER)	0.0527	2.76	13.0	0.150	0.148	12.2
<i>difference</i>	-0.6%	<0.1%	+0.4%	<0.1%	-0.1%	-3%
He production rate (unit in $\times 10^{-8}$ He appm/s)						
JENDL3.3 (NPRIM)	0.272	14.3	42.2	1.39	1.38	1320
ENDF/B-V (SPECTER)	0.283	13.2	38.1	1.38	1.36	1580
<i>difference</i>	-4%	+9%	+11%	+0.7%	+0.9%	-17%

\* Normalized to  $1 \times 10^{17} \text{ m}^{-2} \text{ s}^{-1}$  ( $E > 1.0 \text{ MeV}$ )

#### 4.3. Damage attenuation through pressure vessel of PWR and BWR.

The attenuations of dpa rate and helium production rate through the pressure vessel (RPV) of the PWR and BWR are calculated using the NPRIM code with the JENDL3.3. The chemical composition of the RPVs is assumed to 100% iron. To estimate the spectrum dependence of helium production, typical boron impurity level of 11 wt.ppm is also considered. The 99 group neutron spectra [16] are specified in the water, at 1/4 and 3/4 of RPV thickness, and in the cavity. The spectra at the 1/4 T and 3/4 T of the RPV are shown in Fig.3.

Figure 4 shows the calculated dpa rate attenuation. Two kinds of fast neutron flux, such as  $\phi_{0.1}$  of  $E > 0.1 \text{ MeV}$  and  $\phi_{1.0}$  of  $E > 1 \text{ MeV}$ , are also plotted in this figure. Significant differences are identified for the attenuation ratio of the  $\phi_{0.1}$ , compared with dpa rate in the RPV of PWR and BWR. It seems that the attenuation profiles of the  $\phi_{1.0}$  are similar to the dpa rate, however, the  $\phi_{1.0}$  attenuation ratios at 3/4 T of the RPV are about 56% and 79% of dpa rate in the PWR and BWR, respectively. The calculated helium production rate attenuations are shown in Fig.5. Contribution of two-step helium productions by  $^{58}\text{Ni}(n,\gamma)^{59}\text{Ni}(n,\alpha)^{56}\text{Fe}$  reaction is negligible compared with those from the direct productions of Fe, Ni and Cr, because of the low neutron flux at the RPV. The attenuation profiles of the helium production with  $^{10}\text{B}(n,\alpha)$  reaction are not similar to those without B. Note that the differences between the attenuation rates with and without boron are as almost ten times in the RPV.



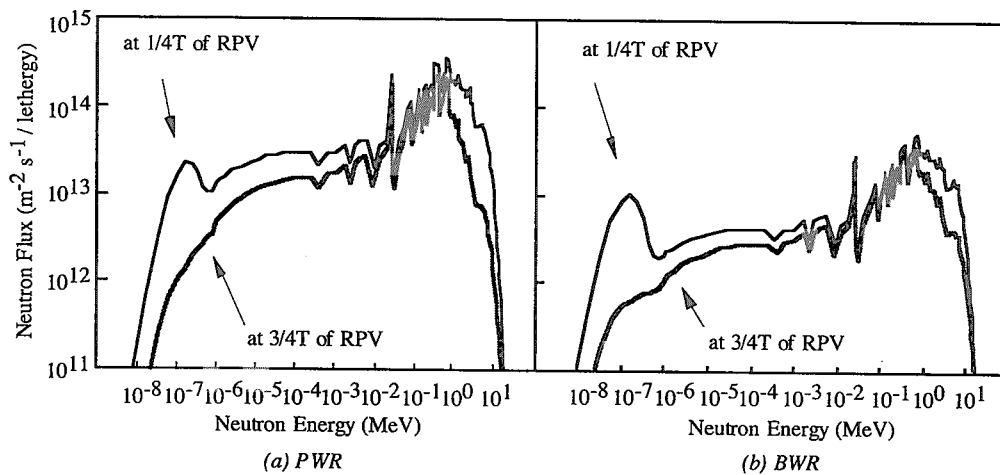


Fig. 3. Neutron Spectra in RPV of PWR and BWR

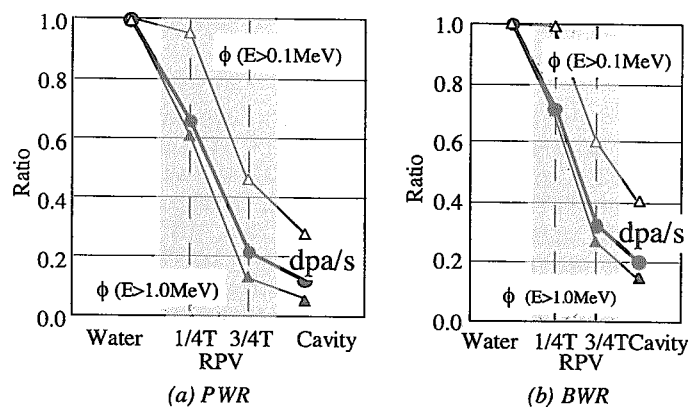


Fig. 4. Attenuation of neutron flux and dpa rate through RPV in PWR and BWR.

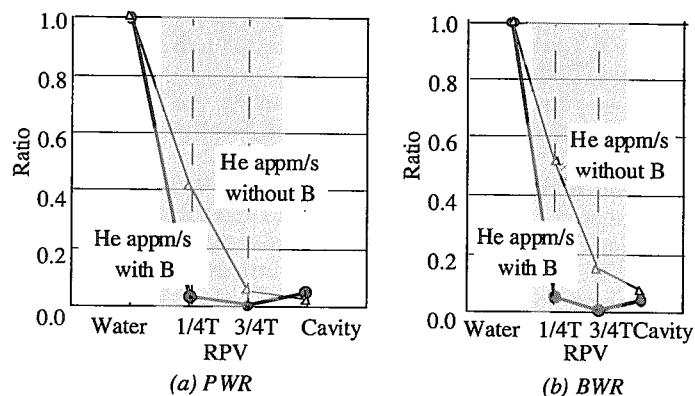


Fig. 5. Attenuation of Helium production rate through RPV in PWR and BWR.

Figure 6 shows the impact of cross sections on dpa rate determination through the RPV of the PWR and BWR. In this figure, the calculation results using JENDL3.2 shows good agreement, about 1% lower through the RPV, with one using ENDF/B-IV in the ASTM Standard E693-94. The dpa rate using JENDL3.3 in the NPRIM code, ENDF/B-V in the

SPECTER code and ENDF/B-VI in new ASTM Standard E693-01 are almost same, and each difference from one using ENDF/B-IV in the ASTM Standard E693-94 becomes larger at the outer position of the RPV. All results of dpa rate indicate good agreement within 6%.

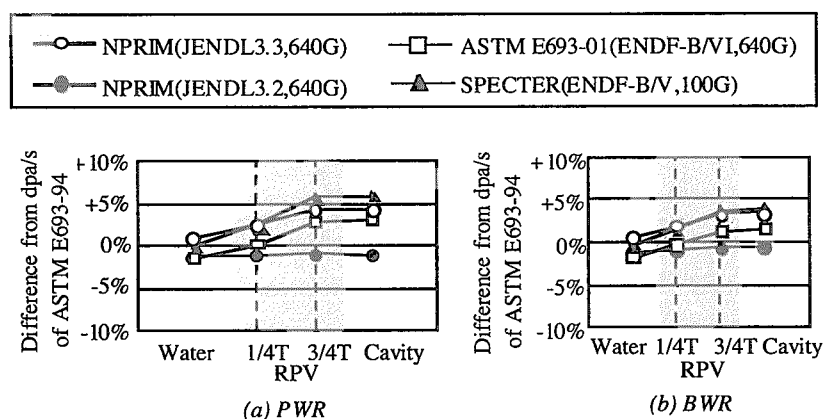


Fig. 6. Impact of cross sections on RPV dpa rate determination.

## 5. Summary

The comparison of the calculation results for iron dpa between the NPRIM code with neutron cross section set based on the JENDL3.3, ASTM Standard E693 based on ENDF/B-IV and SPECTER codes based on ENDF/B-V shows good agreement in six kinds of neutron fields of the HTTR, JMTR, JOYO, PWR, BWR and DT fusion. For neutron irradiation of austenitic stainless steel, no significant difference for dpa rates using JENDL3.3 indicates in comparing with those using ENDF/B-V for the six kinds of neutron fields. The results of dpa rate calculation through the RPV of the PWR and BWR using various cross section libraries, JENDL3.2, JENDL3.3, ENDF/B-V and ENDF/B-VI, indicate good agreement about 6% with one using ENDF/B-IV of ASTM E693-94.

## References

- [1] S. Shimakawa and N. Sekimura, J. Nucl. Mater. (2001) in printing
- [2] S. Shimakawa, ASTM STP 1398, (2000) 244
- [3] K. Yamashita, J. Nucl. Sci. Eng. 122, (1996) 212.
- [4] M. Nakazawa, T. Taniguchi, M. Kato, A. Sekiguchi, K. Kobayashi, K. Sakurai, and S. Suzuki, UTNL-R 0037 (1976)
- [5] T. Sekine, T. Aoyama, A. Yoshida and S. Suzuki. ASTM STP 1398, (2000) 268
- [6] K.R. Thoms and A.F. Rowcliffe, Journal of Neutron. Research Vol.2, No.2, (1994) 71.
- [7] J.W. Rogers and R.A. Anderl, INEL-95/0494 (1995)
- [8] S. Shimakawa et al., Fusion Eng. Des. 28 (1995) 215-219
- [9] JAERI Nuclear Data Center: "Japanese Evaluated Nuclear Data Library Version 3 Revision 3 (JENDL-3.3)", private communication (2002).
- [10] R. E. MacFarlane and D.W. Muir, LA-12740-M, (1994)
- [11] ASTM recommended practice E693-94, Annual Book of ASTM Standard, Part 45 (1994)
- [12] L.R. Greenwood and R.K. Smither, IAEA-TECDOC-263 (1985)
- [13] K. Sone and K. Shiraishi, JAERI-M 6358 (1975)
- [14] ASTM recommended practice E693-01, Annual Book of ASTM Standard, Part 45 (2001)
- [15] K. Asano, S. Nishimura, Y. Sato, H. Sakamoto, Y. Yamada, T. Kato and T. Hashimoto, J. Nucl. Mater. 264(1999) 1-9.
- [16] L.R. Greenwood, private communication (2002)



### 3.29 MCNP and MATXS Cross Section Libraries Based on JENDL-3.3

Kazuaki KOSAKO<sup>1</sup>, Chikara KONNO<sup>2</sup>, Tokio FUKAHORI<sup>2</sup> and Keiichi SHIBATA<sup>2</sup>

<sup>1</sup> *Sumitomo Atomic Energy Industries, Ltd.*

*2-10-14 Ryogoku, Sumida-ku, Tokyo 130-0026*

<sup>2</sup> *Japan Atomic Energy Research Institute*

*Tokai-mura, Naka-gun, Ibaraki-ken 319-1195*

e-mail: kosako@sae.co.jp

The continuous energy cross section library for the Monte Carlo transport code MCNP-4C, FSXLIB-J33, has been generated from the latest version of JENDL-3.3. The multigroup cross section library with the MATXS format, MATXS-J33, has been generated also from JENDL-3.3. Both libraries contain all nuclides in JENDL-3.3 and are processed at 300 K by the nuclear data processing system NJOY99.

#### 1. Introduction

The MCNP-4C code [1] is a recent three-dimensional Monte Carlo code which has been widely used over the world. The cross section data in evaluated nuclear data file are reproduced as precisely as possible in a continuous energy library of MCNP without any averaging of cross sections. The discrete ordinary codes have been used as convenient tool in the field of nuclear design and shielding. Their codes use the multigroup cross section library which needs the average and approximation.

As past continuous energy neutron cross section libraries for MCNP in Japan, FSXLIB-J3 [2] was produced from the Japanese Evaluated Nuclear Data Library Version 3 Revision 1 (JENDL-3.1) [3] in 1991. FSXLIB-J3R2 [4] was produced from JENDL-3.2 [5] in 1994. These libraries have been provided for public use.

JENDL-3 was re-evaluated to yield JENDL-3 Revision 3 (JENDL-3.3) [6], and JENDL-3.3 was released at May 2002. Therefore, the continuous energy cross section libraries for MCNP, FSXLIB-J33, has been produced based on it. The multigroup cross section library with the MATXS format [7], MATXS-J33, has been produced also. A MATXS library is converted to a macroscopic cross section of ANISN multigroup library by the TRANSX-2.15 code [8].

## 2. Modification of NJOY

The NJOY code [7] is a nuclear data processing system used as a standard code throughout the world. NJOY is a unique code to produce a continuous energy library for MCNP and a multigroup library with MATXS format.

The modified version of latest NJOY99.67 was used for processing of JENDL-3.3. The major modifications are as follows (square brackets represent the name of corresponding module in NJOY).

- (1) The nuclides with discontinuous MT in gamma-ray production data are Nb-93 (MT=51), Hg-199 (MT=57) and Pb-207 (MT=53). The energy levels of discontinuous MT were added within code. [HEATR, ACER, GROUPR]
- (2) The energy distribution data (MF=5) has the unit base interpolation (linear-linear of INT=22). The unit base interpolation was allowed in only GROUPR module. [GROUPR]
- (3) The incomplete treatment of input/output part for MF=32 (covariance of resonance parameters) was modified. [MODER]
- (4) Minimum energy for processing unresolved resonance parameters was modified 10 eV to 1 eV, for Pm-148m. [RECONR, UNRESR, PURR]
- (5) The KERMA factors of some nuclides that aren't kept the energy balance in evaluation are negative or large values. The KERMA factors of their nuclides aren't calculated with the energy balance method and then they are done with the kinematics method. [HEATR]
- (6) If probability at an incident energy in LAW=7 angle-energy distribution is zero, the temporary normalization factor is 1 for avoiding division by zero. [ACER]

There is an incomplete modification for the 'rkal' and 'akal' variables in subroutine acelcp (ACER). These variables are rarely undefined variables in the heating calculation of charged particle on MF=6/LAW=1/LANG=2. In this case these are initialized to zero as a tentative measure.

## 3. Production of FSXLIB-J33 and MATXS-J33

First, JENDL-3.3 was processed by the modified NJOY99.67 to produce ACE type cross section data [7] for each nuclide. The ACE type data were compiled into the FSXLIB-J33 library by an exclusive program. FSXLIB-J33 is a library for MCNP-4C as follows: 1) contains a probability distribution table (ptable) as cross section data in unresolved resonance energy region, 2) uses a new format of cumulative angular distribution table (MF=6/LAW=1/LANG=1) by 'newfor=1' input option in NJOY.

The processing parameters for NJOY to process FSXLIB-J33 are shown in Table 1. The precision of 0.1 % was adopted for the numerical processing by expansion of calculation resource. The temperature considered in Doppler broadening is 300 K. The nuclides used kinematics method for KERMA factor are S-33, 34, 36, Ca-42, 46, 48, Ti-47, Mo-92, 94, 95,

96, 97, 98, 100, Eu-151, 153, Hf-174, 176, 177, 178, 179, 180, Ta-181, W-182, 183, 184, 186, Pb-206, 207, 208, Bi-209. The number of resonance ladders is 1000 and the background cross sections for ptable are  $10^{10}$ ,  $10^4$ ,  $10^3$ , 300, 100, 30, 10, 1, 0.1,  $10^{-5}$ . It contains all 337 nuclides in JENDL-3.3. The evaluation identifications in ZAID used to identify nuclide are 42 for elements and isotopes in the ground state and 43 for isotopes in the isomeric states. The data size is about 965 Mbytes in the MCNP type-1 format.

Second, JENDL-3.3 was processed by that to produce MATXS-J33 cross section data for each nuclide. The self-shielding factor is calculated by the PURR module. The photon interaction cross section file for photon transport calculation was the EPDL97 [9]. The processing parameters for NJOY are shown in Table 2. The energy group structure was adopted typical of VITAMIN-J. The basic processing condition is same as FSXLIB-J33. The name of MATXS-J33 data file for each nuclide is "symbol of element", "3 digits of mass number" and ".m" (for example, fe056.m). The total data size of 337 nuclides is about 592 Mbytes in text format. It is note that MATXS-J33 is inadequate for a critical calculation.

#### 4. Plan of Verification

It is inevitable to verify the consistency of FSXLIB-J33 with the original JENDL-3.3 data. Verification of FSXLIB-J33 has been planed by using the MACROS code [4] with both direct comparison of numerical data between JENDL-3.3 and FSXLIB-J33 and visual checking of cross section data plots.

In order to demonstrate reliability of FSXLIB-J33 and MATXS-J33, benchmark calculations are going to carry out for several integral experiments. A test calculation of FXLIB-J33 for MCNP-4C was made of aluminum sphere with radius 50 cm having point source of 15 MeV neutron at center. Figure 1 is comparison of leakage neutron spectra from sphere. FSXLIB-J33 and FSXLIB-J3R2 finely agree.

#### References

- [1] Briesmeister J.F. (Ed.): "MCNP<sup>TM</sup> – A General Monte Carlo N-Particle Transport Code, Version 4C", LA-13709-M (2000).
- [2] Kosako K., et al.: "FSXLIB-J3: MCNP Continuous Cross Section Library Based on JENDL-3", Proc. New Horizons in Radiation Protection and Shielding, Pasco, Washington, April 26 – May 1, 1992, pp. 357-363 (1992).
- [3] Shibata K., et al.: "JENDL-3: Japanese Evaluated Nuclear Data Library, Version-3", JAERI-1319 (1990).
- [4] Kosako K., et al.: "FSXLIB-J3R2: A Continuous Energy Cross Section Library for MCNP Based on JENDL-3.2", JAERI-Data/Code 94-020 (1994).
- [5] Nakagawa T., et al.: "Japanese Evaluated Nuclear Data Library Version 3 Revision-2:

- JENDL-3.2”, J. Nucl. Sci. Technol., 32, 1259 (1995).
- [6] Shibata K., et al.: “Japanese Evaluated Nuclear Data Library Version 3 Revision-3: JENDL-3.3”, J. Nucl. Sci. Technol., 39, 1125 (2002).
- [7] MacFarlane R.E. and Muir D.W.: “The NJOY Nuclear Data Processing System Version 91”, LA-12740-M (1994).
- [8] MacFarlane R.E.: “TRANSX 2: A Code for Interfacing MATXS Cross-Section Libraries to Nuclear Transport Codes”, LA-12312-MS (1992).
- [9] Cullen D.E., et al.: “EPDL97: The Evaluated Photon Data Library, '97 Version”, UCRL-50400, Vol. 6, Rev. 5 (1997)

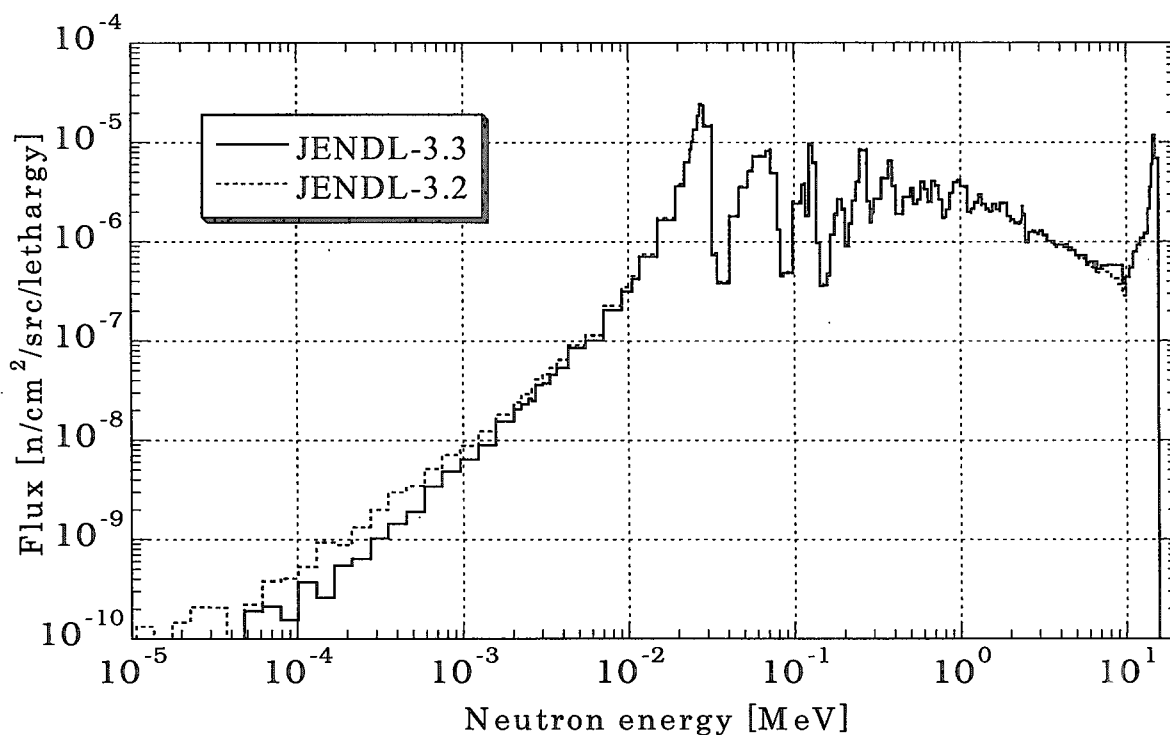


Fig.1 Leakage neutron spectra from Aluminium sphere  
(radius 50 cm; 15 MeV neutron source at center)

Table 1 Processing parameters for NJOY99.67 to produce FSXLIB-J33.

Processing Parameter	Adopted Data
precision of point-wise cross sections	0.1 %
temperature of cross sections	300 K ( $2.53 \times 10^{-8}$ MeV)
upper-limit energy of thermal energy region	4.6 eV
inelastic option of thermal energy region	free gas model
type of gamma-ray production data	detail form
number of equal-probability angular cosine bins	32
probability table of unresolved resonance	with ptable (length=20)
newfor option	1 (LAW61 format)
calculational method of KERMA	energy balance method
evaluation identification in ZAID	42 for ground state isotopes 43 for isomeric state isotopes

Table 2 Processing parameters for NJOY99.67 to produce MATXS-J33.

Processing Parameter	Adopted Data
precision of point-wise cross sections	0.1 %
group structure	VITAMIN-J (neutron 175g, photon 42g)
order of Legendre coefficients	P-6
temperature of cross sections	300 K ( $2.53 \times 10^{-8}$ MeV)
upper-limit energy of thermal energy region	4.6 eV
inelastic option of thermal energy region	free gas model
background cross sections of self-shielding factors	$\sigma_0 = 10^{10}, 10^4, 10^3, 300, 100, 30, 10, 1, 0.1, 10^{-5}$
calculation method of KERMA	energy balance method
storage data	damage (MT=444), $\mu$ (251), $\chi$ (252), $\gamma$ (253), $1/v$ (259)



### 3.30 JOYO MK-II Core Characteristics Database

#### - Upgrade to JENDL-3.2 -

Yasushi OHKAWACHI, Shigetaka MAEDA and Takashi SEKINE  
*Experimental Reactor Division, Irradiation Center, O-arai Engineering Center*  
*Japan Nuclear Cycle Development Institute*  
 4002 Narita, O-arai, Ibaraki 311-1393 JAPAN  
 e-mail : okawachi@oec.jnc.go.jp

#### ABSTRACT

The JOYO core characteristics database, which was published in 1998, was revised based on requests and comments from users. The revisions included changes of group constant set, addition of reactor kinetic parameters and experimental data of the MK-II core start-up test, etc..

#### 1. Introduction

The experimental fast reactor JOYO at O-arai Engineering Center of Japan Nuclear Cycle Development Institute was operated as the MK-II irradiation core for testing fuel and material for FBR development from March 1983 to June 2000.

Through the MK-II operation, extensive data were accumulated on core management calculations and core characteristics tests. These data of thirty-one duty cycle operations and thirteen special test operations were compiled into a database which were recorded on CD-ROM and the first edition<sup>1)</sup> was published in 1998.

This database was widely used for the verification of nuclear calculations and analysis of post irradiation examinations. After that, there were many requests such as the renewal of the group constant set and the addition of reactor kinetic parameters, etc. from many users. The database was then revised in response to these requests.

#### 2. Operating History of JOYO MK-II Core

The operating history of the MK-II core is shown in Fig.1. In 1982, the MK-I breeder core was replaced by the MK-II irradiation core. The MK-II core attained initial criticality on 22nd November 1982, and it achieved a power level of 100MWt in 1983. Thirty-five duty cycle operations and

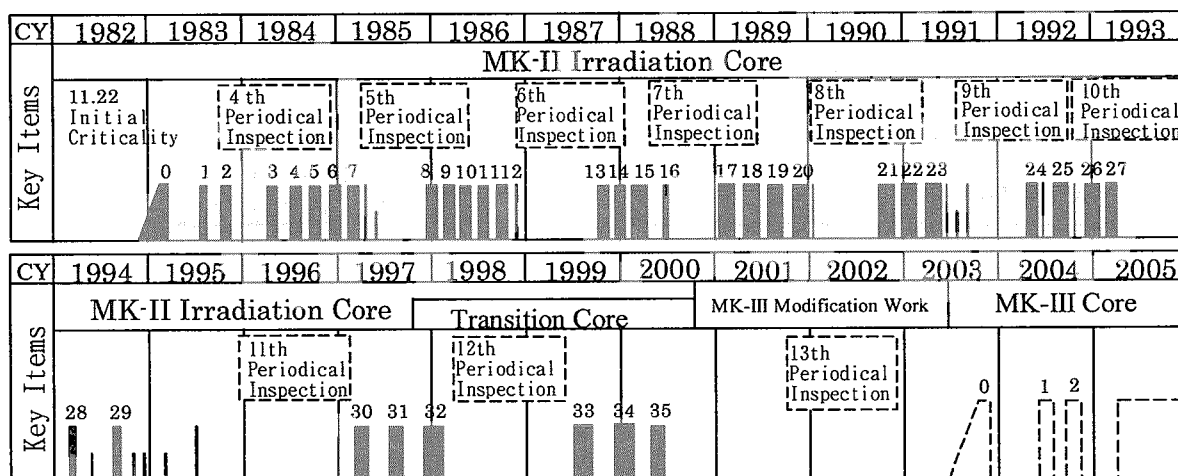


Fig.1 Operating History of JOYO MK-II Core



thirteen special tests were conducted using the MK-II core by June 2000. The thirty-second to thirty-fifth duty cycles were operated as the MK-III transition core, and the fuel region was gradually extended.

The MK-II core and the MK-III transition core were operated in total for 47,757 hours and the integrated power generation was 4,388GWh. During these operations, 362 driver fuel subassemblies and 69 irradiation test subassemblies were irradiated. A pellet peak burn-up of the driver fuel subassembly attained approximately 85GWd/t.

JOYO is currently being upgraded to the MK-III high performance irradiation core,<sup>2), 3), 4)</sup> which will achieve its initial criticality in July 2003.

### 3. Specifications of MK-II Core

JOYO is a sodium cooled fast reactor with mixed oxide (MOX) fuel. The main core parameters of the MK-II core are shown in Table 1, with that of the MK-III core.

The plutonium content of the fuel subassembly was about 30wt%. At the beginning of the MK-II core operation, <sup>235</sup>U enrichment was about 12wt%(J1 fuel), and it was later increased to 18wt%(J2 fuel) to provide enough excess reactivity so that the core burn-up was increased. Consequently, the operational period was extended from 45 days to 70 days.

In the MK-III core, the number of fuel subassemblies and neutron fluence will be increased in comparison with the MK-II core. The fuel region will be divided into inner and outer regions to flatten the neutron flux distribution.

Table 1 Main Core Parameters of JOYO

	MK-II	MK-III
Reactor Power (MWt)	100	140
Inlet / Outlet Temperature (°C)	370/500	350/500
Core Height (cm)	55	50
Core Volume (liter)	230	260
Max. Number of Fuel Subassemblies	67	85
Fuel Type	MOX (UO <sub>2</sub> -PuO <sub>2</sub> )	
Pu Content (wt%)	30	23/30 *
<sup>235</sup> U Enrichment (wt%)	12 (J1) 18 (J2)	18
Max. Fast Neutron Flux ( $E \geq 0.1\text{MeV}$ ) ( $\times 10^{15}\text{n/cm}^2\cdot\text{s}$ )	3.2	4.0
Max. Total Neutron Flux ( $\times 10^{15}\text{n/cm}^2\cdot\text{s}$ )	4.9	5.7
Max. Excess Reactivity (at 100°C) (% $\Delta k/k'$ )	5.5	4.5
Max. Linear Heat Rate (W/cm)	400	420
Max. Burn-up (Pin Average) (MWd/t)	50,000(J1) 75,000(J2)	90,000
Operation Period (days/cycle)	45 (J1) 70 (J2)	60

\*:inner/outer core

### 4. JOYO MK-II Core Management Code System "MAGI"

The "MAGI" calculation code system was developed to predict the reactor parameters required for the core and fuel management of the MK-II core. The calculation flow of MAGI is shown in Fig.2. MAGI is a neutronic and thermo-hydraulic coupling code system that calculates the effective multiplication factor, neutron and gamma flux, power distribution, fuel burn-up, linear heat rate, coolant flow rate, coolant and fuel temperature, etc..

MAGI is based on the diffusion theory with seven neutron energy groups for the neutronic calculation. The cross section is collapsed from the 70 group JFS-3-J3.2R constant set based on JENDL-3.2<sup>3)</sup>. The core configuration is modeled in three-dimensional hexagonal-Z geometry for each operational cycle. The actual reactor power history, which is accumulated using the JOYO data acquisition system, is used in the burn-up calculation based on the matrix exponential method.

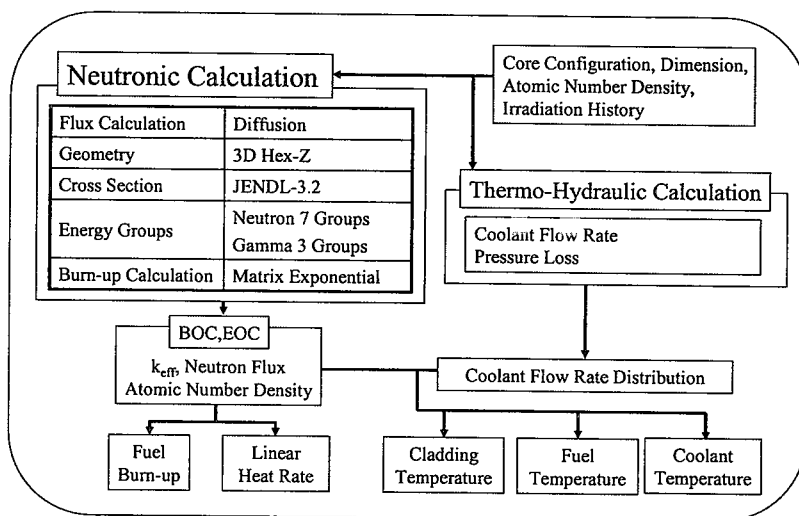


Fig. 2 JOYO MK-II Core Management Code System

In the thermo-hydraulic calculation of MAGI, the coolant flow rate distribution, and the maximum temperature of coolant, cladding and fuel are calculated. These calculation results are compiled in the CD-ROM.

### 5. Core Physics Tests in Each Operational Cycle

The excess reactivity in a zero power critical condition at approximately 250 °C was measured at the reactor start-up of each operational cycle.

JOYO has six control rods containing enriched B<sub>4</sub>C. Every control rod's worth was calibrated with either the positive period method or the inverse kinetics method during the low power test of each operational cycle.

The isothermal reactivity coefficients were measured by taking the difference of reactivity at approximately 250 °C and 370 °C in a zero power critical condition. The measured isothermal reactivity coefficients were constant through the MK-II operation because they were determined mainly by radial expansion of the core support plate, which is independent of burn-up. However, when the core region was gradually extended from the 32<sup>nd</sup> cycle, the isothermal reactivity coefficients were decreased as predicted with the mechanism of the core support plate expansion. The measured isothermal reactivity coefficient is shown in Fig.3.

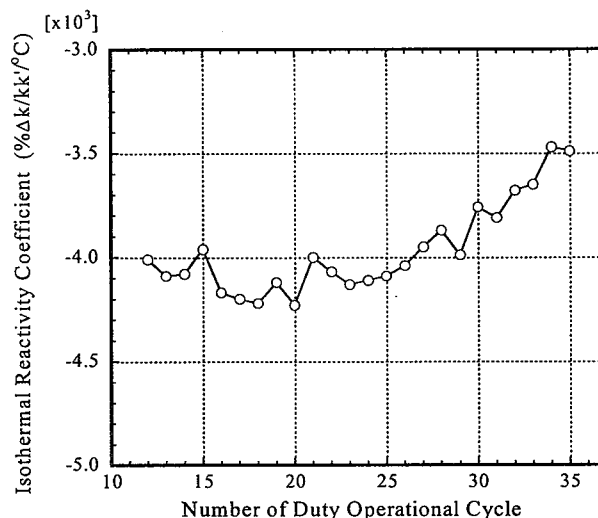


Fig.3 Measured Isothermal Reactivity Coefficient

The power reactivity coefficients were measured at the reactor power increasing and decreasing in each operational cycle. The measured power reactivity coefficients decreased with increasing core burn-up. It was observed that the fuel thermal expansion, which is the major component of the power reactivity coefficient of JOYO, decreases at high burn-up due to fuel restructuring during the irradiation. It was also observed that the power reactivity coefficients varied depending on the reactor power. This phenomenon appeared to be due to a combination of the core bowing effect, fuel thermal expansion and Doppler effects. These causes need further investigation.

The burn-up reactivity coefficients were determined by measuring the reactivity change during rated power operation. Measured values were compared with the MAGI burn-up calculation and both agreed within 5%. It is considered that the decrease of atomic number densities of major fissile nuclides as <sup>235</sup>U and <sup>239</sup>Pu are the dominant factor of burn-up reactivity coefficients because of JOYO's small core size, which results in a hard neutron spectrum and a small internal conversion ratio. Therefore, the burn-up reactivity coefficients can be predicted accurately even at a high burn-up.

### 6. Structure of Database

The MK-II core management data and core characteristics data were recorded on CD-ROM for the convenience of users. The structure of the database, which is shown in Fig.4, is the same as the first edition.

The core management data calculated using MAGI are compiled in text style. The "Configuration Data" includes the core arrangement and refueling record for each operational cycle. The "Subassembly Composition Data" includes the calculation results of MAGI, including atomic number density, neutron fluence, fuel burn-up, integral power of 362 fuel subassemblies and 69 irradiation test subassemblies. The "Irradiation Condition Data" contains the calculated neutron flux, gamma flux, power density, linear heat rate, coolant and fuel temperature distribution of all the fuel subassemblies at the beginning and end of each operational cycle(BOC,EOC). The "Reactor Kinetic Parameter Data" includes effective delayed neutron fraction, decay constant, and prompt neutron

lifetime of each operational cycle.

The "Core Physics Test Data" includes the excess reactivity, control rod worth calibration curve, and reactivity coefficients of temperature, power and burn-up, which were measured in each operational cycle.

Users can edit these core management data with personal computers and analyze the core characteristics of the MK-II core, by forwarding these data to engineering workstations or super computers. By comparing the calculated core characteristics results with the measured values, users will be able to use the estimated results for the core design and the analytical development of the core characteristics.

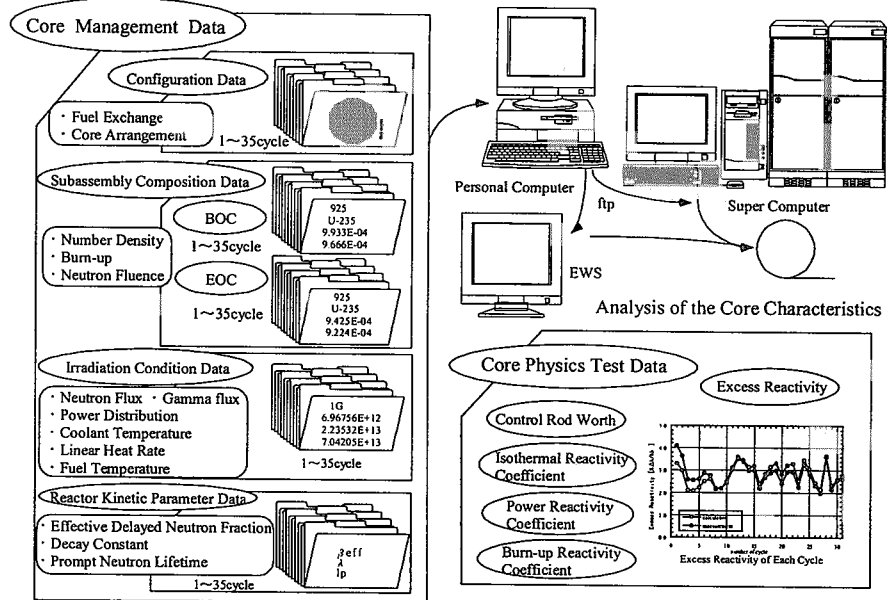


Fig. 4 Structure of JOYO MK-II Core Characteristics Database

## 7. Revised Point

The revisions include changes to the MAGI calculation code system to use the 70 group JFS-3-J3.2R constant set processed from the JENDL-3.2 library. The core characteristics obtained from the 32<sup>nd</sup> to 35<sup>th</sup> operational cycles, which were conducted as the MK-III transition core, were added in this revised edition. Total control rod worth, reactor kinetic parameters and the MK-II core performance test results were included according to users' requests.

### 7.1 Reactor Kinetic Parameter

The effective delayed neutron fraction of each operational cycle is shown in Table 2. Each reactor kinetic parameter was calculated using equation (1) by MAGI.  $\beta$  and  $\chi_d$  evaluated by Tomlinson<sup>6)</sup> were used for the calculations.

$$\beta_{\text{eff}}(i) = \sum_k \frac{\int dr \sum_{g'} \chi_d(i, k, g') \cdot \phi^*(g') \sum_g v \sigma_f(g, k) \cdot N(k) \cdot \phi(g) \cdot \beta(i, k)}{\int dr \sum_{g'} \chi_p(g') \cdot \phi^*(g') \sum_g v \sigma_f(g, k) \cdot N(k) \cdot \phi(g)} \quad (1)$$

$\beta(i, k)$ : delayed neutron fraction

$\chi_d(i, k, g')$ : fission spectrum of delayed neutron

$\chi_p(g')$ : fission spectrum of prompt neutron

$v$ : number of neutrons produced per fission (n)

$\sigma_f(g, k)$ : microscopic fission cross-section (cm<sup>2</sup>)

$N(k)$ : atomic number density (atoms/cm<sup>3</sup>)

$\phi(g)$ : neutron flux (n/cm<sup>2</sup>·s)

$\phi^*(g')$ : adjoint flux

$i$ : delayed neutron precursor group

$k$ : nuclide

$g, g'$ : neutron energy group

Table 2 Effective Delayed Neutron Fraction of Each Operational Cycle

cycle No.	$\beta_1$	$\beta_2$	$\beta_3$	$\beta_4$	$\beta_5$	$\beta_6$	$\beta_{eff}$
0	1.159E-04	8.095E-04	7.108E-04	1.399E-03	5.436E-04	1.562E-04	3.735E-03
1	1.168E-04	8.549E-04	7.477E-04	1.475E-03	5.879E-04	1.659E-04	3.948E-03
2	1.165E-04	8.535E-04	7.464E-04	1.473E-03	5.873E-04	1.658E-04	3.942E-03
...	...	...	...	...	...	...	...
33	1.265E-04	9.206E-04	8.037E-04	1.630E-03	6.391E-04	1.659E-04	4.286E-03
34	1.257E-04	9.165E-04	7.999E-04	1.623E-03	6.365E-04	1.650E-04	4.266E-03
35	1.253E-04	9.152E-04	7.987E-04	1.620E-03	6.365E-04	1.650E-04	4.261E-03

## 7.2 Upgrade to JENDL-3.2

In this revision, the group constant set was changed from JENDL-2<sup>7)</sup> to JENDL-3.2. The effect on the calculation results by changing of the group constant set was examined.

Table 3 shows the burn-up calculation results of a driver fuel subassembly. It was originally irradiated at the core center and it was later moved to the 2<sup>nd</sup> row and irradiation was continued until the pin averaged burn-up reached approximately 62GWd/t. The burn-up calculation was conducted using the matrix exponential method. One group cross-section, which was collapsed from the seven group cross section using the calculated neutron flux at each mesh, was used for the burn-up calculation. The calculation results of main nuclides based on JENDL-3.2 are almost the same as JENDL-2.

Table 3 Comparison of Atomic Number Density  
(unit:  $\times 10^{24}$  atoms/cm<sup>3</sup>)

Library	<sup>235</sup> U	<sup>238</sup> U	<sup>239</sup> Pu	<sup>240</sup> Pu	<sup>241</sup> Pu	<sup>242</sup> Pu
JENDL-3.2	9.06E-04	4.95E-03	1.29E-03	5.43E-04	1.16E-04	8.50E-05
JENDL-2	8.98E-04	4.94E-03	1.29E-03	5.49E-04	1.15E-04	8.55E-05
J3.2/J2	1.01	1.00	1.00	0.99	1.01	0.99

Figure 5 shows the calculated excess reactivity at the beginning of each cycle. By the loading of irradiation test subassemblies, the number of the replaced fuel subassemblies and operation plans, the excess reactivity changed from approximately 1.5 to 4.0% $\Delta k/k$ '. The calculated results using JENDL-3.2 are about 0.45% $\Delta k/k$ ' lower than the results using JENDL-2. It is because  $\nu\sigma_f$  of <sup>235</sup>U and <sup>239</sup>Pu evaluated in JENDL-3.2 are smaller than that of JENDL-2. A similar tendency was shown in the criticality analysis of JUPITER experiment.

Table 4 shows the calculation results of the total neutron flux, fuel power, radial and axial peaking factor, which were calculated using JENDL-3.2 and JENDL-2. The transport cross-sections of uranium, plutonium and sodium of JENDL-3.2 are smaller than that of JENDL-2. Therefore, diffusion coefficients for the fuel region were increased. As a result, fuel power in the core center region decreased and the radial peaking factor decreased by about 3%.

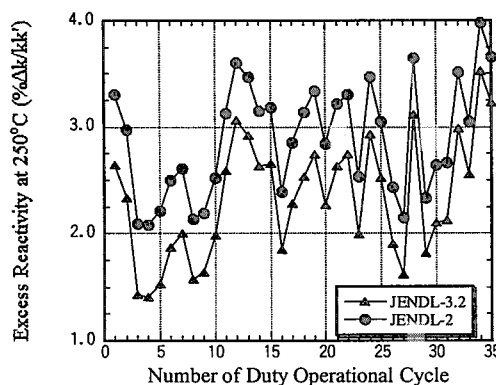


Fig. 5 Calculated Excess Reactivity of Each Operational Cycle

Table 4 Comparison of Calculated Results

Items		JENDL-2	JENDL-3.2	J3.2/J2
Total Neutron Flux (n/cm <sup>2</sup> ·s)*	BOC	4.00E+15	3.99E+15	0.999
	EOC	4.03E+15	4.03E+15	0.999
Fuel Power* (MW / S/A)	BOC	2.15	2.12	0.983
	EOC	2.13	2.09	0.983
Radial Peaking Factor	BOC	1.451	1.405	0.968
	EOC	1.434	1.396	0.974
Axial Peaking Factor	BOC	1.199	1.195	0.997
	EOC	1.190	1.186	0.997

\* Core Center

## 8. Conclusion

The JOYO MK-II core characteristics database was revised in response to the requests from the users. In the revised version, the group constant set was changed from JFS-3-J2 based on JENDL-2 to JFS-3-J3.2R based on JENDL-3.2, and the following data were added: reactor kinetic parameter, MK-II core start-up test results(0 cycle), core characteristics data from the 32<sup>nd</sup> to 35<sup>th</sup> cycles and total

control rod worth.

The effect of updating the group constant set was observed as follows: The calculation results of excess reactivity decreased by about  $0.45\% \Delta k/k$ , radial peaking factor was reduced by about 3%, and fuel composition change of the main nuclides due to burn-up was negligible.

The core characteristics data of JOYO are very valuable data. This database is anticipated to be used in the various fields for, e.g., verification of the nuclear data and nuclear calculation codes. Application of JOYO MK-II database is shown in Fig.6.

The MK-III high performance irradiation core will achieve initial criticality in July 2003. In order to confirm the core characteristics from low power to rated power, core performance tests will be conducted. The power and neutron flux distribution will be measured in detail using about 90 dosimeter sets.

To improve the neutronic calculation accuracy in the MK-III core, the upgraded core management code system "HESTIA" is applied. Three-dimensional triangle-Z model is used in HESTIA to increase the

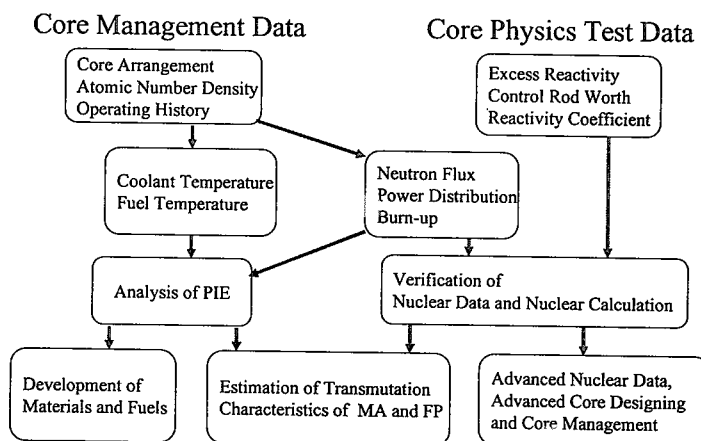


Fig. 6 Application of JOYO MK-II Core Characteristics Database

calculation points. In the horizontal cross section, one hexagonal core subassembly is divided into 24 meshes. In the vertical direction, the fuel region (50cm) is divided into 20 meshes. Eighteen neutron energy groups are adopted to improve the calculation accuracy of the neutron spectrum. Through these upgrades of the core management code system, neutron flux within the driver fuel and irradiation test subassemblies can be calculated in detail.

The calculated and measured results of the MK-III core will be published as the JOYO MK-III core characterization database.

### Acknowledgements

The authors would like to note the contribution of H.Nagasaki of Nuclear Energy System Inc. for collecting and arranging measured core physics test data, and T.Ito of Information Technologies Japan Inc. for the core management calculation using "MAGI".

### References

- 1) S. Tabuchi and T. Aoyama, "Development of JOYO MK-II Core Characteristics Database," *Proc. Symp. on Nuclear Data*, Ibaraki, Japan, Nov. 18-19, 1999, p.149-153 (2000).
- 2) S. Suzuki *et al.*, "Upgrading Program of Experimental Fast Reactor JOYO -The MK-III Program-," *Proc. of 10th Pacific Basin Nuclear Conference*, Kobe, Japan, Vol.1, p.759-768 (1996).
- 3) T. Sekine *et al.*, "Upgrade of irradiation test capability of the experimental fast reactor JOYO," *Proc. of 11th International Symposium on Reactor Dosimetry*, Belgium, Aug. 18-23, 2002, to be published.
- 4) S. Miyakawa *et al.*, "The Fruits and Hope of the Experimental Fast Reactor "JOYO", " *Proc. of The 13th Pacific Basin Nuclear Conference*, Shenzhen, China, Oct. 21-25, 2002.
- 5) T. Nakagawa *et al.*, "Japanese Evaluated Nuclear Data Library Version 3 Revision-2: JENDL-3.2," *J. Nucl. Sci. Technol.*, 32[12], 1259 (1995).
- 6) L. Tomlinson, "Delayed Neutrons from Fission a Compilation and Evaluation of Experimental Data", *AERE-R6993* (1972)
- 7) T. Nakagawa, "Summary of JENDL-2 General Purpose File," *JAERI-M 84-103* (1984)



### 3.31 Measurement of Total Cross-Sections of Natural Dy, In and Cu at the Pohang Neutron Facility

Guinyun Kim,<sup>\*</sup> Rachid Machrafi, Hossain Ahmed, and Dongchul Son  
*Institute of High Energy Physics, Kyungpook National University,  
1370 Sankyuk-Dong, Puk-Gu, Daegu 702-701, Korea*

Vadim Skoy,<sup>†</sup> Young Seok Lee, Hengsik Kang, Moo-Hyun Cho, In Soo Ko, and Won Namkung  
*Pohang Accelerator Laboratory, Pohang University of Science and Technology,  
San 31 Hyoja-Dong, Nam-Gu, Pohang 790 – 784, Korea*

The Pohang Neutron Facility consists of an electron linear accelerator, a water-cooled Ta target, and an 11-m time-of-flight path which has been constructed for nuclear data production. It has been equipped with a new four-position sample changer controlled remotely by a CAMAC data acquisition system, which allows simultaneous accumulation of the neutron time of flight spectra from 4 different detectors. The neutron total cross-sections of natural Dy, In and Cu were measured in the neutron energy range from 0.1 eV to 100 eV by using the neutron time of flight method with the new data acquisition system. A  $^6\text{LiZnS(Ag)}$  glass scintillator was used as a neutron detector and metallic plates of natural Dy, In and Cu samples were used for the neutron transmission measurement. The neutron flight path from the water-cooled Ta target to the neutron detector was  $10.81 \pm 0.02$  m. The background level was determined by using notch-filters of Co, Ta, and Cd sheets. In order to reduce the gamma rays from Bremsstrahlung and those from neutron capture, we employed a neutron-gamma separation system based on their different pulse shapes. The present measurements are in general agreement with the evaluated data in ENDF/B-VI. The resonance parameters of the Dy and In isotopes were extracted from the transmission data and compared with the previous ones.

#### I. INTRODUCTION

Pulsed neutrons based on an electron accelerator (linac) are a powerful tool to measure the energy dependence of cross-sections with high resolution by using time of flight (TOF). The Pohang Neutron Facility (PNF) was proposed in 1997 and constructed at the Pohang Accelerator Laboratory on December 1998 [1]. It consists of a 100-MeV electron linac, water-cooled Ta neutron producing target, and an 11-m-long evacuated flight vertical tube leading to the detector location. Neutrons are produced by the bremsstrahlung process from a tantalum radiator. The facility details of PNF are described elsewhere [2].

The neutron total cross-section is used in nuclear data extraction as well as in nuclear applications such as design of nuclear plants. A few measurements of the neutron total cross-sections for Dy have been reported below 100 eV. Moore [3] and Okamoto [4] measured the total cross-sections of Dy in the thermal neutron energy region by the transmission method. Sailor *et al.* [5] reported the neutron total cross-sections in the energy range from 0.07 to 20 eV measured with a crystal spectrometer. Brunner *et al.* [6] obtained the total cross-sections in the energy range from 0.015 eV to 2.5 eV with a fast-chopper installed in a thermal reactor. Knorr *et al.* [7] reported the total cross-sections in the energy region below  $3.2 \times 10^{-3}$  eV. Recently, Cho *et al.* [8] measured the total cross-sections of Dy in the energy region from 0.002 to 100 keV by using the neutron TOF method with a 46 MeV electron linac of the Research Reactor Institute, Kyoto University. However, there exist discrepancies among the measurements, especially in the resonance energy region.

<sup>\*</sup> E-mail: [gnkim@postech.ac.kr](mailto:gnkim@postech.ac.kr), Tel.: +82-53-950-6328

<sup>†</sup> Permanent address: Frank Laboratory of Neutron Physics, Joint Institute of Nuclear Research, 141980 Dubna, Moscow Region, Russia

The Brookhaven fast chopper Seth has been used to measure the transmission ratio for different elements [9]. The total cross-sections of Cu and other elements have been used to determine the nuclear potential radius and to investigate the predictions of the nuclear optical model. At the ORELA neutron facility, Pandey *et al.* have measured the total cross-sections and resonance parameters of  $^{63,65}\text{Cu}$  [10] in resonance energy range.

The early studies of transmission of In are reported in Refs. 11-13. Harvey *et al.* has measured the transmission of enriched In in the neutron energy range higher than 3 eV and determined the resonance parameters [14]. In the work of Bacher *et al.* [15], to establish more accurately the energy of the resonance above 1.0 eV, they measured the transmission rate covering the energy range from 0.75 to 10 eV, and determined that the resonance energy was between 1.29 and 1.43 eV; later it was defined at 1.35 eV. By studying low-energy neutrons, Havens *et al.* determined the first resonance at 1.44 eV and two others, one at 3.8 eV and the other at 8.6 eV [16]. Bacher *et al.* also investigated the slow neutron energy region of Rh and In, but the poor energy resolution at that time didn't allow them to identify the energy resonance around 1 eV which was fixed with a probable error of about 10%. Later, Boyce and McDaniel fixed this resonance at 1.44 and identified two others, one at 3.7 and the other at 9.0 eV [17]. Using the Nevis synchrocyclotron, Hacken *et al.* investigated the resonance parameters [18]. The most recent work on In was reported by Franke *et al.* [19]. The work was performed for energies of 25 eV up to 500 eV at the Los Alamos Neutron Scattering Center. In this study, 47 unreported resonances were observed; also, new data was obtained for the resonance parameters by combining the total and the capture cross-sections.

The measured result was compared with the evaluated data in ENDF/B-VI [20]. The resonance parameters for Dy isotopes ( $^{161,162,163}\text{Dy}$ ) were determined from the fitting of transmission data by using the Multilevel R-Matrix code SAMMY [21] and compared with Mughabghab's data [22].

## II. EXPERIMENTAL ARRANGEMENT

The experimental arrangement for the transmission measurements is shown in Fig. 1. The target is located in the position where the electron beam hits its center. To reduce the gamma-flash generated by the electron burst in the target, this one was placed 55 mm away from the center of the neutron guide. The target was composed of ten Ta plates with a diameter of 4.9 cm and an effective thickness of 7.4 cm [23]. There was a 0.15-cm water gap between Ta plates in order to cool the target effectively. The housing of the target was made of titanium. This target was set at the center of a cylindrical water moderator contained in an aluminum cylinder with a thickness of 0.5 cm, a diameter of 30 cm, and a height of 30 cm. The water level in the moderator was 3 cm above the target surface, which was decided based on a measurement of the thermal neutron flux. The measurement was also compared with the Monte Carlo N-Particle (MCNP) transport code [24].

The neutron guide tubes were constructed of stainless steel with two different diameters, 15 cm and 20 cm, and were placed perpendicularly to the electron beam. The neutron collimation system was mainly composed of  $\text{H}_3\text{BO}_3$ , Pb and Fe collimators, which were symmetrically tapered from a 10-cm diameter at the beginning, to a 5-cm diameter in the middle position where the sample changer was located, to an 8-cm diameter at the end of guide tube where the neutron detector was placed. There was 1.8-m-thick concrete between the target and the detector room.

The physical parameters of the samples used in the experiment are given in Table 1. A set of notch filters of Co, Ta, and Cd plates with thickness of 0.5 mm, 0.2 mm, and 0.5 mm, respectively, was also used for the background measurement and the energy calibration. The transmission samples were placed at the midpoint of the flight path and were cycled into the neutron beam by using the automatic sample changer with four sample positions.

Table 1. Physical parameters of the samples used in the experiment.

Sample	Purity (%)	Size (cm <sup>2</sup> )	Thickness (mm)	Weight (g)
Dy	99.90	10×10	0.5	42.76
In	99.99	10×10	0.2	9.84
Cu	99.96	10×10	1.5	134.4

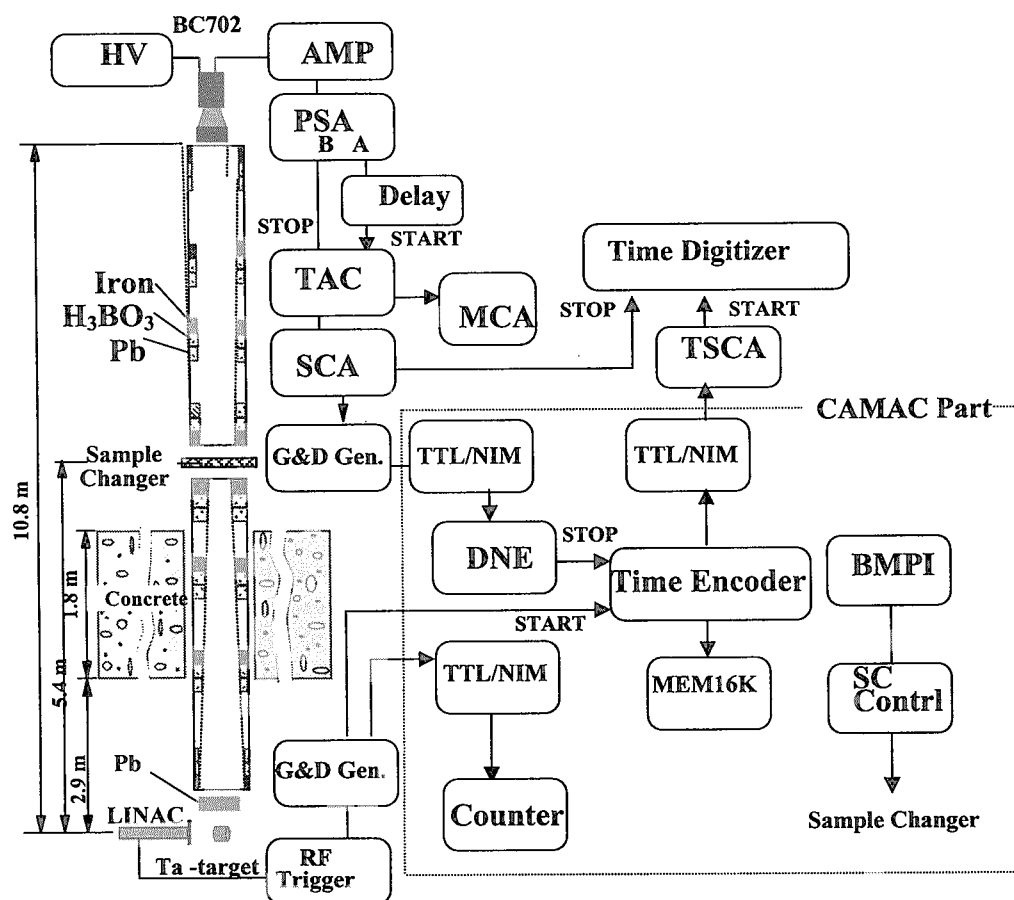


Fig.1. Experimental setup for the transmission measurements.

The neutron detector was located at a distance of 10.81 m from the photo-neutron target. A  $^6\text{Li}$ -ZnS(Ag) scintillator BC702 from Bicron (Newbury, Ohio) with a diameter of 127 mm and a thickness of 15.9 mm mounted on an EMI-93090 photomultiplier was used as a detector for the neutron TOF spectrum measurement. This scintillator consists of a matrix of a lithium compound enriched to 95%  $^6\text{Li}$  dispersed in a fine ZnS(Ag) phosphor powder. The detection process employs the nuclear reaction  $^6\text{Li}(n, \alpha)^3\text{H}$  in which the resulting  $\alpha$ -particle and  $^3\text{H}$  produce scintillations upon interacting with the ZnS(Ag).

During the experiment, the electron linac was operated with a repetition rate of 10 Hz, a pulse width of 1.0  $\mu\text{s}$  and the electron energy of 60 MeV. The peak current in the beam current monitor located at the end of the second accelerator section is above 50 mA, which almost is the same as that in the target.

### III. DATA TAKING AND ANALYSIS

Figure 1 shows the configuration of the data acquisition system used in our measurement. Two different data acquisition systems were used for the neutron TOF spectra measurements: one for the NIM-based system and the other for the CAMAC-based system. The main purpose of the NIM-based system was neutron-gamma separation and the parallel accumulation of the neutron TOF spectra if necessary. The process of neutron-gamma separation was described in details elsewhere [25].

The dynode signal from a BC702 scintillator was connected through an ORTEC-571 amplifier (AMP) to an ORTEC-552 pulse-shape analyzer (PSA) for use in neutron-gamma separation. A fast NIM signal from the "A" output of the PSA was delayed by 60 ns and used as the start signal for an ORTEC-567 time-to-amplitude converter (TAC). The "B" output signal from the PSA was used as the stop signal for the TAC. One of TAC outputs was connected to an ORTEC-550A single channel analyzer (SCA), and the other output signal was fed to a multi-channel pulse-height analyzer (MCA) for neutron-gamma separation. The output signal of the SCA was used as stop signals for a 150-MHz Turbo MCS (Time Digitizer) and for a time encoder of the CAMAC-based system for the neutron TOF spectra measurement. The output of the SCA was sent to an ORTEC-416A gate and delay generator (G&D Gen.) and a TTL/NIM module in order



to form the proper signal for the CAMAC system. This output signal was connected to a time encoder through a detector number encoder (DNE). The DNE allowed data taking from up to 4 detectors simultaneously. The time encoder had 4096 channels and a minimal dwell time of 0.5  $\mu$ s. MEM16K is a memory of 16K capacity and collected the TOF spectra during the measurement.

The 10-Hz RF trigger signal for the modulator of the electron linac was connected to a G&D Gen.; one of output signals was used as the start signal for both the time digitizer and the time encoder, and the other output was sent to the counter through a TTL/NIM converter. The remote control signal from the TTL/NIM was used as the start pulse for the time digitizer for parallel data accumulation. In distinction with the direct use of the start pulse from the RF trigger for the time digitizer, this scheme temporarily interrupts the start pulse sequence while the sample changer moves. The counter has 4 independent inputs, as well as the relevant displays for data and control signals. It is used to accumulate the monitor counts for each position of the sample changer and to control the duration of sample exposure.

Block BMPI sends a request to the sample changer control (SC Contr.) block to change the sample and interrupts the measurement until the next sample reaches its position. The SC Contr. block can be operated automatically (normal mode), as well as manually (manual mode). In the normal mode, it is controlled by software via the BMPI. In the manual mode, one can move the sample changer to any desired position by pressing the relevant knob on the front panel of that block. This mode is usually applied during sample downloading.

The CAMAC part is controlled by PC software via an interface card and crate controller (not shown in Fig. 1). The program sets and controls the following parameters:

- the numbers and quantity of actual detectors used in the measurement;
- the actual number of TOF channels and dwell time for each detector (may be different);
- the duration of the exposition for each sample as the number of starts from the linac.

It also sets the number of full turnovers of the SC and provides a data record from the MEM16K to the relevant files for future processing. Parallel data acquisition with both the Turbo-MCS system and the CAMAC system may be used if one desires to optimize the dwell time for different regions of the TOF spectra. For example, the CAMAC time encoder dwell time may be set to 0.5  $\mu$ s to get good energy resolution in the high-energy part of the TOF spectra while the simultaneous setting for the Turbo-MSC might be 1.5  $\mu$ s to approach, say, 1 meV in the low-energy region of the TOF spectra. A command file written in special script language synchronizes the CAMAC and the Turbo-MCS.

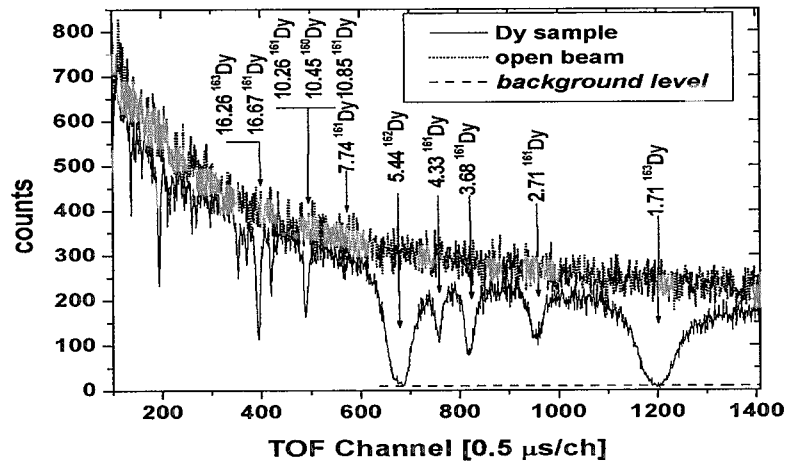
We could estimate the background level by using resonance energies of the neutron TOF spectra of notch-filters of Co, Ta and Cd. The magnitude of the background level was interpolated between the black resonances by using the fitting function  $F(I) = a + bI$ , where  $a$  and  $b$  are constants and  $I$  is the channel number of the time digitizer. In the transmission measurements, we have taken data with sample in and out (open beam) periodically. Total data taking times for sample and open runs of Dy, In, and Cu are 18, 21.5, and 31.25 hours and 16, 21.5 and 31.25 hours, respectively. The net neutron TOF spectra for the sample runs and the open runs for each sample are shown in Fig. 2 together with the estimated background level indicated by dash line. The neutron energy  $E$  in eV corresponding to each channel  $I$  in the TOF spectrum is derived from the relation;  $E = \{72.3 \times L / (I - I_0) \times W\}^2$ , where  $L = 10.81 \pm 0.02$  m is the neutron flight path,  $W = 0.5$   $\mu$ s is the channel width of the time digitizer, and  $I_0$  is the channel of TOF=0 when the neutron burst was produced. In this experiment we found  $I_0$  equals to 5 channels.

The neutron total cross-section is determined by measuring the transmission of neutrons through the sample. The transmission rate of neutrons at the  $i$ -th group energy  $E_i$  is defined as the fraction of incident neutrons passing through the sample compared to that in the open beam. Thus, the neutron total cross-section is related to the neutron transmission rate  $T(E_i)$  as follows:

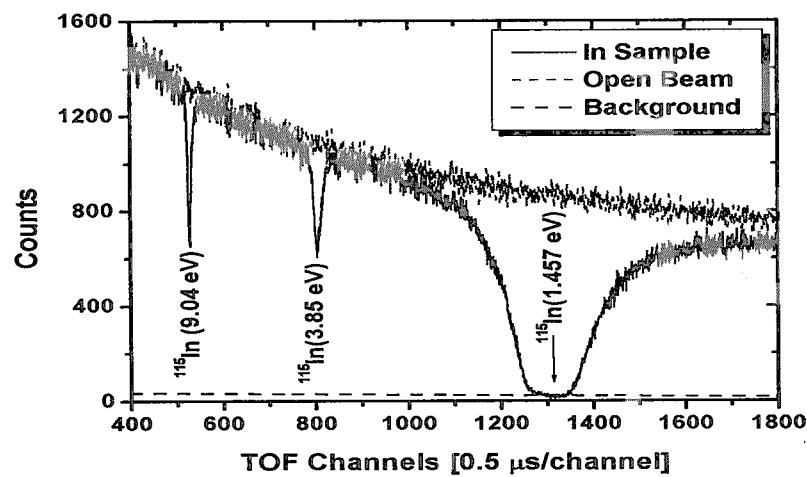
$$\sigma(E_i) = -\frac{1}{\sum_j N_j} \ln T(E_i), \quad (1)$$

$$T(E_i) = \frac{[I(E_i) - IB(E_i)] / M_i}{[O(E_i) - OB(E_i)] / M_o}, \quad (2)$$

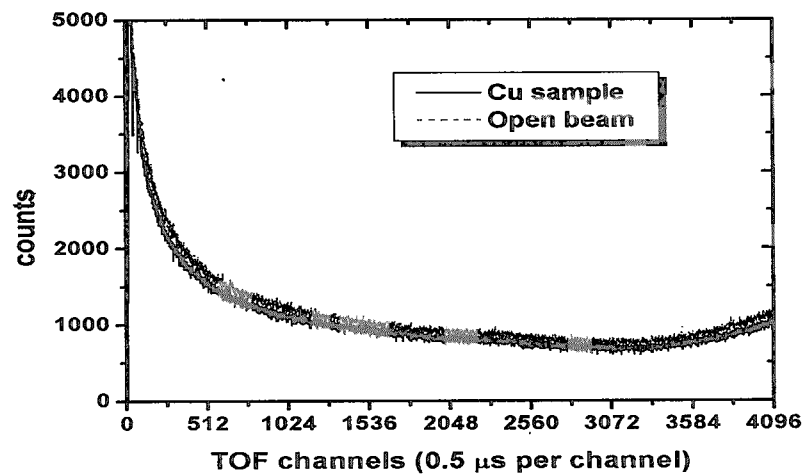
where  $N_j$  is the atomic density per  $\text{cm}^2$  of the  $j$ -th isotope in the sample.  $I(E_i)$  and  $O(E_i)$  are the foreground counts for the sample in and out,  $IB(E_i)$  and  $OB(E_i)$  are the background counts for sample in and out, and  $M_I$  and  $M_O$  are monitor counts for the sample-in and the open beam, respectively. In this measurement, we assumed the monitor counts to be equal during the measurement.



(a)



(b)



(c)

#### IV. RESULTS AND DISCUSSION

Fig.2. The net neutron TOF spectra for sample in and open beam of (a) Dy, (b) In, and (c) Cu samples.

The total cross-sections of natural Dy, In and Cu were obtained in the energy range from 0.1 eV to 100 eV by using the neutron TOF method. We only considered the statistical errors for the present measurements because the other sources of uncertainties, which include the detection efficiencies, the geometric factor for the sample, and the other systematic errors, are negligible. The present measurements for natural Dy, In and Cu are compared with the evaluated data in the ENDF/B-VI, as seen in Fig. 3, 4, and 5, respectively. The error bars in the figures indicate the statistical error only.

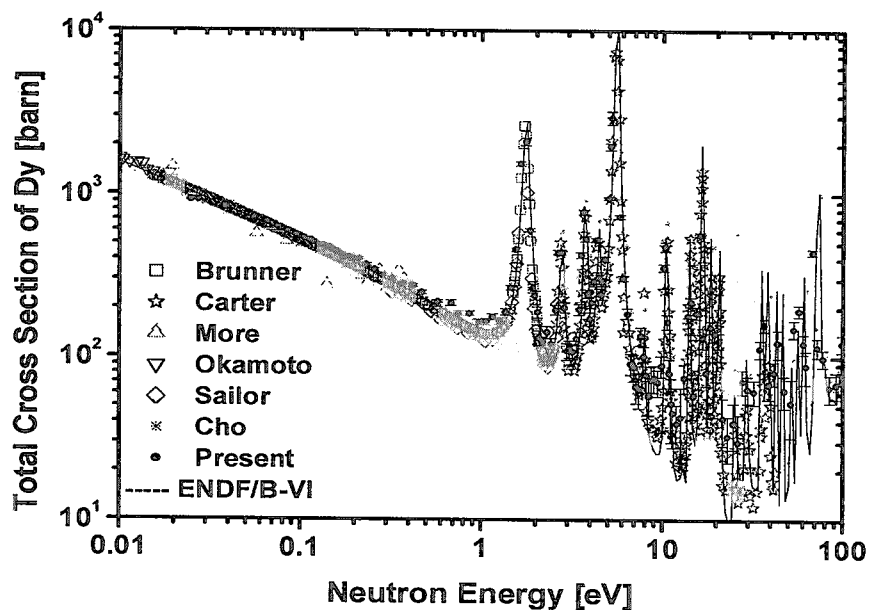


Fig. 3. Comparison of the measured neutron total cross-sections of natural Dy with the previous measurements and the evaluated data in ENDF/B-VI.

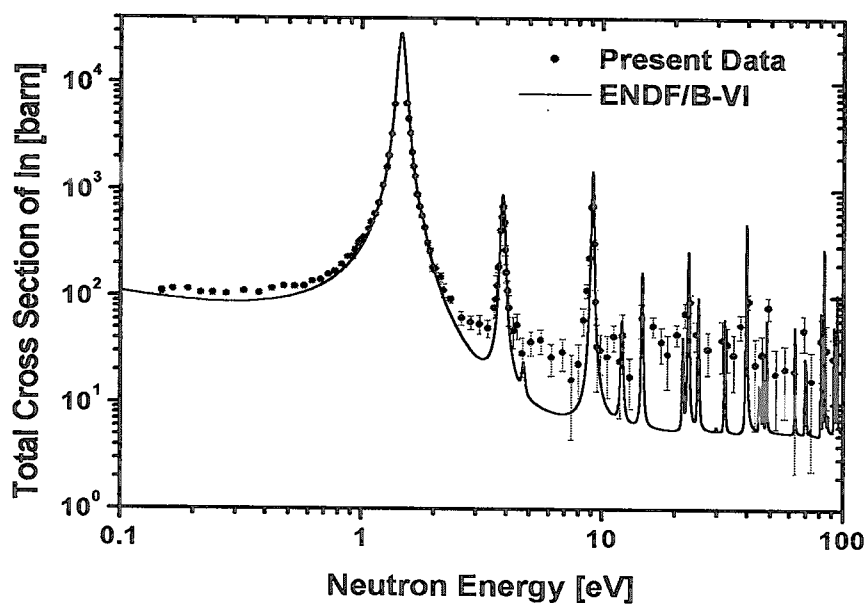


Fig. 4. Comparison of the measured neutron total cross-sections of natural In with the evaluated data in ENDF/B-VI.

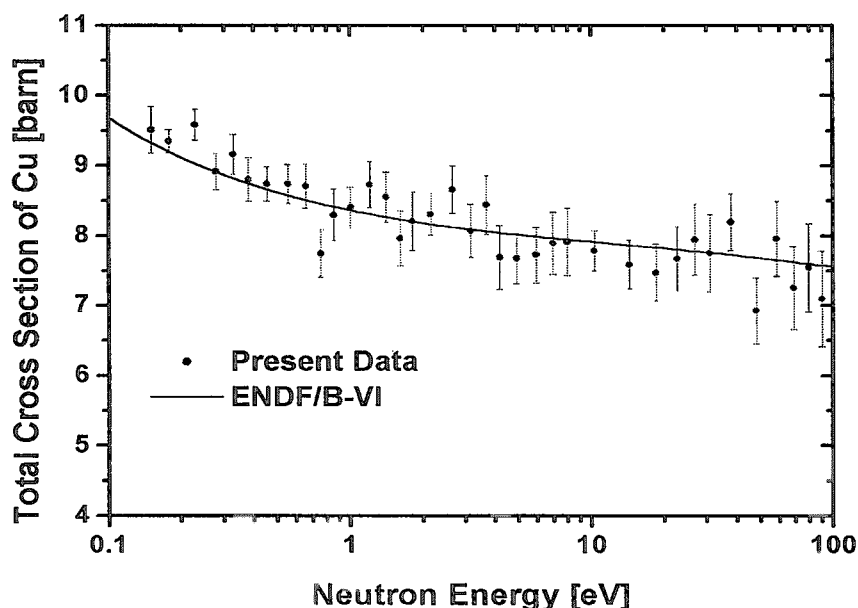


Fig. 5. Comparison of the measured neutron total cross-sections of natural Cu with the evaluated data in ENDF/B-VI.

The present measurement for the neutron total cross-sections of Dy is compared with other data measured by Moore [3], Okamoto [4], Sailor *et al.* [5], Brunner *et al.* [6], Knorr *et al.* [7], Carter [26], and Cho *et al.* [8] and the evaluated data in ENDF/B-VI [20]. The present measurement is generally in good agreement with other data and the evaluated one as shown in Fig. 3.

The present measurements for natural In and Cu are generally in good agreement with the evaluated data in ENDF/B-VI. The quality of these data is not good enough to compare with the previous measurements due to low statistics. The purpose of these measurements was to show the possibility of using the Pohang Neutron Facility equipped with the new data acquisition system as a nuclear data production facility.

There are several resonance peaks in the Dy total cross-sections. In order to get the resonance parameters of each resonance peak, we fit the transmission data with the SAMMY code [21]. This code uses the Reich-Moore approximation [27] in the application of the R-matrix formalism. An implementation of Bayes' theorem is used to fit the requested resonance parameters to the data. For the Doppler broadening and resolution analysis, the MULTI method [28] is applied: the free gas model is applied to the Doppler broadening and the convolution of Gaussian and exponential function to the resolution. Resolution function  $R(E, E')$  used in this calculation is the convolution of Gaussian and exponential function and its mathematical expression is as follows:

$$R_{GE}(E, E') = \frac{1}{\Delta_E \Delta_G \sqrt{\pi}} \int_{E-\Delta E_S}^{\infty} dE^0 \exp\left\{-\frac{(E^0 - (E - \Delta E_S))^2}{\Delta_E^2}\right\} \exp\left\{-\frac{(E' - E^0)^2}{\Delta_G^2}\right\}, \quad (3)$$

where the FWHM of Gaussian resolution function  $\Delta_G$  is given by

$$\Delta_G = E[aE + b]^{1/2} \quad (4)$$

and the width of exponential resolution function  $\Delta_E$  is given by

$$\Delta E = cE^{3/2}. \quad (5)$$

The energy shift  $\Delta E_s$ , which is automatically determined in SAMMY, is introduced in order that the maximum of the broadening function be located at  $E' = E$ . The constant values of  $a$ ,  $b$ , and  $c$  are  $1.3645 \times 10^{-6} \text{ eV}^{-1}$ ,  $9.1281 \times 10^{-6}$ , and  $6.3969 \times 10^{-4} \text{ eV}^{-1/2}$ , respectively.

Thus the resonance parameters, listed in Table 2, have been obtained from the resonance shape in transmission data and are compared with the set of data given between brackets [22]. Quantity  $J$  is the spin of a particular resonance. In Fig. 6, the measured total cross-section of Dy in the neutron energy range from 1 to 10 eV was compared with the SAMMY fitting results. The SAMMY prediction of total cross-section and the present data are in good agreement with each other with  $\chi^2/N=1.04$ .

Table 2. Resonance Parameters for Dy isotopes

Isotope	$J$	$E$ (eV)		$g\Gamma_n$ (meV)	$\Gamma_\gamma$ (meV)
$^{163}\text{Dy}$	2	Present	$1.7093 \pm 0.0007$	$0.9344 \pm 0.0105$	$91.574 \pm 0.827$
		Mughabghab	$(1.713 \pm 0.004)$	$(0.85 \pm 0.05)$	$(102.6 \pm 0.8)$
$^{160}\text{Dy}$	1/2	Present	$1.8871 \pm 0.0321$	$0.1394 \pm 0.0135$	$124.97 \pm 12.32$
		Mughabghab	$(1.88)$	$(0.20)$	$(105.80)$
$^{161}\text{Dy}$	3	Present	$2.6979 \pm 0.0028$	$0.3929 \pm 0.0122$	$130.12 \pm 6.632$
		Mughabghab	$(2.71 \pm 0.02)$	$(0.328 \pm 0.015)$	$(119 \pm 10)$
$^{161}\text{Dy}$	2	Present	$3.6618 \pm 0.0025$	$0.9524 \pm 0.0243$	$139.14 \pm 6.087$
		Mughabghab	$(3.68 \pm 0.03)$	$(0.89 \pm 0.04)$	$(124 \pm 15)$
$^{161}\text{Dy}$	2	Present	$4.2810 \pm 0.0041$	$0.6677 \pm 0.0273$	$130.25 \pm 8.702$
		Mughabghab	$(4.33 \pm 0.02)$	$(0.575 \pm 0.065)$	$(80 \pm 3)$
$^{162}\text{Dy}$	1/2	Present	$5.3697 \pm 0.0022$	$14.492 \pm 0.4007$	$262.08 \pm 11.08$
		Mughabghab	$(5.44 \pm 0.02)$	$(21 \pm 1.5)$	$(148 \pm 15)$
$^{163}\text{Dy}$	2	Present	$5.8377 \pm 0.0775$	$0.0198 \pm 0.0014$	$108.07 \pm 10.81$
		Mughabghab	$(5.81)$	$(0.0135)$	$(108.60)$
$^{161}\text{Dy}$	3	Present	$7.6632 \pm 0.0195$	$0.4284 \pm 0.0340$	$158.01 \pm 14.46$
		Mughabghab	$(7.74)$	$(0.30)$	$(107.00)$

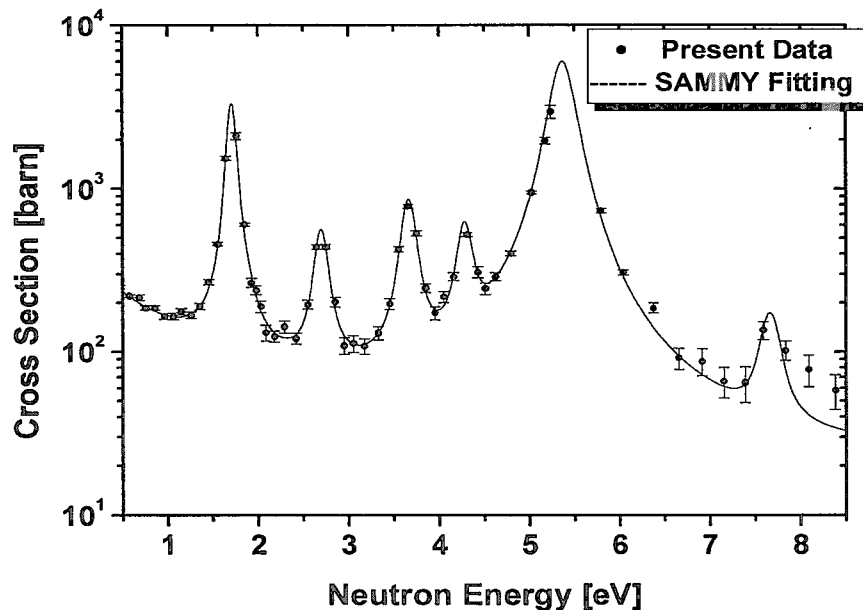


Fig. 6. Comparison of the measured total cross sections of natural Dy with the predicted total cross section from the SAMMY fitting

## V. CONCLUSION

The Pohang Neutron Facility was constructed as a pulsed neutron facility based on an electron linac for producing nuclear data in Korea. It consists of a 100-MeV electron linac, a water cooled Ta target, and an 11-m long TOF path. In order to show the ability to measure nuclear data, we measured the neutron total cross-sections of natural Dy, In and Cu samples in the neutron energy range from 0.1 eV to 100 eV by using the neutron time-of-flight method with the new data acquisition system and a  $^6\text{LiZnS(Ag)}$  glass scintillator as a neutron detector. The present measurements are in general agreement with the evaluated data in ENDF/B-VI. The resonance parameters of the Dy isotopes were extracted from the transmission rate compared with the previous ones.

Based on the present results, this pulsed neutron facility could be used as a user facility for nuclear data production. However, we have to upgrade the electron gun system for high current, wide pulse width, and high repetition rate, and we have to install a neutron monitor in front of the sample changer in order to monitor the neutron intensity. In order to decrease background events, we have to modify the shielding around the detector and the sample changer and add more collimators along the neutron beam tube. For the moment, we can measure the neutron total cross-sections only by using the neutron TOF method. In order to measure the neutron capture cross-sections, we have to construct a set of total energy absorption detectors employing BGO, NaI(Tl), or CsI(Tl).

## ACKNOWLEDGMENTS

The authors would like to express their sincere thanks to the staff of the Pohang Accelerator Laboratory for the excellent electron linac operation and their strong support. This work is partly supported through the Long-term Nuclear R&D program of the Korea Atomic Energy Research Institute and through the Science Research Center (SRC) program of the Institute of High Energy Physics, Kyungpook National University.

## REFERENCES

- [ 1 ] G. N. Kim, J. Y. Choi, M. H. Cho, I. S. Ko, W. Namkung, and J. H. Jang, in *Proceedings International Conference on Nuclear Data for Science and Technology*, edited by G. Reffo, A. Ventura and C. Grandi (Trieste, Italy, May 19-24, 1997), p. 556; H. S. Kang, J. Y. Choi, Y. J. Park, S. H. Kim, G. N. Kim, M. H. Cho, I.

- S. Ko, and W. Namkung, in *Proceedings of First Asian Particle Accelerator Conference*, edited by Y. H. Chin, M. Kihara, H. Kobayashi, N. Akasaka, K. Nigorikawa, and M. Tobiyama (Tsukuba, Japan, Mar. 23-27, 1998), p. 743.
- [2] G. N. Kim, Y. S. Lee, V. Skoy, V. Kovalchuk, M. H. Cho, I. S. Ko, W. Namkung, D. W. Lee, H. D. Kim, S. K. Ko, S. H. Park, D. S. Kim, T. I. Ro, and Y. G. Min, *J. Korean Phys. Soc.* **38**, 14 (2001); G. N. Kim, V. Kovalchuk, Y. S. Lee, V. Skoy, M. H. Cho, I. S. Ko, W. Namkung, D. W. Lee, H. D. Kim, S. K. Ko, S. H. Park, D. S. Kim, T. I. Ro, and Y. G. Min, *Nucl. Instr. Meth. A* **485**, 458 (2002).
  - [3] W. M. Moor, *Bulletin of American Physical Society*, **6**, 70 (1961).
  - [4] K. Okamoto, JAERI Report, JAERI-1069 (1964).
  - [5] V. L. Sailor, H. H. Landon, and H. L. Jr. Foot, *Phys. Rev.* **96**, 1014 (1954).
  - [6] J. Brunner and F. Widder, Report EIR-123 (1967).
  - [7] K. Knorr and W. Schmatz, *Atomk-ernenergie* **16** (9), 49 (1970).
  - [8] H. J. Cho, K. Kobayashi, S. Yamamoto, Y. Fujita, Y. S. Lee, G. N. Kim, I. S. Ko, M. H. Cho, W. Namkung, S. K. Ko, *Annals of Nuclear Energy*, **27**, 1259 (2000).
  - [9] K. K. Seth, D. J. Hughes, R. L. Zimmerman, and R. C. Garth, *Phys. Rev. C* **110**, 692 (1958).
  - [10] M. S. Pandey, G. B. Garg, and J. A. Harvey, *Phys. Rev. C* **15**, 600 (1977).
  - [11] R. G. Allen, T. E. Strehphenson, C. P. Stanford, and S. Bernstein, *Phys. Rev.* **96**, 1297 (1954).
  - [12] H. H. Landon and V. L. Sallor, *Phys. Rev.* **98**, 1267 (1955).
  - [13] W. W. Havens JR. and J. Rainwater, *Phys. Rev.* **73**, 963 (1948).
  - [14] J. A. Harvey, D. J. Hughes, R. S. Cater and V. E. Pilcher, *Phys. Rev.* **99**, 443 (1955).
  - [15] R. F. Bacher, C. P. Baker, and B. D. McDaniel, *Phys. Rev.* **69**, 165 (1946).
  - [16] W. W. Havens, Jr., C. S. Wu, L. J. Rainwater, and C. L. Meaker, *Phys. Rev.* **71**, 165 (1947).
  - [17] D. Boyce and McDaniel, *Phys. Rev.* **70**, 832 (1946).
  - [18] G. Hacken, H. I. Liou, H. S. Camarda, W. J. Makofske, F. Rahn, L. J. Rainwater, M. Slgawitz, and S. Wynchank, *Phys. Rev C* **10**, 1910 (1974).
  - [19] C. M. Frankle, J. D. Dawman, B. E. Crawford, P. P. J. Delheij, C. R. Gould, D. G. Hase, J. N. Knudson, G. E. Mirchel, S. S. Patterson, S. I. Penttila, Yu. P. Popov, N. R. Roberson, S. J. Seestrom, E. I. Sharapov, Yi. Fen Yen, S. H. Yoo, V. W. Yuan, and X. Zhu *Phys. Rev. C* **48**, 1601 (1993).
  - [20] R. F. Ross, ENDF-201, ENDF/B-VI Summary Documentation, BNL-NCS-17541, 4th Ed. (ENDF/B-VI), Brookhaven National Laboratory (1991).
  - [21] N. M. Larson, RSICC Peripheral Shielding Routine Collection SAMMY-M2a: A Code System for Multilevel R-Matrix Fits to Neutron Data Using Bayes' Equations, PSR-158, SAMMY-M2a, Oak Ridge National Laboratory (1999) (unpublished).
  - [22] S. F. Mughabghab, *Neutron Cross-sections* (Academic Press, NY, 1984) Vol. 1.
  - [23] W. Y. Baek, G. N. Kim, M. H. Cho, I. S. Ko, and W. Namkung, in *Proceedings of Workshop on Nuclear Data Production and Evaluation*, edited by J. Chang and G. N. Kim (Pohang, Korea, Aug. 7-8, 1998).
  - [24] MCNP, A general Monte Carlo N-Particle transport code system, Version 4B, Los Alamos National Laboratory, LA-12625-M, (1997).
  - [25] V. Skoy, Y. S. Lee, H. S. Kang, M. H. Cho, I. S. Ko, W. Namkung, G. N. Kim, R. Machrafi, H. Ahmed, and D. Son, *J. Korean Phys. Soc.*, **41**, 314 (2002).
  - [26] R. S. Carter, *Exfor Data File 11897* (1983).
  - [27] C. W. Reich and M. S. Moore, *Phys. Rev.* **111**, 929 (1958).
  - [28] F. A. George, "MULTI, A FORTRAN Code for Least-Square Shape Fitting of Neutron Cross-Section Data Using the Reich-Moore Multilevel Formalism," LA-5473-MS, Los Alamos Scientific Laboratory (1974).



### 3.32 Proposal of experimental facilities for studies of nuclear data and radiation engineering in the Intense Proton Accelerator Project

M. Baba<sup>\*1</sup>, M. Igashira<sup>\*2</sup>, Y. Nagai<sup>\*3</sup>, K. Ishibashi<sup>\*4</sup>

<sup>\*1</sup> Cyclotron and Radioisotope Center, Tohoku University, babam@cyric.tohoku.ac.jp

<sup>\*2</sup> Laboratory for Nuclear Reactors, Tokyo Institute of Technology

<sup>\*3</sup> Research Center for Nuclear Study, Osaka University

<sup>\*4</sup> Graduate School of Engineering, Kyusyu Univ.,

A proposal is given on the facilities and experiments in the Intense Proton Accelerator Project (J-PARC) relevant to the nuclear data and radiation engineering, nuclear astrophysics, nuclear transmutation, accelerator technology and space technology and so on.

#### 1. Introduction

The Intense Proton Accelerator Project named J-PARC is now promoted as the joint project between Japan Atomic Energy Research Institute (JAERI) and High Energy Accelerator Research Organization (KEK) [1,2]. J-PARC is a accelerator complex consisting of intense proton-linac (400, 600 MeV), 3 GeV proton synchrotron and 50 GeV proton-synchrotron. A schematic layout of the facility is shown in Fig.1 [1,2]. The intensity and time-structure of the proton beam are shown in Fig.2. In the project, three major facilities will be constructed [1,2]:

- 1) a facility for nuclear and particle physics, and neutrino science using 50 GeV protons,
- 2) a material and life science facility using an intense moderated neutron beam produced by a spallation reaction of 3 GeV 1MW proton beam, and
- 3) a transmutation facility for basic research on nuclear transmutation of radioactive wastes with an accelerator-driven system (ADS) using a 600 MeV proton beam [1].

Muon science research is also planned in the 3 GeV accelerator facility.

The intense moderated neutron beams and various energy proton beams provided by J-PARC will open new possibilities in the research of neutron nuclear data for the nuclear astrophysics and nuclear transmutation, and the radiation science relevant to the accelerator and space technology. In the present plan of J-PARC, however, such facilities are not included explicitly. Furthermore, we have to remember that the 12 GeV proton synchrotron and the 500 MeV proton booster at KEK which has been a unique particle source in Japan in the high-energy region should be shutdown with the start of operation of J-PARC. Considering these situations, installation of facilities for radiation engineering in J-PARC is very important and indispensable.

From this view point, four divisions in Atomic Energy Society of Japan, i.e.-Reactor Physics, Radiation Science and Technology, Nuclear Data, and Accelerator & Beam Science-, organized a working group to discuss and propose experimental facilities and research for radiation sciences and ADS in J-PARC. The proposals are as follows [3]:

1)An intense moderated neutron beam line in the life science facility for nuclear astrophysics and ADS, 2)radiation science experiments in the 50 GeV beam line in the nuclear and particle physics facility, and 3)a beam course for nuclear data and the radiation science in the transmutation facility as well as 4) proposals for research in the transmutation facility.

The present report describes outlines of proposals 1)-3) relevant to the nuclear data and radiation



science [3]. For more details, see Ref. [3].

## Configuration of the Accelerator Complex

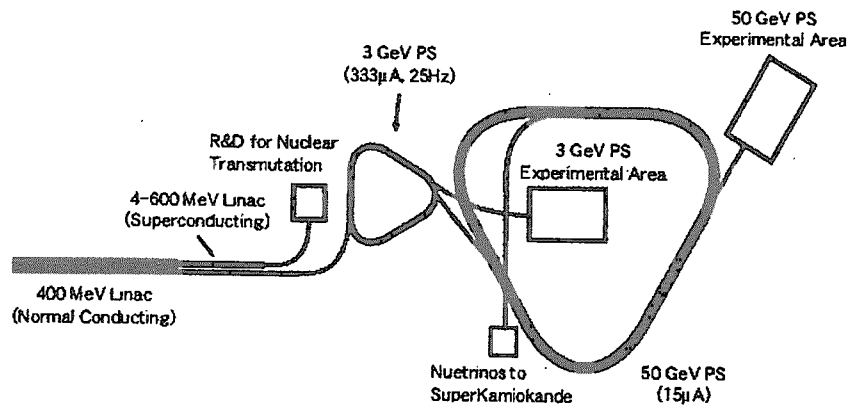


Fig.1 Schematic view of the intense proton accelerator facility, J-PARC [1,2].

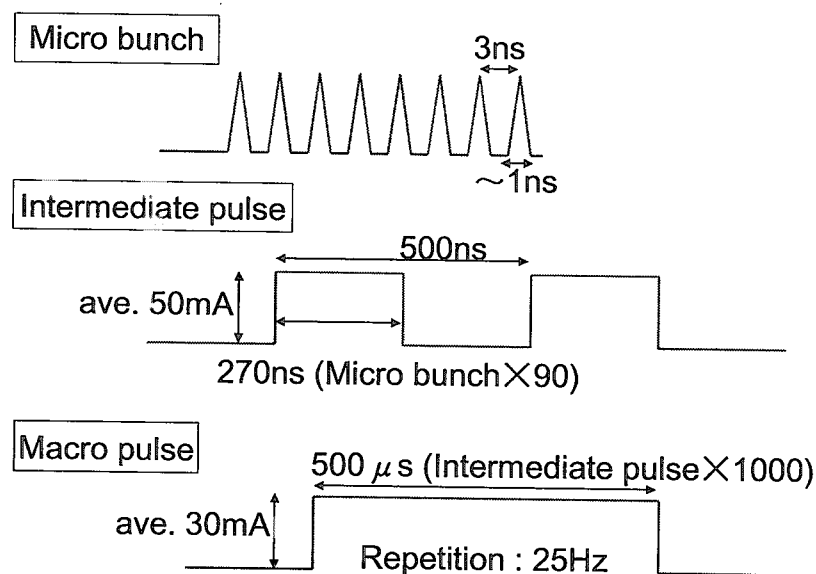


Fig.2. Time structure and intensity of proton beam in J-PASRC [1,2].

## 2. Proposals

The J-PARC project is divided into two phases; 1) in the first phase, 3 GeV and 50 GeV beam will be provided, and materials and life science facility and nuclear & particle physics facility will be installed, 2) in the second phase, the 600 MeV linac and its beam line and the nuclear transmutation facility, and the neutrino science facility will be installed.

The proposals 1) and 2) correspond to phase-I, and 3) and 4) to the periods of phase-II.

### 2.1 Neutron beam line for nuclear data measurements on astrophysics and accelerator-driven system

The schematic view of the proposed beam line is illustrated in Fig.3. The line is expected to be installed as one of the beam lines around the mercury spallation neutron target and the associated moderators. As shown in Fig.3, it is utilized mainly to measure capture and fission cross-sections using a time-of-flight method for the thermal to hundreds of keV region which are of crucial role for the nuclear astrophysics and ADS. The intense neutron beam will newly enable cross-section measurements for elements with very high radio-activity and/or very small sample amount that were not possible thus far. For the advantages, the beam line will provide new generation of neutron nuclear data in the field of nuclear astrophysics and ADS. Figure 4 shows an example of nuclide synthesis chart for Se, Br and Kr where the neutron capture cross-section of  $^{79}\text{Se}$  plays a key role to the synthesis mechanism because it has a relatively long half-life of 65,000 years. Similarly, the nuclear data for actinide nuclei obtained in the facility will greatly contribute to establish the data base for the design and operation of the transmutation facility.

## 2.2 Radiation engineering experiments in 50 GeV nuclear and particle physics facility

The planned experimental facility at 50 GeV beam line is shown in Fig.5 [1,2]. The T0 beam line and associated experimental hall for test experiment enables experiments for GeV range particles using primary and secondary particles and are very useful to perform differential and integral experiments relevant to high-energy accelerator technology and space technology:

- 1) differential cross-sections for the production and scattering of nucleons, muons, and heavy particles,
- 2) integral experiments for the shielding and radiation effects of high energy nucleons, and
- 3) development and characterization of radiation detectors for high energy particles.

The differential experiment 1) provides information on the source term in ADS, the transport and the effects of high-energy accelerator particles and cosmic-rays. These data are required to upgrade theoretical models which are currently used for the design of accelerator shielding and ADS. Figure 6 shows an example of the problem of the nuclear model code presently used. Integral experiments are needed in particular to guarantee the safety designs of accelerator systems based on the differential data. The item 3) is also essential to promote the research experiments that will be carried out in the high-energy facility. In the experiments, secondary beams will be utilized as well as a primary proton beams extracted with a scatterer.

## 2.3 A Beam line in the transmutation facility.

In the transmutation facility, research on basic physics of transmutation and irradiation effects of target elements will be conducted using a critical assembly and an irradiation cell for 600 MeV protons, respectively [1,2]. To promote the research, a comprehensive data base is requested on neutron and charged-particle production by the interaction of primary protons with constituent elements. The data status is, however, quiet unsatisfactory [3]. Therefore, experiments to obtain differential data should be promoted concurrently with the integral experiments using the facility.

In Fig.7, an idea for the beam line is illustrated. In the plan, a "kW target" is newly proposed in addition to "10 W target" in the current design plan [1,2] to get intense and short-burst proton beam required for the differential experiments. A short proton burst is achieved by picking up a fraction ( $< \text{ns}$ ) of micro-bunch (Fig.2) of a beam to the irradiation facility with a laser-charge-exchange and a foil stripping method. In this scheme, it will be possible to provide about a 800 W proton beam to the target guaranteeing that the maximum beam power delivered into the critical assembly is less than 10 W. These lines will be used as powerful facility for differential measurement and integral benchmark experiments on neutron and secondary particle production.

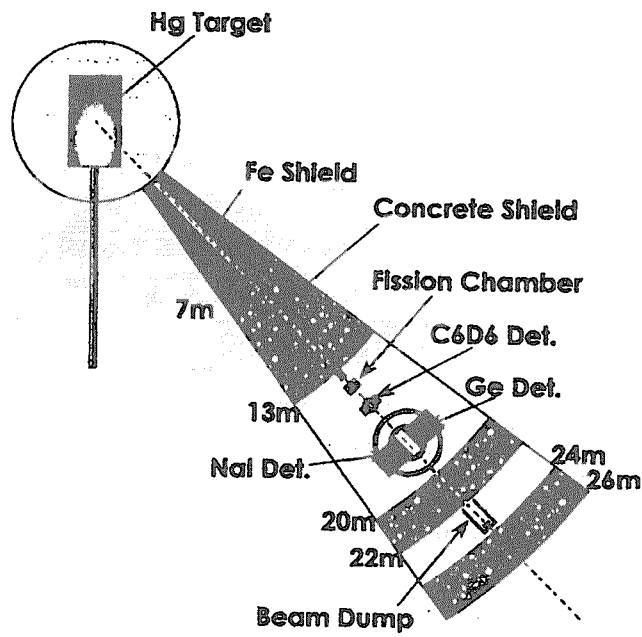


Fig.3: Proposal of neutron beam line in material and life science facility for nuclear astrophysics and ADS [3].

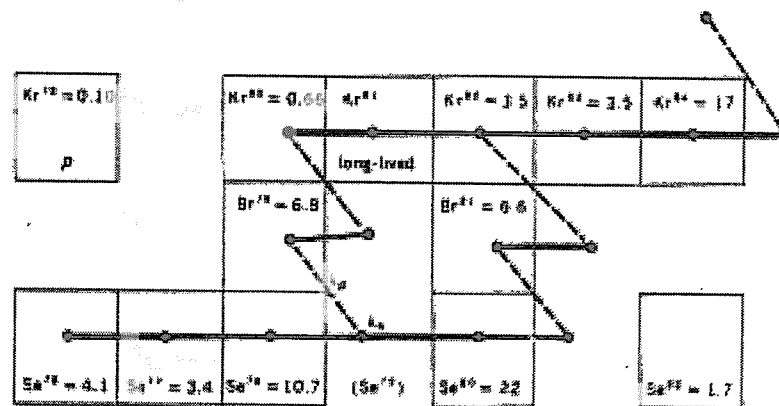


Fig.4: Nuclear synthesis chart for Se, Br and Kr [3].

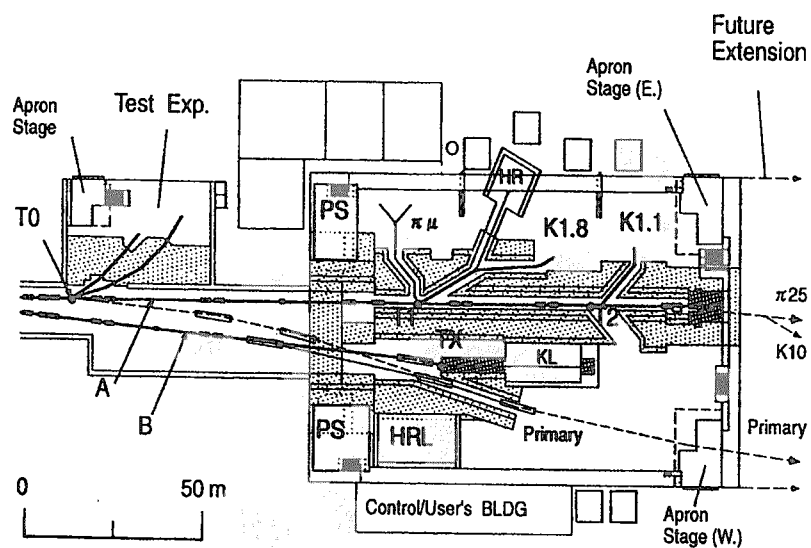


Fig.5: Schematic view of 50 GeV nuclear and particle-physics facility [1,2].

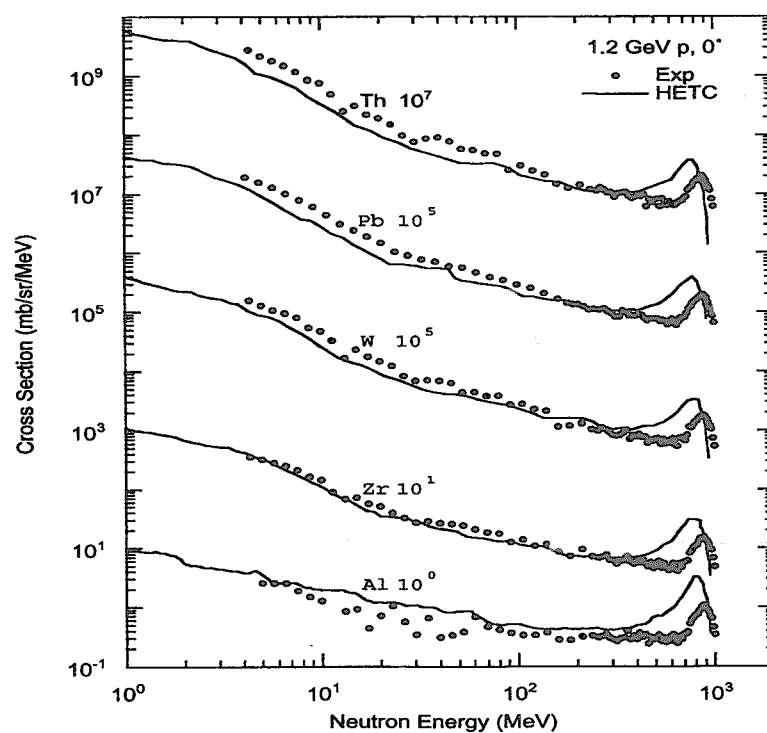


Fig.6: Comparison of the HETC calculation with experimental data for neutron production by the (p,n) reactions with 1.2 GeV protons [3].

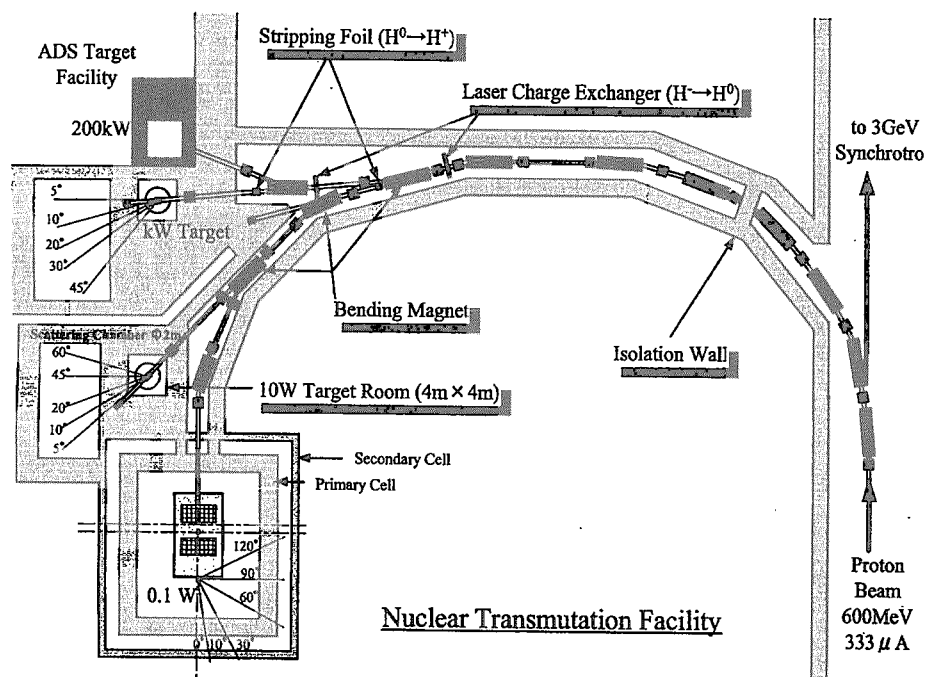


Fig.7: Proposal of "kW beam line" in the nuclear transmutation facility [3]

### 3. Summary

We have presented proposals for facilities and experiments in the intense proton accelerator facility J-PARC relevant to nuclear data and radiation engineering. The facility will be very powerful and productive one owing to distinguished performance such as beam power and/or short burst duration.

We highly expect that the proposals are realized in the near future, and are ready to cooperate with the project team in design and construction of the proposed facilities. About the neutron beam course in the material and life science facility, a letter of intent has been already presented to project management team with the project title of "Neutron beam line for nuclear astrophysics and accelerator-based system".

The authors wish to thank to Drs.Y. Kiyonagi, Y. Yamane, T. Iwasaki, Y. Ikeda, Y. Oyama, H. Oigawa, S. Chiba, H. Nakashima, S. Meigo, Y. Watanabe, N.Yamano for useful discussions and comments.

### References:

- [1] JAERI-Tech 200-003 / KEK Report 99-5 (in Japanese)
- [2] <http://j-parc.jp/>
- [3] Genshikau-Kenkyu Vol.47 (No.1) July 2002 (in Japanese)

This is a blank page.

## Appendix: Participant List

AKINO Fujiyoshi	IRM	KAWASAKI Kenji	JAERI
ANDO Yoshihira	Toshiba Co.	KAWATA Naoki	Tohoku Univ.
ANDOH Masaki	JAERI	KIDO Hiroko	V.I.C.
ARAMAKI Fujio	KIIS	KIM Guinyun	KNU
ARUGA Takeo	JAERI	KIMURA Atsushi	JAERI
BABA Mamoru	Tohoku Univ.	KIN Tadahiro	Kyushu Univ.
CHATANI Hiroshi	Kyoto Univ.	KITAZAWA Hideo	NDA
CHIBA Gou	JNC	KOBAYASHI Katsuhei	Kyoto Univ.
CHIBA Satoshi	JAERI	KOBAYASHI Katsutoshi	JAERI
ENDO Akira	JAERI	KONNO Chikara	JAERI
FUKAHORI Tokio	JAERI	KOSAKO Kazuaki	SAE
FUKETA Toyojiro	JMSF	KOURA Hiroyuki	RIKEN
FUKUYA Koji	INSS	KUROSAWA Naohiro	V.I.C.
FUMIZAWA Motoo	JAERI	LEE Young-Ouk	KAERI
GAIDAROV, M.K.	Kyushu Univ.	Liem Peng Hong	NAIS
HAGIWARA Masayuki	Tohoku Univ.	MAEDA Shigetaka	JNC
HARADA Masahide	JAERI	MARUYAMA Hiromi	GNF-J
HASEGAWA Akira	JAERI	MATSUMURA Tetsuo	CRIEPI
HAZAMA Taira	JNC	MATSUNOBU Hiroyuki	DEI
HIRABAYASHI Naoya	Tohoku Univ.	MATSUSHIMA Takayuki	NDA
HORI Jun-ichi	JAERI	MEIGO Shin-ichiro	JAERI
HUDA, Md. Quamrul	INST	MITSUDA Motoyuki	Osaka Univ.
ICHIHARA Akira	JAERI	MITSUOKA Shin-ichi	JAERI
ICHINOSE Jun	SAE	MIZUMOTO Motoharu	JAERI
IGASHIRA Masayuki	Tokyo Inst. of Tech.	MORI Seiji	KHI
IGUCHI Tetsuo	Nagoya Univ.	MURATA Toru	AITEL
ISHIKAWA Isamu	RIST	NAKAGAWA Tsuneo	JAERI
ISHIKAWA Makoto	JNC	NAKAJIMA Hajime	JAERI
ITOGA Toshiro	Tohoku Univ.	NAKAJIMA Ken	JAERI
IWAMOTO Osamu	JAERI	NAKAJIMA Kyo	Tohoku Univ.
KAI Tetsuya	JAERI	NAKAMURA Hisashi	—
KAISE Yoichiro	ARTECH	NAKAMURA Shoji	JNC
KANEKO Toshiyuki	JRI	NAKAO Makoto	JAERI
KATAKURA Jun-ichi	JAERI	NAKASHIMA Hiroshi	JAERI
KATO Kiyoshi	Hokkaido Univ.	NAUCHI Yasushi	CRIEPI
KAWAI Masayoshi	KEK	NEMOTO Makoto	V.I.C.
KAWANO Toshihiko	Kyushu Univ.	NISHINAKA Ichiro	JAERI
KAWASAKI Hiromitsu	CRC	NISHIO Katsuhisa	JAERI

NISHITANI Takeo	JAERI
NIWA Kimio	Nagoya Univ.
NOJIRI Naoki	JAERI
ODANO Naoteru	NMRI
OHKAWACHI Yasushi	JNC
OHKI Shigeo	JNC
OHKUBO Makio	SOHONRR
OHSAKI Toshiro	Tokyo Inst. of Tech.
OHSAWA Takaaki	Kinki Univ.
OKAJIMA Shigeaki	JAERI
OKUMURA Keisuke	JAERI
OKUNO Hiroshi	JAERI
OTSUKA Naohiko	Hokkaido Univ.
OYAMATSU Kazuhiro	Aichi Shukutoku Univ.
SAIHO Fuminobu	Kyushu Univ.
SAITO Kosuke	Tokyo Inst. of Tech.
SAKURAI Kiyoshi	JAERI
SAKURAI Takeshi	JAERI
SASAKI Kenji	ARTECH
SASAKI Makoto	MHI
SAWAMURA Hidenori	Nagoya Univ.
SEKI Akiyuki	JAERI
SEKINE Takashi	JNC
SHIBATA Keiichi	JAERI
SHIBATA Takemasa	JAERI
SHIGYO Nobuhiro	Kyushu Univ.
SHIMADA Shoichiro	JAERI
SHIMAKAWA Satoshi	JAERI
SHIMIZU Toshiaki	Nagoya Univ.
SHINDO Ryuichi	JAERI
SHIRAKI Takako	MHI
SHONO Akira	JNC
SUGI Teruo	
SUGITA Takeshi	SSL
SUKEGAWA Takenori	JAERI
TACHIBANA Takahiro	Waseda U. Senior High School
TAHARA Yoshihisa	MHI
TAKAI Konomi	JAERI
TAKAMURA Atsusi	SSL
TJAHYANI, D.T.S.	BATAN

TOKASHIKI Mikio	NFI
TSUBOSAKA Akira	NFI
TSUJI Masatoshi	TEC
TSUKAMOTO Yasuyuki	Kyushu Univ.
UDDIN, Md. Shuza	Tohoku Univ.
UMANO Takuya	NUPEC
UMEBARA Youichi	YONDEN
UNO Yoshitomo	JAERI
WATANABE Yukinobu	Kyushu Univ.
WU Zhendong	JAERI
YAMAGUCHI Yasuhiro	JAERI
YAMAMOTO Toshihiro	JAERI
YAMANO Naoki	SAE
YAMAUCHI Michinori	JAERI
YOKAYAMA Kenji	JNC
YOSHIDA Tadashi	Musashi Inst. of Tech.
YOSHIZAWA Michio	JAERI



# 国際単位系 (SI) と換算表

表1 SI基本単位および補助単位

量	名称	記号
長さ	メートル	m
質量	キログラム	kg
時間	秒	s
電流	アンペア	A
熱力学温度	ケルビン	K
物質の量	モル	mol
光度	カンデラ	cd
平面角	ラジアン	rad
立体角	ステラジアン	sr

表3 固有の名称をもつSI組立単位

量	名称	記号	他のSI単位 による表現
周波数	ヘルツ	Hz	s <sup>-1</sup>
力	ニュートン	N	m·kg/s <sup>2</sup>
圧力, 応力	パスカル	Pa	N/m <sup>2</sup>
エネルギー, 仕事, 熱量	ジュール	J	N·m
工率, 放射束	ワット	W	J/s
電気量, 電荷	クーロン	C	A·s
電位, 電圧, 起電力	ボルト	V	W/A
静電容量	ファラド	F	C/V
電気抵抗	オーム	Ω	V/A
コンダクタンス	ジーメンズ	S	A/V
磁束	ウェーバ	Wb	V·s
磁束密度	テスラ	T	Wb/m <sup>2</sup>
インダクタンス	ヘンリー	H	Wb/A
セルシウス温度	セルシウス度	°C	
光束度	ルーメン	lm	cd·sr
照射度	ルクス	lx	lm/m <sup>2</sup>
放射能	ベクレル	Bq	s <sup>-1</sup>
吸収線量	グレイ	Gy	J/kg
線量等量	シーベルト	Sv	J/kg

表2 SIと併用される単位

名称	記号
分, 時, 日	min, h, d
度, 分, 秒	°, ', "
リットル	l, L
トン	t
電子ボルト	eV
原子質量単位	u

1 eV=1.60218×10<sup>-19</sup>J  
1 u=1.66054×10<sup>-27</sup>kg

表5 SI接頭語

倍数	接頭語	記号
10 <sup>18</sup>	エクサ	E
10 <sup>15</sup>	ペタ	P
10 <sup>12</sup>	テラ	T
10 <sup>9</sup>	ギガ	G
10 <sup>6</sup>	メガ	M
10 <sup>3</sup>	キロ	k
10 <sup>2</sup>	ヘクト	h
10 <sup>1</sup>	デカ	da
10 <sup>-1</sup>	デシ	d
10 <sup>-2</sup>	センチ	c
10 <sup>-3</sup>	ミリ	m
10 <sup>-6</sup>	マイクロ	μ
10 <sup>-9</sup>	ナノ	n
10 <sup>-12</sup>	ピコ	p
10 <sup>-15</sup>	フェムト	f
10 <sup>-18</sup>	アト	a

表4 SIと共に暫定的に維持される単位

名称	記号
オングストローム	Å
バ	b
バ	bar
ガ	Gal
キュリー	Ci
レントゲン	R
ラ	rad
レ	rem

1 Å=0.1nm=10<sup>-10</sup>m  
1 b=100fm<sup>2</sup>=10<sup>-28</sup>m<sup>2</sup>  
1 bar=0.1MPa=10<sup>5</sup>Pa  
1 Gal=1cm/s<sup>2</sup>=10<sup>-2</sup>m/s<sup>2</sup>  
1 Ci=3.7×10<sup>10</sup>Bq  
1 R=2.58×10<sup>-4</sup>C/kg  
1 rad=1cGy=10<sup>-2</sup>Gy  
1 rem=1cSv=10<sup>-2</sup>Sv

(注)

- 表1-5は「国際単位系」第5版, 国際度量衡局 1985年刊行による。ただし, 1 eV および 1 u の値はCODATAの1986年推奨値によった。
- 表4には海里, ノット, アール, ヘクトールも含まれているが日常の単位なのでここでは省略した。
- bar は, JIS では流体の圧力を表す場合に限り表2のカテゴリに分類されている。
- E C 閣僚理事会指令では bar, barn および「血圧の単位」mmHgを表2のカテゴリに入れている。

換算表

力	N(=10 <sup>5</sup> dyn)	kgf	lbf
	1	0.101972	0.224809
	9.80665	1	2.20462
	4.44822	0.453592	1

粘度 1 Pa·s(N·s/m<sup>2</sup>)=10 P(ポアズ)(g/(cm·s))

動粘度 1 m<sup>2</sup>/s=10<sup>6</sup>St(ストークス)(cm<sup>2</sup>/s)

圧	MPa(=10bar)	kgf/cm <sup>2</sup>	atm	mmHg(Torr)	lbf/in <sup>2</sup> (psi)
	1	10.1972	9.86923	7.50062×10 <sup>3</sup>	145.038
力	0.0980665	1	0.967841	735.559	14.2233
	0.101325	1.03323	1	760	14.6959
	1.33322×10 <sup>-4</sup>	1.35951×10 <sup>-3</sup>	1.31579×10 <sup>-3</sup>	1	1.93368×10 <sup>-2</sup>
	6.89476×10 <sup>-3</sup>	7.03070×10 <sup>-2</sup>	6.80460×10 <sup>-2</sup>	51.7149	1

エネルギー・仕事・熱量	J(=10 <sup>7</sup> erg)	kgf·m	kW·h	cal(計量法)	Btu	ft·lbf	eV
	1	0.101972	2.77778×10 <sup>-7</sup>	0.238889	9.47813×10 <sup>-4</sup>	0.737562	6.24150×10 <sup>18</sup>
	9.80665	1	2.72407×10 <sup>-6</sup>	2.34270	9.29487×10 <sup>-3</sup>	7.23301	6.12082×10 <sup>19</sup>
	3.6×10 <sup>6</sup>	3.67098×10 <sup>5</sup>	1	8.59999×10 <sup>5</sup>	3412.13	2.65522×10 <sup>6</sup>	2.24694×10 <sup>25</sup>
	4.18605	0.426858	1.16279×10 <sup>-6</sup>	1	3.96759×10 <sup>-3</sup>	3.08747	2.61272×10 <sup>19</sup>
	1055.06	107.586	2.93072×10 <sup>-4</sup>	252.042	1	778.172	6.58515×10 <sup>21</sup>
	1.35582	0.138255	3.76616×10 <sup>-7</sup>	0.323890	1.28506×10 <sup>-3</sup>	1	8.46233×10 <sup>18</sup>
	1.60218×10 <sup>-19</sup>	1.63377×10 <sup>-20</sup>	4.45050×10 <sup>-26</sup>	3.82743×10 <sup>-20</sup>	1.51857×10 <sup>-22</sup>	1.18171×10 <sup>-19</sup>	1

1 cal= 4.18605J (計量法)  
= 4.184J (熱化学)  
= 4.1855J (15℃)  
= 4.1868J (国際蒸気表)  
仕事率 1 PS(仏馬力)  
= 75 kgf·m/s  
= 735.499W

放射能	Bq	Ci
	1	2.70270×10 <sup>-11</sup>
	3.7×10 <sup>10</sup>	1

吸収線量	Gy	rad
	1	100
	0.01	1

照射線量	C/kg	R
	1	3876
	2.58×10 <sup>-4</sup>	1

線量当量	Sv	rem
	1	100
	0.01	1

Proceedings of the 2002 Symposium on Nuclear Data November 21-22, 2002, JAERI, Tokai, Japan